

Discrete Dynamics in Nature and Society

Mathematical Models and Computation in Discrete Dynamics

Lead Guest Editor: Jia-Bao Liu

Guest Editors: Shaohui Wang and M Javid





Mathematical Models and Computation in Discrete Dynamics

Discrete Dynamics in Nature and Society

**Mathematical Models and Computation
in Discrete Dynamics**

Lead Guest Editor: Jia-Bao Liu


Guest Editors: Shaohui Wang and M Javaid






Copyright © 2023 Hindawi Limited. All rights reserved.

This is a special issue published in "Discrete Dynamics in Nature and Society." All articles are open access articles distributed under the Creative Commons Attribution License, which permits unrestricted use, distribution, and reproduction in any medium, provided the original work is properly cited.
























Chief Editor

Paolo Renna , Italy

Associate Editors

Cengiz Çinar, Turkey
Seenith Sivasundaram, USA
J. R. Torregrosa , Spain
Guang Zhang , China
Lu Zhen , China

Academic Editors

Douglas R. Anderson , USA
Viktor Avrutin , Germany
Stefan Balint , Romania
Kamel Barkaoui, France
Abdellatif Ben Makhlof , Saudi Arabia
Gabriele Bonanno , Italy
Florentino Borondo , Spain
Jose Luis Calvo-Rolle , Spain
Pasquale Candito , Italy
Giulio E. Cantarella , Italy
Giancarlo Consolo, Italy
Anibal Coronel , Chile
Binxiang Dai , China
Luisa Di Paola , Italy
Xiaohua Ding, China
Tien Van Do , Hungary
Hassan A. El-Morshedy , Egypt
Elmetwally Elabbasy, Egypt
Marek Galewski , Poland
Bapan Ghosh , India
Cristi Giuseppe , Italy
Gisèle R Goldstein, USA
Vladimir Gontar, Israel
Pilar R. Gordoá , Spain
Luca Guerrini , Italy
Chengming Huang , China
Giuseppe Izzo, Italy
Sarangapani Jagannathan , USA
Ya Jia , China
Emilio Jiménez Macías , Spain
Polinpapiliño F. Katina , USA
Eric R. Kaufmann , USA
Mehmet emir Koksál, Turkey
Junqing Li, China
Li Li , China
Wei Li , China

Ricardo López-Ruiz , Spain
Rodica Luca , Romania
Palanivel M , India
A. E. Matouk , Saudi Arabia
Rigoberto Medina , Chile
Vicenç Méndez , Spain
Dorota Mozyrska , Poland
Jesus Manuel Munoz-Pacheco , Mexico
Yukihiko Nakata , Japan
Luca Pancioni , Italy
Ewa Pawluszewicz , Poland
Alfred Peris , Spain
Adrian Petrusel , Romania
Andrew Pickering , Spain
Tiago Pinto, Spain
Chuanxi Qian , USA
Youssef N. Raffoul , USA
Maria Alessandra Ragusa , Italy
Aura Reggiani , Italy
Marko Robnik , Slovenia
Priyan S , Uzbekistan
Mouquan SHEN, China
Aceng Sambas, Indonesia
Christos J. Schinas , Greece
Mijanur Rahaman Seikh, India
Tapan Senapati , China
Kamal Shah, Saudi Arabia
Leonid Shaikhet , Israel
Piergiulio Tempesta , Spain
Fabio Tramontana , Italy
Cruz Vargas-De-León , Mexico
Francisco R. Villatoro , Spain
Junwei Wang , China
Kang-Jia Wang , China
Rui Wang , China
Xiaoquan Wang, China
Chun Wei, China
Bo Yang, USA
Zaoli Yang , China
Chunrui Zhang , China
Ying Zhang , USA
Zhengqiu Zhang , China
Yong Zhou , China
Zuonong Zhu , China
Mingcheng Zuo, China



Contents

Retracted: Analysis of the Impact of Climate Change on National Vulnerability Based on Fuzzy Comprehensive Evaluation

Discrete Dynamics in Nature and Society

Retraction (1 page), Article ID 9894584, Volume 2023 (2023)

Bounds of Degree-Based Molecular Descriptors for Generalized F -sum Graphs

Jia Bao Liu , Sana Akram, Muhammad Javaid , Abdul Raheem, and Roslan Hasni



Research Article (17 pages), Article ID 8821020, Volume 2021 (2021)

The Distance Laplacian Spectral Radius of Clique Trees

Xiaoling Zhang  and Jiajia Zhou



Research Article (8 pages), Article ID 8855987, Volume 2020 (2020)

First General Zagreb Index of Generalized F -sum Graphs

H. M. Awais, Muhammad Javaid , and Akbar Ali 



Research Article (16 pages), Article ID 2954975, Volume 2020 (2020)

Research on Urban Rainfall Runoff Pollution Prediction Model Based on Feature Fusion

Junping Yao  and Tianle Sun 

Research Article (9 pages), Article ID 8861288, Volume 2020 (2020)

Zagreb Connection Numbers for Cellular Neural Networks

Jia-Bao Liu , Zahid Raza, and Muhammad Javaid 






Review Article (8 pages), Article ID 8038304, Volume 2020 (2020)

Exploring the Impact of Stress on Burnout: A Mathematical Model and Empirical Research

Cheng-Lin Jin, Ting Chen , Shu-Yang Wu, and Yi-Lin Yang


Research Article (8 pages), Article ID 3475324, Volume 2020 (2020)

ARSS: A Novel Aerial Robot Performs Tree Pruning Tasks

Hao Xu , Zhong Yang , Le Chang , Kaiwen Lu , Changliang Xu , and Qiuyan Zhang


Research Article (14 pages), Article ID 8883655, Volume 2020 (2020)

Optimal Simulation of Sandcastle Life in Dynamic Environment Based on Stability Principle

Peng-Hui Yang, Ya-Yu Jiang, Qi Tang, Yi-Fang Li, and Jia-Ming Zhu 


Review Article (7 pages), Article ID 8850110, Volume 2020 (2020)

Research on Optimization of Improved Gray Wolf Optimization-Extreme Learning Machine Algorithm in Vehicle Route Planning

Shijin Li and Fucai Wang 


Research Article (7 pages), Article ID 8647820, Volume 2020 (2020)

The Electrical Analogue Computer of Microtubule's Protofilament

M. C. Ekosso , A. J. Fotue, S. C. Kenfack, H. Fotsin, and L. C. Fai


Research Article (10 pages), Article ID 4916202, Volume 2020 (2020)

Investigating the Mediation and Moderation Effect of Students' Addiction to Virtual Reality Games: A Perspective of Structural Equation Modeling

Xuesong Zhai, Fahad Asmi, Rongting Zhou, Intikhab Ahmad , Muhammad Azfar Anwar, Saba Saneinia, and Man Li


Research Article (13 pages), Article ID 5714546, Volume 2020 (2020)

Stability Analysis of Regular and Chaotic Ca^{2+} Oscillations in Astrocytes

Min Ye and Hongkun Zuo 


Research Article (9 pages), Article ID 9279315, Volume 2020 (2020)

Resolvability in Subdivision of Circulant Networks $C_n[1, k]$

Jianxin Wei , Syed Ahtsham Ul Haq Bokhary, Ghulam Abbas, and Muhammad Imran



Research Article (11 pages), Article ID 4197678, Volume 2020 (2020)

An Exponential Spline Difference Scheme for Solving a Class of Boundary Value Problems of Second-Order Ordinary Differential Equations

Dunqian Cao 


Research Article (16 pages), Article ID 7056254, Volume 2020 (2020)

Multiple Criteria Decision-Making Based on Vector Similarity Measures under the Framework of Dual Hesitant Fuzzy Sets

Juan Luis García Guirao , M. Sarwar Sindhu, Tabasam Rashid , and Agha Kashif


Research Article (11 pages), Article ID 1425487, Volume 2020 (2020)

Some Properties of Double Roman Domination

Hong Yang  and Xiaoqing Zhou



Research Article (5 pages), Article ID 6481092, Volume 2020 (2020)

[Retracted] Analysis of the Impact of Climate Change on National Vulnerability Based on Fuzzy Comprehensive Evaluation

Jia-Ming Zhu, Yang Chen, and Su Zhang 


Research Article (10 pages), Article ID 3527540, Volume 2020 (2020)

Maximum Reciprocal Degree Resistance Distance Index of Unicyclic Graphs

Gai-Xiang Cai , Xing-Xing Li, and Gui-Dong Yu 



Research Article (14 pages), Article ID 7318968, Volume 2020 (2020)

DNA Origami Model for Simple Image Decoding

Risheng Wang, Zhixiang Yin , Jianzhong Cui, Jing Yang, Zhen Tang, Xinmu Yang, and Xianya Geng

Research Article (8 pages), Article ID 3989173, Volume 2020 (2020)

On Face Index of Silicon Carbides



Xiujun Zhang , Ali Raza, Asfand Fahad , Muhammad Kamran Jamil , Muhammad Anwar

Chaudhry , and Zahid Iqbal 

Research Article (8 pages), Article ID 6048438, Volume 2020 (2020)



Contents



Minimum Variable Connectivity Index of Trees of a Fixed Order

Shamaila Yousaf, Akhlaq Ahmad Bhatti , and Akbar Ali 

Research Article (4 pages), Article ID 3976274, Volume 2020 (2020)

On Computation of Face Index of Certain Nanotubes

Ansheng Ye, Aisha Javed, Muhammad Kamran Jamil , Kanza Abdul Sattar, Adnan Aslam , Zahid

Iqbal , and Asfand Fahad 


Research Article (6 pages), Article ID 3468426, Volume 2020 (2020)

Design of Computational Model for Cyanobacterial Pollutant Diffusion Change in Chaohu Lake of China Based on Large Data

Junping Yao  and Guilan He 


Research Article (7 pages), Article ID 2036349, Volume 2020 (2020)

Regulator-Based Risk Statistics for Portfolios

Xiaochuan Deng and Fei Sun 



Research Article (6 pages), Article ID 7015267, Volume 2020 (2020)

A Mathematical Model for Calculating the “Brittleness-Ductility” Drop Coefficient of Sandstone in Mining Zones

Guodong Shi, Baoquan Cheng , and An Li

Research Article (7 pages), Article ID 2621672, Volume 2020 (2020)

Analytical and Approximate Solutions of a Novel Nervous Stomach Mathematical Model

Yolanda Guerrero Sánchez , Zulqurnain Sabir, Hatira Günerhan, and Haci Mehmet Baskonus 

Research Article (9 pages), Article ID 5063271, Volume 2020 (2020)

Retraction

Retracted: Analysis of the Impact of Climate Change on National Vulnerability Based on Fuzzy Comprehensive Evaluation

Discrete Dynamics in Nature and Society

Received 15 August 2023; Accepted 15 August 2023; Published 16 August 2023

Copyright © 2023 Discrete Dynamics in Nature and Society. This is an open access article distributed under the Creative Commons Attribution License, which permits unrestricted use, distribution, and reproduction in any medium, provided the original work is properly cited.

This article has been retracted by Hindawi following an investigation undertaken by the publisher [1]. This investigation has uncovered evidence of one or more of the following indicators of systematic manipulation of the publication process:

- (1) Discrepancies in scope
- (2) Discrepancies in the description of the research reported
- (3) Discrepancies between the availability of data and the research described
- (4) Inappropriate citations
- (5) Incoherent, meaningless and/or irrelevant content included in the article
- (6) Peer-review manipulation

The presence of these indicators undermines our confidence in the integrity of the article's content and we cannot, therefore, vouch for its reliability. Please note that this notice is intended solely to alert readers that the content of this article is unreliable. We have not investigated whether authors were aware of or involved in the systematic manipulation of the publication process.

Wiley and Hindawi regrets that the usual quality checks did not identify these issues before publication and have since put additional measures in place to safeguard research integrity.

We wish to credit our own Research Integrity and Research Publishing teams and anonymous and named external researchers and research integrity experts for contributing to this investigation.

The corresponding author, as the representative of all authors, has been given the opportunity to register their agreement or disagreement to this retraction. We have kept a record of any response received.

References

- [1] J. Zhu, Y. Chen, and S. Zhang, "Analysis of the Impact of Climate Change on National Vulnerability Based on Fuzzy Comprehensive Evaluation," *Discrete Dynamics in Nature and Society*, vol. 2020, Article ID 3527540, 10 pages, 2020.

Research Article

Bounds of Degree-Based Molecular Descriptors for Generalized F -sum Graphs

Jia Bao Liu ¹, Sana Akram,² Muhammad Javaid ², Abdul Raheem,³ and Roslan Hasni⁴

¹School of Mathematics and Physics, Anhui Jianzhu University, Hefei 230601, China

²Department of Mathematics, School of Science, University of Management and Technology, Lahore, Pakistan

³Higher Education Department, Government Post Graduate College, Asghar Mall, Rawalpindi, Pakistan

⁴Faculty of Ocean Engineering Technology and Informatics, University Malaysia Terengganu, Kuala Terengganu, Malaysia

Correspondence should be addressed to Muhammad Javaid; javidmath@gmail.com

Received 12 August 2020; Accepted 8 February 2021; Published 2 March 2021

Academic Editor: Luisa Di Paola

Copyright © 2021 Jia Bao Liu et al. This is an open access article distributed under the Creative Commons Attribution License, which permits unrestricted use, distribution, and reproduction in any medium, provided the original work is properly cited.

A molecular descriptor is a mathematical measure that associates a molecular graph with some real numbers and predicts the various biological, chemical, and structural properties of the underlying molecular graph. Wiener (1947) and Trinajstić and Gutman (1972) used molecular descriptors to find the boiling point of paraffin and total π -electron energy of the molecules, respectively. For molecular graphs, the general sum-connectivity and general Randić are well-studied fundamental topological indices (TIs) which are considered as degree-based molecular descriptors. In this paper, we obtain the bounds of the aforesaid TIs for the generalized F -sum graphs. The foresaid TIs are also obtained for some particular classes of the generalized F -sum graphs as the consequences of the obtained results. At the end, 3 D -graphical presentations are also included to illustrate the results for better understanding.

1. Introduction

A molecular descriptor called by the topological index (TI) is a function from the set of (molecular) graphs to the set of real numbers. TIs are studied as a subtopic of chemical graph theory to predict the chemical reactions, biological attributes, and physical features of the compounds in theoretical chemistry, toxicology, pharmaceutical industry, and environmental chemistry, see [1]. In addition, these TIs are also used to characterize the molecular structure with respect to quantitative structure activity and property relationships which are studied in the subject of cheminformatics, see [2]. TIs have been classified into different classes but degree-based TIs play a significant part in the theory of chemical structures or networks. Firstly, Wiener [3] used the TI to find boiling point of paraffin. Gutman and Trinajstić calculated total π -electron energy of the molecules by a TI that is recognized as the first

Zagreb index in the literature, see [4]. In 2009, Zhou and Trinajstić [5] suggested the sum-connectivity index, which was subsequently generalized in 2010 [6]. The Randić index was defined in 1975 [7]; later on the idea was subsequently extended to the generalized Randić connectivity index by Li and Gutman, see [8]. For more studies, we refer to [9–12].

In chemical graph theory, operations of graphs are frequently used to find the new families of graphs. Yan et al. [13] defined the four subdivision-related operations (S_1^1, S_1^2, S_1^3 , and S_1^4) on a molecular graph M and obtained the Wiener indices of the resultant graphs $S_1^1(M), S_1^2(M), S_1^3(M)$, and $S_1^4(M)$. After that, Eliasi and Taeri [14] defined the F -sum graph $M_1 +_{F_1} M_2$ with the help of Cartesian product of M_1 and $F(M_2)$, where $F_1 \in \{S_1^1, S_1^2, S_1^3, S_1^4\}$. Deng et al. [15] and Akhter and Imran [16] also computed the 1st and 2nd Zagreb and general sum-connectivity indices of the F -sum graphs, respectively. Recently, Liu et al. [17]

generalized these subdivision-related operations and defined the generalized F -sum graphs $M_1 +_{F_k} M_2$ for $F_k \in \{S_k^1, S_k^2, S_k^3, S_k^4\}$, where $k \geq 1$ is an integral value. They also computed the 1st and 2nd Zagreb indices for these newly obtained graphs. For further studies of F -sum and generalized F -sum graphs, see [18–27].

Now, we extend this study by computing the bounds (upper and lower) of the general sum-connectivity and general Randić indices for the generalized F -sum graphs. In the remaining paper, Section 2 consists of main results of bounds and Section 3 has conclusion and applications of the obtained results.

2. Preliminaries

Throughout, we consider undirected, connected, and simple graphs with $V(M) = \{a_i: 1 \leq i \leq n\}$ and $E(M) \subseteq V(M) \times V(M)$ as vertex and edge sets, respectively. In addition, $|V(M)| = n$ and $|E(M)| = m$ are the order and size of M . For a vertex $a \in V(M)$ and $d_M(a)$ as a degree of a in M , $\Delta_M = \max\{d_M(a): a \in V(M)\}$ and $\delta_M(a) = \min\{d_M(a): a \in V(M)\}$ are the maximum and minimum degrees of the graph M . The graphs $V(P_n) = \{a_i: 1 \leq i \leq n\}$ & $E(P_n) = \{a_i a_{i+1}: 1 \leq i \leq n-1\}$, $V(C_n) = \{a_i: 1 \leq i \leq n\}$ & $E(C_n) = \{a_i a_{i+1}: 1 \leq i \leq n-1\} \cup \{a_n a_1\}$ and $V(K_n) = \{a_i: 1 \leq i \leq n\}$ and $E(K_n) = \{a_i a_j: 1 \leq i, j \leq n\}$ are called path (P_n), cycle (C_n), and complete (K_n), respectively. For further basic terminologies, see [28].

Definition 1. For a real number α and (molecular) graph M , the general sum-connectivity index (GSCI) and general Randić index (GRI) are

$$\begin{aligned} \chi_\alpha(M) &= \sum_{x_1, x_2 \in E(M)} [d_M(x_1) + d_M(x_2)]^\alpha, \\ R_\alpha(M) &= \sum_{x_1, x_2 \in E(M)} [d_M(x_1) d_M(x_2)]^\alpha. \end{aligned} \quad (1)$$

Moreover, $\alpha = 1, 2$ and then $\chi_\alpha(M)$ are known as the 1st Zagreb index and hyper-Zagreb index. If $\alpha = (-1/2), 1, (1/2)$, then $R_\alpha(M)$; it is known as Randić, 2nd Zagreb, and reciprocal Randić indices.

Liu [17] defined the following graphs using the generalized subdivision-related operations:

- (i) $S_k^1(M)$ graph is obtained by inserting k -vertices in each edge of M .
- (ii) $S_k^2(M)$ is obtained from $S_k^1(M)$ by joining the old vertices which are adjacent in M .
- (iii) $S_k^3(M)$ is obtained from $S_k^1(M)$ by joining the new vertices lying in an edge to the corresponding new vertices of the other edge, if these edges have some common vertexes in M .
- (iv) $S_k^4(M)$ is the union of $S_k^2(M)$ and $S_k^3(M)$ graphs.

For more details, see Figure 1 for $k = 4$.

Definition 2. Let M_1 and M_2 be two connected graphs, $F_k \in \{S_k^1, S_k^2, S_k^3, S_k^4\}$ and $F_k(M_1)$ be a graph (obtained after applying the operation F_k on M_1 with vertex set $V(F_k(M_1))$ and edge set $E(F_k(M_1))$). Then, the generalized F -sum graph $M_1 +_{F_k} M_2$ is a graph with vertex set $V(M_1 +_{F_k} M_2) = V(F_k(M_1)) \times V(M_2) = (V(M_1) \cup E(M_1)) \times V(M_2)$ in such a way that $(x_1, y_1), (x_2, y_2) \in V(M_1 +_{F_k} M_2)$ are adjacent if $[x_1 = x_2 \in V(M_1) \text{ and } (y_1, y_2) \in E(M_2)]$ or $[y_1 = y_2 \in V(M_2) \text{ and } (x_1, x_2) \in E(F_k(M_1))]$, where $k \geq 1$ is an integral value.

For more details, see Figures 2 and 3.

3. Main Results

In this section, we find out the sharp bounds of GSCI and GRI of generalized F -sum graphs.

Theorem 1. For a real number $\alpha > 0$ and counting number $k \geq 1$, the lower and upper bounds on the GSCI and GRI of generalized F -sum graph $(M_1 +_{S_k^1} M_2)$ are as follows:

- (a) $2^\alpha n_1 m_2 (\Delta_{M_1} + \Delta_{M_2})^\alpha + 2 n_2 m_1 (\Delta_{M_1} + \Delta_{M_2} + 2)^\alpha + 4^\alpha n_2 m_1 (k-1) \leq \chi_\alpha(M_1 +_{S_k^1} M_2) \leq 2^\alpha n_1 m_2 (\delta_{M_1} + \delta_{M_2})^\alpha + 2 n_2 m_1 (\delta_{M_1} + \delta_{M_2} + 2)^\alpha + 4^\alpha n_2 m_1 (k-1)$,
- (b) $n_1 m_2 (\Delta_{M_1} + \Delta_{M_2})^{2\alpha} + 2^{\alpha+1} n_2 m_1 (\Delta_{M_1} + \Delta_{M_2})^\alpha + 4^\alpha n_2 m_1 (k-1) \leq R_\alpha(M_1 +_{S_k^1} M_2) \leq n_1 m_2 (\delta_{M_1} + \delta_{M_2})^{2\alpha} + 2^{\alpha+1} n_2 m_1 (\delta_{M_1} + \delta_{M_2})^\alpha + 4^\alpha n_2 m_1 (k-1)$,

where equalities hold if M_1 and M_2 are regular graphs.

Proof. (a) By the definition of GSCI, we have

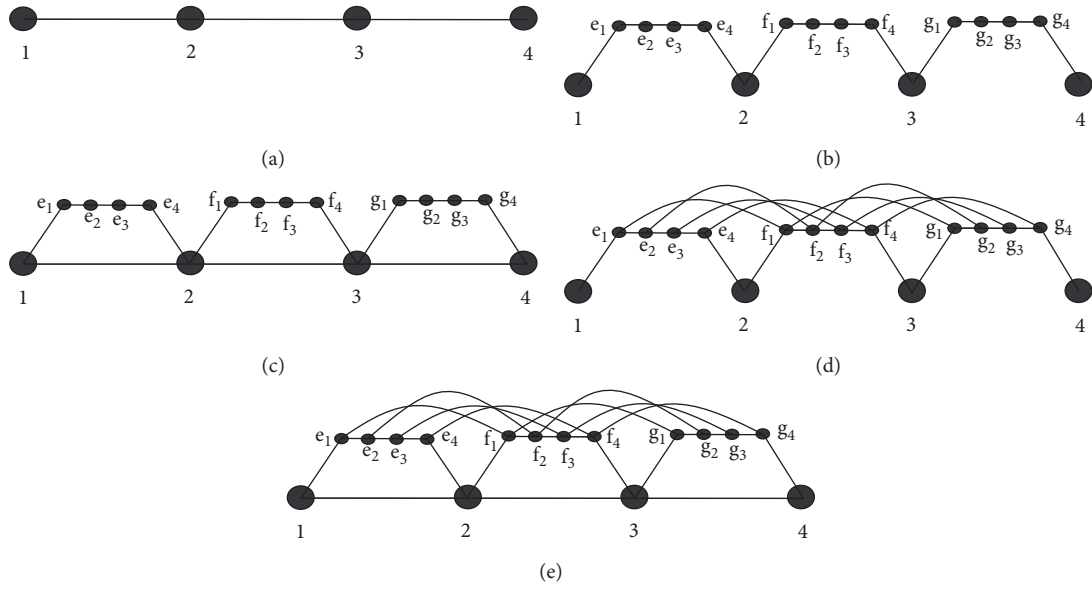


FIGURE 1: (a) $M \cong P_4$, (b) $S_4(M)$, (c) $R_4(M)$, (d) $Q_4(M)$, and (e) $T_4(M)$.

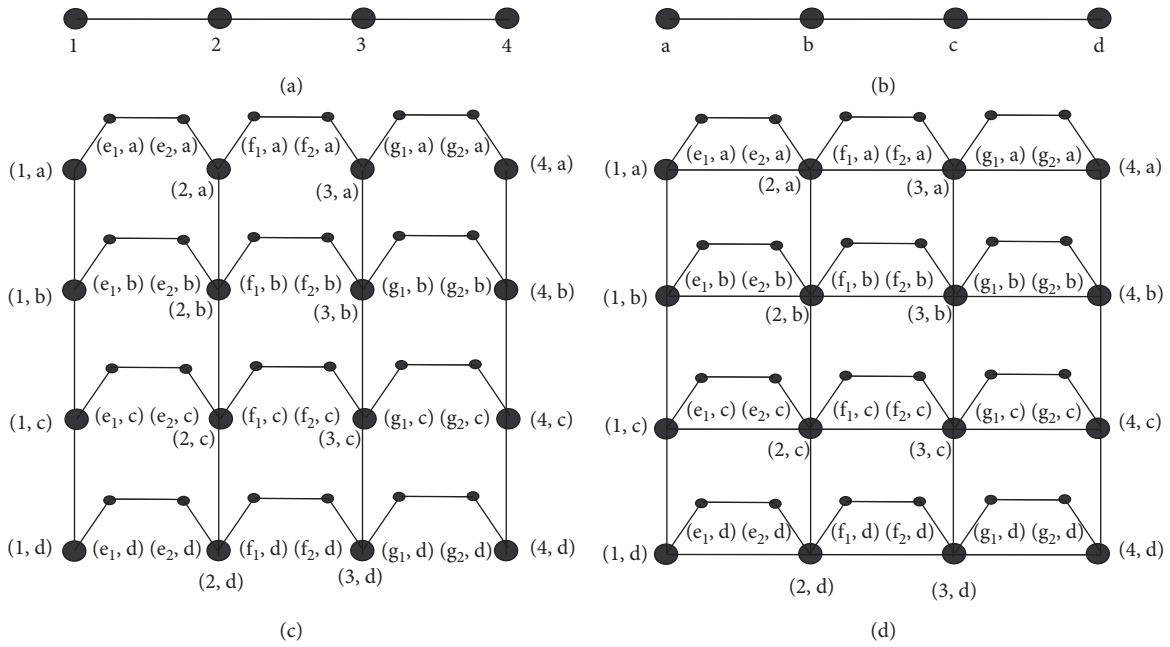
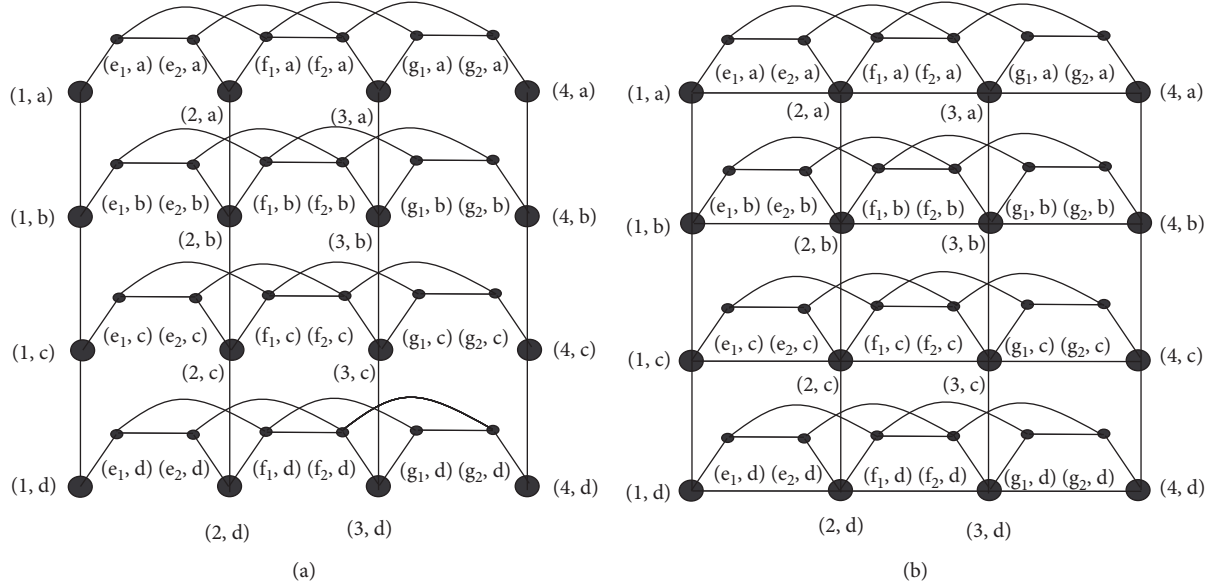


FIGURE 2: (a) $M_1 \cong P_4$, (b) $M_2 \cong P_4$, (c) $M_{1+S_2}M_2$, and (d) $M_{1+R_2}M_2$.

FIGURE 3: (a) $M_{1+Q_2}M_2$. (b) $M_{1+T_2}M_2$.

$$\begin{aligned}
\chi_\alpha(M_1 + S_k^1 M_2) &= \sum_{(x_1, y_1)(x_2, y_2) \in E(M_1 + S_k^1 M_2)} \left[d_{(M_1 + S_k^1 M_2)}(x_1, y_1) + d_{(M_1 + S_k^1 M_2)}(x_2, y_2) \right]^\alpha, \\
&= \sum_{x \in V(M_1)} \sum_{y_1, y_2 \in E(M_2)} \left[d_{(M_1 + S_k^1 M_2)}(x, y_1) + d_{(M_1 + S_k^1 M_2)}(x, y_2) \right]^\alpha \\
&\quad + \sum_{y \in V(M_2)} \sum_{x_1, x_2 \in E(S_k^1(M_1))} \left[d_{(M_1 + S_k^1 M_2)}(x_1, y) + d_{(M_1 + S_k^1 M_2)}(x_2, y) \right]^\alpha \\
&= \sum_{x \in V(M_1)} \sum_{y_1, y_2 \in E(M_2)} \left[d_{(M_1 + S_k^1 M_2)}(x, y_1) + d_{(M_1 + S_k^1 M_2)}(x, y_2) \right]^\alpha \\
&\quad + \sum_{y \in V(M_2)} \sum_{x_1, x_2 \in E(S_k^1(M_1))} \left[d_{(M_1 + S_k^1 M_2)}(x_1, y) + d_{(M_1 + S_k^1 M_2)}(x_2, y) \right]^\alpha \\
&\quad \quad \quad x_1 \in V(M_1), x_2 \in V(S_k^1(M_1) - M_1) \\
&\quad + \sum_{y \in V(M_2)} \sum_{x_1, x_2 \in E(S_k^1(M_1))} \left[d_{(M_1 + S_k^1 M_2)}(x_1, y) + d_{(M_1 + S_k^1 M_2)}(x_2, y) \right]^\alpha = \sum 1 + \sum 2 + \sum 3. \\
&\quad \quad \quad x_1, x_2 \in V(S_k^1(M_1) - M_1)
\end{aligned} \tag{2}$$

Consider

$$\begin{aligned}
\sum 1 &= \sum_{x \in V(M_1)} \sum_{y_1, y_2 \in E(M_2)} \left[d_{(M_1 + S_k^1 M_2)}(x, y_1) + d_{(M_1 + S_k^1 M_2)}(x, y_2) \right]^\alpha \\
&= \sum_{x \in V(M_1)} \sum_{y_1, y_2 \in E(M_2)} \left[2d_{M_1}(x) + d_{M_2}(y_1) + d_{M_2}(y_2) \right]^\alpha \leq 2^\alpha n_1 m_2 (\Delta_{M_1} + \Delta_{M_2})^\alpha.
\end{aligned} \tag{3}$$

Since $|E(S_1^1(M_1))| = 2|E(M_1)|$ and $\Delta_{S_k^1(M_1)} = \Delta_{M_1}$, we have

$$\begin{aligned}
 \sum 2 &= \sum_{y \in V(M_2)} \sum_{\substack{x_1, x_2 \in E(S_k^1(M_1)) \\ x_1, x_2 \in V(S_k^1(M_1) - M_1)}} \left[d_{(M_1 + S_k^1 M_2)}(x_1, y) + d_{(G + S_k^1 M_2)}(x_2, y) \right]^\alpha, \\
 &= \sum_{y \in V(M_2)} \sum_{\substack{x_1, x_2 \in E(S_k^1(M_1)) \\ x_1, x_2 \in V(M_1), x_2 \in V}} (S_k^1(M_1) - V(M_1)) \left[d_{M_1}(x_1) + d_{M_2}(y) + d_{S_k^1 M_1}(x_2) \right]^\alpha \\
 &\leq 2n_2 m_1 (\Delta_{M_1} + \Delta_{M_2} + 2)^\alpha \tag{4} \\
 \sum 3 &= \sum_{y \in V(M_2)} \sum_{\substack{x_1, x_2 \in E(S_k^1(M_1)) \\ x_1, x_2 \in V(S_k^1(M_1) - M_1)}} \left[d_{(M_1 + S_k^1 M_2)}(x_1, y) + d_{(M_1 + S_k^1 M_2)}(x_2, y) \right]^\alpha \\
 &= \sum_{y \in V(M_2)} \sum_{\substack{x_1, x_2 \in E(S_k^1(M_1)) \\ x_1, x_2 \in V(S_k^1(M_1) - M_1)}} [2 + 2]^\alpha.
 \end{aligned}$$

Since in this case $|E(S_k^1(M_1) - E(S_1^1))| = (k - 1)|E(M_1)|$, we have

Consequently,

$$\begin{aligned}
 &= (k - 1)|E(M_1)| \sum_{y \in V(M_2)} (4)^\alpha \tag{5} \\
 &= 4^\alpha (k - 1)|V(M_2)||E(M_1)| = 4^\alpha (k - 1)n_2 m_1.
 \end{aligned}$$

$$\begin{aligned}
 &2^\alpha n_1 m_2 (\Delta_{M_1} + \Delta_{M_2})^\alpha + 2n_2 m_1 (\Delta_{M_1} + \Delta_{M_2} + 2)^\alpha + 4^\alpha n_2 m_1 (k - 1) \leq \chi_\alpha(M_1 + S_k^1 M_2) \tag{6} \\
 &\leq 2^\alpha n_1 m_2 (\delta_{M_1} + \delta_{M_2})^\alpha + 2n_2 m_1 (\delta_{M_1} + \delta_{M_2} + 2)^\alpha + 4^\alpha n_2 m_1 (k - 1),
 \end{aligned}$$

where equalities hold if M_1 and M_2 are regular graphs. \square *Proof.* (b) By the definition of GRI, we have

$$\begin{aligned}
 R_\alpha(M_1 + S_k^1 M_2) &= \sum_{(x_1, y_1), (x_2, y_2) \in E(M_1 + S_k^1 M_2)} \left[d_{(M_1 + S_k^1 M_2)}(x_1, y_1) + d_{(M_1 + S_k^1 M_2)}(x_2, y_2) \right]^\alpha \\
 &= \sum_{x \in V(M_1)} \sum_{y_1, y_2 \in E(M_2)} \left[d_{(M_1 + S_k^1 M_2)}(x, y_1) + d_{(M_1 + S_k^1 M_2)}(x, y_2) \right]^\alpha \\
 &\quad + \sum_{y \in V(M_2)} \sum_{x_1, x_2 \in E(S_k^1(M_1))} \left[d_{(M_1 + S_k^1 M_2)}(x_1, y) + d_{(M_1 + S_k^1 M_2)}(x_2, y) \right]^\alpha \\
 &= \sum_{x \in V(M_1)} \sum_{y_1, y_2 \in E(M_2)} \left[d_{(M_1 + S_k^1 M_2)}(x, y_1) + d_{(M_1 + S_k^1 M_2)}(x, y_2) \right]^\alpha \tag{7} \\
 &\quad + \sum_{y \in V(M_2)} \sum_{\substack{x_1, x_2 \in E(S_k^1(M_1)) \\ x_1, x_2 \in V(M_1), x_2 \in V(S_k^1(M_1) - M_1)}} \left[d_{(M_1 + S_k^1 M_2)}(x_1, y) + d_{(M_1 + S_k^1 M_2)}(x_2, y) \right]^\alpha \\
 &\quad + \sum_{y \in V(M_2)} \sum_{\substack{x_1, x_2 \in E(S_k^1(M_1)) \\ x_1, x_2 \in V(S_k^1(M_1) - M_1)}} \left[d_{(M_1 + S_k^1 M_2)}(x_1, y) + d_{(M_1 + S_k^1 M_2)}(x_2, y) \right]^\alpha = \sum 1 + \sum 2 + \sum 3.
 \end{aligned}$$

Consider

$$\begin{aligned}
 \sum 1 &= \sum_{x \in V(M_1)} \sum_{y_1, y_2 \in E(M_2)} \left[d_{(M_1 + S_k^1 M_2)}(x, y_1) + d_{(M_1 + S_k^1 M_2)}(x, y_2) \right]^\alpha \\
 &= \sum_{x \in V(M_1)} \sum_{y_1, y_2 \in E(M_2)} \left[d_{M_1}(x) + d_{M_2}(y_1) \right] \left[d_{M_1}(x) + d_{M_2}(y_2) \right]^\alpha \\
 &= \sum_{x \in V(M_1)} \sum_{y_1, y_2 \in E(M_2)} \left[d_{M_1}^2(x) + d_{M_1}(x) \left[d_{M_2}(y_1) + d_{M_2}(y_2) \right] + d_{M_2}(y_1) d_{M_2}(y_2) \right]^\alpha \\
 &\leq n_1 m_2 (\Delta_{M_1} + \Delta_{M_2})^{2\alpha}.
 \end{aligned} \tag{8}$$

Since $|E(S_k^1(M_1))| = 2|E(M_1)|$ and $\Delta_{S_k^1(M_1)} = \Delta_{M_1}$, we have

$$\begin{aligned}
 \sum 2 &= \sum_{y \in V(M_2)} \sum_{\substack{x_1, x_2 \in E(S_k^1(M_1)) \\ x_1, x_2 \in V(S_k^1(M_1) - M_1)}} \left[d_{(M_1 + S_k^1 M_2)}(x_1, y) + d_{(M_1 + S_k^1 M_2)}(x_2, y) \right]^\alpha \\
 &= \sum_{y \in V(M_2)} \sum_{\substack{x_1, x_2 \in E(S_k^1(M_1)) \\ x_1, x_2 \in V(S_k^1(M_1) - M_1)}} \left[\left[d_{M_1}(x_1) + d_{M_2}(y) \right] \left[d_{S_k^1(M_1)}(x_2) \right] \right]^\alpha \\
 &= \sum_{y \in V(M_2)} \sum_{\substack{x_1, x_2 \in E(S_k^1(M_1)) \\ x_1, x_2 \in V(S_k^1(M_1) - M_1)}} \left[(\Delta_{M_1} + \Delta_{M_2}) 2 \right]^\alpha \leq 2^{\alpha+1} n_2 m_1 (\Delta_{M_1} + \Delta_{M_2})^\alpha \\
 \sum 3 &= \sum_{y \in V(M_2)} \sum_{\substack{x_1, x_2 \in E(S_k^1(M_1)) \\ x_1, x_2 \in V(S_k^1(M_1) - M_1)}} \left[d_{(M_1 + S_k^1 M_2)}(x_1, y) + d_{(M_1 + S_k^1 M_2)}(x_2, y) \right]^\alpha \\
 &= \sum_{y \in V(M_2)} \sum_{\substack{x_1, x_2 \in E(S_k^1(M_1)) \\ x_1, x_2 \in V(S_k^1(M_1) - M_1)}} [2 \times 2]^\alpha.
 \end{aligned} \tag{9}$$

Since in this case $|E(S_k^1(M_1) - E(S_1^1))| = (k-1)|E(M_1)|$, we have $= (k-1)|E(M_1)| \sum_{y \in V(M_2)} (4)^\alpha = 4^\alpha (k-1) n_2 m_1$.

Consequently,

$$\begin{aligned}
 n_1 m_2 (\Delta_{M_1} + \Delta_{M_2})^{2\alpha} + 2^{\alpha+1} n_2 m_1 (\Delta_{M_1} + \Delta_{M_2})^\alpha + 4^\alpha n_2 m_1 (k-1) &\leq R_\alpha(M_1 + S_k^1 M_2) \\
 \leq n_1 m_2 (\delta_{M_1} + \delta_{M_2})^{2\alpha} + 2^{\alpha+1} n_2 m_1 (\delta_{M_1} + \delta_{M_2})^\alpha + 4^\alpha n_2 m_1 (k-1),
 \end{aligned} \tag{10}$$

where equalities hold if M_1 and M_2 are regular graphs. \square

Theorem 2. For a real number $\alpha > 0$ and counting number $k \geq 1$, the lower and upper bounds on the GSCI and GRI of the generalized F -sum graph $(M_1 + S_k^2 M_2)$ are as follows:

$$(a) \quad 2^\alpha (n_1 m_2 + n_2 m_1) (2\Delta_{M_1} + \Delta_{M_2})^\alpha + 2n_2 m_1 (2\Delta_{M_1} + \Delta_{M_2} + 2)^\alpha + 4^\alpha n_2 m_1 (k-1) \leq \chi_\alpha(M_1 + S_k^1 M_2) \leq 2^\alpha$$

$$(n_1 m_2 + n_2 m_1) (2\delta_{M_1} + \delta_{M_2})^\alpha + 2n_2 m_1 (2\delta_{M_1} + \delta_{M_2} + 2)^\alpha + 4^\alpha n_2 m_1 (k-1),$$

$$(b) \quad (n_1 m_2 + n_2 m_1) (2\Delta_{M_1} + \Delta_{M_2})^{2\alpha} + 2^{\alpha+1} n_2 m_1 (2\Delta_{M_1} + \Delta_{M_2})^\alpha + 4^\alpha n_2 m_1 (k-1) \leq R_\alpha(M_1 + S_k^2 M_2) \leq (n_1 m_2 + n_2 m_1) (2\delta_{M_1} + \delta_{M_2})^{2\alpha} + 2^{\alpha+1} n_2 m_1 (2\delta_{M_1} + \delta_{M_2})^\alpha + 4^\alpha n_2 m_1 (k-1),$$

where equalities hold if and only if M_1 and M_2 are regular graphs.

Proof. (a) By the definition of the GSCI, we have

$$\begin{aligned} \chi_\alpha(M_1 + S_k^2 M_2) &= \sum_{(x_1, y_1), (x_2, y_2) \in E(M_1 + S_k^2 M_2)} \left[d_{(M_1 + S_k^2 M_2)}(x_1, y_1) + d_{(M_1 + S_k^2 M_2)}(x_2, y_2) \right]^\alpha \\ &= \sum_{x \in V(M_1)} \sum_{y_1, y_2 \in E(M_2)} \left[d_{(M_1 + S_k^1 M_2)}(x, y_1) + d_{(M_1 + S_k^1 M_2)}(x, y_2) \right]^\alpha \\ &\quad + \sum_{y \in V(M_2)} \sum_{x_1, x_2 \in E(S_k(M_1))} \left[d_{(M_1 + S_k^2 M_2)}(x_1, y) + d_{(M_1 + S_k^2 M_2)}(x_2, y) \right]^\alpha = \sum 1 + \sum 2. \end{aligned} \tag{11}$$

Consider

$$\begin{aligned} \sum 1 &= \sum_{x \in V(M_1)} \sum_{y_1, y_2 \in E(M_2)} \left[d_{(M_1 + S_k^1 M_2)}(x, y_1) + d_{(M_1 + S_k^1 M_2)}(x, y_2) \right]^\alpha \\ &= \sum_{x \in V(M_1)} \sum_{y_1, y_2 \in E(M_2)} \left[4d_{M_1}(x) + d_{M_2}(y_1) + d_{M_2}(y_2) \right]^\alpha \leq 2^\alpha n_1 m_2 (2\Delta_{M_1} + \Delta_{M_2})^\alpha \\ \sum 2 &= \sum_{x \in V(M_1)} \sum_{x_1, x_2 \in V(M_1)} [d(x_1, y) + d(x_2, y)]^\alpha \\ &= \sum_{y \in V(M_2)} \sum_{\substack{x_1, x_2 \in E(S_k^2(M_1)) \\ x_1, x_2 \in V(M_1)}} [d(x_1, y) + d(x_2, y)]^\alpha \\ &\quad + \sum_{y \in V(M_2)} \sum_{\substack{x_1, x_2 \in E(S_k^2(M_1)) \\ x_1 \in V(M_1) \\ x_2 \in V(S_k^2(M_1) - V(M_1))}} [d(x_1, y) + d(x_2, y)]^\alpha \\ &\quad + \sum_{y \in V(M_2)} \sum_{\substack{x_1, x_2 \in E(S_k^2(M_1)) \\ x_1, x_2 \in V(S_k^2(M_1) - V(M_1))}} [d(x_1, y) + d(x_2, y)]^\alpha = \sum' 2 + \sum'' 2 + \sum''' 2. \end{aligned} \tag{12}$$

Consider for $x_1, x_2 \in V(M_1)$, we have $x_1, x_2 \in E(S_k^2(M_1))$ if $x_1, x_2 \in E(M_1)$; for $x_1 \in V(M_1)$, we obtain $d_{S_{1M_1}^2}(x_1) =$

$2d_{M_1}(x_1)$ and for $x_2 \in V(S_{kM_1}^2) - V(M_1)$, we have $d_{S_{kM_1}^2}(x_2) = 2$.
Now, consider

$$\begin{aligned} \sum' 2 &= \sum_{y \in V(M_2)} \sum_{\substack{x_1, x_2 \in E(M_1) \\ x_1, x_2 \in V(M_1)}} [d(x_1, y) + d(x_2, y)]^\alpha = \sum_{y \in V(M_2)} \sum_{x_1, x_2 \in E(M_1)} [d(x_1, y) + d(x_2, y)]^\alpha \\ &= \sum_{y \in V(M_2)} \sum_{x_1, x_2 \in E(M_1)} [2d_{M_2}(y) + 2d_{M_1}(x_1) + 2d_{M_1}(x_2)]^\alpha \leq 2^\alpha n_2 m_1 (2\Delta_{M_1} + \Delta_{M_2})^\alpha. \end{aligned} \tag{13}$$

Note that $|E(S_1^1(M_1))| = 2|E(M_1)|$ and if $x_1 \in V(M_1)$, then $d_{S_k^2}(M_1)x_1 = 2d_{M_1}(x_1)$, and if $x_2 \in V(S_k^2(M_1) - V(M_1))$, then $d_{S_k^2}(M_1)x_2 = 2$.

$$\begin{aligned}
\sum'' 2 &= \sum_{y \in V(M_2)} \sum_{\substack{x_1, x_2 \in E(S_k^2(M_1)) \\ x_1 \in V(M_1), x_2 \in V(S_k^2(M_1) - V(M_1))}} [d(x_1, y) + d(x_2, y)]^\alpha \\
&= \sum_{y \in V(M_2)} \sum_{\substack{x_1, x_2 \in E(M_1) \\ x_1 \in V(M_1), x_2 \in V(M_1) - V(M_1)}} [2d_{M_1}(x_1) + d_{S_k^2(M_1)}(x_2) + d_{M_2}(y)]^\alpha \\
&= \sum_{y \in V(M_2)} \sum_{\substack{x_1, x_2 \in E((M_1)) \\ x_1 \in V(M_1), x_2 \in V((M_1) - V(M_1))}} [2d_{M_1}(x_1) + 2 + d_{M_2}(y)]^\alpha \leq 2n_2m_1(2\Delta_{M_1} + \Delta_{M_2} + 2)^\alpha
\end{aligned} \tag{14}$$

$$\begin{aligned}
\sum''' 2 &= \sum_{y \in V(M_2)} \sum_{\substack{x_1, x_2 \in E(S_k^2(M_1)) \\ x_1, x_2 \in V(S_k^2(M_1) - V(M_1))}} [d(x_1, y) + d(x_2, y)]^\alpha \\
&= (k-1) \sum_{y \in V(M_2)} \sum_{\substack{x_1, x_2 \in E(S_k^2(M_1)) \\ x_1, x_2 \in V(S_k^2(M_1) - V(M_1))}} [d_{S_k^2(M_1)}(x_1) + d_{S_k^2(M_1)}(x_2)]^\alpha = 4^\alpha(k-1)m_1n_2.
\end{aligned}$$

Hence,

$$\begin{aligned}
2^\alpha(n_1m_2 + n_2m_1)(2\Delta_{M_1} + \Delta_{M_2})^\alpha + 2n_2m_1(2\Delta_{M_1} + \Delta_{M_2} + 2)^\alpha + 4^\alpha n_2m_1(k-1) &\leq \chi_\alpha \\
(M_1 + S_k^2M_2) &\leq 2^\alpha(n_1m_2 + n_2m_1)(2\delta_{M_1} + \delta_{M_2})^\alpha + 2n_2m_1(2\delta_{M_1} + \delta_{M_2} + 2)^\alpha + 4^\alpha n_2m_1(k-1).
\end{aligned} \tag{15}$$

Equality holds if M_1 and M_2 are regular graphs. \square *Proof.* (b) By the definition of GRI, we have

$$\begin{aligned}
R_\alpha(M_1 + S_k^2M_2) &= \sum_{(x_1, y_1)(x_2, y_2) \in E(M_1 + S_k^2M_2)} [d_{(M_1 + S_k^2M_2)}(x_1, y_1)d_{(M_1 + S_k^2M_2)}(x_2, y_2)]^\alpha, \\
&= \sum_{x \in V(M_1)} \sum_{y_1, y_2 \in E(M_2)} [d_{(M_1 + S_k^2M_2)}(x, y_1)d_{(M_1 + S_k^2M_2)}(x, y_2)]^\alpha \\
&\quad + \sum_{y \in V(M_2)} \sum_{x_1, x_2 \in E(S_k^2(M_1))} [d_{(M_1 + S_k^2M_2)}(x, y_1)d_{(M_1 + S_k^2M_2)}(x_2, y)]^\alpha = \sum 1 + \sum 2.
\end{aligned} \tag{16}$$

Consider

$$\begin{aligned}
 \sum 1 &= \sum_{x \in V(M_1)} \sum_{y_1, y_2 \in E(M_2)} \left[d_{(M_1+S_k^2 M_2)}(x, y_1) d_{(M_1+S_k^2 M_2)}(x, y_2) \right]^\alpha, \\
 &= \sum_{x \in V(M_1)} \sum_{y_1, y_2 \in E(M_2)} \left[[2d_{M_1}(x) + d_{M_2}(y_1)][2d_{M_1}(x) + d_{M_2}(y_2)] \right]^\alpha \\
 &= \sum_{x \in V(M_1)} \sum_{y_1, y_2 \in E(M_2)} \left[[4d_{M_1}^2(x) + 2d_{M_1}(x_1)[d_{M_2}(y_1) + d_{M_2}(y_2)] + d_{M_2}(y_1)d_{M_2}(y_2)] \right]^\alpha \\
 &\leq n_1 m_2 (2\Delta_{M_1} + \Delta_{M_2})^{2\alpha}, \\
 \sum 2 &= \sum_{y \in V(M_2)} \sum_{x_1, x_2 \in E(S_k^2(M_1))} [d(x_1, y)d(x_2, y)]^\alpha \tag{17} \\
 &= \sum_{y \in V(M_2)} \sum_{\substack{x_1, x_2 \in E(S_k^2(M_1)) \\ x_1, x_2 \in V(M_1)}} [d(x_1, y)d(x_2, y)]^\alpha + \sum_{y \in V(M_2)} \sum_{\substack{x_1, x_2 \in E(S_k^2(M_1)) \\ x \in V(M_1) \\ x_2 \in V(S_k^2(M_1)) - V(M_1)}} [d(x_1, y)d(x_2, y)]^\alpha \\
 &\quad + \sum_{y \in V(M_2)} \sum_{\substack{x_1, x_2 \in E(S_k^2(M_1)) \\ x_1, x_2 \in V(S_k^2(M_1)) - V(M_1)}} [d(x_1, y)d(x_2, y)]^\alpha = \sum 2 + \sum 2 + \sum 2.
 \end{aligned}$$

Consider for $x_1, x_2 \in V(M_1)$, we have $x_1, x_2 \in E(S_k^2(M_1))$ if $x_1, x_2 \in E(M_1)$; for $x_1 \in V(M_1)$, we obtain $d_{S_k^2(M_1)}(x_1) =$

$2d_{M_1}(x_1)$ and for $x_2 \in V(S_k^2(M_1)) - V(M_1)$, we have $d_{S_k^2(M_1)}(x_2) = 2$. Now, consider

$$\begin{aligned}
 \sum 2 &= \sum_{y \in V(M_2)} \sum_{\substack{x_1, x_2 \in E(S_k^2(M_1)) \\ x_1, x_2 \in V(M_1)}} [d(x_1, y)d(x_2, y)]^\alpha = \sum_{y \in V(M_1)} \sum_{x_1, x_2 \in E(M_1)} [d(x_1, y)d(x_2, y)]^\alpha, \\
 &= \sum_{y \in V(M_2)} \sum_{x_1, x_2 \in E(M_1)} \left[[d_{S_k^2(M_1)}(x_1) + d_{M_2}(y)][d_{S_k^2(M_1)}(x_2) + d_{M_2}(y)] \right]^\alpha \tag{18} \\
 &= \sum_{y \in V(M_2)} \sum_{x_1, x_2 \in E(M_1)} \left[4d_{(M_1)}(x_1)d_{(M_1)}(x_2) + 2d_{(M_1)}(x_1)d_{M_2}(y) + 2d_{(M_1)}(x_2)d_{M_2}(y) + d_{M_2}^2(y) \right]^\alpha \\
 &= \sum_{y \in V(M_2)} \sum_{x_1, x_2 \in E(M_1)} \left[4\Delta_{M_1}\Delta_{M_1} + 2\Delta_{M_2}[\Delta_{M_1} + \Delta_{M_1}] + \Delta_{M_2}^2 \right]^\alpha \leq n_2 m_1 [2\Delta_{M_1} + \Delta_{M_2}]^{2\alpha}.
 \end{aligned}$$

Note that $|E(S_1^2(M_1))| = 2|E(M_1)|$ and if $x_1 \in V(M_1)$, then $d_{S_k^2(M_1)}(x_1) = 2d_{M_1}(x_1)$, and if $x_2 \in V(S_k^2(M_1)) - V(M_1)$, then $d_{S_k^2(M_1)}(x_2) = 2$.

$$\begin{aligned}
 \sum'' 2 &= \sum_{y \in V(M_2)} \sum_{\substack{x_1, x_2 \in E(S_k^2(M_1)) \\ x_1 \in V(M_1), x_2 \in V(S_k^2(M_1)) - V(M_1)}} [d(x_1, y)d(x_2, y)]^\alpha, \\
 &= \sum_{y \in V(M_2)} \sum_{\substack{x_1, x_2 \in E(S_k^2(M_1)) \\ x_1 \in V(M_1) \\ x_2 \in V(S_k^2(M_1)) - V(M_1)}} \left[\left[d_{S_k^2(M_1)}(x_1) + d_{M_2}(y) \right] \left[d_{S_k^2(M_1)}(x_2) \right] \right]^\alpha \\
 &= \sum_{y \in V(M_2)} \sum_{\substack{x_1, x_2 \in E(S_k^2(M_1)) \\ x_1 \in V(M_1) \\ x_2 \in V(S_k^2(M_1)) - V(M_1)}} \left[\left[2d_{M_1}(x_1) + d_{M_2}(y) \right] [2] \right]^\alpha \leq 2^{\alpha+1} n_2 m_1 (2\Delta_{M_1} + \Delta_{M_2})^\alpha
 \end{aligned} \tag{19}$$

$$\begin{aligned}
 \sum''' 2 &= \sum_{y \in V(M_2)} \sum_{\substack{x_1, x_2 \in E(S_k^2(M_1)) \\ x_2 \in V(S_k^2(M_1)) - V(M_1)}} [d(x_1, y)d(x_2, y)]^\alpha, \\
 &= (k-1) \sum_{y \in V(M_2)} \sum_{\substack{x_1, x_2 \in E(S_k^2(M_1)) \\ x_1, x_2 \in V(S_k^2(M_1)) - V(M_1)}} \left[d_{S_k^2(M_1)}(x_1)d_{S_k^2(M_1)}(x_2) \right]^\alpha = 4^\alpha (k-1)m_1 n_2.
 \end{aligned}$$

Hence,

$$\begin{aligned}
 (n_1 m_2 + n_2 m_1)(2\Delta_{M_1} + \Delta_{M_2})^{2\alpha} + 2^{\alpha+1} n_2 m_1 (2\Delta_{M_1} + \Delta_{M_2})^\alpha + 4^\alpha n_2 m_1 (k-1) &\leq R_\alpha \\
 (M_1 + S_k^3 M_2) &\leq (n_1 m_2 + n_2 m_1)(2\delta_{M_1} + \delta_{M_2})^{2\alpha} + 2^{\alpha+1} n_2 m_1 (2\delta_{M_1} + \delta_{M_2})^\alpha + 4^\alpha n_2 m_1 (k-1).
 \end{aligned} \tag{20}$$

Equality holds if M_1 and M_2 are regular graphs. \square

Theorem 3. For a real number $\alpha > 0$ and counting number $k \geq 1$, the lower and upper bounds on the GSCI and GRI of the generalized F-sum graph $(M_1 + S_k^3 M_2)$ are as follows:

$$\begin{aligned}
 (a) \quad & 2^\alpha n_1 m_2 (\Delta_{M_1} + \Delta_{M_2})^\alpha + 2n_2 m_1 (3\Delta_{M_1} + \Delta_{M_2})^\alpha + \\
 & 2(k-1)n_1 [Z_1(M_1)]^\alpha + 4^\alpha \Delta_{M_1}^\alpha n_2 ((1/2)Z_1(M_1) + \\
 & m_1)^\alpha \leq \chi_\alpha(M_1 + S_k^3 M_2) \leq 2^\alpha n_1 m_2 (\delta_{M_1} + \delta_{M_2})^\alpha + \\
 & 2n_2 m_1 (3\delta_{M_1} + \delta_{M_2})^\alpha + 2(k-1)n_1 [Z_1(M_1)]^\alpha + \delta_{M_1}^\alpha n_2 ((1/2)Z_1(M_1) + m_1)^\alpha,
 \end{aligned}$$

$$\begin{aligned}
 (b) \quad & n_1 m_2 (\Delta_{M_1} + \Delta_{M_2})^{2\alpha} + 2^\alpha n_2 m_1 (\Delta_{M_1}^2 + \Delta_{M_1} \Delta_{M_2})^\alpha + \\
 & 2(k-1)n_2 Z_2(M_1)^\alpha + 4^\alpha \Delta_{M_1}^{2\alpha} n_2 \leq R_\alpha(M_1 + S_k^3 M_2) \leq \\
 & n_1 m_2 (\delta_{M_1} + \delta_{M_2})^{2\alpha} + 2^\alpha n_2 m_1 (\delta_{M_1}^2 + \delta_{M_1} \delta_{M_2})^\alpha + \\
 & 2(k-1)n_2 Z_2(M_1)^\alpha + 4^\alpha \delta_{M_1}^{2\alpha} n_2,
 \end{aligned}$$

where equalities hold if and only if M_1 and M_2 are regular graphs.

Proof. (a) By the definition of the GSCI, we have

$$\begin{aligned}
 \chi_\alpha(M_1 + S_k^3 M_2) &= \sum_{(x_1, y_1), (x_2, y_2) \in E(M_1 + S_k^3 M_2)} \left[d_{(M_1 + S_k^3 M_2)}(x_1, y_1) + d_{(M_1 + S_k^3 M_2)}(x_2, y_2) \right]^\alpha \\
 &= \sum_{x \in V(M_1)} \sum_{y_1, y_2 \in E(M_2)} [d(x, y_1) + d(x, y_2)]^\alpha + \sum_{y \in V(M_2)} \sum_{x_1, x_2 \in E(S_k^3(M_2))} [d(x, y_1) + d(x, y_2)]^\alpha \\
 &= \sum 1 + \sum 2.
 \end{aligned} \tag{21}$$

Now,

$$\begin{aligned}
 \sum 1 &= \sum_{x \in V(M_1)} \sum_{y_1, y_2 \in E(M_2)} [d(x, y_1) + d(x, y_2)]^\alpha \\
 &= \sum_{x \in V(M_1)} \sum_{y_1, y_2 \in E(M_2)} [2d_{M_1}(x) + d_{M_2}(y_1) + d_{M_2}(y_2)]^\alpha \leq 2^\alpha n_1 m_2 (\Delta_{M_1} + \Delta_{M_2})^\alpha \\
 \sum 2 &= \sum_{y \in V(M_2)} \sum_{x_1, x_2 \in E(S_k^3(M_1))} [d(x_1, y) + d(x_2, y)]^\alpha \\
 &= \sum_{y \in V(M_2)} \sum_{\substack{x_1, x_2 \in E(S_k^3(M_1)) \\ x_1 \in V(M_1) \\ x_2 \in V(S_k^3(M_1)) - V(M_1)}} [d(x_1, y) + d(x_2, y)]^\alpha \\
 &\quad + \sum_{y \in V(M_2)} \sum_{\substack{x_1, x_2 \in E(S_k^3(M_1)) \\ x_1, x_2 \in V(S_k^3(M_1)) - V(M_1)}} [d(x_1, y) + d(x_2, y)]^\alpha = ' \sum 2 + '' \sum 2.
 \end{aligned}
 \tag{22}$$

Now,

$$\begin{aligned}
 \sum' 2 &= \sum_{y \in V(M_2)} \sum_{\substack{x_1, x_2 \in E(S_k^3(M_1)) \\ x_1 \in V(M_1) \\ x_2 \in V(S_k^3(M_1)) - V(M_1)}} [d(x_1, y) + d(x_2, y)]^\alpha, \\
 &= \sum_{y \in V(M_2)} \sum_{\substack{x_1, x_2 \in E(S_k^3(M_2)) \\ x_1 \in V(M_1) \\ x_2 \in V(S_k^3(M_1)) - V(M_1)}} [d_{S_k^3(M_1)}(x_1) + d_{M_2}(y) + d_{S_k^3(M_1)}(x_2)]^\alpha \\
 &= \sum_{y \in V(M_2)} \sum_{\substack{x_1, x_2 \in E(S_k^3(M_2)) \\ x_1 \in V(M_1) \\ x_2 \in V(S_k^3(M_1)) - V(M_1)}} [d_{S_k^3(M_1)}(x_1) + d_{M_2}(y) + d_{S_k^3(M_1)}(x_2)]^\alpha.
 \end{aligned}
 \tag{23}$$

Note that $d_{S^3(M_1)}(x_2) = d_{M_1}(w_i) + d_{M_1}(w_j)$ for $a_2 \in V(S^3(M_1)) - V(M_1)$, where a_2 is the vertex inserted into the edge $w_i w_j$ of M_1 . Then, we have

$$\begin{aligned}
 &= \sum_{y \in V(M_2)} \sum_{\substack{x_1, x_2 \in E(S_k^3(M_2)) \\ x_1 \in V(M_1), x_2 \in V(S_k^3(M_1)) - V(M_1)}} [d_{S_k^3(M_1)}(x_1) + d_{M_2}(y) + d_{M_1}(w_i) + d_{M_1}(w_j)]^\alpha \\
 &\leq 2n_2 m_1 (3\Delta_{M_1} + \Delta_{M_2})^\alpha
 \end{aligned}
 \tag{24}$$

$$\sum'' 2 = \sum_{y \in V(M_2)} \sum_{\substack{x_1, x_2 \in E(S_k^3(M_1)) \\ x_1, x_2 \in V(S_k^3(M_1)) - V(M_1)}} [d(x_1, y) + d(x_2, y)].$$

We break this sum into two parts $\sum 2 = \sum 3 + \sum 4$, where $\sum 3$ belong the $S_k^3(M)$ edges and $\sum 4$ belong the $S_k^3(M_1)$.

$$\begin{aligned}
\sum 3 &= \sum_{y \in V(M_2)} \sum_{\substack{x_1 x_2 \in E(S_k^3(M_1)) \\ x_1 x_2 \in V(S_k^3(M_1)) - V(M_1)}} \left[d_{S_k^3(M_1)}(x_1) + d_{S_k^3(M_1)}(x_2) \right]^\alpha \\
&= 2(k-1) \sum_{y \in V(M_2)} \sum_{w_i w_j \in E(M)} \left[d_{M_1}(w_i) + d_{M_1}(w_j) \right]^\alpha \leq 2(k-1)n_1 [Z_1(M_1)]^\alpha \\
\sum 4 &= \sum_{y \in V(M_2)} \sum_{\substack{x_1 x_2 \in E(S_k^3(M_1)) \\ x_1 x_2 \in V(S_k^3(M_1)) - V(M_1)}} \left[d(x_1, y) + d(x_2, y) \right]^\alpha, \\
&= \sum_{y \in V(M_2)} \sum_{\substack{x_1 x_2 \in E(S_k^3(M_1)) \\ x_1 x_2 \in V(S_k^3(M_1)) - V(M_1)}} \left[d_{S_k^3(M_1)}(x_1) + d_{S_k^3(M_1)}(x_2) \right]^\alpha.
\end{aligned} \tag{25}$$

Since x_1 is the vertex inserted into the edge $w_i w_j$ of M_1 and a_2 is the vertex inserted into the edge $w_j w_k$ of M_1 ,

$$\begin{aligned}
&= \sum_{y \in V(M_2)} \sum_{\substack{w_i w_j \in E(M_1) \\ w_j w_k \in E(M_1)}} \left[d_{M_1}(w_i) + d_{M_1}(w_j) + d_{M_1}(w_j) + d_{M_1}(w_k) \right]^\alpha \\
&= \sum_{y \in V(M_2)} \sum_{\substack{w_i w_j \in E(M_1) \\ w_j w_k \in E(M_1)}} \left[d_{M_1}(w_i) + d_{M_1}(w_k) + 2d_{M_1}(w_j) \right]^\alpha \leq 4^\alpha k \Delta_{M_1}^\alpha n_2 \left(\frac{1}{2} Z_1(M_1) + m_1 \right)^\alpha.
\end{aligned} \tag{26}$$

Consequently, we have

$$\begin{aligned}
&2^\alpha n_1 m_2 (\Delta_{M_1} + \Delta_{M_2})^\alpha + 2n_2 m_1 (3\Delta_{M_1} + \Delta_{M_2})^\alpha + 2(k-1)n_1 [Z_1(M_1)]^\alpha \\
&+ 4^\alpha \Delta_{M_1}^\alpha n_2 \left(\frac{1}{2} Z_1(M_1) + m_1 \right)^\alpha \leq \chi_\alpha(M_1 + S_k^3 M_2) \leq 2^\alpha n_1 m_2 (\delta_{M_1} + \delta_{M_2})^\alpha + 2n_2 m_1 (3\delta_{M_1} + \delta_{M_2})^\alpha \\
&+ 2(k-1)n_1 [(Z_1(M_1))]^\alpha + 4^\alpha \delta_{M_1}^\alpha n_2 \left(\frac{1}{2} Z_1(M_1) + m_1 \right)^\alpha.
\end{aligned} \tag{27}$$

Proof. (b) By the definition of the GRI, we have

$$\begin{aligned}
R_\alpha(M_1 + S_k^3 M_2) &= \sum_{(x_1, y_1) (x_2, y_2) \in E(M_1 + S_k^3 M_2)} \left[d_{(M_1 + S_k^3 M_2)}(x_1, y_1) d_{(M_1 + S_k^3 M_2)}(x_2, y_2) \right]^\alpha, \\
&= \sum_{x \in V(M_1)} \sum_{y_1 y_2 \in E(M_2)} \left[d(x, y_1) d(x, y_2) \right]^\alpha + \sum_{y \in V(M_2)} \sum_{x_1 x_2 \in E(S_k^3(M_2))} \left[d(x_1, y) d(x_2, y) \right]^\alpha = \sum 1 + \sum 2.
\end{aligned} \tag{28}$$

Now,

$$\begin{aligned}
 \sum 1 &= \sum_{x \in V(M_1)} \sum_{y_1, y_2 \in E(M_2)} \left[d_{(M_1+S_k^3 M_2)}(x, y_1) d_{(M_1+S_k^3 M_2)}(x, y_2) \right]^\alpha, \\
 &= \sum_{x \in V(M_1)} \sum_{y_1, y_2 \in E(M_2)} \left[d_{M_1}(x) + d_{M_2}(y_1) \right] \left[d_{M_1}(x) + d_{M_2}(y_2) \right]^\alpha \\
 &= \sum_{x \in V(M_1)} \sum_{y_1, y_2 \in E(M_2)} \left[d_{M_1}^2(x) + d_{M_1}(x_1) \left[d_{M_2}(y_1) + d_{M_2}(y_2) \right] + d_{M_2}(y_1) d_{M_2}(y_2) \right]^\alpha \\
 &\leq n_1 m_2 \left(\Delta_{M_1}^2 + \Delta_{M_1} (2\Delta_{M_2}) + \Delta_{M_2}^2 \right)^\alpha \leq n_1 m_2 \left(\Delta_{M_1} + \Delta_{M_2} \right)^{2\alpha}, \\
 \sum 2 &= \sum_{y \in V(M_2)} \sum_{x_1, x_2 \in E(S_k^3(M_1))} \left[d(x_1, y) d(x_2, y) \right]^\alpha, \\
 &= \sum_{y \in V(M_2)} \sum_{\substack{x_1, x_2 \in E(S_k^3(M_1)) \\ x_1 \in V(M_1) \\ x_2 \in V(S_k^3(M_1)) - V(M_1)}} \left[d(x_1, y) d(x_2, y) \right]^\alpha \\
 &+ \sum_{y \in V(M_2)} \sum_{\substack{x_1, x_2 \in E(S_k^3(M_1)) \\ x_1, x_2 \in V(S_k^3(M_1)) - V(M_1)}} \left[d(x_1, y) d(x_2, y) \right]^\alpha = \sum' 2 + \sum 2.
 \end{aligned} \tag{29}$$

Now,

$$\begin{aligned}
 \sum' 2 &= \sum_{y \in V(M_2)} \sum_{\substack{x_1, x_2 \in E(S_k^3(M_1)) \\ x_1 \in V(M_1) \\ x_2 \in V(S_k^3(M_1)) - V(M_1)}} \left[d(x_1, y) d(x_2, y) \right]^\alpha, \\
 &= \sum_{y \in V(M_2)} \sum_{\substack{x_1, x_2 \in E(S_k^3(M_1)) \\ x_1 \in V(M_1) \\ x_2 \in V(S_k^3(M_1)) - V(M_1)}} \left[\left[d_{S_k^3(M_1)}(x_1) + d_{M_2}(y) \right] \left[d_{S_k^3(M_1)}(x_2) \right] \right]^\alpha.
 \end{aligned} \tag{30}$$

Note that $d_{S_k^3(M_1)}(x_2) = d_{M_1}(w_i) + d_{M_1}(w_j)$ for $x_2 \in V(S_3(M_1)) - V(M_1)$, where x_2 is the vertex inserted into the edge $w_i w_j$ of M_1 . Then, we have

$$\begin{aligned}
 &= \sum_{y \in V(M_2)} \sum_{\substack{x_1, x_2 \in E(S_k^3(M_1)) \\ x_1 \in V(M_1) \\ x_2 \in V(S_k^3(M_1)) - V(M_1)}} \left[d_{(M_1)}(x_1) + d_{M_2}(y) \right] \left[d_{M_1}(w_i) + d_{M_1}(w_j) \right]^\alpha \\
 &\leq 2^\alpha n_2 m_1 \left(\Delta_{M_1}^2 + \Delta_{M_1} \Delta_{M_2} \right)^\alpha \\
 \sum'' 2 &= \sum_{y \in V(M_2)} \sum_{\substack{x_1, x_2 \in E(S_k^3(M_1)) \\ x_1, x_2 \in V(S_k^3(M_1)) - V(M_1)}} \left[d(x_1, y) d(x_2, y) \right].
 \end{aligned} \tag{31}$$

We break this sum into two parts $\sum'' 2 = \sum 3 + \sum 4$, where $\sum 3$ belong the $S_k^3(M)$ edges and $\sum 4$ belong the $S_k^3(M_1)$.

$$\begin{aligned} \sum 3 &= \sum_{y \in V(M_2)} \sum_{\substack{x_1, x_2 \in E(S_k^3(M_1)) \\ x_1, x_2 \in V(S_k^3(M_1)) - V(M_1)}} \left[d_{S_k^3(M_1)}(x_1) d_{S_k^3(M_1)}(x_2) \right]^\alpha \\ &= 2(k-1) \sum_{y \in V(M_2)} \sum_{w_i, w_j \in E(M)} \left[d_{M_1}(w_i) d_{M_1}(w_j) \right]^\alpha \leq 2(k-1) n_2 Z_2(M_1)^\alpha \\ \sum 4 &= \sum_{y \in V(M_2)} \sum_{\substack{x_1, x_2 \in E(S_k^3(M_1)) \\ x_1, x_2 \in V(S_k^3(M_1)) - V(M_1)}} \left[d(x_1, y) d(x_2, y) \right]^\alpha \\ &= \left[d_{S_k^3(M_1)}(x_1) d_{S_k^3(M_1)}(x_2) \right]^\alpha \left[d_{S_k^3(M_1)}(x_1) d_{S_k^3(M_1)}(x_2) \right]^\alpha. \end{aligned} \tag{32}$$

Since x_1 is the vertex inserted into the edge $w_i w_j$ of M_1 and a_2 is the vertex inserted into the edge $w_j w_k$ of M_1 ,

$$\begin{aligned} &= \sum_{y \in V(M_2)} \sum_{\substack{w_i, w_j \in E(M_1) \\ w_j, w_k \in E(M_1)}} \left[d_{M_1}(w_i) + d_{M_1}(w_j) \right] \\ &\cdot \left[d_{M_1}(w_j) + d_{M_1}(w_k) \right]^\alpha \leq 4^\alpha \Delta_{M_1}^{2\alpha} n_2. \end{aligned} \tag{33}$$

Consequently, we have

$$\begin{aligned} n_1 m_2 (\Delta_{M_1} + \Delta_{M_2})^{2\alpha} + 2^\alpha n_2 m_1 (\Delta_{M_1}^2 + \Delta_{M_1} \Delta_{M_2})^\alpha + 2(k-1) n_2 Z_2(M_1)^\alpha + 4^\alpha \Delta_{M_1}^{2\alpha} n_2 \leq R_\alpha \\ (M_1 + S_k^3 M_2) \leq n_1 m_2 (\delta_{M_1} + \delta_{M_2})^{2\alpha} + 2^\alpha n_2 m_1 (\delta_{M_1}^2 + \delta_{M_1} \delta_{M_2})^\alpha + 2(k-1) n_2 Z_2(M_1)^\alpha + 4^\alpha \delta_{M_1}^{2\alpha} n_2. \end{aligned} \tag{34}$$

Theorem 4. For a real number $\alpha > 0$ and counting number $k \geq 1$, the lower and upper bounds on the GSCI and GRI of the generalized F -sum graph $(M_1 + S_k^1 M_2)$ are

- (a) $2^\alpha n_1 m_2 (\Delta_{M_1} + \Delta_{M_2})^\alpha + 2^\alpha n_2 m_1 (2\Delta_{M_1} + \Delta_{M_2})^\alpha + 2n_2 m_1 (3\Delta_{M_1} + \Delta_{M_2})^\alpha + 2(k-1) n_1 [Z_1(M_1)]^\alpha + 4^\alpha \Delta_{M_1}^{2\alpha} n_2$
 $n_2 ((1/2)Z_1(M_1) + m_1)^\alpha \leq \chi_\alpha(M_1 + S_k^1 M_2) \leq 2^\alpha n_1 m_2 (\delta_{M_1} + \delta_{M_2})^\alpha + 2^\alpha n_2 m_1 (2\delta_{M_1} + \delta_{M_2})^\alpha,$
- (b) $n_1 m_2 (\Delta_{M_1} + \Delta_{M_2})^{2\alpha} + 2^\alpha n_2 m_1 (2\Delta_{M_1} + \Delta_{M_2})^\alpha + 2^\alpha n_2 m_1 (\Delta_{M_1}^2 + \Delta_{M_1} \Delta_{M_2})^\alpha + 2(k-1) n_2 [Z_2(M_1)]^\alpha + 4^\alpha \Delta_{M_1}^{2\alpha} n_2 \leq R_\alpha$
 $(M_1 + S_k^1 M_2) \leq n_1 m_2 (\delta_{M_1} + \delta_{M_2})^{2\alpha} + 2^\alpha n_2 m_1 (2\delta_{M_1} + \delta_{M_2})^\alpha + 2^\alpha n_2 m_1 (\delta_{M_1}^2 + \delta_{M_1} \delta_{M_2})^\alpha + 2(k-1) n_2 Z_2(M_1)^\alpha + 4^\alpha \delta_{M_1}^{2\alpha} n_2,$

where r is the number of common neighbors of x_1 and x_2 in M_1 .

Proof. The proof follows by Theorem 2 and Theorem 3. \square

4. Applications

For a real number $\alpha > 0$, the lower and upper bounds on GSCI and GRI of the generalized F -sum graphs obtained by the particular classes of graphs as the consequences of the obtained results are given in Figures 4–11.

Example 1. For $M_1 = P_n$, $M_2 = P_m$, and $k = 4$, we have

- (a) $mn(6.4^\alpha) + m4^\alpha - 4^\alpha n \leq \chi_\alpha(P_n + S_4^1 P_m) \leq mn(8^\alpha + 2.6^\alpha + 3.4^\alpha) - m(2.6^\alpha - 3.4^\alpha) - 8^\alpha n,$ and
- (b) $mn(2^{4\alpha} + 2^{3\alpha+1} + 3.4^\alpha) - m(2^{3\alpha+1} - 3.4^\alpha) - 2^{4\alpha} n \leq R_\alpha(P_n + S_4^1 P_m) \leq mn(2^{2\alpha} + 2^{2\alpha+1} + 3.4^\alpha) - m(2^{2\alpha+1} - 3.4^\alpha) - 22\alpha n.$

The graphical representation of Example 1(a) is depicted in Figure 4, the lower bounds are represented by the blue graph and the upper bounds are represented by the red graph. The graphical representation of Example 1(b) is depicted in Figure 5, the lower bounds are represented by the green graph and the upper bounds are represented by the blue graph.

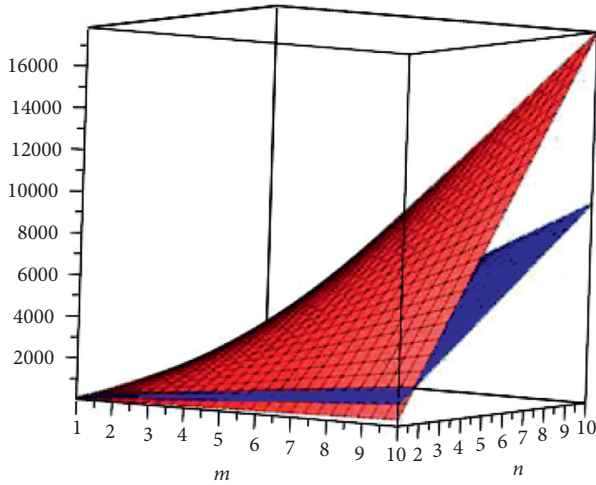


FIGURE 4: Graph for $(\alpha = 2) mn(6 \times 4^2) + 4^2m - 4^2n \leq \chi_\alpha(P_n + S_4^1 P_m) \leq mn(8^2 + 2 \times 6^2 + 3 \times 4^2) - m(2 \times 6^2 - 3 \times 4^2) - 8^2n$.

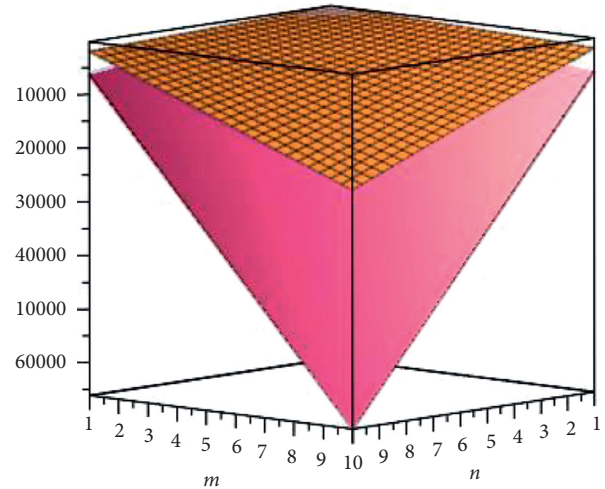


FIGURE 6: Graph for $(\alpha = 2) mn(2.12^2 + 2.8^2 + 3.4^2) - m(12^2 + 2.8^2 + 3.4^2) - 12^2n \leq \chi_\alpha(P_n + S_4^2 P_m) \leq mn(2.6^2 + 2.5^2 + 3.4^2) - m(6^2 + 2.5^2 + 3.4^2) - 6^2n$.

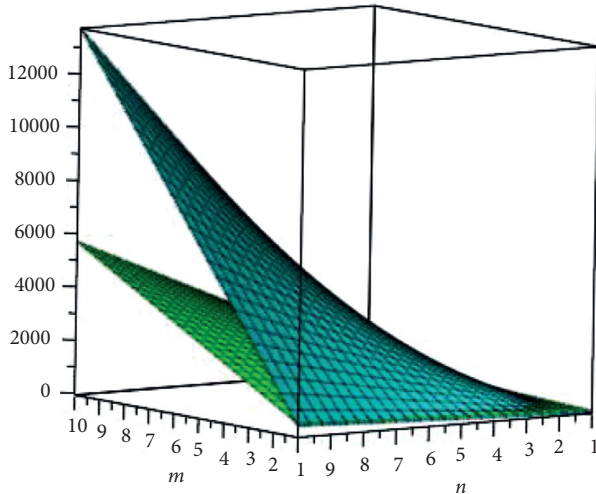


FIGURE 5: Graph for $(\alpha = 2) mn(2^{4^2} + 2^{3^2+1} + 3.4^2) - m(2^{3^2+1} - 3.4^2) - 2^{4^2}n \leq R_\alpha(P_n + S_4^3 P_m) \leq mn(2^{2^2} + 2^{2^2+1} + 3.4^2) - m(2^{2^2+1} - 3.4^2) - 22^2n$.

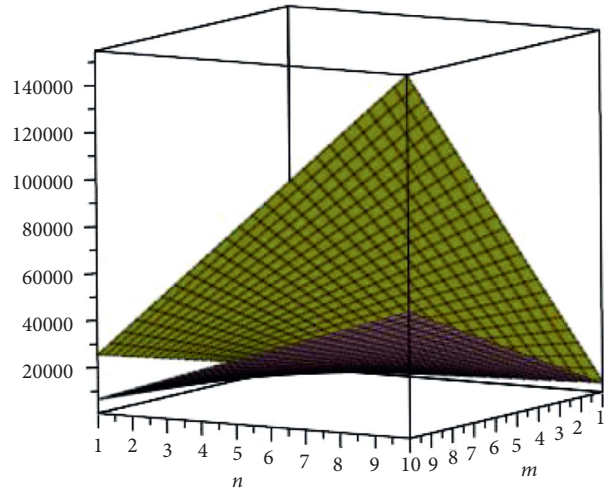


FIGURE 7: Graph for $(\alpha = 2) mn(2.6^{2^2} + 3^2.2^{2^2+1} + 3.4^2) - m(6^{2^2} + 3^2.2^{2^2+1} + 3.4^2) - 6^{2^2}n \leq R_\alpha(P_n + S_4^4 P_m) \leq mn(2.3^{2^2} + 3^2.2^{2^2+1} + 3.4^2) - m(3^{2^2} + 3^2.2^{2^2+1} + 3.4^2) - 3^{2^2}n$.

Example 2. For $M_1 = P_n, M_2 = P_m$, and $k = 4$, we have

- (a) $mn(2.12^\alpha + 2.8^\alpha + 3.4^\alpha) - m(12^\alpha + 2.8^\alpha + 3.4^\alpha) - 12^\alpha n \leq \chi_\alpha(P_n + S_4^1 P_m) \leq mn(2.6^\alpha + 2.5^\alpha + 3.4^\alpha) - m(6^\alpha + 2.5^\alpha + 3.4^\alpha) - 6^\alpha n$,
- (b) $mn(2.6^{2\alpha} + 3^\alpha.2^{2\alpha+1} + 3.4^\alpha) - m(6^{2\alpha} + 3^\alpha.2^{2\alpha+1} + 3.4^\alpha) - 6^{2\alpha}n \leq R_\alpha(P_n + S_4^2 P_m) \leq mn(2.3^{2\alpha} + 3^\alpha.2^{2\alpha+1} + 3.4^\alpha) - m(3^{2\alpha} + 3^\alpha.2^{2\alpha+1} + 3.4^\alpha) - 3^{2\alpha}n$.

The graphical representation of Example 2(a) is depicted in Figure 6. The lower bounds are represented by the Niagara Azure graph and the upper bounds are represented by the gold graph. The graphical representation of Example 2(b) is depicted in Figure 7. The lower bounds are represented by the pink graph and the upper bounds are represented by the yellow graph.

Example 3. For $M_1 = P_n, M_2 = P_m$, and $k = 4$, we have

- (a) $8^\alpha(nm - n) + 2.8^\alpha(mn - m) + 6n(4n - 6)^\alpha + 8^\alpha m(3n - 4)^\alpha \leq \chi_\alpha(P_n + S_4^3 P_m) \leq 4^\alpha(nm - n) + 2.4^\alpha(mn - m) + 6n(4n - 6)^\alpha + 4^\alpha m(3n - 4)^\alpha$,
- (b) $16^\alpha(nm - n) + 16^\alpha(mn - m) + 6m(4m - 6)^\alpha + 16^\alpha \leq R_\alpha(P_n + S_4^4 P_m) \leq 4^\alpha(nm - n) + 4^\alpha(mn - m) + 6m(4m - 6)^\alpha + 4^\alpha$.

The graphical representation of Example 3(a) is depicted in Figure 8. The lower bounds are represented by the blue graph and the upper bounds are represented by the green graph. The graphical representation of Example 3(b) is depicted in Figure 9. The lower bounds are represented by the yellow graph and the upper bounds are represented by the gray graph.

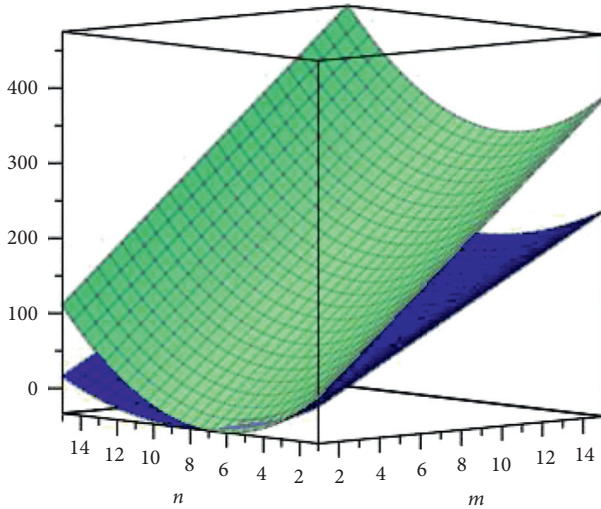


FIGURE 8: Graph for $(\alpha = 2) 8^2 (nm - n) + 2.8^2 (mn - m) + 6n (4n - 6)^2 + 8^2 m (3n - 4)^2 \leq \chi_\alpha (P_n + S_4^3 P_m) \leq 4^2 (nm - n) + 2.4^2 (mn - m) + 6n(4n - 6)^2 + 4^2 m(3n - 4)^2$.

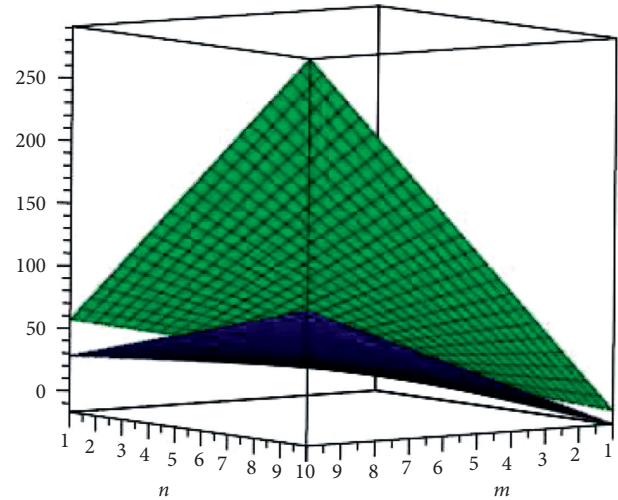


FIGURE 10: Graph for $\alpha = 2 8^2 (nm - n) + 12^2 (mn - m) + 2.8^2 (mn - m) + 6n (4n - 6)^2 + 8^2 m(3n - 4)^2 \leq \chi_\alpha (P_n + S_4^4 P_m) \leq 4^2 (nm - n) + 6^2 (mn - m) + 2.4^2 (mn - m) + 6n(4n - 6)^2 + 4^2 m (3n - 4)^2$.

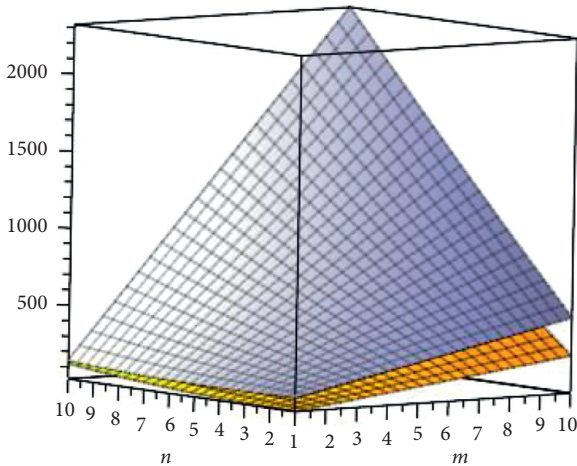


FIGURE 9: Graph for $(\alpha = 2) 16^2 (nm - n) + 16^2 (mn - m) + 6m (4m - 6)^2 + 16^2 \leq R_\alpha (P_n + S_4^3 P_m) \leq 4^2 (nm - n) + 4(mn - m) + 6m (4m - 6)^2 + 4^2$.

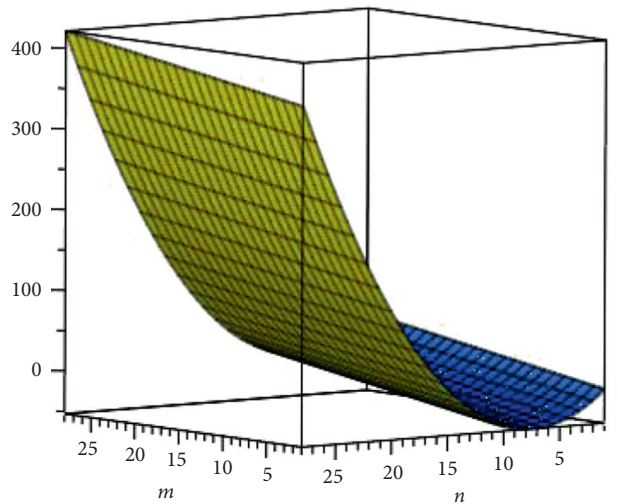


FIGURE 11: Graph for $\alpha = 2 2^{4^2} (nm - n) + 2^{2^2} \cdot 3^2 (mn - m) + 24^2 (mn - m) + 6m (4m - 6)^2 + 24^2 m \leq R_\alpha (P_n + S_4^4 P_m) \leq 2^{2^2} (nm - n) + 6^2 (mn - m) + 22^2 (mn - m) + 6m(4m - 6)^2 + 4^2 m$.

Example 4. For $M_1 = P_n, M_2 = P_m$, and $k = 4$, we have

- (a) $8^\alpha (nm - n) + 12^\alpha (mn - m) + 2.8^\alpha (mn - m) + 6n (4n - 6)^\alpha + 8^\alpha m(3n - 4)^\alpha \leq \chi_\alpha (P_n + S_4^4 P_m) \leq 4^\alpha (nm - n) + 6^\alpha (mn - m) + 2.4^\alpha (mn - m) + 6n(4n - 6)^\alpha + 4^\alpha m(3n - 4)^\alpha$,
- (b) $2^{4^\alpha} (nm - n) + 2^{2^\alpha} \cdot 3^\alpha (mn - m) + 24^\alpha (mn - m) + 6m (4m - 6)^\alpha + 24^\alpha m \leq R_\alpha (P_n + S_4^4 P_m) \leq 2^{2^\alpha} (nm - n) + 6^\alpha (mn - m) + 22^\alpha (mn - m) + 6m (4m - 6)^\alpha + 4^\alpha m$.

The graphical representation of Example 4(a) is depicted in Figure 10. The lower bounds are represented by the blue graph and the upper bounds are represented by the green graph. The graphical representation of Example 4(b) is depicted in Figure 11. The lower bounds are represented by

the yellow graph and the upper bounds are represented by the blue graph.

5. Conclusion

In this paper, the lower and upper bounds of the general sum-connectivity and general Randić indices of the generalized F -sum graphs (F_k -sum graphs) are computed in terms of the order, size, maximum, and/or minimum degree and Zagreb indices of the factor graphs, where the F_k -sum graphs are obtained with the help of four generalized subdivision-related operations and the Cartesian product of graphs. However, the problem is still open for other types of product of graphs.

Data Availability

All the data are included within this paper. However, the reader may contact the corresponding author for more details of the data.

Conflicts of Interest

The authors have no conflicts of interest.

Acknowledgments

This research was funded by the Project of Anhui Jianzhu University under Grant nos. 2016QD116 and 2017dc03.

References

- [1] H. Gonzalez-Diaz, S. Vilar, L. Santana, and E. Uriarte, "Medicinal chemistry and bioinformatics - current trends in drugs discovery with networks topological indices," *Current Topics in Medicinal Chemistry*, vol. 7, no. 10, pp. 1015–1029, 2007.
- [2] A. R. Matamala and E. Estrada, "Simplex optimization of generalized topological index (GTI-simplex): a unified approach to optimize QSPR models," *The Journal of Physical Chemistry A*, vol. 43, no. 109, pp. 9890–9895, 2005.
- [3] H. Wiener, "Structural determination of paraffin boiling points," *Journal of the American Chemical Society*, vol. 69, no. 1, pp. 17–20, 1947.
- [4] I. Gutman and N. Trinajstić, "Graph theory and molecular orbitals. Total ϕ -electron energy of alternant hydrocarbons," *Chemical Physics Letters*, vol. 17, no. 4, pp. 535–538, 1972.
- [5] B. Zhou and N. Trinajstić, "On a novel connectivity index," *Journal of Mathematical Chemistry*, vol. 46, no. 4, pp. 1252–1270, 2009.
- [6] B. Zhou and N. Trinajstić, "On general sum-connectivity index," *Journal of Mathematical Chemistry*, vol. 47, no. 1, pp. 210–218, 2010.
- [7] M. Randić, "Characterization of molecular branching," *Journal of the American Chemical Society*, vol. 97, no. 23, pp. 6609–6615, 1975.
- [8] X. Li and I. Gutman, *Mathematical Aspects of Randić-type Molecular Structure Descriptors: Mathematical Chemistry Monographs No.1*, University of Kragujevac, Kragujevac, Serbia, 2006.
- [9] P. Balister, B. Bollobás, and S. Gerke, "The generalized Randić index of trees," *Journal of Graph Theory*, vol. 56, no. 4, pp. 270–286, 2007.
- [10] R.-M. Tache, "General sum connectivity index with $\alpha \geq 1$ for bicyclic graphs," *MATCH Commun. Math. Comput. Chem.* vol. 72, pp. 761–774, 2014.
- [11] I. Tomescu and S. Kanwal, "Unicyclic graphs of given girth $k \geq 4$ having smallest general sum-connectivity index," *Discrete Applied Mathematics*, vol. 164, pp. 344–348, 2014.
- [12] Z. Zhu and H. Lu, "On the general sum-connectivity index of tricyclic graphs," *Journal of Applied Mathematics and Computing*, vol. 51, no. 1-2, pp. 177–188, 2015.
- [13] W. Yan, B.-Y. Yang, and Y.-N. Yeh, "The behavior of wiener indices and polynomials of graphs under five graph decorations," *Applied Mathematics Letters*, vol. 20, no. 3, pp. 290–295, Mar. 2007.
- [14] M. Eliasi and B. Taeri, "Four new sums of graphs and their wiener indices," *Discrete Applied Mathematics*, vol. 157, no. 4, pp. 794–803, 2009.
- [15] H. Deng, D. Sarala, S. K. Ayyaswamy, and S. Balachandran, "The zagreb indices of four operations on graphs," *Applied Mathematics and Computation*, vol. 275, pp. 422–431, Feb 2016.
- [16] S. Akhter and M. Imran, "The Sharp bounds on general sum-connectivity index of four operations on graphs," *Journal of Inequalities and Applications*, vol. 24110 pages, 2016.
- [17] J.-B. Liu, M. Javaid, and H. M. Awais, "Computing zagreb indices of the subdivision-related generalized operations of graphs," *IEEE Access*, vol. 7, pp. 105479–105488, 2019.
- [18] M. Ahmad, M. Saeed, M. Javaid, and M. Hussain, "Exact formula and improved bounds for general sum-connectivity index of graph-operations," *IEEE Access*, vol. 7, pp. 167290–167299, 2019.
- [19] H. M. Awais, M. Javaid, and M. Jamal, "Forgotten index of generalized F -sum graphs," *Journal of Prime Research in Mathematics*, vol. 15, pp. 115–128, 2019.
- [20] H. M. Awais, M. Javaid, and A. Raheem, "Hyper-zagreb index of graphs based on generalized subdivision related operations," *Punjab University Journal of Mathematics*, vol. 52, no. 5, pp. 89–103, 2019.
- [21] H. M. Awais, M. Javaid, and A. Akbar, "First general zagreb index of generalized F -sum graphs," *Discrete Dynamics in Nature and Society*, vol. 2020, Article ID 2954975, 16 pages, 2020.
- [22] Y.-M. Chu, S. Javed, M. Javaid, and M. Kamran Siddiqui, "On bounds for topological descriptors of ϕ -sum graphs," *Journal of Taibah University for Science*, vol. 14, no. 1, pp. 1288–1301, 2020.
- [23] M. Javaid, S. Javed, A. M. Alanazi, and M. R. Alotaibi, "Computing analysis of zagreb indices for generalized sum graphs under strong product," *Journal of Chemistry*, vol. 2021, Article ID 6663624, 20 pages, 2021.
- [24] M. Javaid, "Masood ur Rehman, and Jinde Cao, topological indices of rhombus type silicate and oxide networks," *Candidian Journal of Chemistry*, vol. 2, no. 95, pp. 134–143, 2017.
- [25] X. Li, M. Ahmad, M. Javaid, M. Saeed, and J.-B. Liu, "Bounds on general randić index for F -sum graphs," *Journal of Mathematics*, vol. 2020, Article ID 9129365, 17 pages, 2020.
- [26] J.-B. Liu, S. Javed, M. Javaid, and K. Shabbir, "Computing first general zagreb index of operations on graphs," *IEEE Access*, vol. 7, pp. 47494–47502, 2019.
- [27] X. Zhang, H. M. Awais, M. Javaid, and M. K. Siddiqui, "Multiplicative zagreb indices of molecular graphs," *Journal of Chemistry*, vol. 2019, Article ID 5294198, 19 pages, 2019.
- [28] D. M. Cvetkovic, M. Doob, and H. Sachs, *Spectra of Graphs: Theory and Applications*, Academic Press, New York, NY, USA, 1980.

Research Article

The Distance Laplacian Spectral Radius of Clique Trees

Xiaoling Zhang  and Jiajia Zhou

School of Mathematics and Information Sciences, Yantai University, Yantai, Shandong 264005, China

Correspondence should be addressed to Xiaoling Zhang; zhangxling04@163.com

Received 7 August 2020; Revised 11 September 2020; Accepted 4 October 2020; Published 9 December 2020

Academic Editor: M Javaid

Copyright © 2020 Xiaoling Zhang and Jiajia Zhou. This is an open access article distributed under the Creative Commons Attribution License, which permits unrestricted use, distribution, and reproduction in any medium, provided the original work is properly cited.

The distance Laplacian matrix of a connected graph G is defined as $\mathcal{L}(G) = \text{Tr}(G) - D(G)$, where $D(G)$ is the distance matrix of G and $\text{Tr}(G)$ is the diagonal matrix of vertex transmissions of G . The largest eigenvalue of $\mathcal{L}(G)$ is called the distance Laplacian spectral radius of G . In this paper, we determine the graphs with maximum and minimum distance Laplacian spectral radius among all clique trees with n vertices and k cliques. Moreover, we obtain n vertices and k cliques.

1. Introduction

In this paper, we consider simple connected graphs [1]. A graph G is represented by $G = (V(G), E(G))$, in which the set $V(G) = \{v_1, v_2, \dots, v_n\}$ represents its vertex set and $E(G)$ is the edge set connecting pairs of distinct vertices. The number $n = |V(G)|$ is referred to as the order of G . The distance matrix of G is the $n \times n$ matrix $D(G) = (d_G(u, v))_{u, v \in V(G)}$, where $d_G(u, v)$ denotes the distance between vertices u and v in G , i.e., the length of a shortest path from u to v in G . For $u \in V(G)$, the transmission of u in G , denoted by $\text{Tr}_G(u)$, is defined as the sum of distances from u to all other vertices of G . Let $\text{Tr}(G)$ be the diagonal matrix of vertex transmissions of G . In 2013, Aouchiche and Hansen [2] first gave the definition of distance Laplacian matrix: for a connected graph G , $\mathcal{L}(G) = \text{Tr}(G) - D(G)$, where $\mathcal{L}(G)$ denotes the distance Laplacian matrix. Obviously, $\mathcal{L}(G)$ is a positive semidefinite, symmetric, and singular matrix. The distance Laplacian eigenvalues of G , denoted by $\lambda_1(G) \geq \lambda_2(G) \geq \dots \geq \lambda_n(G) = 0$, are the eigenvalues of $\mathcal{L}(G)$. Especially, the largest eigenvalue $\lambda_1(G)$ is the distance Laplacian spectral radius of G . The positive unit eigenvector, i.e., all components of the eigenvector are positive, corresponding to $\lambda_1(G)$ is called the Perron eigenvector of $\mathcal{L}(G)$.

For a graph G , two vertices are called adjacent if they are connected by an edge and two edges are called incident if they share a common vertex. The set of vertices that are adjacent to a vertex $v \in V(G)$ is called the neighborhood of v and is presented by $N_G(v)$. As usual, let K_n , $K_{1,n-1}$, and P_n denote the complete graph, the star, and the path with order n , respectively. G is a connected graph, $X \in V(G)$, $G - X$ is not connected, and then X is a cut-vertex set. If X has only vertex v , then v is a cut-vertex. A block of G is a maximal connected subgraph of G that has no cut-vertex. A block is a clique if the block is a complete graph. A graph G is a clique tree if each block of G is a clique. We call $\mathcal{P}_{n_1, n_2, \dots, n_k}$ a clique path if we replace each edge of P_{k+1} by a clique K_{n_i} such that $V(K_{n_i}) \cap V(K_{n_{i+1}}) = v_i$ for $i = 1, 2, \dots, k-2$ and $V(K_{n_i}) \cap V(K_{n_j}) = \emptyset$ for $j \neq i-1, i+1$ and $2 \leq i \leq k-1$. We call $K_{u, n_1, n_2, \dots, n_k}$ a clique star if we replace each edge of the star $K_{1,k}$ with a clique K_{n_i} such that $V(K_{n_i}) \cap V(K_{n_j}) = u$ for $i \neq j$ and $i, j = 1, 2, \dots, k$ (see Figure 1).

Recently, Xing and Zhou [3] characterized the unique graph with minimum distance Laplacian spectral radius among all the bicyclic graphs with fixed number of vertices; Aouchiche and Hansen [4] showed that the star $K_{1,n}$ is the unique tree with the minimum distance Laplacian spectral radius among all trees; Lin et al. [5, 6] determined the unique

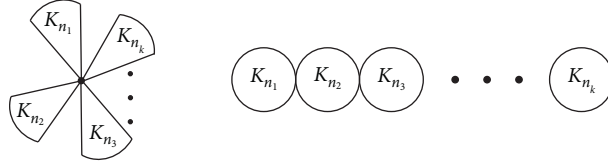


FIGURE 1: A clique star and a clique path.

graph with minimum distance Laplacian spectral radius among all the trees with fixed bipartition, nonstar-like trees, noncaterpillar trees, nonstar-like noncaterpillar trees, and the graph with fixed edge connectivity at most half of the order, respectively; Niu et al. [7] determined the unique graph with minimum distance Laplacian spectral radius among all the bipartite graphs with fixed matching number and fixed vertex connectivity, respectively; Fan et al. [8] determined the graph with minimum distance Laplacian spectral radius among all the unicyclic and bicyclic graphs with fixed numbers of vertices, respectively; Lin and Zhou [9] determined the unique graph with maximum distance Laplacian spectral radius among all the unicyclic graphs with fixed numbers of vertices.

In 2019, Cui et al. [10] investigated a convex combination of $\text{Tr}(G)$ and $D(G)$ in the form of $D_\alpha(G) = \alpha \text{Tr}(G) + (1 - \alpha)D(G)$, $0 \leq \alpha \leq 1$, which is called the generalized distance matrix. Alhevaz et al. [11] gave some new upper and lower bounds for the generalized distance energy of graphs which are established based on parameters including the Wiener index and the transmission degrees and found that the complete graph has the minimum generalized distance energy among all connected graphs; Lin and Drury et al. [12] established some bounds for the generalized distance Gaussian Estrada index of a connected graph, involving the different graph parameters, including the order, the Wiener index, the transmission degrees, and the parameter $\alpha \in [0, 1]$, and characterized the extremal graphs attaining these bounds; Alhevaz et al. [13] obtained some bounds for the generalized distance spectral radius of graphs using graph parameters like the diameter, the order, the minimum degree, the second minimum degree, the transmission degree, and the second transmission degree and characterized the extremal graphs; Alhevaz et al. [14] studied the generalized distance spectrum of join of two regular graphs and join of a regular graph with the union of two different regular graphs; Shang [15] established better lower and upper bounds to the distance Estrada index for almost all graphs.

The distance Laplacian energy is defined as $\text{DLE}(G) = (1/n) \sum_{i=1}^n |\lambda_i(G) - t(G)|$, where $t(G)$ is the average transmission of G and is defined by $t(G) = (1/n) \sum_{i=1}^n \text{Tr}_G(v_i)$. Although there has been extensive work done on the distance Laplacian spectral radius of graphs, relatively little is known in regard to distance Laplacian energy. The distance Laplacian energy was first introduced in [16], where several lower and upper bounds were obtained; Das et al. [17] gave some lower bounds on distance Laplacian energy in terms of n for graphs and trees and characterized the extremal graphs and trees. In this

paper, first, we not only get the distance Laplacian eigenvalues of all clique stars $K_{u, n_1, n_2, \dots, n_k}$ but also get their distance Laplacian energies; second, we prove all clique stars $K_{u, n_1, n_2, \dots, n_k}$ are the graphs with minimum distance Laplacian spectral radius among all clique trees with n vertices and k cliques. Then, we show that the clique path $\mathcal{P}_{m, 2, \dots, 2, n-m-k+3}$ for $m \geq 3$ is the graph with maximum distance Laplacian spectral radius among all clique trees with n vertices and k cliques.

2. Preliminaries

Let $G = (V, E)$ be a connected graph with $V(G) = \{v_1, v_2, \dots, v_n\}$. A column vector $x = (x_{v_1}, x_{v_2}, \dots, x_{v_n})^T \in \mathbb{R}^n$ can be considered as a function defined on $V(G)$ which maps vertex v_i to x_{v_i} , i.e., $x(v_i) = x_{v_i}$ for $i = 1, 2, \dots, n$. Then,

$$x^T \mathcal{L}(G)x = \sum_{\{u, v\} \in V(G)} d_G(u, v)(x_u - x_v)^2, \quad (1)$$

and λ is a distance Laplacian eigenvalue with corresponding eigenvector x if and only if $x \neq 0$, for each $u \in V(G)$,

$$(\lambda - \text{Tr}_G(u))x_u = - \sum_{v \in V(G)} d_G(u, v)x_v, \quad (2)$$

or equivalently

$$\lambda x_u = \sum_{v \in V(G)} d_G(u, v)(x_u - x_v). \quad (3)$$

The above equation is called the eigenequation of G at u .

Note that $1_n = (1, 1, \dots, 1)^T$ is an eigenvector of $\mathcal{L}(G)$ corresponding to $\lambda_n(G) \neq 0$. For $n \geq 2$, if x is an eigenvector of $\mathcal{L}(G)$ corresponding to $\lambda_1(G)$, we have $x^T 1_n = 0$.

For a unit column vector $x \in \mathbb{R}^n$, by Rayleigh's principle, we have $\lambda(G) \geq x^T \mathcal{L}(G)x$ with equality if and only if x is an eigenvector of $\mathcal{L}(G)$ corresponding to $\lambda(G)$.

The following is the well-known Cauchy interlacing theorem.

Lemma 1 (Cauchy interlace theorem) (see [1]). *Let A be a Hermitian matrix with eigenvalues $\lambda_1 \geq \dots \geq \lambda_n$ and B be one of its principal submatrices. Let B have eigenvalues $\mu_1 \geq \dots \geq \mu_m$. Then, the inequalities $\lambda_{n-m+i} \leq \mu_i \leq \lambda_i$ ($i = 1, \dots, m$) hold.*

Lemma 2 (see [6]). *Let G be a connected graph with three induced subgraphs $G_1, G_2,$ and G_3 such that $|V(G_i)| \geq 2$ for $i = 1, 2, 3$ and $V(G_i) \cap V(G_j) = \{u\}$ for $1 \leq i < j \leq 3$ and $\cup_{i=1}^3 V(G_i) = V(G)$ (see Figure 2). For $v \in V(G_2) \setminus \{u\}$ and $y \in V(G_1) \setminus \{u\}$, let $G^1 = G - \{u\} + \{u\}$ and $G^2 = G - \{u\} + \{u\}$.*

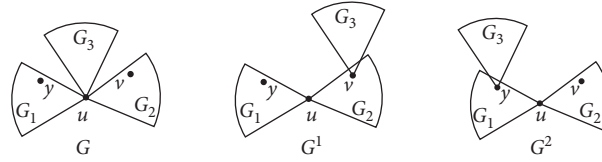


FIGURE 2: A graph transformation from G to G^1 and G^2 .

$N_{G_3}(u)$ and $G^2 = G - \{uw : \omega \in N_{G_3}(u)\} + \{y\omega : \omega \in N_{G_3}(u)\}$. If $N_G(u) = \{y, v\} \cup N_{G_3}(u)$, then $\lambda_1(G) < \lambda_1(G^1)$ or $\lambda_1(G) < \lambda_1(G^2)$.

3. Minimum Distance Laplacian Spectral Radius of Clique Trees

The diameter of a graph is the maximum distance between any pair of vertices.

Lemma 3. Let S be a clique tree with n vertices and k cliques. If $\text{diam}(S) \geq 3$, then $\lambda_1(S) > 2n - 1$.

Proof. For convenience, let $\text{diam}(S) = d$ and $\mathcal{P}_{n_1, n_2, \dots, n_d}$ be a clique path of S . Denote the cliques of $\mathcal{P}_{n_1, n_2, \dots, n_d}$ by $K_{n_1}, K_{n_2}, \dots, K_{n_d}$. Let $V(K_{n_i}) \cap V(K_{n_{i+1}}) = v_i$ for $i = 1, 2, \dots, d - 1$. Let $\{v_0\} \in V(K_{n_1}) \setminus \{v_1\}$ and $\{v_d\} \in V(K_{n_d}) \setminus \{v_{d-1}\}$. Then, $v_0 v_1 \dots v_d$ is a diameter path of S . We can easily get

$$\begin{aligned} \text{Tr}_S(v_0) &\geq (n_1 - 2) + 2(n_2 - 2) + \dots + d(n_d - 2) + 1 + 2 + \dots + d \\ &\quad + 2[n - n_1 - n_2 - \dots - n_d + (d - 1)], \\ \text{Tr}_S(v_d) &\geq (n_d - 2) + 2(n_{d-1} - 2) + \dots + d(n_1 - 2) + 1 + 2 + \dots + d \\ &\quad + 2[n - n_1 - n_2 - \dots - n_d + (d - 1)]. \end{aligned} \tag{4}$$

Then, we have

$$\begin{aligned} \text{Tr}_S(v_0) + \text{Tr}_S(v_d) &\geq (d + 1)[(n_1 - 2) + (n_2 - 2) + \dots + (n_d - 2)] + d(d + 1) + 4n \\ &\quad - 4[(n_1 - 2) + (n_2 - 2) + \dots + (n_d - 2)] - 8d + 4(d - 1) \\ &= (d + 1 - 4)[(n_1 - 2) + (n_2 - 2) + \dots + (n_d - 2)] + d(d + 1) + 4n - 8d + 4(d - 1) \\ &= (d - 3)[(n_1 - 2) + (n_2 - 2) + \dots + (n_d - 2)] + d^2 + 4n - 3d - 4 > 4n + d^2 - 3d - 8. \end{aligned} \tag{5}$$

Let M be the principal submatrix of $\mathcal{L}(S)$ indexed by v_0 and v_d . Then,

$$\begin{aligned} M &= \begin{pmatrix} \text{Tr}_S(v_0) & -d \\ -d & \text{Tr}_S(v_d) \end{pmatrix}, \\ |M - \lambda E| &= \begin{vmatrix} \text{Tr}_S(v_0) - \lambda & -d \\ -d & \text{Tr}_S(v_d) - \lambda \end{vmatrix} \\ &= \lambda^2 - (\text{Tr}_S(v_0) + \text{Tr}_S(v_d))\lambda + \text{Tr}_S(v_0)\text{Tr}_S(v_d) - d^2, \end{aligned} \tag{6}$$

$$\begin{aligned} \lambda_1(M) &= \frac{\text{Tr}_S(v_0) + \text{Tr}_S(v_d) + \sqrt{(\text{Tr}_S(v_0) - \text{Tr}_S(v_d))^2 + 4d^2}}{2} \\ &\geq \frac{\text{Tr}_S(v_0) + \text{Tr}_S(v_d) + 2d}{2} > \frac{4n + d^2 - d - 8}{2} \\ &\geq \frac{4n + 3^2 - 3 - 8}{2} = 2n - 1. \end{aligned} \tag{7}$$

By Lemma 2, we have $\lambda_1(S) \geq \lambda_1(M) > 2n - 1$. \square

Theorem 1. Let $K_{u, n_1, n_2, \dots, n_k}$ be an arbitrary clique star with n vertices and k cliques. Then, $\lambda_1(K_{u, n_1, n_2, \dots, n_k}) = 2n - 1$.

Proof. Obviously, we have $n_1 + n_2 + n_3 + \dots + n_k = n + k - 1$. Let x be a Perron eigenvector of $\mathcal{L}(K_{u, n_1, n_2, \dots, n_k})$ corresponding to $\lambda_1(K_{u, n_1, n_2, \dots, n_k})$. By symmetry, we may assume $x_v = x_i$ for any $v \in V(K_{n_i}) \setminus \{u\}$, $i = 1, 2, \dots, k$. Let $x_0 = x_u$, then we have

$$\begin{cases} \lambda x_0 = (n_1 - 1)(x_0 - x_1) + (n_2 - 1)(x_0 - x_2) + (n_3 - 1)(x_0 - x_3) + \dots + (n_k - 1)(x_0 - x_k), \\ \lambda x_1 = (x_1 - x_0) + 2(n_2 - 1)(x_1 - x_2) + 2(n_3 - 1)(x_1 - x_3) + \dots + 2(n_k - 1)(x_1 - x_k), \\ \lambda x_2 = (x_2 - x_0) + 2(n_1 - 1)(x_2 - x_1) + 2(n_3 - 1)(x_2 - x_3) + \dots + 2(n_k - 1)(x_2 - x_k), \\ \lambda x_3 = (x_3 - x_0) + 2(n_1 - 1)(x_3 - x_1) + 2(n_2 - 1)(x_3 - x_2) + \dots + 2(n_k - 1)(x_3 - x_k), \\ \dots \\ \lambda x_k = (x_k - x_0) + 2(n_1 - 1)(x_k - x_1) + 2(n_2 - 1)(x_k - x_2) + \dots + 2(n_{k-1} - 1)(x_k - x_{k-1}). \end{cases} \tag{8}$$

Thus, λ_1 is the largest root of the equation $f_{n_1, n_2, \dots, n_k}(t) = 0$, where $\beta = \sum_{i=1}^k n_i - k$ and

$$\begin{aligned} f_{n_1, n_2, \dots, n_k}(t) &= \begin{vmatrix} \beta - t & 1 - n_1 & 1 - n_2 & \dots & 1 - n_k \\ -1 & 2(\beta - n_1) + 3 - t & 2 - 2n_2 & \dots & 2 - 2n_k \\ -1 & 2 - 2n_1 & 2(\beta - n_2) + 3 - t & \dots & 2 - 2n_k \\ \vdots & \vdots & \vdots & \ddots & \vdots \\ -1 & 2 - 2n_1 & 2 - 2n_2 & \dots & 2(\beta - n_k) + 3 - t \end{vmatrix} \\ &= \begin{vmatrix} -t & 1 - n_1 & 1 - n_2 & \dots & 1 - n_k \\ -t & 2(\beta - n_1) + 3 - t & 2 - 2n_2 & \dots & 2 - 2n_k \\ -t & 2 - 2n_1 & 2(\beta - n_2) + 3 - t & \dots & 2 - 2n_k \\ \vdots & \vdots & \vdots & \ddots & \vdots \\ -t & 2 - 2n_1 & 2 - 2n_2 & \dots & 2(\beta - n_k) + 3 - t \end{vmatrix} \\ &= \begin{vmatrix} -t & 1 - n_1 & 1 - n_2 & 1 - n_3 & \dots & 1 - n_k \\ -t & 2(\beta - n_1) + 3 - t & 2 - 2n_2 & 2 - 2n_3 & \dots & 2 - 2n_k \\ 0 & 1 - 2n + t & 2n - 1 - t & 0 & \dots & 0 \\ \vdots & \vdots & \vdots & \vdots & \ddots & \vdots \\ 0 & 1 - 2n + t & 0 & 0 & \dots & 2n - 1 - t \end{vmatrix} \tag{9} \\ &= \begin{vmatrix} -t & 1 - n - t & 1 - n_2 & 1 - n_3 & \dots & 1 - n_k \\ -t & 1 - 2t & 2 - 2n_2 & 2 - 2n_3 & \dots & 2 - 2n_k \\ 0 & 0 & 2n - 1 - t & 0 & \dots & 0 \\ \vdots & \vdots & \vdots & \vdots & \ddots & \vdots \\ 0 & 0 & 0 & 0 & \dots & 2n - 1 - t \end{vmatrix} \\ &= (-t)(-1)^2(2n - 1 - t)^{k-1}(1 - 2t) + (-t)(-1)^3(2n - 1 - t)^{k-1}(1 - n - t) \\ &= (2n - 1 - t)^{k-1}[(1 - 2t)(-t) + (1 - n - t)t] \\ &= t(2n - 1 - t)^{k-1}(t - n). \end{aligned}$$

Therefore, we have $\lambda_1(K_{u, n_1, n_2, \dots, n_k}) = 2n - 1 - n$ and 0 are also distance Laplacian eigenvalues of K_{u, n_1, \dots, n_k} .

Combining Lemma 3 and Theorem 1, we have the following result. \square

Theorem 2. *Among all clique trees with n vertices and k cliques, the graphs attaining the minimum distance Laplacian spectral radius are clique stars $K_{u, n_1, n_2, \dots, n_k}$.*

Let I be the identity matrix of order n . The characteristic polynomial of $\mathcal{L}(G)$ can be written as $\psi(G; \lambda) = \det(\lambda I - \mathcal{L}(G))$. Let us label the vertices of $K_{u, n_1, n_2, \dots, n_k}$ such that u is the first vertices, and the first n_1 vertices are from $V(K_{n_1})$, the following $n_2 - 1$ vertices are from $V(K_{n_2}) \setminus \{u\}$, \dots , and the last $n_k - 1$ are from $V(K_{n_k}) \setminus \{u\}$. Let $\det(\lambda I - \mathcal{L}(K_{u, n_1, n_2, \dots, n_k})) = 0$. Combining Theorem 1, by direct calculations, we get the following result.

Corollary 1. *The distance Laplacian eigenvalues of K_{u,n_1,n_2,\dots,n_k} are $2n-1$ of multiplicities $k-1$, $2n-n_i$ of multiplicities n_i-2 ($1 \leq i \leq k$), n , and 0 .*

Theorem 3. *Let K_{u,n_1,n_2,\dots,n_k} be an arbitrary clique star with n vertices and k cliques. Then, we have $DLE(K_{u,n_1,n_2,\dots,n_k}) = (2/n)[2n-1 + (1/n)(k-1 - \sum_{i=1}^k n_i^2)]$.*

Proof. Obviously, we have $n_1 + n_2 + n_3 + \dots + n_k = n + k - 1$. For convenience, let $G = K_{u,n_1,n_2,\dots,n_k}$. For any $v, w \in V(K_{n_i}) \setminus \{u\}$, we have $\text{Tr}_G(v) = \text{Tr}_G(w)$. Let $v_i \in V(K_{n_i}) \setminus \{u\}$, $1 \leq i \leq k$. Then, we have $\text{Tr}_G(v_i) = 2n - n_i - 1$ and $t(G) = (1/n) \sum_{i=1}^n \text{Tr}_G(v_i) = (([\sum_{i=1}^k ((n_i - 1)(2n - n_i - 1)] + n - 1)/n) = ((2n \sum_{i=1}^k 1^k (n_i - 1) - \sum_{i=1}^k (n_i - 1)(n_i + 1) + n - 1)/n) = ((2n(n - 1) - \sum_{i=1}^k n_i^2 + k + n - 1)/n) = 2n - 1 + ((k - 1 - \sum_{i=1}^k 1^k n_i^2)/n)$. By Cauchy-Schwarz inequality, we have $\sum_{i=1}^k n_i^2 \geq (n + k - 1)^2 > n^2$. So, we get $t(G) < 2n - 1 + ((k - 1 - n^2)/n) = n - 1 + (k - 1/n) < n$. By Corollary 1, we know $\lambda_i > n > t(G)$ for $i = 1, 2, \dots, n - 1$, and $\lambda_n = 0$. $DLE(K_{u,n_1,n_2,\dots,n_k}) = (1/n) \sum_{i=1}^n |\lambda_i(G) - t(G)| = ((\sum_{i=1}^{n-1} 1^{n-1} [\lambda_i(G) - t(G)] + t(G))/n) = (\sum_{i=1}^n \lambda_i(G) + (2 - n)t(G)/n) = (2t(G)/n)$ since $\sum_{i=1}^n \lambda_i(G)$ is equal to the trail of $\mathcal{L}(G)$, i.e.,

$\sum_{i=1}^n \lambda_i(G) = \sum_{i=1}^n \text{Tr}_G(v_i)$. So, we get $DLE(K_{u,n_1,n_2,\dots,n_k}) = (2/n)[2n - 1 + (1/n)(k - 1 - \sum_{i=1}^k 1^k n_i^2)]$. \square

4. Maximum Distance Laplacian Spectral Radius of Clique Trees

Lemma 4. *Let H be a connected graph and S be a clique tree with $\text{diam}(S) = d$. Suppose $\mathcal{P}_{n_1,n_2,\dots,n_d}$ is a clique path of S with cliques $K_{n_1}, K_{n_2}, \dots, K_{n_d}$ and $V(K_{n_i}) \cap V(K_{n_{i+1}}) = v_i$ for $i = 1, 2, \dots, d - 1$. Let H_t be the graph obtained by identifying a vertex v of H and a vertex u of K_{n_t} , where $2 \leq t \leq d - 1$. Then, $\lambda_1(H_d) > \lambda_1(H_t)$ or $\lambda_1(H_1) > \lambda_1(H_t)$.*

Proof. By Lemma 2, we may assume $u \neq v_{t-1}$ or $u \neq v_t$ for $2 \leq t \leq d - 1$. Denote the component of $S - v_{t-1}$ which contains vertex v_{t-2} by \mathcal{S}_1 and the component of $S - v_t$ which contains vertex v_{t+1} by \mathcal{S}_2 . Let $S_1 = V(\mathcal{S}_1)$, $S_2 = V(\mathcal{S}_2)$, and $S_3 = V(S) \setminus (V(\mathcal{S}_1) \cup V(\mathcal{S}_2))$. Suppose x is a Perron eigenvector of $\mathcal{L}(H_t)$ corresponding to $\lambda_1(H_t)$. In the following, we will first prove $\lambda_1(H_{t+1}) > \lambda_1(H_t)$ or $\lambda_1(H_{t-1}) > \lambda_1(H_t)$.

Case 1: $\sum_{h \in V(H) \setminus \{v\}} \{v\} \sum_{\omega \in S_1} (x_\omega - x_h)^2 \geq \sum_{h \in V(H) \setminus \{v\}} \sum_{\omega \in S_2} (x_\omega - x_h)^2$. From H_t to H_{t+1} , we have

$$d_{H_t}(\omega, h) - d_{H_{t+1}}(\omega, h) = \begin{cases} -1, & \omega \in S_1 \cup S_3 \setminus \{v_t\}, h \in V(H) \setminus \{v\}, \\ 1, & \omega \in S_2, h \in V(H) \setminus \{v\}, \\ 0, & \text{otherwise,} \end{cases}$$

$$\lambda_1(H_{t+1}) - \lambda_1(H_t) \geq x^T (\mathcal{L}(H_{t+1}) - \mathcal{L}(H_t))x$$

$$= \sum_{h \in V(H) \setminus \{v\}} \left[\sum_{\omega \in S_1 \cup S_3 \setminus \{v_t\}} (x_\omega - x_h)^2 - \sum_{\omega \in S_2} (x_\omega - x_h)^2 \right]$$

$$= \sum_{h \in V(H) \setminus \{v\}} \left[\sum_{\omega \in S_1} (x_\omega - x_h)^2 + \sum_{\omega \in S_3 \setminus \{v_t\}} (x_\omega - x_h)^2 - \sum_{\omega \in S_2} (x_\omega - x_h)^2 \right]$$

$$\geq \sum_{h \in V(H) \setminus \{v\}} \left[\sum_{\omega \in S_1} (x_\omega - x_h)^2 - \sum_{\omega \in S_2} (x_\omega - x_h)^2 \right]$$

$$\geq 0.$$

Thus, $\lambda_1(H_{t+1}) \geq \lambda_1(H_t)$.

In the following, we will prove $\lambda_1(H_{t+1}) > \lambda_1(H_t)$. If $\lambda_1(H_{t+1}) = \lambda_1(H_t)$, then $\sum_{h \in V(H) \setminus \{v\}} \sum_{\omega \in S_3 \setminus \{v_t\}} (x_\omega - x_h)^2 = 0$, which implies $x_\omega = x_h$ for any $\omega \in S_3 \setminus \{v_t\}$, $h \in V(H) \setminus \{v\}$, and x is also a Perron eigenvector of $\mathcal{L}(H_{t+1})$ corresponding to $\lambda_1(H_{t+1})$. For arbitrary $\omega_1 \in S_1$, from the eigenequations of H_{t+1} and H_t at ω_1 , we have

$$\lambda_1(H_{t+1})x_{\omega_1} = \sum_{h \in V(H_{t+1})} d_{H_{t+1}}(\omega_1, h)(x_{\omega_1} - x_h)$$

$$= \sum_{h \in V(H_t)} d_{H_t}(\omega_1, h)(x_{\omega_1} - x_h)$$

$$+ \sum_{h \in V(H) \setminus \{v\}} (x_{\omega_1} - x_h)$$

$$= \lambda_1(H_t)x_{\omega_1} + \sum_{h \in V(H) \setminus \{v\}} (x_{\omega_1} - x_h).$$

So, we have $\sum_{h \in V(H) \setminus \{v\}} (x_{\omega_1} - x_h) = 0$. Similarly, for arbitrary $\omega_2 \in S_2$ and $\omega_3 \in S_3 \setminus \{v_t\}$, we have $\sum_{h \in V(H) \setminus \{v\}} (x_{\omega_2} - x_h) = 0$ and $\sum_{h \in V(H) \setminus \{v\}} (x_{\omega_3} - x_h) = 0$. Then, we have $x_\omega = x_w$ for any $\omega, w \in V(H_t) \setminus \{v_t\}$. Since $x^T \mathbf{1}_{|V(H_t)|} = 0$, we have $(|V(H_t)| - 1)x_{v_1} + x_{v_t} = 0$, which implies $x_{v_1} \neq 0$ and $x_{v_t} \neq 0$.

From the eigenequation of H_t at v_1 and v_2 , we have $0 = \lambda_1(H_t)x_{v_1} - \lambda_1(H_t)x_{v_2} = \sum_{h \in V(H) \setminus \{v\}} (x_{v_1} - x_h) + x_{v_t} = x_{v_t}$, which is a contradiction.

Up to now, we have proved $\lambda_1(H_{t+1}) > \lambda_1(H_t)$.

Case 2: $\sum_{h \in V(H) \setminus \{v\}} \sum_{\omega \in S_1} (x_\omega - x_h)^2 < \sum_{h \in V(H) \setminus \{v\}} \sum_{\omega \in S_2} (x_\omega - x_h)^2$.

From H_t to H_{t-1} , we have

$$d_{H_t}(\omega, h) - d_{H_{t-1}}(\omega, h) = \begin{cases} -1, & \omega \in S_2 \cup S_3 \setminus \{v_{t-1}\}, h \in V(H) \setminus \{v\}, \\ 1, & \omega \in S_1, h \in V(H) \setminus \{v\}, \\ 0, & \text{otherwise.} \end{cases} \quad (12)$$

Then, we have

$$\begin{aligned} \lambda_1(H_{t-1}) - \lambda_1(H_t) &\geq x^T (\mathcal{L}(H_{t-1}) - \mathcal{L}(H_t))x \\ &= \sum_{h \in V(H) \setminus \{v\}} \left[\sum_{\omega \in S_2} (x_\omega - x_h)^2 + \sum_{\omega \in S_3 \setminus \{v_{t-1}\}} (x_\omega - x_h)^2 - \sum_{\omega \in S_1} (x_\omega - x_h)^2 \right] \\ &\geq \sum_{h \in V(H) \setminus \{v\}} \left[\sum_{\omega \in S_2} (x_\omega - x_h)^2 - \sum_{\omega \in S_1} (x_\omega - x_h)^2 \right] \\ &> 0. \end{aligned} \quad (13)$$

Thus, $\lambda_1(H_{t-1}) > \lambda_1(H_t)$.

In the following, we will prove $\lambda_1(H_d) > \lambda_1(H_t)$ or $\lambda_1(H_1) > \lambda_1(H_t)$.

If $\lambda_1(H_{t+1}) > \lambda_1(H_t)$, we may denote the component of $S - v_t$ which contains vertex v_{t-1} by \mathcal{S}'_1 and the component of $S - v_{t+1}$ which contains vertex v_{t+2} by \mathcal{S}'_2 . Let $\mathcal{S}'_1 = V(\mathcal{S}'_1)$, $\mathcal{S}'_2 = V(\mathcal{S}'_2)$, and $\mathcal{S}'_3 = V(S) \setminus (V(\mathcal{S}'_1) \cup V(\mathcal{S}'_2))$. Let x' be a Perron eigenvector of $\mathcal{L}(H_{t+1})$ corresponding to $\lambda_1(H_{t+1})$. If $\sum_{h \in V(H) \setminus \{v\}} \sum_{\omega \in \mathcal{S}'_1} (x'_\omega - x'_h)^2 < \sum_{h \in V(H) \setminus \{v\}} \sum_{\omega \in \mathcal{S}'_2} (x'_\omega - x'_h)^2$, then $\lambda_1(H_t) - \lambda_1(H_{t+1}) \geq \sum_{h \in V(H) \setminus \{v\}} [\sum_{\omega \in \mathcal{S}'_2} (x'_\omega - x'_h)^2 - \sum_{\omega \in \mathcal{S}'_1} (x'_\omega - x'_h)^2]$, and we can get $\lambda_1(H_t) > \lambda_1(H_{t+1})$, which is a contradiction. So, we have $\sum_{h \in V(H) \setminus \{v\}} \sum_{\omega \in \mathcal{S}'_1} (x'_\omega - x'_h)^2 \geq \sum_{h \in V(H) \setminus \{v\}} \sum_{\omega \in \mathcal{S}'_2} (x'_\omega - x'_h)^2$. Then, we have $\lambda_1(H_{t+2}) - \lambda_1(H_{t+1}) \geq \sum_{h \in V(H) \setminus \{v\}} [\sum_{\omega \in \mathcal{S}'_1} (x'_\omega - x'_h)^2 - \sum_{\omega \in \mathcal{S}'_2} (x'_\omega - x'_h)^2] \geq 0$, similar to case 1, and we can get the equal sign in the above inequality does not hold. So, we have $\lambda_1(H_{t+2}) > \lambda_1(H_{t+1})$. Repeating the above procedure, we can get $\lambda_1(H_d) > \dots > \lambda_1(H_{t+2}) > \lambda_1(H_{t+1}) > \lambda_1(H_t)$.

Similarly, if $\lambda_1(H_{t-1}) > \lambda_1(H_t)$, we can prove $\lambda_1(H_1) > \dots > \lambda_1(H_{t-2}) > \lambda_1(H_{t-1}) > \lambda_1(H_t)$. \square

Theorem 4. Among all clique trees with n vertices and k cliques, the graph attaining the maximum distance Laplacian spectral radius is $\mathcal{P}_{m, 2, \dots, 2, n-m-k+3}$ for some $m \geq 3$.

Proof. Let G be the graph with maximum distance Laplacian spectral radius among all clique trees with n vertices and k cliques. By Lemma 4, we get $G = \mathcal{P}_{n_1, n_2, \dots, n_k}$. Let $V(K_{n_i}) \cap V(K_{n_{i+1}}) = v_i$ for $i = 1, 2, \dots, k-1$. If $k \leq 2$, the result holds. Next, we may assume $k \geq 3$. Suppose there exists some $2 \leq t \leq k$ such that $n_t \geq 3$. Denote the component of $G - v_{t-1}$ which contains vertex v_{t-2} by G_1 and the component of $G - v_t$ which contains vertex v_{t+1} by G_2 . Let $S_1 = V(G_1)$, $S_2 = V(G_2)$, and $S_3 = V(G) \setminus (V(G_1) \cup V(G_2))$, i.e., $S_3 = V(K_{n_t})$. Let

$$\begin{aligned} G^{t-1} &= G - \{vv_t | v \in V(K_{n_t}) \setminus \{v_{t-1}, v_t\}\} + \{uv | u \in V(K_{n_{t-1}}) \setminus \{v_{t-1}\}, v \in V(K_{n_t}) \setminus \{v_{t-1}, v_t\}\}, \\ G^{t+1} &= G - \{v_{t-1}v | v \in V(K_{n_t}) \setminus \{v_{t-1}, v_t\}\} + \{uv | u \in V(K_{n_{t-1}}) \setminus \{v_t\}, v \in V(K_{n_t}) \setminus \{v_{t-1}, v_t\}\}, \end{aligned} \quad (14)$$

i.e., $G^{t-1} = \mathcal{P}_{n_1, \dots, n_{t-2}, n_{t-1}+n_t-2, n_{t+1}, \dots, n_k}$ and $G^{t+1} = \mathcal{P}_{n_1, \dots, n_{t-1}, 2, n_{t+1}+n_t-2, n_{t+2}, \dots, n_k}$. Suppose x is a Perron eigenvector of $\mathcal{L}(G)$ corresponding to $\lambda_1(G)$. In the following, we will first prove $\lambda_1(G^{t-1}) > \lambda_1(G)$ or $\lambda_1(G^{t+1}) > \lambda_1(G)$.

Case 1: $\sum_{\omega \in S_2} \sum_{h \in S_3 \setminus \{v_{t-1}, v_t\}} (x_\omega - x_h)^2 \geq \sum_{\omega \in S_1} \sum_{h \in S_3 \setminus \{v_{t-1}, v_t\}} (x_\omega - x_h)^2$.

From G to G^{t-1} , we have

$$\begin{aligned}
 d_G(\omega, h) - d_{G^{t-1}}(\omega, h) &= \begin{pmatrix} -1, & \omega \in S_2 \cup \{v_t\}, h \in S_3 \setminus \{v_{t-1}, v_t\}, \\ 1, & \omega \in S_1, h \in S_3 \setminus \{v_{t-1}, v_t\}, \\ 0, & \text{otherwise.} \end{pmatrix} \\
 \lambda_1(G^{t-1}) - \lambda_1(G) &\geq x^T(\mathcal{L}(G^{t-1}) - \mathcal{L}(G))x \\
 &= \sum_{h \in S_3 \setminus \{v_{t-1}, v_t\}} \left[\sum_{\omega \in S_2 \cup \{v_t\}} (x_\omega - x_h)^2 - \sum_{\omega \in S_1} (x_\omega - x_h)^2 \right] \\
 &= \sum_{h \in S_3 \setminus \{v_{t-1}, v_t\}} \left[\sum_{\omega \in S_2} (x_\omega - x_h)^2 + (x_{v_t} - x_h)^2 - \sum_{\omega \in S_1} (x_\omega - x_h)^2 \right] \\
 &\geq \sum_{h \in S_3 \setminus \{v_{t-1}, v_t\}} \left[\sum_{\omega \in S_2} (x_\omega - x_h)^2 - \sum_{\omega \in S_1} (x_\omega - x_h)^2 \right] \\
 &\geq 0,
 \end{aligned} \tag{15}$$

which implies $\lambda_1(G^{t-1}) \geq \lambda_1(G)$. Similar to Case 1 of Lemma 4, we can get the equal sign in the above inequality does not hold. So, we have $\lambda_1(G^{t-1}) \geq \lambda_1(G)$.

Case 2: $\sum_{\omega \in S_2} \sum_{h \in S_3 \setminus \{v_{t-1}, v_t\}} (x_\omega - x_h)^2 < \sum_{\omega \in S_1} \sum_{h \in S_3 \setminus \{v_{t-1}, v_t\}} (x_\omega - x_h)^2$.
Then, we have

$$\begin{aligned}
 \lambda_1(G^{t+1}) - \lambda_1(G) &\geq x^T(\mathcal{L}(G^{t+1}) - \mathcal{L}(G))x \\
 &= \sum_{h \in S_3 \setminus \{v_{t-1}, v_t\}} \left[\sum_{\omega \in S_1 \cup \{v_{t-1}\}} (x_\omega - x_h)^2 - \sum_{\omega \in S_2} (x_\omega - x_h)^2 \right] \\
 &= \sum_{h \in S_3 \setminus \{v_{t-1}, v_t\}} \left[\sum_{\omega \in S_1} (x_\omega - x_h)^2 + (x_{v_{t-1}} - x_h)^2 - \sum_{\omega \in S_2} (x_\omega - x_h)^2 \right] \\
 &\geq \sum_{h \in S_3 \setminus \{v_{t-1}, v_t\}} \left[\sum_{\omega \in S_1} (x_\omega - x_h)^2 - \sum_{\omega \in S_2} (x_\omega - x_h)^2 \right] \\
 &> 0.
 \end{aligned} \tag{16}$$

Thus, we have $\lambda_1(G^{t+1}) > \lambda_1(G)$.

Doing the above graph transformations until $n_2 = n_3 = \dots = n_{k-1} = 2$, we get G as $\mathcal{P}_{m, 2, \dots, 2, n-m-k+3}$ for some $m \geq 3$. \square

5. Conclusion

This paper mainly determines the extremal graphs with maximum and minimum distance Laplacian spectral radius among all clique trees with n vertices and k cliques. Moreover, we get the distance Laplacian energies of all the clique stars with n vertices and k cliques. Based on our results, we conjecture that the line graphs of S_n^+ and $K_{i_n, 3}$ are the unique graphs with minimum and maximum distance Laplacian spectral radius among all the line graphs of unicyclic graphs, respectively, where S_n^+ is the graph obtained by adding an edge to the star $K_{1, n-1}$ of

order n and $K_{i_n, 3}$ is the graph obtained by adding an edge between a vertex of a triangle and a terminal vertex of a path on $n - 3$ vertices. Moreover, we can study the distance Laplacian spectral radius of diclique trees in the future.

Data Availability

No data were used to support this study.

Conflicts of Interest

The authors declare that they have no conflicts of interest.

Acknowledgments

This work was supported by the NSFC (grant nos. 11501491, 11671347, and 61771019).

References

- [1] A. E. Brouwer and W. H. Haemers, *Spectra of Graphs*, Springer, New York, NY, USA, 2012.
- [2] M. Aouchiche and P. Hansen, “Two Laplacians for the distance matrix of a graph,” *Linear Algebra and Its Applications*, vol. 439, no. 1, pp. 21–33, 2013.
- [3] R. Xing and B. Zhou, “On the distance and distance signless Laplacian spectral radii of bicyclic graphs,” *Linear Algebra and Its Applications*, vol. 439, no. 12, pp. 3955–3963, 2013.
- [4] M. Aouchiche and P. Hansen, “Some properties of the distance Laplacian eigenvalues of a graph,” *Les Czechoslovak Mathem Atical Journal*, vol. 64, no. 139, pp. 751–761, 2014.
- [5] H. Lin and B. Zhou, “On the distance Laplacian spectral radius of graphs,” *Linear Algebra and Its Applications*, vol. 475, pp. 265–275, 2015.
- [6] H. Lin and B. Zhou, “The changes in distance Laplacian spectral radius of graphs resulting from graft transformations,” *Discrete Applied Mathematics*, vol. 219, pp. 147–157, 2017.
- [7] A. Niu, D. Fan, and G. Wang, “On the distance Laplacian spectral radius of bipartite graphs,” *Discrete Applied Mathematics*, vol. 186, pp. 207–213, 2015.
- [8] D. D. Fan, A. H. Niu, and G. P. Wang, “The bicyclic graph with the minimum distance Laplacian spectral radius,” *Journal of Engineering Mathematics*, vol. 37, pp. 121–130, 2020.
- [9] H. Y. Lin and B. Zhou, “The distance Laplacian spectral radius of unicyclic graphs,” *Mathematics Combinatorics*, vol. 45, pp. 35–46, 2017.
- [10] S.-Y. Cui, J.-X. He, and G.-X. Tian, “The generalized distance matrix,” *Linear Algebra and Its Applications*, vol. 563, p. 1, 2019.
- [11] A. Alhevaz, M. Baghipur, H. A. Ganie, and Y. L. Shang, “On the generalized distance energy of graphs,” *Mathematics*, vol. 8, no. 17, 2019.
- [12] H. Q. Lin and S. Drury, “The distance spectrum of complements of trees,” *Linear Algebra and Its Applications*, vol. 530, pp. 185–201, 2017.
- [13] A. Alhevaz, M. Baghipur, H. A. Ganie, and Y. Shang, “Bounds for the generalized distance eigenvalues of a graph,” *Symmetry*, vol. 11, no. 12, p. 1529, 2019.
- [14] A. Alhevaz, M. Baghipur, H. A. Ganie, and Y. L. Shang, “The generalized distance spectrum of the join of graphs,” *Symmetry*, vol. 12, no. 169, 2020.
- [15] Y. Shang, “Distance estrada index of random graphs,” *Linear and Multilinear Algebra*, vol. 63, no. 3, pp. 466–471, 2015.
- [16] J. S. Yang and L. H. Y.I. Gutman, “Bounds on the distance Laplacian energy of graphs,” *Kragujevac Journal of Mathematics*, vol. 37, no. 2, pp. 245–255, 2013.
- [17] K. C. Das, M. Aouchiche, and P. Hansen, “On (distance) Laplacian energy and (distance) signless Laplacian energy of graphs,” *Discrete Applied Mathematics*, vol. 243, pp. 172–185, 2018.

Research Article

First General Zagreb Index of Generalized F -sum Graphs

H. M. Awais,¹ Muhammad Javaid ¹ and Akbar Ali ²

¹Department of Mathematics, School of Science, University of Management and Technology, Lahore, Pakistan

²Department of Mathematics, Faculty of Science, University of Ha'il, Ha'il, Saudi Arabia

Correspondence should be addressed to Akbar Ali; akbarali.maths@gmail.com

Received 14 May 2020; Accepted 10 November 2020; Published 9 December 2020

Academic Editor: Luisa Di Paola

Copyright © 2020 H. M. Awais et al. This is an open access article distributed under the Creative Commons Attribution License, which permits unrestricted use, distribution, and reproduction in any medium, provided the original work is properly cited.

The first general Zagreb (FGZ) index (also known as the general zeroth-order Randić index) of a graph G can be defined as $M^\gamma(G) = \sum_{uv \in E(G)} [d_G^{c-1}(u) + d_G^{c-1}(v)]$, where γ is a real number. As $M^\gamma(G)$ is equal to the order and size of G when $\gamma = 0$ and $\gamma = 1$, respectively, γ is usually assumed to be different from 0 to 1. In this paper, for every integer $\gamma \geq 2$, the FGZ index M^γ is computed for the generalized F -sums graphs which are obtained by applying the different operations of subdivision and Cartesian product. The obtained results can be considered as the generalizations of the results appeared in (IEEE Access; 7 (2019) 47494–47502) and (IEEE Access 7 (2019) 105479–105488).

1. Introduction

Graph theory concepts are being utilized to model and study the several problems in different fields of science, including chemistry and computer science. A topological index (TI) of a (molecular) graph is a numeric quantity that remained unchanged under graph isomorphism [1,2]. Many topological indices have found applications in chemistry, especially in the quantitative structure-activity/property relationships studies; for detail, see [3–13].

Wiener index is the first TI introduced by Harry Wiener in 1947, when he was working on the boiling point of paraffin [14]. In 1972, Trinajstić and Gutman [15] obtained a formula concerning the total energy of π electrons of molecules where the sum of square of valences of the vertices of a molecular structure was appeared. This sum is nowadays known as the first Zagreb index. In this paper, we are concerned with a generalized version of the first Zagreb index, known as the general first Zagreb index as well as the general zeroth-order Randić index.

There are several operations in graph theory such as product, complement, addition, switching, subdivision, and deletion. In many cases, graph operations may be helpful in finding graph quantities of more complicated graphs by considering the less complicated ones. In chemical graph

theory, by using different graph operations, one can develop large molecular structures from the simple and basic structures. Recently, many classes of molecular structures are studied with the assistance of graph operations.

In 2007, Yan et al. [6] listed the five subdivision operations with the help of their vertices and edges. They also discussed the different features of Wiener index of graphs under these operations. After that, Eliasi and Taeri [16] introduced the F_1 -sum graphs $\Gamma_{1+F_1}\Gamma_2$ with the assistance of Cartesian product on graphs $F_1(\Gamma_1)$ and Γ_2 , where $F_1(\Gamma_1)$ is obtained by applying the subdivision operations S_1, R_1, Q_1 , and T_1 . They also defined the Wiener indices of these resulting graphs $\Gamma_{1+S_1}\Gamma_2, \Gamma_{1+R_1}\Gamma_2, \Gamma_{1+Q_1}\Gamma_2$, and $\Gamma_{1+T_1}\Gamma_2$. Later on, Deng et al. [17] calculated the 1st and 2nd Zagreb topological indices, and Imran and Akhtar [18] calculated the forgotten topological index of the F_1 -sums graph. In 2019, Liu et al. [19] computed the first general Zagreb index of F_1 -sums graphs.

Recently, Liu et al. [20] introduced the generalized version of the aforesaid subdivided operations of graphs denoted by S_k, R_k, Q_k , and T_k , where $k \geq 1$ is counting number. They also defined the generalized F -sums graphs using these generalized operations and calculated their 1st and 2nd Zagreb indices. In the present work, we compute the 1st general Zagreb index of the generalized F -sums graphs

$\Gamma_{1+F_k}\Gamma_2$ for $F_k \in \{S_k, R_k, Q_k, T_k\}$. The remaining work is arranged as follows: Section 2 contains some basic definitions, Section 3 contains the key outcomes, and Section 4 contains the some particular applications. Conclusions of the obtained results are presented in Section 5.

2. Preliminaries

Let $\Gamma = (V(\Gamma), E(\Gamma))$ be a simple graph having $|V(\Gamma)|$ the order and $|E(\Gamma)|$ the size of a graph, where $V(\Gamma)$ is considered as node set and $E(\Gamma) \subseteq V(\Gamma) \times V(\Gamma)$ is a bond set. Every vertex is considered as an atom in a graph, and bonding within the two atoms is known as edge. The valency or degree of any node is the number of total edges which are incident to the node. Now, few useful TI's are explained given below:

Definition 1. If Γ be a connected graph, then the 1st and 2nd Zagreb topological indices as

$$\begin{aligned} M_1(\Gamma) &= \sum_{uv \in V(\Gamma)} [d_\Gamma(u) + d_\Gamma(v)], \\ M_2(\Gamma) &= \sum_{uv \in E(\Gamma)} [d_\Gamma(u)d_\Gamma(v)]. \end{aligned} \quad (1)$$

These two descriptors of the graph were introduced by Trinajstić and Gutman [15]. Such type of TI's have been utilized to discuss the QSAR/QSPR of the different chemical structures such as chirality, complexity, hetero-system, ZE-isomers, π electron energy, and branching [9, 10].

Definition 2. If R is the real number, $\gamma \in R - \{0, 1\}$, and Γ be a connected graph, so the 1st general Zagreb topological index is given as

$$M^\gamma(\Gamma) = \sum_{uv \in E(\Gamma)} [d_\Gamma^{\gamma-1}(u) + d_\Gamma^{\gamma-1}(v)]. \quad (2)$$

Definition 3. If R is the real number, $\gamma \in R$, and Γ be a connected graph, so the general Randić is given as

$$R_\gamma(\Gamma) = \sum_{uv \in E(\Gamma)} [d_G(u)d_G(v)]^\gamma, \quad (3)$$

where $R_{-(1/2)}$ is considered as the classical Randić connectivity topological index.

The generalized F -sums graph is defined in [20] as follows:

- (i) $S_k(G)$ graph is obtained by inserting k vertices in each edge of G .
- (ii) $R_k(G)$ is obtained from $S_k(G)$ by joining the old vertices which are adjacent G .
- (iii) $Q_k(G)$ is obtained from $S_k(G)$ by joining the new vertices lying on edge to the corresponding new vertices of other edge, if these edges have some common vertex in G .
- (iv) $T_k(G)$ is union of $R_k(G)$ and $Q_k(G)$ graphs. For further details, see Figure 1.

Definition 4. If Γ_1 & Γ_2 be two connected molecular structures, $F_k \in \{S_k, R_k, Q_k, T_k\}$ and $F_k(\Gamma_1)$ be a structure obtained after using F_k on Γ_1 with bonds (edges) $E(F_k(\Gamma_1))$ and nodes (vertices) $V(F_k(\Gamma_1))$. So, the generalized F -sums graph $(\Gamma_{1+F_k}\Gamma_2)$ is a structure with nodes:

$$\begin{aligned} V(\Gamma_{1+F_k}\Gamma_2) &= V(F_k(\Gamma_1)) \times V(\Gamma_2), \\ &= (V(\Gamma_1) \cup E(\Gamma_1)) \times V(\Gamma_2), \end{aligned} \quad (4)$$

in such a way two nodes (a_1, b_1) & (a_2, b_2) of $V(\Gamma_{1+F_k}\Gamma_2)$ are adjacent if $[a_1 = a_2 \in V(\Gamma_1) \& (b_1, b_2) \in E(\Gamma_2)]$ or $[b_1 = b_2 \in V(\Gamma_2) \& (a_1, a_2) \in E(F_k(\Gamma_1))]$. For more details, see Figures 2 and 3.

Lemma 1. For $F_k \in \{S_k, R_k, Q_k, T_k\}$ and $(x, y) \in \Gamma_{1+F_k}\Gamma_2$, the degree of (x, y) in $\Gamma_{1+F_k}\Gamma_2$ is

$$\begin{aligned} \text{(i)} \quad d(d_{\Gamma_1+S_k\Gamma_2}(x, y)) &= \begin{cases} d_{\Gamma_1}(x) + d_{\Gamma_2}(y), & \text{if } x \in V(\Gamma_1) \wedge y \in V(\Gamma_2), \\ 2, & \text{if } x \in V(S_k(\Gamma_1)) - V(\Gamma_1) \wedge y \in V(\Gamma_2), \end{cases} \\ \text{(ii)} \quad d(d_{\Gamma_1+R_k\Gamma_2}(x, y)) &= \begin{cases} d_{R_k(\Gamma_1)}(x) + d_{\Gamma_2}(y), & \text{if } x \in V(\Gamma_1) \wedge y \in V(\Gamma_2), \\ 2, & \text{if } x \in V(S_k(\Gamma_1)) - V(\Gamma_1) \wedge y \in V(\Gamma_2), \end{cases} \\ \text{(iii)} \quad d(d_{\Gamma_1+Q_k\Gamma_2}(x, y)) &= \begin{cases} d_{\Gamma_1}(x) + d_{\Gamma_2}(y), & \text{if } x \in V(\Gamma_1) \wedge y \in V(\Gamma_2), \\ d_{Q_k(\Gamma_1)}(x), & \text{if } x \in V(Q_k(\Gamma_1)) - V(\Gamma_1) \wedge y \in V(\Gamma_2), \end{cases} \\ \text{(iv)} \quad d(d_{\Gamma_1+T_k\Gamma_2}(x, y)) &= \begin{cases} d_{T_k(\Gamma_1)}(x) + d_{\Gamma_2}(y), & \text{if } x \in V(\Gamma_1) \wedge y \in V(\Gamma_2), \\ d_{T_k(\Gamma_1)}(x), & \text{if } x \in V(T_k(\Gamma_1)) - V(\Gamma_1) \wedge y \in V(\Gamma_2). \end{cases} \end{aligned} \quad (5)$$

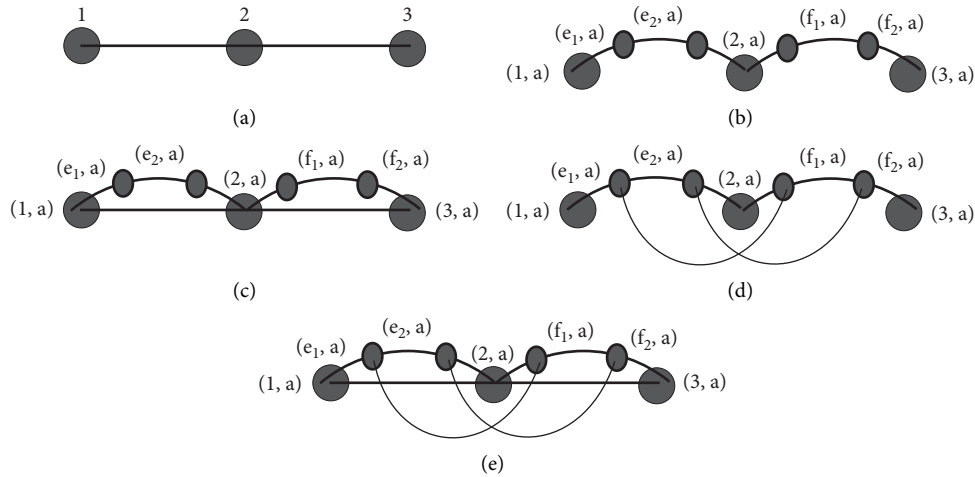


FIGURE 1: (a) Γ , (b). $S_2(\Gamma)$, (c) $R_2(\Gamma)$, (d) $Q_2(\Gamma)$, and (e) $T_2(\Gamma)$.

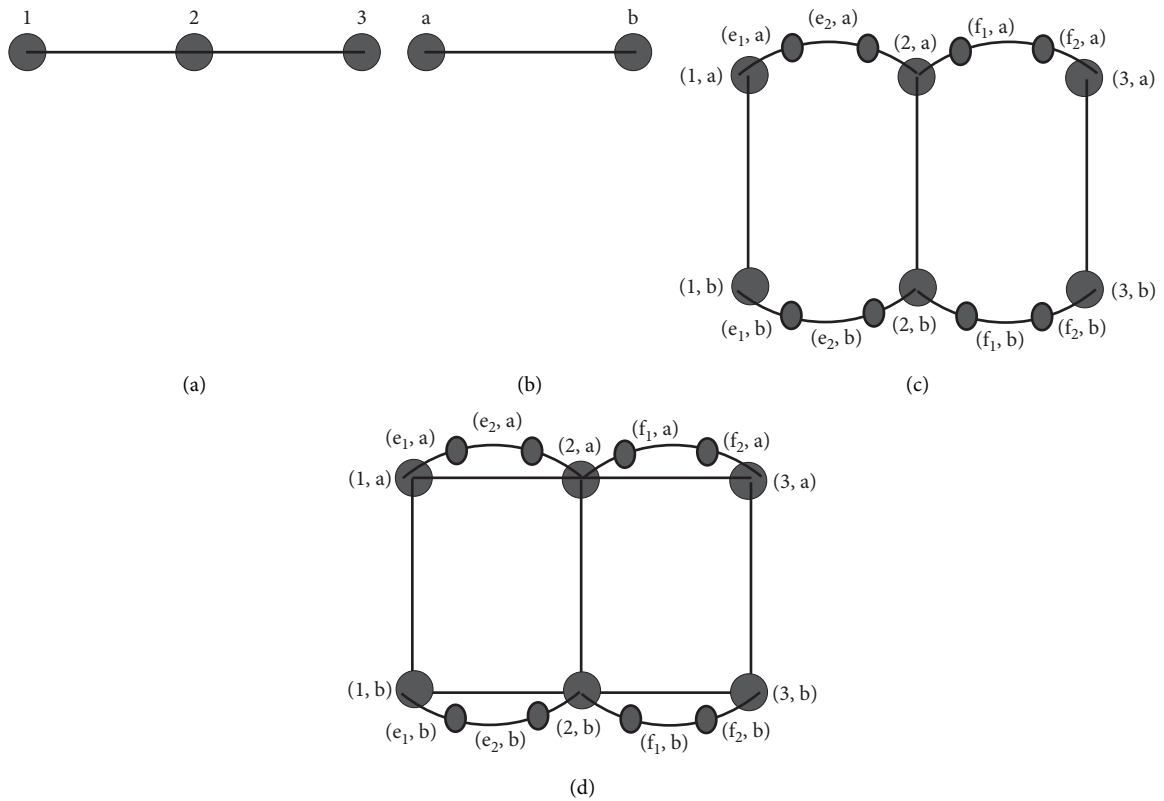


FIGURE 2: (a) $\Gamma_1 \cong P_3$. (b) $\Gamma_2 \cong P_2$. (c) $\Gamma_{1+S_2}\Gamma_2$. (d) $\Gamma_{1+R_2}\Gamma_2$.

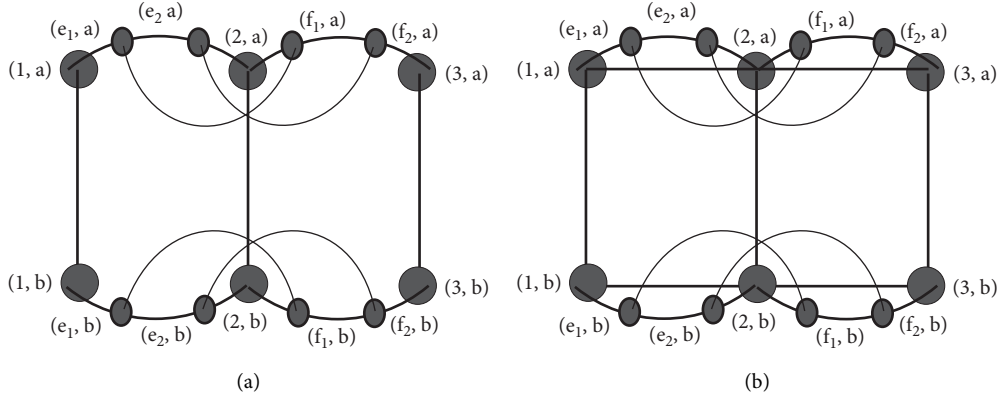
3. Main Results

The main results of FGZ index of the generalized F -sum graphs are presented in this section.

Theorem 1. Let Γ_1 and Γ_2 be two simple graphs and $\gamma \in N - \{0, 1\}$. The FGZ index of the generalized S -sum graph $\Gamma_{1+S_k}\Gamma_2$ is

$$M^\gamma(\Gamma_{1+S_k}\Gamma_2) = \sum_{i=0}^{\alpha} \binom{\alpha}{i} (M_{\Gamma_1}^{\alpha-i})(M_{\Gamma_2}^{i+1}) + n_{\Gamma_2} M_{S_k}^\gamma(\Gamma_1) + \sum_{i=1}^{\alpha} \binom{\alpha}{i} M_{\Gamma_2}^i M_{\Gamma_1}^{\gamma-i} + 2^{\alpha+1} (k-1) n_{\Gamma_2} e_{\Gamma_1}, \tag{6}$$

where N is the set of natural numbers and $\alpha = \gamma - 1$.

FIGURE 3: (a) $\Gamma_{1+Q_2}\Gamma_2$, (b) $\Gamma_{1+T_2}\Gamma_2$.

Proof. Let

$$M^\gamma(\Gamma_{1+S_k}\Gamma_2) = \sum_{(a,b) \in V(\Gamma_{1+S_k}\Gamma_2)} d_{\Gamma_{1+S_k}\Gamma_2}^\gamma(a, b). \quad (7)$$

For $\alpha = \gamma - 1$, then the above equation is considered as

$$\begin{aligned} M^\gamma(\Gamma_{1+S_k}\Gamma_2) &= \sum_{(a,b)(c,d) \in E(\Gamma_{1+S_k}\Gamma_2)} \left[d_{\Gamma_{1+S_k}\Gamma_2}^\alpha(a, b) + d_{\Gamma_{1+S_k}\Gamma_2}^\alpha(c, d) \right] \\ &= \sum_{a \in V(\Gamma_1)} \sum_{b, d \in E(\Gamma_2)} \left[d_{\Gamma_{1+S_k}\Gamma_2}^\alpha(a, b) + d_{\Gamma_{1+S_k}\Gamma_2}^\alpha(a, d) \right] + \sum_{b \in V(\Gamma_2)} \sum_{a \in E(S_k(\Gamma_1))} \left[d_{\Gamma_{1+S_k}\Gamma_2}^\alpha(a, b) + d_{\Gamma_{1+S_k}\Gamma_2}^\alpha(b, c) \right] \\ &= \sum_{a \in V(\Gamma_1)} \sum_{b, d \in E(\Gamma_2)} \left[d_{\Gamma_{1+S_k}\Gamma_2}^\alpha(a, b) + d_{\Gamma_{1+S_k}\Gamma_2}^\alpha(a, d) \right] + \sum_{b \in V(\Gamma_2)} \sum_{a \in E(S_k(\Gamma_1))} \sum_{a \in V(\Gamma_1), c \in V(S_k(\Gamma_1)) - V(\Gamma_1)} \left[d_{\Gamma_{1+S_k}\Gamma_2}^\alpha(a, b) + d_{\Gamma_{1+S_k}\Gamma_2}^\alpha(b, c) \right] \\ &\quad + \sum_{b \in V(\Gamma_2)} \sum_{a \in E(S_k(\Gamma_1))} \sum_{a, c \in V(S_k(\Gamma_1)) - V(\Gamma_1)} \left[d_{\Gamma_{1+S_k}\Gamma_2}^\alpha(a, b) + d_{\Gamma_{1+S_k}\Gamma_2}^\alpha(b, c) \right]. \end{aligned} \quad (8)$$

For every vertex $a \in V(\Gamma_1)$ and edge $b, d \in E(\Gamma_2)$, then 1st term of (8) will be

$$\begin{aligned} &\sum_{a \in V(\Gamma_1)} \sum_{b, d \in E(\Gamma_2)} \left[d_{\Gamma_{1+S_k}\Gamma_2}^\alpha(a, b) + d_{\Gamma_{1+S_k}\Gamma_2}^\alpha(a, d) \right] \\ &= \sum_{a \in V(\Gamma_1)} \sum_{b, d \in E(\Gamma_2)} \left[\sum_{i=0}^{\alpha} \binom{\alpha}{i} d_{\Gamma_1}^{\alpha-i}(a) d_{\Gamma_2}^i(b) + \sum_{i=0}^{\alpha} \binom{\alpha}{i} d_{\Gamma_1}^{\alpha-i}(a) d_{\Gamma_2}^i(d) \right] \\ &= \sum_{a \in V(\Gamma_1)} \sum_{b, d \in E(\Gamma_2)} \left[\sum_{i=0}^{\alpha} \binom{\alpha}{i} d_{\Gamma_1}^{\alpha-i}(a) [d_{\Gamma_2}^i(b) + d_{\Gamma_2}^i(d)] \right] \\ &= \sum_{a \in V(\Gamma_1)} \left[\sum_{i=0}^{\alpha} \binom{\alpha}{i} d_{\Gamma_1}^{\alpha-i}(a) \right] \left[\sum_{b, d \in E(\Gamma_2)} [d_{\Gamma_2}^i(b) + d_{\Gamma_2}^i(d)] \right] \\ &= \sum_{a \in V(\Gamma_1)} \left[\sum_{i=0}^{\alpha} \binom{\alpha}{i} d_{\Gamma_1}^{\alpha-i}(a) \right] (M_{\Gamma_2}^{i+1}) \\ &= \sum_{i=0}^{\alpha} \binom{\alpha}{i} (M_{\Gamma_1}^{\alpha-i}) (M_{\Gamma_2}^{i+1}). \end{aligned} \quad (9)$$

Since $|E(S_k(\Gamma_1))| = 2|E(\Gamma_1)|$. So, for every $b \in V(\Gamma_2)$ and $ac \in E(S_k(\Gamma_1))$ with $a \in V(\Gamma_1)$, and $c \in V(S_k(\Gamma_1)) - V(\Gamma_1)$; then the 2nd term of (8) is

$$\begin{aligned}
 & \sum_{b \in V(\Gamma_2)} \sum_{ac \in E(S_k(\Gamma_1))} \sum_{a \in V(\Gamma_1), c \in V(S_k(\Gamma_1)) - V(\Gamma_1)} \left[d_{\Gamma_1 + S_k \Gamma_2}^\alpha(a, b) + d_{\Gamma_1 + S_k \Gamma_2}^\alpha(b, c) \right] \\
 &= \sum_{b \in V(\Gamma_2)} \sum_{ac \in E(S_k(\Gamma_1))} \left[d_{\Gamma_1 + S_k \Gamma_2}^\alpha(a, b) + d_{\Gamma_1 + S_k \Gamma_2}^\alpha(b, c) \right] \\
 &= \sum_{b \in V(\Gamma_2)} \sum_{ac \in E(S_k(\Gamma_1))} \left[\sum_{i=0}^{\alpha} \binom{\alpha}{i} d_{S_k(\Gamma_1)}^{\alpha-i}(a) d_{\Gamma_2}^i(b) + d_{S_k(\Gamma_1)}^\alpha(c) \right] \\
 &= \sum_{b \in V(\Gamma_2)} \sum_{ac \in E(S_k(\Gamma_1))} \left[d_{S_k(\Gamma_1)}^\alpha(a) + \sum_{i=0}^{\alpha} \binom{\alpha}{i} d_{S_k(\Gamma_1)}^{\alpha-i}(a) d_{\Gamma_2}^i(b) + d_{S_k(\Gamma_1)}^\alpha(c) \right] \\
 &= \sum_{b \in V(\Gamma_2)} \sum_{ac \in E(S_k(\Gamma_1))} \left[d_{S_k(\Gamma_1)}^\alpha(a) + d_{S_k(\Gamma_1)}^\alpha(c) + \sum_{i=1}^{\alpha} \binom{\alpha}{i} d_{S_k(\Gamma_1)}^{\alpha-i}(a) d_{\Gamma_2}^i(b) \right] \tag{10} \\
 &= \sum_{b \in V(\Gamma_2)} \sum_{ac \in E(S_k(\Gamma_1))} \left[d_{S_k(\Gamma_1)}^\alpha(a) + d_{S_k(\Gamma_1)}^\alpha(c) \right] + \sum_{b \in V(\Gamma_2)} \sum_{ac \in E(S_k(\Gamma_1))} \left[\sum_{i=1}^{\alpha} \binom{\alpha}{i} d_{S_k(\Gamma_1)}^{\alpha-i}(a) d_{\Gamma_2}^i(b) \right] \\
 &= \sum_{b \in V(\Gamma_2)} \left[M_{S_k(\Gamma_1)}^{\alpha+1} \right] + \sum_{i=1}^{\alpha} \binom{\alpha}{i} [M_{\Gamma_2}^i] [M_{\Gamma_1}^{\gamma-i}] \\
 &= n_{\Gamma_2} \left[M_{S_k(\Gamma_1)}^\gamma \right] + \sum_{i=1}^{\alpha} \binom{\alpha}{i} [M_{\Gamma_2}^i] [M_{\Gamma_1}^{\gamma-i}],
 \end{aligned}$$

and the 3rd term of equation (8) will be

$$\sum_{b \in V(\Gamma_2)} \sum_{ac \in E(S_k(\Gamma_1))} \sum_{a, c \in V(S_k(\Gamma_1)) - V(\Gamma_1)} \left[d_{\Gamma_1 + S_k \Gamma_2}^\alpha(a, b) + d_{\Gamma_1 + S_k \Gamma_2}^\alpha(c, b) \right] = \sum_{b \in V(\Gamma_2)} \sum_{ac \in E(S_k(\Gamma_1))} \sum_{a, c \in V(S_k(\Gamma_1)) - V(\Gamma_1)} [2^\alpha + 2^\alpha]. \tag{11}$$

Since in this case $|E(S_k(\Gamma_1))| = (k - 1)e_{\Gamma_1}$, we have

$$= 2^{\alpha+1} (k - 1)n_{\Gamma_2} e_{\Gamma_1}. \tag{12}$$

By using (9), (10), & (12) in (8), we get

$$M^\gamma(\Gamma_1 + S_k \Gamma_2) = \sum_{i=0}^{\alpha} \binom{\alpha}{i} (M_{\Gamma_1}^{\alpha-i}) (M_{\Gamma_2}^{i+1}) + n_{\Gamma_2} M_{S_k(\Gamma_1)}^\beta + \sum_{i=1}^{\alpha} \binom{\alpha}{i} M_{\Gamma_2}^i M_{\Gamma_1}^{\gamma-i} + 2^{\alpha+1} (k - 1)n_{\Gamma_2} e_{\Gamma_1}. \tag{13}$$

Theorem 2. Let Γ_1 and Γ_2 be two simple graphs and $\gamma \in N - \{0, 1\}$. The FGZ index of the generalized R-sum $\Gamma_1 + R_k \Gamma_2$ graph is

$$\begin{aligned}
 M^\gamma(\Gamma_1 + R_k \Gamma_2) &= \sum_{i=0}^{\alpha} \binom{\alpha}{i} 2^{\alpha-i} M_{\Gamma_1}^{\alpha-i} M_{\Gamma_2}^{i+1} + 2 \sum_{i=0}^{\alpha} \binom{\alpha}{i} 2^{\alpha-i} M_{\Gamma_1}^{\gamma-i} M_{\Gamma_2}^i \\
 &+ 2^\alpha e_{\Gamma_1} n_{\Gamma_2} + 2^{\alpha+1} (k - 1)n_{\Gamma_2} e_{\Gamma_1},
 \end{aligned} \tag{14}$$

where N is the set of natural numbers and $\alpha = \gamma - 1$.

Proof. Then by definition, we have,

$$M^\gamma(\Gamma_1 + R_k \Gamma_2) = \sum_{(a,b) \in (V(\Gamma_1 + R_k \Gamma_2))} d_{\Gamma_1 + R_k \Gamma_2}^\gamma(a, b). \tag{15}$$

For $\alpha = \gamma - 1$, the above equation is consider as

$$\begin{aligned}
M^y(\Gamma_1 + R_k \Gamma_2) &= \sum_{(a,b)(c,d) \in (E(\Gamma_1 + R_k \Gamma_2))} \left[d_{\Gamma_1 + R_k \Gamma_2}^\alpha(a, b) + d_{\Gamma_1 + R_k \Gamma_2}^\alpha(c, d) \right] \\
&= \sum_{a \in V(\Gamma_1)} \sum_{bd \in (E(\Gamma_2))} \left[d_{\Gamma_1 + R_k \Gamma_2}^\alpha(a, b) + d_{\Gamma_1 + R_k \Gamma_2}^\alpha(a, d) \right] + \sum_{b \in V(\Gamma_2)} \sum_{ac \in (E(R_k(\Gamma_1)))} \left[d_{\Gamma_1 + R_k \Gamma_2}^\alpha(a, b) + d_{\Gamma_1 + R_k \Gamma_2}^\alpha(b, c) \right] \\
&= \sum_{a \in V(\Gamma_1)} \sum_{bd \in (E(\Gamma_2))} \left[d_{\Gamma_1 + R_k \Gamma_2}^\alpha(a, b) + d_{\Gamma_1 + R_k \Gamma_2}^\alpha(a, d) \right] + \sum_{b \in V(\Gamma_2)} \sum_{ac \in (E(R_k(\Gamma_1)))} \sum_{a, c \in V(\Gamma_1)} \left[d_{\Gamma_1 + R_k \Gamma_2}^\alpha(a, b) + d_{\Gamma_1 + R_k \Gamma_2}^\alpha(b, c) \right] \\
&\quad + \sum_{b \in V(\Gamma_2)} \sum_{ac \in (E(R_k(\Gamma_1)))} \sum_{a \in V(\Gamma_1)} \sum_{c \in V(R_k(\Gamma_1)) - V(\Gamma_1)} \left[d_{\Gamma_1 + R_k \Gamma_2}^\alpha(a, b) + d_{\Gamma_1 + R_k \Gamma_2}^\alpha(b, c) \right] \\
&= \sum_{a \in V(\Gamma_1)} \sum_{bd \in (E(\Gamma_2))} \left[d_{\Gamma_1 + R_k \Gamma_2}^\alpha(a, b) + d_{\Gamma_1 + R_k \Gamma_2}^\alpha(a, d) \right] + \sum_{b \in V(\Gamma_2)} \sum_{ac \in (E(R_k(\Gamma_1)))} \sum_{a, c \in V(\Gamma_1)} \left[d_{\Gamma_1 + R_k \Gamma_2}^\alpha(a, b) + d_{\Gamma_1 + R_k \Gamma_2}^\alpha(b, c) \right] \\
&\quad + \sum_{b \in V(\Gamma_2)} \sum_{ac \in (E(R_k(\Gamma_1)))} \sum_{a \in V(\Gamma_1)} \sum_{c \in V(R_k(\Gamma_1)) - V(\Gamma_1)} \left[d_{\Gamma_1 + R_k \Gamma_2}^\alpha(a, b) + d_{\Gamma_1 + R_k \Gamma_2}^\alpha(b, c) \right] \sum_{b \in V(\Gamma_2)} \\
&\quad \cdot \sum_{ac \in E(R_k(\Gamma_1))} \sum_{a, c \in V(R_k(\Gamma_1)) - V(\Gamma_1)} \left[d_{\Gamma_1 + R_k \Gamma_2}^\alpha(a, b) + d_{\Gamma_1 + R_k \Gamma_2}^\alpha(c, b) \right].
\end{aligned} \tag{16}$$

For every vertex $a \in V(\Gamma_1)$ & edge $bd \in E(\Gamma_2)$, then the 1st term of (16) is

$$\begin{aligned}
\sum_{a \in V(\Gamma_1)} \sum_{bd \in (E(\Gamma_2))} \left[d_{\Gamma_1 + R_k \Gamma_2}^\alpha(a, b) + d_{\Gamma_1 + R_k \Gamma_2}^\alpha(a, d) \right] &= \sum_{a \in V(\Gamma_1)} \sum_{bd \in (E(\Gamma_2))} \left[\left[\sum_{i=0}^{\alpha} \binom{\alpha}{i} d_{R_k(\Gamma_1)}^{\alpha-i}(a) \cdot d_{\Gamma_2}^i(b) \right] + \left[\sum_{i=0}^{\alpha} \binom{\alpha}{i} d_{R_k(\Gamma_1)}^{\alpha-i}(a) \cdot d_{\Gamma_2}^i(d) \right] \right] \\
&= \sum_{i=0}^{\alpha} \binom{\alpha}{i} \sum_{a \in V(\Gamma_1)} d_{R_k(\Gamma_1)}^{\alpha-i}(a) \sum_{bd \in (E(\Gamma_2))} d_{\Gamma_2}^i(b) + \sum_{i=0}^{\alpha} \binom{\alpha}{i} \sum_{a \in V(\Gamma_1)} d_{R_k(\Gamma_1)}^{\alpha-i}(a) \\
&\quad \cdot \sum_{bd \in (E(\Gamma_2))} d_{\Gamma_2}^i(d) \\
&= \sum_{i=0}^{\alpha} \binom{\alpha}{i} \sum_{a \in V(\Gamma_1)} (2d_{\Gamma_1}(a))^{\alpha-i} \sum_{bd \in (E(\Gamma_2))} d_{\Gamma_2}^i(b) + \sum_{i=0}^{\alpha} \binom{\alpha}{i} \sum_{a \in V(\Gamma_1)} (2d_{\Gamma_1}(a))^{\alpha-i} \\
&\quad \cdot \sum_{bd \in (E(\Gamma_2))} d_{\Gamma_2}^i(d) \\
&= \sum_{i=0}^{\alpha} \binom{\alpha}{i} (2)^{\alpha-i} M_{\Gamma_1}^{\alpha-i} \sum_{bd \in (E(\Gamma_2))} [d_{\Gamma_2}^i(b) + d_{\Gamma_2}^i(d)] \\
&= \sum_{i=0}^{\alpha} \binom{\alpha}{i} (2)^{\alpha-i} M_{\Gamma_1}^{\alpha-i} M_{\Gamma_2}^{i+1}.
\end{aligned} \tag{17}$$

For every vertex $b \in V(\Gamma_2)$ & edge $ac \in E(R_k(\Gamma_1))$, then the 2nd term of (16) will be

$$\begin{aligned}
 & \sum_{b \in V(\Gamma_2)} \sum_{ac \in (E(R_k(\Gamma_1)))} \left[d_{\Gamma_1+R_k\Gamma_2}^\alpha(a, b) + d_{\Gamma_1+R_k\Gamma_2}^\alpha(b, c) \right] \\
 &= \sum_{b \in V(\Gamma_2)} \sum_{ac \in (E(R_k(\Gamma_1)))} \left[\left[\sum_{i=0}^{\alpha} \binom{\alpha}{i} d_{R_k(\Gamma_1)}^{\alpha-i}(a) \cdot d_{\Gamma_2}^i(b) \right] + \left[\sum_{i=0}^{\alpha} \binom{\alpha}{i} d_{R_k(\Gamma_1)}^{\alpha-i}(c) \cdot d_{\Gamma_2}^i(b) \right] \right] \\
 &= \sum_{b \in V(\Gamma_2)} \sum_{ac \in (E(R_k(\Gamma_1)))} \left[\sum_{i=0}^{\alpha} \binom{\alpha}{i} d_{\Gamma_2}^i(b) \left[d_{R_k(\Gamma_1)}^{\alpha-i}(a) + d_{R_k(\Gamma_1)}^{\alpha-i}(c) \right] \right] \\
 &= \sum_{ac \in (E(R_k(\Gamma_1)))} \sum_{a, c \in V(\Gamma_1)} \left[\left[\sum_{i=0}^{\alpha} \binom{\alpha}{i} \left[\sum_{b \in V(\Gamma_2)} d_{\Gamma_2}^i(b) \left[d_{R_k(\Gamma_1)}^{\alpha-i}(a) + d_{R_k(\Gamma_1)}^{\alpha-i}(c) \right] \right] \right] \right] \\
 &= \sum_{ac \in (E(R_k(\Gamma_1)))} \sum_{a, c \in V(\Gamma_1)} \left[\left[\sum_{i=0}^{\alpha} \binom{\alpha}{i} M_{\Gamma_2}^i \left[(2d_{\Gamma_1}(a))^{\alpha-i} + (2d_{\Gamma_1}(c))^{\alpha-i} \right] \right] \right] \\
 &= \sum_{ac \in (E(R_k(\Gamma_1)))} \sum_{a, c \in V(\Gamma_1)} \sum_{i=0}^{\alpha} \binom{\alpha}{i} M_{\Gamma_2}^i \left[(2)^{\alpha-i} \left(d_{\Gamma_1}^{\alpha-i}(a) + d_{\Gamma_1}^{\alpha-i}(c) \right) \right] \tag{18} \\
 &= \sum_{i=0}^{\alpha} \binom{\alpha}{i} M_{\Gamma_2}^i \sum_{ac \in (E(R_k(\Gamma_1)))} \sum_{a, c \in V(\Gamma_1)} \left[(2)^{\alpha-i} \left(d_{\Gamma_1}^{\alpha-i}(a) + d_{\Gamma_1}^{\alpha-i}(c) \right) \right] \\
 &= \sum_{i=0}^{\alpha} \binom{\alpha}{i} M_{\Gamma_2}^i \sum_{ac \in (E(R_k(\Gamma_1)))} \sum_{a, c \in V(\Gamma_1)} \left[(2)^{\alpha-i} \left(d_{\Gamma_1}^{\alpha-i}(a) + d_{\Gamma_1}^{\alpha-i}(c) \right) \right] \\
 &= \sum_{i=0}^{\alpha} \binom{\alpha}{i} M_{\Gamma_2}^i (2)^{\alpha-i} \sum_{ac \in (E(R_k(\Gamma_1)))} \sum_{a, c \in V(\Gamma_1)} \left[d_{\Gamma_1}^{\alpha-i}(a) + d_{\Gamma_1}^{\alpha-i}(c) \right] \\
 &= \sum_{i=0}^{\alpha} \binom{\alpha}{i} M_{\Gamma_2}^i (2)^{\alpha-1} \left[M_{\Gamma_1}^{\alpha-i} \right] \\
 &= \sum_{i=0}^{\alpha} \binom{\alpha}{i} M_{\Gamma_2}^i (2)^{\alpha-1} M_{\Gamma_1}^{\alpha-i}.
 \end{aligned}$$

For every vertex $b \in V(\Gamma_2)$ & edge $ac \in E(R_k(\Gamma_1))$, $a \in V(\Gamma_1)$, $c \in V(R_k(\Gamma_1)) - V(\Gamma_1)$. Since we have

$d_{R_k(\Gamma_1)}(a) = 2d_{\Gamma_1}(a) \forall a \in V(\Gamma_1)$ also $d_{R_k(\Gamma_1)}(c) = 2 \forall c \in V(R_k(\Gamma_1)) - V(\Gamma_1)$. So the 3rd term of (16) will be

$$\begin{aligned}
 &= \sum_{b \in V(\Gamma_2)} \sum_{ac \in (E(R_k(\Gamma_1)))} \sum_{a \in V(\Gamma_1)} \sum_{c \in V(R_k(\Gamma_1)) - V(\Gamma_1)} \left[d_{\Gamma_1+R_k\Gamma_2}^\alpha(a, b) + d_{\Gamma_1+R_k\Gamma_2}^\alpha(b, c) \right] \\
 &= \sum_{b \in V(\Gamma_2)} \sum_{ac \in (E(R_k(\Gamma_1)))} \sum_{a \in V(\Gamma_1)} \sum_{c \in V(R_k(\Gamma_1)) - V(\Gamma_1)} \left[\sum_{i=0}^{\alpha} \binom{\alpha}{i} d_{R_k(\Gamma_1)}^{\alpha-i}(a) \cdot d_{\Gamma_2}^i(b) + d_{R_k(\Gamma_1)}^\alpha(c) \right], \tag{19}
 \end{aligned}$$

Here $d_{R_k(\Gamma_1)}^\alpha = 2^\alpha$ and $d_{R_k(\Gamma_1)}^{\alpha-i}(a) = (2d_{\Gamma_1}(a))^{\alpha-i}$:

$$\begin{aligned}
&= \sum_{b \in V(\Gamma_2)} \sum_{ac \in (E(R_k(\Gamma_1)))} \sum_{a \in V(\Gamma_1) c \in V(R_k(\Gamma_1)) - V(\Gamma_1)} \left[\sum_{i=0}^{\alpha} \binom{\alpha}{i} (2d_{\Gamma_1}(a))^{\alpha-i} d_{\Gamma_2}^i(b) + 2^\alpha \right] \\
&= \sum_{b \in V(\Gamma_2)} \sum_{ac \in (E(R_k(\Gamma_1)))} \sum_{a \in V(\Gamma_1) c \in V(R_k(\Gamma_1)) - V(\Gamma_1)} \left[\sum_{i=0}^{\alpha} \binom{\alpha}{i} (2)^{\alpha-i} (d_{\Gamma_1}(a))^{\alpha-i} d_{\Gamma_2}^i(b) + 2^\alpha \right] \\
&= \sum_{i=0}^{\alpha} \binom{\alpha}{i} \left[\sum_{b \in V(\Gamma_2)} \sum_{ac \in (E(R_k(\Gamma_1)))} \sum_{a \in V(\Gamma_1) c \in V(R_k(\Gamma_1)) - V(\Gamma_1)} (2)^{\alpha-i} (d_{\Gamma_1}^{\alpha-i}(a)) d_{\Gamma_2}^i(b) \right. \\
&\quad \left. + \sum_{b \in V(\Gamma_2)} \sum_{ac \in (E(R_k(\Gamma_1)))} \sum_{a \in V(\Gamma_1) c \in V(R_k(\Gamma_1)) - V(\Gamma_1)} 2^\alpha \right] \\
&= \sum_{i=0}^{\alpha} \binom{\alpha}{i} (2)^{\alpha-i} \cdot M_{\Gamma_2}^i \cdot M_{\Gamma_1}^{\gamma-i} + 2^\alpha e_{\Gamma_1} n_{\Gamma_2} \\
&= \sum_{i=0}^{\alpha} \binom{\alpha}{i} (2)^{\alpha-i} \cdot M_{\Gamma_2}^i \cdot M_{\Gamma_1}^{\gamma-i} + 2^\alpha e_{\Gamma_1} n_{\Gamma_2},
\end{aligned} \tag{20}$$

and the 4th term of (5) is

$$\sum_{b \in V(\Gamma_2)} \sum_{ac \in E(R_k(\Gamma_1))} \sum_{a, c \in V(R_k(\Gamma_1)) - V(\Gamma_1)} \left[d_{\Gamma_1 + R_k \Gamma_2}^\alpha(a, b) + d_{\Gamma_1 + R_k \Gamma_2}^\alpha(c, b) \right] = \sum_{b \in V(\Gamma_2)} \sum_{ac \in E(R_k(\Gamma_1))} \sum_{a, c \in V(R_k(\Gamma_1)) - V(\Gamma_1)} [2^\alpha + 2^\alpha]. \tag{21}$$

Since in this case $|E(S_k(\Gamma_1))| = (k-1)e_{\Gamma_1}$, we have

$$= 2^{\alpha+1} (k-1) n_{\Gamma_2} e_{\Gamma_1}. \tag{22}$$

Using (17), (18), (20), and (22) in (16), then we have

$$M(\Gamma_1 + R_k \Gamma_2) = \sum_{i=0}^{\alpha} \binom{\alpha}{i} 2^{\alpha-i} M_{\Gamma_1}^{\alpha-i} M_{\Gamma_2}^{i+1} + 2 \left[\sum_{i=0}^{\alpha} \binom{\alpha}{i} 2^{\alpha-i} M_{\Gamma_1}^{\gamma-i} M_{\Gamma_2}^i \right] + 2^\alpha e_{\Gamma_1} n_{\Gamma_2} + 2^{\alpha+1} (k-1) n_{\Gamma_2} e_{\Gamma_1}. \tag{23}$$

Theorem 3. Let Γ_1 and Γ_2 be two simple graphs and $\gamma \in N - \{0, 1\}$. The FGZ index of the generalized Q-sum $\Gamma_1 +_{Q_k} \Gamma_2$ graph is

$$\begin{aligned}
M^\gamma(\Gamma_1 +_{Q_k} \Gamma_2) &= \sum_{i=0}^{\alpha} \binom{\alpha}{i} (M_{\Gamma_1}^{\alpha-i}) (M_{\Gamma_2}^{i+1}) + \sum_{i=0}^{\alpha} \binom{\alpha}{i} (M_{\Gamma_1}^{\gamma-i}) (M_{\Gamma_2}^i) + 2n_{\Gamma_2} \sum_{i=0}^{\alpha} \binom{\alpha}{i} (d_{\Gamma_1}^{\alpha-i}(u) \cdot d_{\Gamma_1}^i(v)) \\
&\quad + n_{\Gamma_2} \sum_{uv \in E(\Gamma_1)} \sum_{vw \in E(\Gamma_1)} \left[\left[\sum_{i=0}^{\alpha} \binom{\alpha}{i} d_{\Gamma_1}^{\alpha-i}(u) \cdot d_{\Gamma_1}^i(v) \right] + \left[\sum_{i=0}^{\alpha} \binom{\alpha}{i} d_{\Gamma_1}^{\alpha-i}(v) \cdot d_{\Gamma_1}^i(w) \right] \right] \\
&\quad + 2(k-1)n_{\Gamma_2} \sum_{uv \in E(\Gamma_1)} [d_{\Gamma_1}^\alpha(u) + d_{\Gamma_1}^\alpha(v)],
\end{aligned} \tag{24}$$

where N is the set of natural numbers and $\alpha = \gamma - 1$.

Proof. Then by definition, we have

$$\begin{aligned}
 M^\gamma(\Gamma_1+Q_k\Gamma_2) &= \sum_{(a,b)\in V(\Gamma_1+Q_k\Gamma_2)} d_{\Gamma_1+Q_k\Gamma_2}^\gamma(a,b) = \sum_{(a,b)(c,d)\in E(\Gamma_1+Q_k\Gamma_2)} \left[d_{\Gamma_1+Q_k\Gamma_2}^\alpha(a,b) + d_{\Gamma_1+Q_k\Gamma_2}^\alpha(c,d) \right] \\
 &= \sum_{a\in V(\Gamma_1)} \sum_{b,d\in E(\Gamma_2)} \left[d_{\Gamma_1+Q_k\Gamma_2}^\alpha(a,b) + d_{\Gamma_1+Q_k\Gamma_2}^\alpha(a,d) \right] + \sum_{b\in V(\Gamma_2)} \sum_{ac\in E(Q_k(\Gamma_1))} \left[d_{\Gamma_1+Q_k\Gamma_2}^\alpha(a,b) + d_{\Gamma_1+Q_k\Gamma_2}^\alpha(b,c) \right].
 \end{aligned} \tag{25}$$

For every vertex $a \in V(\Gamma_1)$ & edge $bd \in E(\Gamma_2)$, then the 1st term of (25) will be

$$\begin{aligned}
 &\sum_{a\in V(\Gamma_1)} \sum_{b,d\in E(\Gamma_2)} \left[d_{\Gamma_1+Q_k\Gamma_2}^\alpha(a,b) + d_{\Gamma_1+Q_k\Gamma_2}^\alpha(a,d) \right] \\
 &= \sum_{a\in V(\Gamma_1)} \sum_{b,d\in E(\Gamma_2)} \left[\sum_{i=0}^{\alpha} \binom{\alpha}{i} d_{Q_k(\Gamma_1)}^{\alpha-i}(a) d_{\Gamma_2}^i(b) + \sum_{i=0}^{\alpha} \binom{\alpha}{i} d_{Q_k(\Gamma_1)}^{\alpha-i}(a) d_{\Gamma_2}^i(d) \right] \\
 &= \sum_{a\in V(\Gamma_1)} \sum_{b,d\in E(\Gamma_2)} \left[\sum_{i=0}^{\alpha} \binom{\alpha}{i} d_{\Gamma_1}^{\alpha-i}(a) [d_{\Gamma_2}^i(b) + d_{\Gamma_2}^i(d)] \right] \\
 &= \sum_{a\in V(\Gamma_1)} \left[\sum_{i=0}^{\alpha} \binom{\alpha}{i} d_{\Gamma_1}^{\alpha-i}(a) \right] \sum_{b,d\in E(\Gamma_2)} [d_{\Gamma_2}^i(b) + d_{\Gamma_2}^i(d)] \\
 &= \sum_{a\in V(\Gamma_1)} \left[\sum_{i=0}^{\alpha} \binom{\alpha}{i} d_{\Gamma_1}^{\alpha-i}(a) \right] (M_{\Gamma_2}^{i+1}) \\
 &= \sum_{i=0}^{\alpha} \binom{\alpha}{i} (M_{\Gamma_1}^{\alpha-i}) (M_{\Gamma_2}^{i+1}).
 \end{aligned} \tag{26}$$

For every vertex $b \in V(\Gamma_2)$ & edge $ac \in E(Q_k(\Gamma_1))$ $a, c \in V(\Gamma_1)$, then the 2nd term of equation (25) will be

$$\begin{aligned}
 &\sum_{b\in V(\Gamma_2)} \sum_{ac\in E(Q_k(\Gamma_1))} \left[d_{\Gamma_1+Q_k\Gamma_2}^\alpha(a,b) + d_{\Gamma_1+Q_k\Gamma_2}^\alpha(b,c) \right] \\
 &= \sum_{b\in V(\Gamma_2)} \sum_{ac\in E(Q_k(\Gamma_1))} \sum_{a\in V(\Gamma_1), c\in V(Q_k(\Gamma_1))-V(\Gamma_1)} \left[d_{\Gamma_1+Q_k\Gamma_2}^\alpha(a,b) + d_{\Gamma_1+Q_k\Gamma_2}^\alpha(b,c) \right] \\
 &\quad + \sum_{b\in V(\Gamma_2)} \sum_{ac\in E(Q_k(\Gamma_1)) \setminus \{a,c\} \in V(Q_k(\Gamma_1))-V(\Gamma_1)} \left[d_{\Gamma_1+Q_k\Gamma_2}^\alpha(a,b) + d_{\Gamma_1+Q_k\Gamma_2}^\alpha(b,c) \right].
 \end{aligned} \tag{27}$$

Now $\forall b \in V(\Gamma_2)$, $ac \in E(Q_k(\Gamma_1))$ if $a \in V(\Gamma_1)$ and $c \in V(Q_k(\Gamma_1)) - V(\Gamma_1)$; the 1st term of (27) will be

$$\begin{aligned}
& \sum_{b \in V(\Gamma_2)} \sum_{ac \in E(Q_k(\Gamma_1))} \sum_{a \in V(\Gamma_1)} \sum_{c \in V(Q_k(\Gamma_1)) - V(\Gamma_1)} \left[\left[d_{\Gamma_1 + Q_k \Gamma_2}^\alpha(a, b) \right] + \left[d_{\Gamma_1 + Q_k \Gamma_2}^\alpha(b, c) \right] \right] \\
&= \sum_{b \in V(\Gamma_2)} \sum_{ac \in E(Q_k(\Gamma_1))} \sum_{a \in V(\Gamma_1)} \sum_{c \in V(Q_k(\Gamma_1)) - V(\Gamma_1)} \left[\left[d_{Q_k(\Gamma_1)}(a) + d_{\Gamma_2}(b) \right]^\alpha + \left[d_{Q_k(\Gamma_1)}(c) \right]^\alpha \right] \\
&= \sum_{b \in V(\Gamma_2)} \sum_{ac \in E(Q_k(\Gamma_1))} \sum_{a \in V(\Gamma_1)} \sum_{c \in V(Q_k(\Gamma_1)) - V(\Gamma_1)} \left[\sum_{i=0}^{\alpha} \binom{\alpha}{i} d_{Q_k(\Gamma_1)}^{\alpha-i}(a) \cdot d_{\Gamma_2}^i(b) + d_{Q_k(\Gamma_1)}^\alpha(c) \right] \\
&= \sum_{b \in V(\Gamma_2)} \sum_{ac \in E(Q_k(\Gamma_1))} \sum_{a \in V(\Gamma_1)} \sum_{c \in V(Q_k(\Gamma_1)) - V(\Gamma_1)} \left[\sum_{i=0}^{\alpha} \binom{\alpha}{i} d_{Q_k(\Gamma_1)}^{\alpha-i}(a) \cdot d_{\Gamma_2}^i(b) \right] \\
&\quad + \sum_{b \in V(\Gamma_2)} \sum_{ac \in E(Q_k(\Gamma_1))} \sum_{a \in V(\Gamma_1)} \sum_{c \in V(Q_k(\Gamma_1)) - V(\Gamma_1)} \left[d_{Q_k(\Gamma_1)}^\alpha(c) \right] \\
&= \sum_{i=0}^{\alpha} \binom{\alpha}{i} \sum_{b \in V(\Gamma_2)} d_{\Gamma_2}^i(b) \sum_{ac \in E(Q_k(\Gamma_1))} \sum_{a \in V(\Gamma_1)} \sum_{c \in V(Q_k(\Gamma_1)) - V(\Gamma_1)} d_{Q_k(\Gamma_1)}^{\alpha-i}(a) \\
&\quad + \sum_{b \in V(\Gamma_2)} \sum_{ac \in E(Q_k(\Gamma_1))} \sum_{a \in V(\Gamma_1)} \sum_{c \in V(Q_k(\Gamma_1)) - V(\Gamma_1)} \left[d_{Q_k(\Gamma_1)}^\alpha(c) \right] \\
&= \sum_{i=0}^{\alpha} \binom{\alpha}{i} M_{\Gamma_2}^i M_{\Gamma_1}^{\alpha-i} + n_{\Gamma_2} \cdot \sum_{ac \in E(Q_k(\Gamma_1))} \sum_{a \in V(\Gamma_1)} \sum_{c \in V(Q_k(\Gamma_1)) - V(\Gamma_1)} \left[d_{Q_k(\Gamma_1)}^\alpha(c) \right] \\
&= \sum_{i=0}^{\alpha} \binom{\alpha}{i} M_{\Gamma_2}^i M_{\Gamma_1}^{\alpha-i} + n_{\Gamma_2} \left[2 \sum_{uv \in E(\Gamma_1)} (d_{\Gamma_1}(u) + d_{\Gamma_1}(v))^\alpha \right] \\
&= \sum_{i=0}^{\alpha} \binom{\alpha}{i} M_{\Gamma_2}^i M_{\Gamma_1}^{\alpha-i} + 2n_{\Gamma_2} \left[\sum_{i=0}^{\alpha} \binom{\alpha}{i} \sum_{uv \in E(\Gamma_1)} (d_{\Gamma_1}^{\alpha-i}(u) \cdot d_{\Gamma_1}^i(v)) \right].
\end{aligned} \tag{28}$$

Now $\forall b \in V(\Gamma_2)$ & edge $ac \in E(Q_k(\Gamma_1))$ if the vertex $a, c \in V(Q_k(\Gamma_1)) - V(\Gamma_1)$. Then the 2nd term of equation

(27) splits into two parts for the vertices a and c , then the equation will be

$$\begin{aligned}
 &= \sum_{b \in V(\Gamma_2)} \sum_{a \in E(Q_k(\Gamma_1))} \sum_{c \in V(Q_k(\Gamma_1)) - V(\Gamma_1)} \left[d_{\Gamma_1+Q_k\Gamma_2}(a, b)^\alpha + d_{\Gamma_1+Q_k\Gamma_2}(b, c)^\alpha \right] \\
 &= \sum_{b \in V(\Gamma_2)} \sum_{a \in E(Q_k(\Gamma_1))} \sum_{c \in V(Q_k(\Gamma_1)) - V(\Gamma_1)} \left[d_{\Gamma_1+Q_k\Gamma_2}(a)^\alpha + d_{\Gamma_1+Q_k\Gamma_2}(c)^\alpha \right] \\
 &= \sum_{b \in V(\Gamma_2)} \sum_{uv \in E(\Gamma_1), vw \in E(\Gamma_1)} \left[d_{\Gamma_1}(u) + d_{\Gamma_1}(v) \right]^\alpha + \left[d_{\Gamma_1}(v) + d_{\Gamma_1}(w) \right]^\alpha \\
 &= c_{\Gamma_2} \sum_{uv \in E(\Gamma_1), vw \in E(\Gamma_1)} \left[\left[\sum_{i=0}^{\alpha} \binom{\alpha}{i} d_{\Gamma_1}^{\alpha-i}(u) \cdot d_{\Gamma_1}^i(v) \right] + \left[\sum_{i=0}^{\alpha} \binom{\alpha}{i} d_{\Gamma_1}^{\alpha-i}(v) \cdot d_{\Gamma_1}^i(w) \right] \right],
 \end{aligned} \tag{29}$$

$$\begin{aligned}
 \sum_{b \in V(\Gamma_2)} \sum_{a \in E(Q_k(\Gamma_1))} \sum_{c \in V(Q_k(\Gamma_1)) - V(\Gamma_1)} \left[d_{Q_k(\Gamma_1)}^\alpha(a) + d_{Q_k(\Gamma_1)}^\alpha(c) \right] &= 2(k-1) \sum_{b \in V(\Gamma_2)} \sum_{uv \in E(\Gamma_1)} \left[d_{\Gamma_1}^\alpha(u) + d_{\Gamma_1}^\alpha(v) \right] \\
 &= 2(k-1)n_{\Gamma_2} \sum_{uv \in E(\Gamma_1)} \left[d_{\Gamma_1}^\alpha(u) + d_{\Gamma_1}^\alpha(v) \right].
 \end{aligned} \tag{30}$$

Using (26), (28), (29), and (30) in (25), we get the required result:

$$\begin{aligned}
 &= \sum_{i=0}^{\alpha} \binom{\alpha}{i} (M_{\Gamma_1}^{\alpha-i} (M_{\Gamma_2}^{i+1} + \sum_{i=0}^{\alpha} \binom{\alpha}{i} M_{\Gamma_2}^i M_{\Gamma_1}^\alpha) \\
 &\quad + 2n_{\Gamma_2} \sum_{i=0}^{\alpha} \binom{\alpha}{i} \sum_{uv \in E'(\Gamma_1)} (d_{\Gamma_1}^{\alpha-i}(u) \cdot d_{\Gamma_1}^i(v)) \\
 &\quad + n_{\Gamma_2} \sum_{uv \in E'(\Gamma_1), vw \in E'(\Gamma_1)} \left[\sum_{i=0}^{\alpha} \left[\binom{\alpha}{i} d_{\Gamma_1}^{\alpha-i}(u) \cdot d_{\Gamma_1}^i(v) \right] \right] + \left[\sum_{i=0}^{\alpha} \binom{\alpha}{i} d_{\Gamma_1}^{\alpha-i}(v) \cdot d_{\Gamma_1}^i(w) \right] + 2(k-1)n_{\Gamma_2} \sum_{uv \in E(\Gamma_1)} \left[d_{\Gamma_1}^\alpha(u) + d_{\Gamma_1}^\alpha(v) \right] \\
 &= \sum_{i=0}^{\alpha} \binom{\alpha}{i} (M_{\Gamma_1}^{2\gamma-2-i} (M_{\Gamma_2}^{2i+1}) + 2n_{\Gamma_2} \sum_{i=0}^{\alpha} \binom{\alpha}{i} \sum_{uv \in E(\Gamma_1)} (d_{\Gamma_1}^{\alpha-i}(u) \cdot d_{\Gamma_1}^i(v)) + n_{\Gamma_2} \sum_{uv \in E(\Gamma_1), vw \in E(\Gamma_1)} \left[\sum_{i=0}^{\alpha} \binom{\alpha}{i} d_{\Gamma_1}^{\alpha-i}(u) \cdot d_{\Gamma_1}^i(v) \right] \\
 &\quad + \left[\sum_{i=0}^{\alpha} \binom{\alpha}{i} d_{\Gamma_1}^{\alpha-i}(v) \cdot d_{\Gamma_1}^i(w) \right] + 2(k-1)n_{\Gamma_2} \sum_{uv \in E(\Gamma_1)} \left[d_{\Gamma_1}^\alpha(u) + d_{\Gamma_1}^\alpha(v) \right].
 \end{aligned} \tag{31}$$

Theorem 4. Let Γ_1 and Γ_2 be two simple graphs. The FGZ index of the generalized T -sum graph $\Gamma_1+_{T_k}\Gamma_2$ is

$$\begin{aligned}
 M^\gamma(\Gamma_1+_{T_k}\Gamma_2) &= \sum_{i=0}^{\alpha} \binom{\alpha}{i} (2)^{\alpha-i} M_{\Gamma_1}^{\alpha-i} M_{\Gamma_2}^{i+1} + \sum_{i=0}^{\alpha} \binom{\alpha}{i} M_{\Gamma_2}^i (2)^{\alpha-i} M_{\Gamma_1}^{\gamma-i} + \sum_{i=0}^{\alpha} \binom{\alpha}{i} (2)^{\alpha-i} M_{\Gamma_2}^i M_{\Gamma_1}^{\gamma-i} \\
 &\quad + 2n_{\Gamma_2} \sum_{i=0}^{\alpha} \binom{\alpha}{i} \sum_{uv \in E(\Gamma_1)} (d_{\Gamma_1}^{\alpha-i}(u) \cdot d_{\Gamma_1}^i(v)) + n_{\Gamma_2} \\
 &\quad \cdot \sum_{uv \in E(\Gamma_1), vw \in E(\Gamma_1)} \left[\left[\sum_{i=0}^{\alpha} \binom{\alpha}{i} d_{\Gamma_1}^{\alpha-i}(u) \cdot d_{\Gamma_1}^i(v) \right] + \left[\sum_{i=0}^{\alpha} \binom{\alpha}{i} d_{\Gamma_1}^{\alpha-i}(v) + d_{\Gamma_1}^i(w) \right] \right] \\
 &\quad + 2(k-1)n_{\Gamma_2} \sum_{uv \in E(\Gamma_1)} \left[d_{\Gamma_1}^\alpha(u) + d_{\Gamma_1}^\alpha(v) \right],
 \end{aligned} \tag{32}$$

where $\gamma \in N^+ - \{0, 1\}$ and $\alpha = \gamma - 1$.

Proof. Since we have $d_{\Gamma_1 + T_k \Gamma_2}(a, b) = d_{\Gamma_1 + R_k \Gamma_2}(a, b)$ for every vertex $a \in V(\Gamma_1)$ and $b \in V(\Gamma_2)$, also $d_{\Gamma_1 + T_k \Gamma_2}(a, b) = d_{\Gamma_1 + Q_k \Gamma_2}(a, b)$ for every vertex $a \in V(T_k(\Gamma_1)) - V(\Gamma_1)$ and $b \in V(\Gamma_2)$, the result follows by the proof of Theorems 2 and 3.

Theorem 5. Assume that Γ_1 and Γ_2 are two simple graphs and $\alpha = \gamma - 1$, where $\gamma \in \mathfrak{R} - \{0, N^+\}$ and \mathfrak{R} is a set of real number. Then, the FGZ index of generalized F-sum graphs $(\Gamma_1 + S_k \Gamma_2, \Gamma_1 + R_k \Gamma_2, \Gamma_1 + Q_k \Gamma_2, \text{ and } \Gamma_1 + T_k \Gamma_2)$ are

$$\begin{aligned}
 \text{(i) } M^\gamma(\Gamma_1 + S_k \Gamma_2) &= \sum_{i=0}^{\infty} \binom{\alpha}{i} (M_{\Gamma_1}^i)(M_{\Gamma_2}^{\alpha-i+1}) + n_{\Gamma_2} M_{S_k(\Gamma_1)}^i + \sum_{i=1}^{\infty} \binom{\alpha}{i} M_{\Gamma_2}^{\alpha-1} M_{\Gamma_1}^{i+1} + 2^{\gamma+1} (k-1) n_{\Gamma_2} e_{\Gamma_1} \\
 \text{(ii) } M^\gamma(\Gamma_1 + R_k \Gamma_2) &= \sum_{i=0}^{\infty} \binom{\alpha}{i} 2^i M_{\Gamma_1}^i M_{\Gamma_2}^{\alpha-i+1} + 2 \left[\sum_{i=0}^{\infty} \binom{\alpha}{i} 2^i M_{\Gamma_1}^{i+1} M_{\Gamma_2}^{\alpha-i} \right] + 2^\gamma e_{\Gamma_1} n_{\Gamma_2} + 2^{\gamma+1} (k-1) n_{\Gamma_2} e_{\Gamma_1} \\
 \text{(iii) } M_{\Gamma_1 + Q_k \Gamma_2}^\gamma &= \sum_{i=0}^{\infty} \binom{\alpha}{i} (M_{\Gamma_1}^i)(M_{\Gamma_2}^{\alpha-i+1}) + \sum_{i=0}^{\infty} \binom{\alpha}{i} (M_{\Gamma_1}^{i+1})(M_{\Gamma_2}^{\alpha-i}) + 2n_{\Gamma_2} \left[\sum_{i=0}^{\infty} \binom{\alpha}{i} (d_{\Gamma_1}^i(u) \cdot d_{\Gamma_1}^{\alpha-i}(v)) \right] \\
 &\quad + n_{\Gamma_2} \sum_{uv \in E(\Gamma_1), vw \in E(\Gamma_1)} \left[\left[\sum_{i=0}^{\infty} \binom{\alpha}{i} d_{\Gamma_1}^i(u) \cdot d_{\Gamma_1}^{\alpha-i}(v) \right] + \left[\sum_{i=0}^{\infty} \binom{\alpha}{i} d_{\Gamma_1}^i(v) \cdot d_{\Gamma_1}^{\alpha-i}(w) \right] \right] \\
 &\quad + 2(k-1)n_{\Gamma_2} \sum_{uv \in E(\Gamma_1)} [d_{\Gamma_1}^\gamma(u) + d_{\Gamma_1}^\gamma(v)] \tag{33} \\
 \text{(iv) } M^\gamma(\Gamma_1 + T_k \Gamma_2) &= \sum_{i=0}^{\infty} \binom{\alpha}{i} 2^i M_{\Gamma_1}^i M_{\Gamma_2}^{\alpha-i+1} + \left[\sum_{i=0}^{\infty} \binom{\alpha}{i} 2^i M_{\Gamma_1}^{i+1} M_{\Gamma_2}^{\alpha-i} \right] \\
 &\quad + \sum_{i=0}^{\infty} \binom{\alpha}{i} (M_{\Gamma_1}^{i+1})(M_{\Gamma_2}^{\alpha-i}) + 2n_{\Gamma_2} \sum_{i=0}^{\infty} \binom{\alpha}{i} \sum_{uv \in E(\Gamma_1)} (d_{\Gamma_1}^i(u) \cdot d_{\Gamma_1}^{\alpha-i}(v)) \\
 &\quad + n_{\Gamma_2} \sum_{uv \in E(\Gamma_1), vw \in E(\Gamma_1)} \left[\left[\sum_{i=0}^{\infty} \binom{\alpha}{i} d_{\Gamma_1}^i(u) \cdot d_{\Gamma_1}^{\alpha-i}(v) \right] + \left[\sum_{i=0}^{\infty} \binom{\alpha}{i} d_{\Gamma_1}^i(v) \cdot d_{\Gamma_1}^{\alpha-i}(w) \right] \right] \\
 &\quad + 2(k-1)n_{\Gamma_2} \sum_{uv \in E(\Gamma_1)} [d_{\Gamma_1}^\gamma(u) + d_{\Gamma_1}^\gamma(v)].
 \end{aligned}$$

Proof. The above proof is similar as of Theorems 1–4.

Let Γ_1 be a negative integer, so from Theorem 5, Corollary 1 is obtained.

Corollary 1. Assume that $\Gamma_1 \notin \Gamma_2$ are two simple graphs and $\alpha = \gamma - 1$, where γ is a negative real number. The FGZ index of the generalized F -sums graphs $(\Gamma_1 +_{S_k} \Gamma_2, \Gamma_1 +_{R_k} \Gamma_2, \Gamma_1 +_{Q_k} \Gamma_2, \text{ and } \Gamma_1 +_{T_k} \Gamma_2)$ are

$$\begin{aligned}
 (i) M^\gamma(\Gamma_1 +_{S_k} \Gamma_2) &= \sum_{i=0}^{\infty} (-1)^i \binom{\alpha+i-1}{i} (M_{\Gamma_1}^i)(M_{\Gamma_2}^{\alpha-i+1}) + n_{\Gamma_2} M_{S_k(\Gamma_1)}^i + \sum_{i=1}^{\infty} (-1)^i \binom{\alpha+i-1}{i} M_{\Gamma_2}^{\alpha-1} M_{\Gamma_1}^{i+1} + 2^{\gamma+1} (k-1) n_{\Gamma_2} e_{\Gamma_1} \\
 (ii) M^\gamma(\Gamma_1 +_{R_k} \Gamma_2) &= \sum_{i=0}^{\infty} (-1)^i \binom{\alpha+i-1}{i} 2^i M_{\Gamma_1}^i M_{\Gamma_2}^{\alpha-i+1} + 2 \left[\sum_{i=0}^{\infty} (-1)^i \binom{\alpha+i-1}{i} 2^i M_{\Gamma_1}^{i+1} M_{\Gamma_2}^{\alpha-i} \right] + 2^\gamma e_{\Gamma_1} n_{\Gamma_2} + 2^{\gamma+1} (k-1) n_{\Gamma_2} e_{\Gamma_1} \\
 (iii) M_{\Gamma_1 +_{Q_k} \Gamma_2}^\gamma &= \sum_{i=0}^{\infty} (-1)^i \binom{\alpha+i-1}{i} (M_{\Gamma_1}^i)(M_{\Gamma_2}^{\alpha-i+1}) + \sum_{i=0}^{\infty} (-1)^i \binom{\alpha+i-1}{i} (M_{\Gamma_1}^{i+1})(M_{\Gamma_2}^{\alpha-i}) \\
 &\quad + 2n_{\Gamma_2} \sum_{i=0}^{\infty} (-1)^i \binom{\alpha+i-1}{i} \sum_{uv \in E(\Gamma_1)} (d_{\Gamma_1}^i(u) \cdot d_{\Gamma_1}^{\alpha-i}(v) + n_{\Gamma_2} \sum_{uv \in E(\Gamma_1), vw \in E(\Gamma_1)} \left[\sum_{i=0}^{\infty} (-1)^i \binom{\alpha+i-1}{i} d_{\Gamma_1}^i(u) \cdot d_{\Gamma_1}^{\alpha-i}(v) \right] \\
 &\quad + \left[\sum_{i=0}^{\infty} (-1)^i \binom{\alpha+i-1}{i} d_{\Gamma_1}^i(v) \cdot d_{\Gamma_1}^{\alpha-i}(w) \right]) + 2(k-1)n_{\Gamma_2} \sum_{uv \in E(\Gamma_1)} [d_{\Gamma_1}^\gamma(u) + d_{\Gamma_1}^\gamma(v)] \\
 (iv) M^\gamma(\Gamma_1 +_{T_k} \Gamma_2) &= \sum_{i=0}^{\infty} (-1)^i \binom{\alpha+i-1}{i} 2^i M_{\Gamma_1}^i M_{\Gamma_2}^{\alpha-i+1} + \left[\sum_{i=0}^{\infty} (-1)^i \binom{\alpha+i-1}{i} 2^i M_{\Gamma_1}^{i+1} M_{\Gamma_2}^{\alpha-i} \right] \\
 &\quad + \sum_{i=0}^{\infty} (-1)^i \binom{\alpha+i-1}{i} (M_{\Gamma_1}^{i+1})(M_{\Gamma_2}^{\alpha-i}) + 2n_{\Gamma_2} \sum_{i=0}^{\infty} (-1)^i \binom{\alpha+i-1}{i} \sum_{uv \in E(\Gamma_1)} (d_{\Gamma_1}^i(u) \cdot d_{\Gamma_1}^{\alpha-i}(v) \\
 &\quad + n_{\Gamma_2} \sum_{uv \in E(\Gamma_1), vw \in E(\Gamma_1)} \left[\sum_{i=0}^{\infty} (-1)^i \binom{\alpha+i-1}{i} d_{\Gamma_1}^i(u) \cdot d_{\Gamma_1}^{\alpha-i}(v) \right] + \left[\sum_{i=0}^{\infty} (-1)^i \binom{\alpha+i-1}{i} d_{\Gamma_1}^i(v) \cdot d_{\Gamma_1}^{\alpha-i}(w) \right]) \\
 &\quad + 2(k-1)n_{\Gamma_2} \sum_{uv \in E(\Gamma_1)} [d_{\Gamma_1}^\gamma(u) + d_{\Gamma_1}^\gamma(v)].
 \end{aligned} \tag{34}$$

4. Applications

Now, we present some examples as applications of the obtained results Theorems 1–4. Also the numerical comparisons are represented in Tables 1–4, and the graphical representations are depicted in Figures 4–7.

Example 1. Let P_m and P_n be two simple graphs with $m \geq 2$ and $n \geq 2$. Then, we have

$$\begin{aligned}
 1. M^\gamma(P_{m+S_k} P_n) &= \sum_{t=0}^{\gamma} C_T^{\gamma-1} [2^{\gamma-1-t} (m-2) + 2] [2^{t+1} (n-2) + 2] + \sum_{t=0}^{\gamma} C_T^{\gamma-1} [2^{\gamma-t} (m-2) + 2] [2^t (n-2) + 2] \\
 &\quad + n(2^\gamma (2m-3) + 2) + 4(k-1)n(m-1).
 \end{aligned} \tag{35}$$

From Figure 4, it is clear that the behavior of FGZ index of the generalized S -sum graph $\Gamma_1 +_{S_k} \Gamma_2$ at $t = 2$ is more better than $t = 0$ and $t = 1$:

$$\begin{aligned}
 2. M^\gamma(P_{m+R_k} P_n) &= \sum_{t=0}^{\gamma} C_T^{\gamma-1} 2^{\gamma-1-t} [2^{\gamma-1-t} (m-2) + 2] \cdot [2^{t+1} (n-2) + 2] + 2 \sum_{t=0}^{\gamma} C_T^{\gamma-1} 2^{\gamma-1-t} [2^{\gamma-t} (m-2) + 2] [2^t (n-2) + 2] \\
 &\quad + 2(m-1)n + 4(k-1)n(m-1).
 \end{aligned} \tag{36}$$

TABLE 1: Numerical comparison for $M^y(P_{m+s_k}P_n)$.

$[m, n, k]$	$T=0$	$T=1$	$T=2$
[1, 1, 1]	-4	-4	-13
[2, 2, 2]	28	28	28
[3, 3, 3]	124	124	133
[4, 4, 4]	308	308	326
[5, 5, 5]	604	604	631
[6, 6, 6]	1036	1036	1072
[7, 7, 7]	1628	1628	1673
[8, 8, 8]	2404	2404	2458
[9, 9, 9]	3388	3388	3451
[10, 10, 10]	4604	4604	4676

TABLE 2: Numerical comparison for $M^y(P_{m+R_k}P_n)$.

$[m, n, k]$	$T=0$	$T=1$	$T=2$
[1, 1, 1]	-8	-2	-6.5000
[2, 2, 2]	36	24	18
[3, 3, 3]	164	110	90.5000
[4, 4, 4]	400	280	235
[5, 5, 5]	768	558	475.000
[6, 6, 6]	1292	968	836
[7, 7, 7]	1996	1534	1340.5
[8, 8, 8]	2904	2280	2013
[9, 9, 9]	4040	3230	2877.5
[10, 10, 10]	5428	4408	3958

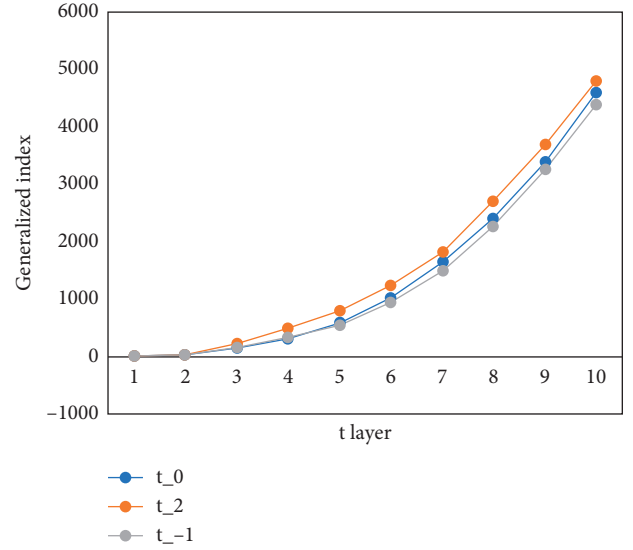
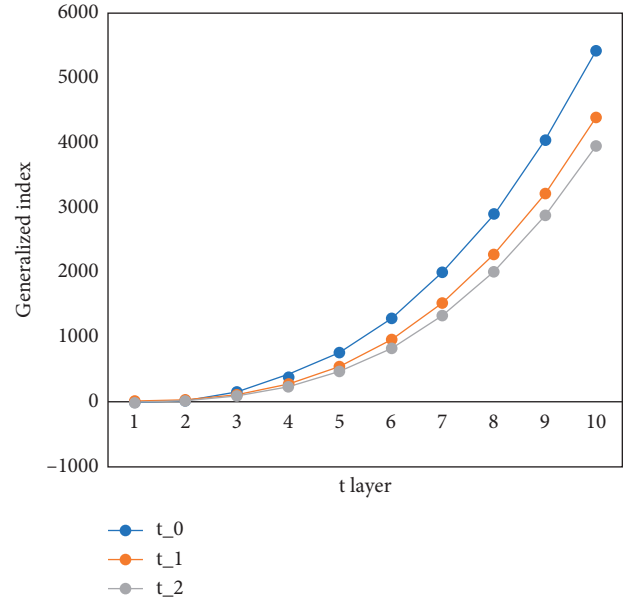
TABLE 3: Numerical comparison for $M^y(P_{m+Q_k}P_n)$.

$[m, n, k]$	$T=0$	$T=1$	$T=2$
[1, 1, 1]	3	3	-1.5000
[2, 2, 2]	38	38	47
[3, 3, 3]	157	157	179.5000
[4, 4, 4]	408	408	444
[5, 5, 5]	839	839	888.5000
[6, 6, 6]	1498	1498	1561
[7, 7, 7]	2433	2433	2509.5
[8, 8, 8]	3692	3692	3782
[9, 9, 9]	5323	5323	5426.5
[10, 10, 10]	7374	7374	7491

TABLE 4: Numerical comparison for $M^y(P_{m+T_k}P_n)$.

$[m, n, k]$	$T=0$	$T=1$	$T=2$
[1, 1, 1]	-3	3	3
[2, 2, 2]	54	42	45
[3, 3, 3]	227	173	167
[4, 4, 4]	564	444	417
[5, 5, 5]	1113	903	843
[6, 6, 6]	1922	1598	1493
[7, 7, 7]	3039	2577	2415
[8, 8, 8]	4512	3888	3657
[9, 9, 9]	6389	5579	5267
[10, 10, 10]	8718	7698	7293

From Figure 5, it is clear that the behavior of FGZ index of the generalized R -sum graph $\Gamma_{1+R_k}\Gamma_2$ at $t=0$ is more better than $t=1$ and $t=2$:

FIGURE 4: Numerical behavior of $M^y(P_{m+s_k}P_n)$ using Table 1.FIGURE 5: Numerical behavior of $M^y(P_{m+R_k}P_n)$ using Table 2.

$$\begin{aligned}
3. M^y(P_{m+Q_k}P_n) &= \sum_{t=0}^y C_T^{y-1} [2^{y-1-t} (m-2) + 2] [2^{t+1} (n-2) + 2] \\
&+ \sum_{t=0}^y C_T^{y-1} [2^{y-t} (m-2) + 2] [2^t (n-2) + 2] \\
&+ 2n \sum_{t=0}^y C_T^{y-1} [2^{y-1-t} + (m-2)2^{y-1} + 2^t] \\
&+ n \sum_{t=0}^y C_T^{y-1} [2^t + 2(m-1)2^{y-1} + 2^{y-1-t}] \\
&\cdot 2(k-1)n [2^{\alpha+1} (m-2) + 2].
\end{aligned}$$

(37)

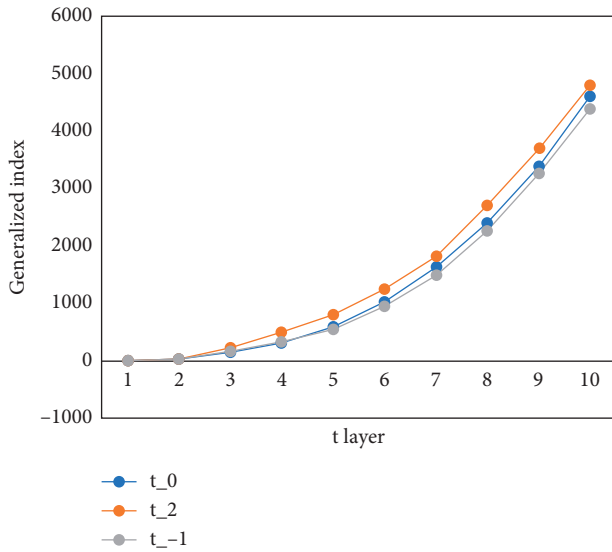


FIGURE 6: Numerical behavior of $M^\gamma(P_{m+Q_k}P_n)$ using Table 3.

From Figure 6, it is clear that the behavior of FGZ index of the generalized Q -sum graph $\Gamma_{1+Q_k}\Gamma_2$ at $t = 2$ is more better than $t = 0$ and $t = 1$:

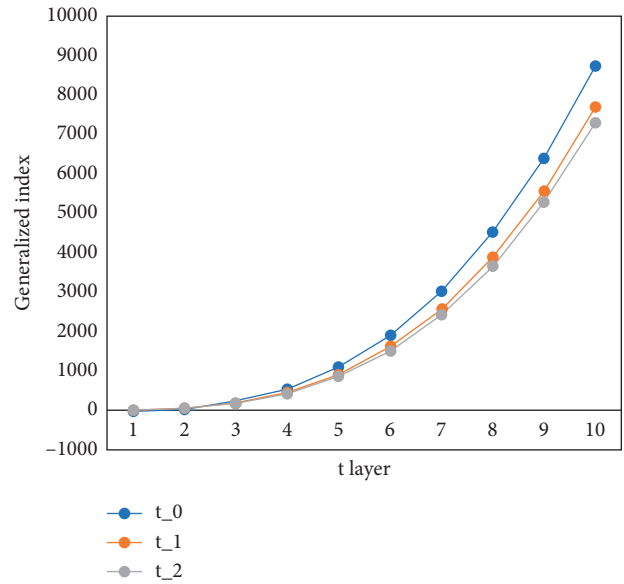


FIGURE 7: Numerical behavior of $M^\gamma(P_{m+T_k}P_n)$.

From Figure 7, it is clear that the behavior of FGZ index of the generalized T -sum graph $\Gamma_{1+T_k}\Gamma_2$ at $t = 0$ is more better than $t = 1$ and $t = 2$.

5. Conclusions

Now, we close our discussion with the following remarks:

- (i) For positive integer k and two graphs Γ_1 & Γ_2 , we have computed FGZ index of the generalized F -sums graphs $\Gamma_{1+F_k}\Gamma_2$, where generalized F -sums graphs are obtained by the different operations of subdivision and Cartesian product on Γ_1 & Γ_2 .
- (ii) The obtained results are also verified and illustrated for the particular classes of graphs.
- (iii) The behavior of FGZ index is also analyzed with the help of numerical and graphical presentations.
- (iv) However, the problem is still open to compute the different topological indices (degree and distance based) for the generalized F -sum graphs.

$$\begin{aligned}
 4. M^\gamma(P_{m+T_k}P_n) &= \sum_{t=0}^{\gamma} C_T^{\gamma-1} 2^{\gamma-1-t} [2^{\gamma-1-t} (m-2) + 2] [2^{t+1} (n-2) + 2] + 2 \sum_{t=0}^{\gamma} C_T^{\gamma-1} 2^{\gamma-1-t} [2^{\gamma-t} (m-2) + 2] [2^t (n-2) + 2] \\
 &+ 2n \sum_{t=0}^{\gamma} C_T^{\gamma-1} [2^{\gamma-1-t} + (m-2)2^{\gamma-1} + 2^t] + n \sum_{t=0}^{\gamma} C_T^{\gamma-1} [2^t + 2(m-1)2^{\gamma-1} + 2^{\gamma-1-t}] 2(k-1)n [2^{\alpha+1} (m-2) + 2].
 \end{aligned}
 \tag{38}$$

Data Availability

All the data are included within this paper. However, the reader may contact the corresponding author for more details of the data.

Conflicts of Interest

The authors have no conflicts of interest.

Acknowledgments

The authors are also thankful to Dr. Muhammad Kamran Siddiqui who helped in the graphical analysis. The University of Hail, Saudi Arabia, partially supported the study.

References

- [1] H. Gonzalez-Diaz, S. Vilar, L. Santana, and E. Uriarte, "Medicinal chemistry and bioinformatics-current trends in drugs discovery with networks topological indices," *Current Topics in Medicinal Chemistry*, vol. 7, pp. 1025–1039, 2007.
- [2] R. Gozalbes, J. Doucet, and F. Derouin, "Application of topological descriptors in QSAR and drug design: history and

- new trends,” *Current Drug Target-Infectious Disorders*, vol. 2, no. 1, pp. 93–102, 2002.
- [3] G. Rücker and C. Rücker, “On topological indices, boiling points, and cycloalkanes,” *Journal of Chemical Information and Computer Sciences*, vol. 39, no. 5, pp. 788–802, 1999.
- [4] M. Randić, “On characterization of molecular branching,” *Journal of the American Chemical Society*, vol. 97, pp. 6609–6615, 1975.
- [5] A. R. Matamala and E. Estrada, “Generalised topological indices: optimisation methodology and physico-chemical interpretation,” *Chemical Physics Letters*, vol. 410, no. 4–6, pp. 343–347, 2005.
- [6] W. Yan, B.-Y. Yang, and Y.-N. Yeh, “The behavior of Wiener indices and polynomials of graphs under five graph decorations,” *Applied Mathematics Letters*, vol. 20, no. 3, pp. 290–295, 2007.
- [7] H. Gonzglez-Diaz, S. Vilar, L. Santana, and E. Uriarte, “Medicinal chemistry and bioinformatics-current trends in drugs discovery with networks topological indices,” *Current Topics in Medicinal Chemistry*, vol. 7, no. 10, pp. 1015–1029, 2007.
- [8] L. H. Hall and L. B. Kier, *Molecular Connectivity in Chemistry and Drug Research*, Academic Press, Boston, MA, USA, 1976.
- [9] M. V. Diudea, *QSPR/QSAR Studies by Molecular Descriptors*, NOVA, New York, NY, USA, 2001.
- [10] J. Devillers and A. T. Balaban, *Topological Indices and Related Descriptors in QSAR and QSPR*, Gordon & Breach, Amsterdam, Netherlands, 1999.
- [11] R. Todeschini, V. Consonni, R. Mannhold, H. Kubinyi, and H. Timmerman, *Handbook of Molecular Descriptors*, Wiley-VCH, Weinheim, Germany, 2002.
- [12] I. Gutman and O. Polansky, *Mathematical Concepts in Organic Chemistry*, Springer-Verlag, Berlin, Germany, 1986.
- [13] I. Gutman, “Degree-based topological indices,” *Croatica Chemica Acta*, vol. 86, no. 4, pp. 351–361, 2013.
- [14] H. Wiener, “Structural determination of paraffin boiling points,” *Journal of the American Chemical Society*, vol. 69, no. 1, pp. 17–20, 1947.
- [15] N. Trinajstić and I. Gutman, “Graph theory and molecular orbitals. Total ϕ -electron energy of alternant hydrocarbons,” *Chemical Physics Letters*, vol. 17, no. 4, pp. 535–538, 1972.
- [16] M. Eliaşi and B. Taeri, “Four new sums of graphs and their Wiener indices,” *Discrete Applied Mathematics*, vol. 157, no. 4, pp. 794–803, 2009.
- [17] H. Deng, D. Sarala, S. K. Ayyaswamy, and S. Balachandran, “The Zagreb indices of four operations on graphs,” *Applied Mathematics and Computation*, vol. 275, pp. 422–431, 2016.
- [18] S. Akhter and M. Imran, “Computing the forgotten topological index of four operations on graphs,” *AKCE International Journal of Graphs and Combinatorics*, vol. 14, no. 1, pp. 70–79, 2017.
- [19] J.-B. Liu, S. Javed, M. Javaid, and K. Shabbir, “Computing first general Zagreb index of operations on graphs,” *IEEE Access*, vol. 7, pp. 47494–47502, 2019.
- [20] J.-B. Liu, M. Javaid, and H. M. Awais, “Computing Zagreb indices of the subdivision-related generalized operations of graphs,” *IEEE Access*, vol. 7, pp. 105479–105488, 2019.

Research Article

Research on Urban Rainfall Runoff Pollution Prediction Model Based on Feature Fusion

Junping Yao ¹ and Tianle Sun ²

¹School of Electronic and Information Engineering, Chongqing Radio & TV University, Chongqing, China

²College of Horticulture Sichuan Agricultural University, Chengdu, China

Correspondence should be addressed to Junping Yao; yao_junping@126.com and Tianle Sun; suntianle2002@163.com

Received 20 August 2020; Revised 19 October 2020; Accepted 9 November 2020; Published 20 November 2020

Academic Editor: Jia-Bao Liu

Copyright © 2020 Junping Yao and Tianle Sun. This is an open access article distributed under the Creative Commons Attribution License, which permits unrestricted use, distribution, and reproduction in any medium, provided the original work is properly cited.

In this paper, a rainfall runoff pollution prediction method based on grey neural network algorithm is proposed in consideration of the current situation that the accuracy of research results related to rainfall runoff pollution prediction needs to be improved. Meanwhile, the characteristics of rainfall runoff pollution are analyzed from the perspectives of the main sources of rainfall runoff pollution, the types of rainfall runoff pollution, and the initial erosion. The neural network algorithm is optimized and trained according to the sample data to obtain the sample features; the sample data are predicted according to the extracted sample features, and the prediction model is generated by using the feature fusion technology for two groups of prediction results to generate the prediction model and realize the water drop prediction. The pollution concentration of runoff was obtained by the exponential function method. The experimental results show that the predicted values of discharge and pollution concentration are well fitted with the actual values, indicating that the proposed method has high accuracy and feasibility. Finally, from the viewpoint of non-engineering measures and engineering measures, the suggestions for treating runoff pollution and relevant supports for ecological environment protection are given.

1. Introduction

As one of the natural disasters that threaten the public life and property safety, the flood disaster caused by rainfall is generating more and more serious harms in today's society with various types of disasters [1]. Therefore, it is of great guiding role in ecological management by reducing the pollution caused by flooding and erosion through improving the accuracy of rainfall runoff pollution prediction [2].

Due to the accelerated urbanization in China, the proportion of the total area of permeable ground is getting smaller. As a result, the emergent and impactful pollutions caused by rainfall runoff have already become the main source of ecological environmental pollutions [3]. Due to the large-scale pollutants contained in rainfall runoff, its initial runoff load is much heavier than that of domestic sewage [4]. Thus, the prediction and treatment of rainfall runoff pollution is an urgent problem to be solved in ecological environment management, which has aroused extensive

attentions and received in-depth researches by relevant experts and scholars [5].

By combining with strengths of relevant research achievements, the method of rainfall runoff prediction based on grey neural network algorithm is proposed so as to effectively enhance the prediction accuracy. At the same time, the feasibility of this method was verified to better improve the prediction of rainfall runoff pollution and treatment of environmental containment.

2. Rainfall Runoff Pollution Prediction Based on Grey Neural Network Algorithm

2.1. Characteristics of Rainfall Runoff Pollution Extract. The urban runoff, as being classified according to certain principles, belongs to non-point source pollution [6]. Strictly speaking, rainfall runoff has the characteristics of both surface source and point source. Among them, the surface source characteristic is mainly embodied in the following

aspects: the pollutants accumulate on the surface on sunny days but will be discharged to different places with the surface runoff on rainy days, so there are intermittent emission characteristics of surface source [7]. In regard to the point source characteristic, the pollutants are discharged to the storage water body, so there are the characteristics of centralized discharge [8].

2.1.1. Main Source of Rainfall Runoff Pollution. Surface pollution is the most important among the different sources of rainfall runoff pollution. The following analysis focuses on the accumulation and erosion in road surface pollution [9].

The total content of various pollutants on the surface, during the process of pollutant accumulation, will be affected by atmospheric dustfall, land use, and traffic [10]. In addition to particulates, dustfall also contains many types of pollutants; the influence of land use on surface pollution is diverse; traffic has a great impact on the cumulative rate of pollutions in cities or adjacent road sections, such as the toxic metal substances, especially lead, produced by friction between the ground and vehicle exhaust as well as auto parts. Road pollutants are also correlated with the type of urban industry and the surrounding geological conditions. The particles present in the rubbish on the road are generally transmitted from nearby soil and industrial dust by air. In summary, the consideration shall be given to the above factors while analyzing the accumulation of road surface pollution [11].

During the rainfall, the surface pollutants are eroded and there is correlation in the nature of pollutants. For example, the reactions of washing soluble and insoluble materials are different [12]. Besides, the water permeability of road surface will also have a certain impact on the erosion of pollutants. Furthermore, the differences in the depth and flow velocity of surface runoff in different regions also directly affect the performance of pollutant erosion.

On the impervious area, some soluble pollutants will be eroded first by rainfall. At the beginning of rainfall, it only moistens the road surface and the pollutants [13]. As a result, the loose pollutants will be splashed by raindrops, thereby enhancing the dissolution efficiency. Gradually, sufficient rainfall wets the ground and forms runoff, so that the low-lying places are filled and the soluble pollutants on the road surface are dissolved, especially the location with accumulated pollutants, such as street side ditch and roof collecting pipe [14]. The continuous formation and flow of surface runoff will take away large-scale soluble pollutants, while the insoluble pollutants will only move as soon as the local surface runoff reaches a certain speed. Once the flow rate exceeds the initial speed, the solid particles on the road surface begin to move, and so do the contaminants adsorbed on these particles. There are some differences in the movement due to the different sizes of the particles, but these pollutants will eventually flow into the gutter inlet with the rainfall runoff and gradually move downward through the pipe network. In the permeable area, some of the soluble and insoluble pollutants will adhere to the surface particles due to the upward penetration of rainwater, while others may move into the groundwater along

with the seepage, so that groundwater pollution is formed. When the surface runoff occurs as the rainfall intensity exceeds the soil infiltration performance, various soluble and insoluble pollutants entrained during the rainfall runoff will flow into the rainwater well [15].

2.1.2. Types of Rainfall Runoff Pollution. At present, most of the domestic and overseas researches pay attention to the pollutants such as suspended sediments, bacteria, and some toxic pollutants.

The rainfall runoff carries a lot of sediments. Generally speaking, the soil erosion in the old city is more serious; the mixed sediments in urban area mainly come from the various substances generated by the rust of vehicles, the wastes generated by motor vehicles, and the smoke exhausted from household chimneys, especially in industrial and commercial areas, highways, and some construction sites. Rainfall runoff contains many nutrients, which, after flowing to rivers or lakes and then into large estuaries and oceans, will lead to eutrophication of water bodies and damage the ecological environment. The runoff contains large scale of various organic substances, including domestic garbage and wastes, which will consume large amounts of oxygen in the water once starting to decompose. Therefore, after the rainstorm, the oxygen present in lakes or rivers will be consumed up, of which the oxygen consumption of runoff from the old city is the highest. Bacteria mainly come from animals and sewer overflows. The toxic substances present in rainfall runoff include heavy metals, pesticides, and polycyclic aromatic hydrocarbons, where the most typical pollutants of heavy metals derive from motor vehicles.

2.1.3. Initial Erosion. In rainfall runoff, the initial erosion refers to the occurrence of runoff since the start of rainfall, during which the pollutant content is the highest with large-scale pollutants flowing into the receiving water body. As can be observed from relevant researches, the total contents of pollutants during initial rainfall runoff are affected by indicators such as confluence area and rainfall intensity. Therefore, the research is complex and the concept of initial rainfall erosion remains to be determined.

2.2. Precipitation Prediction. Considering the close relationship between precipitation and runoff pollution, the grey neural network method is adopted to accurately predict rainwater runoff pollution. At present, neural network and grey system prediction models are widely adopted in various aspects. As can be concluded from analyzing the advantages and disadvantages of the grey waveform method as well as the neural network, the grey prediction method is more suitable for small data volume prediction because it can constantly approach the complex nonlinear functions. However, there will be prediction errors and the prediction accuracy is low when applying the grey prediction method to the system in poor stability. Compared with the grey prediction method, artificial neural network is better in nonlinear mapping, which can not only properly predict various mutation data through learning but also predict some special cases. The disadvantage is that the prediction

accuracy of neural network is relatively low because the large-scale representative information data are needed for practical training during prediction, but there is no enough data in practical application [16]. For this reason, to organically combine the neural network with grey prediction and realize complementarity will help overcome the limitations of the single prediction model and prevent the loss of effective information, so that the prediction accuracy of rainfall runoff pollution will be promoted.

With respect to the model of combining the grey model NGM (1,1,k) with neural network WNN, it means to effectively integrate grey system theory with WNN to gain more useful information, design and construct a grey neural network prediction model, and then improve the prediction accuracy. The main combination modes are divided into serial combination, parallel combination, grey compensation combination, and deep fusion. In the serial combination, the output result of one side is regarded as the input data of the other side, where the output result of the latter is the final prediction result; the parallel combination means to separately predict the two sides, so as to obtain the combined prediction result by weighing the weight values, which is also the final result of prediction model; the grey compensation combination is to acquire the mapping correlation between grey algorithm residuals and grey prediction method after conducting iterative training on the neural network, and then correct the grey prediction result according to the compensation value of neural network algorithm; in deep fusion, the two sides are fused into a grey waveform-WNN to achieve mutual complementarity in the prediction.

The parallel combination mode is selected after in-depth analysis, as shown in Figure 1. The optimal combined prediction model is constructed by combining the improved grey algorithm with the neural network prediction model.

The main ideas for designing and constructing the combined feature extraction model are as follows:

- (1) The ant colony algorithm is applied to optimize the neural network algorithm and conduct training based on the sample data, so that the first group of eigenvalues is obtained and set to $Y_1 = \{y_{1i}|t, n qih =_1 x, 7 \dots C, ; N\}$, and the error set is defined as $E_1 = \{e_{1i}|t, n qih =_1 x, 7 \dots C, ; N\}$.
- (2) The sample data is predicted according to the improved NGM (1,1,k) method, so that the second group of eigenvalues is obtained and set to $Y_2 = \{y_{2i}|t, n qih =_1 x, 7 \dots C, ; N\}$, and the error set is defined as $E_2 = \{e_{2i}|t, n qih =_1 x, 7 \dots C, ; N\}$.
- (3) The linear combination operations are performed on the two groups of feature extraction results (1) and (2) through feature fusion, so that a model is generated.

Among them, the feature fusion is calculated as follows.

After that, the optimal combination method is used to solve the weight coefficients of each feature extraction method based on the basic principle of minimum combination error value in the process of extracting features. At the same time, the weight coefficients of each single feature extraction method are fixed values in each prediction period.

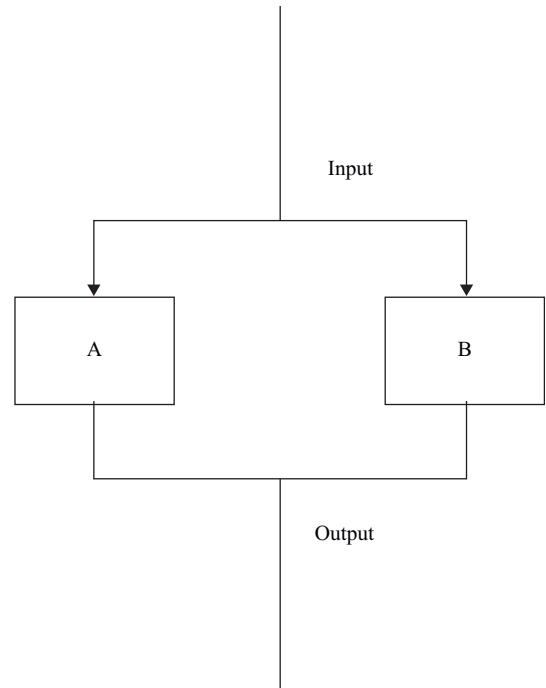


FIGURE 1: Schematic diagram of parallel combination mode.

Assume that there are currently m ways to implement combined prediction, in which each prediction method has a weight coefficient of $k_1, \dots, k_i, \dots, k_m$ and satisfies $k_1, \dots, k_i, \dots, k_m$. Suppose that e_{it} represents the error of the i -th mode in the time bucket t , and there are a total of n time buckets; then, the total error values of the combined prediction time buckets are

$$\begin{aligned}
 e_t &= k_1 e_{1t} + \dots + k_i e_{it} + \dots + k_m e_{mt} \\
 &= k_1 e_{1t} + \dots + k_i e_{it} + \dots + k_{m-1} e_{(m-1)t} \\
 &\quad + (1 - k_1 - \dots - k_{m-1}) e_{mt} \\
 &= k_1 (e_{1t} - e_{mt}) + \dots + k_2 (e_{2t} - e_{mt}) + \dots + k_i (e_{it} - e_{mt}) \\
 &\quad + \dots + k_{m-1} (e_{(m-1)t} - e_{mt}) + e_{mt}.
 \end{aligned} \tag{1}$$

Let

$$f_{it} = e_{it} - e_{mt} \quad (i = 1, \dots, m-1). \tag{2}$$

Then, the equation for calculating errors is

$$e_t = k_1 f_{1t} + \dots + k_i f_{it} + \dots + k_{m-1} f_{(m-1)t} + f_{mt}. \tag{3}$$

According to the above analysis, the prediction target is to minimize the sum of squared errors, that is, obtaining k_1, k_i, \dots, k_m to minimize equation (4).

$$Q = \sum_{i=1}^n e_{2t} = \sum_{i=1}^n (k_1 f_{1t} + \dots + k_i f_{it} + \dots + k_{m-1} f_{(m-1)t} + f_{mt})^2. \tag{4}$$

The way of obtaining the extremum through multivariate functions is

$$\begin{cases} \frac{\partial Q}{\partial k_1} = 2(k_1 \sum f_{1t}^2 + \cdots + k_{m-1} \sum f_{1t}f_{(m-1)t} + \cdots) = 0, \\ \vdots \\ \frac{\partial Q}{\partial k_{m-1}} = 2(k_1 \sum f_{1t}f_{(m-1)t} + \cdots + k_{m-1} \sum f_{(m-1)t}^2 + \cdots + \sum f_{(m-1)t}f_{mt}) = 0. \end{cases} \quad (5)$$

Equation (5) can be presented as

$$\begin{bmatrix} \sum f_{1t}^2 & \sum f_{1t}f_{2t} & \cdots & \sum f_{1t}f_{(m-1)t} \\ \sum f_{1t}f_{2t} & \sum f_{2t}^2 & \cdots & \sum f_{2t}f_{(m-1)t} \\ \vdots & \vdots & \ddots & \vdots \\ \sum f_{1t}f_{(m-1)t} & \sum f_{2t}f_{(m-1)t} & \cdots & \sum f_{(m-1)t}^2 \end{bmatrix} \begin{bmatrix} k_1 \\ k_2 \\ \vdots \\ k_{m-1} \end{bmatrix} = \begin{bmatrix} \sum f_{1t}f_{mt} \\ \sum f_{2t}f_{mt} \\ \vdots \\ \sum f_{mt}^2 \end{bmatrix}. \quad (6)$$

Let

$$\begin{aligned} D &= \begin{bmatrix} f_{11} & \cdots & \cdots & f_{1n} \\ f_{21} & \cdots & \cdots & f_{2n} \\ \vdots & \vdots & \vdots & \vdots \\ f_{(m-1)1} & f_{(m-1)2} & \cdots & f_{(m-1)n} \end{bmatrix}, \\ k &= \begin{bmatrix} k_1 \\ k_2 \\ \vdots \\ k_{m-1} \end{bmatrix}, \\ F &= \begin{bmatrix} f_{m1} \\ f_{m2} \\ \vdots \\ f_{mn} \end{bmatrix}. \end{aligned} \quad (7)$$

Then,

$$DD^T K = -DF. \quad (8)$$

Let there be no linear correlation between the above m ways, only $n \geq m - 1$; then, $m - 1$ rows of vectors are linearly independent, so DD^T is reversible; that is, there is a unique solution in the equations, which is the form of equation (4).

As can be observed from the above, there is a unique stagnation point $K = -(DD^T)^{-1}DF$. When $m = 2$, the optimal combined coefficients for the two prediction modes are expressed as

$$\begin{aligned} K_1 &= \frac{\sum f_{1t}f_{2t}}{\sum f_{1t}^2} = \frac{\sum (e_{1t} - e_{2t})e_{2t}}{\sum (e_{1t} - e_{2t})^2} = \frac{\sum e_{2t}^2 - \sum e_{1t}e_{2t}}{\sum e_{1t}^2 + \sum e_{2t}^2 - 2\sum e_{1t}e_{2t}}, \\ K_2 &= 1 - K_1. \end{aligned} \quad (9)$$

By means of the optimal weight coefficient, the linear combination of feature extraction results and rainfall runoff pollution prediction based on feature fusion are realized.

2.3. Prediction of Rainfall Runoff Pollution. It is found from analyzing the characteristics of rainfall runoff pollutions that floating dust, surface debris, and dirt are the main sources of runoff pollutants. Pollutants during rainfall mainly produced the rainfall runoff pollution, which is especially obvious in industrial areas. The rainfall pollutants are composed of two contents: one is the background value of rainfall pollutants being more stable and the other is the wet deposition caused by the atmosphere during rainfall. Ground pollutants are considered as a critical part of runoff pollutants, because the pollutants accumulate in various forms on the impervious areas such as streets, gutters, and drainage systems. The impact of urban sewer transport system on water quality mainly lies in the sewage diffused from sediments and drainage systems, of which the non-point source pollution caused by erosion of the sewer at the beginning of rainfall runoff is the main source. This is because the water body remained in the sedimentation pond from previous runoff and the solids are prone to spoilage; the runoff generated during rainfall will take away the sediments and sewage in the sewer.

The main influencing factors of rainfall runoff pollution include precipitation, surface pollutants, and land use. To some extent, the rainfall intensity determines the ability of the ground pollutants; the precipitation determines the amount of diluted pollutants; the rainfall duration determines the time of pollutant erosion and the period of transmitting pollutants to the ground; the type of land use determines the nature and accumulation rate of pollutants; the accumulation of ground pollutants on sunny days will directly affect the runoff pollutions. All these indicate that the factors affecting rainfall runoff pollutions are many and random.

In summary of the above analysis and calculation, the basic characteristics and main influencing factors of rainfall runoff pollution are obtained. The key to generating rainfall runoff pollution depends on the accumulation of surface pollutions on sunny days and the rainfall erosion, of which the latter is directly correlated with precipitation. That means the erosion phenomenon only occurs when precipitation reaches a certain level, so that the rainfall runoff pollution is formed. The total cumulative amount of surface pollutants is correlated with the cumulative time before rainfall pollution. The methods for simulating the accumulation model of pollutants on sunny days mainly include power function method, exponential function method, and saturation function method. For the power function method, the cumulative pollution amount $B_{T'}$ per unit area is calculated according to the following:

$$B_{T'} = \min(B_0, B_1 T'^{B_2}), \quad (10)$$

where T' represents the time of pollution accumulation before rainfall, B_0 represents the maximum pollution cumulative amount per unit area, B_1 represents the constant of pollution cumulative rate, and B_2 represents the time index.

The second is the exponential function method, whose equation is

$$B_{T'} = B_L + (B_0 - B_L) \times \exp(-B_1 \times T'), \quad (11)$$

where B_L represents the amount of pollutions that remained on the surface before the pollution accumulation.

The third is saturation function method, whose equation is

$$B_{T'} = B_L + (B_0 - B_L) \frac{T'}{B_3 + T'}, \quad (12)$$

where B_3 represents the half-saturation constant in the process of pollution accumulation.

In the construction of rainfall pollutant erosion model, the index function method is compared with the calibration curve method. In the exponential function method, the total pollution erosion amount per unit area in unit time W is expressed as

$$W = K_1 K_2 C_1' q^{C_2'} B, \quad (13)$$

where C_1' represents erosion coefficient, C_2' represents erosion index, and q represents total runoff per unit area.

In the calibration curve method, the total pollution erosion amount per unit area in unit time W is expressed as

$$W = K_1 K_2 C_1' q^{C_2'}. \quad (14)$$

The saturation function method of total accumulative pollution on sunny days and the rain erosion exponential function method are calculated and analyzed as an example. Based on equation (13),

$$dB = -W dt = C_1' q^{C_2'} B dt. \quad (15)$$

To sum up, the concentration values for rainfall runoff pollutants C' can be obtained:

$$\begin{aligned} C' &= C_0' + \frac{W}{q} = C_0' + C_1' q^{C_2'-1} B_{T'} \exp\left(-C_1' \int_0^t q(t)^{C_2'} dt\right) \\ &= C_0' + C_1' q^{C_2'-1} \left(B_L + (B_0 - B_L) \frac{T'}{B_1 + T'} \right) \\ &\quad \times \exp\left(-C_1' \int_0^t q(t)^{C_2'} dt\right), \end{aligned} \quad (16)$$

where C_0' represents the total concentration of atmospheric pollutants contained before the falling of raindrops and $q(t)$ represents the function of rainfall runoff generated under time variation.

3. Experimental Results and Analysis

The urban non-point source includes the erosion and washing of rainfall runoff. Mainly in the form of confluence system and discharged by drainage system, the rainfall runoff pollution plays a significant role in the initial stage. In the process of verifying the rainfall runoff pollution prediction method based on the grey neural network algorithm, the corresponding analysis and calculation are performed after a typical heavy rain, and the experimental platform is built on Mathematica. Figure 2 shows the process curve of rainstorm. Figure 3 presents the results of simulating the whole process of rainstorm runoff in the confluence area, the pollution factors, and indicators under urban non-point source pollution. In order to reduce the experiment complexity, the fitting between the actual situation and the predicted SS as well as COD pollution values is taken as the representative to verify the accuracy of proposed method.

Due to the poor water permeability at water-logged area with relatively large rainfall runoff coefficient, the rainfall runoff is formed quickly and the total runoff at initial stage increases dramatically, reaching the peak in a relatively short period of time. The overall changes of SS and COD are basically the same. The calculated values of water volume and quality are roughly consistent with the actual amount with strong fitting. The calculated error in water quality, that is, the predicted value of rainfall runoff pollution concentration, is small, and the accuracy can meet the actual engineering demands.

For the sake of verifying the practicability of the proposed method, the experiment was carried out in a specific simulation scenario on the test platform. First, the pre-rain drought period in the water quality simulation hypothesis area was set at 8 days, the accumulated rainfall was set at 72 mm, 120 min of rainfall duration was set as the standard parameter, and the annual rainfall was set at 1875.4 mm. For the evaporation amount, solar radiation, and cloud cover, the real-time data of the National Meteorological Observatory was taken as the reference. The specific pollutant calculation formula is shown in Table 1.

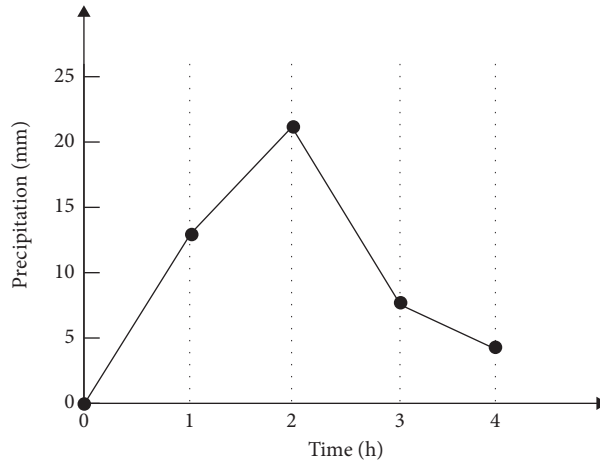


FIGURE 2: Diagram of rainstorm process curve.

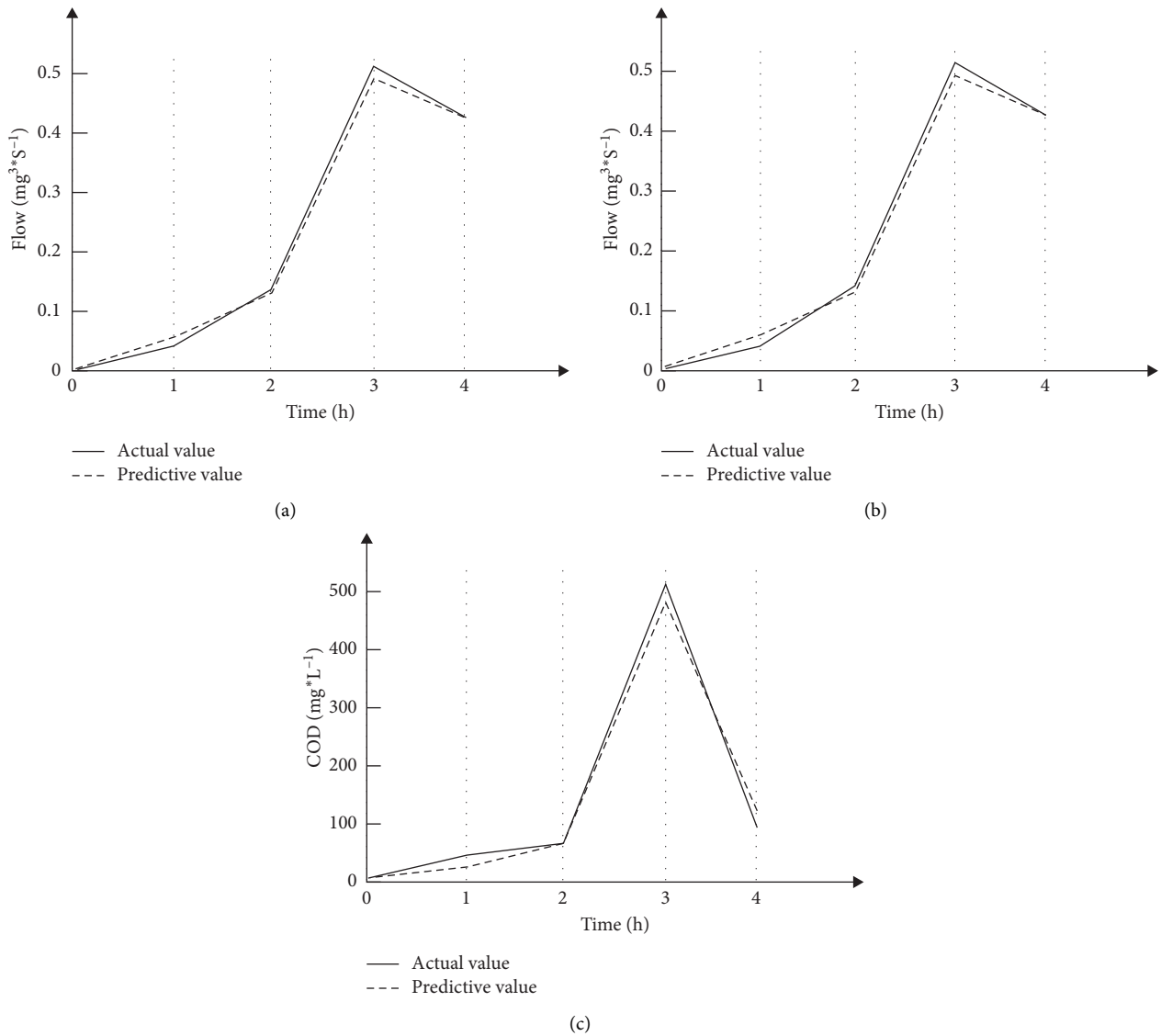


FIGURE 3: Results of rainfall runoff pollution prediction based on grey neural network algorithm. (a) Predicted flow value and fitting with actual value, (b) predicted SS concentration value and fitting with actual value, (c) predicted COD concentration value and fitting with actual value.

TABLE 1: Calculation formula for five pollutants.

Contaminant	Formula	R^2
TN	$y = 0.7646x - 0.8886$	0.9971
TP	$y = 0.1602x$	0.9708
COD _{cr}	$y = 10.879x + 9.8454$	0.9869
SS	$y = 71.488x$	0.9538
$NH_3 - N$	$y = 0.362x$	0.9707

The variation range of the above five pollutants is collected as the accumulated pollution. Under the above-mentioned scenario, the continuous increase of precipitation triggers the increase of runoff amount. Meanwhile, comparative test is carried out by predicting the accumulated pollution load. Figure 4 shows the results of comparing the experimental results with the prediction methods in literature.

According to Figures 4 and 5, in the prediction curve of the accumulated pollution load based on the proposed method, with the increase of accumulated runoff, the higher predicted cumulative pollution load can be reached under the condition of less accumulated runoff, which explains that the proposed method can prevent the loss of effective and available information. Although the designed rainfall only starts from the rainfall event control rate without giving consideration to the specific water quality conditions, the above pollution load will be affected by the original water quality since the concentration of runoff pollutants will usually decrease in the latter stage. However, all of the three prediction methods are conducted in the same parameter setting, indicating that the proposed prediction method not only overcomes the limitations of single prediction model but also improves the accuracy of rainfall runoff pollution prediction and enhances the practicability as well as robustness.

4. Suggestions on Pollution Control

After a long time study and exploration of measures for treating the runoff pollution, developed countries have designed and developed systematic control as well as technical system. Among them, the engineering and non-engineering measures are most representative. The following is the analysis of these two measures, respectively.

4.1. Non-Engineering Measures. With the focuses on the source of control, the natural and ecological governance options, and non-engineering approaches, these measures intend to achieve ecological pollution control through the enhanced management. The detailed plans include the prevention and control via diversion system, increase of urban greening area, cleaning of sewage pipeline system, waste sorting, reduction of garbage dumping, efficient management of construction site and machinery repair plant, and scientific control of urban greenfield fertilization and pesticide use. In addition to formulating the reasonable policies, it is also necessary to strengthen the publicity and education on public ecological environmental protection.

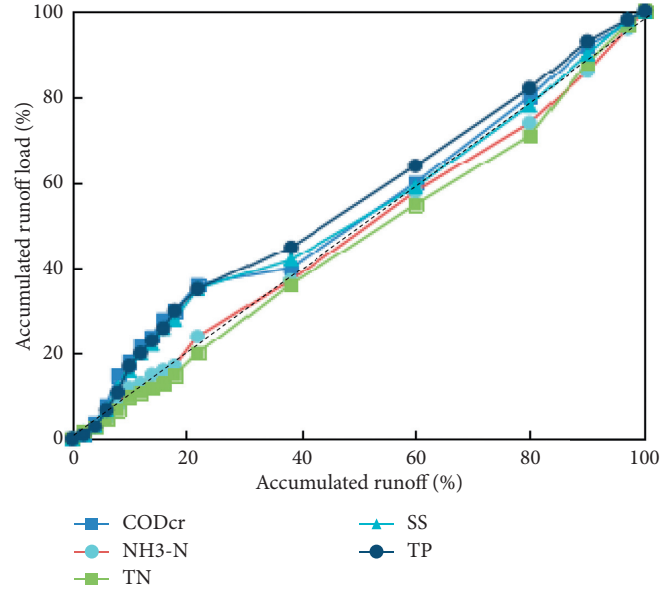


FIGURE 4: Prediction results of real-time pollution simulation through the proposed method.

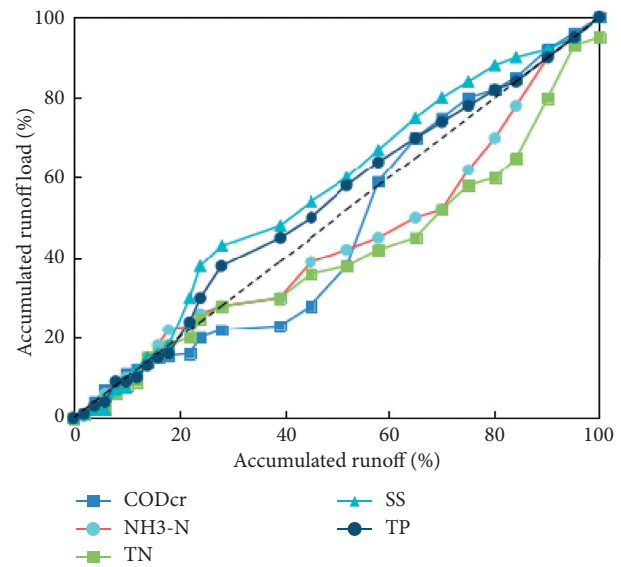


FIGURE 5: Prediction results of real-time pollution simulation through methods in the literature.

4.2. Engineering Measures. The source control shall not only cover management measures, that is, non-engineering measures, but also focus on the measures for reducing heavy pollutants in runoff. Street runoff usually flows directly into the drainage network system, so it is of great significance in reducing and controlling the pollutants by selecting the appropriate gullies, such as applying the water quality-based gullies to filter out various sediments and oils in road runoff. In regard to the control of the runoff of community road surface, it is suggested to increase the community green area and enhance the water permeability and then collect and simply process the internal runoff for watering green space and spraying road surface. Considering that the roof runoff

pollution is affected by dust and roofing materials, the green space or artificial soil layer may be utilized to penetrate underground, so as to reduce rainfall runoff pollution in urban areas.

By means of adopting appropriate treatment programs based on the basic principle of rainfall runoff pollution transmission and diffusion, the discharge of pollutants into underground or surface water bodies can be efficiently reduced. For the precipitation runoff that does not flow into the sewer, the forest grass buffer area may be constructed through natural channels and constructed wetlands so as to significantly reduce the total amount of pollutants in transit. Because the drainage system in urban areas is one of the key approaches to spread pollution, the planning and control of rainwater pipelines shall be effectively integrated with the urban runoff source control system as well as the terminal treatment system.

The old drainage systems in many domestic cities adopt the combined system, which means that the rainwater and sewage are parallel to the drainage pipe. As a result, the normal treatment of the sewage will be seriously affected due to the high fluctuation of rainwater, so the straight drainage often occurs in combined pipelines. The intercept combined drainage system is usually applied in the process of optimizing the old combined flow system, which can transfer the initial rainwater and street waste water to the sewage treatment plant. The diversion system is superior to the combined system in terms of operational performance, so it is generally adopted in China's new urban areas.

The above-mentioned terminal treatment means achieving effective degradation of runoff pollutants by utilizing natural ecological technology or artificial purification technology. The main measures include rainwater regulation tanks, storage ponds, and constructed wetlands. Among them, the load of various pollutants in the water storage pond is very high, but the pond can form an ecosystem based on the contained floating matter and aquatic plants to degrade and digest various pollutants in the runoff, thereby improving the water storage in the pond and optimizing the overall ecological environment around. Rainwater regulation tank is a widely used rainfall runoff pollution control solution, which can effectively prevent and control rainfall runoff pollution through physical, chemical, and biological methods. The rainwater regulation tank is generally composed of a water storage tank and a sedimentation tank, where the former is usually added subsequently for recycling.

5. Conclusions

A rainfall runoff pollution prediction method based on feature fusion is proposed for the prediction and treatment of rainfall runoff pollution. On the basis of analysis, the characteristics of rainfall runoff pollution are extracted through combining with the grey algorithm and neural network method, which are further organically integrated via feature fusion so as to construct a model of rainfall runoff pollution prediction. As proved by the experiment, the proposed method can effectively predict runoff pollution

with good fitting between the predicted value and the actual value. For the sake of better strengthening the urban ecological construction and providing a reliable basis for non-point source pollution control, the rainfall runoff pollution process will be simulated, and the performance of the proposed method will be further verified via different rain types.

Data Availability

All data are available upon request to the corresponding author.

Conflicts of Interest

The authors declare that they have no conflicts of interest.



References

- [1] Y. Luo, K. Yang, Z. Yu et al., "Dynamic monitoring and prediction of dianchi lake cyanobacteria outbreaks in the context of rapid urbanization," *Environmental Science and Pollution Research*, vol. 24, no. 6, pp. 5335–5348, 2016.
- [2] A. Zmy, B. S. Mo, and B. Shen, "An enhanced extreme learning machine model for river flow forecasting: state-of-the-art, practical applications in water resource engineering area and future research direction," *Journal of Hydrology*, vol. 569, pp. 387–408, 2019.
- [3] I. Iskender and N. Sajikumar, "Evaluation of surface runoff estimation in ungauged watersheds using SWAT and GIUH," *Procedia Technology*, vol. 24, pp. 109–115, 2016.
- [4] L. Chen, C. Sun, G. Wang, H. Xie, and Z. Shen, "Event-based nonpoint source pollution prediction in a scarce data catchment," *Journal of Hydrology*, vol. 552, pp. 13–27, 2017.
- [5] X. Li, H. R. Maier, and A. C. Zecchin, "Improved pmi-based input variable selection approach for artificial neural network and other data driven environmental and water resource models," *Environmental Modelling & Software*, vol. 65, pp. 15–29, 2015.
- [6] N. V. Bhattacharjee and E. W. Tollner, "Improving management of windrow composting systems by modeling runoff water quality dynamics using recurrent neural network," *Ecological Modelling*, vol. 339, pp. 68–76, 2016.
- [7] M. A. Paule-Mercado, J. S. Ventura, S. A. Memon, D. Jahng, J.-H. Kang, and C.-H. Lee, "Monitoring and predicting the fecal indicator bacteria concentrations from agricultural, mixed land use and urban stormwater runoff," *Science of The Total Environment*, vol. 550, pp. 1171–1181, 2016.
- [8] K. Chinen, S.-L. Lau, M. Nonezyan et al., "Predicting runoff induced mass loads in urban watersheds: linking land use and pyrethroid contamination," *Water Research*, vol. 102, pp. 607–618, 2016.
- [9] A. K. Kadam, V. M. Wagh, A. A. Muley, B. N. Umrikar, and R. N. Sankhua, "Prediction of water quality index using artificial neural network and multiple linear regression modelling approach in Shivganga River basin, India," *Modeling Earth Systems and Environment*, vol. 5, no. 3, pp. 951–962, 2019.
- [10] A. Elzwayie, A. El-Shafie, Z. M. Yaseen, H. A. Afan, and M. F. Allawi, "RBFNN-based model for heavy metal prediction for different climatic and pollution conditions," *Neural Computing & Applications*, vol. 28, no. 8, pp. 1–13, 2017.

- [11] L. Bo, Z. Yi-Fan, Z. Bei-Bei, and W. Xian-Qing, "A risk evaluation model for karst groundwater pollution based on geographic information system and artificial neural network applications," *Environmental Geology*, vol. 77, no. 9, pp. 341–344, 2018.
- [12] L. Qian, J. Li, C. Liu, J. Tao, and F. Chen, "River flow sequence feature extraction and prediction using an enhanced sparse autoencoder," *Journal of Hydroinformatics*, vol. 22, no. 5, pp. 1391–1409, 2020.
- [13] P. Zhang, Y. Cai, and J. Wang, "A simulation-based real-time control system for reducing urban runoff pollution through a stormwater storage tank," *Journal of Cleaner Production*, vol. 183, pp. 641–652, 2018.
- [14] S. Thorndahl and M. R. Rasmussen, "Short-term forecasting of urban storm water runoff in real-time using extrapolated radar rainfall data," *Journal of Hydroinformatics*, vol. 15, no. 3, pp. 897–912, 2013.
- [15] X. X. Sun, S. H. Mo, B. Shen, M. Liu, and Y. J. Li, "Runoff predicting model based on improved Markov chain," *Journal of Shenyang Agricultural University*, vol. 37, no. 6, pp. 872–877, 2006.
- [16] Y. Zheng, X. Luo, W. Zhang et al., "Enrichment behavior and transport mechanism of soil-bound PAHs during rainfall-runoff events," *Environmental Pollution*, vol. 171, pp. 85–92, 2012.

Review Article

Zagreb Connection Numbers for Cellular Neural Networks

Jia-Bao Liu ¹, Zahid Raza,² and Muhammad Javaid ³

¹School of Mathematics and Physics, Anhui Jianzhu University, Hefei 230601, China

²Department of Mathematics, College of Sciences, University of Sharjah, Sharjah, UAE

³Department of Mathematics, School of Science, University of Management and Technology, Lahore, Pakistan

Correspondence should be addressed to Muhammad Javaid; javaidmath@gmail.com

Received 25 July 2020; Revised 28 September 2020; Accepted 5 October 2020; Published 23 October 2020

Academic Editor: Maria Alessandra Ragusa

Copyright © 2020 Jia-Bao Liu et al. This is an open access article distributed under the Creative Commons Attribution License, which permits unrestricted use, distribution, and reproduction in any medium, provided the original work is properly cited.

Neural networks in which communication works only among the neighboring units are called cellular neural networks (CNNs). These are used in analyzing 3D surfaces, image processing, modeling biological vision, and reducing nonvisual problems of geometric maps and sensory-motor organs. Topological indices (TIs) are mathematical models of the (molecular) networks or structures which are presented in the form of numerical values, constitutional formulas, or numerical functions. These models predict the various chemical or structural properties of the under-study networks. We now consider analogous graph invariants, based on the second connection number of vertices, called Zagreb connection indices. The main objective of this paper is to compute these connection indices for the cellular neural networks (CNNs). In order to find their efficiency, a comparison among the obtained indices of CNN is also performed in the form of numerical tables and 3D plots.

1. Introduction

A neural system that consists of a multidimensional cluster of neurons and neighborhood-connected associations between the cells is called a cellular neural network (CNN) as shown in Figure 1. This kind of system presented in [1] is a consistent time network in the form of an $n \times m$ rectangular matrix array having n rows and m columns (see Figures 1–3 for some values of m and n).

A component of the rectangular array corresponds to a cell in a neural arrangement. But it is noted that the geometry exhibited requires not only to be rectangular, but also such shapes can be triangles or hexagons [2]. Multiple clusters can be represented with a proper interconnected structure to construct a multilayered cell neural system (Figure 4).

A cell $C(h; k)$, where $1 \leq h \leq n$ and $1 \leq k \leq m$ with its l th neighborhood, can be presented as $Nr(h; k)$ and is described as the set of cells $C(p; q)$, where $1 \leq p \leq n$ and $1 \leq q \leq m$, such that $|p - h| \leq l$ and $|q - k| \leq l$. The cells in l th neighborhood of a cell $C(h, k)$ are directly interconnected with cell $C(h, k)$ through $A(p, q, h, k)$, $A(h, k, p, q)$, $B(p, q, h, k)$, and $B(h, k, p, q)$, where $A(p, q, h, k)$ and $A(h, k, p, q)$ are known

as the feedback weights and $B(p, q, h, k)$ and $B(h, k, p, q)$ known as the feedforward weights. The index pair (p, q, h, k) describes the direction of signal from $C(h, k)$ to $C(p, q)$. The cell $C(h, k)$ is connected directly with its adjacent cells $C(p, q) \in Nr(h, k)$. Since every $C(p, q)$ has its adjacent cells, the cell $C(h, k)$ can also be linked with all other cells indirectly as shown in Figure 5.

The CNN has a lot of applications that are indicated by their spatial dynamics. The filtering image processing is one of the good applications of CNN [3]. For more related works about CNN and PNN, one can consult the references [4–13].

Thoroughly, we take the graph $G = (V, E)$ which does not contain loops and multiple or directed edges, where the sets V and $E \subseteq V \times V$ are of vertices and edges, respectively. The length of the shortest path from u to v (denoted by $d(u, v)$) is called its distance and $d_u = |N|$ is known by the degree of u , where $N = \{v \in V: d(v, u) = 1\}$. A topological index (TI) defined with the help of the degrees of nodes of the (molecular) network is a class of indices which are used to find out and model the certain properties of the chemical compounds of the (molecular) networks (see [14–16]). In particular, the degree-based topological properties for the CNN are studied in [17].

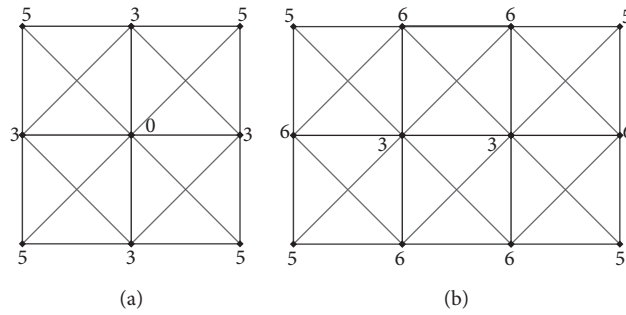


FIGURE 1: Cellular neural network CNN(3,3) (a) and CNN(4,3) (b).

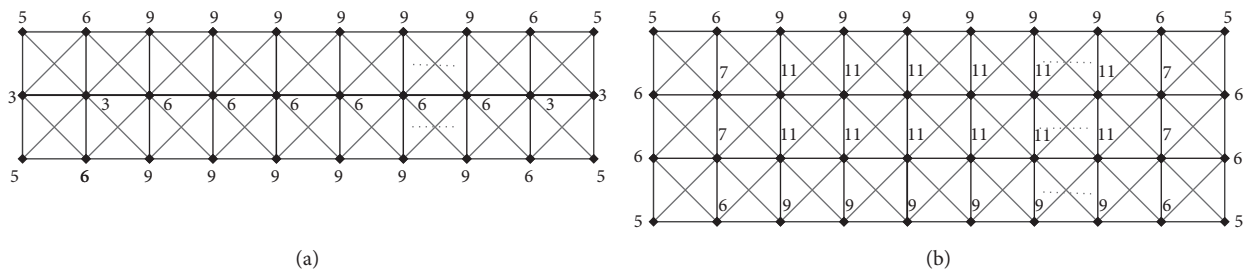


FIGURE 2: Cellular neural network CNN(m,3) (a) and CNN(m,4) (b).

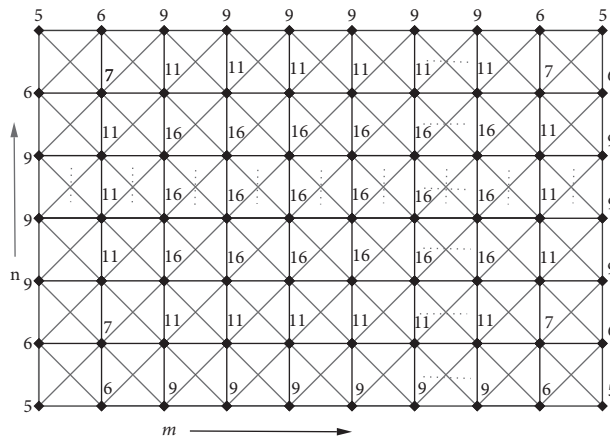


FIGURE 3: Cellular neural network CNN(m,n).

The first Zagreb index is studied for the total π -electron energy [18], and the second Zagreb index appeared to compute molecular branching [19]; they are denoted by M_1 and M_2 , respectively:

$$\begin{aligned} M_1(G) &= \sum_{u \in V(G)} [d_u]^2, \\ M_2(G) &= \sum_{u \in E(G)} d_u d_v. \end{aligned} \tag{1}$$

In relation to the above equations, the first and second Zagreb connection indices (ZCIs) have been put forward in [20, 21] independently:

$$\begin{aligned} ZC_1(G) &= \sum_{u \in V(G)} (\tau_u)^2, \\ ZC_2(G) &= \sum_{uv \in E(G)} \tau_u \tau_v, \\ ZC_1^*(G) &= \sum_{u \in V(G)} d_u \tau_u, \end{aligned} \tag{2}$$

where τ_u denotes the number of vertices $v \in G$ such that $d(u, v) = 2$. It has been proved by Ali and Trinajstić [20] that the topological index ZC_1^* can be written as

$$ZC_1^*(G) = \sum_{uv \in E(G)} (\tau_u + \tau_v). \tag{3}$$

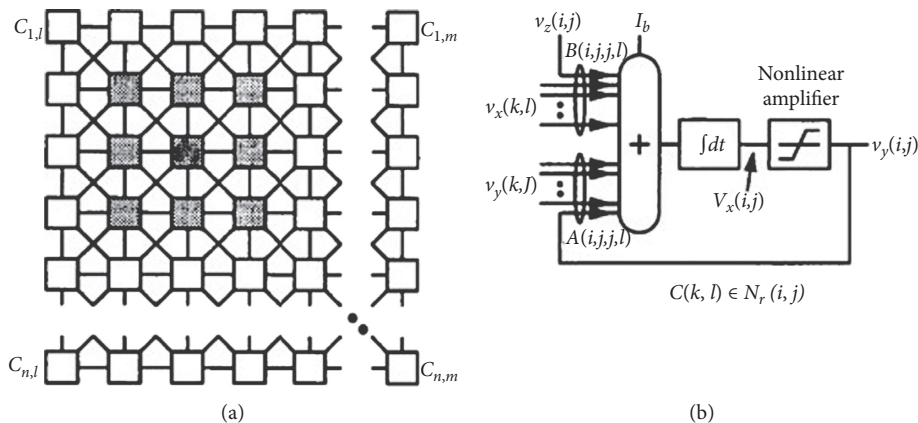


FIGURE 4: Cellular neural network.

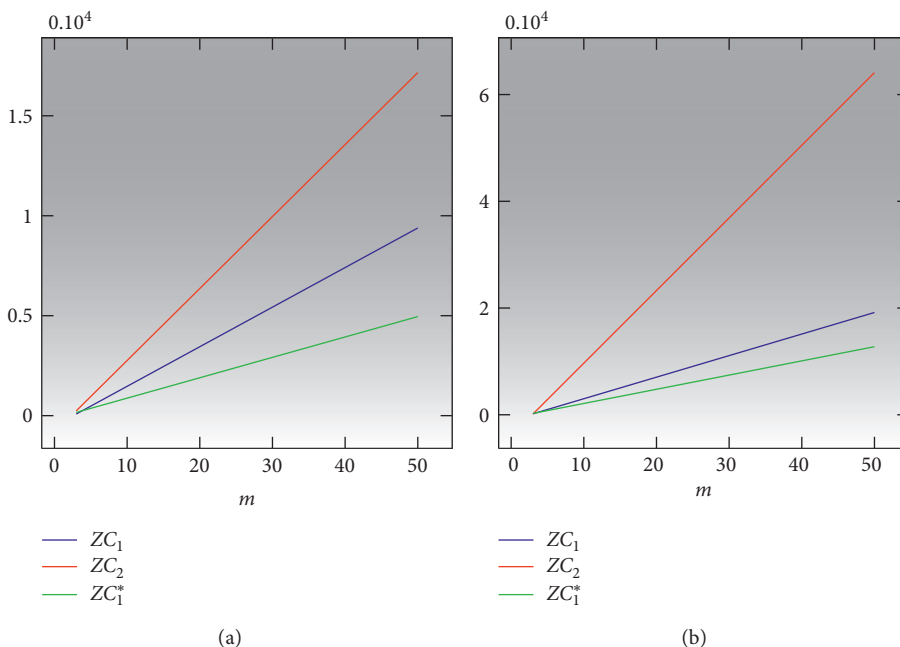


FIGURE 5: Differences of indices for CNN(m,3) (a) and for CNN(m,4) (b).

In [17], the authors checked the chemical applicability of these three Zagreb connection indices on the set of octane isomers, and they found that $ZC_1^*(G)$ has better correlating ability than the other two Zagreb connection indices in the cases of entropy, enthalpy of vaporization, standard enthalpy of vaporization, and acentric factor. Basavanagoud and Jakkannavar checked the chemical applicability of ZC_1 and found that the index has a very good correlation with physical properties of chemical compounds such as boiling point, entropy, enthalpy of evaporation, standard enthalpy of vaporization, and acentric factor (see [23]).

Ali and Trinajstić [20] checked the chemical applicability of ZC_1^* , and they found that this TI correlates well with the entropy and acentric factor of octane isomers. A large number of networks has been studied with the help of connection number-based TIs such as T -sum networks [24], resultant networks [25, 26], connected networks [27, 28], alkanes [22, 29, 30],

dendrimer nanostars [31], trees, and unicyclic networks [32] and subdivided and semitotal point networks [33].

2. Main Results and Discussion

Let $c_k(G)$ denote the number of vertices in G with connection number k and $m_{k,l}(G)$ denote the number of edges in G whose vertices have connection numbers k and l .

The following formulas for the ZCIs are equivalent to the previous definitions:

$$ZC_1(G) = \sum_{0 \leq k \leq n-2} c_k(G)k^2, \tag{4}$$

$$ZC_2(G) = \sum_{0 \leq l \leq k \leq n-2} m_{k,l}(G)(k.l), \tag{5}$$

$$ZC_1^*(G) = \sum_{0 \leq l \leq k \leq n-2} m_{k,l}(G)(k+l). \quad (6)$$

From Figure 1 and definition of the ZCIs, we have the following:

- (1) For $m = 3$ and $n = 3$,
 - (a) $ZC_1(\text{CNN}(3, 3)) = 100$
 - (b) $ZC_2(\text{CNN}(3, 3)) = 156$
 - (c) $ZC_1^*(\text{CNN}(3, 3)) = 88$
- (2) For $m = 4$ and $n = 3$,
 - (a) $ZC_1(\text{CNN}(4, 3)) = 280$
 - (b) $ZC_2(\text{CNN}(4, 3)) = 555$
 - (c) $ZC_1^*(\text{CNN}(4, 3)) = 258$
- (3) For $m = 4$ and $n = 4$,
 - (a) $ZC_1(\text{CNN}(4, 4)) = 584$
 - (b) $ZC_2(\text{CNN}(4, 4)) = 1634$
 - (c) $ZC_1^*(\text{CNN}(4, 4)) = 524$

Theorem 1. Let $m \geq 5$ and $\text{CNN}(m, 3)$ be the CNN. Then,

- (1) $ZC_1(\text{CNN}(m, 3)) = 198m - 512$
- (2) $ZC_2(\text{CNN}(m, 3)) = 360m - 840$
- (3) $ZC_1^*(\text{CNN}(m, 3)) = 102m - 144$

Proof. In order to prove our result, we will compute c_k , the number of vertices of connection number k , and $y_{k,l}(G)$ is the edge of $\text{CNN}(m, 3)$ whose vertices have connection numbers k and l . It is easy to see from the structure of $\text{CNN}(m, n)$ that $c_3 = 4, c_5 = 4, c_6 = m$, and $c_9 = 2m - 8$. Thus, from equation (4), we have the following:

$$\begin{aligned} ZC_1(\text{CNN}(m, 3)) &= \sum_{0 \leq k \leq n-2} c_k(G)k^2 = c_3(3^2) + c_5(5)^2 \\ &\quad + c_6(6)^2 + c_9(9)^2 \\ &= 36 + 100 + 36m + 81(2m - 8) \\ &= 198m - 512. \end{aligned} \quad (7)$$

The edge set of $\text{CNN}(m, 3)$ can be partitioned into different classes depending upon the edge types of $y_{k,l}(G)$ as listed in Table 1.

From the definition of the second ZCI and substitution of $y_{k,l}$ from Table 1 in (5), it follows that

$$\begin{aligned} ZC_2(\text{CNN}(m, 3)) &= y_{3,5}(3 \times 5) + y_{3,6}(3 \times 6) + y_{3,9}(3 \times 9) \\ &\quad + y_{5,6}(5 \times 6) + y_{6,6}(6 \times 6) + y_{6,9}(6 \times 9) \\ &= 8(15) + 8(18) + 4(27) + 4(30) \\ &\quad + (m-1)(36) + (6m-24)(54) \\ &= 360m - 840. \end{aligned} \quad (8)$$

Similarly, from substitution of $y_{k,l}(G)$ from Table 1 in (6), we have

$$\begin{aligned} ZC_1^*(\text{CNN}(m, 3)) &= y_{3,5}(3+5) + y_{3,6}(3+6) + y_{3,9}(3+9) \\ &\quad + y_{5,6}(5+6) + y_{6,6}(6+6) + y_{6,9}(6+9) \\ &= 8(8) + 8(9) + 4(12) + 4(11) \\ &\quad + (m-1)(12) + (6m-24)(15) \\ &= 102m - 144. \end{aligned} \quad (9)$$

Theorem 2. Let $m \geq 5$ and $\text{CNN}(m, 4)$ be the CNN. Then,

- (1) $ZC_1(\text{CNN}(m, 4)) = 404m - 1032$
- (2) $ZC_2(\text{CNN}(m, 4)) = 1361m - 3940$
- (3) $ZC_1^*(\text{CNN}(m, 4)) = 266m - 540$

Proof. It is easy to see from the structure of $\text{CNN}(m, 4)$ that $c_5 = 4, c_6 = 8, c_7 = 4, c_9 = 2m - 8$, and $c_{11} = 2m - 8$. Thus, from equation (4), we have the following:

$$\begin{aligned} ZC_1(\text{CNN}(m, 4)) &= \sum_{0 \leq k \leq n-2} c_k(G)k^2 = c_5(5)^2 + c_6(6)^2 \\ &\quad + c_7(7)^2 + c_9(9)^2 + c_{11}(11)^2 \\ &= 4(25) + 8(36) + 4(49) + (2m-8)(81) \\ &\quad + (2m-8)(121) = 404m - 1032. \end{aligned} \quad (10)$$

The edge set of $\text{CNN}(m, 4)$ can be partitioned into different classes depending upon the edge types of $y_{k,l}(G)$ as listed in Table 2.

From the definition of the second ZCI and substitution of $y_{k,l}$ from Table 2 in (5), it follows that

$$\begin{aligned} ZC_2(\text{CNN}(m, 4)) &= y_{5,6}(5 \times 6) + y_{5,7}(5 \times 7) + y_{6,6}(6 \times 6) + y_{6,7}(6 \times 7) + y_{6,9}(6 \times 9) \\ &\quad + y_{6,11}(6 \times 11) + y_{7,7}(7 \times 7) + y_{7,9}(7 \times 9) + y_{7,11}(7 \times 11) + y_{9,9}(9 \times 9) + y_{9,11}(9 \times 11) + y_{11,11}(11 \times 11) \\ &= 8(30) + 4(35) + 6(36) + 12(42) + 4(54) + 4(66) + 2(49) + 4(63) + 8(77) + (2m-10)(81) \\ &\quad + (6m-28)(99) + (5m-24)(121) = 1361m - 3940. \end{aligned}$$

(11)

TABLE 1: Partition of edge set of CNN ($m, 3$).

Edges of type $y_{k,l}$	Number of edges
$y_{3,5}$	8
$y_{3,6}$	8
$y_{3,9}$	4
$y_{5,6}$	4
$y_{6,6}$	$m - 1$
$y_{6,9}$	$6m - 24$

TABLE 2: Partition of edge set of CNN ($m, 4$).

Edges of type $y_{k,l}$	Number of edges
$y_{5,6}$	8
$y_{5,7}$	4
$y_{6,6}$	6
$y_{6,7}$	12
$y_{6,9}$	4
$y_{6,11}$	4
$y_{7,7}$	2
$y_{7,9}$	4
$y_{7,11}$	8
$y_{9,9}$	$2m - 10$
$y_{9,11}$	$6m - 28$
$y_{11,11}$	$5m - 24$

Similarly, from substitution of $y_{k,l}(G)$ from Table 2 in (6). we have

$$\begin{aligned}
 ZC_1^*(CNN(m, 4)) &= y_{5,6}(5 + 6) + y_{5,7}(5 + 7) \\
 &\quad + y_{6,6}(6 + 6) + y_{6,7}(6 + 7) \\
 &\quad + y_{6,9}(6 + 9) + y_{6,11}(6 + 11) \\
 &\quad + y_{7,7}(7 + 7) + y_{7,9}(7 + 9) \\
 &\quad + y_{7,11}(7 + 11) + y_{9,9}(9 + 9) \\
 &\quad + y_{9,11}(9 + 11) + y_{11,11}(11 + 11) \\
 &= 8(11) + 4(12) + 6(12) + 12(13) \\
 &\quad + 4(15) + 4(17) \\
 &\quad + 2(14) + 4(16) + 8(18) \\
 &\quad + (2m - 10)(18) + (6m - 28)(20) \\
 &\quad + (5m - 24)(22) \\
 &= 266m - 540.
 \end{aligned}
 \tag{12}$$

$$(1) ZC_1(CNN(m, n)) = 256mn - 700m - 700n + 1448$$

TABLE 3: Partition of edge set of CNN (m, n).

Edges of type $y_{k,l}$	Number of edges
$y_{5,6}$	8
$y_{5,7}$	4
$y_{6,6}$	4
$y_{6,7}$	8
$y_{6,9}$	8
$y_{6,11}$	8
$y_{7,9}$	8
$y_{7,11}$	8
$y_{7,16}$	4
$y_{9,9}$	$2m + 2n - 20$
$y_{9,11}$	$6m + 6n - 56$
$y_{11,11}$	$2m + 2n - 16$
$y_{11,16}$	$6m + 6n - 56$
$y_{16,16}$	$4mn - 19m - 19n + 90$

$$(2) ZC_2(CNN(m, n)) = 1024mn - 2808m - 2808n + 7474$$

$$(3) ZC_1^*(CNN(m, n)) = 128mn - 246m - 246n - 100$$

Theorem 3. Let $m, n \geq 5$ and $CNN(m, n)$ be the CNN. Then,

Proof. In order to prove our result, we will compute c_k , the number of vertices of connection number k , and $y_{k,l}(G)$ is the edge of $CNN(m, n)$ whose vertices have connection numbers k and l . It is easy to see from the structure of $CNN(m, n)$ that $c_5 = 4, c_6 = 8, c_7 = 4, c_9 = 2m + 2n - 16, c_{11} = 2m + 2n - 16$, and $c_{16} = (m - 4)(n - 4)$. Thus, from equation (4), we have the following:

$$\begin{aligned}
 ZC_1(CNN(m, n)) &= c_5(5)^2 + c_6(6)^2 + c_7(7)^2 + c_9(9)^2 \\
 &\quad + c_{11}(11)^2 + c_{16}(16)^2 \\
 &= 4(25) + 8(36) + 4(49) \\
 &\quad + (2m + 2n - 16)(81) + (m - 4) \\
 &\quad \cdot (n - 4)(256) + (2m + 2n - 16)(121) \\
 &= 256mn - 700m - 700n + 1448.
 \end{aligned}
 \tag{13}$$

The edge set of $CNN(m, n)$ can be partitioned into different classes depending upon the edge types of $y_{k,l}(G)$ as listed in Table 3.

From the definition of the second ZCI and substitution of $y_{k,l}$ from Table 3 in (5), it follows that

$$\begin{aligned}
 Z_2(CNN(m, n)) &= y_{5,6}(5 \times 6) + y_{5,7}(5 \times 7) + y_{6,6}(6 \times 6) + y_{6,7}(6 \times 7) + y_{6,9}(6 \times 9) \\
 &\quad + y_{6,11}(6 \times 11) + y_{7,9}(7 \times 9) + y_{7,11}(7 \times 11) + y_{7,16}(7 \times 16) + y_{9,9}(9 \times 9) + y_{9,11}(9 \times 11) \\
 &\quad + y_{11,11}(11 \times 11) + y_{11,16}(11 \times 16) + y_{16,16}(16 \times 16) = 8(30) + 4(35) + 4(36) + 8(42) + 8(54) \\
 &\quad + 8(66) + 8(63) + 8(77) + 4(112) + (2m + 2n - 20)81 + 99(6m + 6n - 56) + 121(2m + 2n - 16) \\
 &\quad + (6m + 6n - 56)(176) + (4mn - 19m - 19n + 90)(256) = 1024mn - 2808m - 2808n + 7474.
 \end{aligned}
 \tag{14}$$

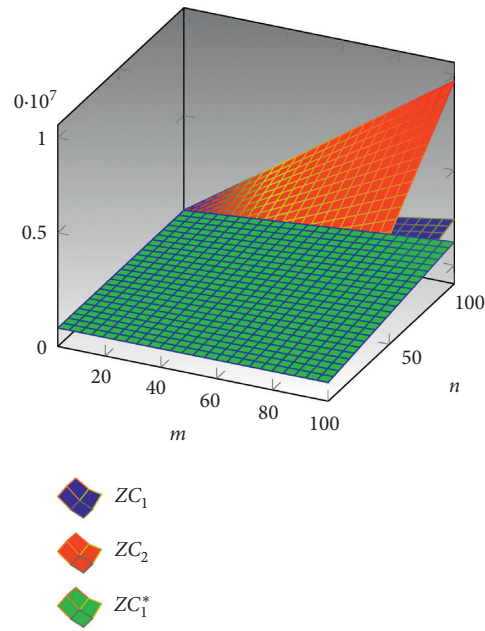


FIGURE 6: Differences of indices for CNN(m, n).

TABLE 4: Differences of indices for CNN($m, 3$).

m	ZC_1	ZC_2	ZC_1^*
5	478	960	366
6	676	1320	468
7	874	1680	570
8	1072	2040	672
9	1270	2400	774
10	1468	2760	876
11	1666	3120	978
12	1864	3480	1080
13	2062	3840	1182
14	2260	4200	1284
15	2458	4560	1386

TABLE 5: Differences of indices for CNN($m, 4$).

m	ZC_1	ZC_2	ZC_1^*
5	988	2865	790
6	1392	4226	1056
7	1796	5587	1322
8	2200	6948	1588
9	2604	8309	1854
10	3008	9670	2120
11	3412	11031	2386
12	3816	12392	2652
13	4220	13753	2918
14	4624	15114	3184
15	5028	16475	3450

TABLE 6: Differences of indices for CNN (m, n) .

(m, n)	ZC_1	ZC_2	ZC_1^*
(5, 5)	848	4994	640
(6, 5)	1428	7306	1034
(7, 5)	2008	9618	1428
(8, 5)	2588	11930	1822
(9, 5)	3168	14242	2216
(10, 5)	3748	16554	2610
(6, 6)	2264	10642	1556
(7, 6)	3100	13978	2078
(8, 6)	3936	17314	2600
(9, 6)	4772	20650	3122
(10, 6)	5608	23986	3644

Similarly, from substitution of $y_{k,l}(G)$ from Table 3 in (6), we have

$$\begin{aligned}
 Z_1^* (\text{CNN}(m, n)) &= y_{5,6}(5 + 6) + y_{5,7}(5 + 7) + y_{6,6}(6 + 6) + y_{6,7}(6 + 7) + y_{6,9}(6 + 9) + y_{6,11}(6 + 11) \\
 &\quad + y_{7,9}(7 + 9) + y_{7,11}(7 + 11) + y_{7,16}(7 + 16) + y_{9,9}(9 + 9) + y_{9,11}(9 + 11) \\
 &\quad + y_{11,11}(11 + 11) + y_{11,16}(11 + 16) \\
 &\quad + y_{16,16}(16 + 16) = 8(11) + 4(12) + 4(12) + 8(13) + 8(15) + 8(17) + 8(16) + 8(18) + 4(23) \quad (15) \\
 &\quad + (2m + 2n - 20)18 + 20(6m + 6n - 56) + 22(2m + 2n - 16) + 27(6m + 6n - 56) \\
 &\quad + 32(4mn - 19m - 19n + 90) \\
 &= 128mn - 246m - 246n - 100.
 \end{aligned}$$

3. Numerical and Graphical Comparisons

In this section, we will give numerical and graphical comparisons of the Zagreb connection indices with respect to the cellular neural network. Maple software is used to construct a simple comparison of the Zagreb connection indices related to the cellular neural network into 3D plots (Figures 5 and 6). The numerical comparison is given in Tables 4–6. We can see from the 3D plots and numerical tables that the second Zagreb index is always greater than the other two indices.

4. Conclusion

The Zagreb connection indices for the cellular neural system on a rectangular grid have been computed. Later on, the obtained results for the Zagreb connection indices, has an application; with the help of numerical tables and 3D plots, the determination of detailed comparisons among these indices of CNN has been outlined. It is notable that the obtained results for these networks are all quadratic in terms of the order of the network, which showed that one can build efficient graph algorithms to compute the indices within polynomial time.

Data Availability

All the data are included within this paper. However, the reader may contact the corresponding author for more details of the data.

Conflicts of Interest

The authors declare no conflicts of interest.

Acknowledgments

Zahid Raza has been funded during this work by the University of Sharjah under Project #1802144068 and MASEP Research Group.

References

- [1] L. O. Chua and L. Yang, "Cellular neural networks: Theory," *IEEE Transactions on Circuits and Systems*, vol. 35, no. 10, pp. 1257–1272, 1988.
- [2] T. Roska and L. O. Chua, "Cellular neural networks with non-linear and delay-type template elements and non-uniform grids," *International Journal of Circuit Theory and Applications*, vol. 20, no. 5, pp. 469–481, 1992.
- [3] T. Matsumoto, T. Yokohama, H. Suzuki, and R. Furukawa, "Several image processing examples by CNN," in *Proceedings of the IEEE International Workshop on Cellular Neural Networks and their Application*, pp. 100–111, Budapest, Hungary, December 1990.
- [4] L. C. Jain and V. R. Vemuri, *Industrial Applications of Neural Networks*, CRC Press, Boca Raton, FL, USA, 1988.
- [5] A. Slavova and V. Mladenov, *Cellular Neural Networks: Theory and Applications*, Nova Publishers, Hauppauge, NY, USA, 2004.

- [6] M. Javaid and J. Cao, "Computing topological indices of probabilistic neural network," *Neural Computing and Applications*, vol. 30, no. 12, pp. 3869–3876, 2018.
- [7] J.-B. Liu, J. Zhao, S. Wang, M. Javaid, and J. Cao, "On the topological properties of the certain neural networks," *Journal of Artificial Intelligence and Soft Computing Research*, vol. 8, no. 4, pp. 257–268, 2018.
- [8] M. Javaid, M. Abbas, J.-B. Liu, W. C. Teh, and J. Cao, "Topological properties of four-layered neural networks," *Journal of Artificial Intelligence and Soft Computing Research*, vol. 9, no. 2, pp. 111–122, 2019.
- [9] S. Chen and Kandlur, "Addressing, routing, and broadcasting in hexagonal mesh multiprocessors," *IEEE Transactions and Computations*, vol. 39, no. 6, pp. 10–18, 1990.
- [10] G. Ducoffe, G. R. Marinescu, C. Obreja, A. Popa, and R. M. Tache, "Extremal graphs with respect to the modified first Zagreb connection index," in *Proceedings of the 16th Cologne-Twente Workshop on Graphs and Combinatorial Optimization, CNAM*, pp. 65–68, Paris, France, June 2018.
- [11] L. N. Lester and J. Sandor, "Computer graphics on a hexagonal grid," *Computers & Graphics*, vol. 8, no. 4, pp. 401–409, 1984.
- [12] D. Maji and G. Ghorai, "A novel graph invariant: the third leap Zagreb index under several graph operations," *Discrete Mathematics, Algorithms and Applications*, vol. 11, no. 5, Article ID 1950054, 2019.
- [13] F. G. Nocetti, I. Stojmenovic, and J. Zhang, "Addressing and routing in hexagonal networks with applications for tracking mobile users and connection rerouting in cellular networks," *IEEE Transactions on Parallel and Distributed Systems*, vol. 13, no. 9, pp. 963–971, 2002.
- [14] A. T. Balaban, "Chemical graph theory and the Sherlock Holmes principle," *International Journal for Philosophy of Chemistry*, vol. 9, no. 1, pp. 107–137, 2013.
- [15] A. T. Balaban, "Can topological indices transmit information on properties but not on structures?" *Journal of Computer-Aided Molecular Design*, vol. 19, no. 9–10, pp. 651–660, 2005.
- [16] D. Basak and B. Subhash, "Use of graph invariants in quantitative structure-activity relationship studies," *Croatica Chemica Acta*, vol. 89, no. 4, pp. 419–429, 2016.
- [17] M. Imran, M. K. Siddiqui, A. Q. Baig, W. Khalid, and H. Shaker, "Topological properties of cellular neural networks," *Journal of Intelligent & Fuzzy Systems*, vol. 37, no. 3, pp. 3605–3614, 2019.
- [18] I. Gutman and N. Trinajstić, "Graph theory and molecular orbitals. Total ϕ -electron energy of alternant hydrocarbons," *Chemical Physics Letters*, vol. 17, no. 4, pp. 535–538, 1972.
- [19] I. Gutman, B. Rui, Trinajstic, and Wilcox Jr., "Graph theory and molecular orbitals. XII. Acyclic polyenes," *The Journal of Chemical Physics*, vol. 62, no. 9, pp. 33–99, 1975.
- [20] A. Ali and N. Trinajstic, "A novel/old modification of the first Zagreb index," *Molecular Informatics*, vol. 37, no. 6-7, p. 1800008, 2018.
- [21] I. Gutman, A. M. Naji, and D. Soner, "On leap Zagreb indices of graphs," *Communications in Combinatorics and Optimization*, vol. 2, no. 2, pp. 99–117, 2017.
- [22] Z. Du, A. Ali, and N. Trinajstic, "Alkanes with the first three maximal/minimal modified first Zagreb connection indices," *Molecular Informatics*, vol. 38, no. 4, Article ID 1800116, 2019.
- [23] B. Basavanagoud and P. Jakkannavar, "Computing first leap Zagreb index of some nano structures," *International Journal of Mathematics And Its Applications*, vol. 6, no. 2-B, pp. 35–39, 2018.
- [24] U. Ali, M. Javaid, and A. Kashif, "Modified Zagreb connection indices of the T-sum graphs," *Main Group Metal Chemistry*, vol. 43, no. 1, pp. 43–55, 2020.
- [25] J. Cao, U. Ali, M. Javaid, and C. Huang, "Zagreb connection indices of molecular graphs based on operations," *Complexity*, vol. 2020, Article ID 7385682, 15 pages, 2020.
- [26] A. M. Naji and N. D. Soner, "First leap Zagreb index of some graph operations," *International Journal of Applied Graph Theory*, vol. 2, pp. 7–18, 2018.
- [27] A. M. Naji, B. Davvaz, S. S. Mahde, and N. D. Soner, "A study on some properties of leap graphs," *Communications in Combinatorics and Optimization*, vol. 5, no. 1, pp. 9–17, 2020.
- [28] Z. Raza, "Leap Zagreb connection numbers for some networks models," *Indonesian Journal of Chemistry*, 2020, In press.
- [29] S. Noreen, A. A. Bhatti, and A. Ali, "Extremum modified first Zagreb connection index of n-vertex trees with fixed number of pendent vertices," *Discrete Dynamics in Nature and Society*, vol. 2020, Article ID 3295342, 6 pages, 2020.
- [30] S. Noreen, A. A. Bhatti, and A. Ali, "Extremal trees for the modified first Zagreb connection index with fixed number of segments or vertices of degree 2," *Journal of Taibah University for Science*, vol. 14, no. 1, pp. 31–37, 2020.
- [31] N. Fatima, A. A. Bhatti, A. Ali, and W. Gao, "Zagreb connection indices of two dendrimer nanostars," *Acta Chemica Iasi*, vol. 27, no. 1, pp. 1–14, 2019.
- [32] Z. Shao, I. Gutman, Z. Li, S. Wang, and P. Wu, "Leap Zagreb indices of trees and unicyclic graphs," *Communications in Combinatorics and Optimization*, vol. 3, pp. 179–194, 2018.
- [33] J.-H. Tang, U. Ali, M. Javaid, and K. Shabbir, "Zagreb connection indices of subdivision and semi-total point operations on graphs," *Journal of Chemistry*, vol. 2019, Article ID 9846913, 14 pages, 2019.

Research Article

Exploring the Impact of Stress on Burnout: A Mathematical Model and Empirical Research

Cheng-Lin Jin,^{1,2} Ting Chen ,² Shu-Yang Wu,³ and Yi-Lin Yang³

¹School of Management, University of Science and Technology of China, Hefei 230088, China

²School of Business, Anhui Xinhua University, Hefei 230088, China

³School of Humanities, University of Science and Technology of China, Hefei, China

Correspondence should be addressed to Ting Chen; Chenting026@163.com

Received 3 May 2020; Revised 26 June 2020; Accepted 16 July 2020; Published 16 October 2020

Guest Editor: Shaohui Wang

Copyright © 2020 Cheng-Lin Jin et al. This is an open access article distributed under the Creative Commons Attribution License, which permits unrestricted use, distribution, and reproduction in any medium, provided the original work is properly cited.

Educational management and social psychology researchers have frequently suggested that job burnout and even turnover intention of college teachers can be induced by stress, which is an inherent part of fast-changing environments and advanced educational technology. However, studies about the contingency effect remain limited. We articulate the effect of role stress and technostress by integrating organizational behaviour and educational management literature. Particularly, this study tries to investigate the moderating effect of teacher agility and leader-member exchange differentiation on suppressing burnout. According to the job demands-resources model, we proposed that the negative effect of stress on burnout depends on the degree of agility and leader-member change quality (LMXD). A study of 271 samples supports the propositions. Specifically, the adverse effect of role stress on job burnout is strengthened by both employee agility and LMXD. We further elaborate theoretical implications on educational management, social psychology, and job demands-resources model.

1. Introduction

Job burnout refers to a series of negative mental experiences from chronic exposure to stress [1]. Prior job burnout literature was involved in social psychological research [2, 3] and organization behavior research [1]. Some studies started to explore the influencing factors and functional mechanisms in a special organization, such as in the healing domain [4, 5], and the accounting field [6, 7]. Recently, some scholars emphasized teacher job burnout [8, 9], yet we still know little about how it occurs and how to constrain teacher occupational burnout.

Prior studies demonstrated that burnout was frequently associated with negative outcomes, such as turnover intention [10, 11], negative emotions [12, 13], poor task performance [14], and commitment to the organization [15]. Likewise, teacher burnout brings about psychological disorder [7] and emotional exhaustion [16, 17]. Teachers' beliefs, attitudes, and emotions affect teaching behaviors and students profoundly [18]. It is not hard to imagine how deep

the despair of an "audience" full of eagerness and curiosity is when confronting an "actor" of emotional exhaustion [14]. Thus, it is extremely essential to be aware what factors account for the occurrence of burnout and it is necessary to investigate what factors can suppress the adverse effect

Burnout is an inherent part of stress [5], which will happen naturally while teachers are exposed to chronic pressure [15]. Some teachers deal with pressure successfully. Yet, for some teachers, burnout might be inevitable because they fail to successfully manage the stress [16]. To reduce and alleviate the negative effect, some researches explore the role of security-related stress on constraining burnout [19], which is verified as an important factor affecting an employee's perception of burnout [20], including two dimensions, security-related role stress (SRRS) and security-related technostress (SRTS).

Prior studies emphasize that the efficacy of stress on burnout is contingent on the context. However, the contingency effect has only received scarce research attention. According to the job demands-resources model [21],

security-related stresses are considered as “job demands” and leader-member change quality (LMXD) and teacher agility as “job resources.” Thereby, we examined the contingency effect of LMXD and teacher agility on the role of security-related stress in suppressing teacher job burnout.

Thus, our study makes several contributions to psychological research and to education management literature. First, we extend the JD-R model, and we provide a more comprehensive understanding on the efficacy of the stress on teacher burnout that is moderated by the value of teacher-subjective effort and the leader-member relationship. Second, we remind teachers and their administrators of potential countermeasures and policies based on different kinds of personal characteristics and interpersonal relationships. Our study sheds a new light on the differential coping strategies in constraining job burnout under various types of stress that teachers suffer from.

2. Theory and Hypotheses Development

The JD-R model was developed to perceive the causes and consequences of burnout. Reference [22], which was first raised by Evangelia Demerouti in *Journal of Applied Psychology*. This theory further indicates two types of working conditions: JDs (job demands) and JRs (job resources). JDs are regarded as “negative factor” [21], which refers to the physical or psychological aspect of the job, and JDs are frequently related to the physical and/or mental costs. In addition, JRs are viewed as “positive factors” [21], which refers to the physical or mental aspect of a job, and they contribute to accomplish work targets, reducing JDs, or aspects relating to physical or physiological expenses and promoting personal working performance.

In our study, security-related stresses correspond with JDs’ definition, which take up teachers’ precious time and efforts. Meanwhile, teacher agility and LMXD pertain to the concept of JRs, which are beneficial for teachers in order to gain necessary resources and make right decision to complete tasks and accomplish targets. Inherent in the definition of JRs is the assumption that JRs may buffer the influence of JDs on job burnout [23]. Teacher agility and LMXD, which are types of JRs, can contribute to prevent and reduce burnout [12].

Our study develops a mathematic model, and the equations of teacher job burnout (TJB) can be written as equation (1) [24]. $SRRS$ and $SRTS$ are considered as antecedents of TJB . Teacher agility (TA) and leader-member exchange differentiation ($LMXD$) indicate the moderating effect on the impacts of TJB . Age, Edu, Acat, and Ole are demographic variables. Based on the job demands-resources model, we try to achieve these following research targets: (1) to elaborate the $SRRS$ and $SRTS$ as essential antecedents to understand teacher burnout; and, specifically, (2) to explore moderating variables changing the extent of efficacy to which $SRRS$ and $SRTS$ impact on teacher burnout.

$$\begin{aligned}
 TJB = & \alpha + \beta_1 SRRS + \beta_1 SRTS + \beta_1 LMXD + \beta_1 TA \\
 & + \beta_1 (SRRS * LMXD) + \beta_1 (SRRS * TA) \\
 & + \beta_1 (SRTS * LMXD) + \beta_1 (SRTS * TA) + \beta_1 Age \\
 & + \beta_1 Edu + \beta_1 Acat + \beta_1 Ole + \mu.
 \end{aligned} \tag{1}$$

2.1. Role Stress, Technostress, and Job Burnout. Burnout is a condition where an employee’s physical, emotional, and mental energies exhaust or run out [25]. There is a strong connection between pressure and burnout [26]. Teacher burnout is consequent when exposed to chronic pressure or when there is a lack of job security [10, 27]. Severe occupational stress may obsessively exhaust teachers’ energy and related JRs and eventually result in a severe status of occupational burnout [15, 28, 29].

Security-related stress is divided into two concepts, security-related role stress ($SRRS$) and security-related technostress ($SRTS$) [20]. $SRRS$ is workers’ response to the situations where multiple roles are provided [20], which is associated with poorer decision-making [4]. Teachers frequently have to do a lot of work besides teaching and scientific research, e.g., the administrative task [25, 29]. Teachers experience role stress and are consequently unsure of their superiors’ expectations and how they will judge the outcomes of their decisions. Teachers will “hesitate to make decisions and will have to rely on a trial and error approach.” Teachers with ambiguous roles would waste more time in struggling to define and understand their own roles, which is bad for decision-making and problem-solving [26], resulting in increasing job burnout.

$SRTS$ is “a kind of modern social disease for technology inadaptation,” when the new technologies cannot be mastered and applied while working [20]. The lack of applying various technologies into educational environment has been considered as a key obstacle to their development [25] and teachers’ capability of integrating the technology into their daily pedagogical work is beneficial for personal development and improvement [30]. More and more teachers are increasingly dependent on education-related technologies. However, at the same time, they are inclined to feel more stressed in a situation where various education-related technologies emerge successively and change rapidly [31]. Thus, as teachers strive to change conventional occupational practices and habits [32], it is inevitable that teachers will experience $SRTS$, which results in losing confidence and missing the previous catching-up opportunity through mastering educational technologies [20, 32], resulting in increasing job burnout. Therefore, we propose the following hypotheses.

- (i) H1a: $SRRS$ is related to teacher burnout positively.
- (ii) H1b: $SRTS$ is related to teacher burnout positively.

2.2. Moderating Effect of Teachers’ Agility. Employee agility, a vital job resource, means a competence to respond promptly and accurately to variation [33, 34] and avail

themselves of chances emerging from the changes. When encountering role stress, teachers with high agility will actively seek for solutions and leader support to break through the role dilemma and make decisions effectively and efficiently [35]. Meanwhile, those teachers with high agility are more adept at capitalizing on an emerging chance, in the ever-changing situation of education-related technologies [36]. Agility adapts teachers to ever-changing technological environments and avails them to modify themselves to better adapt to them. Thus, agility is beneficial for teachers to function efficiently when they are under technostress [37].

Drawing on the JD-R model [23], we propose that teachers with a high level of agility will weaken the efficacy of role stress and technostress, leading to a suppressing of teacher burnout. Therefore, this study attempts to explore the moderating effect of teacher agility on the link of security-related role stress and technostress on teacher burnout. Based on the agreement above, when teacher agility is high, role stress and technostress are less salient in intriguing burnout. Therefore, we propose the following hypotheses.

- (i) H2a: the negative efficacy of SRRS on teacher burnout is weaker when teachers' agility is high rather than low.
- (ii) H2b: the negative efficacy of SRTS on teacher burnout is weaker when teachers' agility is high rather than low.

2.3. The Moderating Effect of LMXD. Leader-member exchange quality differentiation (LMXD) was regarded as the extent of differentiation to which superiors develop distinct quality relationships with their staff [38]. A low LMXD value means a favorable leader-member relationship and a crucial job resource [39]. Prior studies report evidence that LMXD generates negative mood, for instance, distrust or disgust [40], group conflict [39], poor coordination [41], and assistance [42] from both leaders and colleagues.

A high LMXD value further strengthens the adverse effect of stress on job burnout. Firstly, when LMXD is high, for the relationship boundaries, it is unlikely for some teachers to receive resources and leader support [43], yet they receive passive information regarding role differentiation [44]. Thus, for those teachers who are suffering from role stress, it is more difficult to get out of their own role dilemma and to make a right decision. Secondly, when LMXD is high, it is more difficult for some teachers to obtain critical help and support from leaders or other teachers who might have been proficient at some cutting-edge education-related technologies [45], and thus they might feel more insecure.

Drawing on the JD-R model, we propose that the presence of differentiation in the relationship quality with supervisors will strengthen security-related role stress and technostress in aggravating teacher burnout. We attempt to explore the moderating effect of LMXD upon the link of SRRS and SRTS on teacher burnout. Based on the above agreement, when LMXD is high, SRRS and SRTS are more salient in burnout. Therefore, we propose that

- (i) H3a: compared with being low, the negative effect of SRRS on job burnout is more salient when LMXD is high.
- (ii) H3b: compared with being low, the negative effect of SRTS on job burnout is more salient when LMXD is high.

3. Methodology

3.1. Sample and Data Collection. Our research sample frame came from high educational teachers located in China, whose majors are economics, management, engineering, science, philosophy, and literature. To test the hypotheses, we integrated some previously validated items and designed an original questionnaire. With the assistance of some university pro vice-chancellors, in charge of teaching and learning, we conducted in-depth interviews about job burnout with some departmental director and teachers, respectively. Based on the proceeding literature review and field interviews, we redesigned and modified our questionnaire.

Data collection involves two kinds, an online survey and an offline survey. First, we emailed electronic questionnaires to 524 teachers directly, and we received 56 feedbacks. Table 1 presents the profile of the sample. Secondly, with the support of some pro vice-presidents, we effectively adopted the on-site questionnaire distribution and collection. We collected 243 valid questionnaires of 400 distributed questionnaires, of which 28 were removed for being incomplete. Finally, we got 271 samples, with response rate of 28.3%.

3.2. Measures. To validate the conceptual model, our study conducted an empirical investigation and developed the survey instrument in three steps. First, we adapted the measures from preceding studies and then translated the English questionnaire into Chinese while assuring conceptual precision [46]. Second, we asked three academic researchers with expertise in high education research to evaluate the questionnaire for questionnaire flow, design, and content validity. Third, we pilot-tested the questionnaire with 20 teachers and revised the survey instrument based on the feedback received.

3.2.1. Job Burnout. We measured job burnout with 9 items adapted from Chong et al. [6, 47], which is regarded as a series of negative mental experiences from chronic exposure to organizational stress. Example items included "I sense burned out from my work."

3.2.2. Technostress and Role Stress. We adopted scales from Hwang and Cha [20] to measure SRRS and SRTS [20]. SRRS was measured with 8 items, which is associated with workers' response to the situations where multiple roles are provided [20]. Examples included "I often receive assignments without adequate resources and materials to execute them." SRRS was defined as the complexity or uncertainty of education-related technology which induce teacher mental

TABLE 1: Sample demographic ($N = 271$).

	N	Percentage (%)
Gender		
Male	77	28.4
Female	194	71.6
Age		
20–30	89	32.8
30–40	116	42.8
40–50	48	17.7
50–60	16	5.9
≥ 60	2	0.7
Education (Edu)		
Below bachelor	19	7.0
Bachelor	82	30.3
Master	142	52.4
Doctor	28	10.3
Academic title (Acat)		
Research assistant	72	26.6
Lecturer	103	38.0
Associate professor	68	25.1
Professor	28	10.3
Overseas learning experience (Ole)		
Yes	41	15.1
No	230	84.9

pressure [26]. Example items included “*I am forced by education-related technology to work much faster than before.*”

3.2.3. LMXD. We measured LMXD adapted from Chiniara and Bentein [38] which was evaluated for 3 items on the degree of differentiation of the exchange quality between superiors and their staff [38, 42]. Examples include “*Some departmental members have a positive working relationship with my leader while other team members do not.*”

3.2.4. Teacher Agility. We measured the teacher agility adapted from Pitafi et al. [34], which was assessed for 15 items on the capability of a teacher to respond and accommodate themselves to variation rapidly and correctly [34]. Examples include “*I search for the chances to improve myself at my work.*”

4. Result

4.1. Construct Validity. We applied SPSS 21 and Lisrel in our study. Our CFA is to evaluate construct validity, and its results revealed that the measurement model fits the data well as advised ($c^2/df = 2347.25/1016 = 2.31$, CFI = 0.94, IFI = 0.94, NNFI = 0.93, RMSEA = 0.07). All item loadings were statistically significant. Meanwhile, the value of Cronbach’s α and CR were all higher than 0.7. The results of our research further showed good convergent validity and discriminant validity as well, because all values of the square root of the average variances extracted exceeded the thresholds of 0.70 [48] and were higher than the correlations with other constructs [49] (see Table 2). Therefore, in our study, our measures have appropriate reliability and validity.

4.2. Common Method Bias. We conducted one post hoc test to alleviate common method bias. The results of Harman’s single-factor test displayed the first factor only contributed to 19.18 percent of the total variance, indicating a lack of evidence of common method bias. Moreover, the single-factor model showed unacceptable fit indices ($c^2/df = 1130.88/170 = 6.65$, CFI = 0.79, IFI = 0.79, NNFI = 0.77, RMSEA = 0.19, SRMR = 0.12), which were worse than that of our measurement model. Hence, common method bias was not likely to become a major issue.

4.3. Hypothesis Testing. To test the hypotheses in our study, we applied hierarchical regression because it is a usual way recommended to measure moderating effects. In order to reduce concerns of multicollinearity, we standardized all hypothesized variables. The results showed that multicollinearity was not a serious issue because all variance inflation factors (VIF) are less than 7, which is well below the acceptable maximum cutoff value of 10 [50].

In H1a and H1b, we anticipated that role stress and technostress associate positively to teacher burnout. Model 2, in Table 3, indicated that role stress ($\beta = 0.46$, $p < 0.001$, 0.000) and technostress ($\beta = 0.17$, $p < 0.01$, 0.005) both have a significant effect on teacher burnout (see Figure 1). Moreover, compared to technostress, role stress exerted a more salient impact on teacher burnout. Therefore, H1a and H1b were both supported (see Figure 1).

H2a and H2b anticipated the significant moderating impact of teacher agility upon the connection between security-related stress and teacher burnout. We predicted that teacher agility would weaken the effectiveness of role stress in constraining teacher burnout in H2a. On the contrary, the regression results indicated that the interactions of teacher agility with SRRS aggravating teacher burnout ($\beta = 0.18$,

TABLE 2: Descriptive statistics and correlations.

Variable	1	2	3	4	5	6	7	8	9	10
1. JB	—									
2. TS	0.36	0.79								
3. RS	0.54	0.46	0.77							
4. LMXD	-0.21	-0.06	-0.1	0.87						
5. EA	-0.10	0.22	0.20	0.16	0.82					
6. Gender ^a	0.08	-0.14	-0.03	0.08	-0.04	—				
7. Age ^a	0.02	0.04	-0.04	-0.11	-0.04	0.29	—			
8. Edu ^a	0.06	0.02	0.01	0.01	0.01	0.27	0.34	—		
9. Title ^a	0.08	-0.02	-0.02	0.02	-0.05	0.32	0.60	0.53	—	
10. Exp ^a	0.01	0.08	-0.07	0.16	0.03	0.17	0.13	0.24	0.35	—
M	3.00	3.41	3.23	1.71	3.82	0.28	1.99	2.66	2.19	0.15
SD	0.59	0.51	0.65	0.68	0.57	0.45	0.90	0.76	0.95	0.36

Note. The diagonal elements (i.e., italic values) are the square roots of average variances extracted (AVEs). The absolute value of the correlations above 0.14 is statistically significant at $p < 0.05$ (two-tailed tests). ^aDummy variable.

TABLE 3: Hierarchical regression results.

	DV: teacher burnout			
	Model 1	Model 2	Model 3	Model 4
Security-related technostress (SRTS)		0.17*	0.20***	0.21***
Security-related role stress (SRRS)		0.46***	0.48***	0.40***
LMXD			-0.13**	-0.17**
Teacher agility (TA)			-0.21***	-0.14**
SRTS × LMXD				-0.08
SRRS × LMXD				0.15*
SRTS × TA				0.02
SRRS × TA				0.18**
Gender	0.07	0.10	0.12*	0.11*
Age	-0.06	-0.05	-0.07	-0.09
Education	0.01	-0.01	-0.01	0.02
Academic title	0.10	0.10	0.08	0.12
Experience	-0.04	-0.02	0.01	-0.03
R ²	-0.01	0.30	0.38	0.41
ΔR ²		0.31	0.07	0.04
F	6.82	17.828***	18.428***	15.348***
ΔF		59.933***	14.243***	5.536***

Note. * $p < 0.05$; ** $p < 0.01$; *** $p < 0.001$; All tests are two-tailed. (N = 271)

$p < 0.05$, 0.03), which fails to support H2a. Figure 2 reveals that role stress has stronger negative effects on teacher burnout when there is high ($\beta = 0.61$, $p < 0.001$, 0.000) than when there is low teacher agility ($\beta = 0.48$, $p < 0.001$, 0.000). In H2b, although we predicted that teacher agility would weaken the effectiveness of technostress in suppressing teacher burnout, the regression result shows their interactions between teacher agility with SRTS on teacher burnout is not significant ($\beta = 0.02$, $p > 0.05$, 0.80), which fails to support H2b.

H3a and H3b anticipated a positive and significant moderating impact of LMXD upon the connection between role stress, technostress, and teacher burnout. The interaction between LMXD and role stress on teacher burnout is significant ($\beta = 0.15$, $p < 0.05$, 0.03; see Table 3, Model 4), supporting H3a. Model 4, in Table 3, showed higher levels of LMXD strengthening the negative effects of role stress on teacher burnout, in support of H3a. Figure 3 reveals that role stress has stronger negative effects on teacher burnout when

there is high LMXD ($\beta = 0.53$, $p < 0.001$, 0.000) than when there is low LMXD ($\beta = 0.47$, $p < 0.001$, 0.000). In H3b, although we predicted that LMXD would strengthen the efficacy of technostress on teacher burnout, the regression result showed that interaction between LMXD and SRTS on teacher burnout is not significant ($\beta = -0.08$, $p < 0.05$, 0.24), which fails to support H3b.

5. Discussion and Implication

5.1. *Theoretical Implications.* Teacher occupational burnout and stress have attracted attention from theoretical research and management practice, complicating social educational management research [14, 19] and setting higher requirements for the competencies of educational administrators [10]. Although there is widespread recognition of the role of stress, including role stress and technostress, in suppressing teacher burnout, the influences of the leader-member relationship quality and teacher subjective initiative in shaping

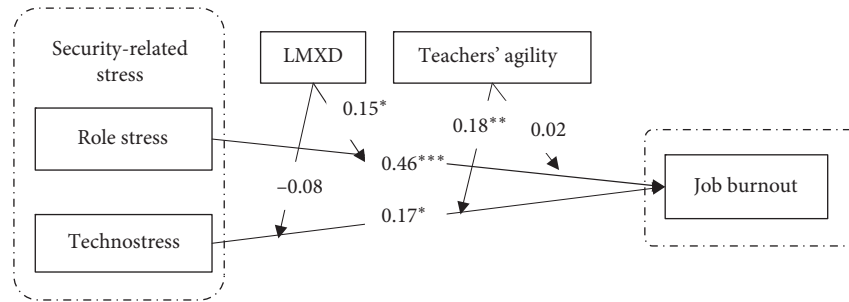


FIGURE 1: Path analysis of the research model. * $p < 0.05$; ** $p < 0.01$; *** $p < 0.001$;

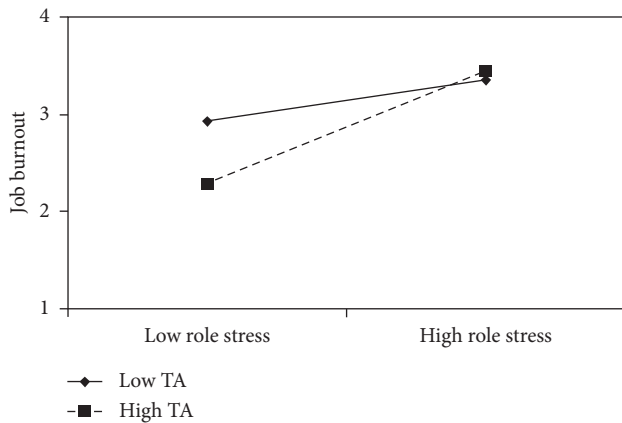


FIGURE 2: Role stress and teacher agility. The moderating effect of teacher agility on role stress-job burnout link.

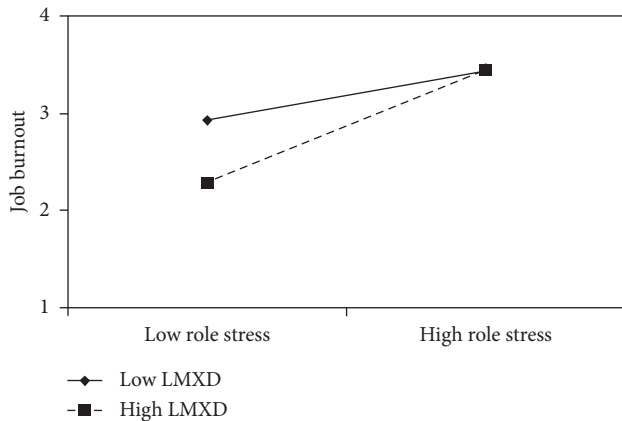


FIGURE 3: Role stress and LMXD. The moderating effect of LMXD on role stress-job burnout link.

their roles remain underexplored. With a survey of 271 teacher samples in China, we found that role stress plays a stronger role in deteriorating teacher burnout than technostress. LMXD enhances role stress in alleviating job burnout. What is surprising and interesting is that teacher agility also worsens job burnout, which is distinct from what we anticipated above. These findings make several contributions to the education management literature.

First, we provided a leadership contingent view of education management by explicating the moderating role of leader-member exchange quality differentiation. Some researches center on the impact of superior leadership [14, 45], but our study represents the first trial to investigate how the relationship of SRRS and SRTS and teacher burnout vary with different levels of leader-member exchange differentiation. When LMXD is high [44], role stress turns more effective in irritating teacher occupational burnout, because an unequal working situation restrains to pursue necessary resources imaginable for university teachers and consequently worsens the level of burnout.

Second, our study enriches the contingent view of JD-R by accounting for different levels of teacher agility. Unlike LMXD, teacher agility varies from person to person [21, 43, 45]. Perhaps most of teachers may make wrong efforts for the lack of appropriate supervision and instruction. Our findings show that role stress has a more salient role in teacher burnout when the level of agility is high for aggravating teacher burnout. Our studies also discovered that the interplay of teacher agility with technostress has a nonsignificant effect on teacher burnout, perhaps because teachers may not be able to overcome technical obstacles only with their own endeavour [25]. Our findings extend prior literature by showing that teacher agility may worsen teacher burnout rather than restrict it.

5.2. Practical Implications. Our study provides several guidelines for practitioners of educational management. Firstly, to lighten the negative efficacy, educational managers should attach emphasis on security-related stress and ought to take effective measures to reduce the adverse effect. Security-related stress, including role stress and technostress, both have a significant negative implication on job burnout. Secondly, role stress has a more salient negative influence than technostress does, especially when LMXD is high. University administrators should prioritize teachers' confusion regarding their role requirements, particularly when leader-member relationship quality is low. However, when teachers are stuck in the technostress, if universities try to optimize the leader-member relationship, the results may disappoint them.

Our findings also have important implications for teachers themselves. Some teachers are struggling from security-related stress [29], such as a large workload, role

conflict or ambiguity, education-related technology complexity, and leader-member exchange relationship, all of which cause psychological and physical passive and exhaustion perception toward work [23]. Our finding confirms stress as a direct cause of job burnout among teachers. Thus, teachers shall take both role stress and technostress seriously and actively [51]; otherwise, they might lose their enthusiasm for educational research and teaching and suffer severe job burnout. As our findings indicate, teachers should attach more emphasis to develop their own agility toward the correct direction. Teachers who have been stuck in role stress may not be clear about what they can or should do. Thus, the more efforts they make, perhaps the more confused they get, and the less progress they will make naturally.

5.3. Limitation and Future Research. Our research consists of two limitations. The impact of agility may vary with time and person. Firstly, the cross-sectional data cannot support us to test the causal link in our concept model. Longitudinal studies might capture the dynamic effects of teacher agility on suppressing the negative impacts between security-related stress and job burnout. Secondly, we gathered data by the virtue of convenient sample methods, and thus we cannot collect data of teachers who are experiencing a distinct degree of security-related stress. Teachers with different experiences show different levels of agility, so the interaction of teacher agility with security-related stress displays distinct characteristics and effects. The teacher's capability to apply education-related technology and getting support from their superiors vary tremendously with development levels of the university and the local economy development [25]. We could conduct stratified sampling studies with large-scale participants in the future in order to gain more sound conclusions and thorough understanding.

Data Availability

The data used to support the findings of this study are available from the corresponding author upon request.

Conflicts of Interest

The authors declare no conflicts of interest.

Acknowledgments

This study was supported by three Key Project Funds from Anhui Education Ministry (no. SK2019A0730, no. SK2019A0749, and no. gxyqZD2016383). The authors thank University of Science and Technology of China for providing laboratory and test system for this study.

References

- [1] E. d. Mol, V. T. Ho, and J. M. Pollack, "Predicting entrepreneurial burnout in a moderated mediated model of job fit," *Journal of Small Business Management*, vol. 56, no. 3, pp. 392–411, 2018.
- [2] M. P. Leiter and C. Maslach, "The social context of burnout," *International Journal of Psychology*, vol. 51, p. 732, 2016.
- [3] X. Wu, H. K. Kwan, L.-Z. Wu, and J. Ma, "The effect of workplace negative gossip on employee proactive behavior in China: the moderating role of traditionality," *Journal of Business Ethics*, vol. 148, no. 4, pp. 801–815, 2015.
- [4] H. S. Jung, H. H. Yoon, and Y. J. Kim, "Effects of culinary employees' role stress on burnout and turnover intention in hotel industry: moderating effects on employees' tenure," *The Service Industries Journal*, vol. 32, no. 13, pp. 2145–2165, 2012.
- [5] C. Maslach and M. P. Leiter, "New insights into burnout and health care: strategies for improving civility and alleviating burnout," *Medical Teacher*, vol. 39, no. 2, pp. 160–163, 2017.
- [6] V. K. Chong, G. S. Monroe, and S. Cahan, "The impact of the antecedents and consequences of job burnout on junior accountants' turnover intentions: a structural equation modelling approach," *Accounting & Finance*, vol. 55, no. 1, pp. 105–132, 2015.
- [7] T. Fagarty, J. Singh, G. K. Rhoads, and R. K. Moore, "Antecedents and consequences of burnout in accounting beyond the role stress model," *Behavioral Research in Accounting*, vol. 12, 2000.
- [8] R. Agcam and M. P. Babanoglu, "An investigation on EFL teachers' attitude toward teaching profession," *Higher Education Studies*, vol. 6, no. 3, p. 21, 2016.
- [9] X. Wang, S. C. Tan, and L. Li, "Technostress in university students' technology-enhanced learning: an investigation from multidimensional person-environment misfit," *Computers in Human Behavior*, vol. 105, p. 106208, 2020.
- [10] Y. H. Lee, "Emotional labor, teacher burnout, and turnover intention in high-school physical education teaching," *European Physical Education Review*, vol. 25, no. 1, pp. 236–253, 2017.
- [11] Y.-N. Cho, B. N. Rutherford, S. B. Friend, G. A. Hamwi, and J. Park, "The role of emotions on frontline employee turnover intentions," *Journal of Marketing Theory and Practice*, vol. 25, no. 1, pp. 57–68, 2016.
- [12] G. M. Alarcon, "A meta-analysis of burnout with job demands, resources, and attitudes," *Journal of Vocational Behavior*, vol. 79, no. 2, pp. 549–562, 2011.
- [13] M.-T. Tsai and H. Ya-Ti, "A resource-based perspective on retention strategies for nurse epidemiologists," *Journal of Advanced Nursing*, vol. 61, no. 2, pp. 188–200, 2008.
- [14] S. Mo and J. Shi, "Linking ethical leadership to employee burnout, workplace deviance and performance: testing the mediating roles of trust in leader and surface acting," *Journal of Business Ethics*, vol. 144, no. 2, pp. 293–303, 2015.
- [15] Y. Wang, A. Ramos, H. Wu et al., "Relationship between occupational stress and burnout among Chinese teachers: a cross-sectional survey in Liaoning, China," *International Archives of Occupational and Environmental Health*, vol. 88, no. 5, pp. 589–597, 2015.
- [16] E. Oberle and K. A. Schonert-Reichl, "Stress contagion in the classroom? The link between classroom teacher burnout and morning cortisol in elementary school students," *Social Science & Medicine*, vol. 159, pp. 30–37, 2016.
- [17] E. M. Skaalvik and S. Skaalvik, "Teacher self-efficacy and teacher burnout: a study of relations," *Teaching and Teacher Education*, vol. 26, no. 4, pp. 1059–1069, 2010.
- [18] S. C. Srivastava, S. Chandra, and A. Shirish, "Technostress creators and job outcomes: theorising the moderating influence of personality traits," *Information Systems Journal*, vol. 25, no. 4, pp. 355–401, 2015.
- [19] C. Maslach, M. P. Leiter, and S. E. Jackson, "Making a significant difference with burnout interventions: researcher and

- practitioner collaboration,” *Journal of Organizational Behavior*, vol. 33, no. 2, pp. 296–300, 2012.
- [20] I. Hwang and O. Cha, “Examining technostress creators and role stress as potential threats to employees’ information security compliance,” *Computers in Human Behavior*, vol. 81, pp. 282–293, 2018.
- [21] D. Xanthopoulou, A. B. Bakker, E. Demerouti, and W. B. Schaufeli, “The role of personal resources in the job demands-resources model,” *International Journal of Stress Management*, vol. 14, no. 2, pp. 121–141, 2007.
- [22] A. Bakker, E. Demerouti, and W. Schaufeli, “The job demands-resources model of burnout,” *Journal of Applied Psychology*, vol. 86, no. 3, pp. 499–512, 2001.
- [23] M. Yankelevich, A. Broadfoot, J. Z. Gillespie, M. A. Gillespie, and A. Guidroz, “General job stress: a unidimensional measure and its non-linear relations with outcome variables,” *Stress and Health*, vol. 28, no. 2, pp. 137–148, 2012.
- [24] J.-B. Liu, J. Zhao, J. Min, and J. D. Cao, “On the Hosoya index of graphs formed by a fractal graph,” *Fractals—Complex Geometry Patterns and Scaling in Nature and Society*, vol. 27, no. 8, pp. 19–35, 2019.
- [25] Y. Dong, C. Xu, C. S. Chai, and X. Zhai, “Exploring the structural relationship among teachers’ technostress, technological pedagogical content knowledge (TPACK), computer self-efficacy and school support,” *The Asia-Pacific Education Researcher*, vol. 29, no. 2, p. 147, 2019.
- [26] S. Zhang, R. C.-W. Kwok, P. B. Lowry, Z. Liu, and J. Wu, “The influence of role stress on self-disclosure on social networking sites: a conservation of resources perspective,” *Information & Management*, vol. 56, no. 7, p. 103147, 2019.
- [27] C.-C. Yang, C.-W. Fan, K.-M. Chen, S.-C. Hsu, and C.-L. Chien, “As a happy kindergarten teacher: the mediating effect of happiness between role stress and turnover intention,” *The Asia-Pacific Education Researcher*, vol. 27, no. 6, pp. 431–440, 2018.
- [28] J. Peng, D. Li, Z. Zhang et al., “How can core self-evaluations influence job burnout? The key roles of organizational commitment and job satisfaction,” *Journal of Health Psychology*, vol. 21, no. 1, pp. 50–59, 2016.
- [29] X. Yu, P. Wang, X. Zhai, H. Dai, and Q. Yang, “The effect of work stress on job burnout among teachers: the mediating role of self-efficacy,” *Social Indicators Research*, vol. 122, no. 3, pp. 701–708, 2014.
- [30] F. O. Pineida, “Competencies for the 21st century: integrating ICT to life, school and economical development,” *Procedia—Social and Behavioral Sciences*, vol. 28, pp. 54–57, 2011.
- [31] S. Krishnan, “Personality and espoused cultural differences in technostress creators,” *Computers in Human Behavior*, vol. 66, pp. 154–167, 2017.
- [32] T. S. Ragu-Nathan, M. Tarafdar, B. S. Ragu-Nathan, and Q. Tu, “The consequences of technostress for end users in organizations: conceptual development and empirical validation,” *Information Systems Research*, vol. 19, no. 4, pp. 417–433, 2008.
- [33] S. Alavi, D. A. Wahab, N. Muhamad, and B. Arbab Shirani, “Organic structure and organisational learning as the main antecedents of workforce agility,” *International Journal of Production Research*, vol. 52, no. 21, pp. 6273–6295, 2014.
- [34] A. H. Pitafi, H. Liu, and Z. Cai, “Investigating the relationship between workplace conflict and employee agility: the role of enterprise social media,” *Telematics and Informatics*, vol. 35, no. 8, pp. 2157–2172, 2018.
- [35] D. Cumming, I. Filatotchev, J. Reinecke, and G. Wood, “New investor categories, agility and HRM: the case of Sovereign Wealth Funds,” *Human Resource Management Review*, vol. 30, no. 1, p. 100694, 2020.
- [36] X. Wang and B. Li, “Technostress among university teachers in higher education: a study using multidimensional person-environment misfit theory,” *Frontiers in Psychology*, vol. 10, p. 1791, 2019.
- [37] Y. J. Joo, K. Y. Lim, and N. H. Kim, “The effects of secondary teachers’ technostress on the intention to use technology in South Korea,” *Computers & Education*, vol. 95, pp. 114–122, 2016.
- [38] M. Chiniara and K. Bentein, “The servant leadership advantage: when perceiving low differentiation in leader-member relationship quality influences team cohesion, team task performance and service OCB,” *The Leadership Quarterly*, vol. 29, no. 2, pp. 333–345, 2018.
- [39] A. Yu, F. K. Matta, and B. Cornfield, “Is leader-member exchange differentiation beneficial or detrimental for group effectiveness? A meta-analytic investigation and theoretical integration,” *Academy of Management Journal*, vol. 61, no. 3, pp. 1158–1188, 2018.
- [40] R. C. Liden, B. Erdogan, S. J. Wayne, and R. T. Sparrowe, “Leader-member exchange, differentiation, and task interdependence: implications for individual and group performance,” *Journal of Organizational Behavior*, vol. 27, no. 6, pp. 723–746, 2006.
- [41] X.-P. Chen, W. He, and L.-C. Weng, “What is wrong with treating followers differently? The basis of leader-member exchange differentiation matters,” *Journal of Management*, vol. 44, no. 3, pp. 946–971, 2015.
- [42] C. Emery, J. E. Booth, G. Michaelides, and A. J. Swaab, “The importance of being psychologically empowered: buffering the negative effects of employee perceptions of leader-member exchange differentiation,” *Journal of Occupational and Organizational Psychology*, vol. 92, no. 3, pp. 566–592, 2019.
- [43] K. Lee, Y. J. Chae, and I. Shin, “Motivational antecedents of leader-member exchange differentiation: evidence from South Korea,” *Asia Pacific Journal of Management*, vol. 33, no. 1, pp. 87–112, 2016.
- [44] S. Auh, D. E. Bowen, C. Aysuna, and B. Menguc, “A search for missing links,” *Journal of Service Research*, vol. 19, no. 3, pp. 260–275, 2016.
- [45] C. H. Thomas and M. J. Lankau, “Preventing burnout: the effects of LMX and mentoring on socialization, role stress, and burnout,” *Human Resource Management*, vol. 48, no. 3, pp. 417–432, 2009.
- [46] L. Poppo, K. Z. Zhou, and J. J. Li, “When can you trust “trust”? Calculative trust, relational trust, and supplier performance,” *Strategic Management Journal*, vol. 37, no. 4, pp. 724–741, 2016.
- [47] W. B. Schaufeli, M. P. Leiter, and C. Maslach, “Burnout: 35 years of research and practice,” *Career Development International*, vol. 14, no. 3, pp. 204–220, 2009.
- [48] C. E. Lance, M. M. Butts, and L. C. Michels, “The sources of four commonly reported cutoff criteria,” *Organizational Research Methods*, vol. 9, no. 2, pp. 202–220, 2006.
- [49] C. Fornell and D. F. Larcker, “Evaluating structural equation models with unobservable variables and measurement error,” *Journal of Marketing Research*, vol. 18, no. 1, pp. 39–50, 1981.
- [50] J. Neter, M. H. Kutner, C. J. Nachtsheim, and W. Wasserman, *Applied Linear Statistical Models*, Irwin, Chicago, IL, USA, 1996.
- [51] C. Maier, S. Laumer, C. Weinert, and T. Weitzel, “The effects of technostress and switching stress on discontinued use of social networking services: a study of Facebook use,” *Information Systems Journal*, vol. 25, no. 3, pp. 275–308, 2015.

Research Article

ARSS: A Novel Aerial Robot Performs Tree Pruning Tasks

Hao Xu ^{1,2}, Zhong Yang ¹, Le Chang ¹, Kaiwen Lu ¹, Changliang Xu ¹
and Qiuyan Zhang³

¹College of Automation Engineering, Nanjing University of Aeronautics and Astronautics, Nanjing 211106, China

²School of Mathematics & Physics, Anhui University of Technology, Anhui 243032, Ma'anshan, China

³Guizhou Electric Power Research Institute, Guizhou Power Grid Co. Ltd., Guiyang, Guizhou 550000, China

Correspondence should be addressed to Zhong Yang; yangzhong@nuaa.edu.cn

Received 7 August 2020; Revised 10 September 2020; Accepted 28 September 2020; Published 14 October 2020

Academic Editor: Jia-Bao Liu

Copyright © 2020 Hao Xu et al. This is an open access article distributed under the Creative Commons Attribution License, which permits unrestricted use, distribution, and reproduction in any medium, provided the original work is properly cited.

In this article, we present a novel aerial robot with a suspended saw (ARSS) for pruning trees that are close to electric power lines. The Robot's movement process includes free flight and aerial pruning. We first established a dynamic model and designed a controller based on the Active Disturbance Rejection Control (ADRC) on the model. Aiming at the problem of saw swing and residual oscillation during the free flight movement, we adopt the linear state feedback to design a swing angle controller. Finally, we use Matlab/Simulink and CoppeliaSim for simulation, and the simulation results verify the effectiveness and feasibility of the controller.

1. Introduction

As Aerial Robots are increasingly deployed in a broad spectrum of real-world, there is a growing demand to broaden their application scenario [1]. The Robot has the advantages of small size, strong maneuverability, and the ability to hover at a fixed point. It has become an excellent aerial work platform, and it has been used in cargo transportation [2], spraying pesticides [3], etc. Tree barrier pruning is a new application of aerial robots. A tree barrier is a tree that grows near the power line. Its branches will grow between the power lines and may cause a short circuit on the power line. These problems are caused due to contact tree branches with wires of power towers. This contact is one of the significant reasons for interrupting power services. The traditional method is that a person carries a pruning tool to climb the tree to cut the branches that will cause a short circuit of the power line. This method is hazardous and quickly causes personal injury. However, using aerial robots to carry pruning tools and fly to the vicinity of the branches to be cut will improve work efficiency and safety.

Moreover, the installation position of the cutting tool on the aerial Robot will cause differences in modeling and

control. To the best of our knowledge, the pruning tool can be installed on the top [4–6], front [7], and bottom of the fuselage [8]. The branches that need to be cut are generally at the crown of the tree. Moving the drone to the top of the tree can improve the pruning efficiency. Therefore, our design is to install the pruning tool under the fuselage through a rope hanging method. This installation method is the mode for a multirotor helicopter with suspended loads [9]. When the robot performs tasks, there are several difficulties to overcome. First, because of the movement of the fuselage and its own inertia, the load will swing in the air. The swing will increase the control difficulty and model uncertainty of the robot. Second, due to the limited space under the fuselage and the problem that the shape of the load does not match the fuselage, there are a lot of restrictions on the choice of load.

To the best of our knowledge, research on the multirotor helicopter with suspended loads has been receiving attention, and many effective control methods have been proposed. In [10], a nonlinear controller based on the backstepping control algorithm is designed so that the drone can still perform a good trajectory tracking when the hanging load swings significantly; Alothman and Gu [11]

uses a differential smoothing method to design a four-rotor UAV controller with suspended load, which realizes the trajectory generation and tracking of this system; Faust et al. [12] denotes an iterative linear-quadratic optimal controller, which realizes the trajectory tracking control of the UAV and suppresses the swing of the hanging load. Palunko et al. [13] adopts a reinforcement learning method to train the helicopter flight control system and realize the trajectory planning of hanging load. In [14], the researchers studied the take-off process of a quadcopter drone with a load. Yang et al. [15] solved the problem of the quadrotor achieving safe take-off under the condition that the hanging load is unknown, and the simulation results confirmed the effectiveness of its algorithm. Complex network theory [16, 17] can plan the tasks of aerial robots.

However, the research results of multirotor drones with hanging systems are remarkable, but many methods still have some limitations. The controller designed in [10] can achieve reasonable trajectory tracking control but does not control the position of the hanging load. The control effect of the controller designed in [11, 12] is significant, but the controller is complex and requires high computing resources for the onboard computer. The controller in [13] can only be used under a load of a specific weight. When changing the load, reinforcement learning is required again, and the portability is not good. The authors of [14, 15] focused on the take-off and landing issues, but did not focus on the entire flight process. References [16, 17] only analyze and prove mission planning but do not involve specific controller design.

In this article, we present the ARSS, an Aerial Robot with Suspended Saws. ARSS can use the hanging saw to cut and clean horizontally growing tree barrier. In order to solve the model uncertainty and disturbance in the execution of aerial pruning tasks, we used the Active Disturbance Rejection Control (ADRC) [18] to design the controller. The main components of ADRC include Tracking-Differentiator (TD) [19], Extended State Observer (ESO) [20, 21], and Nonlinear State Error Feedback (NLSEF) [22], all of which we have covered. We summarize the contributions as follows:

- (1) A novel a novel aerial robot can prune trees well.
- (2) As the position and attitude are controlled by the ADRC method without linearizing the system model, this robot system can achieve better control results when it is far from the equilibrium point, and the system has high robustness.
- (3) In addition, the controller has a simple structure and does not require high calculation speed of the onboard microprocessor.

In the rest of the article, we first discuss the dynamic model of ARSS; next, the controller based on ADRC is introduced including attitude control, position control and control allocation. We also verified the entire Robot under Matlab/Simulink and CoppeliaSim. Finally, we give some conclusions and future work.

2. Mathematical Model

2.1. Coordinates and Conventions. Overall, two coordinate frames were used. The inertial frame $E\{O_E, X_E, Y_E, Z_E\}$ is fixed on the ground, and its z axis points upward. And the body frame $B\{O_B, X_B, Y_B, Z_B\}$ is fixed on the COG, the z axis of the frame points upward, as seen in Figure 1. The Suspended Saws system is shown in Figure 2, L is the length of the rope, and l is the distance from the motor axis to the COG. ϕ_L is the angle between the projection of the connecting rod in the $O_b X_b Z_b$ plane and the z_b axis, θ_L is the angle between the connecting rod and the above projection.

2.2. Assumptions. For the sake of model simplicity and algorithm efficiency, the following assumptions were made:

- (1) The body structure is rigid and symmetric
- (2) The geometric center and CoG of the Robot are the same
- (3) The rope is rigid, non-stretchable, and of no quality
- (4) The load is always under the body

2.3. Notation. Throughout the article, we use right-hand rules for the coordinate system. The attitude angles of the body are $[\theta, \phi, \psi]^T \in \mathbb{R}^3$ including Pitch angle θ , Roll angle ϕ , and Yaw angle ψ , and $[p, q, r]^T \in \mathbb{R}^3$ denote the angular velocity in the body frame. $[x, y, z]^T \in \mathbb{R}^3$ denotes the position in the inertial frame.

The matrix ${}^B_E R$ stands for the rotation matrix that rotates a vector represented in the inertial frame $\{E\}$ to the body frame $\{B\}$. The rotation matrix is defined as

$${}^B_E R = \begin{bmatrix} c_\theta c_\psi & c_\theta s_\psi & -s_\theta \\ s_\theta s_\phi c_\psi - c_\phi s_\psi & s_\theta s_\phi s_\psi + c_\phi c_\psi & c_\theta s_\phi \\ s_\theta c_\phi c_\psi + s_\phi s_\psi & s_\theta c_\phi s_\psi - s_\phi c_\psi & c_\theta c_\phi \end{bmatrix}, \quad (1)$$

where ${}^B_E R \in SO(3)$, $SO(3) \triangleq \{R | R^T R = \mathbf{I}_3, \det(R) = 1, R \in \mathbb{R}^{3 \times 3}\}$ with $s_{(\cdot)}$ representing the sine and $c_{(\cdot)}$ the cosine.

2.4. Body Dynamic Model. For the modeling of the body dynamics, the Newton–Euler formalism was used. The Equilibrium equation is as follows:

$$M [\ddot{x} \ \ddot{y} \ \ddot{z}] = \begin{bmatrix} F_x \\ F_y \\ F_z \end{bmatrix}, \quad (2)$$

$$I_b \begin{bmatrix} \dot{p} \\ \dot{q} \\ \dot{r} \end{bmatrix} + \begin{bmatrix} p \\ q \\ r \end{bmatrix} \times I_b \begin{bmatrix} p \\ q \\ r \end{bmatrix} = \begin{bmatrix} \tau_x \\ \tau_y \\ \tau_z \end{bmatrix},$$

with M being the mass of the aerial Robot and I_b the moment of inertia. I_b is defined as follows:

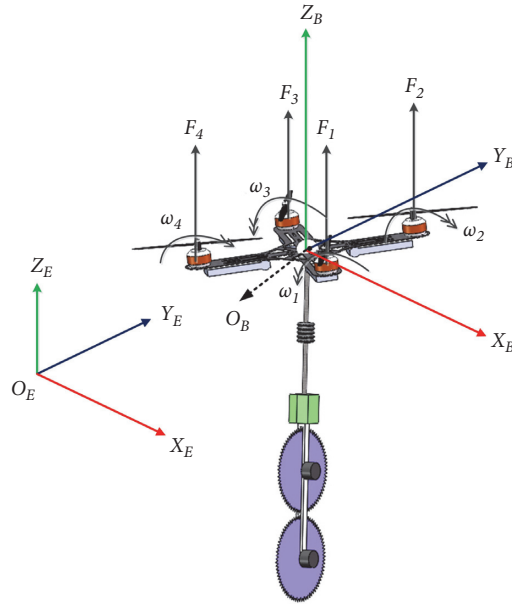


FIGURE 1: The inertial and body frames.

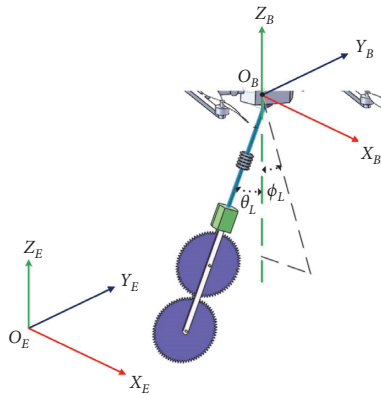


FIGURE 2: The suspended saws system.

$$I_b = \begin{bmatrix} I_{11} & -I_{12} & -I_{13} \\ -I_{12} & I_{22} & -I_{23} \\ -I_{13} & -I_{23} & I_{33} \end{bmatrix}, \quad (3)$$

where I_{12}, I_{13}, I_{23} are smaller than I_{11}, I_{22}, I_{33} , respectively. Define

$$\begin{aligned} I_x &= I_{11}, \\ I_y &= I_{22}, \\ I_z &= I_{33}. \end{aligned} \quad (4)$$

The solution to equation (3) is

$$I_b = \text{diag}(I_x, I_y, I_z). \quad (5)$$

According to equation (4), the forces ${}^B F = [F_x \ F_y \ F_z]^T$ and torques $\tau^B = [\tau_x \ \tau_y \ \tau_z]^T \in \mathbb{R}^3$ act on the COG of the body. Then the relation between

angular velocity $[p, q, r]^T$ and attitude angle $[\theta, \phi, \psi]^T$ can expressed as

$$\begin{bmatrix} p \\ q \\ r \end{bmatrix} = \mathbf{R}_c \begin{bmatrix} \dot{\phi} \\ \dot{\theta} \\ \dot{\psi} \end{bmatrix}, \quad (6)$$

$$\mathbf{R}_c = \begin{bmatrix} 1 & 0 & -\sin \theta \\ 0 & \cos \phi & \sin \phi \cos \theta \\ 0 & -\sin \phi & \cos \phi \cos \theta \end{bmatrix}.$$

Regardless of external disturbances, the aerial Robot is mainly subjected to the gravity in the negative direction of the $O_e X_e$ axis and the lift $F_i, i = 1, 2, 3, 4$ generated by the four rotors pointed by the positive direction of the $O_b Z_b$ axis. F_i is related to lift coefficient C_T and rotating speed ω_i , which is given by

$$F_i = C_T \omega_i^2. \quad (7)$$

Therefore, let F_t be the total lift so that

$$F_t = \sum_{i=1}^4 F_i = C_T \sum_{i=1}^4 \omega_i^2. \quad (8)$$

According to equation (1), ${}^B F = [F_x \ F_y \ F_z]^T$ is obtained as follows:

$$\begin{aligned} \begin{bmatrix} F_x \\ F_y \\ F_z \end{bmatrix} &= {}^B_E \mathbf{R}^T \begin{bmatrix} 0 \\ 0 \\ -F_t \end{bmatrix} + \begin{bmatrix} 0 \\ 0 \\ mg \end{bmatrix} \\ &= \begin{bmatrix} -(\cos \phi \sin \theta \cos \psi + \sin \phi \sin \psi) F_t \\ -(\cos \phi \sin \theta \sin \psi - \sin \phi \cos \psi) F_t \\ mg - \cos \phi \cos \theta F_t \end{bmatrix}. \end{aligned} \quad (9)$$

Based on assumption (2), the resultant torque is mainly generated by the lift and counter torque at the rotor that does not pass through the center of mass, while gravity does not produce torque. The torque generated by the rotor lift constitutes the moment around the $O_b X_b$ and $O_b Y_b$ axis, and the antitorque of the rotor constitutes the moment around the $O_b Z_b$ axis, given by

$$\begin{aligned} \tau_x &= L(-F_1 + F_2 + F_3 - F_4), \\ \tau_y &= L(F_1 + F_2 - F_3 - F_4), \\ \tau_z &= C_M(\omega_1^2 - \omega_2^2 + \omega_3^2 - \omega_4^2), \end{aligned} \quad (10)$$

where L is the distance between the center point of the rotor and the centroid of the Robot.

On the basis of Equations (8) and (10), one has

$$\begin{pmatrix} \tau_x \\ \tau_y \\ \tau_z \end{pmatrix} = \begin{pmatrix} -C_T L & C_T L & C_T L & -C_T L \\ C_T L & C_T L & -C_T L & -C_T L \\ C_M & -C_M & C_M & -C_M \end{pmatrix} \begin{pmatrix} \omega_1^2 \\ \omega_2^2 \\ \omega_3^2 \\ \omega_4^2 \end{pmatrix}. \quad (11)$$

By combining Equations (2), (9), and (11), the body dynamic model is expressed as

$$\begin{aligned} \ddot{x} &= -(\cos \phi \sin \theta \cos \psi + \sin \phi \sin \psi) \frac{F_t}{m}, \\ \ddot{y} &= -(\cos \phi \sin \theta \sin \psi - \sin \phi \cos \psi) \frac{F_t}{m}, \\ \ddot{z} &= g - \cos \phi \cos \theta \frac{F_t}{m}, \\ \dot{p} &= \frac{I_y - I_z}{I_x} qr + \frac{1}{I_x} \tau_x, \\ \dot{q} &= \frac{I_z - I_x}{I_y} pr + \frac{1}{I_y} \tau_y, \\ \dot{r} &= \frac{I_x - I_y}{I_z} pq + \frac{1}{I_z} \tau_z. \end{aligned} \quad (12)$$

2.5. Suspended Saws Model. For the modeling of the saws dynamics, the Lagrange formalism was used. Its general form is the following:

$$\frac{d}{dt} \left(\frac{\partial \mathcal{L}}{\partial \dot{\Theta}} \right) - \frac{\partial \mathcal{L}}{\partial \Theta} = Q, \quad (13)$$

where $\mathcal{L}(\Theta, \dot{\Theta}) = k(\Theta, \dot{\Theta}) - u(\Theta)$, $k(\Theta, \dot{\Theta})$ represents the kinetic energy and $u(\Theta)$ expresses potential energy; Θ denotes the generalized coordinate and Q is generalized forces.

As shown in Figure 1, the equation set from Saws position (x_L, y_L, z_L) to the body position (x, y, z) is further obtained as

$$\begin{aligned} x_L &= x + l \cos \theta_L \sin \phi_L, \\ y_L &= y + l \sin \theta_L, \\ z_L &= z - l \cos \theta_L \cos \phi_L, \end{aligned} \quad (14)$$

where l represents the rod length.

Combining equation (14), kinetic energy $k(\Theta, \dot{\Theta})$ is expressed as

$$k(\Theta, \dot{\Theta}) = \frac{1}{2} M(\dot{x}^2 + \dot{y}^2 + \dot{z}^2) + \frac{1}{2} m(\dot{x}_L^2 + \dot{y}_L^2 + \dot{z}_L^2). \quad (15)$$

Then potential energy is

$$u(\Theta) = Mgz + mgz_L. \quad (16)$$

Among the saws dynamic model, generalized coordinate $\Theta = [x, y, z, \theta_L, \phi_L]^T$ and generalized forces $Q = [F_x, F_y, F_z, 0, 0]^T$. By combining equations (13)–(17), the ARSS dynamic model is expressed as

$$M(\Theta)\ddot{\Theta} + C(\Theta, \dot{\Theta}) + G(\Theta) = Q, \quad (17)$$

where

$$M(\Theta) = \begin{bmatrix} M+m & 0 & 0 & mlc_{\theta_L}c_{\phi_L} & -m s_{\theta_L}s_{\phi_L} \\ 0 & M+m & 0 & 0 & mlc_{\theta_L} \\ 0 & 0 & M+m & mlc_{\theta_L}s_{\phi_L} & m s_{\theta_L}c_{\phi_L} \\ mlc_{\theta_L}c_{\phi_L} & 0 & mlc_{\theta_L}s_{\phi_L} & ml^2c_{\theta_L}^2 & 0 \\ -m s_{\theta_L}s_{\phi_L} & mlc_{\theta_L} & m s_{\theta_L}c_{\phi_L} & 0 & ml^2 \end{bmatrix},$$

$$C(\Theta, \dot{\Theta}) = \begin{bmatrix} 0 & 0 & 0 & -ml(c_{\theta_L}s_{\phi_L}\dot{\phi}_L + s_{\theta_L}c_{\phi_L}\dot{\theta}_L) & -ml(s_{\theta_L}c_{\phi_L}\dot{\phi}_L + c_{\theta_L}s_{\phi_L}\dot{\theta}_L) \\ 0 & 0 & 0 & 0 & -m s_{\theta_L}\dot{\theta}_L \\ 0 & 0 & 0 & ml(c_{\theta_L}c_{\phi_L}\dot{\phi}_L - s_{\theta_L}s_{\phi_L}\dot{\theta}_L) & -ml(s_{\theta_L}s_{\phi_L}\dot{\phi}_L - c_{\theta_L}c_{\phi_L}\dot{\theta}_L) \\ 0 & 0 & 0 & -ml^2c_{\theta_L}s_{\phi_L}\dot{\theta}_L & -ml^2c_{\theta_L}s_{\phi_L}\dot{\phi}_L \\ 0 & 0 & 0 & ml^2c_{\theta_L}s_{\phi_L}\dot{\phi}_L & 0 \end{bmatrix}, \quad (18)$$

$$G(\Theta) = [0 \ 0 \ (M+m)g \ mglc_{\theta_L}s_{\phi_L} \ mgl s_{\theta_L}c_{\phi_L}]^T,$$

$$Q = \begin{bmatrix} {}^B_E R^T [0 \ 0 \ F_t]^T \\ 0 \\ 0 \end{bmatrix} = [F_x \ F_y \ F_z \ 0 \ 0]^T,$$

$$\begin{aligned} \ddot{x} &= \frac{ml}{M+m} (c^3\theta s\phi\dot{\phi}^2 + c\theta s\phi\dot{\theta}^2) + \frac{1}{M} (M+m - m\sin^2\phi\cos^2\theta) \\ &\quad - \frac{m}{M} \sin\theta\cos\theta\sin\phi F_y + \frac{m}{M} \sin\phi\cos\phi\cos^2\theta F_z, \\ \ddot{y} &= \frac{ml}{M+m} (\cos^2\theta\sin\theta\dot{\phi}^2 + \sin\theta\dot{\theta}^2) - \frac{m}{M} \sin\theta\cos\theta\sin\phi F_x \\ &\quad + \left(1 + \frac{m}{M}\cos^2\theta\right) F_y + \frac{m}{M} \sin\theta\cos\theta\cos\phi F, \\ \ddot{z} &= -\frac{ml}{M+m} (\cos^3\theta\cos\phi\dot{\phi}^2 + \cos\theta\cos\phi\dot{\theta}^2) + \frac{m}{M(M+m)} \sin\phi\cos\phi\cos^2\theta F_x \\ &\quad - \frac{m}{M(M+m)} \sin\theta\cos\theta\cos\phi F_y + \frac{1}{M(M+m)} (M+m - m\cos^2\phi\cos^2\theta) F_z - g, \end{aligned} \quad (19)$$

$$\begin{aligned} L\cos\theta_L\ddot{\phi}_L - 2l\sin\theta_L\dot{\theta}_L\dot{\phi}_L + \cos\phi_L\ddot{x} + (\ddot{z} + g)\sin\phi_L &= 0, \\ L\ddot{\theta}_L + l\sin\theta_L\cos\theta_L\dot{\phi}_L^2 + g\cos\phi_L\sin\theta_L - \sin\phi_L\sin\theta_L\ddot{x} + \cos\theta_L\dot{y} + \cos\phi_L\sin\theta_L\ddot{z} &= 0. \end{aligned} \quad (20)$$

3. Controller Design

The general aerial Robot only needs to control the position and attitude, and ARSS not only needs to control the position and attitude, but also needs to control the swing angle of suspended saw. The position change of the Robot will cause the saw swing. If the swing angle is not controlled, the saw may swing violently, affecting the robot stability, so it is necessary to control the swing angle of the suspended saw. ADRC has the advantages of low model

dependence and strong anti-disturbance, and it has good applicability to ARSS with complex model and large disturbance.

In this section, we present a baseline controller for the ARSS platform. The controller is based on ADRC including attitude and position control, and uses a linear state feedback to design the swing angle controller. The controller is a double-loop structure, the outer loop is position control, and the inner one is attitude control. Control structure shown in Figure 3.

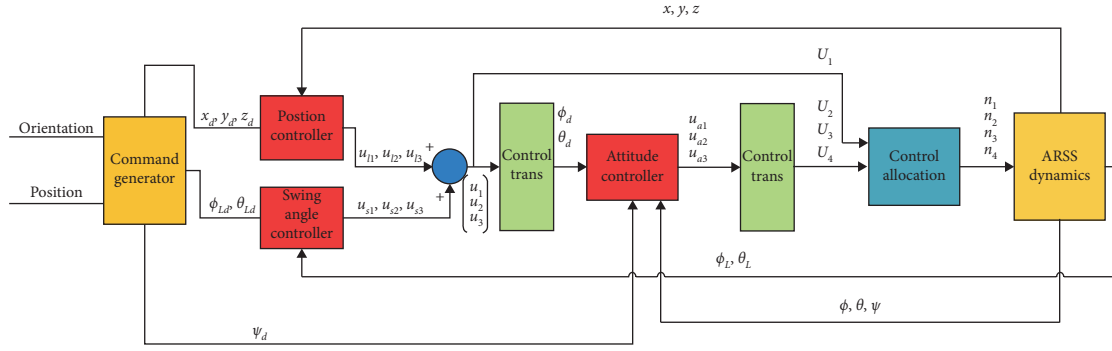


FIGURE 3: The control diagram of ARSS.

3.1. Attitude Control. The attitude controller controls the attitude angle α , so equation (6) needs to be transformed to obtain the expression of Euler angle. Because the expression contains a large number of non-linear elements and coupling terms, a common solution is the small angle approximation method, which limits the attitude angle change in a small range, so that the Euler angle change $(\dot{\phi}, \dot{\theta}, \dot{\psi})$ is approximately equal to the angular velocity (p, q, r) . However, such a processing method can only allow the controller to have a good control effect within a small range of attitude angle changes. If the attitude angle changes too much, the performance of the controller will be greatly reduced. The other method is to add a layer of angular velocity loop on the basis of the small angle approximation method to make the attitude controller into a double-loop structure. Although this method has a certain effect, it will make the structure of the controller very complicated and many parameters, it is difficult to adjust the parameters.

ADRC can solve this problem well. ADRC has low dependence on the mathematical model of the controlled object. It can treat the coupling item as an unmodeled part of the system and compensate the coupling item by Extended State Observer (ESO). Therefore, we adopt ADRC to design ARSS attitude controller.

First, the derivative of equation (6) can be obtained:

$$\begin{bmatrix} \dot{p} \\ \dot{q} \\ \dot{r} \end{bmatrix} = \mathbf{R}_c \begin{bmatrix} \ddot{\phi} \\ \ddot{\theta} \\ \ddot{\psi} \end{bmatrix} + \begin{bmatrix} 0 & -\cos \theta & 0 \\ -\sin \phi & -\sin \phi \sin \theta & \cos \phi \cos \theta \\ -\cos \phi & -\sin \phi \cos \theta & -\cos \phi \sin \theta \end{bmatrix} \begin{bmatrix} \dot{\phi} \dot{\theta} \\ \dot{\theta} \dot{\psi} \\ \dot{\phi} \dot{\psi} \end{bmatrix}. \quad (21)$$

Then, combining equations (3)–(5) with equation (21), one has

$$\begin{bmatrix} \dot{p} \\ \dot{q} \\ \dot{r} \end{bmatrix} = I_b^{-1} \text{diag}(I_y - I_z, I_z - I_x, I_x - I_y) \begin{bmatrix} qr \\ pr \\ pq \end{bmatrix} + I_b^{-1} \begin{bmatrix} \tau_x \\ \tau_y \\ \tau_z \end{bmatrix}. \quad (22)$$

Consequently,

$$\begin{bmatrix} \ddot{\phi} \\ \ddot{\theta} \\ \ddot{\psi} \end{bmatrix} = \mathbf{R}_c^{-1} \mathbf{I}_b^{-1} \text{diag}(I_y - I_z, I_z - I_x, I_x - I_y) \begin{bmatrix} qr \\ pr \\ pq \end{bmatrix} + \mathbf{R}_c^{-1} \mathbf{I}_b^{-1} \begin{bmatrix} \tau_x \\ \tau_y \\ \tau_z \end{bmatrix} - \mathbf{R}_c^{-1} \begin{bmatrix} 0 & -\cos \theta & 0 \\ -\sin \phi & -\sin \phi \sin \theta & \cos \phi \cos \theta \\ -\cos \phi & -\sin \phi \cos \theta & -\cos \phi \sin \theta \end{bmatrix} \begin{bmatrix} \dot{\phi} \dot{\theta} \\ \dot{\theta} \dot{\psi} \\ \dot{\phi} \dot{\psi} \end{bmatrix}, \quad (23)$$

where \mathbf{R}_c is reversible and k is an integer when $\theta \neq (2k + 1)\pi/2$ and $\phi \neq (2k + 1)\pi/2$.

Equation (23) is very complicated and there are non-linear and coupling terms, it is very difficult to design the controller directly for this model. ADRC can simplify the model and treat the nonlinear and coupling terms as unmodeled parts. Consequently, the equation (23) becomes

$$\begin{bmatrix} \ddot{\phi} \\ \ddot{\theta} \\ \ddot{\psi} \end{bmatrix} = \begin{bmatrix} s_1(p, q, r, \phi, \theta, \psi, \dot{\phi}, \dot{\theta}, \dot{\psi}) \\ s_2(p, q, r, \phi, \theta, \psi, \dot{\phi}, \dot{\theta}, \dot{\psi}) \\ s_3(p, q, r, \phi, \theta, \psi, \dot{\phi}, \dot{\theta}, \dot{\psi}) \end{bmatrix} + \begin{bmatrix} u_1 \\ u_2 \\ u_3 \end{bmatrix}, \quad (24)$$

$$\begin{bmatrix} u_1 \\ u_2 \\ u_3 \end{bmatrix} = \mathbf{R}_c^{-1} \mathbf{I}_b^{-1} \begin{bmatrix} U_2 \\ U_3 \\ U_4 \end{bmatrix},$$

where (s_1, s_2, s_3) denote coupling and nonlinear part, (u_1, u_2, u_3) are virtual control and the relationship with input torque is shown in equation (24). From this, the desired control input can be obtained

$$\begin{bmatrix} U_2 \\ U_3 \\ U_4 \end{bmatrix} = \mathbf{I}_b \mathbf{R}_c \begin{bmatrix} u_1 \\ u_2 \\ u_3 \end{bmatrix} = \begin{bmatrix} I_x & 0 & -I_x \sin \theta \\ 0 & I_y \cos \phi & I_y \sin \phi \cos \theta \\ 0 & -I_z \sin \phi & I_z \cos \phi \cos \theta \end{bmatrix} \begin{bmatrix} u_1 \\ u_2 \\ u_3 \end{bmatrix}. \quad (25)$$

Here, the math model required by the attitude controller can be obtained, the decoupling of pitch, roll and yaw is

completed, and this multiple input multiple output (MIMO) model is converted into three single-input single-output (SISO) subsystems. From equation (25), these subsystems are second-order linear systems.

Taking the roll angle θ for example, we established the ADRC attitude controller to roll motion, and the structure diagram is shown in Figure 4.

When $z_1 = \theta$, $\dot{z}_1 = \dot{\theta}$, equation (24) is rewritten as

$$\begin{aligned} \dot{z}_1 &= z_2, \\ \dot{z}_2 &= s_2(p, q, r, \phi, \theta, \psi, \dot{\phi}, \dot{\theta}, \dot{\psi}) + u_2 + w_\theta, \\ \theta &= z_1, \end{aligned} \quad (26)$$

where w_θ represents the disturbance to θ ; $s_2(p, q, r, \phi, \theta, \psi, \dot{\phi}, \dot{\theta}, \dot{\psi}) + w_\theta$ represents the sum of internal and external disturbances estimated by the Expanded State Observer (ESO). Equation (26) complies with the second-order form of the ADRC standard and can be designed as a second-order attitude controller. The specific design steps are as follows:

3.1.1. *Design TD.* TD is shown in equation (27):

$$\begin{aligned} v_1(k+1) &= v_1(k) + Tv_2(k), \\ v_2(k+1) &= v_2(k) + Tfh, \\ fh &= fhan(v_1(k) - v(k), v_2(k), r, h), \end{aligned} \quad (27)$$

where $v(k)$ is the desired pitch angle θ_d which is given by the position controller, $v_1(k)$ is the tracking signal of θ_d , and $v_2(k)$ is the derivative of $v_1(k)$. T is the sampling period of the discrete signal, $fhan(v_1(k) - v(k), v_2(k), r, h)$ is the nonlinear function, and its expression is as follows:

$$\begin{aligned} d &= rh, \\ d_0 &= dh, \\ y &= v_1(k) - v(k) + hv_2(k), \\ a_0 &= (d^2 + 8r|y|)^{(1/2)}, \\ a &= \begin{cases} v_2(k) + \frac{(a_0 - d)}{2}, & |y| > d_0, \\ v_2(k) + \frac{y}{h}, & |y| \leq d_0, \end{cases} \\ fhan &= \begin{cases} -\frac{ra}{d}, & a \leq d_0, \\ -r\text{sgn}(a), & a > d_0, \end{cases} \end{aligned} \quad (28)$$

where r and h are adjustable gains. r is called the fast factor, and a suitably large one can achieve a faster tracking speed; h is called the filter factor, and the larger the h , the better the filtering effect. But the increase of h will bring about an increase in phase delay, generally h takes 5 ~ 10 T.

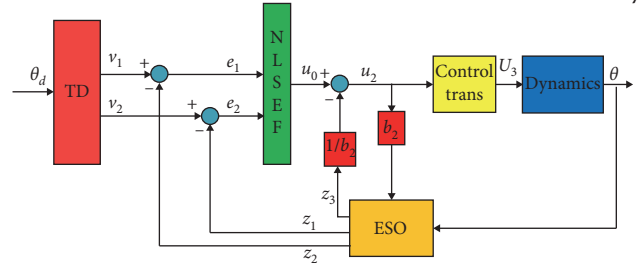


FIGURE 4: Structure diagram in rolling channel.

3.1.2. *Design ESO.* The ESO is as shown in equation (29)

$$\begin{aligned} e &= z_1(k) - y(k), \\ z_1(k+1) &= z_1(k) + T[z_2(k) - \beta_{01}e], \\ z_2(k+1) &= z_2(k) + T[z_3(k) - \beta_{02}\text{fal}(e, \alpha_1, \delta) + bu(k)], \\ z_3(k+1) &= z_3(k) - T\beta_{03}\text{fal}(e, \alpha_2, \delta), \end{aligned} \quad (29)$$

where $y(k)$ denotes the actual pitch angle of θ ; z_1 is the estimated value of θ , z_2 is the estimated value of $\dot{\theta}$, z_3 is the estimated value of total disturbance; u represents the virtual control u_2 which mentioned in equation (24), and $b = 1$.

3.1.3. *Design SEF.* We use the fastest control synthesis function, which is expressed as

$$u_0 = -fhan(e_1, ce_2, r, h), \quad (30)$$

where r and h are consistent with the description in equation (29), c denotes damping coefficient. When $c \in (0, 1)$, the system Underdamped; when $c > 1$, the system overdamped.

From equation (30), the control output u_0 of SEF can be obtained, then combining equation (31) to compensate for disturbances observed by ESO, we get the total control output u_2 of the rolling channel. Equation (31) is

$$u = u_0 - \left(\frac{z_3}{b}\right), \quad (31)$$

where z_3 and b are the same as equation (29)

Using the same method, the control outputs u_1, u_3 of the roll, yaw channel attitude controllers can be obtained, respectively. In this case, according to equation (25), the control input $[U_2, U_3, U_4]^T$ is acquired. The attitude controller is shown in Figure 5.

3.2. *Position Control.* When designing a position controller, we need to control the position of the aerial Robot and suspended saw. The position change will cause the swing of the saw. If the swing angle is not controlled, the saw may swing violently, affecting the stability of the aerial Robot, so it is necessary to control the swing angle of the hanging saw. ADRC has the advantages of low model dependence and strong anti-disturbance, and it has good applicability to ARSS with more complex models and larger disturbances.

Similar to the attitude controller, equation (12) is rewritten as

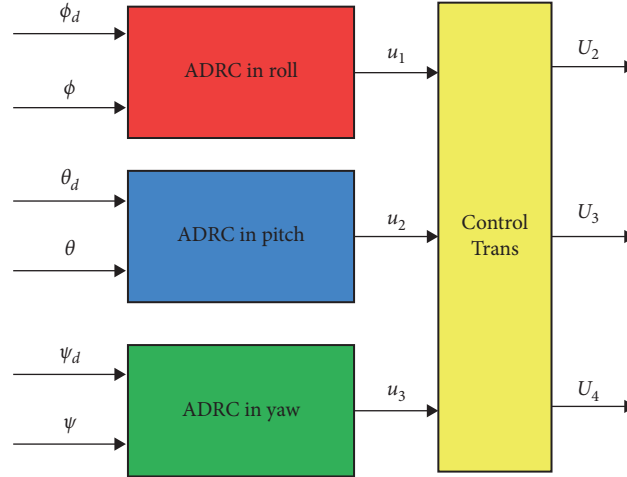


FIGURE 5: Attitude controller structure diagram.

$$(\ddot{x} \ \ddot{y} \ \ddot{z}) = \begin{pmatrix} s_1(\theta, \dot{\theta}, \phi, \dot{\phi}) \\ s_2(\theta, \dot{\theta}, \phi, \dot{\phi}) \\ s_3(\theta, \dot{\theta}, \phi, \dot{\phi}) \end{pmatrix} + \begin{pmatrix} u_1 \\ u_2 \\ u_3 \end{pmatrix}, \quad (32)$$

$$\begin{pmatrix} u_1 \\ u_2 \\ u_3 \end{pmatrix} = T^{-1} \begin{pmatrix} F_x \\ F_y \\ F_z \end{pmatrix}. \quad (33)$$

where

T is defined as follows:

$$T = \begin{bmatrix} \frac{1}{M}(M + m - ms^2\phi_L c^2\theta_L) & -\frac{m}{M}s_{\theta_L}c_{\theta_L}s_{\phi_L} & \frac{m}{M}s_{\phi_L}c_{\phi_L}c^2\theta_L \\ -\frac{m}{M}s_{\theta_L}c_{\theta_L}s_{\phi_L} & 1 + \frac{m}{M}c^2\theta_L & \frac{m}{M}s_{\theta_L}c_{\theta_L}c_{\phi_L} \\ \frac{m(s_{\phi_L}c_{\phi_L}c^2\theta_L)}{M(M+m)} & \frac{m(s_{\theta_L}c_{\theta_L}c_{\phi_L})}{M(M+m)} & \frac{M+m - mc^2\phi_L c^2\theta_L}{M(M+m)} \end{bmatrix}. \quad (34)$$

During the flight of the Aerial Robot, the swing angle of the suspended saw is small. According to the Small-Angle Approximation, the approximate solution is given by

$$\begin{aligned} \sin \phi_L &\approx \phi_L, \\ \cos \phi_L &\approx 1, \\ \sin \theta_L &\approx \theta_L, \\ \cos \theta_L &\approx 1. \end{aligned} \quad (35)$$

Thus, equations (19) and (20) are simplified as

$$\begin{aligned} \ddot{x} + l\ddot{\phi}_L + g\phi_L &= 0, \\ \ddot{y} + l\ddot{\theta}_L + g\theta_L &= 0. \end{aligned} \quad (36)$$

The ARSS is decomposed into the aerial robot part of the standard second-order model and the suspended saw part of the linear model. Position control is changed to control the aerial Robot while ensuring the stability of the linear part, so that the saw swing during flight is gradually reduced.

First, design the position controller of the aerial robot part. Similar to the attitude controller, equation (32) is

converted into three SISO subsystems, and these subsystems are second-order standard.

Taking x for example. When $z_1 = x$ and $\dot{z}_1 = \dot{x}$, equation (32) is rewritten as

$$\begin{aligned} \dot{z}_1 &= z_2, \\ \dot{z}_2 &= u_1 + w_x, \\ x &= z_1, \end{aligned} \quad (37)$$

where w_x represents the disturbance to x and u_1 denotes virtual control. Similar to the attitude controller, the specific design steps are as follows.

3.2.1. Design TD. TD is defined as

$$\begin{aligned} v_1(k+1) &= v_1(k) + T_s v_2(k), \\ v_2(k+1) &= v_2(k) + T_s f h, \\ f h &= \text{fhan}(v_1(k) - v_1(k), v_2(k), r, h), \end{aligned} \quad (38)$$

where $v(k)$ is the desired position x_d which is given by the position controller, $v_1(k)$ is the tracking signal of x_d , and $v_2(k)$ is the derivative of $v_1(k)$. T_s is the sampling period of the discrete signal. r and h are adjustable gains. $\text{fhan}(v_1(k) - v(k), v_2(k), r, h)$ is the non-linear function, and its expression is as follows:

$$\begin{aligned} d &= rh, \\ d_0 &= dh, \\ y &= x_1 + hx_2, \\ a_0 &= (d^2 + 8r|y|)^{1/2}, \\ a &= \begin{cases} x_2 + \frac{(a_0 - d)}{2}, & |y| > d_0, \\ x_2 + \frac{y}{h}, & |y| \leq d_0, \end{cases} \quad (39) \\ \text{fhan} &= \begin{cases} -\frac{ra}{d}, & a \leq d_0, \\ -r\text{sgn}(a), & a > d_0. \end{cases} \end{aligned}$$

3.2.2. *Design ESO.* The ESO is shown as

$$\begin{aligned} e &= z_1(k) - y(k), \\ z_1(k+1) &= z_1(k) + T[z_2(k) - \beta_{01}e], \\ z_2(k+1) &= z_2(k) + T[z_3(k) - \beta_{02}\text{fal}(e, \alpha_1, \delta) + bu(k)], \\ z_3(k+1) &= z_3(k) - T\beta_{03}\text{fal}(e, \alpha_2, \delta), \end{aligned} \quad (40)$$

where $y(k)$ denotes the actual position x ; z_1 is the estimated value of x , z_2 is the estimated value of \dot{x} , and z_3 is the estimated value of total disturbance w_x ; u represents the virtual control u_1 and $b = 1$; β_{01} , β_{02} , β_{03} , α_1 and α_2 are parameters.

$\text{fal}(\ast)$ is a non-linear function, and its expression is shown as

$$\text{fal}(e, \alpha, \delta) = \begin{cases} \frac{e}{\delta^{1-\alpha}}, & |e| \leq \delta, \\ |e|^\alpha \text{sign}(e), & |e| > \delta, \end{cases} \quad (41)$$

where α and δ are parameters, with $0 < \alpha < 1$ and $\delta > 0$.

3.2.3. *Design State Error Feedback (SEF).* The position control does not have strict requirements for fast response, so a linear SEF with simple structure and easy parameter adjustment can be used. We have

$$u_0 = \beta_1 \text{fal}(e_1) + \beta_2 \text{fal}(e_2), \quad (42)$$

where β_1 and β_2 are parameters.

From equation (40), we compensate the disturbances observed by ESO, we get the total control output u_2 of the channel x . With the same method, the output and of the other two channels can be obtained, and the required control amount can be obtained according to equation (25). The position controller structure is shown in Figure 6.

3.3. *Suspended Saw Controller.* In the Suspended Saw model, ϕ_L and θ_L describe the swing state of the suspended saw. ϕ_L denotes the angle between the projection of the connecting rod in the $O_b X_b Z_b$ plane and the z_b axis, the acceleration of the aerial Robot in the x and z axes will affect ϕ_L . Similarly, the acceleration in the y -axis and z -axis directions will affect θ_L . The height and horizontal position are generally not controlled at the same time, so the influence of the acceleration in the z -axis direction on the swing angle can be ignored. Considering that ARSS performs position control, it also needs to control swing angle, equation (36) is rewritten as

$$\begin{aligned} u'_1 &= u_1 - K_1 \dot{\phi}_L - K_2 \phi_L, \\ u'_2 &= u_2 - K_3 \dot{\theta}_L - K_4 \theta_L. \end{aligned} \quad (43)$$

When designing the position controller, the linear dynamic compensation method of ADRC is used to transform the non-linear model of the aerial Robot into a series model, that is,

$$\begin{aligned} \ddot{x} &= u'_1, \\ \ddot{y} &= u'_2. \end{aligned} \quad (44)$$

Then, combining equations (43) and (44) with equation (36), the system is described by

$$\begin{aligned} l\ddot{\phi}_L - K_1 \dot{\phi}_L + (g - K_2)\phi_L &= 0, \\ l\ddot{\theta}_L - K_3 \dot{\theta}_L + (g - K_4)\theta_L &= 0, \end{aligned} \quad (45)$$

where $K_i, i = 1, \dots, 4$ are gains.

For this linear closed-loop system, sufficient and necessary conditions for its asymptotic stability are that all the characteristic roots are in the left half of the complex plane; that is, the real parts of all the characteristic roots are all negative. According to the Routh criterion, its characteristic roots are all in the left half of the complex plane and need to satisfy

$$\begin{aligned} l &> 0, \\ -K_1 &> 0, \\ g - K_2 &> 0, \\ -K_3 &> 0, \\ g - K_4 &> 0. \end{aligned} \quad (46)$$

As long as the parameter K_i satisfies, the swing angle of the hanging saw can be gradually stabilized.

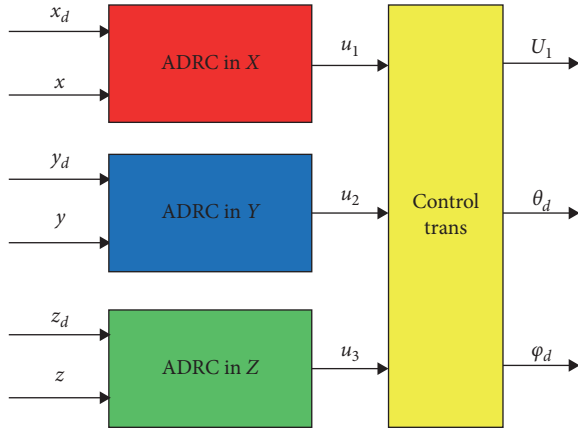


FIGURE 6: Position controller structure diagram.

4. Evaluation

In this section, we present our experiment. In each experiment, we simulate a complete tree-barrier removal task. Each task is divided into two stages: free flight and aerial pruning. The controller was tested in simulation, which used CoppeliaSim [23] as a physics environment and to model the Robot. The controller is programmed under MATLAB/Simulink. Table 1 summarizes the numerical values used to simulate, and Table 2 shows the controller parameters. The parameters in Table 2 are adjusted by a parameter self-learning algorithm CARLA-ADRC [24].

All experiments have considered numerical indicators, including integral of squared of tracking error, integral of squared of control signal. In the next section, we will choose one experiment sample to explain.

4.1. Attitude Control Experiment. First, verify the attitude controller and design the attitude tracking experiment. For example, the desired signals of roll, pitch, and yaw of 10° are given in the first, fourth, and seventh seconds, respectively. The experiment result is shown in Figure 7.

It can be seen from Figure 7 that the attitude controller can quickly track the desired signal, in which the tracking response time of pitch and roll angle is 1 s, the tracking response time of the yaw angle is 1.3 s, and there is no overshoot in each channel of the attitude angle. It proves that the attitude controller has good speed and stability.

4.2. Free-Flight Experiments. When performing the pruning task, we first fly ARSS to a desired position close to the tree. Suppose that in an experiment, the ARSS is controlled to fly to the desired position $[2, 2, 1.5]^T \in \mathbb{R}^3$ in the inertial frame. At 0 s, give an 1.5 m step signal in the z axis; at 5 s, give a 2 m step signal in the x -axis; at 10 s, give a 2 m step signal in the y -axis, and then keep hovering. The simulation duration is 25 s in total. The curves of position and swing angle during the simulation are shown in Figure 8.

It can be seen from Figure 8(a) that because the swing of the saw cannot be too large, the aerial Robot cannot fly too fast, so the transition process of the TD link arrangement is

TABLE 1: Simulation parameters.

Parameter	Value
M	8.5 kg
l	0.4 m
m	1.0 kg
L	1.0 m
g	9.81 m/s ²

TABLE 2: Controller parameters.

ADRC	ϕ	θ	ψ	x	y	z
TD- r	3000	3000	3000	4	4	4
TD- h	0.01	0.01	0.01	0.01	0.01	0.01
ESO- β_{01}	1000	1000	1000	1000	1000	1000
ESO- β_{02}	19764	19764	19764	19764	19764	19764
ESO- β_{03}	462902	462902	462902	462902	462902	462902
ESO- α_1	0.5	0.5	0.5	0.5	0.5	0.5
ESO- α_2	0.25	0.25	0.25	0.25	0.25	0.25
ESO- δ	0.001	0.001	0.001	0.001	0.001	0.001
ESO- b	1	1	1	1	1	1
SEF- c	0.95	1.05	0.95	—	—	—
SEF- r	108.73	108.73	108.73	—	—	—
SEF- h	0.05	0.05	0.05	—	—	—
SEF- k_1	—	—	—	50	50	400
SEF- k_2	—	—	—	41	41	50

relatively smooth. The response curve shows that the position error in the x and y axes is always kept within 0.4 m, and there is no overshoot; the error in the x -axis is kept within 0.05 m, and there is no overshoot. It is verified that the position controller has faster tracking speed and accuracy.

Figure 8(b) shows the tracking response curve of the swing angle. It can be seen that the swing angle is always controlled within 6° . The maximum swing angle appeared in 8 s and 13 s, respectively, reached 5.7° . This is because the deceleration occurs when the ARSS is close to the expected position at this time. After 2 s, the swing angle has dropped to within 2° , and when ARSS hovers, it can gradually stabilize to the equilibrium point and remain stable. This shows that the swing angle controller can well reduce the swing amplitude of the saw and can gradually stabilize after reaching the destination.

4.3. Aerial Pruning Experiments. The purpose of ARSS is to perform tree pruning operations. The pruning process is difficult to describe accurately, and the cutting process is not exactly the same for tree bars of different thickness. This experiment will simulate the cutting of a 6 cm diameter tree branch growing laterally to verify the controller. In the early stage, through the actual branch cutting experiment on the ground, the test results were counted and empirical conclusions were drawn: to cut a tree branch with a diameter of 6 cm, a squeezing force of 2 N is required between the saw and the branch, and contact with the tree barrier 2 s, the swing angle reaches -11.5 deg. It can be calculated from this that the body needs to be 20 cm ahead of COG of the saw in the direction of advancement. Considering that the saw

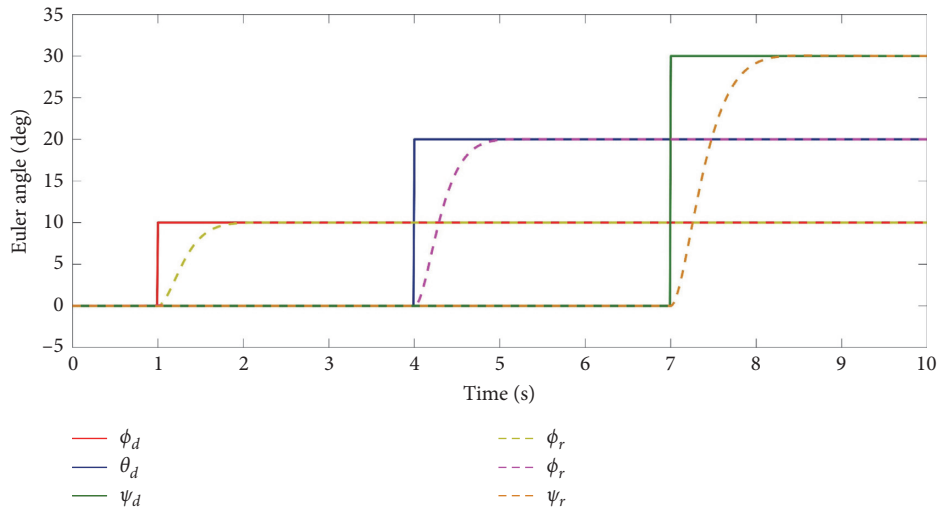
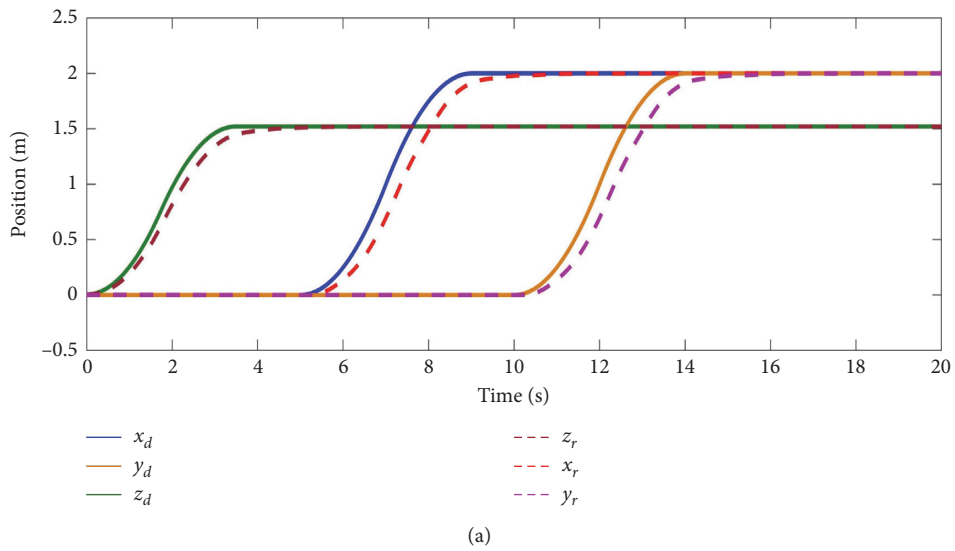
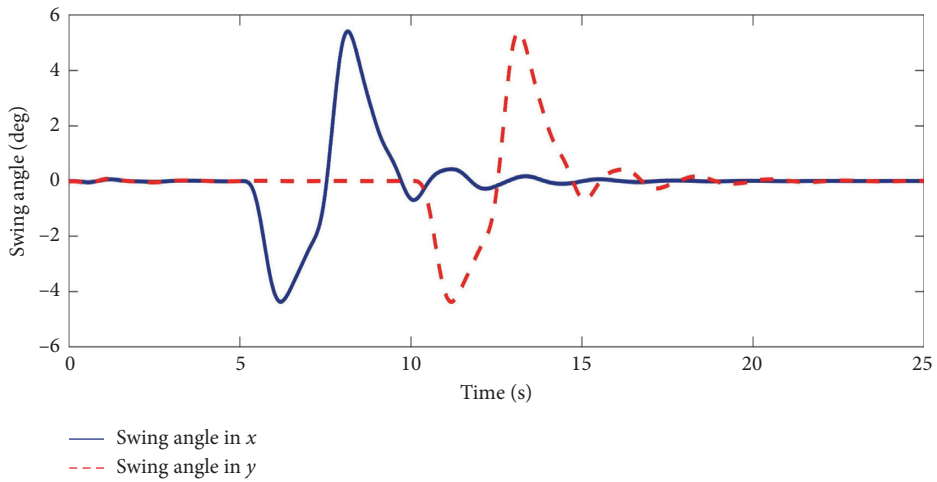


FIGURE 7: Attitude tracking response.



(a)



(b)

FIGURE 8: Position and Swing angle during simulation. (a) Position tracking response. (b) Swing angle tracking response.

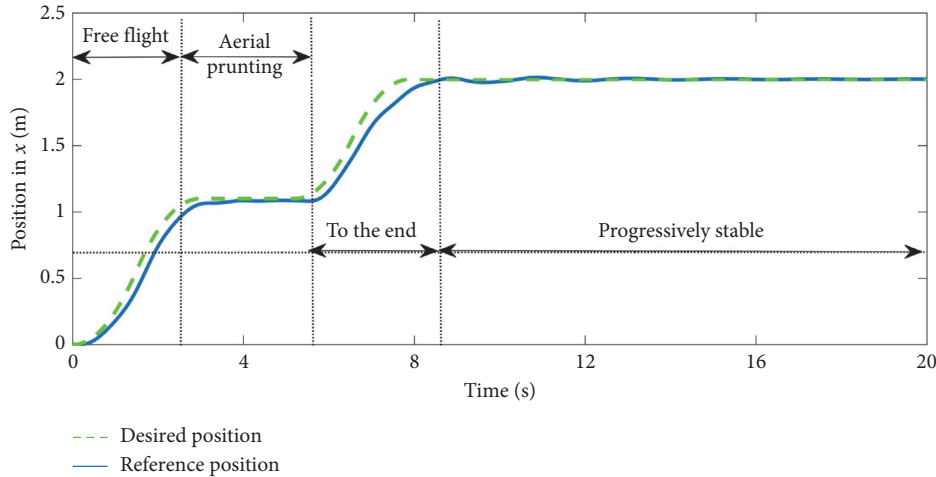


FIGURE 9: Position changes of ARSS during the pruning.

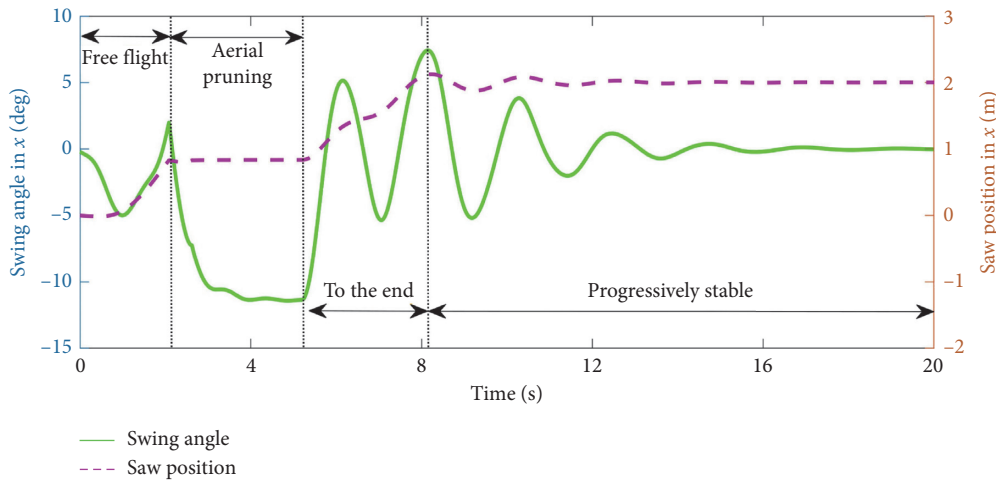


FIGURE 10: Swing angle changes of ARSS during the pruning.

diameter used in this article is 14 cm and the branch diameter is 6 cm, so during the cutting process, the flying platform needs to be 0.1 m in front of the tree branch. In this process, the saw will also receive a cutting force of 50 N.

Based on the above analysis, the cutting process can be approximated as follows: the saw is in continuous contact with the branch for 2 s at a swing angle of -11.5° and disturbed by a cutting force of 50 N. The experimental process is designed as follows: the initial state of ARSS is hovering, and a tree barrier is placed at a distance of 1 m from the ARSS. On the 0 s, give a step signal of 1.1 m in the x -axis and set the desired swing angle to -11.5° . After the aerial Robot reaches the desired position, hover for 2 s and then perform the cutting operation. During this process, a cutting force of 50 N is applied to the saw, and then a step signal of 2 m on the x -axis is given and the desired swing angle is set to 0° , leaving the Working area. The entire simulation process lasts 20 s. This test mainly tests the position of the X direction and the performance of the swing angle controller, so only the curve of the x -axis position and

the swing angle during the simulation process is given, as shown in Figures 9 and 10.

In order to more intuitively explain the simulation results, the simulation process is divided into four stages, as shown in Figure 11.

From Figure 11, ARSS made contact with the tree barrier in 2.2 s, and the swing angle before contact was 2° (in Figure 11(a)). After the contact, due to the tree barrier blocking the saw, the saw stayed at the position of 1 m, while the flying platform continued to fly, reached 1.1 m in the 3.2 s and hovered, the swing angle gradually increased to -11.5° , and keep the angle until 5.2 s (in Figure 11(b)). After the pruning is completed, due to the loss of the barrier to the saw, the saw quickly swings forward. Under the action of the swing angle controller, it reaches a maximum of 7° , and stays within 7° when going to the destination (in Figure 11(c)), and it can gradually stabilize after reaching the destination (in Figure 11(d)). In terms of position control, the Robot can always quickly track the desired position, and the

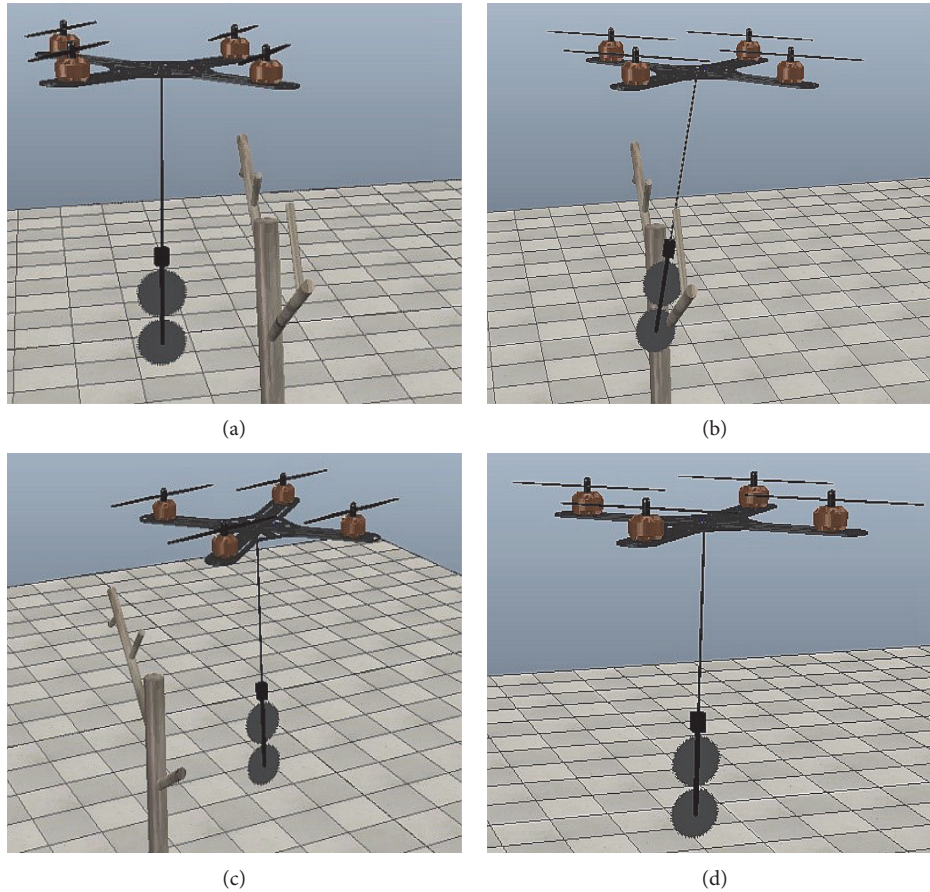


FIGURE 11: Snapshots of ARSS during the pruning.

maximum tracking error is within 0.4 m. After reaching the destination, due to the need to control the swing angle, there is an overshoot of 0.1 m, which can gradually stabilize after a period of time. The experiments demonstrated that the position controller and the swing angle controller can complete the task of aerial pruning well.

5. Discussion and Conclusions

Throughout the development of ARSS, a range of issues were encountered on which we are developing a novel aerial platforms. While building the novel robot for the tree pruning has a range of advantages, it also has the following limitations:

- (1) Physical testing still needs to be carried out in future research.
- (2) The control of the swing angle is linearized by a Small-Angle-Approximation to the dynamic model, and the model uncertainty cannot be completely solved.
- (3) The knife and saw will generate force after contact with the tree. The research does not directly control the force, but indirectly realizes the force control through the control of the position, attitude and swing angle.

However, the article introduces how a novel aerial robot can realize flying motion and aerial pruning and designs a position and attitude controller based on the ADRC method, and a swing angle controller via the linear SEF method. The methodology not only realize the fast, accurate, and stable flight movement to the specified position, but also effectively suppress the swing of the hanging load and the residual oscillation after reaching the specified position. The control effect is remarkable, with good speed and robustness.

Data Availability

The figures, tables, and other data used to support this study are included within the article.

Conflicts of Interest

The authors declare that there are no conflicts of interest regarding the publication of this paper.

Acknowledgments

This work was supported by the Guizhou Provincial Science and Technology Projects (Grant no. (2020)2Y044), the Science and Technology Projects of China Southern Power Grid Co., Ltd. (Grant no. 066600KK52170074), the Key Laboratory Projects of Aeronautical Science Foundation of

China (Grant no. 201928052006), and the National Natural Science Foundation of China (Grant no. 61473144).

References

- [1] R. Mahony, V. Kumar, and P. Corke, "Multirotor aerial vehicles: modeling, estimation, and control of quadrotor," *IEEE Robotics & Automation Magazine*, vol. 19, no. 3, pp. 20–32, 2012.
- [2] X. Liang, Y. Fang, N. Sun, and H. Lin, "A novel energy-coupling-based hierarchical control approach for unmanned quadrotor transportation systems," *IEEE/ASME Transactions on Mechatronics*, vol. 24, no. 1, pp. 248–259, 2019.
- [3] D. Yallappa, M. Veerangouda, D. Maski, V. Palled, and M. Bheemanna, "Development and evaluation of drone mounted sprayer for pesticide applications to crops," in *Proceedings of the GHTC 2017—IEEE Global Humanitarian Technology Conference*, pp. 1–7, San Jose, CA, USA, October 2017.
- [4] J. Molina and S. Hirai, "Pruning tree-branches close to electrical power lines using a skew-gripper and a multirotor helicopter," in *Proceedings of the IEEE/ASME International Conference on Advanced Intelligent Mechatronics, AIM*, pp. 1123–1128, Munich, Germany, July 2017.
- [5] J. Molina and S. Hirai, "Aerial pruning mechanism, initial real environment test," *Robotics and Biomimetics*, vol. 4, p. 15, 2017.
- [6] J. Molina and S. Hirai, "Kinematic analysis of a novel skew-gripper for aerial pruning tasks," in *Proceedings of the 3rd International Conference on Mechatronics and Robotics Engineering*, pp. 134–138, Paris, France, February 2017.
- [7] Q. Zhang, Z. Yang, S. Wang, and Y. Jiang, "Attitude controller design for the aerial trees-pruning robot based on nonsingular fast terminal sliding mode," *International Journal of Advanced Robotic Systems*, vol. 16, no. 4, pp. 1–14, 2019.
- [8] N. Azami, P. Zarafshan, A. M. Kermani, M. Khashehchi, and S. Kouravand, "Design and analysis of an armed-ocrotor to prune trees near the power lines," in *Proceedings of the International Conference of Iranian Aerospace Society*, Tehran, Iran, February 2017.
- [9] K. Klausen, T. I. Fossen, and T. A. Johansen, "Suspended load motion control using multicopters," in *Proceedings of the 2014 22nd Mediterranean Conference on Control and Automation, MED 2014*, pp. 1371–1376, Palermo, Italy, June 2014.
- [10] K. Sreenath, N. Michael, and V. Kumar, "Trajectory generation and control of a quadrotor with a cable-suspended load—a differentially-flat hybrid system," in *Proceedings of the IEEE International Conference on Robotics and Automation*, pp. 4888–4895, Karlsruhe, Germany, May 2013.
- [11] Y. Allothman and D. Gu, "Quadrotor transporting cable-suspended load using iterative linear quadratic regulator (iLQR) optimal control," in *Proceedings of the 2016 8th Computer Science and Electronic Engineering Conference, CEEC 2016*, pp. 168–173, Colchester, UK, September 2016.
- [12] A. Faust, I. Palunko, P. Cruz, R. Fierro, and L. Tapia, "Learning swing-free trajectories for UAVs with a suspended load," in *Proceedings of the IEEE International Conference on Robotics and Automation*, pp. 4902–4909, Karlsruhe, Germany, May 2013.
- [13] I. Palunko, R. Fierro, and P. Cruz, "Trajectory generation for swing-free maneuvers of a quadrotor with suspended payload: a dynamic programming approach," in *Proceedings of the IEEE International Conference on Robotics and Automation*, pp. 2691–2697, Saint Paul, MN, USA, May 2012.
- [14] S. Yang and B. Xian, "Energy-based nonlinear adaptive control design for the quadrotor UAV system with a suspended payload," *IEEE Transactions on Industrial Electronics*, vol. 67, no. 3, pp. 2054–2064, 2020.
- [15] S. Yang, L. Kunqin, and J. Shi, "Design and simulation of the longitudinal autopilot of UAV based on self-adaptive fuzzy PID control," in *Proceedings of the CIS International Conference on Computational Intelligence and Security*, pp. 634–638, Beijing, China, December 2009.
- [16] J.-B. Liu, S. Wang, C. Wang, and S. Hayat, "Further results on computation of topological indices of certain networks," *IET Control Theory & Applications*, vol. 11, no. 13, pp. 2065–2071, 2017.
- [17] J.-B. Liu, J. Cao, A. Alofi, A. AL-Mazrooei, and A. Elaiw, "Applications of Laplacian spectra for n -prism networks," *Neurocomputing*, vol. 198, pp. 69–73, 2016.
- [18] J. Han, "From PID to active disturbance rejection control," *IEEE Transactions on Industrial Electronics*, vol. 56, no. 3, pp. 900–906, 2009.
- [19] X. Yang and Y. Huang, "Capabilities of extended state observer for estimating uncertainties," in *Proceedings of the American Control Conference*, pp. 3700–3705, St. Louis, MO, USA, June 2009.
- [20] Q. Zheng, L. Q. Gao, and Z. Gao, "On validation of extended state observer through analysis and experimentation," *Journal of Dynamic Systems, Measurement, and Control*, vol. 134, no. 2, pp. 1–6, 2012.
- [21] B.-Z. Guo and Z.-l. Zhao, "On the convergence of an extended state observer for nonlinear systems with uncertainty," *Systems & Control Letters*, vol. 60, no. 6, pp. 420–430, 2011.
- [22] Z. X. Zhou, Y. Y. Qu, J. D. Yang, and D. J. Liu, "Suspension position control of precise planar magnetic bearing," *Kongzhi yu Juece/Control and Decision*, vol. 25, no. 3, pp. 437–444, 2010.
- [23] CoppeliaSim: <https://www.coppeliarobotics.com/>.
- [24] L. Wu, H. Bao, J. L. Du, and C. S. Wang, "A learning algorithm for parameters of automatic disturbances rejection controller," *Zidonghua Xuebao/Acta Automatica Sinica*, vol. 40, no. 3, pp. 556–560, 2014.

Review Article

Optimal Simulation of Sandcastle Life in Dynamic Environment Based on Stability Principle

Peng-Hui Yang, Ya-Yu Jiang, Qi Tang, Yi-Fang Li, and Jia-Ming Zhu 

School of Statistics and Applied Mathematics, Anhui University of Finance and Economics, Bengbu 233030, China

Correspondence should be addressed to Jia-Ming Zhu; zhujm1973@163.com

Received 21 August 2020; Revised 28 September 2020; Accepted 29 September 2020; Published 13 October 2020

Academic Editor: Shaohui Wang

Copyright © 2020 Peng-Hui Yang et al. This is an open access article distributed under the Creative Commons Attribution License, which permits unrestricted use, distribution, and reproduction in any medium, provided the original work is properly cited.

This paper mainly studies to explore a three-dimensional geometric model including three modules of a sandcastle foundation with optimal stability. Firstly, based on the knowledge of streamline structure, structural mechanics, and fluid mechanics, the most stable sand pile foundation model under the action of tidal current and wave is established. Secondly, by limiting the degree of allowable aggregation, the discrete global optimization algorithm based on the continuous descent method is adopted to find out the optimal water-sand ratio. Finally, we apply the above results to verify the reliability of the optimal model by comprehensively considering the influence of rainfall factors on sandcastles.

1. Introduction

Playing is the nature of humans, but it is not easy to come to a kind of inspiration while playing. There are castles of various shapes on the beach; how to make our castles more durable is a question that most people are curious about. There are numerous factors which influence the firmness of sandcastles [1], such as sand-to-water mixture proportion, the type of sand, weather, etc. In this paper, we attempt to explore a three-dimensional geometric model of a sandcastle foundation having the best stability.

Our model is formulated on a certain theoretical basis. After consulting a lot of literature, we carefully selected the parameters of the model. In this way, we can make our model as close to reality as possible [2]. Based on the streamlined structure and the knowledge of structural mechanics and fluid mechanics, the most stable sand pile foundation model under the action of tides and waves is established. The water-sand ratio is limited to a reasonable range by limiting the degree of allowable polymerization. The discrete global optimization algorithm based on successive descent method was used to efficiently find the optimal water-sand mix ratio [3]. Meanwhile, we divide the impact of rain on sandcastles into two parts: scour and

infiltration. Through the calculation and analysis of the model, it is found that the sandcastle with streamlined structure is still the most durable, which proves the reliability of the model.

2. Basic Assumptions

In order to solve the problem, we make assumptions as follows: (i) it is assumed that, in the process of natural erosion, one should ignore the situation of huge waves and winds sweeping the sandcastle far from the original location. (ii) It is assumed that there is no significant difference in the sand quality of our sandcastle foundation. (iii) It is assumed that there is negligible chemical erosion of sandcastle foundations. (iv) There are no unexpected factors affecting our assessment during the study period.

3. Construction of the Best Sandcastle Shape Model Based on Dynamics

3.1. Sandcastle-Erosion Model. Based on the streamlined structure, the most durable sand pile foundation model under the action of tides and waves is established by the optimization model. Based on the knowledge of structural

mechanics and fluid mechanics, this method can mitigate the impact of water flow on sandcastle as much as possible. Under certain conditions such as sandcastle base volume and distance from the sea, the ratio of the horizontal impact force to the volume of sandcastle can be as small as feasible, which can reduce the loss of sand grains and ensure its stability [4].

3.1.1. Model Preparation. The damage of waves and tides on the foundation of sandcastle is mainly manifested as the tangential impact force parallel to the beach and the impact force close to the horizontal direction. The smaller the projected area of wave front influence is, the smaller the impact force of the entire foundation will be. The water flowed along the side of the sandcastle foundation. The smaller the angle between the water flow and the contact surface, the smaller the local impact force. The sand base is subject to the impact force of the water flow [5]. For example, when the tangential force of the sand element is greater than the adhesion force between the sand grains, the sand grains will go with the water flow and the sandcastle will be destroyed. In order to guarantee the stability of the foundation, we change the shape of the foundation to reduce the resultant force of water flow in the tangential direction.

3.1.2. Model Establishing and Solving. Sand under certain water flow under the force is divided into two kinds: the friction force and pressure difference; the friction is caused by fluid viscosity, close to flow around objects surface boundary layer, within the scope of the boundary layer thickness; flow around fluid velocity increased dramatically by objects close to the wall of a stationary speed where V_0 is outflow velocity; thus, the object surface has larger friction shear stress.

On the other hand, when there is a relative motion and fluid flow field around the quantities that causes disturbance, surface pressure distribution of symmetry is broken, the unbalanced pressure leads to flow around objects flow period, and period of pressure difference exists in the object moving direction; through the above analysis, the friction force and differential pressure can be expressed as follows. As shown in Figure 1, ds is an area of an object's surface, T is friction shear stress, and P is the compressive stress.

Friction and differential pressure force, respectively, are as follows:

$$\begin{aligned} F_f &= \int_S \tau \cos \alpha ds, \\ F_p &= \int_S P \sin \alpha ds. \end{aligned} \quad (1)$$

From formula (1), we get the total force:

$$F = F_f + F_p = \int_S \tau \cos \alpha ds + \int_S P \sin \alpha ds. \quad (2)$$

It is assumed that the water flowing towards each part of the sand base at high tide is the same in nature, and the

smaller the ratio between the resistance of the part in contact with the sea water and the base volume is, the smaller the amount of sand taken away by the sea water after the impact can be regarded as the smallest damage caused by the sea water impact on the sand base and the most stable in nature [6]. Since the streamlined structure is subject to less resistance in the water, the streamlined structure of sand infrastructure can mitigate the impact of waves and tides on the sandcastle. From the kinetic energy loss of water flow in the process of high tide to low tide, we preliminarily designed the structure of sandcastle as a semi-elliptic and parabolic streamlined semi-rotating body. The top view is shown in Figure 2.

The streamline inlet section of the sand pile foundation close to the sea water is a semi-ellipse, which can be expressed as follows:

$$y = \pm \frac{K_0}{2L_z} \sqrt{L_z^2 - x^2}. \quad (3)$$

In formula (3), the variable K_0 represents the maximum cross section diameter of the rotary body, and the variable L_z represents the length of incoming flow segment; the units are mm. The seawater first passes through the incoming flow section and then through the outgoing flow section. The outgoing flow section is a parabola, which can be expressed as follows:

$$y = \pm \frac{K_0}{2} \left(1 - \frac{x^2}{L_Y^2} \right). \quad (4)$$

In formula (4), L_Y represents the length of the outlet section; the units are mm. Since only the influence of the basic shape on its stability is considered, we assume that the water flow is laminar for the convenience of calculation. For a semi-rotary body, it is necessary to integrate the march surface in the direction of its length when calculating its frictional resistance; since the cross section of a rotary body is a semicircle, it is only necessary to integrate the function of the length in the y direction [7–9]:

$$F = 2\pi \int_0^l r \tau_0 dx. \quad (5)$$

For incoming flow segments,

$$r = \frac{K_0}{2L_z} \sqrt{L_z^2 - x^2}. \quad (6)$$

The friction shear force of the laminar flow on the plate is expressed as follows:

$$\tau_0 = 0.343\rho V_0^2 \sqrt{\frac{1}{\text{Re}}}. \quad (7)$$

In the formula, the variable V_0 represents the coming flow speed, the units are m/s, and Re represents Reynolds number; it is a dimensionless quantity; then, the laminar frictional resistance in the incoming flow section is

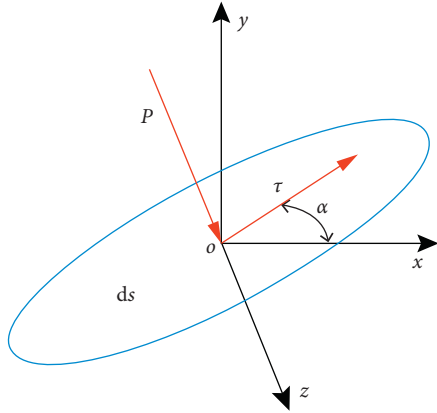


FIGURE 1: Simplified diagram of sandcastle model section.

$$F_{L_z} = \frac{0.343\pi K_0 \sqrt{\mu\rho V_0^3}}{L_z} \int_{-L_z}^0 \sqrt{\frac{L_z^2 - x^2}{x + L_z}} dx. \quad (8)$$

In the formula, the Gauss three-point interpolation formula with fifth-degree algebraic precision was used for an approximate calculation, and the laminar frictional resistance in the incoming flow segment was obtained as follows:

$$F_{L_z} = 0.5145\pi K_0 \sqrt{\mu\rho V_0^3 L_z}. \quad (9)$$

Therefore, the frictional resistance in the reaching flow section is

$$F_{L_y} = 2\pi \int_0^{L_y} 0.343 \sqrt{\frac{\mu\rho V_0^3}{x}} \cdot \frac{K_0}{2} \left(1 - \frac{x^2}{L_y^2}\right) dx. \quad (10)$$

Finally, from formula (5) to formula (10), the total frictional resistance of semi-elliptic and parabolic streamlined rotating bodies under laminar flow is obtained as follows:

$$F_L = F_{L_z} + F_{L_y} = 0.05145\pi K_0 \sqrt{\mu\rho V_0^3 L_z} + 0.5488\pi K_0 \sqrt{\mu\rho V_0^3 L_y}. \quad (11)$$

As the flow velocity, Reynolds number, and other parameters are all certain, and only the influence of the foundation shape on stability is considered, ρ , μ , V_0 values are set to 1, and the total frictional resistance of the rotary body is as follows:

$$F = 0.5145\pi K_0 \sqrt{L_z} + 0.5488\pi K_0 \sqrt{L_y}. \quad (12)$$

From formula (11) to formula (12), the optimal solution is obtained by calculation: $X = 0.63$, $Y = 0.22$.

Therefore, the function expression of the basic model is as follows:

$$f(x, y) = \frac{30.87\sqrt{x} + 32.928\sqrt{1-x}}{xy + 4y}. \quad (13)$$

3.1.3. Result Analysis. The effect of waves and tides on the stability of a sandcastle foundation is converted into a

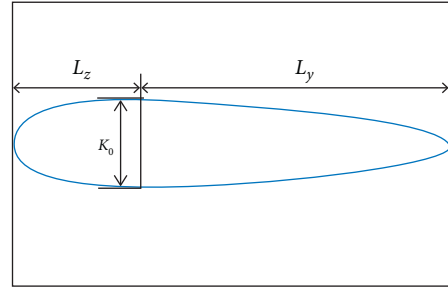


FIGURE 2: Top view of sandcastle structure.

functional relationship between the impact force and volume ratio of sandcastle foundation and the three-dimensional shape parameters of sandcastle foundation, and the minimum ratio of impact force and volume is obtained [10].

Three-dimensional shape parameters of sand fort foundation: in order to mitigate the effects of water flow on the sand, as best as possible to reduce the loss of sand, on the basis of sandcastle simple structural mechanics and fluid mechanics analysis, the optimal model determines the best 3D sand foundation model.

3.2. Optimal Water-to-Sand Mixture Proportion. The ratio of water to sand will directly affect the antierosion ability of sandcastle foundation. By introducing the relation equation between water-sand polymerization degree and water-sand ratio, we limited the allowable range of polymerization degree to obtain a reasonable range of water-sand ratio and then solved the optimal water-sand ratio through models [11, 12].

3.2.1. Model Preparation. We considered the aggregation of water and sand, leading to the concept of the degree of aggregation of water and sand [13]. We defined the degree of water and sand polymerization according to the volume change of water and sand specific gravity before and after polymerization:

$$W = \left(1 - \frac{((M_1/C_1) + (M_2/C_2))}{(M_1 + M_2)}\right) \times 100\%, \quad (14)$$

where M_1 and M_2 represent the volume of sand and water before mixing and C_1 and C_2 represent water absorption coefficient and water solubility coefficient, respectively. Let us use these two coefficients to express the polymerization capacity of water and sand.

3.2.2. Model Establishing and Solving. Let us use water-sand ratio NR to simplify this equation:

$$W = \left(1 - \frac{((N_R/C_1) + (1/C_2))}{(N_R + 1)}\right) \times 100\%. \quad (15)$$

From formula (13) to formula (15), MATLAB was used to solve the equation, and the relation curve between water-

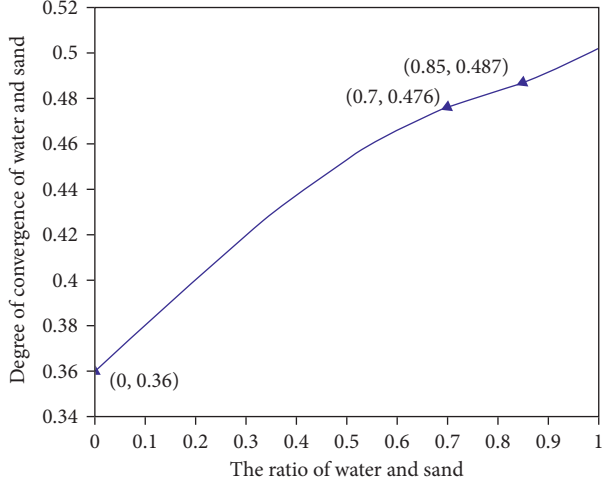


FIGURE 3: Convergence of water and sand.

sand polymerization degree and water-sand ratio was obtained, as shown in Figure 3.

With the increase of water-sand ratio, the polymerization degree of water-sand increases. In order to ensure the longest erosion resistance time of sandcastles, not only the relatively larger adhesion but also the optimization of erosion resistance performance should be considered. In combination with the actual situation, the two-point interval with a wide viscosity range as shown in the figure was selected as the optimization parameter [14, 15].

Based on the optimal proportion of the best shape selected above and the initial value of water-sand ratio N_R as a variable, the target T was discretized in the same way. According to the variation of foundation ΔS and Δh , the relationship between the damage index and time, the constraint is added:

$$0.7 < N_R < 0.85.$$

Obtain the continuous schedule record of N_R equidistant points, as shown in Table 1.

Using the above model, we can get that when the water-sand ratio is $N_R = 0.74$, under the condition of good shape adhesion, the maximum service life of sandcastle foundation can be achieved.

3.3. Sandcastle-Rain-Erosion Model. When considering rainfall, a sandcastle-rain-erosion model is established, and the influence of rainfall is directly superimposed with that of seawater; that is, the rainfall directly affects the sandcastles eroded by seawater. Suppose the raindrops were particles of mass, hitting the sandcastle vertically, with the same force as the waves [16–18].

3.3.1. Model Preparation. To study the effect of rain on sandcastles, we first need to understand some of the motion characteristics of rain. Let us say the rain falls straight down. Raindrops have a lot of kinetic energy [19]. When they hit a sandcastle, they destroy the structure of the sandcastle and change the water content of the sandcastle. Therefore, we

TABLE 1: Different water-sand ratios correspond to duration.

Water-sand ratio	0.70	0.72	0.74	0.76	0.78	0.80	0.82	0.84
Duration	4.7	4.9	5.2	4.8	5.1	5.0	4.6	4.4

divide the impact of rain on sandcastles into two parts: scour and infiltration [20, 21].

Formula for calculating the final velocity of raindrop is as follows.

If $d \leq 3$ mm, we have

$$V_{\max} = \sqrt{\left(38.9 \frac{v}{d}\right)^2 + 2400gd} - 38.9 \frac{v}{d} \quad (16)$$

If $3 \text{ mm} < d \leq 6$ mm, we have

$$V_{\max} = \frac{d}{(0.113 + 0.845d)}. \quad (17)$$

In the formula, v is the viscosity coefficient of air motion. When $T = 293$ K, $v = 1.810741555 \times 10^{-5}$ Pa·S.

Think of raindrops as spheres. According to the momentum formula $q = mV_{\max}$ and energy formula $E = (mV_{\max}^2)/2$, the momentum and energy contained in each raindrop can be obtained, and then the relationship between raindrop diameter and momentum and energy can be obtained [22–24].

3.3.2. Model Establishing and Solving. However, in the actual calculation of rainfall characteristics such as rainfall kinetic energy, only the data of rainfall or rainfall intensity are usually available, and the observed data of raindrop diameter are not available. In order to facilitate production and application, the final raindrop velocity can be expressed as a function of rain intensity [25]. According to the analysis of the measured data, there is a power function relationship between the median raindrop diameter and rainfall intensity:

$$d_m = 2.52i^{0.32}. \quad (18)$$

In the formula, d_m represents median diameter of raindrops; the units are mm. i represents rain intensity; the units are mm/min. The final velocity of raindrop is determined by rainfall intensity through substitution and calculation.

If $i \leq 2.13$, we have

$$V_{\max} = \sqrt{\left(1.544 \frac{v}{i^{0.23}}\right)^2 + 6.048gi^{0.23}} - 1.544 \frac{v}{i^{0.23}}. \quad (19)$$

If $2.13 < i \leq 43.46$, we have

$$V_{\max} = \frac{i^{0.23}}{(0.0448 + 0.0845i^{0.23})}. \quad (20)$$

From formula (16) to formula (20), the relationship between precipitation and raindrop velocity, energy, and momentum is calculated, as shown in Figures 4–6.

After understanding the motion parameters of raindrops, we also need to analyze the influence of raindrops on sandcastles [26]. The Sartor–Boyd scour model is mainly

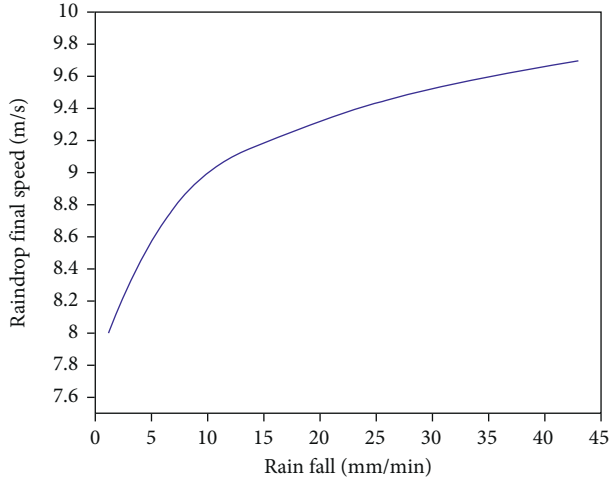


FIGURE 4: Relationship between precipitation and raindrop speed.

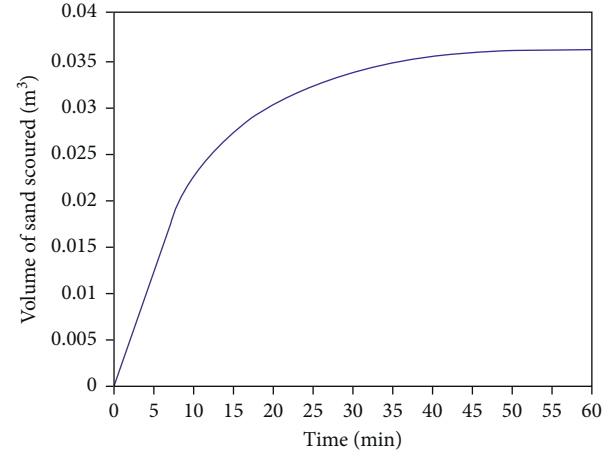


FIGURE 7: Changes in the amount of sand washed away by precipitation.

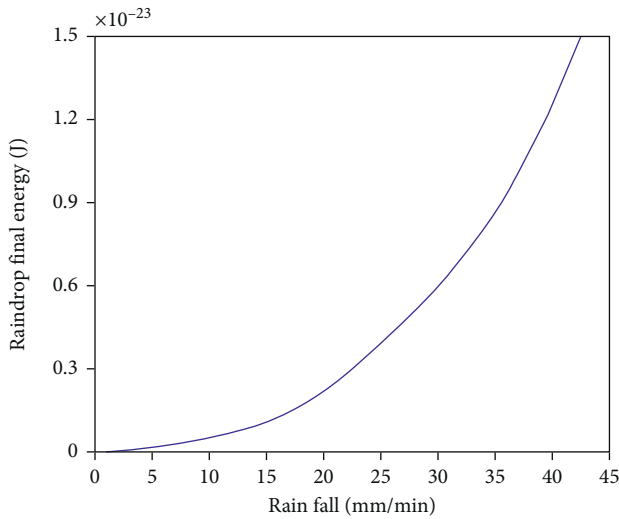


FIGURE 5: Relationship between precipitation and raindrop energy.

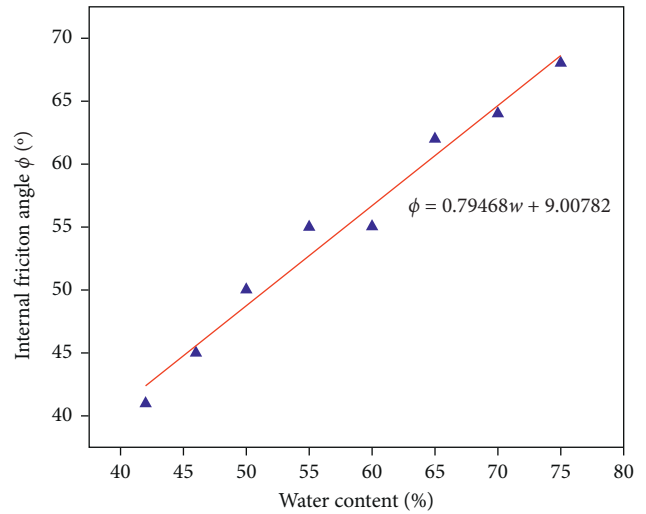


FIGURE 8: Relationship between water content and internal friction angle caused by rainfall on sandcastle.

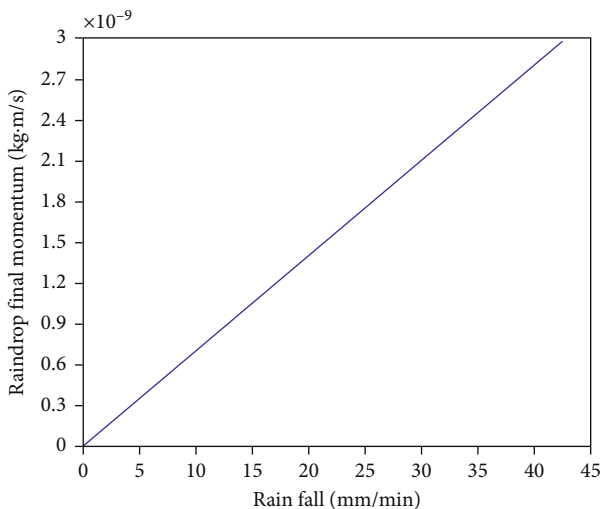


FIGURE 6: Relationship between precipitation and raindrop momentum.

applicable to the rainfall process with initial scour effect, as shown in the following equation:

$$\frac{dV_p}{dt} = K_e V_p R_p. \tag{21}$$

In formula (21), K_e represents the erosion coefficient, the units are mm^{-1} ; V_p represents the volume of sandcastle at the beginning, the units are m^3 ; R_p represents rainwater runoff per unit time per unit area, the units are mm/min ; t represents time, the unit is min . In our model, take K_e as 0.2 to get the change of sand grain quantity washed away by precipitation, as shown in Figure 7.

3.3.3. *Result Analysis.* When the sandcastle is affected by rainfall, MATLAB is used to fit the relationship between the internal friction angle and water content of the sandcastle, as shown in Figure 8.

In the precipitation model, we get the formula for calculating the final velocity of raindrop. Then, the water content of sandcastle and the angle of internal friction during rainfall are calculated. Finally, compare the relationship between the two and draw a conclusion. The results show that the rain has a certain effect on the structural stability of the sandcastle. Through the establishment and solution of the above model, we find that streamline is still the optimal geometric shape, which verifies the reliability of the model.

4. Conclusions

On the basis of the simulation results, the destructive power of seawater, rainy days, and other environments is summarized, which is an important threat to the sandcastle foundation [27–31]. Several models established in the detailed mathematical analysis provided answers to the required questions, including a view of the exterior of the sandcastle with the longest period of stability in the natural state.

In general, a sandcastle foundation with a gentle slope is good at resisting seawater erosion, while a foundation with a large top is good at resisting rain. After many iterations, all initial sandcastle foundation transfers have similar structures. As mentioned earlier, the optimal sand-water mixture ratio is about 0.74. Due to the trade-off between friction and fluidity, three measures can be taken to strengthen the sandcastle foundation, such as adjusting construction time, adding support structure, and improving the building. Those are all practical measures one can take in order to obtain a better sandcastle foundation.

Data Availability

The data in this paper come from Question B of the 2020 American College Students Mathematical Modeling Competition.

Conflicts of Interest

The authors declare that there are no conflicts of interest regarding the publication of this paper.

Acknowledgments

This study was funded by the Humanities and Social Sciences Research Major Project of the Education Department of Anhui Province (SK2017A0452), the Teaching and Research Fund Project of the Education Department of Anhui Province (2018jyxm1305), and the Teaching and Research Fund Project of the Anhui University of Finance and Economics (acxkjsjy201803zd and acjyyb2020011).

References

- [1] J. P. Bouchaud, M. E. Cates, J. R. Prakash, and S. F. Edwards, "Hysteresis and metastability in a continuum sandpile model," *Physical Review Letters*, vol. 74, no. 11, pp. 1982–1985, 1995.
- [2] Y. L. Chen, G. Y. Liu, N. Li, X. Du, S.-R. Wang, and R. Azzam, "Stability evaluation of slope subjected to seismic effect combined with consequent rainfall," *Engineering Geology*, vol. 266, Article ID 105461, 2020.
- [3] M. Pakpour, M. Habibi, P. Møller, and D. Bonn, "How to construct the perfect sandcastle," *Scientific Reports*, vol. 2, no. 1, pp. 1–3, 2012.
- [4] S. Dumont and I. Noureddine, "On a dual formulation for the growing sand pile problem," *European Journal of Applied Mathematics*, vol. 20, no. 2, pp. 169–185, 2009.
- [5] N. Fraysse, H. Thomé, and L. Petit, "Humidity effects on the stability of a sand pile," *The European Physical Journal B-Condensed Matter and Complex Systems*, vol. 11, no. 4, pp. 615–619, 1999.
- [6] T. Gröger, U. Tüzün, and D. M. Heyes, "Modelling and measuring of cohesion in wet granular materials," *Powder Technology*, vol. 133, no. 3, pp. 203–215, 2003.
- [7] T. C. Halsey and A. J. Levine, "How sandcastles fall," *Physical Review Letters*, vol. 80, no. 14, pp. 31–41, 1998.
- [8] G. L. George, "Magic sand: modeling the hydrophobic effect and reversed-phase liquid chromatography," *Journal of Chemical Education*, vol. 67, no. 6, pp. 512–515, 1990.
- [9] M. Scheel, R. Seemann, M. Brinkmann et al., "Morphological clues to wet granular pile stability," *Nature Materials*, vol. 7, no. 3, pp. 189–193, 2008.
- [10] S. Dumontl and N. Igbida, "On the collapsing sandpile problem," *Communications on Pure and Applied Analysis*, vol. 10, no. 2, pp. 625–638, 2010.
- [11] C. Mejia and J. A. Montoya, "On the complexity of sand pile critical avalanches," *Theoretical Computer Science*, vol. 412, no. 30, pp. 3964–3974, 2011.
- [12] S. Qiao, S. Qin, J. Chen, X. Hu, and Z. Ma, "The application of a three-dimensional deterministic model in the study of debris flow prediction based on the rainfall-unstable soil coupling mechanism," *Processes*, vol. 7, no. 2, 2019.
- [13] N. Igbida and N. Noureddine, "A partial integrodifferential equation in granular matter and its connection with a stochastic model," *Siam Journal on Mathematical Analysis*, vol. 44, no. 3, pp. 1950–1975, 2012.
- [14] N. Igbida, "A generalized collapsing sandpile model," *Archiv Der Mathematik*, vol. 94, no. 2, pp. 193–200, 2010.
- [15] A. Sotirov and S. H. Yu, "On the solution of a Boltzmann system for gas mixtures," *Archive for Rational Mechanics & Analysis*, vol. 195, no. 2, pp. 675–700, 2010.
- [16] G. Sorbino and M. V. Nicotera, "Unsaturated soil mechanics in rainfall-induced flow landslides," *Engineering Geology*, vol. 165, pp. 105–132, 2013.
- [17] M. Burylo, C. Hudek, and F. Rey, "Soil reinforcement by the roots of six dominant species on eroded mountainous marly slopes (Southern Alps, France)," *CATENA*, vol. 84, no. 1-2, pp. 70–78, 2011.
- [18] Y. Hong, R. Chen, C. Wu, and J. Chen, "Shaking table tests and stability analysis of steep nailed slopes," *Canadian Geotechnical Journal*, vol. 42, no. 5, pp. 1264–1279, 2011.
- [19] H. Moriwaki, T. Inokuchi, T. Hattani, K. Sassa, H. Ochiai, and G. Wang, "Failure processes in a full-scale landslide experiment using a rainfall simulator," *Landslides*, vol. 1, no. 4, pp. 277–288, 2004.
- [20] M. Lin and K. Wang, "Seismic slope behavior in a large-scale shaking table model test," *Engineering Geology*, vol. 86, no. 2-3, pp. 118–133, 2006.
- [21] K. Sasahara and N. Sakai, "Development of shear deformation due to the increase of pore pressure in a sandy model slope

- during rainfall,” *Engineering Geology*, vol. 170, pp. 43–51, 2014.
- [22] L. Pantelidis and D. V. Griffiths, “Stability of earth slopes. Part II: three dimensional analysis in closed-form,” *International Journal for Numerical and Analytical Methods in Geomechanics*, vol. 37, no. 13, pp. 1987–2004, 2013.
- [23] N. Iwata, R. Yoshinaka, and T. Sasaki, “Applicability of the seismic response analysis using multiple yield model for discontinuous rock,” *International Journal of Rock Mechanics and Mining Sciences*, vol. 60, pp. 196–207, 2013.
- [24] H. Yuehua, Z. Cheng, and L. I. Hongmei, “Combined effects of trees and macropores on slope stability subjected to rainfall,” *Journal of Water Resources & Architectural Engineering*, 2018.
- [25] Z. Yu, Y. L. Kun, G. Z. Zheng et al., “Evaluation of the stability of Maliulin landslide under the reservoir water level fluctuation combined with rainfall,” *Geological Science and Technology Information*, 2019.
- [26] A. Chinkulkijniwat, T. Tirametatarat, C. Supotayan et al., “Stability characteristics of shallow landslide triggered by rainfall,” *Journal of Mountain Science*, vol. 16, pp. 2171–2183, 2019.
- [27] J. B. Liu, J. Zhao, J. Cao, and J. Min, “On the Hosoya index of graphs formed by a fractal graph,” *Fractals-Complex Geometry Patterns and Scaling in Nature and Society*, vol. 27, no. 8, pp. 19–35, 2019.
- [28] J. B. Liu, J. Zhao, H. He, and Z. Shao, “Valency-based Topological descriptors and structural property of the generalized Sierpiński networks,” *Journal of Statistical Physics*, vol. 177, no. 6, pp. 1131–1147, 2019.
- [29] J. B. Liu, J. Zhao, and Z. Cai, “On the generalized adjacency, Laplacian and signless Laplacian spectra of the weighted edge corona networks,” *Physica A: Statistical Mechanics and its Applications*, vol. 540, pp. 12–30, 2020.
- [30] J. M. Zhu, W. Y. Xia, J. J. Sun, J.-B. Liu, and F.-H. Yu, “The spread pattern on Ebola and the control schemes,” *International Journal of Innovative Computing and Applications*, vol. 9, no. 2, pp. 77–89, 2018.
- [31] J.-M. Zhu, L. Wang, and J.-B. Liu, “Eradication of Ebola based on dynamic programming,” *Computational and Mathematical Methods in Medicine*, vol. 2016, p. 9, Article ID 1580917, 2016.

Research Article

Research on Optimization of Improved Gray Wolf Optimization-Extreme Learning Machine Algorithm in Vehicle Route Planning

Shijin Li¹ and Fucai Wang² 

¹Academic Affairs Office, Yunnan University of Finance and Economics, Kunming, Yunnan 650221, China

²Yunnan Business Information Engineering School, Kunming, Yunnan 650000, China

Correspondence should be addressed to Fucai Wang; wangfucai_km@sina.com

Received 2 August 2020; Revised 16 September 2020; Accepted 22 September 2020; Published 6 October 2020

Academic Editor: Jia-Bao Liu

Copyright © 2020 Shijin Li and Fucai Wang. This is an open access article distributed under the Creative Commons Attribution License, which permits unrestricted use, distribution, and reproduction in any medium, provided the original work is properly cited.

With the rapid development of intelligent transportation, intelligent algorithms and path planning have become effective methods to relieve traffic pressure. Intelligent algorithm can realize the priority selection mode in realizing traffic optimization efficiency. However, there is local optimization in intelligence and it is difficult to realize global optimization. In this paper, the antilearning model is used to solve the problem that the gray wolf algorithm falls into local optimization. The positions of different wolves are updated. When falling into local optimization, the current position is optimized to realize global optimization. Extreme Learning Machine (ELM) algorithm model is introduced to accelerate Improved Gray Wolf Optimization (IGWO) optimization and improve convergence speed. Finally, the experiment proves that IGWO-ELM algorithm is compared in path planning, and the algorithm has an ideal effect and high efficiency.

1. Introduction

Traffic congestion has become a common problem faced by many cities and even most countries in the world. Traffic congestion will not only increase the waiting time people spend on the road and cause urban traffic paralysis but also aggravate environmental pollution. According to understanding, when vehicles are in traffic jams, gasoline is not fully burned in the engine due to the low speed of the vehicle, resulting in pollutants that are several times higher than that when driving at normal speed. Path planning plays an important role in the urban transportation system. A well-planned transportation system can not only reduce the pressure of urban traffic but also bring great convenience to people's travel, and it has a great role in improving the urban landscape, enhancing the image of the city, and providing people with a good working and learning environment [1]. The main purpose of path planning is to design a traffic route that best meets the actual needs of travelers, provide travelers with the most time-saving and least expensive route, reduce

traffic congestion, improve road traffic conditions, and realize urban traffic continued development [2]. As artificial intelligence plays an increasingly obvious role in traffic forecasting, it can plan the traffic path and greatly reduce the time of congestion on the road.

Path planning has been widely used in high technology, daily life, decision management, and other fields [3–6]. According to different classification types, the classification of path planning is also different. When classified according to the degree of mastery of the current path, it is mainly divided into two parts: global path planning and local path planning. As the core of autonomous planning and navigation technology for mobile intelligent vehicles, researchers at home and abroad have done a lot of research in recent years. Mrazovic et al. [7] used big data analysis technology to calculate the current vehicle circulation and parking utilization rate and developed a multivehicle routing algorithm to reduce road congestion caused by parking or specific areas. In this paper, a two-layer local search algorithm (greedy random adaptive) is used to train a large number of

historical data collected. Through algorithm optimization comparison and analysis, urban road optimization management and reasonable route planning are realized. Gündüz et al. [8] proposed a new path planning method based on an improved genetic algorithm. The evaluation index and optimization function are given through path length and path energy. The three-dimensional path layer structure is established based on fuzzy neural network, and then the genetic algorithm is used to solve the optimal path. Lin et al. [9] proposed a path optimization algorithm for dynamic programming based on PSO, which adopts multi-objective PSO method and can realize parallel processing of different optimization objectives. Ant colony algorithm adopts a positive feedback mechanism, and the search process converges continuously. It has parallelism and greatly improves the operation efficiency of the algorithm. Heuristic probabilistic search has better global optimization ability. However, the disadvantage of ant colony algorithm is that the computation is large [10]. Mauricio et al. [11] adopted a particle swarm optimization method to solve the nonuniform vehicle routing problem with terminal. Through adaptive inertia weight and local search strategy, a better vehicle route scheme is solved. Experimental results show that this method can effectively save the total delivery cost and the number of vehicles required for distribution. Vareias et al. [12] proposed a random time vehicle routing optimization method, which assigns corresponding time to vehicles to solve the optimization problem. The time-consuming and time-consuming of vehicles in the planned route are evaluated, a time window is set for each vehicle, and a penalty and restraint mechanism is set for vehicles late and early. A two-level solution method is implemented, and the cost of the path is optimized and the time window is decomposed into subwindows to evaluate the optimization effect. Hiraishi [13] proposed a route optimization scheme with passengers as the criteria for judging the vehicle status. The route is planned by judging the passenger status. For example, if the passenger is judged to be tired, a time-consuming route is planned. Saed et al. [14] used memory storage mode through the optimal route, adaptive decision-making cognitive framework; this method can memorize, store, and optimize the route of vehicle information and update the optimal route mode through continuous learning. These algorithms have a certain ability to intelligently process and optimize information, but they do not evaluate historical time and consumption. The restraint mechanism and real-time road conditions cannot be better evaluated, and the road conditions cannot be predicted in real time. The above-mentioned documents have certain advantages in solving real-time path optimization and have a good prediction effect in a short time.

2. Gray Wolf Optimization Algorithm Strategies

2.1. Standard Wolf Optimization Algorithm. Gray Wolf Optimization (GWO) algorithm is a population intelligence algorithm proposed by Mirjalili Seyedali inspired by gray wolf predation behavior in 2014. The gray wolf pack has a 4-layer hierarchical mechanism of α , β , δ , and ω . Among them, wolf α

is the leader with the best adaptability among the gray wolves. β and δ are the two individuals with the second best fitness. Their task is to assist wolf α in managing the wolf pack and making decisions in the hunting process. ω is the remaining common wolf pack. The predation process is described as follows: first, wolf α leads the gray wolves to search, track, and approach their prey; then, wolves β and δ besiege the prey under the command of wolf α and summon ordinary wolves to attack the prey until they capture the prey. GWO algorithm completes the predation behavior by imitating the predation tasks such as gray wolf surrounding, hunting, and attacking, thus realizing the process of global optimization.

2.2. Mathematical Model of GWO. In GWO's leadership system, wolf α has the highest level, and wolves β and δ led by wolf α are also better individuals. Wolf ω searches paths under wolf α , wolf β , and wolf δ . As ω continuously optimizes the target, while α , β , and δ wolves continuously update the location information, other ω also continuously optimize the target.

Assuming that in D -dimensional space, the gray wolf pack $\{X_i, i = 1, 2, \dots, N\}$ consists of N gray wolves. The GWO algorithm is described as follows:

Encirclement stage: after the wolves determine the position of their prey, they first encircle the prey. The mathematical description is as follows:

$$\begin{aligned} D &= |C \cdot X_p(t) - X(t)|, \\ X(t+1) &= X_p(t) - A \cdot D, \end{aligned} \quad (1)$$

where D is the distance between the gray wolf and its prey; $X_p(t)$ is the position of the prey after the t -th iteration (the current optimal solution); $X(t)$ is the position of the gray wolf (the position of the feasible solution) after the t -th iteration; A and C are coefficient factors, defined as follows:

$$\begin{aligned} A &= 2a \times r_1 - a, \\ C &= 2 \times r_2, \end{aligned} \quad (2)$$

where r_1 and r_2 are random numbers within $[0, 1]$; t is the number of iterations of the algorithm; and \max is the maximum number of iterations. $a = 2 \rightarrow 0$ with the increase of iteration times t :

$$a = 2 - 2\left(\frac{t}{\max}\right). \quad (3)$$

Hunting stage: wolf α can quickly find the position of the prey and search for the prey. When wolf α finds the position of the prey, wolves α , β , and δ have a certain understanding of the position of the prey and require ω

to approach the position of the prey. This is the prey process of wolves.

After the siege phase is completed, wolf α leads wolves β and δ to hunt down their prey. In the process of hunting, the position of individual wolves will move with the escape of prey:

$$\begin{aligned} X_1 &= X_\alpha - A_1 |C_1 X_\alpha(t) - X(t)|, \\ X_2 &= X_\beta - A_2 |C_2 X_\beta(t) - X(t)|, \\ X_3 &= X_\delta - A_3 |C_3 X_\delta(t) - X(t)|, \end{aligned} \quad (4)$$

where X_α , X_β , and X_δ represent the current positions of wolves α , β , and δ ; $X(t)$ indicates the current gray wolf position; C_1, C_2, C_3 are random vectors.

Update the location of wolf α :

$$X(t+1) = \frac{X_1 + X_2 + X_3}{3}. \quad (5)$$

By continuously updating the location information, ω wolf continuously updates the location to obtain the optimal location information. The candidate solution in the gray wolf algorithm updates its own position by taking the position information of the leadership level. Candidate solutions are distributed in a random circle defined by the leadership level. From the above formula and schematic diagram, it can be summarized that the optimization process of gray wolf algorithm is to elect wolves α, β , and δ in turn and then use the elected elite individuals to evaluate the possible positions of the prey, and then other individuals in the group randomly update the positions around the prey with reference to the position information of wolves α, β , and δ .

3. Improved Gray Wolf Optimization Algorithm

Gray Wolf Optimization algorithm is a naturally inspired search algorithm, which has good performance and efficiency in solving various optimization problems. The ‘‘flame’’ variable in the process of lateral orientation is an important parameter used by GWO to update the new position of the population. However, the reduction of flame will slow down the convergence speed, thus affecting the quality of the final solution. In order to overcome this shortcoming, a new antilearning (OBL) moth flame algorithm is proposed. In addition, for cross-border moths, a mirror cross-border strategy is adopted to ensure that moths are within the dimension range and improve population diversity.

3.1. Antilearning Algorithm. OBL was first proposed by Tizhoosh in 2005. It is described as follows: suppose the point $\mathbf{X} = (x_1, x_2, \dots, x_i, \dots, x_d)$ in d -dimensional space, where $x_1, x_2, \dots, x_i, \dots, x_d \in R$ and $x_i \in [a_i, b_i]$. Its reverse point $\tilde{\mathbf{X}} = (\tilde{x}_1, \tilde{x}_2, \dots, \tilde{x}_i, \dots, \tilde{x}_d)$ is defined as follows:

$$\tilde{x}_i = a_i + b_i - x_i. \quad (6)$$

On the basis of GWO, a supplementary function H based on antilearning strategy is added to speed up the

convergence of GWO, and a high-precision solution is obtained. The H function is described as follows:

$$H = (A + B) - C \times \text{rand}() \quad (7)$$

$$M_i = H, \quad (8)$$

$$A = \begin{cases} \Gamma, & s > \text{rand}() \\ U, & \text{otherwise,} \end{cases} \quad (9)$$

$$B = \begin{cases} \Theta, & s > \text{rand}() \\ L, & \text{otherwise,} \end{cases} \quad (10)$$

where $s = (\text{Current number of iterations} / \text{Maximum number of iterations})$, Γ and Θ are the largest and smallest positions of gray wolf respectively, U and L are the upper and lower limits of the search space, C is that optimal flame position in any iteration process, and rand is a random number between (0, 1). Equation (7) is a new form of antilearning. H function generates a new reverse solution according to the reverse position of gray wolf.

3.2. Gray Wolf Cross-Border Mirror Strategy. In the GWO optimization process, the gray wolf updates its position according to formula (5), and its position coordinates will cross the border and be continuously placed on the boundary, which not only reduces the diversity of the gray wolf population but also easily makes the algorithm fall into local optimization, thus affecting the optimization performance of the algorithm. In view of this situation, use equation (11) to update the cross-border gray wolf:

$$X(t+1)_{i,j} = \begin{cases} 2L_j - \text{rand}() \times X(t+1)_{i,j}, & X(t+1)_{i,j} \leq L_j, \\ 2U_j - \text{rand}() \times X(t+1)_{i,j}, & X(t+1)_{i,j} > U_j, \end{cases} \quad (11)$$

where $X(t+1)_{i,j}$ is the j -dimensional cross-border position in the i -th gray wolf; L_j and U_j are the value range of the j -th dimension. Repeated operation formula (11) can map $X(t+1)_{i,j}$ to the range of dimensions, ensure population diversity, and effectively improve the optimization performance of GWO algorithm.

3.3. Steps to Improve Gray Wolf Optimization Algorithm. An Improved Gray Wolf Optimizer (IGWO) is proposed by improving the gray wolf algorithm. The implementation steps of IGWO are summarized as follows:

Step 1: set algorithm parameters, including population size N , maximum iteration times max , search space dimension dim , search space upper bound U , and lower bound L .

Step 2: initialize that population according to the method in Section 2.2, $p = 2 * \text{dim} + 3$.

Step 3: calculate and sort the fitness values of gray wolf individuals according to the objective function, find out the individuals with the highest fitness according to the

fitness values, and save their positions as X_α , X_β , and X_δ , respectively.

Step 4: update the position according to the step size segment step size update mechanism of formulae (4) and (5).

Step 5: update the gray wolf population position according to the algorithm designed by formula (11).

Step 6: update parameters a , A , and C , where the original linear convergence factor a is changed to exponential nonlinear convergence factor.

Step 7: determine whether the maximum number of iterations has been reached, and if so, stop the iteration and output.

4. Extreme Learning Machine (ELM)

Professor Huang et al. [15] proposed the Extreme Learning Machine in 2006. ELM algorithm is an improved new algorithm based on SLFN. The biggest advantage of ELM algorithm over traditional SLFN algorithm is that it does not need to update the parameters in training, such as the weight between the input layer and the hidden layer and the threshold value of hidden layer neurons. Once the number of hidden layer nodes is determined, ELM algorithm can obtain a unique global optimal solution with good generalization and general approximation capability.

Extreme Learning Machine is a kind of single-hidden layer feedforward neural network (SLFN), which has been widely concerned and applied because of its fast convergence and fast learning ability and good nonlinear classification ability.

Set n different training samples (x_i, y_i) , of which the k -th input $x = [x_1, x_2, \dots, x_N]^T \in R^N$ corresponds to the output $y = [y_1, y_2, \dots, y_m]^T \in R^m$, set the number of input layer nodes of the network as N , set the number of hidden layer nodes as M , and the activation function is expressed as $g(x)$; then the unified model of SLFN is

$$\sum_{j=1}^M \beta_j g(x_i) = \sum_{j=1}^M \beta_j g(w_j \cdot x_i + b_j) = y_i, \quad i = 1, \dots, n, \quad (12)$$

where w_j represents the j -th weight of the input layer and the hidden layer, b is the node bias of the hidden layer, $g(\cdot)$ is the excitation function of the hidden layer, the output of the output layer is $y = [y_1, y_2, \dots, y_m]^T \in R^m$, the expected output is $e = [e_1, e_2, \dots, e_m]^T \in R^m$, $w = \{w_{ij}\}$ represents the connection weight between neurons and neurons (i and j , resp., represent the serial numbers of neurons in the input layer and the hidden layer), and $\beta = \{\beta_{ij}\}$ represents the connection weight between neurons and neurons (i and j , resp., represent the serial numbers of neurons in the hidden layer and the output layer). Then the output of each sample is

$$y = [g(w_1 x + b_1)g(w_2 x + b_2), \dots, g(w_m x + b_m)]\beta_i + b_i. \quad (13)$$

The equation is expressed as

$$h(x) = g(w_1 x + b_1)g(w_2 x + b_2), \dots, g(w_m x + b_m). \quad (14)$$

$H(x)$ refers to the response of all neurons in the hidden layer to the input vector x and calculates the output:

$$y = h(x) \cdot \beta_i + b_i. \quad (15)$$

The system output for N samples is

$$Y = H \cdot \beta + b_i. \quad (16)$$

The error function is defined as

$$E = \|T - Y\| = \|T - (H \cdot \beta + b_i)\|, \quad (17)$$

where $\|\cdot\|$ represents norm. The above is the basic mathematical reasoning process of a single-hidden layer feedforward neural network. All its parameter values are continuously updated, and the thresholds and weights of both the hidden layer and the output layer will be optimized.

5. Experimental Scheme

In this paper, a directed graph $G = (V, E)$ is defined for urban intersections to represent the key intersection conditions of the city, as shown in Figure 1, where $V = (v_1, v_2, \dots, v_n)$ represents N key intersections in the city and $E = (e_1, e_2, \dots, e_m)$ represents all roads in the city, totaling m roads. The traffic flow between each key intersection is expressed by matrix $D = \{d_{ij}\}$, $1 \leq i, j \leq n$, where d_{ij} represents the number of vehicles from stations v_i to v_j . However, the cost matrix $C = \{c_{ij}\}$, $1 \leq i, j \leq n$, of vehicles passes between intersections. It shows that c_{ij} represents the cost of vehicles arriving at v_j from station v_i , which generally refers to time or distance. Because time is proportional to distance when the vehicle speed is the same, the cost is the same regardless of time or distance. However, if there is no road between station v_i and station v_j , c_{ij} is defined as a large number. For example, $c_{01} = 6, c_{10} = 4$ means that the two reintersections communicate at different times and the road conditions between the two intersections are different.

In Figure 1, the passing time before different intersections in the city at a certain moment shows different passing time at different times, different seasons, and different months, different time points in the day show different passing time, and the road conditions show different, specifically showing congestion, slow movement, and smooth flow. In Figure 1, the traffic conditions of different roads back and forth are shown, and the numbers represent specific locations. The number between location and location represents the cost that can be done between locations and generally refers to the time or cost that can be done.

Through the relevant statistical analysis of GPS data, the longitude and latitude of different sections at different times and the road conditions of the current map are analyzed. Relevant statistics and analysis are carried out on longitude, latitude, and geographic information in GPS data, vehicle information at different time points of road sections in GPS

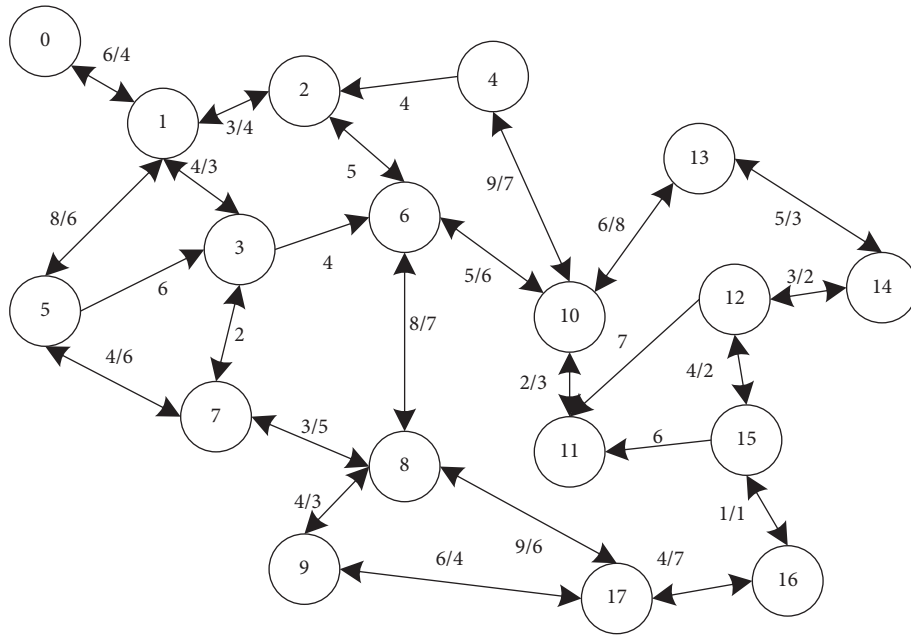


FIGURE 1: Abstract diagram of the route of the key intersection of urban traffic at a certain moment.

TABLE 1: Statistical table of road conditions of vehicles.

Road ID	Vehicles ID	Road length (m)	Entry time	Leave time	Speed (km/h)	Road condition
3	15	478.6	08:03:18	08:04:23	32.6	3
2	18	1242.8	12:52:00	12:54:10	23.2	2
1	121	1254.4	21:18:15	21:20:15	25.1	3
9	128	521.3	10:57:06	10:59:10	10.5	1
3	675	613.2	18:47:59	18:50:23	9.2	1
...						

data is counted, key intersections are numbered, and the sorted data are described in Table 1.

The above is the statistics of a certain point in time, and the road condition information is usually counted every 5 minutes. Generally, the statistical results of the current real-time road conditions can be divided into three states: blockage, slow travel, and comfort. 1, 2, and 3 are used, respectively. The threshold judgment criteria are as follows: blockage is less than 12 km/h, slow travel is 12~25 km/h, and unblocked is greater than 25 km/h. The data in Table 1 is obtained through raw data statistics. Road ID denotes the number of the road in the map; vehicle ID denotes the number of the vehicle; road section length denotes the actual length of a road section; entry time denotes the start time when the vehicle enters the road section; departure time denotes the end time when the vehicle leaves the road section; speed denotes general passing calculated by dividing the length of the road segment by the time; road conditions denotes classify road conditions by speed.

Through the gray wolf algorithm to predict the key intersections of urban traffic, predicting the key routes through

different intersections is the focus of this paper. In order to be able to predict the optimal route from the starting point to the ending point and to predict different intersections, Figure 2 compares the prediction effects of different routes.

The optimal route in Figure 2 is the route selection when the current key route is unblocked, which is referred to herein as the optimal route. The route selection recommended by IGWO-ELM algorithm is basically in high agreement with the optimal route in terms of route, but this is the actual route selection, considering the road conditions at different times. IGWO-ELM algorithm is ideal in execution effect, which shows that the algorithm has a good execution effect. In order to reflect the performance effect of the algorithm, the comparison effect between PSO and GWO algorithms is shown in Figure 3.

In Figure 3, compared with the time under different paths, the time of IGWO-ELM algorithm in practical application is close to the theoretical value. PSO and GWO algorithms may have differences in running time. In some paths, the running efficiency of the two algorithms is the same, sometimes PSO is better than GWO, and the time efficiency of the two algorithms alternates.

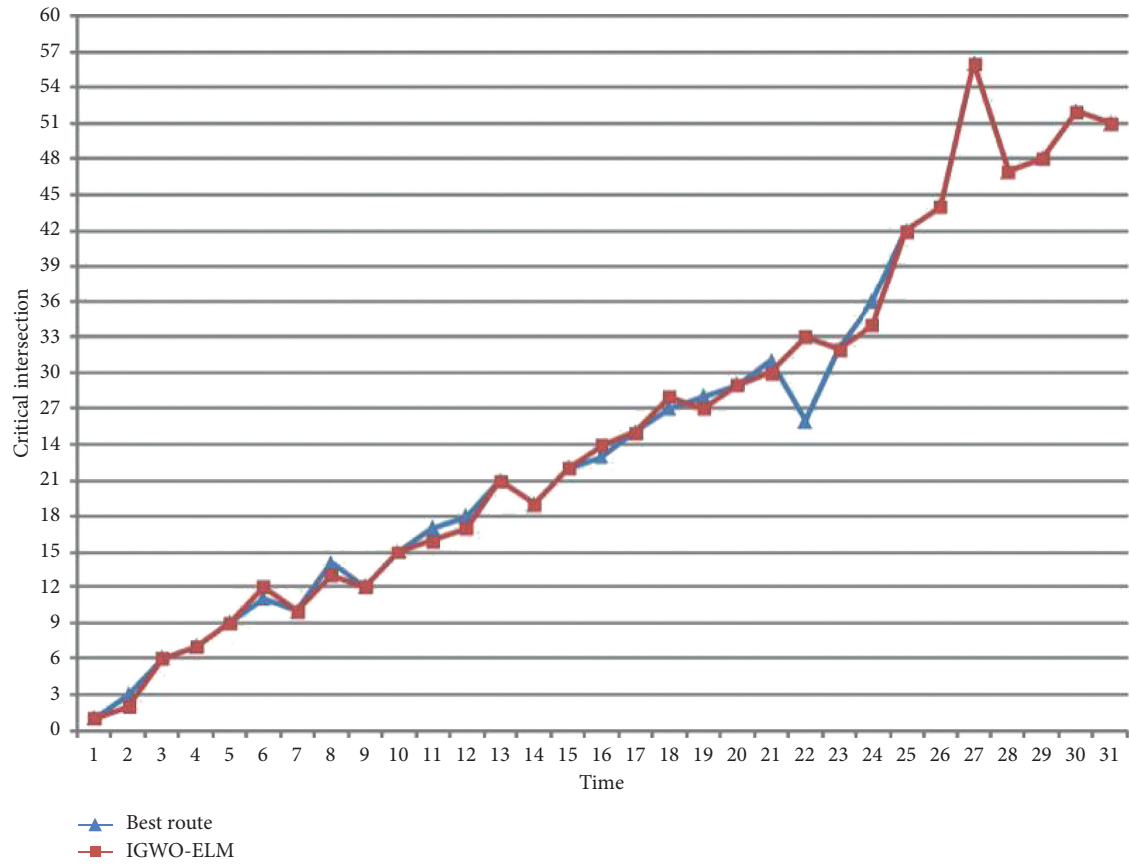


FIGURE 2: Comparison of IGWO-ELM route and optimal route in Figure 2.

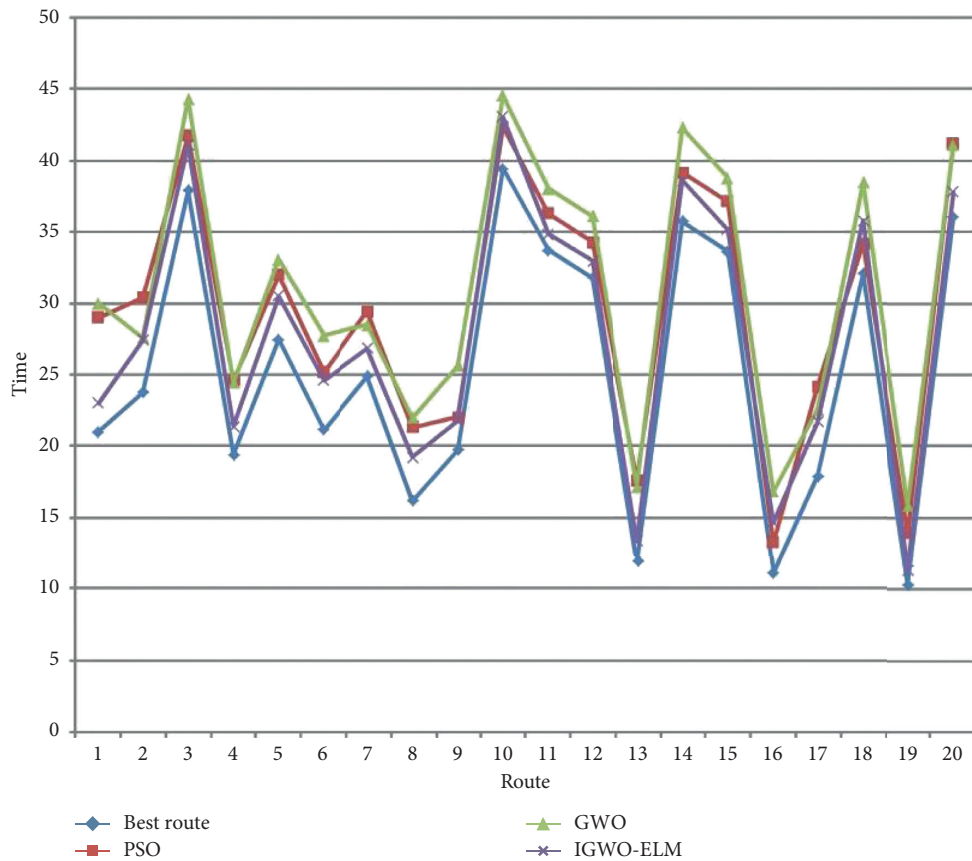


FIGURE 3: Comparisons of three algorithms under different route.

6. Conclusion

This paper proposes an improved gray wolf algorithm to be applied to urban traffic path planning. Reasonable traffic path planning can improve traffic operation efficiency and save a lot of time. The basic gray wolf algorithm is easy to fall into local optimization, and it is difficult to obtain global total optimization. The gray wolf algorithm is improved through the antilearning model; thus, the actual global optimization is achieved. Finally, the experimental comparison shows that IGWO-ELM algorithm has obvious advantages in execution efficiency and time. Considering the comparative advantage of IGWO-ELM algorithm in efficiency, different time points or seasonal points will be used as research objects in the later period. The historical data are trained to predict the traffic planning for a period of time in the future, and the vehicles are reasonably planned to alleviate the traffic congestion.

Data Availability

The data used to support the findings of this study are included within the article.

Conflicts of Interest

The authors declare that they have no conflicts of interest.

Authors' Contributions

All authors contributed equally to the writing of this paper. All authors read and approved the final manuscript.

Acknowledgments

This work was supported by the Design and Application of Intelligent Teaching Model Based on Rain Classroom Grant no. 41620200001/002, Data Mining Research on MOOC Learning Behavior Based on Internet Environment under Grant no. 80059900227, and Research on the Model of Flip Classroom Teaching Based on Micro-Lectures under Grant no. 80059900253.

References

- [1] W.-H. Wang, Y. Wang, Z. Li, C.-Z. Wei, J.-C. Zhao, and L.-q. Sun, "Effect of a strengthened ecological floating bed on the purification of urban landscape water supplied with reclaimed water," *Science of the Total Environment*, vol. 622-623, pp. 1630-1639, 2018.
- [2] S. Zhao, Y. Liu, M. Sundhararajan et al., "Evaluation system for the sustainable development of urban transportation and ecological environment based on SVM," *Journal of Intelligent & Fuzzy Systems*, vol. 34, no. 2, pp. 831-838, 2018.
- [3] J. B. Liu, J. Zhao, and Z. Cai, "On the generalized adjacency, Laplacian and signless Laplacian spectra of the weighted edge corona networks," *Physica A*, vol. 540, pp. 1-11, 2020.
- [4] W. Liu, J. Li, L. Ren et al., "Exploring livelihood resilience and its impact on livelihood strategy in rural China," *Social Indicators Research*, vol. 150, no. 3, pp. 977-998, 2020.
- [5] J.-B. Liu, J. Zhao, H. He, and Z. Shao, "Valency-based topological descriptors and structural property of the generalized sierpiński networks," *Journal of Statistical Physics*, vol. 177, no. 6, pp. 1131-1147, 2019.
- [6] W. Jiang, D. R. Carter, H. L. Fu et al., "The impact of the biomass crop assistance program on the United States forest products market: an application of the global forest products model," *Forests*, vol. 10, no. 3, pp. 1-12, 2019.
- [7] P. Mrazovic, E. Eser, H. Ferhatosmanoglu et al., "Multi-vehicle route planning for efficient urban freight transport," in *Proceedings of the 2018 international conference on intelligent systems (IS), IEEE, Funchal-Madeira, Portugal*, September 2019.
- [8] M. G. Gündüz, M. S. Kiran, and E. Özceylan, "A hierarchic approach based on swarm intelligence to solve the traveling salesman problem," *Turkish Journal of Electrical Engineering & Computer Sciences*, vol. 23, pp. 103-117, 2015.
- [9] Y.-H. Lin, L.-C. Huang, S.-Y. Chen, and C.-M. Yu, "The optimal route planning for inspection task of autonomous underwater vehicle composed of MOPSO-based dynamic routing algorithm in currents," *Applied Ocean Research*, vol. 75, pp. 178-192, 2018.
- [10] W. Y. H. Adoni, T. Nahhal, B. Aghezzaf et al., "The Map-Reduce-based approach to improve the shortest path computation in large-scale road networks: the case of A* algorithm," *Journal of Big Data*, vol. 5, no. 1, p. 16, 2018.
- [11] G. E. Mauricio, R. I. Bolaños, and J. W. Escobar, "A meta-heuristic algorithm for the MultiDepot vehicle routing problem with heterogeneous fleet," *International Journal of Industrial Engineering Computations*, vol. 9, no. 4, pp. 461-478, 2018.
- [12] A. D. Vareias, P. P. Repoussis, and C. D. Tarantilis, "Assessing customer service reliability in route planning with self-imposed time windows and stochastic travel times," *Transportation Science*, vol. 53, no. 1, pp. 256-281, 2019.
- [13] H. Hiraishi, "Passenger condition based route-planning for cognitive vehicle system," *International Journal of Software Science and Computational Intelligence*, vol. 10, no. 2, pp. 25-35, 2018.
- [14] Y. Saeed, K. Ahmed, M. Zareei et al., "In-vehicle cognitive route decision using fuzzy modeling and artificial neural network," *IEEE Access*, vol. 7, pp. 20262-20272, 2019.
- [15] G. B. Huang, Q. Y. Zhu, C. K. Siew et al., "Extreme learning machine: theory and applications," *Neurocomputing*, vol. 70, no. 1-3, pp. 489-501, 2006.

Research Article

The Electrical Analogue Computer of Microtubule's Protofilament

M. C. Ekosso ¹, A. J. Fotue,¹ S. C. Kenfack,¹ H. Fotsin,² and L. C. Fai¹

¹Mesoscopic and Multilayers Structures Laboratory, Department of Physics, Faculty of Science, University of Dschang, P.O. Box 479, Dschang, Cameroon

²Laboratory of Electronics and Signal Processing, Department of Physics, Faculty of Science, University of Dschang, P.O. Box 67, Dschang, Cameroon

Correspondence should be addressed to M. C. Ekosso; christekosso@gmail.com

Received 2 July 2020; Revised 6 September 2020; Accepted 13 September 2020; Published 27 September 2020

Academic Editor: Giancarlo Consolo

Copyright © 2020 M. C. Ekosso et al. This is an open access article distributed under the Creative Commons Attribution License, which permits unrestricted use, distribution, and reproduction in any medium, provided the original work is properly cited.

Microtubules as essential biopolymers implicated into electrical intracellular transport open a lot of questions about their intrinsic character of dynamic instability. Both experimental and theoretical investigations are used to understand their behavior in order to mimic and build powerful and smart biomaterials. So, in this paper, by analytical and computational approaches, we proposed an electrical analogue computer of microtubule's protofilament drawing from the partial differential equation which describes microtubule's motion. Using the computing elements, namely, operational amplifiers, capacitors, and resistors, we designed analytically the bioelectronic circuit of the microtubule's protofilament. To validate our model, Runge-Kutta code was used to solve the partial differential equation of MT's motion on software Matlab, and then, the results obtained are used as a controller to fit and validate numerical results obtained by running the bioelectronic circuit on software PSpice. It is shown that the analogue circuit displayed spontaneous electrical activity consistent with self-sustained electrical oscillations. We found out that two behaviors were exhibited by the voltage generated from the electrical analogue computer of MT's protofilament; amplification and damping behaviors are modulated by the values of the resistor of the summing operational amplifier. From our study, it is shown that low values of the resistor promote damping behavior while high values of the resistor promote an amplification behavior. So microtubule's protofilament exhibits different spontaneous regimes leading to different oscillatory modes. This study put forward the possibility to build microtubule's protofilament as a biotransistor.

1. Introduction

At the nanoscale, biological systems displayed electrical activity that cares biological communication via electrical signals [1]. Microtubules (MTs), made up of electrically polar tubulin heterodimer subunits α -tubulin (negatively charged) and β -tubulin (positively charged) monomers forming an electric dipole are essential cellular biopolymers, playing an important role in the intracellular signaling and information processing [2], recognized to participate in eukaryote vesicle trafficking and cell division, implicated in cognitive processing by contributing to neuronal developmental structures such as axons and dendrites [3–5]. MTs contribute to the processing of electrical activity of excitable cells and signals within neuron via ion channel regulation [6–8]. They are the source of electromagnetic fields in the form of electric

pulses [9]. In that way, they are good conductors of electrical signals at nanolevel and are assimilated to cellular automata [10, 11]. Besides, microtubules perform mechanical dynamics revealing vibration characteristics and nanoscale effects on their structure [12–16]. Recently, some research studies summarize the possibility of MTs to application in novel bioinspired nanoelectronic components [17]. In fact, because of their self-organization intrinsic character, through dynamic instability phenomenon modulated by temperature physical control, they facilitate the fabrication of nanowires, nodes, and networks in the future for bionanotechnology applications [18]. The field of nanotechnology applications of biomolecular motors is a young and evolving area of research. While the field has advanced significantly in recent decades, it is fraught with several engineering challenges. Both experimental and theoretical

approaches are used to conduct nanotechnology research on MT. In 2020, Kalra et al. quantified at physiological tubulin concentration the capacitance and resistance of the microtubule network. They reported that through counterionic condensation, microtubules act as charge storage devices across a broad frequency spectrum [19]. Tuszynski et al., by a theoretical basis and experimental support, showed that MTs behave consistently with the definition of a memristor. They provided an estimation of MT memristance and discussed the significance of biology, especially neuroscience, and the potential for nanotechnology applications [20]. In 2006, Priel et al. investigated MT electrodynamic properties. They reported that MTs behave as biomolecular transistors capable of amplifying electrical information [8]. Recently, Gutierrez et al. reported that isolated brain MTs are electrical oscillators that behave as “ionic-based” transistors and amplify electrical signals which may have important implications in neuronal computational capabilities [21]. All the abovementioned studies have been done experimentally. In the theoretical viewpoint, MT’s bioelectronic circuits were first established by Sekulić and Sataric, who was inspired by electrical nonlinear transmission line: RLC circuit [2]. Moreover, Ilić et al. have modelled microtubules as nanowires capable of enhancing ionic transport using a similar approach than Sekulić [22]. In fact, in the theoretical viewpoint, researchers were inspired by a general RLC-cell circuit by considering the values of elements usually estimated experimentally. This consideration is powerful but not sufficient to generate a realistic and unique circuit characterizing the natural MTs. Thus, in this work, we propose an electrical analogue computer of microtubule by drawing from the partial differential equation describing the dynamics of the system. Composed by electrical computing elements such as resistors, capacitors, and operational amplifiers, an electrical analogue computer is an active network capable of simulating any set of linear and non-linear partial differential equations. The voltage waveform generated from the electrical analogue computer is usually encoded into the time evolution, providing powerful computational real-time operation and complete parallelism. What we will do is to compare numerical results obtained from the partial differential equation using Runge–Kutta code to numerical results obtained from the analogue computer simulated on PSpice. The paper is organized as follows: Section 2 gives an overview about computing elements; in Section 3, the analogue computer of MT’s protofilament is presented, Section 4 investigates numerical results on Matlab and PSpice, and Section 5 concludes the study.

2. The Computing Elements

In this section, we summarize the relation between output and input voltages of each computing analogue element that can be useful to design the analogue computer. The relations are derived using the common node laws at the entrance of each operational amplifier (Figure 1).

The principal component in an analogue computer is the operational amplifier. When two impedances Z_i and Z_f are

connected to such an amplifier as shown in Figure 1(a), it can be shown that the input and output voltages to the circuit are related by summing the currents:

$$i_1 + i_2 = 0 \implies \left(\frac{v_i}{Z_i}\right) + \left(\frac{v_o}{Z_f}\right) = 0. \quad (1)$$

The output voltage is given by

$$v_o = -\left(\frac{Z_f}{Z_i}\right)v_i. \quad (2)$$

Thus, the quantity (Z_f/Z_i) acts as an operator on the input voltage v_i to produce the output v_o . When Z_f and Z_i are chosen to be two resistors, the operator simply becomes a multiplying constant and equation (1) takes the following form:

$$v_o = -\left(\frac{R_f}{R_i}\right)v_i. \quad (3)$$

If $R_f = R_i$, the output and the input are inversely related as follows:

$$v_o = -v_i. \quad (4)$$

This type of circuit given in equation (4) is known as the inverting operational amplifier because of the phase inverting property (negative sign) associated with it. Most inverting amplifiers, which are part of the standard computing setup, usually have multiplication constants of 1, 4, and 10. In general, the amplifier may have more than one input port as shown in Figure 1(b). The result is a summing amplifier, whose output v_o is given by

$$v_o = -R_f \left(\frac{v_1}{R_1} + \frac{v_2}{R_2} + \frac{v_3}{R_3} \right). \quad (5)$$

When a capacitor C and a resistor of resistance R_i are connected as shown in Figure 1(c), the output voltage is evaluated as follows:

Assuming $i_1 + i_2 = 0 \implies i_1 = -i_2$

$$i_2 = C \frac{d(v_o - v_-)}{dt} = C \frac{dv_o}{dt}. \quad (6)$$

Knowing that $v_- \rightarrow 0$

$$i_1 = \left(\frac{v_i - v_-}{R_i}\right) = \left(\frac{v_i}{R_i}\right). \quad (7)$$

Using equations (6) and (7), the corresponding node law relation can be written as follows:

$$i_1 + i_2 = \left(\frac{v_i}{R_i}\right) + C \left(\frac{dv_o}{dt}\right) = 0. \quad (8)$$

From equation (8), the output voltage is given by the following expression:

$$v_o = -\left(\frac{1}{R_i C}\right) \int v_i dt. \quad (9)$$

In the case of many input voltages, the output is evaluated by summing all the input currents (Figure 1(d)): $i_1 +$

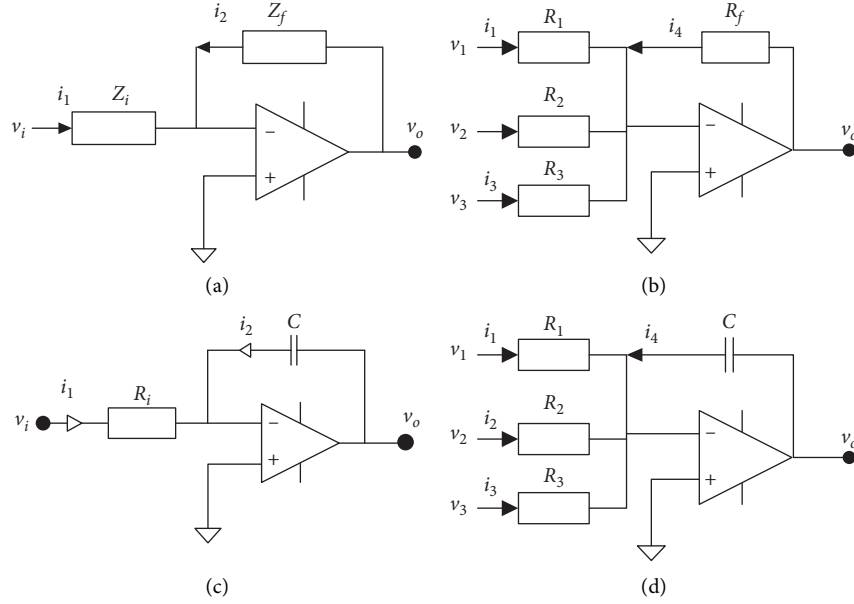


FIGURE 1: Computing elements. (a) High gain dc amplifier with feedback and input impedances, (b) summing amplifier, (c) integrating amplifier, and (d) summing integrating amplifier.

$i_2 + i_3 + i_4 = 0$, with $i_1 = C(dv_o/dt)$, $i_3 = (v_2/R_2)$, $i_2 = (v_1/R_1)$, $i_4 = (v_3/R_3)$

So $C(dv_o/dt) + (v_1/R_1) + (v_2/R_2) + (v_3/R_3) = 0$, the output voltage in this case is expressed as follows:

$$v_o = -\left(\frac{1}{C}\right) \int \left(\left(\frac{v_1}{R_1}\right) + \left(\frac{v_2}{R_2}\right) + \left(\frac{v_3}{R_3}\right) \right) dt. \quad (10)$$

3. Analogue Computer of MT's Protofilament

In this section, the differential equation describing the motion of a protofilament is presented. The time encode equation is then expressed as 2 parametric equations. By using these parametric equations and the suitable computing components summarized above, the electrical analogue circuit is designed. From the designed circuit, the electrical equation of motion is performed and compared to the original differential equation in order to derive the network of resistors necessary to run the circuit on PSpice.

3.1. Differential Equation of Motion. The model assumes only one degree of freedom per dimer, which is common for, more or less, each model describing microtubule dynamics. According to the model, the dimers perform angular oscillations, but the coordinate u is the projection of the top of the dimer on the direction of protofilament and the model can be regarded as the longitudinal one [23, 24]. The general equation describing MT's protofilament motion using Hamilton equations is expressed as follows:

$$\alpha \left(\frac{d^2 \psi}{d\xi^2} \right) - \rho \left(\frac{d\psi}{d\xi} \right) - \beta \psi + \delta \psi^3 - \sigma = 0. \quad (11)$$

By assuming the dimensionless parameters:

$\alpha = ((m\omega^2 - kl^2\kappa^2)/A)$, $\rho = (\gamma\omega/A)$, $\sigma = (qE/A\sqrt{(A/B)})$, and $\beta \approx \delta \rightarrow 1$ in which m is a mass of the dimer, k is an intradimer stiffness parameter, $q > 0$ represents the excess charge within the dipole, $E > 0$ is internal electric field and the integer, A is a constant depending on temperature and B is an arbitrary constant, γ is a viscosity coefficient of the cytosol, and l is a length of a tubulin dimer. Since $\zeta = \kappa X - \omega_0 t$, α measures the competition between the kinetic energy of the tubulin dimer and the potential energy of pertaining chemical bonds [23, 24], ρ is a constant related to viscosity coefficient of the cytosol. Parameters β and δ are arbitrary and related to the nonlinearity of the system. σ characterizes the electrical force, and this parameter was evaluated by Zdravkovic et al. [23, 24]; equation (11) depends on both space and time. But in this study, we shall consider only the temporal variation of the wave function generated during the dynamic instability phenomenon of MT. The spatial term in ξ will be considered invariant. So, the time dependence of the equation of motion is written as follows:

$$\alpha \ddot{x} - \rho \dot{x} - \beta x + \delta x^3 - \sigma = 0. \quad (12)$$

$\tau = \omega_0 t$ and $\dot{x} = (dx/d\tau)$, and x represents the part of the wave function that depends only on time. It is assumed that equations (11) and (12) represent a first approximation of the system with a single degree of freedom related to longitudinal displacement.

Let us proceed by parametric equation by supposing $\dot{x} = y$, equation (12) can be written as a set of 2 equations as follows:

$$\begin{cases} \dot{x} = y, \\ \dot{y} = \left(\frac{\rho}{\alpha}\right)y + \left(\frac{\beta}{\alpha}\right)x - \left(\frac{\delta}{\alpha}\right)x^3 + \left(\frac{\sigma}{\alpha}\right). \end{cases} \quad (13)$$

So,

$$\begin{cases} x = \int y \, d\tau, \\ y = \int \left(\left(\frac{\rho}{\alpha} \right) y + \left(\frac{\beta}{\alpha} \right) x - \left(\frac{\delta}{\alpha} \right) x^3 + \left(\frac{\sigma}{\alpha} \right) \right) d\tau. \end{cases} \quad (14)$$

Using equation (13) and considering the computing elements previously study, we can generate the electrical analog computer that corresponds to MT's protofilament equation of motion over time as shown in Figure 2.

In fact, the procedure used to design the circuit is as follows.

Step 1. The circuit will be built using 2 input voltages corresponding to \dot{x} and \dot{y} . We have to derive the exact corresponding expression of each input voltage using capacitors and resistors. As shown in equation (14), it is suitable to build x and y using integrating amplifier in Figure 1(c) corresponding to equation (9). Let us use equation (9) to evaluate the input voltage as follows:

$v_o = -(1/R_i C) \int v_i dt \rightarrow R_i C v_o = - \int v_i dt$, meaning that $R_i C \dot{v}_o = -v_i$. We have to keep in mind that if we integrate the input \dot{x} by using equation (9), we shall get $-x$ as an output. Thus, the expression $R_i C \dot{v}_o = -v_i$ will be rewritten as follows: $-v_{i_1} = R_1 C_1 (-\dot{x})$ for the first parametric equation and $-v_{i_2} = R_2 C_2 (-\dot{y})$ for the second parametric equation in equation (13) as shown in Figure 2, respectively.

Step 2. By observing the second parametric equation in equation (13), we should generate y , x , x^3 and a constant input V_{CC} corresponding to a last term of the expression. The first term y is built using inverting amplifier of Figure 1(a) with $Z_i = Z_f = R$ to inverse the input $-y$ to the output y as expressed in equation (4). The same procedure is done to get x from $-x$. The input x is then multiplied 3 times to get x^3 as shown in Figure 2.

Step 3. In this stage, we have to connect all the components together with respect to equation (13). From the first parametric equation, the input \dot{x} will be connected to the output y of the second parametric equation. From the second parametric equation of equation (13), we have to sum $-y$, $-x$, x^3 , and $-V_{CC}$ by using summing amplifier of Figure 1(b) where the corresponding expression of the output is given by equation (5). The input $-V_{CC}$ is added such that the summing amplifier is constituted by 4 input voltages corresponding to each term. All terms in the second parametric equation of equation (13) are signed negative except x^3 which is signed positive, as the sign in the formula of equation (5) can suitably be corresponded to the expression of equation (13). R_f in equation (5) corresponds to R' in Figure 2. The output of the summing amplifier is then connected to the input voltage $R_2 C_2 \dot{y}$ to balance the right side to the left side of the second parametric equation of equation (13).

3.2. Derivation of Electrical Equation of Motion. The objective now is to evaluate the corresponding values of each computing component according to MT's parameters (Figure 2). In fact, the electrical equation of vibration of the corresponding circuit of a protofilament is computed by using the inverse procedure.

From Figure 2, we get directly

$$\begin{cases} R_1 C_1 \dot{x}' = y, \\ R_2 C_2 \dot{y}' = -R' \left(\left(\frac{-y}{R_3} \right) - \left(\frac{x}{R_4} \right) + \left(\frac{x^3}{R_5} \right) - \left(\frac{V_{cc}}{R_6} \right) \right), \end{cases} \quad (15)$$

where $\dot{x}' = dx/dt$, and (15) can be rewritten as follows:

$$\begin{cases} \dot{x}' = \frac{1}{R_1 C_1} y, \\ \dot{y}' = \frac{R'}{R_3 R_2 C_2} y + \frac{R'}{R_4 R_2 C_2} x - \frac{R'}{R_5 R_2 C_2} x^3 + \frac{R'}{R_6 R_2 C_2} V_{cc}. \end{cases} \quad (16)$$

As stated earlier, we make the change of time variable as $\tau = \omega_0 t \Rightarrow d\tau = \omega_0 dt$. Equation (16) is then recast to

$$\begin{cases} \omega_{01} \left(\frac{dx}{d\tau} \right) = \omega_{01} \dot{x} = \frac{1}{R_1 C_1} y, \\ \omega_{02} \left(\frac{dy}{d\tau} \right) = \omega_{02} \dot{y} = \left(\frac{R'}{R_3 R_2 C_2} \right) y + \left(\frac{R'}{R_4 R_2 C_2} \right) x \\ - \left(\frac{R'}{R_5 R_2 C_2} \right) x^3 + \left(\frac{R'}{R_6 R_2 C_2} \right) V_{cc}. \end{cases} \quad (17)$$

The final expression can be written as follows:

$$\begin{cases} \dot{x} = \frac{1}{R_1 C_1 \omega_{01}} y, \\ \dot{y} = \left(\frac{R'}{R_3 R_2 C_2 \omega_{02}} \right) y + \left(\frac{R'}{R_4 R_2 C_2 \omega_{02}} \right) x \\ - \left(\frac{R'}{R_5 R_2 C_2 \omega_{02}} \right) x^3 + \left(\frac{R'}{R_6 R_2 C_2 \omega_{02}} \right) V_{cc}. \end{cases} \quad (18)$$

By identifying equation (13) to (18), we can get the following relations:

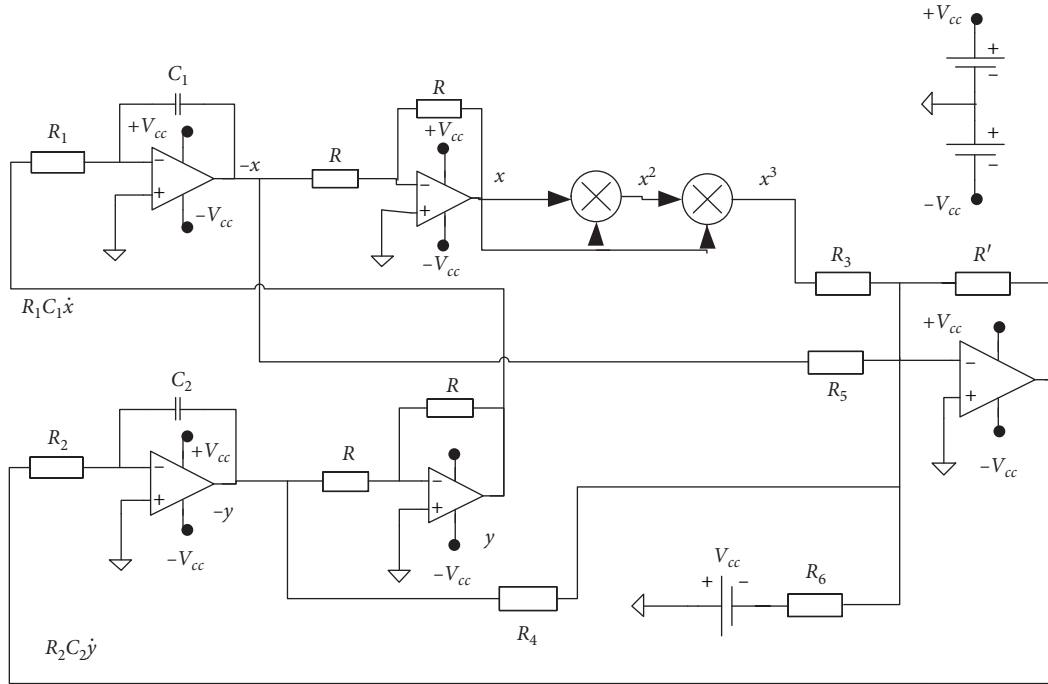


FIGURE 2: Electrical analogue computer of microtubule's protofilament.

$$\left\{ \begin{array}{l} \left(\frac{1}{R_1 C_1 \omega_{01}} \right) = 1, \\ \left(\frac{R'}{R_3 R_2 C_2 \omega_{02}} \right) = \left(\frac{\rho}{\alpha} \right), \\ \left(\frac{R'}{R_4 R_2 C_2 \omega_{02}} \right) = \left(\frac{\beta}{\alpha} \right), \\ \left(\frac{R'}{R_5 R_2 C_2 \omega_{02}} \right) = \left(\frac{\delta}{\alpha} \right), \\ \left(\frac{R'}{R_6 R_2 C_2 \omega_{02}} V_{cc} \right) = \left(\frac{\sigma}{\alpha} \right). \end{array} \right. \Rightarrow \left\{ \begin{array}{l} R_1 = \left(\frac{1}{C_1 \omega_{01}} \right), \\ R_3 = \frac{R'}{R_2 C_2 \omega_{02} * (\rho/\alpha)}, \\ R_4 = \frac{R'}{R_2 C_2 \omega_{02} * (\beta/\alpha)}, \\ R_5 = \frac{R'}{R_2 C_2 \omega_{02} * (\delta/\alpha)}, \\ R_6 = \frac{R' V_{cc}}{R_2 C_2 \omega_{02} * (\sigma/\alpha)}. \end{array} \right. \quad (19)$$

4. Numerical Results

In this section, we have solved the equation of motion numerically using Runge-Kutta code and then run the corresponding circuit on PSpice. The purpose of this procedure is to have an idea about the general behavior of the waveforms propagating along protofilament.

By varying the values of α, ρ, σ at constant parameters β, δ related to the nonlinearity. The following solutions are obtained.

It is observed that the nature of waves depends on the value of α . For low values of α , waves generated are subsonic

waves as shown in Figures 3 and 4. For high values of α , waves generated are supersonic as shown in Figure 5. As previously mentioned, α measures the competition between the kinetic energy and the chemical potential of pertaining bonds. We assume that high values of α mean the highest of kinetic energy in front of chemical potential promotes supersonic behavior while low values of α promote subsonic behavior when the chemical potential of pertaining bonds is higher.

In the case of subsonic behavior (see Figures 3 and 4), it is shown that by increasing the value of α , the wave amplitude increases and oscillations are promoted. Moreover, parameter σ that relates to electric force promotes oscillations as well. As parameter ρ related to cytosol viscosity increases, the signal amplitude decreases over time. Parameters δ and β do not affect the signal amplitude; we consider them equal to 1. So, for subsonic cases, α and σ promote oscillations and increase the signal amplitude. The damping parameter ρ collapses oscillations and promotes a linear and constant signal over time. In the case of supersonic behaviour (see Figure 5), it is observed that the increase in α and σ do not change the signal amplitude, but it is well observed that their increase promotes oscillations, while the increase of parameter ρ collapses oscillations. In this last case, it is observed that the amplification phenomenon can arise infinitely for high values of α and σ and for low values of ρ . This situation is an ideal case and difficult to occur in nature in general and particularly in biological systems. Generally, the switch between amplification and damping behaviors of a signal generated cares the transmission process during the dynamics of biological systems. This allows to balance the energy used and procedure in the system. Besides, each transmitted signal is amplified or

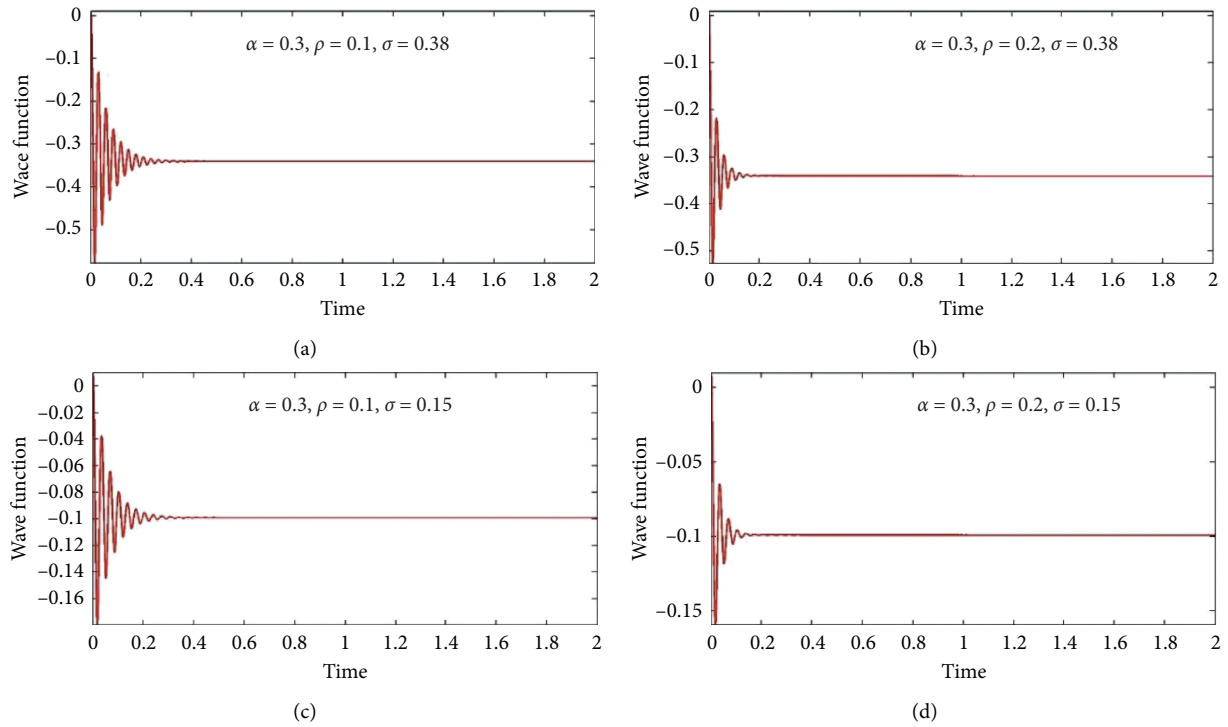


FIGURE 3: Wave function generated from the partial differential equation at low kinetic energy. (a) $\alpha = 0.3, \rho = 0.1, \sigma = 0.38$; (b) $\alpha = 0.3, \rho = 0.2, \sigma = 0.38$; (c) $\alpha = 0.3, \rho = 0.1, \sigma = 0.15$; (d) $\alpha = 0.3, \rho = 0.2, \sigma = 0.15$.

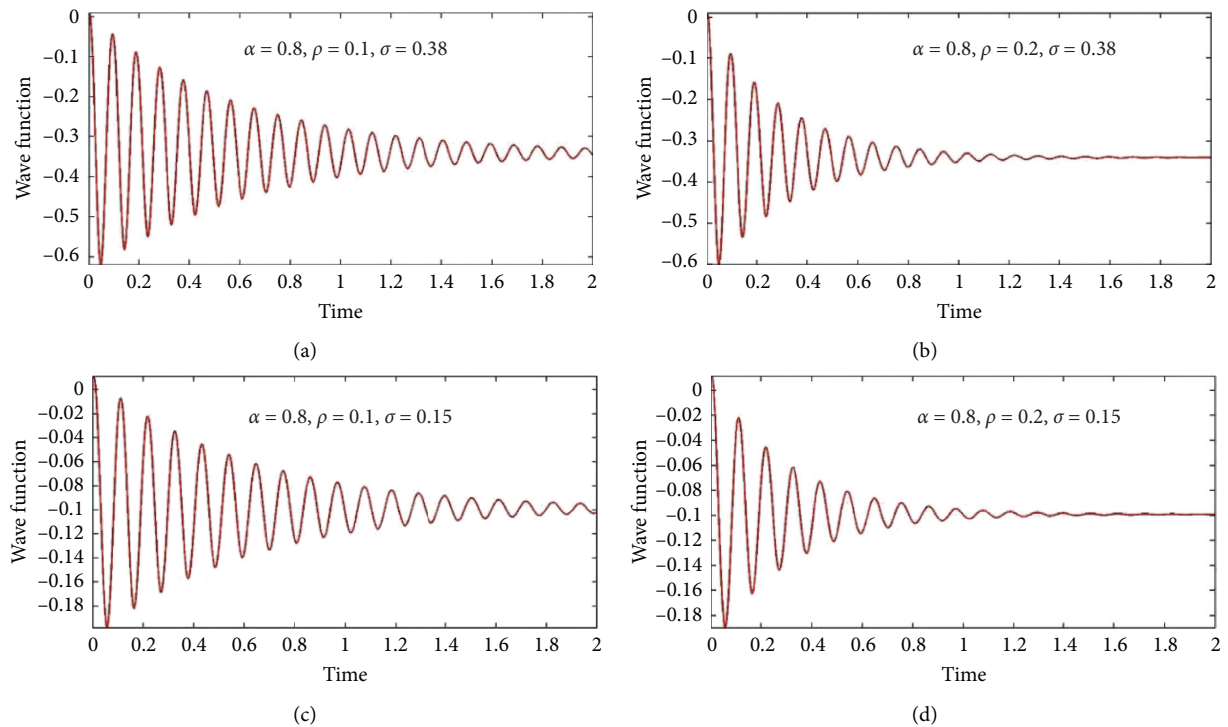


FIGURE 4: Wave function generated from the partial differential equation at high kinetic energy. (a) $\alpha = 0.8, \rho = 0.1, \sigma = 0.38$; (b) $\alpha = 0.8, \rho = 0.2, \sigma = 0.38$; (c) $\alpha = 0.8, \rho = 0.1, \sigma = 0.15$; (d) $\alpha = 0.8, \rho = 0.2, \sigma = 0.15$.

damped for a given time and then usually becomes constant or totally vanishes or switches to an opposite behavior over time. In the case of the dynamic instability of natural

microtubule, we assume that the energy modulating the polymerization/depolymerization cannot care an infinite amplification over time. In fact, the energy produced during

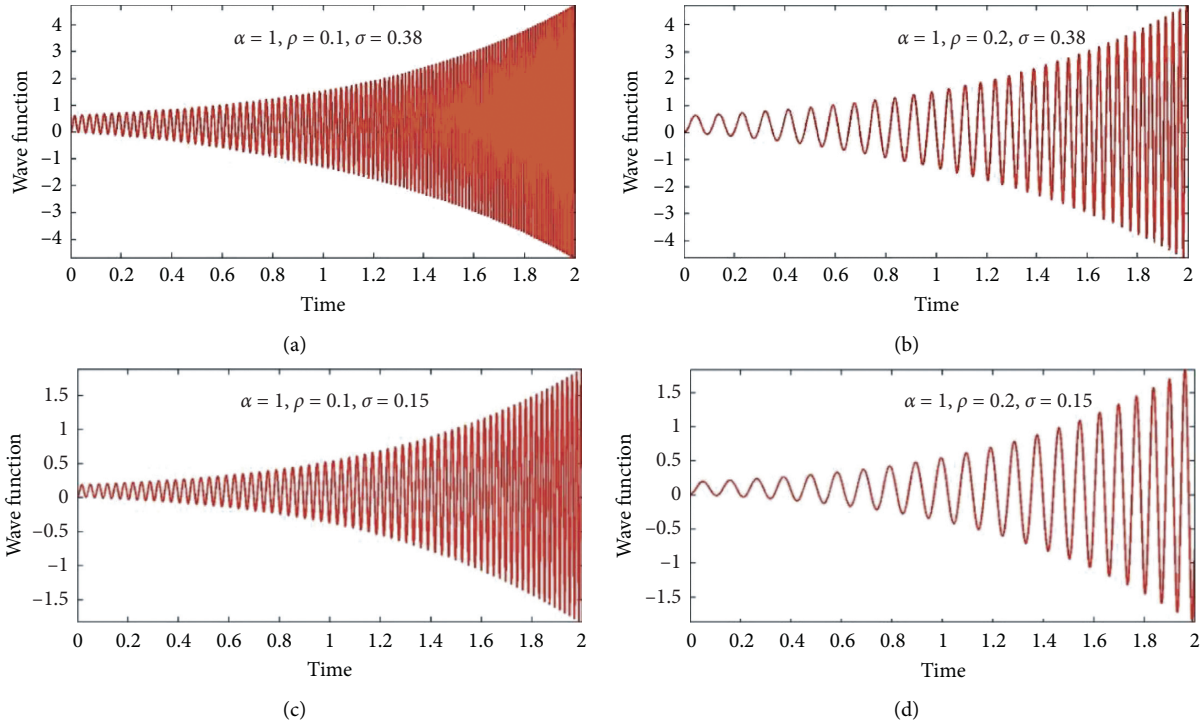


FIGURE 5: Wave function generated from the partial differential equation at very high kinetic energy. (a) $\alpha = 1, \rho = 0.1, \sigma = 0.38$; (b) $\alpha = 1, \rho = 0.2, \sigma = 0.38$; (c) $\alpha = 1, \rho = 0.1, \sigma = 0.15$; (d) $\alpha = 1, \rho = 0.2, \sigma = 0.15$.

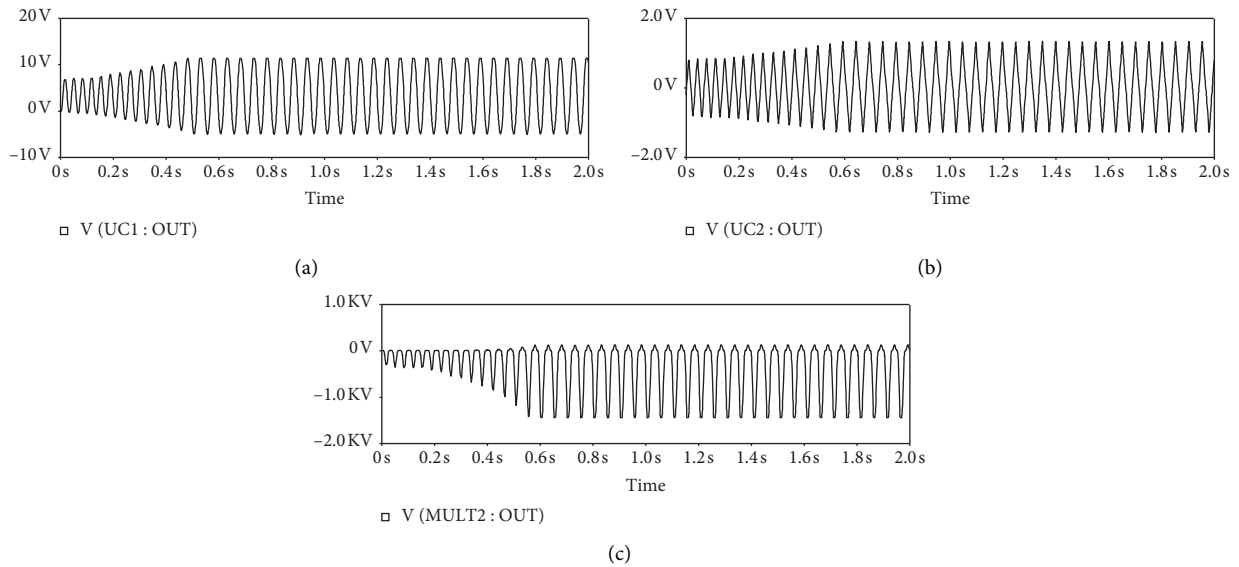


FIGURE 6: Output voltages of (a) amplifier with capacitor C_1 , (b) amplifier with capacitor C_2 , and (c) the nonlinear part x^3 for $R' = 10K\Omega$, $C_1 = 100\text{ nF}$, $C_2 = 10\text{ uF}$, $R = R_1 = R_2 = R_3 = R_5 = 10\text{ K}\Omega$, $V_{cc} = 12\text{ V}$, $R_4 = 5\text{ K}\Omega$, $R_6 = 2.77\text{ K}\Omega$.

the polymerization is used during the depolymerization. During this situation, the energy carried by the waveform moving along protofilament varies constantly and the oscillations generated during the vibration are probably affected. So the chemical energy of pertaining bonds can increase or decrease the kinetic energy as the corresponding parameter α remains low. From the above mentioned, we argue that the real system cannot be designed in the situation

of very high kinetic energy. Thus to run the electrical analogue on PSpice, we will stay in the situation of Figures 3 and 4 and mimic both the amplification and damping behaviors.

Let us run the electrical analogue computer using the software PSpice by considering appropriate values of each parameter as given in Figures 3 and 4. The circuit is run for the case where $\alpha = 0.3, \rho = 0.1, \sigma = 0.38$, but similar curves

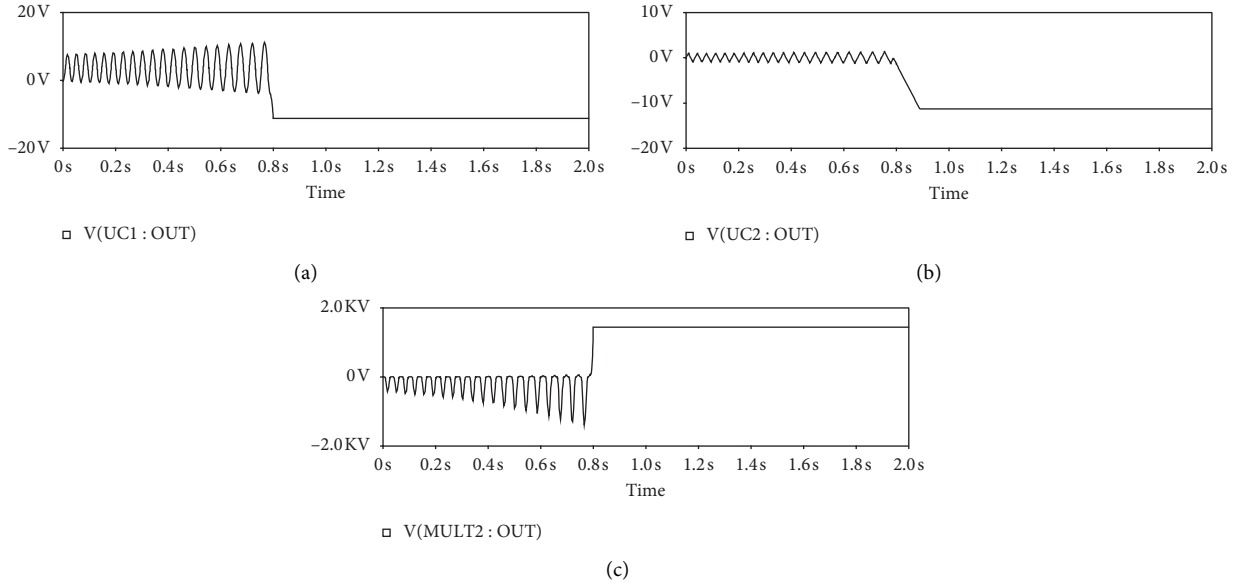


FIGURE 7: Output voltages of (a) amplifier with capacitor C_1 , (b) amplifier with capacitor C_2 , and (c) the nonlinear part x^3 for $R' > 10K\Omega$, $C_1 = 100\text{ nF}$, $C_2 = 10\text{ uF}$, $R = R_1 = R_2 = R_3 = R_5 = 10\text{ K}\Omega$, $V_{cc} = 12\text{ V}$, $R_4 = 5\text{ K}\Omega$, $R_6 = 2.77\text{ K}\Omega$.

are obtained by using values of α less than 1 and $\sigma < \sigma_{\max} = (2/3\sqrt{3})$. These values of parameters are reported in [23, 24] and were evaluated within the situation of a favorable configuration that promotes information processing during the dynamic instability.

By varying resistances, we will try to mimic amplifying or damping behaviors from the electrical signal. For the following simulation values $C_1 = 100\text{ nF}$, $C_2 = 10\text{ uF}$, $R = 10\text{ K}\Omega$ chosen, the signal generated will be convergent. Other values can be used. By fixing these parameters, we use equation (19) to compute other resistances useful for our simulations. The lecturer needs to keep in mind that for each value of R' , he has to evaluate the corresponding network of resistances.

Numerical results previously obtained from MATLAB (Figures 3–5) are used as a controller to find suitable values of resistors. Suitable values of MT parameters are chosen as the electrical analog computer can mimic the behaviour generated by Runge–Kutta code. Voltage is measured at the output of memory computing elements (amplifiers) and the output of the nonlinear proportion x^3 . The increase or decrease behaviour of the output voltage of the electrical analogue computer is modulated by the values of R' .

For $R' = 10\text{ K}\Omega$ as shown in Figure 6, the output voltages exhibit an increasing behaviour and maintain the same amplitude over time. In Figure 6, spontaneous oscillations showed changes in signal's regime and amplitude, namely, amplification regime where signal's amplitude increases with time from 0 s to 0.6 s and constant regime where signal's amplitude remains constant over time (from 0.6 s to 2 s). These results showed the ability of a single microtubule's protofilament to handle amplification of electrical activity and self-controlled the amplification by maintaining the behaviour constant over time. This situation puts forward realistic behaviour of the physical system as previously

mentioned. Spontaneous changes are well observed in signal's amplitude, suggesting that intracellular electrical signaling may heavily obey to the assembly and organization of the various cytoskeletal structures over time [21]. For $R' > 10\text{ K}\Omega$ as shown in Figure 7, the oscillations collapse over time and the output voltages become linear. In fact, by increasing the value of R' up to $10\text{ K}\Omega$, the output voltages also exhibit two regimes: spontaneous amplification of oscillations from 0 s until 0.8 s with a clear change in the signal's amplitude and then a constant and linear response from 0.8 s until 2 s. These changes in regime and amplitude can suggest changes in polarity of the holding potential and conductance as reported by Gutierrez et al. [21] in the case of isolated microtubule.

By decreasing the value R' as $R' \leq 1\text{ K}\Omega$ (Figures 8 and 9), the output voltages exhibit a decreasing behaviour of the oscillation amplitude over time, without becoming linear similar to the behaviour shown in Figures 3 and 4). Results obtained in Figures 8 and 9 are similar to those obtained by Gutierrez et al. [21]. By decreasing the values of R_3 and R_5 as shown in Figure 9, the same behaviour as in Figure 8 is obtained. In general, the behavior of the output voltages depends on the values taken by R' . For $R' \in]1\text{ K}\Omega - 10\text{ K}\Omega[$, the same output voltages as in Figure 6 are generated. According to the results obtained, it is observed that low values of resistance R' act as damping parameter but care oscillations over time while high values of resistance R' act as amplifier parameter but maintain the amplitude of output constant by increasing time. For these cases, it is also observed that the signal exhibits approximately two regimes as previously (Figure 6). However, an interesting difference became evident, namely, that the richer oscillatory behavior drastically changed to damping one and sustained spontaneous stronger oscillations over time. In fact, it is a well-observed fast spontaneous damping regime, followed by smoothly damping regime over time (Figures 8

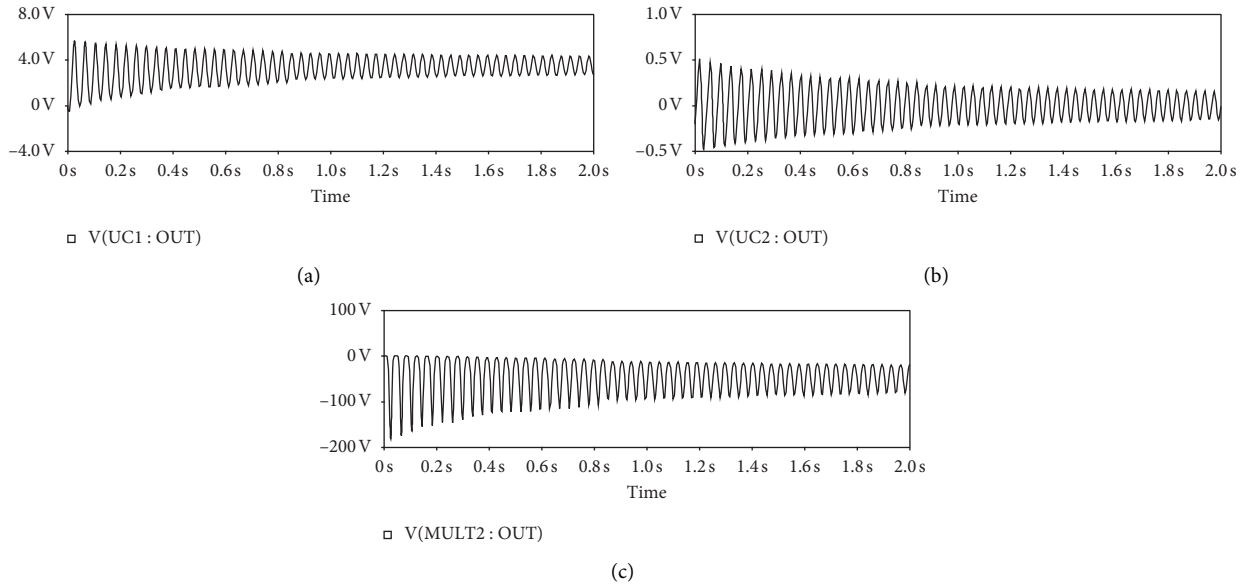


FIGURE 8: Output voltages of (a) amplifier with capacitor C_1 , (b) amplifier with capacitor C_2 , and (c) the nonlinear part x^3 for $R' \leq 1K\Omega$, $C_1 = 100\text{ nF}$, $C_2 = 10\text{ uF}$, $R = R_1 = R_2 = R_3 = R_5 = 10\text{ K}\Omega$, $V_{cc} = 12\text{ V}$, $R_4 = 5\text{ K}\Omega$, $R_6 = 2.77\text{ K}\Omega$.

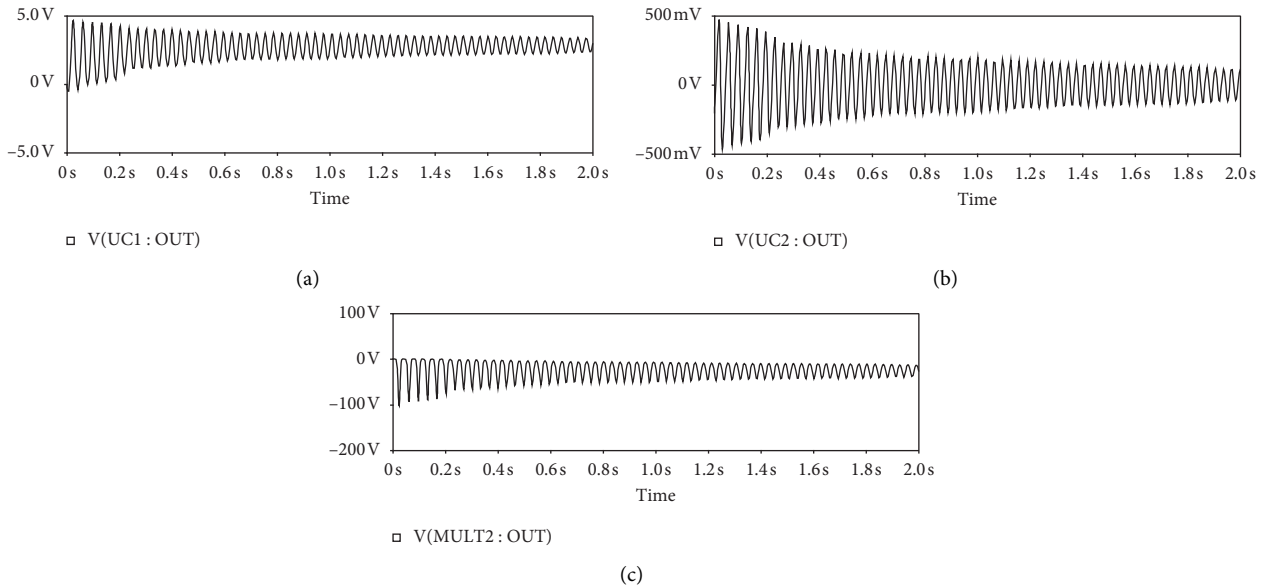


FIGURE 9: Output voltages of (a) amplifier with capacitor C_1 , (b) amplifier with capacitor C_2 , and (c) the nonlinear part x^3 for $R' \leq 1\text{ K}\Omega$, $C_1 = 100\text{ nF}$, $C_2 = 10\text{ uF}$, $R = R_1 = R_2 = 10\text{ K}\Omega$, $V_{cc} = 12\text{ V}$, $R_4 = 5\text{ K}\Omega$, $R_6 = 2.77\text{ K}\Omega$, $R_3 = R_5 = 5\text{ K}\Omega$.

and 9). In these environmental conditions, electrical oscillations are cared over time. But the signal's amplitude decreases continuously.

Other simulations have been carried out by varying resistors' values of R_4 and R_6 . In general, the same behavior is obtained, So the behavior of the output voltages depends on the values of R' . Results obtained from numerical investigations put forward spontaneous electrical activity consistent with self-sustained electrical oscillations during the dynamics of the microtubule's protofilament.

5. Conclusion

In this work, we tantalized to build an electrical analogue computer of MT's protofilament drawing from the partial differential equation of MT's motion. By using the suitable values of MT's parameters, we have been able to find suitable values of computing elements. Numerical results have shown that the behaviour of the output voltage generated by the electrical analogue computer is modulated by the resistance R' . High values of R' promote increase in the behavior of the signal that can become linear for very high

values of R' while low values of R' promote decrease in the behavior of the electrical voltage and care the oscillation over time. To build a more realistic analogue computer, one needs to use the exact values of MT parameters to derive the suitable computing elements. The behaviour of the output voltage obtained for $R' \leq 1 K\Omega$ is similar to the results obtained by experimental studies. This study put forward the electrical activity of microtubule protofilament by electrical oscillations occurring at different regimes with amplitude changes as mechanism for intracellular signaling and communications inside neurons. So designing microtubule as an electrical analogue computer can be useful to better understand the dynamics of the entire system and to build new biological nanowires and biotransistors.

Data Availability

No data were used to support this study.

Conflicts of Interest

The authors declare that they have no conflicts of interest.

References

- [1] J. Zimmerman, R. Parameswaran, and B. Tian, "Nanoscale semiconductor devices as new biomaterials," *Biomaterial Science*, vol. 2, no. 5, pp. 619–626, 2014.
- [2] D. Sekulić and M. Satarić, "Microtubule as nanobioelectronic nonlinear circuit," *Serbian Journal of Electrical Engineering*, vol. 9, no. 1, pp. 107–119, 2012.
- [3] C. Conde and A. Cáceres, "Microtubule assembly, organization and dynamics in axons and dendrites," *Nature Reviews Neuroscience*, vol. 10, no. 5, pp. 319–332, 2009.
- [4] M. Stiess and F. Bradke, "Neuronal polarization: The cytoskeleton leads the way," *Developmental Neurobiology*, vol. 71, no. 6, pp. 430–444, 2011.
- [5] A. Priel, A. J. Ramos, J. A. Tuszynski, and H. F. Cantiello, "The dendritic cytoskeleton as a computational device: An hypothesis," "The dendritic cytoskeleton as a computational device: An hypothesis," in *The Emerging Physics of Consciousness*, J. A. Tuszynski, Ed., Springer, Berlin, Germany, pp. 293–325, 2006.
- [6] B. D. Johnson and L. Byerly, "Ca²⁺ channel Ca(2⁺)-dependent inactivation in a mammalian central neuron involves the cytoskeleton," *Pflügers Archiv European Journal of Physiology*, vol. 429, no. 1, pp. 14–21, 1994.
- [7] D. Johnston, J. C. Magee, C. M. Colbert, and B. R. Christie, "Active properties of neuronal dendrites," "Active properties of neuronal dendrites," in *The Structure and Function of Nervous Tissue*, G. H. Bourne, Ed., pp. 205–267, Academic Press, Cambridge, MA, USA, 1996.
- [8] A. Priel, A. J. Ramos, J. A. Tuszynski, and H. F. Cantiello, "A biopolymer transistor: Electrical amplification by microtubules," *Biophysical Journal*, vol. 90, no. 12, pp. 4639–4643, 2006.
- [9] D. Havelka, M. Cifra, and O. Kučera, "Multi-mode electro-mechanical vibrations of a microtubule: In silico demonstration of electric pulse moving along a microtubule," *Applied Physics Letters*, vol. 104, no. 24, pp. 1–4, Article ID 243702, 2014.
- [10] J. Pokorný, J. Pokorný, and J. Kobilková, "Postulates on electromagnetic activity in biological systems and cancer," *Integrative Biology*, vol. 5, no. 12, pp. 1439–1446, 2013.
- [11] S. R. Hameroff and R. Penrose, "Orchestrated reduction of quantum coherence in brain microtubules," "Orchestrated reduction of quantum coherence in brain microtubules," in *Toward a Science of Consciousness*, S. Hameroff, A. K. Kaszaniak, and A. C. Scott, Eds., MIT Press, Cambridge, MA, USA, 1996.
- [12] F. Daneshmand, E. Ghavanloo, and M. Amabili, "Wave propagation in protein microtubules modeled as orthotropic elastic shells including transverse shear deformations," *Journal of Biomechanics*, vol. 44, no. 10, pp. 1960–1966, 2011.
- [13] F. Daneshmand, H. Farokhi, and M. Amabili, "A higher-order mathematical modeling for dynamic behavior of protein microtubule shell structures including shear deformation and small-scale effects," *Mathematical Biosciences*, vol. 252, pp. 67–82, 2014.
- [14] F. Daneshmand and M. Amabili, "Coupled oscillations of a protein microtubule immersed in cytoplasm: An orthotropic elastic shell modeling," *Journal of Biological Physics*, vol. 38, no. 3, pp. 429–448, 2012.
- [15] E. Ghavanloo, F. Daneshmand, and M. Amabili, "Vibration analysis of a single microtubule surrounded by cytoplasm," *Physica E: Low-Dimensional Systems and Nanostructures*, vol. 43, no. 1, pp. 192–198, 2010.
- [16] E. Ghavanloo, F. Daneshmand, and M. Amabili, "Prediction of bending stiffness and deformed shape of non-axially compressed microtubule by a semi-analytical approach," *Journal of Biological Physics*, vol. 36, no. 4, pp. 427–435, 2010.
- [17] S. Sahu, S. Ghosh, K. Hirata, D. Fujita, and A. Bandyopadhyay, "Multi-level memory-switching properties of a single brain microtubule," *Applied Physics Letters*, vol. 102, pp. 1–4, Article ID 123701, 2013.
- [18] J. A. Tuszynski, T. J. A. Craddock, and E. J. Carpenter, "Bio-ferroelectricity at the nanoscale," *Journal of Computational and Theoretical Nanoscience*, vol. 5, no. 10, pp. 2022–2032, 2008.
- [19] A. P. Kalra, S. D. Patel, A. F. Bhuiyan et al., "Investigation of the electrical properties of microtubule ensembles under cell-like conditions," *Nanomaterials*, vol. 10, no. 2, p. 265, 2020.
- [20] J. A. Tuszynski, D. Friesen, H. Freedman et al., "Microtubules as sub-cellular memristors," *Scientific Reports*, vol. 10, no. 1, pp. 1–11, 2020.
- [21] B. C. Gutierrez, H. F. Cantiello, and M. del Rocío Cantero, "Electrical oscillations of brain microtubules," *Biology*, 2020.
- [22] D. I. Ilić, M. V. Satarić, and N. Ralević, "Microtubule as a transmission line for ionic currents," *Chinese Physics Letters*, vol. 26, no. 7, Article ID 073101, 2009.
- [23] S. Zdravković, L. Kavitha, M. V. Sataric, S. Zekovic, and J. Petrović, "Modified extended tanh-function method and nonlinear dynamics of microtubules," *Chaos, Solitons & Fractals*, vol. 45, no. 11, pp. 1378–1386, 2012.
- [24] S. Zdravkovic, M. V. Sataric, A. Maluckov, and A. Balaz, "A nonlinear model of the dynamics of radial dislocations in microtubules," *Applied Mathematics and Computation*, vol. 237, no. 15, pp. 227–237, 2014.

Research Article

Investigating the Mediation and Moderation Effect of Students' Addiction to Virtual Reality Games: A Perspective of Structural Equation Modeling

Xuesong Zhai,¹ Fahad Asmi,² Rongting Zhou,² Intikhab Ahmad ²,
Muhammad Azfar Anwar,² Saba Saneinia,² and Man Li³

¹College of Education, Zhejiang University, Hangzhou, China

²Department Science and Technology Communication and Policy, University of Science and Technology of China, Hefei, China

³Hefei Institute of Adolescent Psychology, Hefei, China

Correspondence should be addressed to Intikhab Ahmad; intikhabahmad@mail.ustc.edu.cn

Received 28 July 2020; Revised 23 August 2020; Accepted 4 September 2020; Published 24 September 2020

Academic Editor: Shaohui Wang

Copyright © 2020 Xuesong Zhai et al. This is an open access article distributed under the Creative Commons Attribution License, which permits unrestricted use, distribution, and reproduction in any medium, provided the original work is properly cited.

Virtual reality (VR) games construct an immersive context for the youth's entertainment and learning. VR game addiction (VAD) occurs simultaneously and brings about psychological issues. The current research employed a maximum likelihood estimation method to construct a structural equation model, by which learners' VR consumption behaviors were examined. The bootstrapping approach was adopted to explore further the mediation of VR realism (VRR) and the moderation of VR affordance on learners' VAD, which potentially leads to distressing behavioral and psychological circumstances. Data were collected from 575 students recruited in the survey, which was followed by a test of reliability and validity through confirmative factor analysis. Results concluded that VRR and consumers' cognitive satisfaction played a significant role as mediators while conceptualizing addictive behavior based on VR-perceived experience of consumers, self-efficacy, and interactivity. Moreover, this study conceptualized addictive behavior toward VR games through a structural equation model in a media-rich environment and suggested practical implications to reduce addictive behavior.

1. Introduction

Virtual reality (VR) refers to the gadget that simulates interactive virtual settings in a 3D image, which offers an immersive environment than another display screen (i.e., desktop, television, or mobile phone). Previous studies have illuminated that VR brought about various benefits in gaming. For example, it provides opportunities to socialize with other players online. Some users prefer to experience various emotions in VR games to satisfy their psychological needs, whereas others aim to pass the time or escape reality for the time being [1]. Students are a dominant group in VR games, and many researchers have begun to investigate the use of VR games in enhancing learners' fulfillment in the educational domain. VR games provide virtual conditions, where people could improve

their skills that could be positively used in real life. For example, memory games are used to improve cognitive abilities, and adventure games help people cope with qualms [2].

However, the use of VR games may have a negative influence on learners' relationships with their family, education, and social life and may lead to VAD. To quantify the addictive behavior of VR game users, the current study, which is based on the cognitive-behavioral framework, employed structural equation modeling (SEM) to construct a holistic model that reflects the driving mechanism leading to VAD. The structural equation is a reliable modeling approach to explain the relationship between variables and latent constructs systematically. To evaluate the model fitness and path coefficient of the proposed model, this study employed a maximum likelihood estimation (MLE) to

estimate the parameters of a probability distribution by maximizing a likelihood function.

2. Literature Review on VR Addiction

Information technology (IT) has become an essential part of modern society, and its application ranges from education to entertainment and even health. Life is becoming more manageable with IT; however, research has indicated various severe concerns about this exposure (e.g., IT addiction and stress) [3]. Similarly, some studies on technology addiction have discussed that addictions have different types. Specifically, Internet-addicted users are keen toward porn, gambling, and e-gaming addiction. Some researchers have argued that addiction can also have positive effects [4]. Researchers still disagree on definitions. The American Society for Addiction Medicine defines addiction as a primary, acute illness of brain reward, consciousness, and associated circuitry. Moreover, addiction is defined as the incapacity to abstain constantly, the impairment of cognitive command, and the reduced awareness and dysfunctional reaction to important cognitive issues and interpersonal relations [5]. Addiction is a progressive disability and results in premature death without treatment or rehabilitation. A research review identified the four most frequently studied types of IT addiction, namely, Internet addiction, gambling disorder, smartphone addiction, and social network addiction. These types of IT addiction share some common symptoms but also have some unique features [6].

Studies have discussed that Internet addiction and FBA are interconnected. Facebook is widely used in SNS research. Facebook claimed to have 2414 million active users per month [7]. Moreover, the Pew Research Center's Internet and American Life Program describes technology use as essential to everyday life, particularly for teenagers and adults who use smart phones [8]. College-aged students are more attached to and reliant on smartphones; according to a Pew research survey, 94% of young people aged 18–24 years have smartphones [9]. Gökçeşlan et al. [10] stated that frequently using smartphones is an indication of addiction to smartphones. Smartphone addiction leads to serious health issues for young people. Researchers have further argued that young people have nomophobia, which is the fear of being without smartphones [11]. Similarly, online game addiction (OGA) is considered the most critical issue in public health among other related fields. Game addiction is defined as prolonged gaming that leads to behavioral symptoms, including the loss of self-control. Moreover, Internet gaming disorder (IGD) is now included in DMS-5 and ICD-II, but the addiction debate continues. DSM-5 identified addicts of digital games as “gamers” who compulsively play Internet games and exclude other activities, which may lead to psychosocial impairment or stress. Previous studies have used the time spent playing as a gaming disorder indicator, but research still needs to determine whether both are the same or considered similar [12]. Studies have identified that adolescents who are addicted to games have a negative relationship with their parents, feel insecure in their society, and spend more time

with online friends, and all of which are problematic in real life [13]. Therefore, researchers have argued that users addicted to Internet games are aggressive and have disorders, such as insomnia, anxiety, and vision syndrome. Internet game users are loyal. VR technology maybe useful, but its excessive use may influence addictive behavior. Moreover, VR technology has been used for treatment and in learning environments in the beginning, but researchers believe that consumers' access to VR has a negative impact on their behavior [14]. Considering previous research, the present study finds no statistical evidence that has used VR and e-games together. The VR gaming industry is growing slowly because of the cost of the required equipment and the few games on the market. Furthermore, researchers believe that the decreasing prices of VR headsets and software may lead consumers toward pornography and VR game addiction (VAD) [15]. Moreover, previous papers have mainly focused on other ICT addictions, such as SNS, games, and online gambling, as mentioned in Appendix A (Supplementary Materials). The present study helps to enrich the current literature on the dark aspect of VR, specifically VAD.

3. Theoretical Framework

VR research studies are ongoing in different fields, including architectural [16], medical [17, 18], and education [19] fields, because of the development in VR technologies and the rise of the VR industry. The technology acceptance model (TAM) was the paradigm most narrowly tailored to illustrate customers' expectations and interventions about devices [20]. VR technology was used in different experiments by incorporating external influences [21]. Technology acceptance theories primarily focus on benefits and overlook the critical assessments of consumer's potential risks [22, 23]. These include TAM2 [24], UTAUT [25], and UTAUT2 [26], which demonstrate the development of technical adaptation models over time. Nevertheless, none of the technology-related behavioral models was suitable to underline the dark side of technological progress. The present study proposed that high media richness appreciates the user's VR addictive nature to games. In conceptual terms, technological attributes (i.e., VR interactivity (VRI), self-efficacy, and realism) and cognitive attributes (e.g., perceived experience and satisfaction) map the distal and proximal factor spectrum. Previous studies have identified the cognitive-behavioral framework of the problematic use of IT and the combined results of distal and proximal causes. The cognitive-behavioral framework emphasizes thoughts as a significant cause of unusual behavior [27] but is unable to affect problematic use directly as opposed to proximal factors, which are the main attribute of distal causes to factors that contribute significantly to the problematic use of IT [28]. The present study proposed that high media richness increases individuals' game addiction. In other words, it urges irresistible desire [29] and related emotion, which can be mapped in terms of cognitive-behavior modeling [30]. Thus, this study adopted a cognitive-behavioral framework, which identified problematic Internet usage with the combined results of distal and proximal causes. Distal causes

emphasize the factors that indirectly activate addiction [28], whereas proximal causes directly contribute to developing VAD. This paradigm is widely used for different types of behavioral addictions [30], such as game addiction [31]. The cognitive-behavioral model provides a logical basis to explain emotional dependence [32]. Thus, this study assumed and attempted to verify that the cognitive-behavioral framework is exceptionally suitable to map VAD.

For distal cause, the constructs of perceived quality (PQ), VR self-efficacy (VSE), and VRI are considered absolute terms to define the scale of VAD. Hwang and Kim [33] referred to a positive association between brand usage and user experience, which is linked with the users' PQ. Moreover, a service's PQ and technology advancement with brand extension have optimistic domination over the user's satisfaction, willingness to use, purchase of the game, and purchase of additional offers by the provider. Bandura [34] derived self-efficacy from social cognitive theory; furthermore, several studies have argued that self-efficacy could be defined as the individuals' confidence level and ability to tackle unambiguous behavior [35]. Moreover, self-efficacy has beneficial and bleak effects on gamers' behavior, depending on their personality [36]. Specifically, VSE is used as a unique contribution to the current context. The authors assumed VSE as a game player's level of understanding and access to equipment and interfaces with VR games. Thus, VSE is assumed to be one of the most important factors to define VAD. VRI is a state where users participate and modify in real-time. Previous studies have argued that interactivity contributes to VAD and impacts an individual's cognitive growth and social routine [37, 38].

Proximal causes emphasize constructs that hold a direct effect on consumers' game addiction. First, this study considers VR realism (VRR), which is followed by consumers' cognitive satisfaction. Proximal causes directly contribute to game addiction as a behavioral outcome. VRR has a significant contribution to VAD. Previous studies have argued that the actual purpose of VR is to enhance realism such that players can experience and enjoy the game better. Formulators should concentrate on many particular aspects, particularly realism, to attract users [39]. Moreover, studies have argued that realism and the feeling of presence could affect users' emotions, which can negatively and positively affect their attitude [40]. The present study did not find any studies that argued or discussed possible factors related to VRR and game addiction having inter-related connections. Thus, the authors assumed that VRR is one of the most important factors to measure the addictive behavior of the game players, particularly VR game players in the modern era. Moreover, studies have argued that access to related resources encourages individuals' sense of satisfaction. Positive and negative satisfaction can be created with unbiased dimensions of psychosomatic requirements [41]. Moreover, evidence shows that satisfaction and dissatisfaction explain significant factors in IGD [41]. Wu et al. [42] conducted a study in China, concluded that satisfaction is significantly negatively associated with problematic video game playing and argued that competence satisfaction and autonomy show indirect effects on game users' life [43].

Therefore, VR cognitive satisfaction (VCS) is the proximal cause of VR-based EPC addiction. Becker and Murphy [44] stated that addiction rationality applies to a coherent strategy of balanced expectations for the anticipation of future decisions and the maximization of use over time. In the context of VAD, the authors hypothesized PQ, VSE, and VRI as distal causes that further lead to VRR and VCS as proximal causes of VAD in society.

A new study project adopted virtual realism as VR technology and VCS as the neurological component of proximal triggers for individuals with gaming addiction. VRR is a state where users realistically feel the environment. The VR project perfectly simulates virtual realism besides technological advancement because it guarantees valid knowledge about the scenario [45]. Users tend to play VR games because of their rich environment and realism. VRR has an immersive environment, where an individual feels a customized and personal experience. In this context, VRR can be proposed as a proximal cause while mapping VAD. In comparison, the literature suggests a feeling of satisfaction with exposure to the games concerned, and this feeling may contribute to addictive behavior. Moreover, players always give positive feedback to express their satisfaction in playing video games [46]. Thus, the authors conclude that VRR and VCS can be captioned as the proximal causes of VR-based EPC addiction.

3.1. Distal Causes (*Excitement, Interactivity, and Efficacy*).

Zeithaml [47] stated that perceived experience excitement (PEX) is "the customer measure of product/service perfection or dominance." Bitner and Hubbert [48] described it as "the general impression of the customer of an institution and its services' relative dominance or inferiority." Hwang and Kim [33] propose that a positive association between brand usage and user experience is linked with users' PEX. Moreover, services' PEX and technology advancement with brand extension have been observed to positively influence users' satisfaction, willingness to use, purchase of the game, and purchase of the additional offers by the provider [49]. In the last few decades, the widespread use of Internet and web technologies and the implications for every aspect of society have led to the technological revolution. The literature contains full accounts on the web technology integration of organizations of various types and sizes. Experience is not a new concept in IT. Practitioners of information systems have always known the necessity to improve the functioning of information systems to react to external and internal pressures and meet critical problems for its growth and survival. Consumer fidelity for Internet games is difficult and expensive [4] and requires a consumer-friendly service to experience excitement. Numerous surveys have found that the increased perception of customer service and excitement results in increased profitability (satisfaction) [50]. Studies have suggested that PEX is an essential part of a store's image and can influence the behavior of gamers in the new electronic environment. Increasing the level of realism is important to generate more excitement [51]. Slater et al. [52] stated that VRR causes a high level of presence and produces

excitement in users. No study has used excitement with VRR. Thus, the present study proposed the following hypotheses:

H1: Perceived VR experience excitement holds a significant effect on the proximal causes (VRR and VSC) of VAD.

Bandura's [53] personal cognitive philosophy revolves around the concept of self-efficacy. Self-effectiveness refers to an evaluation of people's ability to develop and execute action courses needed to achieve success [34]. It is unique to the area and significantly linked to behavior. Self-effectiveness is about the skills and having the trust to use those skills [54]. Psychological literature shows that self-confidence or self-control and self-efficacy are individual resources [55]. Compared with other personal psychosomatic factors (i.e., self-esteem), self-efficacy encourages the self-appreciation of persons for their capability to perform a given task and accomplish a particular purpose. The authors identified different areas of self-efficiency on this theoretical basis. Self-efficiency in several areas, such as learning [56], worker behavior [57], user responses [58], and video gaming [59], has been examined and validated. In the self-efficiency literature, different technologies were explored, such as the self-efficacy of the computer or the Internet [60]. However, the study has seldom examined the self-efficacy of the video game or online shopping sector. The only study conducted by Ketelhut [59] analyzed the scope of self-efficacy with video games by incorporating self-effectiveness while playing video games. Some studies have used general self-efficacy and personality with games [61]. Moreover, self-efficacy rises to favorable feelings (satisfaction) when computers are experienced and used and is only possible with the trust of users [62]; VR HDM provides a sense of realism [63], where users' self-efficacy pushes them to use VR. Similarly, no research has discussed the use of VSE with VAD. Therefore, the authors assumed that VSE is the most crucial factor in VAD. On the basis of the above arguments, the present study proposed the following hypothesis.

H2: VSE holds significant effects on the proximal causes (VRR and VSC) of VAD.

Consumers participate in a virtual environment for fun, socialization, and interactivity [64]. Therefore, brands create products that allow consumers to be highly involved and have the meaning of using VR gadgets. Studies have found that users lose the sense of experience and interactivity in online shopping. Similarly, the degree of interactivity may affect the sense of telepresence. Bogost [65] argued that the interactivity of the game could give users a top scale of experience and enjoyment (satisfaction). Juul [66] illustrated Doom II and stated the difficulty to find the expanse between story-time, narrative-time, and viewing-time. Moreover, he argued that the narration of the game and interactivity cannot be felt at the same time.

Furthermore, interactivity allows users to decorate themselves according to their preference. Belk [67] argued that users believe that the avatar should be like the users. Interactivity also allows users to make their indent in the virtual world according to their preference. Realism in the virtual world makes users more interactive in a realistic manner through their own created and specially designed avatar. In addition, interactivity increases user satisfaction, but their satisfaction decreases because they do not gain new adventures in games. The authors assume that VRI is one of the essential factors for adopting addictive behavior, specifically in VAD. Therefore, the present study proposed the following hypothesis.

H3: VRI holds significant effects on the proximal causes (VRR and VSC) of VAD.

3.2. Proximal Causes (Realism and Cognitive Satisfaction).

The social scientist Murphy [68] performed a comprehensive literary analysis of VR to confirm and expand the "common-sense assertion that VR" feels true "rather than conventional screen-based games." Realism is with an essential concept within the artistic culture and is plausibly seen as more practical than others for some aesthetic technologies and forms, including VR. Realism is also of significant interest to art theorists, even if it has always contributed to conflict and discussion. The real main question is whether specific media models are more realistic than others and, if so, what this realism is. Chalmers [69] disputed that VR entity can be considered to include fantasy when an imaginary environment, artifacts, or characters are portrayed at any point by certain VR events. The most crucial purpose for the representation of the literature is to use VR in video games. Moreover, other situations use VR to mediate a nonfictional experience with real things in the real world. Disney's work on ball capturing in virtual worlds is one event. Robson and Tavinor [70] insisted that the ball-grabbing case may be described as "aggressive reality" if an encounter with a simulated cannibal is deemed to be "true fictionality." Moreover, studies have suggested that VR can create a highly realistic environment that can negatively impact users' addictive behavior [71]. Therefore, the authors assume that VRR is one of the most important and significant factors and leads users toward addictive behavior. Thus, the present study proposed the following hypotheses:

H4: VRR positively influences VAD.

Oliver [72] pointed out that satisfaction is the after-sales appraisal of the customer and an affective reaction to the overall experience of products or services. Research has suggested that the performance of users is measured by two major dependent variables, namely, machine fear (computer anxiety) and happiness (satisfaction) [62]. Positive feedback and enjoyment can be gained by using virtual simulation games. Consumers are more pleased with the use of model games when they believe that they are characters with positive results [73]. Studies have shown that satisfaction is closely

related to the user profile created by consumers on VR [74]. Lu and Wang [75] stated that addiction to gambling contributed directly to loyalty and reduced loyalty to satisfaction. Researchers have claimed that their results partially clarified why online gamers remain loyal even if they are disappointed [4]. In daily life and video games, fulfillment and dissatisfaction with core psychological needs are accurate predictors of IGD. Powerful video games have to meet players' needs and make them incredibly pleased. They can also make the games risky, mostly for people whose psychosomatic needs are not satisfied in the real world. Consequently, the authors assumed that VR content is one of the most significant and essential factors, assuming that game satisfaction leads users to an IGD. Misra et al. [46] found that emotional dependence (satisfaction) is a significant predictor of game addiction behavior. Therefore, the present study proposed the following hypothesis.

H5: VCS positively influences VAD.

3.3. Moderating Role of VR Affordance (VA). Shin [76] claimed that, for the operation to be accepted, affordance should be correctly viewed by consumers; inquiring how VA is obtained for the industry and the academia is necessary. Nelson et al. [77] acknowledged the idea of affordance as an important tool to explore how VR is united by various interaction trends. Moreover, researchers have discussed [76] presence affordance, questioned whether the existence of VR influences user sensation, and discussed the difference between technical and emotional affordability, which contributes to behavioral shifts in the perception of the consumer. Furthermore, a study related affordance and satisfaction in consumer behavior, but no study has used affordance and VCS together. Ke et al. [19] used affordance in a virtual learning environment, but no study has used affordance and VRR in games, specifically VR games. Based on this argument, the authors assumed that VA is a moderator in modeling for VRR and VCS, which means that the function of VRR and VCS in creating enjoyment in the VR game would cause addictive behavior.

H6: VA (in economic terms) moderates the relationship between proximal causes (VRR and VCS) and VAD behavior.

4. Methodology

4.1. Participants. VR game players were approached in the referral network and accessible gaming zones and cafes in different cities of Anhui (which can be considered as a kind of convenience sampling). However, to maximize the data response rate and coverage of the population, different regions within the mainland were considered. Overall, during the data collection phase, more than 900 VR game players were approached or invited within mainland China. However, 684 respondents were recorded. Among the collected responses, 109 were rejected due to incomplete and ambiguous responses. The survey rate is 63.88%. The

demographics of the collected response set of 575 were explored. The sample size was acceptable according to Cochran. The *t*-test was computed to examine the validity and reliability (nonresponse biases) of the collected sample. The difference between the initial and later collected subsets of the collected sample was checked. The sample can be classified as nonresponse and bias-free based on computed results because no difference was noted among the subset of the collected sample. Table 1 holds the demographic profile of respondents.

4.2. Development of Instruments. The items were taken from authentic sources and were used in different contextual scenarios to ensure reliability and validity. PEX was mapped using three items on VR-based experience excitement and enjoyment from Tokel [78]. VSE was reflected in the three-item instrument, which emphasizes consumers' ability, skills, and confidence in ability and skills in using VR gadgets [79]. VRI was highlighted by the three-item scale, which discussed consumers' participation in the VR environment for interactivity, fun, and visual perspectives, adopted from Kim and Jae [80]. VRR was measured by instruments (items) adopted from Ribbens et al. [81] to emphasize consumers' perception of the VR environment as real in the context of VR addiction. VCS was reflected by a three-item scale adapted from Kim et al. [82] to capture consumers' cognitive satisfaction. VAD was reflected by a three-item scale adopted from Gong et al. [83] to emphasize consumers' VR addiction and related effects. VA was represented by VR hardware purchase intentions, which were measured by a three-item scale proposed by Manis and Choi [84] to capture the effect of consumers' intentions to purchase VR hardware as inventory/resource; this effect can be examined while defining the association of VRR and VCS (as proximal causes) and VR addiction. A Likert scale, which ranges from 1 as highly disagree to 5 as highly agree, was employed to measure each construct. Table 2 shows a list of items adapted.

An instrument with three main sections was developed to collect reliable responses. The first section introduced the purpose of the study. The second section presented the questions related to demographics. The third section enclosed the construct items to collect responses using the Likert scale. To ensure the quality of data collection, reverse coded items were included in the questionnaire, and responses with ambiguities were excluded. To accommodate the concerns related to comprehension and meaningful communication, a prior study was piloted with 25 respondents in the study area. The revised questionnaire was adopted on the basis of suggestions and observations made by participants of the pilot study. The digital medium was considered such that the target population (generation Z) can be approached and invited to participate in the survey. To maximize the response rate, the hyperlink for the survey was shared through the social networking application "WeChat." Data were collected throughout the second and third quarters of 2019.

TABLE 1: Surveyed sample profile.

Characteristic	Detail	Frequency	Percentage
Gender	Male	440	76.50
	Female	135	23.50
Age	Under 20	154	26.78
	20–25	413	71.83
	Above 25	8	01.39
Using VR to play games for the last	Less than 12 months	149	25.91
	1 to 2 years	300	52.17
	2 years or more	126	21.91

TABLE 2: Constructs, instruments, and sources.

Construct	Code	Items description	Source
Perceived experience excitement (PEX)	PEX1	I find playing VR games enjoyable	[78]
	PEX2	I find playing VR games pleasant	
	PEX3	I have fun playing VR games	
VR self-efficacy (VSE)	VSE1	I am confident and can understand the basic concepts of a VR environment	[79]
	VSE2	I am confident that I can excellently perform while using a VR environment	
	VSE3	I expect to do well in a VR environment	
VR interactivity (VRI)	VRI1	I feel that I have a lot of control over the content of the game	[80]
	VRI2	I interactively play a VR game	
	VRI3	I feel I can control my visual perspective	
VR realism (VRR)	VRR1	While playing this game, I felt like I was present in the video game world	[81]
	VRR2	While playing this game, I felt that I was part of the video game world	
	VRR3	While playing this game, I felt as if I was a part of the action	
VR cognitive satisfaction (VCS)	VCS1	My choice to use VR games was a wise one	[82]
	VCS2	The VR games provide me with a real environment, which I idealize	
	VCS3	VR games provide me with what is needed from a gaming environment	
VR game addiction (VAD)	VAD1	Using VR games sometimes interferes with other things	[83]
	VAD2	When I play VR games, I often feel agitated	
	VAD3	I have made unsuccessful attempts to reduce the time I use VR gadgets to play games	
VR affordance (VA)	AV1	The likelihood that I will purchase VR hardware within the foreseeable future is high	[84]
	AV2	I intend to purchase VR hardware within the foreseeable future	
	AV3	Purchasing VR hardware in the foreseeable future is important to me	

4.3. Data Analysis. The current research employed the MLE method to construct a structural equation model, by which learners' VR consumption behavior was examined. The bootstrapping method was adopted to explore further the mediation of VRR and the moderation of VA on learners' VAD.

SEM is a reliable approach to illustrate the relations between variables and latent constructs systematically and simultaneously. Statistically, MLE is typically employed as a universal theory estimation technique to estimate the parameters of a probability distribution by maximizing a likelihood function simultaneously. The point that maximizes the likelihood function in the parameter space is regarded as the MLE. As shown in equation (1), a $\{\mathbf{x}_1, \mathbf{x}_2, \dots, \mathbf{x}_n\}$ random sample is assumed to have descended from a multivariate normal distribution $N(\boldsymbol{\mu}_0, \boldsymbol{\Sigma}_0)$. Assuming a population matrix function with $\boldsymbol{\Sigma}_0$, $q \times 1$ size, and $\boldsymbol{\theta}_0$ unknown parameter, $\boldsymbol{\Sigma}_0 = \boldsymbol{\Sigma}(\boldsymbol{\theta}_0)$ is achieved. In this case, tr denotes the trace of a matrix, \mathbf{S} denotes the sample covariance matrix, p indicates the number of manifests, and

the variable $\boldsymbol{\Sigma}(\boldsymbol{\theta}_0)$ represents the covariance matrix of the hypothesized model (Cangur and Ercan):

$$F_{\text{MLE}}(\boldsymbol{\theta}) = \log \sum (\boldsymbol{\theta}) + \text{tr}(\mathbf{S} \sum (\boldsymbol{\theta})^{-1}) - \log \mathbf{S} - p. \quad (1)$$

In response to the flexibility and intuition of maximum likelihood, the method was dominantly utilized as a means of statistical inference in SEM.

5. Analysis

The current subsection started with the reliability testing of the collected survey and was followed by hypotheses testing, which included mediation and moderation examination. CFA was conducted, which comprised inter- and intra-construct level measures, as presented in Table 3.

Table 4 shows that external reliability computed further the examination of recorded AVE scores for each construct and its square root, which is recommended to be above the interconstruct correlation scores, as advised by the previous

TABLE 3: Reliability and validity analysis through CFA.

Construct	Items	Λ	α	CR	AVE
Perceived experience excitement (PEX)	PEX1	0.832	0.776	0.855	0.662
	PEX2	0.819			
	PEX3	0.790			
VR self-efficacy (VSE)	VSE1	0.804	0.824	0.810	0.587
	VSE2	0.753			
	VSE3	0.741			
VR interactivity (VRI)	VRI1	0.847	0.848	0.870	0.691
	VRI2	0.830			
	VRI3	0.816			
VR realism (VRR)	VRR1	0.851	0.874	0.863	0.678
	VRR2	0.833			
	VRR3	0.784			
VR cognitive satisfaction (VCS)	VCS1	0.844	0.903	0.878	0.706
	VCS2	0.839			
	VCS3	0.838			
VR game addiction (VAD)	VAD1	0.866	0.864	0.849	0.655
	VAD2	0.861			
	VAD3	0.688			
VR affordance (VA)	VA1	0.960	0.936	0.958	0.884
	VA2	0.935			
	VA3	0.926			

TABLE 4: Correlation scores and external validity test.

Construct	M(SD)	VIF	PEX	VSE	VRI	VRR	VCS	VAD	VA
PEX	2.826(.827)	1.177	0.813						
VSE	3.957(.827)	1.572	0.264**	0.766					
VRI	2.769(.770)	1.387	0.339**	0.353**	0.813				
VRR	3.502(.821)	1.576	0.251**	0.466**	0.459**	0.823			
VCS	4.012(.631)	1.549	0.259**	0.533**	0.304**	0.468**	0.840		
VAD	3.840(.645)	--	0.189**	0.601**	0.290**	0.404**	0.506**	0.809	
VA	3.583(.824)	1.012	0.040	0.015	0.059	0.085*	0.071	0.015	0.940

literature [85]. Multicollinearity is a challenge for regression analysis and is calculated by recording the VIF scores of each construct, which were observed within the continuum of 1.012 to 1.576, as advised by Hair et al. [86]. To examine data reliability, Harman’s approach was used to examine factor analysis. Podsakoff et al. [87] recommended the upper cut off limit of 50% by examining a single factor. In the current study, the construct with 29.24% variance was recorded, which indicated that no single factor compromised the proposed model. These results allowed the researchers to proceed with the computation for hypotheses testing.

In the structural model, the chi-square value was 425.147, and the degree of freedom was 124. All the fitness indices in Table 5 were within the satisfactory threshold limits, as advised by Hu and Bentler [88].

The explanation is extracted by using statistical tools (SPSS-Statistics and AMOS), which computed the standardized estimates. The proposed demographic constructs (as control factors) were significant and had noticeable scores while measuring VR addiction. The determinate constructs in the proposed model, namely, VRR, VCS, and VAD, were noted with a variance of 40.3%, 36.7%, and 38.9%, respectively. The study observed PEX as the least

TABLE 5: Model fitness indices computed through AMOS.

Fitness indices	Recommended value	Measurement	Proposed
Chi-square		320.224	425.147
Df		120	124
Chi-square/df	≤5.0	2.669	3.068
GFI	0.90	0.943	0.938
AGFI	0.85	0.919	0.909
TLI	0.95	0.957	0.946
IFI	0.95	0.966	0.959
NFI	0.95	0.947	0.941
CFI	0.95	0.966	0.959
RMSEA	≤0.08	0.054	0.060

Note. df=degree of freedom; GFI, AGFI, TLI, NFI, CFI, and RMSEA =recommended values followed cutoffs, as advised by Hu and Bentler [88].

influencing factor while defining VRR and VCS. PEX’s effect on VRR was insignificant, and that on VCS was minimal, as listed in Table 6.

This argument led to findings from the literature, which reflected that consumers’ excitement to experience VR gadgets did not necessarily explain their after-use satisfaction and perception that the VR environment is real. The

TABLE 6: Hypotheses testing (path analysis).

Sr.	Description	Beta (β)	Significance	Result
H1(a)	PEX \rightarrow VRR	0.032	$p \geq 0.05$	Not supported
H1(b)	PEX \rightarrow VCS	0.100	$p \leq 0.05$	Supported
H2(a)	VSE \rightarrow VRR	0.366	$p \leq 0.001$	Supported
H2(b)	VSE \rightarrow VCS	0.523	$p \leq 0.05$	Supported
H3(a)	VRI \rightarrow VRR	0.384	$p \leq 0.001$	Supported
H3(b)	VRI \rightarrow VCS	0.100	$p \leq 0.001$	Supported
H4	VRR \rightarrow VAD	0.179	$p \leq 0.001$	Supported
H5	VCS \rightarrow VAD	0.240	$p \leq 0.001$	Supported
H6(a)	VRR*VA \rightarrow VAD	0.087	$p \leq 0.05$	Supported
H6(b)	VCS*VA \rightarrow VAD	0.026	$p \geq 0.05$	Not supported

highest impact on VRR was observed by VRI. Consumers' VRI enhanced their perception about the VR environment as real. The second highest effect for VRR is observed by VSE. Consumers have confidence in their ability to use VR gadgets and are likely to perceive the VR environment as real. VSE explained that VCS is stronger than VRI. VSE has a strong impact on VCS. In other words, high self-efficacy to operate and use VR gadgets enhances consumers' satisfaction because more control provides less cognitive dissonance, which makes them more confident and satisfied. While incorporating the effects of endogenous variables, Figure 1 shows that VCS had more explanatory power than VRR in explaining VAD.

The results indicated some interesting findings of the study "VR environment as if real," which showed less effect on VAD than consumers' cognitive satisfaction on VAD. The results concluded that high cognitive satisfaction makes consumers more addicted than experiencing the VR environment as real. The moderation effect of VA was minimal in the case of VRR, where its impact in the case of VCS was insignificant. The results emphasized that VA moderated the effect of VRR in explaining VR addiction but did not perform this moderation in the case of VCS and VAD.

The present study employed Preacher and Hayes's [89] approach to quantify and measure the mediating behavior of the proposed factors (VRR and VSC). Through the recommended approach, the scores of the confidence intervals (CIs) of the bootstrapping method were employed, and CIs computed for each of the hypotheses were satisfactory and are documented in Table 7.

Baron and Kenny followed test mediation. The outputs from the adopted method are listed in Table 8. The present study can conclude that the sense of realism and cognitive satisfaction in the context of VAD usage behavior are partial mediators while examining the role of interactivity, excitement, and self-efficacy of VR content consumption among VR game users.

6. Discussion

This study has two main findings. First, VSE has a significant role as an exogenous factor while measuring VAD among consumers. Second, VCS has a strong significant association

with VAD. Similarly, the authors found that the respondents believe that VSE is a dominating contributor in defining VRR and cognitive satisfaction and creates an addiction to VR games; VSE has a significant hold while mapping the perception and actions of VR game players [61]; the authors also found that VSE has a nonsignificant role in leading VRR to game addiction. Moreover, VRI was observed to be the strongest proposed candidate to define VRR. Studies have suggested immediate interaction on player participation [90], which had a strong effect on addictive behavior. Previous literature has supported the relationship between PEX and VRC. The results created negative and positive emotions.

Furthermore, researchers have argued that felicitous music followed cheerful endings, where in a character experiences joy and satisfaction over a defeated enemy [91]; however, in the current study, observing the fully mediating role of VSC and understanding the relationship between PEX and addiction contributed to the literature. This study concluded that PEX holds a unique behavior while mapping VAD. While defining VAD, VRR was observed to be less dominant to VSC. Moreover, VRR was not as highly significant as VSC when adopting addictive behavior toward VR games. VA was found to be psychological but not from an economic perspective. Furthermore, VA was considered an individual's stance toward the adoption of VR gadgets. VA did not create satisfaction among users who can afford VR for VRR.

6.1. Theoretical Implications. This study provided profound and useful additions to the academic literature. First, this study is the first of its nature to understand the behavior of VAD. Previous studies have been conducted with other research factors, whereas the present study used the behavioral aspect/change of gamers from a multiperspective approach, which enhanced the comprehension of gamers' behavioral changes. Moreover, VSE was used to inquire and understand gamers' addictive behavior toward VR games. Second, this study is highly unique compared with previous studies. Few studies have been found where researchers have adopted gaming addiction with behavioral modeling, specifically in the context of VR games. The authors adopted cognitive behavioral modeling. Previous studies have concluded that excess usage of video games could have a serious health concern [92]. Gackebach et al. [93] stated that, besides addiction, serious physical health concerns are dangerous for users who excessively use Internet games. The present study used the instrument of VSE, whereas previous studies have not used it, specifically in the context of game addiction. Therefore, the authors claimed that this usage is the novelty of this study. Moreover, VRI and VSE are the novelty in the context of games. The authors examined published studies and did not find any data that used VRI or VSE in the context of games.

Furthermore, the authors found that PEX fully mediates VCS and VAD, which means that VCS can create a strong addiction behavior when it comes to PEX and VCS. For

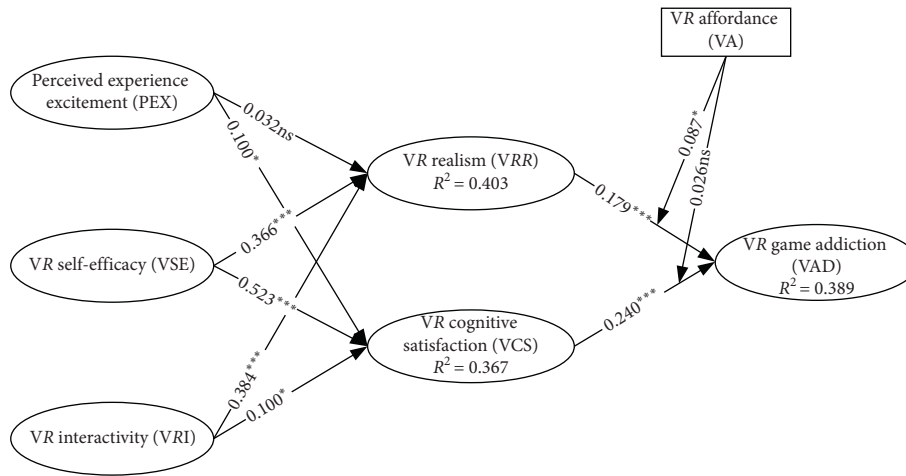


FIGURE 1: Graphical view of the path analysis of the proposed model.

TABLE 7: Mediation analysis (by bootstrapping).

Hypo	IV	M	DV	Effect of IV on M (a)	Effect of M on DV (b)	Direct (c')	Indirect (a*b)	Total effect (c)	95% (CI)	Mediation
H7(a)	PEX	VRR	VAD	0.249***	0.164***	0.025 ^{ns}	0.040**	0.147***	(0.020, 0.064)	Supported
H7(b)	VSE	VRR	VAD	0.693***	0.073*	0.702***	(0.007, 0.095)	Supported		
H7(c)	VRI	VRR	VAD	0.489***	0.140***	0.074*	0.067*	0.243***	(0.034, 0.109)	Supported
H8(a)	PEX	VCS	VAD	0.198***	0.409***	0.025 ^{ns}	0.081***	0.147***	(0.053, 0.115)	Supported
H8(b)	VSE	VCS	VAD	0.609***	0.236***	0.508***	0.143***	0.702***	(0.084, 0.205)	Supported
H8(c)	VRI	VCS	VAD	0.249***	0.404***	0.074*	0.101***	0.243***	(0.072, 0.138)	Supported

TABLE 8: Mediation (as advised by Baron and Kenny’s approach).

Hypo	IV	DV	IV → DV	IV → M	IV + M → DV		Mediation
					IV → DV	M → DV	
H7(a)	PEX	VAD	0.147***	0.250***	0.073*	0.299***	Partial
H7(b)	VSE	VAD	0.703***	0.694***	0.616***	0.124***	Partial
H7(c)	VRI	VAD	0.243***	0.490***	0.111**	0.269***	Partial
H8(a)	PEX	VAD	0.147***	0.198***	0.048 ^{ns}	0.501***	Full
H8(b)	VSE	VAD	0.703***	0.609***	0.541***	0.265***	Partial
H8(c)	VRI	VAD	0.243***	0.249***	0.126***	0.470***	Partial

instance, VSE with realism and satisfaction plays a significant role not only in game addiction but also in general addiction. VA in an economic perspective strengthens addiction behavior. Similarly, VR satisfaction does not rely on affordance but is an individual act. Using a four-cognition-level analysis, the authors found that psychological construct dominates in creating addictive behavior. They also found that a high level of interactivity leads to a high level of game addiction. The authors also suggested that further studies carry out interactivity and self-efficacy and further investigate arcades and VR arcades. Self-efficacy in the games addiction perspective can be further studied. Specifically,

VSE can be studied in the context of different types of games. For instance, VA has been observed while examining individuals’ behavior toward game addiction. However, VA’s moderating effect while mapping the intentions of individuals was rarely observed. No study has used VA as a moderator for VR games players. The present study is the first to use it.

6.2. *Practical Implications.* The results of this study showed that VRI creates a high level of satisfaction among users. Similarly, previous studies have suggested that interactivity

with advanced technology (VR) affects attitude and creates a positive attitude [94]. Moreover, researchers have expressed serious concerns about health and addiction toward Internet games. Gamers' addictions to Internet games have been argued to cause mental health problems [95]. Specifically, among children, the argument is that addiction to games can affect learning and thinking abilities. Similarly, VR games can be restricted with time limitations and demographic usage. VSE is revolving around one's ability to accomplish given tasks. Similarly, from the analysis of the current results, self-efficacy is proven to affect addiction with the help of VRR. Therefore, the quality of games in the sense of realism can be improved to attract the users toward the VR games. Users' involvement becomes more robust when it comes to the sense of realism. Moreover, users feel presence in the game when realism and experience excitement are strong. It can also be used for learning purposes [56]. Studies have indicated that VRR has an important role in learning. For instance, the authors recommend academicians to carry out further research to fill the literature gap on VR games. The environment needs to be more realistic such that users can feel the real sense of presence in the game. The authors did not find any study based on VAD. Thus, VAD can be studied more to fill the literature gap. Satisfaction among users needs excitement and quality experience. To attract users toward VR games, developers need to develop exciting fantasies in the game environment. Balakrishnan and Gri [4] stated that ensuring the loyalty of consumers toward Internet games is difficult; therefore, with the advancement of the technology, more advanced features must be developed to attract users and make them continue playing VR games. Moreover, it can have a negative impact on satisfaction and can disturb the daily routine of users. It can also be considered such that users' daily routines are not disturbed with extra satisfaction. Therefore, satisfied users are likely to experience VAD. The level of satisfaction can be increased for learning or psychological treatment, where students are involved and can learn easily and psychological patients can be treated appropriately. Furthermore, many games require substantial mental ability. Computer games are often considered to be mentally oriented, particularly competitive games.

7. Conclusion and Limitations

This study utilized the cognitive-behavioral model to examine users' addiction toward VR games. The authors found that VRI has the uppermost potential for appreciating situations. Similarly, PEX and VSE are shown to have significant deterministic power to explain users' behavior toward game addiction. Moreover, VRR has an important role in creating a negative impact on addiction among users. Games that offer exciting experiences and a sense of realism can be improved such that more users use them. They should be used for academic purposes more than for entertainment. Furthermore, this study focused on the general population, and the focus could be further extended by adding a cross-cultural view to find the VR addiction behavior of different countries. Moreover, this study adopted a quantitative

survey, and this approach could be improved by adding qualitative techniques for data collection and analysis. This study has the following limitations, which could lead to further studies. First, this study only adopted a cognitive-behavioral frame, which could be further extended and revised with other behavioral methods. Second, this study focused on the general population, which could be further extended to a demographic approach (i.e., gender or socioeconomic factors). Third, this study adopted a quantitative survey, and this approach could be improved by adding qualitative techniques for data collection and analysis.

Data Availability

The data used to support the findings of this study are available from the corresponding author upon request.

Conflicts of Interest

No conflicts of interest were found.

Authors' Contributions

Xuesong Zhai, Fahad Asmi, and Ronting Zhou contributed equally.

Acknowledgments

This research work was supported by the National Social Science Fund of China (grant ID: 17BXW034) and the 2020 Humanities and Social Science Projects of the Ministry of Education (grant ID: 20YJC880118).

Supplementary Materials

Appendix A: studies on addictive behavior. (*Supplementary Materials*)

References

- [1] R. M. Ryan, C. S. Rigby, and A. Przybylski, "The motivational pull of video games: a self-determination theory approach," *Motivation and Emotion*, vol. 30, pp. 347–363, 2006.
- [2] B. Behzadnia, P. J. C. Adachi, E. L. Deci, and H. Mohammadzadeh, "Associations between students' perceptions of physical education teachers' interpersonal styles and students' wellness, knowledge, performance, and intentions to persist at physical activity: a self-determination theory approach," *Psychology of Sport and Exercise*, vol. 39, pp. 10–19, 2018.
- [3] Q.-Q. Liu, D.-J. Zhang, X.-J. Yang, C.-Y. Zhang, C.-Y. Fan, and Z.-K. Zhou, "Perceived stress and mobile phone addiction in Chinese adolescents: a moderated mediation model," *Computers in Human Behavior*, vol. 87, pp. 247–253, 2018.
- [4] J. Balakrishnan and M. D. Griffiths, "Loyalty towards online games, gaming addiction, and purchase intention towards online mobile in-game features," *Computers in Human Behavior*, vol. 87, pp. 238–246, 2018.
- [5] S. Horwood and J. Anglim, "Problematic smartphone usage and subjective and psychological well-being," *Computers in Human Behavior*, vol. 97, pp. 44–50, 2019.

- [6] A. Blachnio and A. Przepiorka, "Personality and positive orientation in Internet and Facebook addiction. An empirical report from Poland," *Computers in Human Behavior*, vol. 59, pp. 230–236, 2016.
- [7] J. Clement, *Number of Monthly Active Facebook Users Worldwide as of 2nd quarter 2019 (in millions)*, Statista, Hamburg, Germany, 2019.
- [8] C. York and J. Turcotte, "Vacationing from facebook: adoption, temporary discontinuance, and re-adoption of an innovation," *Communication Research Reports*, vol. 32, no. 1, pp. 54–62, 2015.
- [9] T. Nam, "Technology usage, expected job sustainability, and perceived job insecurity," *Technological Forecasting and Social Change*, vol. 138, pp. 155–165, 2019.
- [10] Şö Gökçearsan, F. K. Mumcu, T. Haşlamam, and Y. D. Çevik, "Modelling smartphone addiction: the role of smartphone usage, self-regulation, general self-efficacy and cyberloafing in university students," *Computers in Human Behavior*, vol. 63, pp. 639–649, 2016.
- [11] Q. Jiang, Y. Li, and V. Shypenka, "Loneliness, individualism, and smartphone addiction among international students in China," *Cyberpsychology, Behavior, and Social Networking*, vol. 21, no. 11, pp. 711–718, 2018.
- [12] Ás Zsila, G. Orosz, B. Bóthe et al., "An empirical study on the motivations underlying augmented reality games: the case of Pokémon Go during and after Pokémon fever," *Personality and Individual Differences*, vol. 133, pp. 56–66, 2018.
- [13] F. Bányai, M. D. Griffiths, O. Király, and Z. Demetrovics, "The psychology of esports : a systematic literature review," *Journal of Gambling Studies*, vol. 35, no. 2, 2018.
- [14] H. Cash, C. Rae, A. Steel, and A. Winkler, "Internet addiction: a brief summary of research and practice," *Current Psychiatry Reviews*, vol. 8, no. 4, pp. 292–298, 2012.
- [15] D. L. King and P. H. Delfabbro, "An introduction to gaming and IGD," in *Internet Gaming Disorder*, pp. 1–21, Academic Press, Cambridge, MA, USA, 2018.
- [16] M. E. Portman, A. Natapov, and D. Fisher-Gewirtzman, "To go where no man has gone before: virtual reality in architecture, landscape architecture and environmental planning," *Computers, Environment and Urban Systems*, vol. 54, pp. 376–384, 2015.
- [17] E. K. Yuen, E. M. Goetter, M. J. Stasio et al., "A pilot of acceptance and commitment therapy for public speaking anxiety delivered with group videoconferencing and virtual reality exposure," *Journal of Contextual Behavioral Science*, vol. 12, pp. 47–54, 2019.
- [18] D. Lafortune, L. Dion, and P. Renaud, "Virtual reality and sex therapy: future directions for clinical research," *Journal of Sex & Marital Therapy*, vol. 46, no. 1, pp. 1–17, 2019.
- [19] F. Ke, M. Pachman, and Z. Dai, "Investigating educational affordances of virtual reality for simulation-based teaching training with graduate teaching assistants," *Journal of Computing in Higher Education*, 2020.
- [20] H. Yang, J. Yu, H. Zo, and M. Choi, "User acceptance of wearable devices: an extended perspective of perceived value," *Telematics and Informatics*, vol. 33, no. 2, pp. 256–269, 2016.
- [21] J. Lee, J. Kim, and J. Y. Choi, "The adoption of virtual reality devices: the technology acceptance model 918 integrating enjoyment, social interaction, and strength of the social ties," *Telematics and Informatics*, vol. 39, pp. 37–48, 2019.
- [22] F. D. Davis, "Perceived usefulness, perceived ease of use, and user acceptance of information technology," *MIS Quarterly*, vol. 13, no. 3, 1989.
- [23] R. Agarwal and E. Karahanna, "Time flies when you're having fun: cognitive absorption and beliefs about information technology usage," *MIS Quarterly*, vol. 24, no. 4, pp. 665–694, 2000.
- [24] V. Venkatesh and F. D. Davis, "Theoretical extension of the technology acceptance model: four longitudinal field studies," *Management Science*, vol. 46, no. 2, 2000.
- [25] V. Vankatesh, M. G. Morris, M. Hall, G. B. Davis, F. D. Davis, and S. M. Walton, "User acceptance OF information technology : toward a unified view," *MIS Quarterly*, vol. 27, pp. 425–478, 2003.
- [26] V. Venkatesh, J. Y. L. Thong, and X. Xu, "Consumer acceptance and use of information technology: extending the unified theory of acceptance and use of technology," *MIS Quarterly*, vol. 36, no. 1, pp. 157–178, 2012.
- [27] R. A. Davis, "Cognitive-behavioral model of pathological Internet use," *Computers in Human Behavior*, vol. 17, no. 2, 2001.
- [28] X. Zheng and M. K. O. Lee, "Excessive use of mobile social networking sites: negative consequences on individuals," *Computers in Human Behavior*, vol. 65, pp. 65–76, 2016.
- [29] E. Karadağ and B. Kılıç, "Öğretmen görüşlerine göre öğrencilerdeki teknoloji bağımlılığı," *Psikiyatride Guncel Yaklasimler - Current Approaches in Psychiatry*, vol. 11, no. 1, pp. 101–117, 2019.
- [30] M. H. Orzack, A. C. Voluse, D. Wolf, and J. Hennen, "An ongoing study of group treatment for men involved in problematic internet-enabled sexual behavior," *Cyber Psychology & Behavior*, vol. 9, no. 3, pp. 348–360, 2006.
- [31] M. Moital, A. Bain, H. Thomas et al., "The psychology of esports : a systematic literature review," *Journal of Gambling Studies*, vol. 1321, pp. 1–5, 2018.
- [32] C. Wang, M. K. O. Lee, and Z. Hua, "A theory of social media dependence: evidence from microblog users," *Decision Support Systems*, vol. 69, pp. 40–49, 2015.
- [33] S. Hwang and S. Kim, "Does mIM experience affect satisfaction with and loyalty toward O2O services?" *Computers in Human Behavior*, vol. 82, pp. 70–80, 2019.
- [34] A. Bandura, *Social Foundations of Thought and Action : A Social Cognitive Theory/Albert Bandura*, Prentice-Hall, Upper Saddle River, NJ, USA, 1986.
- [35] N. Jimenez, S. San-Martin, and N. Puente, "The path to mobile shopping compatibility," *The Journal of High Technology Management Research*, vol. 30, no. 1, pp. 15–26, 2019.
- [36] T. Strohäker, "The relationship between self-limitation and gambling behavior among German gambling arcade visitors," *Journal of Gambling Studies*, vol. 35, no. 4, pp. 1229–1248, 2019.
- [37] J.-H. T. Lin, "Fear in virtual reality (VR): fear elements, coping reactions, immediate and next-day fright responses toward a survival horror zombie virtual reality game," *Computers in Human Behavior*, vol. 72, pp. 350–361, 2017.
- [38] B. Y. Park, G. Wilson, J. Berger et al., "Is internet pornography causing sexual dysfunctions? A review with clinical reports," *Behavioral Sciences*, vol. 6, 2016.
- [39] P. Krompiec and K. Park, "Enhanced player interaction using motion controllers for first-person shooting games in virtual reality," *IEEE Access*, vol. 7, pp. 124548–124557, 2019.
- [40] K. Zibrek, S. Martin, and R. McDonnell, "Is photorealism important for perception of expressive virtual humans in virtual reality?" *ACM Transactions on Applied Perception*, vol. 16, 2019.
- [41] B. P. H. Hui, A. M. S. Wu, N. Y. F. Siu, M. L. Chung, and N. Pun, "The effects of need satisfaction and dissatisfaction on

- flourishing among young Chinese gamers: the mediating role of internet gaming disorder,” *International Journal of Environmental Research and Public Health*, vol. 16, pp. 1–14, 2019.
- [42] A. M. S. Wu, L. L. M. Lei, and L. Ku, “Psychological needs, purpose in life, and problem video game playing among Chinese young adults,” *International Journal of Psychology*, vol. 48, no. 4, pp. 583–590, 2013.
- [43] I. Tóth-Király, B. Bóthe, A. N. Márki, A. Rigó, and G. Orosz, “Two sides of the same coin: the differentiating role of need satisfaction and frustration in passion for screen-based activities,” *European Journal of Social Psychology*, vol. 49, pp. 1190–1205, 2019.
- [44] G. S. Becker and K. M. Murphy, “A theory of rational addiction,” *Journal of Political Economy*, vol. 96, no. 41, 1988.
- [45] L. g. Pujol, “Realism in virtual reality applications for cultural heritage,” *International Journal of Virtual and Augmented Reality*, vol. 10, pp. 41–49, 2011.
- [46] R. Misra, S. Singh, and N. Singh, “Assessing behavioral patterns for online gaming addiction,” *International Journal of Cyber Behavior, Psychology and Learning*, vol. 10, no. 2, pp. 43–64, 2020.
- [47] V. A. Zeithaml, “Consumer perceptions of price, quality, and value: a means-end model and synthesis of evidence,” *Journal of Marketing*, vol. 52, no. 3, pp. 2–22, 1988.
- [48] M. J. Bitner and A. R. Hubbert, “Encounter satisfaction versus overall satisfaction versus quality: the customer’s voice,” in *Service Quality: New Directions in Theory and Practice* SAGE Publications, Thousand Oaks, CA, USA, 2012.
- [49] S. Lee, J. Park, and S. Bryan Lee, “The interplay of internet addiction and compulsive shopping behaviors,” *Social Behavior and Personality: An International Journal*, vol. 44, no. 11, pp. 1901–1912, 2016.
- [50] C. L. Hsu and M. C. Chen, “How does gamification improve user experience? An empirical investigation on the antecedents and consequences of user experience and its mediating role,” *Technological Forecasting and Social Change*, vol. 132, pp. 118–129, 2018.
- [51] M. van Gisbergen, M. Kovacs, F. Campos, M. van der Heeft, and V. Vugts, “What we don’t know. the effect of realism in virtual reality on experience and behaviour,” *Augmented Reality and Virtual Reality*, Springer, Berlin, Germany, pp. 45–57, 2019.
- [52] M. Slater, “Place illusion and plausibility can lead to realistic behaviour in immersive virtual environments,” *Philosophical Transactions of the Royal Society B: Biological Sciences*, vol. 364, no. 1535, pp. 3549–3557, 2009.
- [53] A. Bandura, “Self-efficacy: toward a unifying theory of behavioral change,” *Advances in Behaviour Research and Therapy*, vol. 1, no. 4, pp. 139–161, 1978.
- [54] A. Bandura, G. V. Caprara, C. Barbaranelli, M. Gerbino, and C. Pastorelli, “Role of affective self-regulatory efficacy in diverse spheres of psychosocial functioning,” *Child Development*, vol. 74, no. 3, pp. 769–782, 2003.
- [55] L. Mallalieu and K. M. Palan, “How good A shopper Am I? Conceptualizing teenage girls’ perceived shopping competence,” *Academy of Marketing Science Review*, vol. 2006, pp. 1–28, 2006.
- [56] E. Zetou, N. Vernadakis, V. Derri, E. Bebetso, and F. Filippou, “The effect of game for understanding on backhand tennis skill learning and self-efficacy improvement in elementary students,” *Procedia - Social and Behavioral Sciences*, vol. 152, pp. 765–771, 2014.
- [57] L. Schjoedt and J. B. Craig, “Development and validation of a unidimensional domain-specific entrepreneurial self-efficacy scale,” *International Journal of Entrepreneurial Behavior & Research*, vol. 23, no. 1, pp. 98–113, 2017.
- [58] Y. Peng, H.-H. Hsiung, and K.-H. Chen, “The level of concern about FengShui in house purchasing: the impacts of self-efficacy, superstition, and the big five personality traits,” *Psychology & Marketing*, vol. 30, pp. 461–469, 2010.
- [59] D. J. Ketelhut, “Assessing gaming, computer and scientific inquiry self-efficacy in a virtual environment,” in *Serious Educational Game Assessment*, L. Annetta and S. C. Bronack, Eds., pp. 1–18, Sense Publishers, Rotterdam, Netherlands, 2011.
- [60] S. F. Verkijika, “If you know what to do, will you take action to avoid mobile phishing attacks”: self-efficacy, anticipated regret, and gender,” *Computers in Human Behavior*, vol. 101, pp. 286–296, 2019.
- [61] M. Dindar and Y. Akbulut, “Role of self-efficacy and social appearance anxiety on gaming motivations of MMOFPS players,” *Computers & Education*, vol. 81, pp. 26–34, 2015.
- [62] J. M. Pina and V. Bordonaba-Juste, “Students’ experience with online simulation games: from computer anxiety to satisfaction,” *Interacting with Computers*, vol. 30, no. 2, pp. 162–171, 2018.
- [63] Y. Shu, Y. Z. Huang, S. H. Chang, and M. Y. Chen, “Do virtual reality head-mounted displays make a difference? A comparison of presence and self-efficacy between head-mounted displays and desktop computer-facilitated virtual environments,” *Virtual Reality*, vol. 23, no. 3, 2018.
- [64] M. Eisenbeiss, B. Blechschmidt, K. Backhaus, and P. A. Freund, “The (real) world is not enough:” motivational drivers and user behavior in virtual worlds,” *Journal of Interactive Marketing*, vol. 26, no. 1, pp. 4–20, 2012.
- [65] I. Bogost, *Persuasive Games: The Expressive Power of Video Games*, MIT Press, Cambridge, MA, USA, 2007.
- [66] J. Juul, “Games telling stories?” *International Journal of Computing*, vol. 1, 2001.
- [67] R. W. Belk, “Extended self in a digital world: table 1,” *Journal of Consumer Research*, vol. 40, no. 3, pp. 477–500, 2013.
- [68] D. Murphy, “Virtual reality is “finally here”: a qualitative exploration of formal determinants of player experience in VR,” in *Proceedings of the 2017 DiGRA International Conference*, Melbourne, Australia, July 2017.
- [69] D. J. Chalmers, “The virtual and the real,” *Disputatio*, vol. 9, pp. 309–352, 2017.
- [70] J. Robson and G. Tavinor, “Videogames and virtual media,” in *The Aesthetics of Videogames*, pp. 146–160, Routledge, Abingdon, UK, 2018.
- [71] R. Lavoie, K. Main, C. King, and D. King, “Virtual experience, real consequences: the potential negative emotional consequences of virtual reality gameplay,” *Virtual Reality*, 2020.
- [72] R. L. Oliver, “A cognitive model of the antecedents and consequences of satisfaction decisions,” *Journal of Marketing Research*, vol. 17, no. 4, pp. 460–469, 1980.
- [73] J. M. Vervoort, “New frontiers in futures games: leveraging game sector developments,” *Futures*, vol. 105, pp. 174–186, 2018.
- [74] T. Waltemate, D. Gall, D. Roth, M. Botsch, and M. E. Latoschik, “The impact of avatar personalization and immersion on virtual body ownership, presence, and emotional response,” *IEEE Transactions on Visualization and Computer Graphics*, vol. 24, no. 4, pp. 1643–1652, 2018.
- [75] H. P. Lu and S. m. Wang, “The role of Internet addiction in online game loyalty: an exploratory study,” *Internet Research*, vol. 18, no. 5, pp. 499–519, 2008.

- [76] D. H. hin, "The role of affordance in the experience of virtual reality learning: technological and affective affordances in virtual reality," *Telematics and Informatics*, vol. 34, no. 8, pp. 1826–1836, 2017.
- [77] S. B. Nelson, M. H. Jarrahi, and L. Thomson, "Mobility of knowledge work and affordances of digital technologies," *International Journal of Information Management*, vol. 37, no. 2, pp. 54–62, 2017.
- [78] S. T. Tokel and V. İsler, "Acceptance of virtual worlds as learning space," *Innovations in Education and Teaching International*, vol. 52, no. 3, pp. 254–264, 2015.
- [79] G. Makransky and G. B. Petersen, "Investigating the process of learning with desktop virtual reality: a structural equation modeling approach," *Computers & Education*, vol. 134, pp. 15–30, 2019.
- [80] D. Kim and Y. J. Ko, "The impact of virtual reality (VR) technology on sport spectators' flow experience and satisfaction," *Computers in Human Behavior*, vol. 93, pp. 346–356, 2019.
- [81] W. Ribbens, S. Malliet, R. Van Eck, and D. Larkin, "Perceived realism in shooting games: towards scale validation," *Computers in Human Behavior*, vol. 64, pp. 308–318, 2016.
- [82] M. Kim, M. Park, J. Park et al., "The role of multidimensional switching barriers on the cognitive and affective satisfaction-loyalty link in mobile communication services: coupling in moderating effects," *Computers in Human Behavior*, vol. 87, 2018.
- [83] M. Gong, L. Yu, and A. Luqman, "Understanding the formation mechanism of mobile social networking site addiction: evidence from WeChat users," *Behaviour & Information Technology*, vol. 0, pp. 1–16, 2019.
- [84] K. T. Manis and D. Choi, "The virtual reality hardware acceptance model (VR-HAM): extending and individuating the technology acceptance model (TAM) for virtual reality hardware," *Journal of Business Research*, vol. 100, pp. 503–513, 2019.
- [85] C. Fornell and D. F. Larcker, "Structural equation models with unobservable variables and measurement error: algebra and statistics," *Journal of Marketing Research*, vol. 18, no. 3, 1981.
- [86] J. F. Hair, W. C. Black, B. J. Babin, and R. E. Anderson, *Multivariate Data Analysis*, Pearson Education, Upper Saddle River, NJ, USA, 7th edition, 2014.
- [87] P. M. Podsakoff, S. B. MacKenzie, and N. P. Podsakoff, "Common method biases in behavioral research: a critical review of the literature and recommended remedies," *Journal of Applied Psychology*, vol. 88, no. 5, p. 879, 2003.
- [88] L. t. Hu and P. M. Bentler, "Cutoff criteria for fit indexes in covariance structure analysis: conventional criteria versus new alternatives," *Structural Equation Modeling: A Multidisciplinary Journal*, vol. 6, no. 1, pp. 1–55, 1999.
- [89] K. J. Preacher and A. F. Hayes, "Asymptotic and resampling strategies for assessing and comparing indirect effects in multiple mediator models," *Behavior Research Methods*, vol. 40, no. 3, 2008.
- [90] G. Crawford, D. Muriel, and S. Conway, "A feel for the game: exploring gaming 'experience' through the case of sports-themed video games," *Convergence*, vol. 25, no. 5-6, pp. 937–952, 2019.
- [91] J.-H. T. Lin, D.-Y. Wu, and C.-C. Tao, "So scary, yet so fun: the role of self-efficacy in enjoyment of a virtual reality horror game," *New Media & Society*, vol. 20, no. 9, pp. 3223–3242, 2018.
- [92] P. Dullur and P. Hay, "Problem internet use and internet gaming disorder: a survey of health literacy among psychiatrists from Australia and New Zealand," *Australasian Psychiatry*, vol. 25, pp. 140–145, 2017.
- [93] J. Gackenbach, D. Wijeyaratnam, and C. Flockhart, *The Video Gaming Frontier*, Elsevier, Amsterdam, Netherlands, 2017.
- [94] C. L. Huang, Y. F. Luo, S. C. Yang, C. M. Lu, and A.-S. Chen, "Influence of students' learning style, sense of presence, and cognitive load on learning outcomes in an immersive virtual reality learning environment," *Journal of Educational Computing Research*, vol. 58, no. 3, 2019.
- [95] M. D. Griffiths, D. J. Kuss, and D. L. King, "Video game addiction: past, present and future," *Current Psychiatry Reviews*, vol. 8, no. 4, 2012.

Research Article

Stability Analysis of Regular and Chaotic Ca^{2+} Oscillations in Astrocytes

Min Ye¹ and Hongkun Zuo² 

¹School of Education Science, Guangxi University for Nationalities, Nanning 530006, Guangxi, China

²School of Finance and Mathematics, Huainan Normal University, Huainan 232038, Anhui, China

Correspondence should be addressed to Hongkun Zuo; hk_zuo@163.com

Received 13 July 2020; Revised 5 September 2020; Accepted 12 September 2020; Published 23 September 2020

Academic Editor: Jia-Bao Liu

Copyright © 2020 Min Ye and Hongkun Zuo. This is an open access article distributed under the Creative Commons Attribution License, which permits unrestricted use, distribution, and reproduction in any medium, provided the original work is properly cited.

Ca^{2+} oscillations play an important role in various cell types. Thus, understanding the dynamical mechanisms underlying astrocytic Ca^{2+} oscillations is of great importance. The main purpose of this article was to investigate dynamical behaviors and bifurcation mechanisms associated with astrocytic Ca^{2+} oscillations, including stability of equilibrium and classification of different dynamical activities including regular and chaotic Ca^{2+} oscillations. Computation results show that part of the reason for the appearance and disappearance of spontaneous astrocytic Ca^{2+} oscillations is that they embody the subcritical Hopf and the supercritical Hopf bifurcation points. In more details, we theoretically analyze the stability of the equilibrium points and illustrate the regular and chaotic spontaneous calcium firing activities in the astrocytes model, which are qualitatively similar to actual biological experiment. Then, we investigate the effectiveness and the accuracy of our nonlinear dynamical mechanism analysis via computer simulations. These results suggest the important role of spontaneous Ca^{2+} oscillations in conjunction with the adjacent neuronal input that may help correlate the connection of both the glia and neuron.

1. Introduction

There are two types of cells (namely, the neuron and the glia) in the central nervous system (CNS). Neuron is the basic structural and functional elements of the CNS and has the function of contacting and integrating input information and transmitting information [1, 2]. With the aid of electron microscope, it was found that the neuron is divided into two parts: the cell body and the protrusion. The role of the protrusion is to receive the impulse from the axon of other neurons and transfer to the cell body. Unlike the neuron, as another type of cell, the glia also has the protrusion, but without the dendrites or the axons. It is demonstrated that the glia, of which ratio of the amount to neuron is about 10 : 1, is widely distributed in the CNS. The glia includes astrocyte, oligodendrocyte (combined with the astrocyte as macroglia), and microglia. In the past decades, the role of astrocytes in the CNS has been recognized that the transmission and integration of information is performed by network of neurons. The glia is the only passive auxiliary role, supporting, providing nutrition, and assisting metabolism [3, 4]. In recent

years, lots of studies have attempted to show that the glia has great potential to provide new insight into other roles (assisting the functional activities of neuron) besides having an effect on supporting and isolating the neighboring neurons [5]. The evidences that indicate that the glia cooperates with the neuron come from a large number of experiments by Newman and Zahs [6]. As the second messenger, calcium oscillation is referred to cytoplasmic calcium ions as transducing information in a manner of concentration oscillation, which affects various processes such as cell differentiation, maturation, and apoptosis. One of the earliest reactions produced by all cells after physiological stimulation is of an increase in the concentration of calcium ions in the cytoplasm [1]. The astrocyte located near synapse of neighboring neuron responds to glutamate, ATP, etc., with evaluation of calcium oscillations. Excitatory glutamate released by neuron can activate not only the neighboring neuron but also glutamate receptor of astrocyte increasing the calcium ion concentration [7]. It is shown that calcium oscillation is not only the basic way of astrocyte excitement but also the basic mode of biological information exchange between the neuron and

astrocyte [8, 9]. In contrast with the neuron, astrocyte generates neuronal-dependent and spontaneous calcium oscillation, which is similar to the glutamate-dependent calcium waves, releasing glutamate affected by the neuron [10].

In the last decades, based on biological background of calcium oscillation in the neuron and astrocyte, a wide variety of mathematical models are constructed to investigate in detail the stability and dynamical mechanism of calcium activities in the neuron and astrocyte [11–15]. It has long been appreciated that the location of the bifurcations is of great interest in many dynamical systems and it has emerged as a major component in the analysis of mathematical models. It is well known that there are three traditional software packages (Matlab and AUTO) that are used to solve the continuation and the bifurcation of mathematical models [16, 17]. Therefore, flexible, yet computable, and dynamical analysis of calcium oscillations (separately, firing, bursting, quasi-periodic, and chaotic activity), as well as waves involved in the biological process in the CNS is required. Regular oscillatory activity is classified into firing and bursting, which is based on the dynamics of fast and slow systems [18]. For quasiperiodic and chaotic activity, it refers to seemingly random irregular motion that occurs in a deterministic system described by deterministic theory with uncertainty and unpredictability. In a large number of the free calcium oscillation experiments of the neuron and astrocyte, it was found that bursting is of an important role in information transmission [19–23].

There is strong experimental evidence for bidirectional information communication between the glia and neuron in biological signaling pathway [22]. As the major neurotransmitter, glutamate released from the neuron may have an autonomous effect on the adjacent glia by the intracellular calcium oscillations. Trying to recognize the dynamical mechanism of different phenomena of calcium oscillatory activities, based on the bidirectional signaling pathway between the neuron and glia of the CNS in different brain regions, critical and constructive analysis of existing published review literatures are provided both from experimental and theoretical point of view [24–26]. The establishment of the first dynamic model describing the process of generating neuronal firing activities began with a series of work by Hodgkin and Huxley in the 1950s. Based on the bioelectric theory and giant axon experiment, they

successfully established a mathematical neuron model for the first time through a series of nonlinear differential equations that reproduce different oscillatory patterns of neuron observed in the experiment. On this neurophysiological basis of their finds, many other mathematical models associated with cell membrane ion channels were established with purpose of describing rich firing oscillations of different types of neurons in the experiment [27]. Although these neuron models are the mathematical reduction of the HH model, they can simulate the experimental phenomena from a wide variety of cell types and thus have been extensively studied [28].

In order to understand the dynamical mechanisms involved in spontaneous Ca^{2+} oscillations in the astrocyte, Lavrentovich and Hemkin proposed a dynamical model of how the different types of Ca^{2+} oscillations occur in real astrocyte in the CNS [29]. Spontaneous Ca^{2+} oscillations have been extensively observed in the cytosol of the glia both in situ and in vivo originating in the hippocampus and thalamus of the brain [30]. Although the functional and structural perspective of spontaneous behaviors is not yet well understood, many physiological experimental results indicate that, in conjunction with outer input, spontaneous Ca^{2+} oscillations may help correlate the connection between the glia and neuron. It is known that different types of these oscillatory activities in astrocytes vary with bifurcation principles, stability analysis, and simulations that underlie activation and inhibition of regular and chaotic Ca^{2+} oscillations which should be discussed in detail both from theoretical and experimental point of view.

2. Model Description

In this study, we analyze a two-compartment astrocyte model proposed by Lavrentovich and Hemkin as an example of a system that exhibits regular and chaotic calcium oscillations. This model involves currents such as the free calcium concentration (Ca_{cyt}) in cytosol and in ER (Ca_{er}), and IP_3 concentration as intracellular messenger in astrocyte (IP_3). V_{CICR} and V_{serca} denote calcium flux from ER to cytosol and sarcoplasmic reticulum ATPase that reach ER from cytosol, respectively [31–34]. The model can be described as follows:

$$\begin{cases} \frac{d\text{Ca}_{\text{cyt}}}{dt} = v_{\text{in}} + V_{\text{CICR}} - 0.5\text{Ca}_{\text{cyt}} - v_{\text{M2}} \left(\frac{\text{Ca}_{\text{cyt}}^2}{\text{Ca}_{\text{cyt}}^2 + 10^{-2}} \right) + 0.5(\text{Ca}_{\text{er}} - \text{Ca}_{\text{cyt}}), \\ \frac{d\text{Ca}_{\text{er}}}{dt} = v_{\text{M2}} \left(\frac{\text{Ca}_{\text{cyt}}^2}{\text{Ca}_{\text{cyt}}^2 + k_2^2} \right) - k_f(\text{Ca}_{\text{er}} - \text{Ca}_{\text{cyt}}) - V_{\text{CICR}}, \\ \frac{d\text{IP}_3}{dt} = 0.05 \left(\frac{\text{Ca}_{\text{cyt}}^2}{\text{Ca}_{\text{cyt}}^2 + k_p^2} \right) - 0.08 \text{IP}_3, \end{cases} \quad (1)$$

where

$$V_{CICR} = 4(Ca_{er} - Ca_{cyt})v_{M3} \left(\frac{0.27^n Ca_{cyt}^n}{(Ca_{cyt}^n + 0.27^n)(Ca_{cyt}^n + k_{CaI}^n)} \right) \times \left(\frac{IP_3^m}{IP_3^m + k_{ip3}^m} \right). \quad (2)$$

Since the parameter v_{in} is calcium ion flux from outer extracellular space through membrane of the astrocyte and into the cytosol, in this work, we choose v_{in} to be the bifurcation parameter to control the spontaneous calcium oscillatory activities. The other physiological parameter values are $v_{M3} = 40 \text{ s}^{-1}$, $k_{CaI} = 0.27 \text{ } \mu\text{M s}^{-1}$, $k_{ip3} = 0.1 \text{ } \mu\text{M s}^{-1}$, $v_{M2} = 15 \text{ } \mu\text{M s}^{-1}$, $k_2 = 0.1 \text{ } \mu\text{M}$, $k_f = 0.5 \text{ } \mu\text{M s}^{-1}$, and $k_p = 0.164 \text{ } \mu\text{M}$.

3. Stability Analysis and Bifurcation of Equilibrium

Let $x = (x, y, z)^T = (Ca_{cyt}, Ca_{er}, IP_3)^T$, $r = v_{in}$, system (1) can be rewritten as

$$\begin{cases} \dot{x} = \frac{1}{2}y + (r - x) - 15 \quad d1 - 11.4x^n d2z^m d3, \\ \dot{y} = \frac{1}{2}(x - y) + 15 \quad d1 + 11.4x^n d2z^m d3, \\ \dot{z} = 10^{-2}(5x^2 d4 - 8z), \end{cases} \quad (3)$$

where $d1 = x^2/(x^2 + 10^{-2})$, $d2 = (x-y)/(x^n + 7 \times 10^{-2})$, $d3 = 1/(z^m + 6 \times 10^{-3})$, and $d4 = 1/(x^2 + 27 \times 10^{-3})$.

Equilibrium of (3) takes the form

$$\begin{cases} x = 2r, \\ z = \frac{5}{8}x^2 d4, \\ y = 2(15 \quad d1 - 11.4x^{2.02}z^{2.2}d2 \quad d3 + r). \end{cases} \quad (4)$$

Let $(x_0, y_0, z_0)^T$ be the root of (3) and $x_1 = x - x_0$, $y_1 = y - y_0$, and $z_1 = z - z_0$, and we are able to obtain the following equations:

$$\begin{cases} \dot{x}_1 = r - x + \frac{1}{2} \left(2y - \frac{p_2 x^2}{d2} \right) - \frac{p_3 x^{2.02} z^{2.2} (x - y)}{d2 \quad d3}, \\ \dot{y}_1 = \frac{1}{2}(x - y + p_2 d1) + p_3 x^n d2 p_3 d3, \\ \dot{z}_1 = 10^{-2}(5x^2 d4 - 8z). \end{cases} \quad (5)$$

The Jacobian matrix is

$$A = (a_{ij})_{3 \times 3}, \quad i, j = 1, 2, 3, \quad (6)$$

where

$$a_{11} = p_2 d1 - q_1 \frac{p_3 - p_4 q_2}{\sigma} + p_5 d2 \quad d3 \frac{1}{\sigma} - 1,$$

$$a_{12} = \frac{p_3 q_1}{\sigma} + \frac{1}{2},$$

$$a_{13} = \frac{p_1 x^{2.02} q_2 z^{3.04} d3}{\sigma} - \frac{p_1 q_1 q_2}{\sigma z},$$

$$a_{21} = -x p_1 + d1 p_2 + \frac{p_3 q_1 + p_4 q_2}{\sigma x} - \frac{p_5 x^{3.04} q_2 q_1 d1}{\sigma} + \frac{1}{2},$$

$$a_{22} = -\frac{p_3 q_1}{\sigma} - \frac{1}{2},$$

$$a_{23} = -\frac{d3 p_1 x^{2.02} q_2 z^{3.04}}{\sigma} + \frac{p_1 q_1 q_2}{\sigma z},$$

$$a_{31} = x \quad d1 - 10^{-1} x^3 p_1 q_2,$$

$$a_{32} = 0,$$

$$a_{33} = -\frac{2}{25},$$

$$\sigma = \frac{d2}{d3},$$

$$p_1 = 25,$$

$$p_2 = 30,$$

$$p_3 = 11,$$

$$p_4 = 23,$$

$$p_5 = 46,$$

$$q_1 = x^n z^m,$$

$$q_2 = x - y. \quad (7)$$

Clearly, the characteristic equation of system (5) is

$$\lambda^3 + Q_3 \lambda^2 + Q_2 \lambda + Q_1 = 0. \quad (8)$$

The Hurwitz matrix with the coefficients Q_i of the matrix characteristic polynomial can be rewritten as follows:

$$\begin{aligned} H_1 &= (Q_1), \\ H_2 &= \begin{pmatrix} Q_1 & 1 \\ Q_3 & Q_2 \end{pmatrix}. \end{aligned} \quad (9)$$

By simple computation, one can easily verify that the eigenvalues are negative or of negative real parts if the determinants of Hurwitz matrix are positive:

$$\text{de } t(\mathbf{H}_i) > 0, \quad i = 1, 2, 3. \quad (10)$$

Now, motivating the Routh–Hurwitz method, we analyze the bifurcation points of system (4) for the parameter r (that is, v_{in}):

$$\begin{aligned} r_1 &= 0.0193, \\ r_2 &= 0.0772. \end{aligned} \quad (11)$$

Summarizing the above stability analysis, we have linearized the model at the origin of portrait state and the following results can be described as follows:

- (1) System (5) has a stable node as $0r < 0.0193$
- (2) System (5) has a nonhyperbolic equilibrium $O_1 = (0.03858, 2.66776, 0.03277)$ as $r = 0.0193$
- (3) System (5) has a saddle node as $0.0193r < 0.0772$
- (4) System (5) has a nonhyperbolic equilibrium $O_2 = (0.15432, 0.675115, 0.29351)$ as $r = 0.0772$
- (5) System (5) has a stable node as $r > 0.0772$

We denote $r = r_0$, $x_1 = x - x_0$, $y_1 = y - y_0$, $z_1 = z - z_0$, and $r_1 = r - r_0$, and the equilibrium of system (5) is (x_0, y_0, z_0) . For the purpose of applying the Hopf bifurcation theory, a new variable r_1 is added to the model, where $dr_1/dt = 0$. The system takes the form

$$\begin{cases} \dot{x}_1 = (r_1 + r_0) - d2 \quad d3p_3x^{2.02}z^{2.2}q_2 - (p_1 - 1)d1 - \frac{1}{2}p_2, \\ \dot{y}_1 = \frac{1}{2} + (p_1 - 1)d1 + p_3q_1q_1d1 \quad d3, \\ \dot{z}_1 = -(z_1 + z_0) \frac{x^2}{x^2 + Q_3}, \\ \dot{r}_1 = 0. \end{cases} \quad (12)$$

For $r_1 = 0$, the point $(0, 0, 0, 0)$ is the equilibrium of system (12), which has the same stability as the one in (3). For $r_0 = 0.01929$, the Jacobian matrix of system (12) is

$$\begin{pmatrix} -6 \times 10 & 7 \times 10^{-1} & 4 \times 10 & 1 \\ 6 \times 10 & -7 \times 10^{-1} & -4 \times 10 & 0 \\ 10^{-1} & 0 & -8 \times 10^{-2} & 0 \\ 0 & 0 & 0 & 0 \end{pmatrix}. \quad (13)$$

Four eigenvalues of (5) are $\xi_1 = -58.0969$, $\xi_2 = 0.0225i$, $\xi_3 = -0.0225i$, and $\xi_4 = 0$, respectively. Therefore, we can have the associated eigenvector:

$$\begin{pmatrix} \mathbf{x}_* \\ \mathbf{y}_* \\ \mathbf{z}_* \\ \mathbf{r}_* \end{pmatrix} = \mathbf{U} \begin{pmatrix} \mathbf{u} \\ \mathbf{v} \\ \mathbf{w} \\ \mathbf{s} \end{pmatrix}. \quad (14)$$

Therefore, system (12) can be written as

$$\begin{pmatrix} \dot{u} \\ \dot{v} \\ \dot{w} \\ \dot{s} \end{pmatrix} = \mathbf{A} \begin{pmatrix} \mathbf{u} \\ \mathbf{v} \\ \mathbf{w} \\ \mathbf{s} \end{pmatrix} + \mathbf{S}, \quad (15)$$

where

$$\begin{aligned} \mathbf{A} &= \begin{pmatrix} -38 & 0 & 0 & 0 \\ 0 & 0 & -2 \times 10^{-2} & 0 \\ 0 & 2 \times 10^{-2} & 0 & 0 \\ 0 & 0 & 0 & 0 \end{pmatrix}, \\ \mathbf{S} &= \mathbf{U}^{-1} \begin{pmatrix} \mathbf{f}_1 \\ \mathbf{f}_2 \\ \mathbf{f}_3 \\ 0 \end{pmatrix} - \mathbf{A} \begin{pmatrix} \mathbf{u} \\ \mathbf{v} \\ \mathbf{w} \\ \mathbf{s} \end{pmatrix}. \end{aligned} \quad (16)$$

Next, we analyze the center manifold of system (12). By simple computation, we have

$$\mathbf{W}_{\text{loc}}^c(\mathbf{O}_1) = \{(\mathbf{u}, \mathbf{v}, \mathbf{w}, \mathbf{s}) \in \mathbb{R}^4 \mid \mathbf{u} = \mathbf{h}^*(\mathbf{v}, \mathbf{w}, \mathbf{s}), \mathbf{Dh}^* = 0\}. \quad (17)$$

Substituting (17) into (15), we have

$$\begin{pmatrix} \mathbf{h}^*(\mathbf{v}, \mathbf{w}, \mathbf{s}) \\ \dot{v} \\ \dot{w} \\ \dot{s} \end{pmatrix} = \mathbf{A} \begin{pmatrix} \mathbf{h}^*(\mathbf{v}, \mathbf{w}, \mathbf{s}) \\ \mathbf{v} \\ \mathbf{w} \\ \mathbf{s} \end{pmatrix} + \mathbf{S}. \quad (18)$$

Let $h(v, w, s) = av^2 + bw^2 + cs^2 + dv \quad w + evs + fws + \dots$, and the center manifold of (12) is

$$\mathbf{N}(\mathbf{h}) = 0, \quad (19)$$

where $a = 0.000567$, $b = -0.1828$, $c = -1.95096$, $d = 0.049818$, $e = -1638.5116$, and $f = -0.75265$. Then, system (12), which is confined to the manifold, is

$$\begin{pmatrix} \dot{v} \\ \dot{w} \end{pmatrix} = \mathbf{B} \begin{pmatrix} \mathbf{v} \\ \mathbf{w} \end{pmatrix} + \begin{pmatrix} \mathbf{f}^*(\mathbf{v}, \mathbf{w}) \\ \mathbf{f}^*(\mathbf{v}, \mathbf{w}) \end{pmatrix}. \quad (20)$$

Thus, we can obtain

$$\mathbf{d} = \frac{\mathbf{d}(\text{Re}(\xi(s)))}{\mathbf{ds}} \Big|_{\mathbf{O}_1} < 0. \quad (21)$$

Having applied the above formulas and computations, the sufficient conditions for stability can be obtained.

Conclusion 1. System (3) has a subcritical Hopf bifurcation at $r_0 = 0.01929$. If $r > r_0$, the equilibrium loses its stability, which means that a periodic solution occurs and the system oscillates.

Using the same notations above, we construct the eigenvalues of equilibrium point $O_2 = (0, 0, 0, 0)$ as

$\xi_1 = -0.08959$, $\xi_2 = 3.3864i$, $\xi_3 = -3.3864i$, and $\xi_4 = 0$, respectively, as $r_0 = 0.07716$. On the center manifold, system (12) has the form

$$\begin{pmatrix} \dot{u} \\ \dot{v} \\ \dot{w} \\ \dot{s} \end{pmatrix} = \mathbf{U}^{-1} \begin{pmatrix} \mathbf{u} \\ \mathbf{v} \\ \mathbf{w} \\ \mathbf{s} \end{pmatrix} + \mathbf{S}, \quad (22)$$

where

$$\mathbf{S} = \mathbf{U}^{-1} \mathbf{f} - \mathbf{B} \begin{pmatrix} \mathbf{u} \\ \mathbf{v} \\ \mathbf{w} \\ \mathbf{s} \end{pmatrix}. \quad (23)$$

Note that, on the above center manifold of the system, we have

$$\mathbf{N}(\mathbf{h}) = 0. \quad (24)$$

In this case, the system confined to the center manifold is as follows:

$$\begin{aligned} \mathbf{a} &= 6 \times 10^{-1} \mathbf{f}_1 + 2 \times 10^{-2} \mathbf{f}_2 = -2265.4 > 0, \\ \mathbf{d} &= -7 \times 10^{-4} < 0. \end{aligned} \quad (25)$$

Based on the above analysis and computation, we can obtain the following result:

Conclusion 2. System (3) has a supercritical Hopf bifurcation when $r_0 = 0.07716$. If $r < r_0$, the equilibrium becomes unstable, system (3) begins to oscillate.

4. Numerical Examples

In this section, we study the effects of calcium ion flux from outer space through membrane of astrocyte and into cytosol on the dynamics of full system. Regular Ca^{2+} oscillations of the full system as v_{in} increases from $v_{\text{in}} = 0.02 \mu\text{M/s}$ and $v_{\text{in}} = 0.04 \mu\text{M/s}$ (blue curve) are plotted in Figure 1. These figures are the result achieved by solving the ordinary differential equations in model of Lavrentovich and Hemkin using Matlab software.

As expected, regular periodic oscillations in cytosolic are generated from numerical simulations. In Figure 1, time evolution of Ca_{cyt} are illustrated for two examples of regular calcium oscillations, that is, a simple spike oscillation with a period of the order of 2000 s at $v_{\text{in}} = 0.02 \mu\text{M/s}$ (Figure 1(a)), a burst oscillation with a period of the order of 400 s at $v_{\text{in}} = 0.04 \mu\text{M/s}$ (Figure 1(c)). The corresponding three-dimensional phase portrait diagram in (x, y, z) -plane for $v_{\text{in}} = 0.02 \mu\text{M/s}$ (Figure 1(b)) and $v_{\text{in}} = 0.04 \mu\text{M/s}$ (Figure 1(d)) are also plotted, respectively. In Figure 1(c), free calcium ion flux from the

outer space into the cytosol caused a large initial peak, which is followed by a small one. In this case, the 3D phase portrait diagram in (x, y, z) -plane is also significantly different.

Based on the stability analysis, we concluded that, in this case, the model has a saddle node for the value of v_{in} . It is seen that the number of peak and the magnitude of each burst increase accordingly, as shown in Figure 2 as $v_{\text{in}} = 0.045 \mu\text{M/s}$. Compared to spike oscillation, burst is found to be one of the elementary modes in many cell types, including the neuron and glia. Unlike the case of $v_{\text{in}} = 0.04 \mu\text{M/s}$, the free calcium ion current from the outer space into the cytosol caused a large initial peak, which is followed by three small ones, as shown in Figure 2(a). At the same time, the phase portrait diagram in (x, y, z) -plane is rotated at least three times. In order to study the variation of this regular oscillations in detail, two examples of chaotic burst spontaneous Ca^{2+} oscillations are also performed, as shown in Figure 3.

Chaotic oscillation means the system is of total confusion with no order. Figures 1(c), 2(a), 3(a), and 3(c) show the corresponding time series of Ca_{cyt} for two parameter values of $v_{\text{in}} = 0.05025 \mu\text{M/s}$ and $v_{\text{in}} = 0.050252 \mu\text{M/s}$, respectively, for which the number of peak and the magnitude of each burst increase with no order, indicating a state of total confusion. In Figures 3(b) and 3(d), the phase portrait diagram simultaneously exhibits the corresponding attractor, which has been rarely reported in the previous literatures in this astrocyte model. The main difference between the two chaotic burst calcium oscillations is that the order of the chaotic burst oscillation in Figure 3(a) is less than that of the chaotic burst oscillation in Figure 3(c) in both frequency and amplitude.

As the parameter v_{in} increases to $v_{\text{in}} = 0.050254 \mu\text{M/s}$, it is observed that each burst comprises two similar spike which means that a small correlation exists between each burst. Compared with the previous finds, in this case, the time evolution and the phase portrait would develop into the long-term depression, as shown in Figures 4(a) and 4(b), respectively. We can predict that as the parameter v_{in} increases further, a simple spike calcium oscillation would occur. To further investigate the generation with respect to the parameter v_{in} , we perform a detailed Hopf bifurcation analysis to the model.

Bifurcation diagram of the whole system with respect to the parameter v_{in} versus Ca_{cyt} (Ca_{er}) is displayed in Figure 5(a) and 5(b). The system begins to oscillate due to a subcritical Hopf bifurcation at point H1 with $v_{\text{in}} = 0.01929 \mu\text{M/s}$; meanwhile, a stable limit cycle occurs. With the parameter increasing further, the oscillatory activities terminate and the steady state turns stable again after the parameter $v_{\text{in}} = 0.07716 \mu\text{M/s}$ at the supercritical Hopf bifurcation point H2. The solid (dashed) curve in Figure 3 denotes the stable (unstable) equilibrium of the steady state. The Matlab software package enables one to simulate the time series and the corresponding phase portrait diagram to verify the effectiveness of our previous prediction.

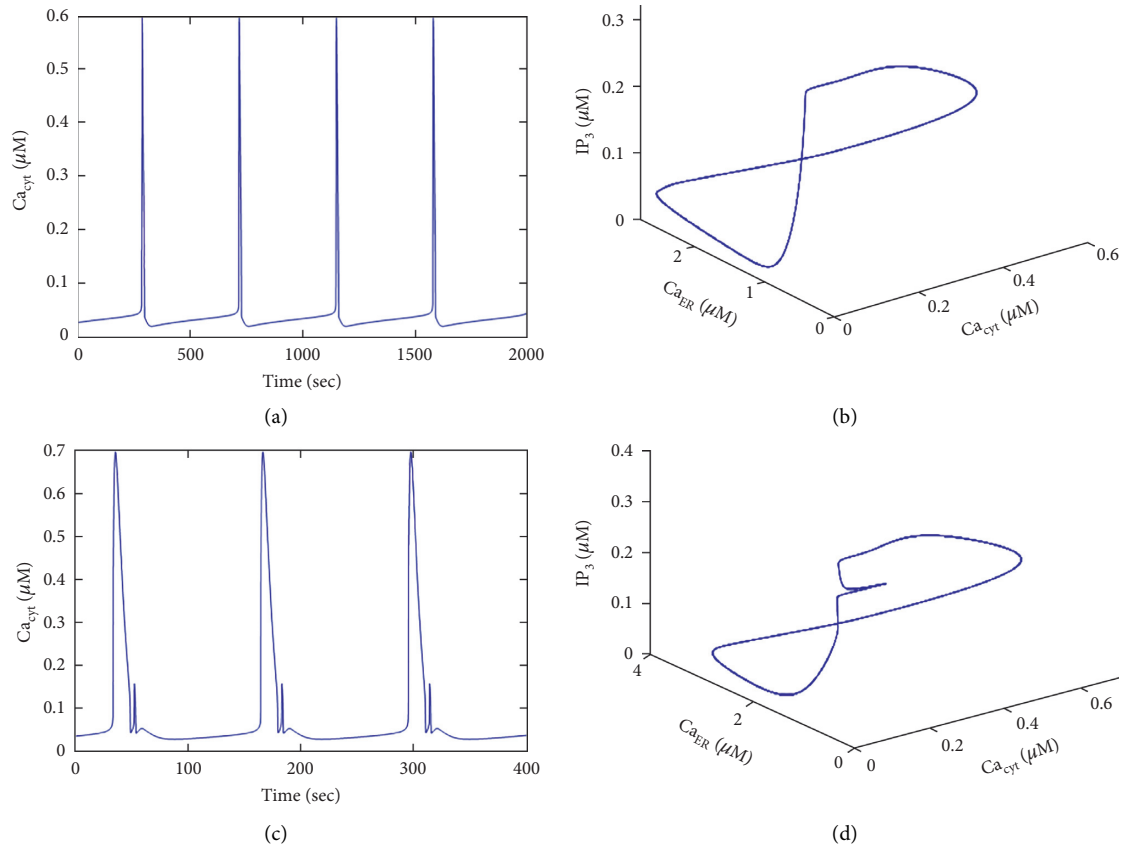


FIGURE 1: Time evolution of regular spontaneous Ca^{2+} oscillations in astrocytes. (a) Simple spike Ca^{2+} oscillations for $v_{in} = 0.02 \mu M/s$. (b) 3D phase portrait diagram in (x, y, z) -plane for $v_{in} = 0.02 \mu M/s$. (c) Burst Ca^{2+} oscillations for $v_{in} = 0.04 \mu M/s$. (d) 3D phase portrait diagram in (x, y, z) -plane for $v_{in} = 0.04 \mu M/s$.

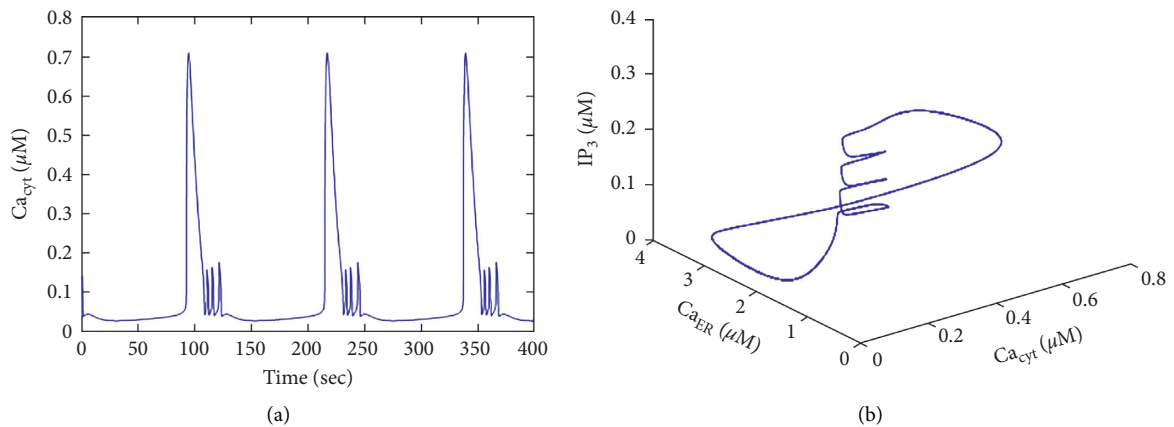


FIGURE 2: Time evolution of regular burst spontaneous Ca^{2+} oscillations in astrocytes. (a) $v_{in} = 0.045 \mu M/s$. (b) 3D phase portrait diagram in (x, y, z) -plane for $v_{in} = 0.045 \mu M/s$.

5. Summary

In summary, we have theoretically analyzed a spontaneous Ca^{2+} oscillatory model in astrocyte based on the stability and Hopf bifurcation theory. Firstly, we obtained the sufficient conditions to ensure the model to be stable and the existence of Hopf bifurcation by increasing the parameter v_{in} and the

calcium ion current from extracellular space through the membrane of astrocyte and into the cytosol. As v_{in} is slightly more than a critical value, these spontaneous Ca^{2+} oscillations will disappear. Moreover, we concluded that a sub-critical Hopf bifurcation point and a supercritical Hopf bifurcation point may be important for the occurrence of spontaneous Ca^{2+} oscillations in astrocytes by applying the

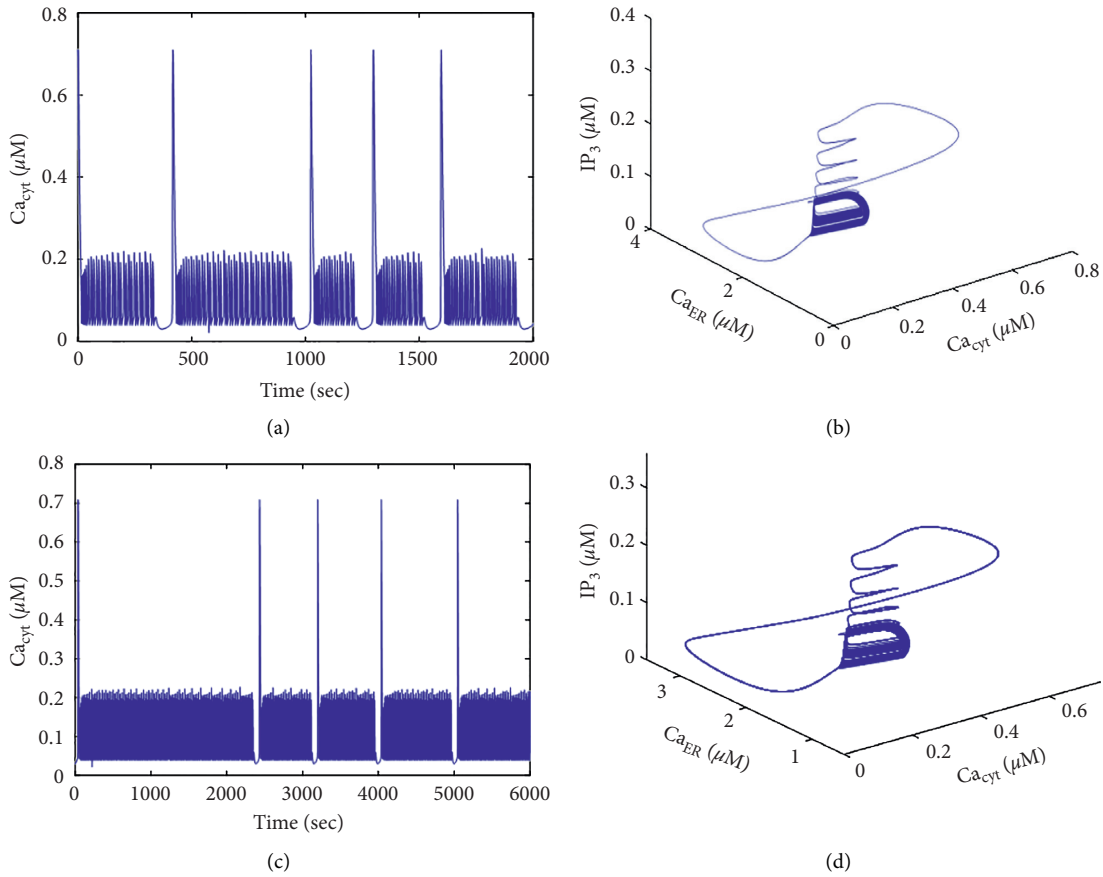


FIGURE 3: Time evolution of chaotic burst spontaneous Ca^{2+} oscillations in astrocytes. (a) $v_{in} = 0.05025 \mu M/s$. (b) 3D phase portrait diagram in (x, y, z) -plane for $v_{in} = 0.05025 \mu M/s$. (c) $v_{in} = 0.050252 \mu M/s$. (d) 3D phase portrait diagram in (x, y, z) -plane for $v_{in} = 0.050252 \mu M/s$.

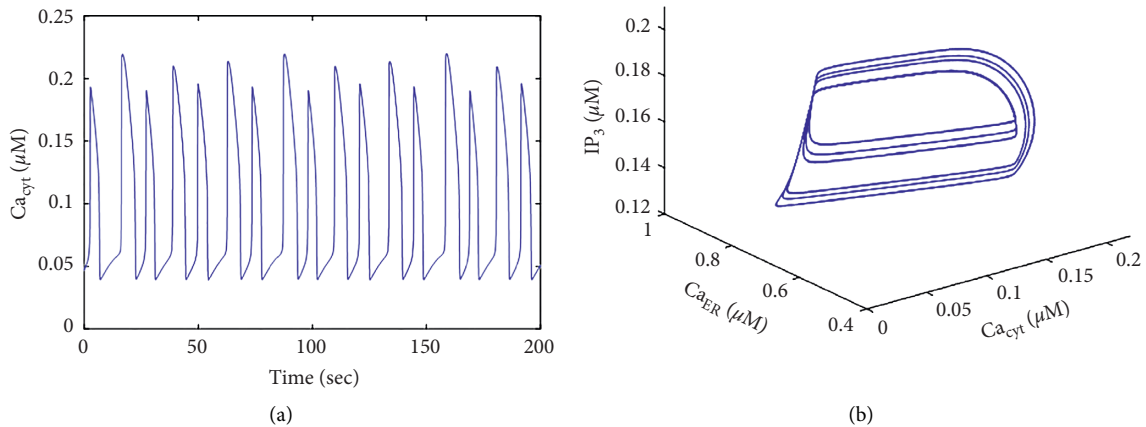


FIGURE 4: Time evolution of regular burst spontaneous Ca^{2+} oscillations in astrocytes. (a) $v_{in} = 0.050254 \mu M/s$. (b) 3D phase portrait diagram in (x, y, z) -plane for $v_{in} = 0.050254 \mu M/s$.

Hopf bifurcation theorem. Moreover, the domain of oscillatory activities with respect to v_{in} is determined by computation using the Hurwitz stability criterion. Finally, based on our theoretical analysis, we give some numerical examples to illustrate the regular and chaotic spontaneous Ca^{2+} oscillations at some certain parameter values. These

results demonstrate and enhance our understanding of the generation and transition mechanisms of complex Ca^{2+} oscillations in the astrocyte. These results may be potentially able to better understand the bidirectional signaling pathway between the neuron and glia from a mathematical point of view. Future experimental studies should be undertaken to

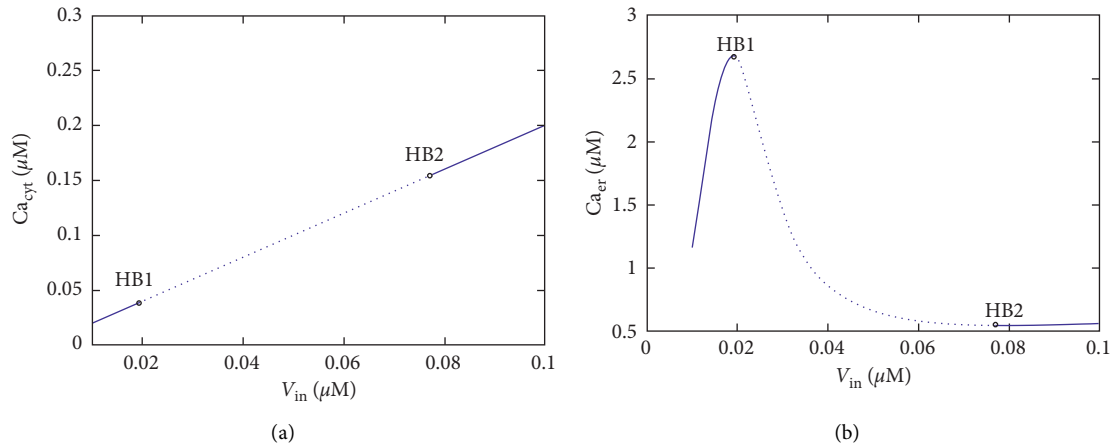


FIGURE 5: (a) Bifurcation diagram of the whole system versus the parameter v_{in} in the (v_{in}, Ca_{cyt}) -plane. (b) Bifurcation diagram of the whole system versus the parameter v_{in} in the (v_{in}, Ca_{er}) -plane. The points HB1 and HB2 represent the subcritical Hopf bifurcation point and the supercritical Hopf bifurcation point, respectively.

discover mechanisms underlying spontaneous Ca^{2+} oscillations in the astrocyte in detail.

Data Availability

All the data utilized in this study have been included within the article, and the sources from where they were adopted were cited accordingly.

Conflicts of Interest

All authors declare no conflicts of interest.

Authors' Contributions

All authors read and approved the last version of the manuscript.

Acknowledgments

This work was supported by the Natural Science Foundation of China under Grant no. 11872084 and Natural Science Foundation of the Anhui Higher Education Institutions of China under Grant nos. KJ2016SD54 and KJ2017A460.

References

- [1] M. V. Sofroniew and H. V. Vinters, "Astrocytes: biology and pathology," *Acta Neuropathologica*, vol. 119, no. 1, pp. 7–35, 2010.
- [2] B. Reynolds and S. Weiss, "Generation of neurons and astrocytes from isolated cells of the adult mammalian central nervous system," *Science*, vol. 255, no. 5052, pp. 1707–1710, 1992.
- [3] N. J. Abbott, L. Rönnbäck, and E. Hansson, "Astrocyte-endothelial interactions at the blood-brain barrier," *Nature Reviews Neuroscience*, vol. 7, no. 1, pp. 41–53, 2006.
- [4] J. W. Fawcett and R. A. Asher, "The glial scar and central nervous system repair," *Brain Research Bulletin*, vol. 49, no. 6, pp. 377–391, 1999.
- [5] V. Parpura, T. A. Basarsky, F. Liu, K. Jeftinija, S. Jeftinija, and P. G. Haydon, "Glutamate-mediated astrocyte-neuron signalling," *Nature*, vol. 369, no. 6483, pp. 744–747, 1994.
- [6] E. A. Newman and K. R. Zahs, "Modulation of neuronal activity by glial cells in the retina," *The Journal of Neuroscience*, vol. 18, no. 11, pp. 4022–4028, 1998.
- [7] A. Cornell-Bell, S. Finkbeiner, M. Cooper, and S. Smith, "Glutamate induces calcium waves in cultured astrocytes: long-range glial signaling," *Science*, vol. 247, no. 4941, pp. 470–473, 1990.
- [8] V. V. Matrosov and V. B. Kazantsev, "Bifurcation mechanisms of regular and chaotic network signaling in brain astrocytes," *Chaos: an Interdisciplinary Journal of Nonlinear Science*, vol. 21, no. 2, Article ID 023103, 2011.
- [9] M. V. Sofroniew, "Molecular dissection of reactive astrogliosis and glial scar formation," *Trends in Neurosciences*, vol. 32, no. 12, pp. 638–647, 2009.
- [10] M. Pekny and M. Nilsson, "Astrocyte activation and reactive gliosis," *Glia*, vol. 50, no. 4, pp. 427–434, 2005.
- [11] M. Zonta, M. C. Angulo, S. Gobbo et al., "Neuron-to-astrocyte signaling is central to the dynamic control of brain microcirculation," *Nature Neuroscience*, vol. 6, no. 1, pp. 43–50, 2003.
- [12] D. E. Postnov, R. N. Koreschkov, N. A. Brazhe, A. R. Brazhe, and O. V. Sosnovtseva, "Dynamical patterns of calcium signaling in a functional model of neuron-astrocyte networks," *Journal of Biological Physics*, vol. 35, no. 4, pp. 425–445, 2009.
- [13] J. J. Wade, L. J. McDaid, J. Harkin, V. Crunelli, and J. A. Kelso, "Bidirectional coupling between astrocytes and neurons mediates learning and dynamic coordination in the brain: a multiple modeling approach," *PLoS One*, vol. 6, no. 12, Article ID e29445, 2011.
- [14] G. Karimi, M. Ranjbar, M. Amirian, and A. Shahim-aeen, "A neuromorphic real-time VLSI design of Ca^{2+} dynamic in an astrocyte," *Neurocomputing*, vol. 272, no. 10, pp. 197–203, 2018.
- [15] S. Mederos, C. Gonzalezarias, G. Perea et al., "Astrocyte-neuron networks: a multilane highway of signaling for homeostatic brain function," *Frontiers in Synaptic Neuroscience*, vol. 6, p. 32343, 2018.
- [16] B. Ermentrout, *Simulating, Analyzing, and Animating Dynamical Systems: A Guide to XPPAUT for Researchers and*

- Students*, Society for Industrial and Applied Mathematics, Philadelphia, PA, USA, 2002.
- [17] Y. A. Kuznetsov and V. V. Levitin, *CONTENT: A Multiplatform Environment for Analyzing Dynamical Systems*, Dynamical Systems Laboratory, Amsterdam, The Netherlands, 1997.
- [18] Y.-X. Li and J. Rinzel, "Equations for InsP3 receptor-mediated $[Ca^{2+}]_i$ oscillations derived from a detailed kinetic model: a Hodgkin-Huxley like formalism," *Journal of Theoretical Biology*, vol. 166, no. 4, pp. 461–473, 1994.
- [19] Q. Ji and Y. Lu, "Bifurcations and continuous transitions in a nonlinear model of intracellular calcium oscillations," *International Journal of Bifurcation and Chaos*, vol. 23, no. 02, p. 1350033, 2013.
- [20] Q. Ji, Y. Zhou, Z. Yang, and X. Meng, "Evaluation of bifurcation phenomena in a modified Shen-Larter model for intracellular Ca^{2+} bursting oscillations," *Nonlinear Dynamics*, vol. 84, no. 3, pp. 1281–1288, 2016.
- [21] F. Oschmann, H. Berry, K. Obermayer, and K. Lenk, "From in silico astrocyte cell models to neuron-astrocyte network models: a review," *Brain Research Bulletin*, vol. 136, pp. 76–84, 2018.
- [22] V. Matrosov, S. Gordleeva, N. Boldyreva, E. Ben-Jacob, V. Kazantsev, and M. De Pittà, "Emergence of regular and complex calcium oscillations by inositol 1, 4, 5-trisphosphate signaling in astrocytes," *Springer Series in Computational Neuroscience*, vol. 2019, pp. 151–176, 2019.
- [23] M. Enomoto and S. Kawazu, "Blockage of spontaneous Ca^{2+} oscillation causes cell death in intraerythrocytic *Plasmodium falciparum*," *PLoS One*, vol. 7, no. 7, Article ID e39499, 2012.
- [24] M. Zonta and G. Carmignoto, "Calcium oscillations encoding neuron-to-astrocyte communication," *Journal Physiology-Paris*, vol. 96, no. 3-4, pp. 193–198, 2002.
- [25] S. Zeng, B. Li, S. Zeng, and S. Chen, "Simulation of spontaneous Ca^{2+} oscillations in astrocytes mediated by voltage-gated calcium channels," *Biophysical Journal*, vol. 97, no. 9, pp. 2429–2437, 2009.
- [26] C. Agulhon, T. A. Fiacco, and K. D. McCarthy, "Hippocampal short- and long-term plasticity are not modulated by astrocyte Ca^{2+} signaling," *Science*, vol. 327, no. 5970, pp. 1250–1254, 2010.
- [27] Y. Otsu, K. Couchman, D. G. Lyons et al., "Calcium dynamics in astrocyte processes during neurovascular coupling," *Nature Neuroscience*, vol. 18, no. 2, pp. 210–218, 2015.
- [28] M. Naeem, L. J. McDaid, J. Harkin, J. J. Wade, and J. Marsland, "On the role of astroglial syncytia in self-repairing spiking neural networks," *IEEE Transactions on Neural Networks and Learning Systems*, vol. 26, no. 10, pp. 2370–2380, 2015.
- [29] M. Lavrentovich and S. Hemkin, "A mathematical model of spontaneous calcium (II) oscillations in astrocytes," *Journal of Theoretical Biology*, vol. 251, no. 4, pp. 553–560, 2008.
- [30] B. Chander and V. Chakravarthy, "A computational model of neuro-glio-vascular loop interactions," *PLoS ONE*, vol. 7, Article ID e48802, 2012.
- [31] J. Li, J. Tang, J. Ma, M. Du, R. Wang, and Y. Wu, "Dynamic transition of neuronal firing induced by abnormal astrocytic glutamate oscillation," *Scientific Reports*, vol. 6, Article ID 32343, 2016.
- [32] J. Li, Y. Xie, Y. Yu, M. Du, R. Wang, and Y. Wu, "A neglected GABAergic astrocyte: calcium dynamics and involvement in seizure activity," *Science China Technological Sciences*, vol. 60, no. 7, pp. 1003–1010, 2017.
- [33] T. Manninen, R. Havela, M. Linne et al., "Computational models for calcium-mediated astrocyte functions," *Frontiers in Computational Neuroscience*, vol. 201814 pages, 2018.
- [34] H. Wang, Q. Wang, and Q. Lu, "Bursting oscillations, bifurcation and synchronization in neuronal systems," *Chaos, Solitons & Fractals*, vol. 44, no. 8, pp. 667–675, 2011.

Research Article

Resolvability in Subdivision of Circulant Networks $C_n[1, k]$

Jianxin Wei ¹, Syed Ahtsham Ul Haq Bokhary,² Ghulam Abbas,² and Muhammad Imran³

¹School of Mathematics and Statistics Science, Ludong University, Yantai 264025, Shandong, China

²Centre for Advanced Studies in Pure and Applied Mathematics, Bahauddin Zakariya University, Multan, Pakistan

³Department of Mathematical Sciences, United Arab Emirates University, P.O. Box 15551, Al Ain, UAE

Correspondence should be addressed to Jianxin Wei; wjx0426@ldu.edu.cn

Received 25 June 2020; Accepted 25 August 2020; Published 14 September 2020

Academic Editor: M. Javaid

Copyright © 2020 Jianxin Wei et al. This is an open access article distributed under the Creative Commons Attribution License, which permits unrestricted use, distribution, and reproduction in any medium, provided the original work is properly cited.

Circulant networks form a very important and widely explored class of graphs due to their interesting and wide-range applications in networking, facility location problems, and their symmetric properties. A resolving set is a subset of vertices of a connected graph such that each vertex of the graph is determined uniquely by its distances to that set. A resolving set of the graph that has the minimum cardinality is called the basis of the graph, and the number of elements in the basis is called the metric dimension of the graph. In this paper, the metric dimension is computed for the graph $G_n[1, k]$ constructed from the circulant graph $C_n[1, k]$ by subdividing its edges. We have shown that, for $k = 2$, $G_n[1, k]$ has an unbounded metric dimension, and for $k = 3$ and 4 , $G_n[1, k]$ has a bounded metric dimension.

1. Introduction

Resolvability of graphs becomes an important parameter in graph theory due to its wide applications in different branches of mathematics, such as facility location problems, chemistry, especially molecular chemistry [1], the method of positioning robot networks [2], the optimization problem in combinatorics [3], applications in pattern recognition and image processing [4], and the problems of sonar and Coast Guard LORAN [5].

The resolvability of graphs depends on the distances in graphs. The distance between two vertices in a connected graph is the smallest distance connecting those two vertices. The representation of a vertex u with respect to the set W is denoted by $r(u, W)$ and is defined as a k -tuple $(d(u, w_1), \dots, d(u, w_n))$, where $w_1, \dots, w_n \in W$. The set W is called the resolving set [1] or sometimes locating set [5] if each vertex of the graph has a unique representation with respect to W . A resolving set of the graph that has the minimum cardinality is called the basis of the graph, and the number of elements in the basis is called the metric dimension of the graph, generally denoted by $\beta(G)$.

Motivated by the problem of uniquely determining the location of an intruder in a network, the concept of metric

dimension was first introduced by Slater in [5, 6] and studied independently by Harary and Melter in [7]. Applications of this invariant to the navigation of robots in networks are discussed in [2], and applications to chemistry are given in [1], while applications to the problem of pattern recognition and image processing, some of which involve the use of hierarchical data structures, are given in [4].

A family of connected graphs F is said to have a bounded metric dimension if the metric dimension of each graph in F is bounded above by a positive integer. Otherwise, F has an unbounded metric dimension.

If every graph F has a constant metric dimension, then F is said to have constant metric dimension. A connected graph G has $\beta(G) = 1$ if and only if G is the path [1]; cycles C_n have metric dimension 2 for every $n \geq 3$. Also, generalized Peterson graphs $P(n, 2)$, antiprism A_n , and circulant graphs $C_n[1, 2]$ are families of graphs with constant metric dimension. The families of graphs having constant metric dimension are studied in [8–23].

It is important to note that to determine the graph has a bounded metric dimension is an NP-complete problem [19]. Some bounds for this parameter, in terms of the diameters of the graph, are given in [2], and it was shown in [1, 2, 4, 20] that the metric dimension of the tree can be determined efficiently. However, it is highly unlikely to determine the

dimension of the graph unless the graph belongs to such family for which the distance between vertices can be computed systematically.

Geometrically, by subdividing an edge, we mean to insert a new vertex in the edge such that the existing edge is divided into two edges. The subdivision of the graph G is a graph obtained after performing a sequence of edge subdivision. Subdivision of graphs is an important tool to determine whether the graph is planar or not. In [24], plane graphs are characterized using subdivision as follows:

A necessary and sufficient condition of a graph to be planar is that each of its subdivision is planar

A necessary and sufficient condition of a graph to be planar is if it does not contain a subdivision of K_5 or $K_{3,3}$

In this paper, we have investigated the resolvability of subdivision of circulant graph $C_n[1, k]$ for $k \geq 2$. It is shown that, for $k = 2$, this class has an unbounded metric dimension, and for $k = 3$ and 4, it has a bounded metric dimension.

2. Metric Dimension of Subdivision of Circulant Graph $C_n[1, k]$ for $k \geq 2$

The circulant graphs are an important class of graphs that can be used in local area networks.

A circulant graph on n vertices and m parameters a_1, \dots, a_m , where each parameter a_i is at most half of n , is denoted by $C_n[a_1, a_2, \dots, a_m]$. If $\{v_1, \dots, v_n\}$ are vertices of $C_n[a_1, a_2, \dots, a_m]$, then there is an edge between two vertices v_i and v_j if and only if $|i - j|$ is one of a_i . The parameters of a_i are called generators of $C_n[a_1, a_2, \dots, a_m]$.

The graph $G_n[a_1, \dots, a_k]$ is a graph obtained from $C_n[a_1, a_2, \dots, a_m]$ by subdividing all the edges of $C_n[a_1, a_2, \dots, a_m]$ except the edges between vertices v_i and v_{i+1} .

In this paper, the resolvability of $G_n[1, k]$ is investigated. Let u_i be the added vertex in each of the edge $v_i v_{i+k}$. Thus, the graph $G_n[1, k]$ has $2n$ vertices and $3n$ edges. Let x_i and x_j be two vertices of $G_n[1, k]$; then, the gap between vertices x_i and x_j is defined to be $|i - j|$, where $1 \leq i < j \leq n$.

In the following theorem, it is shown that the metric dimension of the graph $G_n[1, 2]$ is unbounded.

Theorem 1. For $n \geq 9$,

$$\beta(G_n[1, 2]) = \left\lceil \frac{n}{3} \right\rceil. \quad (1)$$

Proof. Let $W = \{x_i: 1 \leq i \leq q\}$ be a minimum resolving set of $G_n[1, 2]$. We have two cases: either $x_i = v_i$ or $x_i = u_i$, for some i \square .

Claim 1. If $x_i = v_i$ for some i , then v_{i+2} also belongs to W because, otherwise, v_{i+2} and u_{i+1} will have the same representation.

Claim 2. If $x_i = u_i$ for some i , then u_{i+3} must belong to W because, otherwise, v_{i+3} and u_{i+2} will have the same representation.

Both these cases imply that the two consecutive vertices in W can have at most distance 3. Thus, the gap between two vertices of W is at most 3. Since vertices presented on the outer cycle are n , therefore, $q \geq \lceil n/3 \rceil$. Hence,

$$\beta(G_n[1, 2]) \geq \left\lceil \frac{n}{3} \right\rceil. \quad (2)$$

To prove the upper bound, consider the set $W = \{u_{3i-2}: i = 1, 2, \dots, \lfloor n/3 \rfloor\}$ of vertices of $G_n[1, 2]$. The construction of W shows that every vertex in W determines a gap of size 3.

For $1 \leq i \leq \lfloor n/3 \rfloor$, let $S = \{v_i, v_{i+1}, v_{i+2}, v_{i+3}, u_{i+1}, u_{i+2}\}$ be the set of vertices determined by the two consecutive vertices u_i and u_{i+3} . It is enough to show that every vertex in S is uniquely determined by some vertices in W .

The vertices v_i and v_{i+2} are the only vertices in $G_n[1, 2]$ that are at distance 1 from u_i , but $d(v_i, u_{i+3}) = 4$ and $d(v_{i+2}, u_{i+3}) = 2$.

The vertices v_{i-1} , v_{i+1} , v_{i+3} , u_{i+2} , and u_{i-2} are the only vertices in $G_n[1, 2]$ that are at distance 2 from u_i . The vertices v_{i-1} and u_{i-2} also have the same distance 5 from u_{i+3} , but they can be resolved by the vertex $u_{4\lfloor n/3 \rfloor - 1}$. The vertices v_{i+1} and u_{i+2} also have the same distance 3 from u_{i+3} , but they can be resolved by the vertex u_{i+6} . The vertex v_{i+3} is the unique vertex in $G_n[1, 2]$ such that $d(v_{i+3}, u_{i+3}) = 1$ and $d(v_{i+3}, u_i) = 2$.

The vertex u_{i+1} is the unique vertex in $G_n[1, 2]$ such that $d(u_{i+1}, u_{i+3}) = 2$ and $d(u_{i+1}, u_i) = 3$.

This shows that every vertex in the set S is uniquely determined by some vertices in the set W . Thus, W becomes a resolving set, and

$$\beta(G_n[1, 2]) \leq \left\lceil \frac{n}{3} \right\rceil. \quad (3)$$

From equations (2) and (3), we have $\beta(G_n[1, 2]) = \lceil n/3 \rceil$.

In the next results, it is shown that the graph $G_n[1, k]$ has constant metric dimension for $3 \leq k \leq 4$.

Theorem 2. For $n \geq 14$, if $n = 2(rm\{\text{mod}\}3)$, then,

$$\beta(G_n[1, 3]) = 3. \quad (4)$$

Proof. Let $W = \{u_1, u_3, u_5\}$ be the set of vertices in $G_n[1, 3]$. It is enough to show that every vertex of the graph $G_n[1, 3]$ is determined uniquely by some of the vertices in W . For this, the representations of each vertex are calculated as follows.

The vertices v_1, \dots, v_7 have representations $(1, 3, 4)$, $(2, 2, 3)$, $(2, 1, 3)$, $(1, 2, 2)$, $(2, 2, 1)$, $(3, 1, 2)$, $(3, 2, 2)$, respectively.

The representations of the remaining vertices $v_i: 7 \leq i \leq n$ of $G_n[1, 3]$ are calculated as follows:

$$r(v_i, W) = \begin{cases} \left(\left\lfloor \frac{2i-5}{3} \right\rfloor, \left\lfloor \frac{2i-9}{3} \right\rfloor, \left\lfloor \frac{2i-13}{3} \right\rfloor \right), & \text{for } 8 \leq i \leq \left\lfloor \frac{n}{2} \right\rfloor + 2, \\ \left(\frac{2n+2}{3} - \left\lfloor \frac{2i-5}{3} \right\rfloor, \left\lfloor \frac{2i-9}{3} \right\rfloor, \left\lfloor \frac{2i-13}{3} \right\rfloor \right), & \text{for } i = \left\lfloor \frac{n}{2} \right\rfloor + 3, \\ \left(\frac{2n+2}{3} - \left\lfloor \frac{2i-5}{3} \right\rfloor, \frac{2n+11}{3} - \left\lfloor \frac{2i}{3} \right\rfloor, \left\lfloor \frac{2i-13}{3} \right\rfloor \right), & \text{for } i = \left\lfloor \frac{n}{2} \right\rfloor + 4, \\ \left(\frac{2n+2}{3} - \left\lfloor \frac{2i-5}{3} \right\rfloor, \frac{2n+11}{3} - \left\lfloor \frac{2i}{3} \right\rfloor, \frac{2n+2}{3} - \left\lfloor \frac{2i-9}{3} \right\rfloor \right), & \text{for } i = \left\lfloor \frac{n}{2} \right\rfloor + 5, \\ \left(\frac{2n+2}{3} - \left\lfloor \frac{2i-5}{3} \right\rfloor, \frac{2n+2}{3} - \left\lfloor \frac{2i-9}{3} \right\rfloor, \frac{2n+2}{3} - \left\lfloor \frac{2i-9}{3} \right\rfloor \right), & \text{for } \left\lfloor \frac{n}{2} \right\rfloor + 6 \leq i \leq n. \end{cases} \quad (5)$$

The vertices $u_2, u_4, u_6, u_7, u_{n-1}, u_n$ of $G_n[1, 3]$ have representations $(3, 3, 2), (2, 3, 3), (4, 2, 3), (4, 3, 3), (3, 3, 4), (3, 2, 4)$, respectively.

For the remaining vertices, we have

$$r(u_i, W) = \begin{cases} \left(\left\lfloor \frac{2i-2}{3} \right\rfloor, \left\lfloor \frac{2i-6}{3} \right\rfloor, \left\lfloor \frac{2i-10}{3} \right\rfloor \right), & \text{for } 8 \leq i \leq \left\lfloor \frac{n}{2} \right\rfloor + 1, \\ \left(\frac{2n-1}{3} - \left\lfloor \frac{2i-5}{3} \right\rfloor, \left\lfloor \frac{2i-8}{3} \right\rfloor, \left\lfloor \frac{2i-11}{3} \right\rfloor \right), & \text{for } i = \left\lfloor \frac{n}{2} \right\rfloor + 2, \\ \left(\frac{2n-1}{3} - \left\lfloor \frac{2i-5}{3} \right\rfloor, \frac{2n+8}{3} - \left\lfloor \frac{2i}{3} \right\rfloor, \left\lfloor \frac{2i-10}{3} \right\rfloor \right), & \text{for } i = \left\lfloor \frac{n}{2} \right\rfloor + 3, \\ \left(\frac{2n-1}{3} - \left\lfloor \frac{2i-5}{3} \right\rfloor, \frac{2n+8}{3} - \left\lfloor \frac{2i}{3} \right\rfloor, \frac{2n+2}{3} - \left\lfloor \frac{2i-6}{3} \right\rfloor \right), & \text{for } i = \left\lfloor \frac{n}{2} \right\rfloor + 4, \\ \left(\frac{2n+2}{3} - \left\lfloor \frac{2i-2}{3} \right\rfloor, \frac{2n+2}{3} - \left\lfloor \frac{2i-6}{3} \right\rfloor, \frac{2n+2}{3} - \left\lfloor \frac{2i-10}{3} \right\rfloor \right), & \text{for } \left\lfloor \frac{n}{2} \right\rfloor + 5 \leq i \leq n-2. \end{cases} \quad (6)$$

This shows that every vertex of the graph $G_n[1, 3]$ is determined uniquely by some of the vertices in W . Hence, W becomes a resolving set, and

$$\beta(G_n[1, 3]) \leq 3. \quad (7)$$

Now, to compute the lower bound, suppose, on contrary, that W is a minimum resolving set of $G_n[1, 3]$ of cardinality 2. We have the following possibilities to choose the vertices of W . \square

2.1. If W Contains Both Vertices from v_i . One can suppose without losing any generality that $W = \{v_1, v_j; 2 \leq j \leq n\}$. However, in this case, if $j \equiv 2 \pmod{3}$, then

$$r(u_j, W) = r(v_{j+1}, W) = \begin{cases} \left(\left\lfloor \frac{2j}{3} \right\rfloor, 1 \right), & \text{for } 2 \leq j \leq \left\lfloor \frac{n}{2} \right\rfloor, \\ \left(\left\lfloor \frac{2n-2j}{3} \right\rfloor, 1 \right), & \text{for } \left\lfloor \frac{n}{2} \right\rfloor + 1 \leq j \leq n, \end{cases} \quad (8)$$

and if $j \equiv 0, 1 \pmod{3}$, then

$$r(u_{j+1}, W) = r(v_{j+2}, W) = \begin{cases} \left(\left\lfloor \frac{2j+2}{3} \right\rfloor, 2 \right), & \text{for } 2 \leq j \leq \left\lfloor \frac{n}{2} \right\rfloor, \\ \left(\left\lfloor \frac{2n-2j-2}{3} \right\rfloor, 2 \right), & \text{for } \left\lfloor \frac{n}{2} \right\rfloor + 1 \leq j \leq n. \end{cases} \quad (9)$$

2.2. If W Contains Both Vertices from u_i . One can suppose without losing any generality that $W = \{u_1, u_j; 2 \leq j \leq n\}$. However, in this case, if $j \equiv 0 \pmod{3}$, then

$$r(u_{j+1}, W) = r(v_{j+2}, W) = \begin{cases} \left(\left\lfloor \frac{2j}{3} \right\rfloor, 3 \right), & \text{for } 2 \leq j \leq \left\lfloor \frac{n}{2} \right\rfloor, \\ \left(\left\lfloor \frac{2n-2j}{3} \right\rfloor, 3 \right), & \text{for } \left\lfloor \frac{n}{2} \right\rfloor + 1 \leq j \leq n, \end{cases} \quad (10)$$

and if $j \equiv 1, 2 \pmod{3}$,

$$\begin{aligned} r(u_{j+3}, W) &= r(v_{j+4}, W) \\ &= \begin{cases} \left(\left\lfloor \frac{2j+3}{3} \right\rfloor, 2 \right), & \text{for } 2 \leq j \leq \left\lfloor \frac{n}{2} \right\rfloor, \\ \left(\left\lfloor \frac{2n-2j-3}{3} \right\rfloor, 2 \right), & \text{for } \left\lfloor \frac{n}{2} \right\rfloor + 1 \leq j \leq n. \end{cases} \end{aligned} \quad (11)$$

2.3. *If One Each from v_i and u_j Belongs to W .* One can suppose without losing any generality that $W = \{v_i, u_j: 1 \leq i \leq j \leq n\}$. However, in this case, if $j \equiv 0 \pmod{3}$, then

$$\begin{aligned} r(u_{j+4}, W) &= r(v_{j+5}, W) \\ &= \begin{cases} \left(\left\lfloor \frac{2j}{3} \right\rfloor + 3, 3 \right), & \text{for } 3 \leq j \leq \left\lfloor \frac{n}{2} \right\rfloor - 2, \\ \left(\left\lfloor \frac{2n-2j-8}{3} \right\rfloor, 3 \right), & \text{for } \left\lfloor \frac{n}{2} \right\rfloor - 1 \leq j \leq n, \end{cases} \end{aligned} \quad (12)$$

and if $j \equiv 1, 2 \pmod{3}$,

$$\begin{aligned} r(u_{j+3}, W) &= r(v_{j+4}, W) \\ &= \begin{cases} \left(\left\lfloor \frac{2j}{3} \right\rfloor + 2, 2 \right), & \text{for } 1 \leq j \leq \left\lfloor \frac{n}{2} \right\rfloor, \\ \left(\left\lfloor \frac{2n-2j-6}{3} \right\rfloor, 2 \right), & \text{for } \left\lfloor \frac{n}{2} \right\rfloor + 1 \leq j \leq n. \end{cases} \end{aligned} \quad (13)$$

Thus, there is no resolving set of $G_n[1, 3]$ having two vertices. This implies that

$$\beta(G_n[1, 3]) \geq 3. \quad (14)$$

From (7) and (14), we get

$$\beta(G_n[1, 3]) = 3. \quad (15)$$

Theorem 3. *For $n \geq 15$, if $n \equiv 0, 1 \pmod{3}$, then*

$$\beta(G_n[1, 3]) = 4. \quad (16)$$

Proof. Let $W = \{v_1, v_2, v_3, v_4\}$ be the set of vertices in $G_n[1, 4]$. It is enough to show that every vertex of the graph $G_n[1, 4]$ is uniquely determined by some vertices in W . For this, the representations of each vertex are calculated as follows.

The representations of outer vertices $v_i: 1 \leq i \leq n$ of $G_n[1, 3]$ are calculated as follows:

$$r(v_i, W) = \begin{cases} \left[\frac{2i-2}{3}, \left[\frac{2i-4}{3}, \left[\frac{2i-6}{3}, \left[\frac{2i-8}{3} \right] \right] \right] \right], & \text{for } 5 \leq i \leq \left\lfloor \frac{n+1}{2} \right\rfloor, \\ \left[\frac{2n-2i+2}{3}, \left[\frac{2n-2i+4}{3}, \left[\frac{2n-2i+6}{3}, \left[\frac{2n-2i+8}{3} \right] \right] \right] \right], & \text{for } \left\lfloor \frac{n+1}{2} \right\rfloor + 4 \leq i \leq n. \end{cases} \quad (17)$$

If $i = \lfloor (n+1)/2 \rfloor + 1$,

$$r(v_i, W) = \begin{cases} \left[\left[\frac{2i-6}{3}, \left[\frac{2i-6}{3}, \left[\frac{2i-6}{3}, \left[\frac{2i-8}{3} \right] \right] \right] \right] \right], & \text{for } n = 6k \text{ and } k \geq 3, \\ \left[\left[\frac{2i-4}{3}, \left[\frac{2i-4}{3}, \left[\frac{2i-4}{3}, \left[\frac{2i-7}{3} \right] \right] \right] \right] \right], & \text{for } n = 6k + 1 \text{ and } k \geq 3, \\ \left[\left[\frac{2i-4}{3}, \left[\frac{2i-4}{3}, \left[\frac{2i-6}{3}, \left[\frac{2i-6}{3} \right] \right] \right] \right] \right], & \text{for } n = 6k + 3 \text{ and } k \geq 2, \\ \left[\left[\frac{2i-5}{3}, \left[\frac{2i-3}{3}, \left[\frac{2i-5}{3}, \left[\frac{2i-8}{3} \right] \right] \right] \right] \right], & \text{for } n = 6k + 4 \text{ and } k \geq 2. \end{cases} \quad (18)$$

If $i = \lfloor (n+1)/2 \rfloor + 2$,

$$r(v_i, W) = \begin{cases} \left[\frac{2i-10}{3} \right], \left[\frac{2i-8}{3} \right], \left[\frac{2i-8}{3} \right], \left[\frac{2i-8}{3} \right], & \text{for } n = 6k \text{ and } k \geq 3, \\ \left[\frac{2i-6}{3} \right], \left[\frac{2i-6}{3} \right], \left[\frac{2i-6}{3} \right], \left[\frac{2i-6}{3} \right], & \text{for } n = 6k+1 \text{ and } k \geq 3, \\ \left[\frac{2i-8}{3} \right], \left[\frac{2i-6}{3} \right], \left[\frac{2i-6}{3} \right], \left[\frac{2i-8}{3} \right], & \text{for } n = 6k+3 \text{ and } k \geq 2, \\ \left[\frac{2i-10}{3} \right], \left[\frac{2i-7}{3} \right], \left[\frac{2i-4}{3} \right], \left[\frac{2i-7}{3} \right] & \text{for } n = 6k+4 \text{ and } k \geq 2. \end{cases} \quad (19)$$

If $i = \lfloor (n+1)/2 \rfloor + 3$,

$$r(v_i, W) = \begin{cases} \left[\frac{2i-14}{3} \right], \left[\frac{2i-12}{3} \right], \left[\frac{2i-10}{3} \right], \left[\frac{2i-10}{3} \right], & \text{for } n = 6k \text{ and } k \geq 3, \\ \left[\frac{2i-11}{3} \right], \left[\frac{2i-8}{3} \right], \left[\frac{2i-8}{3} \right], \left[\frac{2i-8}{3} \right], & \text{for } n = 6k+1 \text{ and } k \geq 3, \\ \left[\frac{2i-10}{3} \right], \left[\frac{2i-10}{3} \right], \left[\frac{2i-8}{3} \right], \left[\frac{2i-8}{3} \right], & \text{for } n = 6k+3 \text{ and } k \geq 2, \\ \left[\frac{2i-12}{3} \right], \left[\frac{2i-12}{3} \right], \left[\frac{2i-9}{3} \right], \left[\frac{2i-6}{3} \right], & \text{for } n = 6k+4 \text{ and } k \geq 2. \end{cases} \quad (20)$$

The vertices $u_1, u_2, u_3, u_4, u_{n-1}, u_n$ have representations $(1, 2, 2, 1)$, $(2, 1, 2, 2)$, $(3, 2, 1, 2)$, $(3, 3, 2, 1)$, $(2, 1, 2, 3)$, $(2, 2, 1, 2)$, respectively.

The representations of the remaining vertices u_i of $G_n[1, 3]$ are calculated as follows:

$$r(u_i, W) = \begin{cases} \left[\frac{2i+1}{3} \right], \left[\frac{2i-1}{3} \right], \left[\frac{2i-3}{3} \right], \left[\frac{2i-5}{3} \right], & \text{for } 5 \leq i \leq \left\lfloor \frac{n}{2} \right\rfloor - 1, \\ \left[\frac{2n-2i-1}{3} \right], \left[\frac{2n-2i+1}{3} \right], \left[\frac{2n-2i+3}{3} \right], \left[\frac{2n-2i+5}{3} \right], & \text{for } \left\lfloor \frac{n}{2} \right\rfloor + 3 \leq i \leq n-2. \end{cases} \quad (21)$$

If $i = \lfloor n/2 \rfloor$,

$$r(u_i, W) = \begin{cases} \left[\frac{2i-1}{3} \right], \left[\frac{2i-1}{3} \right], \left[\frac{2i-3}{3} \right], \left[\frac{2i-3}{3} \right], & \text{for } n = 6k \text{ and } k \geq 3, \\ \left[\frac{2i-2}{3} \right], \left[\frac{2i+1}{3} \right], \left[\frac{2i-2}{3} \right], \left[\frac{2i-5}{3} \right], & \text{for } n = 6k+1 \text{ and } k \geq 3, \\ \left[\frac{2i-1}{3} \right], \left[\frac{2i-1}{3} \right], \left[\frac{2i-1}{3} \right], \left[\frac{2i-4}{3} \right], & \text{for } n = 6k+3 \text{ and } k \geq 2, \\ \left[\frac{2i-1}{3} \right], \left[\frac{2i-1}{3} \right], \left[\frac{2i-1}{3} \right], \left[\frac{2i-4}{3} \right], & \text{for } n = 6k+4 \text{ and } k \geq 2. \end{cases} \quad (22)$$

If $i = \lfloor n/2 \rfloor + 1$,

$$r(u_i, W) = \begin{cases} \left\lfloor \frac{2i-6}{3} \right\rfloor, \left\lfloor \frac{2i-4}{3} \right\rfloor, \left\lfloor \frac{2i-4}{3} \right\rfloor, \left\lfloor \frac{2i-6}{3} \right\rfloor, & \text{for } n = 6k \text{ and } k \geq 3, \\ \left\lfloor \frac{2i-7}{3} \right\rfloor, \left\lfloor \frac{2i-4}{3} \right\rfloor, \left\lfloor \frac{2i-1}{3} \right\rfloor, \left\lfloor \frac{2i-4}{3} \right\rfloor, & \text{for } n = 6k + 1 \text{ and } k \geq 3, \\ \left\lfloor \frac{2i-6}{3} \right\rfloor, \left\lfloor \frac{2i-4}{3} \right\rfloor, \left\lfloor \frac{2i-4}{3} \right\rfloor, \left\lfloor \frac{2i-4}{3} \right\rfloor, & \text{for } n = 6k + 3 \text{ and } k \geq 2, \\ \left\lfloor \frac{2i-3}{3} \right\rfloor, \left\lfloor \frac{2i-3}{3} \right\rfloor, \left\lfloor \frac{2i-3}{3} \right\rfloor, \left\lfloor \frac{2i-3}{3} \right\rfloor, & \text{for } n = 6k + 4 \text{ and } k \geq 2. \end{cases} \quad (23)$$

If $i = \lfloor n/2 \rfloor + 2$,

$$r(u_i, W) = \begin{cases} \left\lfloor \frac{2i-7}{3} \right\rfloor, \left\lfloor \frac{2i-7}{3} \right\rfloor, \left\lfloor \frac{2i-5}{3} \right\rfloor, \left\lfloor \frac{2i-5}{3} \right\rfloor, & \text{for } n = 6k \text{ and } k \geq 3, \\ \left\lfloor \frac{2i-9}{3} \right\rfloor, \left\lfloor \frac{2i-9}{3} \right\rfloor, \left\lfloor \frac{2i-6}{3} \right\rfloor, \left\lfloor \frac{2i-3}{3} \right\rfloor, & \text{for } n = 6k + 1 \text{ and } k \geq 3, \\ \left\lfloor \frac{2i-11}{3} \right\rfloor, \left\lfloor \frac{2i-9}{3} \right\rfloor, \left\lfloor \frac{2i-7}{3} \right\rfloor, \left\lfloor \frac{2i-7}{3} \right\rfloor, & \text{for } n = 6k + 3 \text{ and } k \geq 2, \\ \left\lfloor \frac{2i-8}{3} \right\rfloor, \left\lfloor \frac{2i-5}{3} \right\rfloor, \left\lfloor \frac{2i-5}{3} \right\rfloor, \left\lfloor \frac{2i-5}{3} \right\rfloor, & \text{for } n = 6k + 4 \text{ and } k \geq 2. \end{cases} \quad (24)$$

This shows that every vertex of the graph $G_n[1, 4]$ is uniquely determined by some of the vertices in W . Hence, W become a resolving set, and

$$\beta(G_n[1, 4]) \leq 4. \quad (25)$$

Let $n = 6k + l$ and $l \in \{0, 1, 3, 4\}$. We show that there is no resolving set of $G_n[1, 4]$ with three elements. Suppose, on contrary, that W is a minimum resolving set of $G_n[1, 4]$ of

cardinality 3. We have the following possibilities to choose the vertices of W . \square

2.4. If Only $v_i \in W$. One can suppose without losing any generality that $W = \{v_1, v_i, v_j\}$, where $2 \leq i \leq 3k$ and $i + 1 \leq j \leq 6k$. In this case, the vertices of $G_n[1, 4]$ that have the same representation for all choices of the resolving set are given as follows:

$$\left\{ \begin{array}{ll} r(u_{n-3}) = r(v_{n-1}) = \left(2, \left\lfloor \frac{2i+3}{3} \right\rfloor, \left\lfloor \frac{2j+4}{3} \right\rfloor\right), & \text{for } i \equiv 0 \pmod{3}, j \equiv 0, 1 \pmod{3} \text{ and for every value of } l, \\ r(u_{(n+3)/2}) = r(v_{(n+5)/2}) = \left(\frac{n-3}{3}, \left\lfloor \frac{n-i+1}{3} \right\rfloor, \left\lfloor \frac{n-2j+5}{3} \right\rfloor\right), & \text{for } l = 1, 3 \text{ and } i \equiv 0 \pmod{3}, j \equiv 2 \pmod{3}, \\ r(u_{n/2}) = r(v_{(n+2)/2}) = \left(\frac{n}{3}, \left\lfloor \frac{n-i+1}{3} \right\rfloor, \left\lfloor \frac{n-2j+3}{3} \right\rfloor\right), & \text{for } l = 0, 4 \text{ and } i \equiv 0 \pmod{3}, j \equiv 2 \pmod{3}, \\ r(u_{n-2}) = r(v_n) = \left(1, \left\lfloor \frac{2i}{3} \right\rfloor, \left\lfloor \frac{2j+1}{3} \right\rfloor\right), & \text{otherwise and for all } l. \end{array} \right. \quad (26)$$

2.5. If Two Vertices from v_i and One Vertex from u_j Belong to W . One can suppose without losing any generality that $W = \{v_1, v_i, u_j\}$, where $2 \leq i \leq 3k$ and $i \leq j \leq 6k$.

In this case, the vertices of $G_n[1, 4]$ that have the same representation for all choices of the resolving set are given as follows:

$$\left\{ \begin{array}{l} r(u_{n-3}) = r(v_{n-1}) = \left(2, \left\lfloor \frac{2i+3}{3} \right\rfloor, \left\lfloor \frac{2j+4}{3} \right\rfloor\right), \\ r(u_{(n+3)/2}) = r(v_{(n+5)/2}) = \left(\frac{n-3}{3}, \left\lfloor \frac{n-i+1}{3} \right\rfloor, \left\lfloor \frac{n-2j+5}{3} \right\rfloor\right), \\ r(u_{n/2}) = r(v_{(n+2)/2}) = \left(\frac{n}{3}, \left\lfloor \frac{n-i+1}{3} \right\rfloor, \left\lfloor \frac{n-2j+3}{3} \right\rfloor\right), \\ r(u_{n-2}) = r(v_n) = \left(1, \left\lfloor \frac{2i}{3} \right\rfloor, \left\lfloor \frac{2j+1}{3} \right\rfloor\right), \end{array} \right. \quad \begin{array}{l} \text{for } i \equiv 0 \pmod{3}, j \equiv 0, 1 \pmod{3} \text{ and for all } l, \\ \text{for } l = 1, 3 \text{ and } i \equiv 0 \pmod{3}, j \equiv 2 \pmod{3}, \\ \text{for } l = 0, 4 \text{ and } i \equiv 0 \pmod{3}, j \equiv 2 \pmod{3}, \\ \text{otherwise and for all } l. \end{array} \quad (27)$$

2.6. If Two Vertices from u_i and One Vertex from v_j Belong to W . One can suppose without losing any generality that $W = \{v_1, u_i, u_j\}$, where $1 \leq i \leq 3k$ and $i \leq j \leq 6k$.

In this case, the vertices of $G_n[1, 4]$ that have the same representation for all choices of the resolving set are given as follows:

$$\left\{ \begin{array}{l} r(u_{n-3}) = r(v_{n-1}) = \left(2, \left\lfloor \frac{2i+3}{3} \right\rfloor, \left\lfloor \frac{2j+4}{3} \right\rfloor\right), \\ r(u_{(n+3)/2}) = r(v_{(n+5)/2}) = \left(\frac{n-3}{3}, \left\lfloor \frac{n-i+1}{3} \right\rfloor, \left\lfloor \frac{n-2j+5}{3} \right\rfloor\right), \\ r(u_{n/2}) = r(v_{(n+2)/2}) = \left(\frac{n}{3}, \left\lfloor \frac{n-i+1}{3} \right\rfloor, \left\lfloor \frac{n-2j+3}{3} \right\rfloor\right), \\ r(u_{n-2}) = r(v_n) = \left(1, \left\lfloor \frac{2i}{3} \right\rfloor, \left\lfloor \frac{2j+1}{3} \right\rfloor\right), \end{array} \right. \quad \begin{array}{l} \text{for } i \equiv 0 \pmod{3}, j \equiv 0, 1 \pmod{3} \text{ and for all } l, \\ \text{for } l = 1, 3 \text{ and } i \equiv 0 \pmod{3}, j \equiv 2 \pmod{3}, \\ \text{for } l = 0, 4 \text{ and } i \equiv 0 \pmod{3}, j \equiv 2 \pmod{3} \text{ and for } l =, \\ \text{otherwise and for all } l. \end{array} \quad (28)$$

2.7. If W Contains All Three Vertices from u_i . One can suppose without losing any generality that $W = \{u_1, u_i, u_j\}$ is a resolving set, where $2 \leq i \leq 3k$ and $i + 1 \leq j \leq 6k$.

In this case, the vertices of $G_n[1, 4]$ that have the same representation for all choices of the resolving set are given as follows:

$$\left\{ \begin{array}{l} r(u_{n-3}) = r(v_{n-1}) = \left(2, \left\lfloor \frac{2i+3}{3} \right\rfloor, \left\lfloor \frac{2j+4}{3} \right\rfloor\right), \\ r(u_{(n+3)/2}) = r(v_{(n+5)/2}) = \left(\frac{n-3}{3}, \left\lfloor \frac{n-i+1}{3} \right\rfloor, \left\lfloor \frac{n-2j+5}{3} \right\rfloor\right), \\ r(u_{n/2}) = r(v_{(n+2)/2}) = \left(\frac{n}{3}, \left\lfloor \frac{n-i+1}{3} \right\rfloor, \left\lfloor \frac{n-2j+3}{3} \right\rfloor\right), \\ r(u_{n-2}) = r(v_n) = \left(1, \left\lfloor \frac{2i}{3} \right\rfloor, \left\lfloor \frac{2j+1}{3} \right\rfloor\right), \end{array} \right. \quad \begin{array}{l} \text{for } i \equiv 0 \pmod{3}, j \equiv 0, 1 \pmod{3} \text{ and for all } l, \\ \text{for } l = 1, 3 \text{ and } i \equiv 0 \pmod{3}, j \equiv 2 \pmod{3}, \\ \text{for } l = 0, 4 \text{ and } i \equiv 0 \pmod{3}, j \equiv 2 \pmod{3}, \\ \text{otherwise and for all } l. \end{array} \quad (29)$$

Thus, there is no resolving set of $G_n[1, 4]$ having three elements. Hence,

From equations (25) and (30), we get

$$\beta(G_n[1, 4]) \geq 4. \quad (30)$$

$$\beta(G_n[1, 4]) = 4. \quad (31)$$

Theorem 4. For $n \geq 20$, if $n \equiv 3 \pmod{4}$, then

$$\beta(G_n[1, 4]) = 4. \tag{32}$$

Proof. Let $W = \{u_1, u_4, u_7, u_{10}\}$ be the set of vertices in $G_n[1, 4]$. It is enough to show that every vertex of the graph $G_n[1, 4]$ is uniquely determined by some vertices in W . For

this, the vertices v_1, \dots, v_{11} have representations $(1, 4, 5, 6)$, $(2, 3, 4, 5)$, $(3, 2, 3, 6)$, $(2, 1, 4, 5)$, $(1, 2, 3, 4)$, $(2, 3, 2, 3)$, $(3, 2, 1, 4)$, $(4, 1, 2, 3)$, $(3, 2, 3, 2)$, $(4, 3, 2, 1)$, $(5, 4, 1, 2)$, respectively.

Let $W' = \{u_1, u_4, u_7\}$. Then, the representations of the vertices v_i : $12 \leq i \leq n$ of $G_n[1, 4]$ with respect to W' and the vertex u_{10} are calculated as follows:

$$r(v_i | W') \equiv \begin{cases} \left(\left\lfloor \frac{i}{2} \right\rfloor, \left\lfloor \frac{i-6}{2} \right\rfloor, \left\lfloor \frac{i-8}{2} \right\rfloor \right), & \text{if } i \text{ is divisible by } 4 \text{ and } 12 \leq i \leq \left\lfloor \frac{n+9}{2} \right\rfloor, \\ \left(\left\lfloor \frac{n-i+3}{2} \right\rfloor, \left\lfloor \frac{n-i+9}{2} \right\rfloor, \left\lfloor \frac{n-i+11}{2} \right\rfloor \right), & \text{if } i \text{ is divisible by } 4 \text{ and } \left\lfloor \frac{n+9}{2} \right\rfloor + 1 \leq i \leq n, \\ \left(\left\lfloor \frac{i-3}{2} \right\rfloor, \left\lfloor \frac{i-5}{2} \right\rfloor, \left\lfloor \frac{n-i+11}{2} \right\rfloor \right), & \text{if } i-1 \text{ is divisible by } 4 \text{ and } 13 \leq i \leq \left\lfloor \frac{n+9}{2} \right\rfloor, \\ \left(\left\lfloor \frac{n-i+6}{2} \right\rfloor, \left\lfloor \frac{n-i+8}{2} \right\rfloor, \left\lfloor \frac{n-i+10}{2} \right\rfloor \right), & \text{if } i-1 \text{ is divisible by } 4 \text{ and } \left\lfloor \frac{n+9}{2} \right\rfloor + 1 \leq i \leq n, \\ \left(\left\lfloor \frac{i-3}{2} \right\rfloor, \left\lfloor \frac{i-4}{2} \right\rfloor, \left\lfloor \frac{i-6}{2} \right\rfloor \right), & \text{if } i-2 \text{ is divisible by } 4 \text{ and } 14 \leq i \leq \left\lfloor \frac{n+9}{2} \right\rfloor, \\ \left(\left\lfloor \frac{n-i+5}{2} \right\rfloor, \left\lfloor \frac{n-i+7}{2} \right\rfloor, \left\lfloor \frac{n-i+9}{2} \right\rfloor \right), & \text{if } i-2 \text{ is divisible by } 4 \text{ and } \left\lfloor \frac{n+9}{2} \right\rfloor + 1 \leq i \leq n, \\ \left(\left\lfloor \frac{i-1}{2} \right\rfloor, \left\lfloor \frac{i-3}{2} \right\rfloor, \left\lfloor \frac{i-9}{2} \right\rfloor \right), & \text{if } i-3 \text{ is divisible by } 4 \text{ and } 15 \leq i \leq \left\lfloor \frac{n-1}{2} \right\rfloor, \\ \left(\left\lfloor \frac{n-i+4}{2} \right\rfloor, \left\lfloor \frac{n-i+6}{2} \right\rfloor, \left\lfloor \frac{n-i+12}{2} \right\rfloor \right), & \text{if } i-3 \text{ is divisible by } 4 \text{ and } \left\lfloor \frac{n-1}{2} \right\rfloor + 1 \leq i \leq n, \end{cases} \tag{33}$$

$$r(v_i | v_{10}) = \begin{cases} \left\lfloor \frac{i-6}{2} \right\rfloor, & \text{if } i \text{ is divisible by } 4 \text{ and } i = 12, \\ \left\lfloor \frac{i-10}{2} \right\rfloor, & \text{if } i \text{ is divisible by } 4 \text{ and } 13 \leq i \leq \left\lfloor \frac{n+17}{2} \right\rfloor, \\ \left\lfloor \frac{n-i+12}{2} \right\rfloor, & \text{if } i \text{ is divisible by } 4 \text{ and } \left\lfloor \frac{n+17}{2} \right\rfloor + 1 \leq i \leq n, \\ \left\lfloor \frac{i-9}{2} \right\rfloor, & \text{if } i-1 \text{ is divisible by } 4 \text{ and } 13 \leq i \leq \left\lfloor \frac{n+17}{2} \right\rfloor + 1, \\ \left\lfloor \frac{n-i+12}{2} \right\rfloor, & \text{if } i-1 \text{ is divisible by } 4 \text{ and } \left\lfloor \frac{n+17}{2} \right\rfloor + 2 \leq i \leq n, \\ \left\lfloor \frac{i-12}{2} \right\rfloor, & \text{if } i-2 \text{ is divisible by } 4 \text{ and } 14 \leq i \leq \left\lfloor \frac{n+17}{2} \right\rfloor + 3, \\ \left\lfloor \frac{n-i+15}{2} \right\rfloor, & \text{if } i-2 \text{ is divisible by } 4 \text{ and } \left\lfloor \frac{n+17}{2} \right\rfloor + 4 \leq i \leq n, \\ \left\lfloor \frac{i-11}{2} \right\rfloor, & \text{if } i-3 \text{ is divisible by } 4 \text{ and } 15 \leq i \leq \left\lfloor \frac{n+17}{2} \right\rfloor + 3, \\ \left\lfloor \frac{n-i+14}{2} \right\rfloor, & \text{if } i-3 \text{ is divisible by } 4 \text{ and } \left\lfloor \frac{n+17}{2} \right\rfloor + 4 \leq i \leq n. \end{cases}$$

The representations of the vertices u_i : $1 \leq i \leq 11$ of $G_n[1, 4]$ are calculated as follows: $r(u_2, W) = (3, 4, 3, 4)$, $r(u_3, W) = (4, 3, 2, 5)$, $r(u_5, W) = (2, 3, 4, 3)$, $r(u_6, W) =$

$(3, 4, 3, 2)$, $r(u_8, W) = (5, 2, 3, 4)$, $r(u_9, W) = (4, 3, 4, 3)$, $r(u_{11}, W) = (6, 5, 2, 3)$, $r(u_{n-2}, W) = (3, 4, 5, 6)$, $r(u_{n-1}, W) = (4, 3, 4, 7)$, $r(u_n, W) = (3, 2, 5, 6)$.

The remaining vertices $u_i: 12 \leq i \leq n$ of $G_n[1, 4]$ have the following representation with respect to W' , and the vertex u_{10} is calculated as follows:

$$\begin{aligned}
 r(u_i | W') = & \begin{cases} \left(\left\lfloor \frac{i+7}{2} \right\rfloor, \left\lfloor \frac{i-4}{2} \right\rfloor, \left\lfloor \frac{i-6}{2} \right\rfloor \right), & \text{if } i \text{ is divisible by } 4 \text{ and } 12 \leq i \leq \left\lfloor \frac{n+7}{2} \right\rfloor, \\ \left(\left\lfloor \frac{n-i+11}{2} \right\rfloor, \left\lfloor \frac{n-i+7}{2} \right\rfloor, \left\lfloor \frac{n-i+9}{2} \right\rfloor \right), & \text{if } i \text{ is divisible by } 4 \text{ and } \left\lfloor \frac{n+7}{2} \right\rfloor + 1 \leq i \leq n-3, \\ \left(\left\lfloor \frac{i-1}{2} \right\rfloor, \left\lfloor \frac{i-3}{2} \right\rfloor, \left\lfloor \frac{i-5}{2} \right\rfloor \right), & \text{if } i-1 \text{ is divisible by } 4 \text{ and } 13 \leq i \leq \left\lfloor \frac{n+7}{2} \right\rfloor, \\ \left(\left\lfloor \frac{n-i+3}{2} \right\rfloor, \left\lfloor \frac{n-i+6}{2} \right\rfloor, \left\lfloor \frac{n-i+7}{2} \right\rfloor \right), & \text{if } i-1 \text{ is divisible by } 4 \text{ and } \left\lfloor \frac{n+7}{2} \right\rfloor + 1 \leq i \leq n-3, \\ \left(\left\lfloor \frac{i+6}{2} \right\rfloor, \left\lfloor \frac{i-2}{2} \right\rfloor, \left\lfloor \frac{i-4}{2} \right\rfloor \right), & \text{if } i-2 \text{ is divisible by } 4 \text{ and } 14 \leq i \leq \left\lfloor \frac{n+7}{2} \right\rfloor, \\ \left(\left\lfloor \frac{n-i+5}{2} \right\rfloor, \left\lfloor \frac{n-i+5}{2} \right\rfloor, \left\lfloor \frac{n-i+7}{2} \right\rfloor \right), & \text{if } i-2 \text{ is divisible by } 4 \text{ and } \left\lfloor \frac{n+7}{2} \right\rfloor + 1 \leq i \leq n-3, \\ \left(\left\lfloor \frac{n-i}{2} \right\rfloor, \left\lfloor \frac{i+5}{2} \right\rfloor, \left\lfloor \frac{i-7}{2} \right\rfloor \right), & \text{if } i-3 \text{ is divisible by } 4 \text{ and } 15 \leq i \leq \left\lfloor \frac{n+7}{2} \right\rfloor, \\ \left(\left\lfloor \frac{n-i+4}{2} \right\rfloor, \left\lfloor \frac{n-i+4}{2} \right\rfloor, \left\lfloor \frac{n-i+10}{2} \right\rfloor \right) & \text{if } i-3 \text{ is divisible by } 4 \text{ and } \left\lfloor \frac{n+7}{2} \right\rfloor + 1 \leq i \leq n-3, \end{cases} \\
 r(u_i | u_{10}) = & \begin{cases} \left\lfloor \frac{i-4}{2} \right\rfloor, & \text{if } i \text{ is divisible by } 4 \text{ and } i = 12, \\ \left\lfloor \frac{i-6}{2} \right\rfloor, & \text{if } i \text{ is divisible by } 4 \text{ and } 13 \leq i \leq \left\lfloor \frac{n+9}{2} \right\rfloor + 4, \\ \left\lfloor \frac{n-i+11}{2} \right\rfloor, & \text{if } i \text{ is divisible by } 4 \text{ and } \left\lfloor \frac{n+9}{2} \right\rfloor + 5 \leq i \leq n-3, \\ \left\lfloor \frac{i-7}{2} \right\rfloor, & \text{if } i-1 \text{ is divisible by } 4 \text{ and } 13 \leq i \leq \left\lfloor \frac{n+9}{2} \right\rfloor + 1, \\ \left\lfloor \frac{n-i+10}{2} \right\rfloor, & \text{if } i-1 \text{ is divisible by } 4 \text{ and } \left\lfloor \frac{n+9}{2} \right\rfloor + 2 \leq i \leq n-3, \\ \left\lfloor \frac{i-10}{2} \right\rfloor, & \text{if } i-2 \text{ is divisible by } 4 \text{ and } 14 \leq i \leq \left\lfloor \frac{n+9}{2} \right\rfloor + 6, \\ \left\lfloor \frac{n-i+13}{2} \right\rfloor, & \text{if } i-2 \text{ is divisible by } 4 \text{ and } \left\lfloor \frac{n+9}{2} \right\rfloor + 7 \leq i \leq n-3, \\ \left\lfloor \frac{i-9}{2} \right\rfloor, & \text{if } i-3 \text{ is divisible by } 4 \text{ and } 15 \leq i \leq \left\lfloor \frac{n+9}{2} \right\rfloor + 3, \\ \left\lfloor \frac{n-i+12}{2} \right\rfloor, & \text{if } i-3 \text{ is divisible by } 4 \text{ and } \left\lfloor \frac{n+9}{2} \right\rfloor + 4 \leq i \leq n-3. \end{cases} \tag{34}
 \end{aligned}$$

One can easily verify that each vertex of $G_n[1, 4]$ has unique representation with respect to W . Hence, W is a resolving set, and

$$\beta(G_n[1, 3]) \leq 4. \tag{35}$$

Now, to prove the lower bound, it is sufficient to show that there is no resolving set of $G_n[1, 4]$ with three elements. Suppose, on contrary, that W is a minimum resolving set of $G_n[1, 4]$ of cardinality 3. Define

$$\begin{aligned}
A &= \left\{ u_{4i-3}, v_{4i+1}, 1 \leq i \leq \frac{n-1}{2} \right\}, \\
B &= \left\{ u_{4i-2}, v_{4i+2}, 1 \leq i \leq \frac{n-1}{2} \right\}, \\
C &= \left\{ u_{4i-1}, v_{4i+3}, 1 \leq i \leq \frac{n-1}{2} \right\}, \\
D &= \left\{ u_{4i}, v_{4i+4}, 1 \leq i \leq \frac{n-1}{2} \right\}.
\end{aligned} \tag{36}$$

It is easy to see that these are disjoint subsets of the vertex set of $G_n[1, 4]$. We make the following claims.

Claim 3. Let x be an arbitrary vertex of the resolving set W that does not belong to A . Then,

$$\begin{aligned}
d(v_{i-1}, x) &= d(u_{i-4}, x) \\
&= \left\lfloor \frac{i+2}{2} \right\rfloor \text{ or } \left\lfloor \frac{i+4}{2} \right\rfloor.
\end{aligned} \tag{37}$$

Thus, to resolve u_{i-4} and v_{i-1} , either u_{i-4} or v_{i-1} or one of the vertices from the set $A = \{u_{4i-3}, v_{4i+1}, 1 \leq i \leq \lfloor (n-1)/2 \rfloor\}$ must belong to W .

Claim 4. Let x be an arbitrary vertex of the resolving set W that does not belong to B . Then,

$$\begin{aligned}
d(v_i, x) &= d(u_{i-3}, x) \\
&= \left\lfloor \frac{i}{2} \right\rfloor \text{ or } \left\lfloor \frac{i+2}{2} \right\rfloor.
\end{aligned} \tag{38}$$

Thus, to resolve u_{i-3} and v_i , either u_{i-3} or v_i or one of the vertices from the set $B = \{u_{4i-2}, v_{4i+2}, 1 \leq i \leq \lfloor (n-1)/2 \rfloor\}$ must belong to W .

Claim 5. Let x be an arbitrary vertex of the resolving set W that does not belong to C . Then,

$$\begin{aligned}
d(v_{i+1}, x) &= d(u_{i+2}, x) \\
&= \left\lfloor \frac{i-1}{2} \right\rfloor \text{ or } \left\lfloor \frac{i+1}{2} \right\rfloor.
\end{aligned} \tag{39}$$

Thus, to resolve u_{i+2} and v_{i+1} , either u_{i+2} or v_{i+1} or one of the vertices from the set $C = \{u_{4i-1}, v_{4i+3}, 1 \leq i \leq \lfloor (n-1)/2 \rfloor\}$ must belong to W .

Claim 6. Let x be an arbitrary vertex of the resolving set W that does not belong to D . Then,

$$\begin{aligned}
d(v_{i+2}, x) &= d(u_{i-1}, x) \\
&= \left\lfloor \frac{i-2}{2} \right\rfloor \text{ or } \left\lfloor \frac{i}{2} \right\rfloor.
\end{aligned} \tag{40}$$

Thus, to resolve u_{i-1} and v_{i+2} , either u_{i-1} or v_{i+2} or one of the vertices from the set $D = \{u_{4i}, v_{4i+4}, 1 \leq i \leq \lfloor (n-1)/2 \rfloor\}$ must belong to W .

The above claims imply that W contains at least four elements. Thus,

$$\beta(G_n[1, 4]) \geq 4. \tag{41}$$

From equations (35) and (41), we get

$$\beta(G_n[1, 4]) = 4. \tag{42}$$

3. Conclusion

The resolvability of the circulant graphs $C_n[1, 2, \dots, k]$ has been investigated by different authors [15, 17, 18, 25]. The resolvability of barycentric subdivision of circulant graphs was investigated by Imran et al. in [8, 25], where they showed that some of these families had constant metric dimension. In this paper, we have studied the metric dimension of subdivision of circulant graphs $C_n[1, k]$ denoted by $G_n[1, k]$ for $2 \leq k \leq 4$. It is proved that the metric dimension of this family of graphs $G_n(1, k)$ has unbounded metric dimension when $n \geq 9$ and $k = 2$. It is also shown that for $k = 3$ and 4, the graph $G_n[1, k]$ has constant metric dimension. This family of graphs $G_n[1, k]$ which is obtained from subdivision of circulant graphs has interesting metric properties. The family has an unbounded metric dimension for $k = 2$ and bounded metric dimension for $k = 3, 4$. We also believe that the metric dimension increases as the value of k increases. In this context, we arise the following open question.

Open problem: compute the exact value of metric dimension or determine some good bounds in terms of other graphical parameters for the subdivision of circulant graphs $G_n[1, k]$ when $k \geq 5$. Also, characterize the classes of $G_n[1, 2, \dots, k]$ that has bounded or unbounded metric dimension.

Data Availability

The data used to support the findings of this study are included within the article.

Conflicts of Interest

The authors declare that there are no conflicts of interest regarding the publication of this paper.

Acknowledgments

The research work of the first author was sponsored by the Shandong Provincial Natural Science Foundation, China (ZR2018MA010). This research was also supported by UPAR Grants of United Arab Emirates University (UAEU), UAE, via Grant nos. G00002590 and G00003271.

References

- [1] G. Chartrand, L. Eroh, M. A. Johnson, and O. R. Oellermann, "Resolvability in graphs and the metric dimension of a graph," *Discrete Applied Mathematics*, vol. 105, no. 1-3, pp. 99-113, 2000.

- [2] S. Khuller, B. Raghavachari, and A. Rosenfeld, *Localization in Graphs*, Technical Report CS-TR-3326, University of Maryland at College Park, College Park, MD, USA, 1994.
- [3] A. Sebö and E. Tannier, “On metric generators of graphs,” *Mathematics of Operations Research*, vol. 29, pp. 383–393, 2004.
- [4] R. A. Melter and I. Tomescu, “Metric bases in digital geometry,” *Computer Vision, Graphics, and Image Processing*, vol. 25, no. 1, pp. 113–121, 1984.
- [5] P. J. Slater, “Leaves of trees, congress,” *Numer*, vol. 14, pp. 549–559, 1975.
- [6] P. J. Slater, “Dominating and reference sets in graph,” *Journal of Mathematical Physics*, vol. 22, pp. 445–455, 1988.
- [7] F. Harary and R. A. Melter, “On the metric dimension of a graph,” *Ars Combinatoria*, vol. 2, pp. 191–195, 1976.
- [8] A. Ahmad, M. Imran, O. AL-Mushayt, and S. A. U. H. Bokhary, “On the metric dimension of barycentric subdivision of Cayley graphs $Cay(Z_n \oplus Z_m)$,” *Miskolc Math Notes*, vol. 16, no. 2, pp. 637–646, 2015.
- [9] U. Ali, S. A. Bokhary, K. Wahid, and G. Abbas, “On resolvability of a graph associated to a finite vector space,” *Journal of Algebra and Its Applications*, vol. 18, no. 2, pp. 1–10, Article ID 1950028, 2018.
- [10] A. Borchert and S. Gosselin, “The metric dimension of circulant graphs and Cayley hypergraphs,” *Utilitas Mathematica*, vol. 106, pp. 125–147, 2018.
- [11] K. Chau and S. Gosselin, “The metric dimension of circulant graphs and their cartesian products,” *Opuscula Mathematica*, vol. 37, no. 4, pp. 509–534, 2017.
- [12] C. Grigorious, T. Kalinowski, J. Ryan, and S. Stephen, “The metric dimension of the circulant graph $C(n, \pm 1, 2, 3, 4)$,” *Australasian Journal of Combinatorics*, vol. 69, pp. 417–441, 2017.
- [13] M. Imran, S. A. Ul Haq Bokhary, and A. Q. Baig, “On families of convex polytopes with constant metric dimension,” *Computers & Mathematics with Applications*, vol. 60, no. 9, pp. 2629–2638, 2010.
- [14] M. Imran, F. Bashir, A. Q. Baig, S. A. Bokhary, A. Riasat, and I. Tomescu, “On metric dimension of flower graphs $f_{n \times m}$ and convex polytopes,” *Utilitas Mathematica*, vol. 92, pp. 389–409, 2013.
- [15] M. Imran and S. A. Bokhary, “On resolvability in double-step circulant graphs,” *UPB Scientific Bulletin, Series A: Applied Mathematics*, vol. 76, no. 2, pp. 31–42, 2014.
- [16] M. Imran, S. A. U. H. Bokhary, A. Ahmad, and A. Semaničová-Feňovčíková, “On classes of regular graphs with constant metric dimension,” *Acta Mathematica Scientia*, vol. 33, no. 1, pp. 187–206, 2013.
- [17] L. D. Toit and T. Vertik, “On the metric dimension of circulant graphs with 2 generators,” *Kragujevac Journal of Mathematics*, vol. 43, no. 1, pp. 49–58, 2019.
- [18] T. Vertik, “On the metric dimension of circulant graphs with 4 generators,” *Discrete mathematics*, vol. 12, no. 2, pp. 104–114, 2017.
- [19] M. R. Garey and D. S. Johnson, *Computer and Intractability: A Guide to the Theory of NP-Completeness*, Freeman, New York, NY, USA, 1979.
- [20] O. R. Oellermann and J. Peters-Fransen, “Metric dimension of cartesian products of graphs,” *Utilitas Mathematica*, vol. 69, pp. 33–41, 2006.
- [21] P. S. Buczkowski, G. Chartrand, C. Poisson, and P. Zhang, “On k -dimensional graphs and their basis,” *Periodica Mathematica Hungarica*, vol. 46, no. 1, pp. 9–15, 2003.
- [22] G. Chartrand and P. Zhang, “The theory and applications of resolvability in graphs,” *Congress Numer*, vol. 160, pp. 47–68, 2003.
- [23] T. Vertik, “The metric dimension of circulant graphs,” *Canadian Mathematical Bulletin*, vol. 60, pp. 206–216, 2017.
- [24] J. L. Gross and J. Yellen, *Graph Theory and its Applications*, Chapman and Hall/CRC, New York, NY, USA, 2006.
- [25] M. Imran, A. Q. Baig, S. A. U. H. Bokhary, and I. Javaid, “On the metric dimension of circulant graphs,” *Applied Mathematics Letters*, vol. 25, no. 3, pp. 320–325, 2012.

Research Article

An Exponential Spline Difference Scheme for Solving a Class of Boundary Value Problems of Second-Order Ordinary Differential Equations

Dunqian Cao 

School of Mathematics and Physics, Guangxi University for Nationalities, Nanning 530006, China

Correspondence should be addressed to Dunqian Cao; caodunqian@gxun.edu.cn

Received 8 May 2020; Revised 2 July 2020; Accepted 3 July 2020; Published 28 August 2020

Academic Editor: Juan L. G. Guirao

Copyright © 2020 Dunqian Cao. This is an open access article distributed under the Creative Commons Attribution License, which permits unrestricted use, distribution, and reproduction in any medium, provided the original work is properly cited.

In this paper, we mainly study an exponential spline function space, construct a basis with local supports, and present the relationship between the function value and the first and the second derivative at the nodes. Using these relations, we construct an exponential spline-based difference scheme for solving a class of boundary value problems of second-order ordinary differential equations (ODEs) and analyze the error and the convergence of this method. The results show that the algorithm is high accurate and conditionally convergent, and an accuracy of $(1/240)h^6$ was achieved with smooth functions.

1. Introduction

In physics, chemistry, biology, sociology, and many other disciplines, there are tremendous problems that can be described by differential equations (DEs), but it is difficult to get their explicit expressions. So, people began to seek the numerical solutions of these problems, which can also be applied to scientific research and engineering practice if their accuracy satisfies the needs. Especially the advent of computers makes it possible to quickly carry out a large number of calculations, which also makes the numerical solution method of DEs become one of the most important branches of computational mathematics. Due to its high smoothness, low power, and easy calculation, the spline function has been widely used in computer graphics, data interpolation and fitting, shape control, and numerical solutions of DEs. There are two main schemes in numerical solutions of DEs using spline functions: the spline finite element method and the spline difference method. The first has a wide range of application and can be applied to many types of equations, but it requires a large amount of calculation. While the second is simple process with a small amount of calculation and high accuracy, but it can only be applied to specific types of equations.

In this paper, we mainly focus a class of second-order ordinary differential equations (ODEs):

$$u'' + q(x)u' + p(x)u = g(x), \quad x \in [a, b], \quad (1)$$

which meets one of the following boundary conditions.

(1) First boundary condition:

$$\begin{aligned} u(a) &= \mu_0, \\ u(b) &= \mu_1. \end{aligned} \quad (2)$$

(2) Second boundary condition:

$$\begin{aligned} u^{(1)}(a) &= \mu_0, \\ u^{(1)}(b) &= \mu_1. \end{aligned} \quad (3)$$

(3) Third boundary condition:

$$\begin{aligned} u(a) &= \mu_0, \\ u^{(1)}(b) &= \mu_1. \end{aligned} \quad (4)$$

(4) Fourth boundary condition:

$$\begin{aligned} u^{(1)}(a) &= \mu_0, \\ u(b) &= \mu_1. \end{aligned} \quad (5)$$

where μ_0 and μ_1 are constants and $p(x)$, $q(x)$, and $g(x)$ are continuous functions in the interval of $[a, b]$.

Many scholars have been studying such two-point boundary value problems. Albasiny and Hoskins [1] and Raghavarao et al. [2] used cubic polynomial splines to solve such problems. Blue [3] used quintic polysplines to solve such problems. Caglar et al. [4] used cubic B-splines in their solving scheme. Chawla and Shiva Kumar[5] extended the problem to semi-infinite regions.

In recent years, with the deepening of research, people have begun to use nonpolynomial splines to solve such problems. Zahra [6], Rao and Kumar [7], Tirmizi et al. [8], Ramadan et al. [9], Surla and Stojanović [10], Jha [11, 12], and Kadalbajoo and Patidar [13] have carried out a lot of research in this area and achieved very high computational accuracy.

However, there are still many theoretical problems to be broken in the study of nonpolynomial splines. Due to the diversity of nonpolynomial splines, it is crucial to choose the basis and parameters in solving the problem. However, there is still no reference in this regard. In this paper, a selected set of spline basis functions was used to deduce the relationship between the derivative and the function value and then to obtain the second-order difference scheme for solving second-order ODEs, which provides a method for solving such problems.

2. Exponential Spline Function Space

Exponential spline refers to a type of spline in which the nonpolynomial factors of spline basis functions contain only exponential functions. The exponential spline in this sense is not very specific; it can contain many forms of exponential spline, which can produce substantially different splines, and is inconvenient to study. Therefore, the exponential spline refers to that with a specific form in the rest of this work.

Next, we define an exponential spline function space. Let

$$s_i(x) = a_i + b_i(x - x_i) + c_i e^{\tau_1(x - x_i)} + d_i e^{\tau_2(x - x_i)}, \quad (6)$$

$$i = 1, 2, \dots, n,$$

where a_i , b_i , c_i , and d_i are coefficients and τ_1 and τ_2 are parameters with $\tau_1 \neq \tau_2$.

Definition 1. The following function space

$$\begin{aligned} \mathcal{E}_3^r(\Delta_n) &= \{s: s(x) = s_i(x), x \in I_i, i = 1, 2, \dots, \\ &ns(x) \in C^r[a, b], r < 3\}, \end{aligned} \quad (7)$$

is called the cubic r -order exponential spline function space.

Obviously, the function $s(x)$ in $\mathcal{E}_3^2(\Delta_n)$ must meet

$$s_i^{(r)}(x_i) = s_{i+1}^{(r)}(x_i), \quad r = 0, 1, 2; i = 1, 2, \dots, n - 1. \quad (8)$$

The dimension of $\mathcal{E}_3^2(\Delta_n)$ is $n + 3$. Then, we find a set of basic functions with local supports for $\mathcal{E}_3^2(\Delta_n)$.

Assume $s(x) \in \mathcal{E}_3^2(\Delta_n)$, for given j , $2 \leq j \leq n - 2$; let

$$\begin{cases} s_{j-1}^{(r)}(x_{j-2}) = 0, & r = 0, 1, 2, \\ s_{j+2}^{(r)}(x_{j+2}) = 0, & r = 0, 1, 2, \\ s_{j+k}^{(r)}(x_{j+k}) = s_{j+k+1}^{(r)}(x_{j+k}), & k = -1, 0, 1, r = 0, 1, 2, \\ s_j(x_j) = 1. \end{cases} \quad (9)$$

We can obtain

$$\begin{aligned} a_{i-1} &= \frac{|\mathbf{A}_1|}{|\mathbf{A}|}, & b_{i-1} &= \frac{|\mathbf{A}_2|}{|\mathbf{A}|}, & c_{i-1} &= \frac{|\mathbf{A}_3|}{|\mathbf{A}|}, & d_{i-1} &= \frac{|\mathbf{A}_4|}{|\mathbf{A}|}, \\ a_i &= \frac{|\mathbf{A}_5|}{|\mathbf{A}|}, & b_i &= \frac{|\mathbf{A}_6|}{|\mathbf{A}|}, & c_i &= \frac{|\mathbf{A}_7|}{|\mathbf{A}|}, & d_i &= \frac{|\mathbf{A}_8|}{|\mathbf{A}|}, \\ a_{i+1} &= \frac{|\mathbf{A}_9|}{|\mathbf{A}|}, & b_{i+1} &= \frac{|\mathbf{A}_{10}|}{|\mathbf{A}|}, & c_{i+1} &= \frac{|\mathbf{A}_{11}|}{|\mathbf{A}|}, & d_{i+1} &= \frac{|\mathbf{A}_{12}|}{|\mathbf{A}|}, \\ a_{i+2} &= \frac{|\mathbf{A}_{13}|}{|\mathbf{A}|}, & b_{i+2} &= \frac{|\mathbf{A}_{14}|}{|\mathbf{A}|}, & c_{i+2} &= \frac{|\mathbf{A}_{15}|}{|\mathbf{A}|}, & d_{i+2} &= \frac{|\mathbf{A}_{16}|}{|\mathbf{A}|}, \end{aligned} \quad (10)$$

where

$$\mathbf{A} = [\mathbf{A}'_1 \mathbf{A}'_2],$$

$$\mathbf{A}'_1 = \begin{bmatrix}
 1 & -h_{i-1} & e^{(-\theta_{i-1})} & e^{(-\eta_{i-1})} & 0 & 0 & 0 & 0 \\
 0 & 1 & \tau_1 e^{(-\theta_{i-1})} & \tau_2 e^{(-\eta_{i-1})} & 0 & 0 & 0 & 0 \\
 0 & 0 & \tau_1^2 e^{(-\theta_{i-1})} & \tau_2^2 e^{(-\eta_{i-1})} & 0 & 0 & 0 & 0 \\
 1 & 0 & 1 & 1 & -1 & h_i & -e^{(-\theta_i)} & -e^{(-\eta_i)} \\
 0 & 1 & \tau_1 & \tau_2 & 0 & -1 & -\tau_1 e^{(-\theta_i)} & -\tau_2 e^{(-\eta_i)} \\
 0 & 0 & \tau_1^2 & \tau_2^2 & 0 & 0 & -\tau_1^2 e^{(-\theta_i)} & -\tau_2^2 e^{(-\eta_i)} \\
 0 & 0 & 0 & 0 & 1 & 0 & 1 & 1 \\
 0 & 0 & 0 & 0 & 0 & 1 & \tau_1 & \tau_2 \\
 0 & 0 & 0 & 0 & 0 & 0 & \tau_1^2 & \tau_2^2 \\
 0 & 0 & 0 & 0 & 0 & 0 & 0 & 0 \\
 0 & 0 & 0 & 0 & 0 & 0 & 0 & 0 \\
 0 & 0 & 0 & 0 & 0 & 0 & 0 & 0 \\
 0 & 0 & 0 & 0 & 0 & 0 & 0 & 0 \\
 0 & 0 & 0 & 0 & 0 & 0 & 0 & 0 \\
 0 & 0 & 0 & 0 & 0 & 0 & 0 & 0 \\
 0 & 0 & 0 & 0 & 1 & 0 & 1 & 1
 \end{bmatrix},$$

$$\mathbf{A}'_2 = \begin{bmatrix}
 0 & 0 & 0 & 0 & 0 & 0 & 0 & 0 \\
 0 & 0 & 0 & 0 & 0 & 0 & 0 & 0 \\
 0 & 0 & 0 & 0 & 0 & 0 & 0 & 0 \\
 0 & 0 & 0 & 0 & 0 & 0 & 0 & 0 \\
 0 & 0 & 0 & 0 & 0 & 0 & 0 & 0 \\
 0 & 0 & 0 & 0 & 0 & 0 & 0 & 0 \\
 -1 & h_{i+1} & -e^{(-\theta_{i+1})} & -e^{(-\eta_{i+1})} & 0 & 0 & 0 & 0 \\
 0 & -1 & -\tau_1 e^{(-\theta_{i+1})} & -\tau_2 e^{(-\eta_{i+1})} & 0 & 0 & 0 & 0 \\
 0 & 0 & -\tau_1^2 e^{(-\theta_{i+1})} & -\tau_2^2 e^{(-\eta_{i+1})} & 0 & 0 & 0 & 0 \\
 1 & 0 & 1 & 1 & -1 & h_{i+2} & -e^{(-\theta_{i+2})} & -e^{(-\eta_{i+2})} \\
 0 & 1 & \tau_1 & \tau_2 & 0 & -1 & -\tau_1 e^{(-\theta_{i+2})} & -\tau_2 e^{(-\eta_{i+2})} \\
 0 & 0 & \tau_1^2 & \tau_2^2 & 0 & 0 & -\tau_1^2 e^{(-\theta_{i+2})} & -\tau_2^2 e^{(-\eta_{i+2})} \\
 0 & 0 & 0 & 0 & 1 & 0 & 1 & 1 \\
 0 & 0 & 0 & 0 & 0 & 1 & \tau_1 & \tau_2 \\
 0 & 0 & 0 & 0 & 0 & 0 & \tau_1^2 & \tau_2^2 \\
 0 & 0 & 0 & 0 & 0 & 0 & 0 & 0
 \end{bmatrix}.$$

(11)

\mathbf{A}_k ($k = 1, 2, \dots, 16$) is the matrix obtained by replacing the k column of \mathbf{A} with $[0, \dots, 0, 1]^T$, $\theta_i = \tau_1 h_i$, and $\eta_i = \tau_2 h_i$.

For even splitting, i.e., $h_i = h, i = 1, 2, \dots, n$, and $\tau_2 = -\tau_1 = \tau \neq 0$, the results obtained are

$$\begin{aligned}
a_{j-1} &= -\frac{\omega\theta}{\sigma}, \\
b_{j-1} &= -\frac{\omega\theta}{h\sigma}, \\
c_{j-1} &= \frac{1}{2} \frac{\omega(-\cosh(\theta) + \sinh(\theta))}{\sigma}, \\
d_{j-1} &= \frac{1}{2} \frac{\omega(\cosh(\theta) + \sinh(\theta))}{\sigma}, \\
a_j &= \frac{\theta(-4 \sinh(3\theta) + \sinh(4\theta) - 4 \sinh(\theta) + 6 \sinh(2\theta))}{\sigma}, \\
b_j &= \frac{\theta(-3 \sinh(3\theta) + 2 \sinh(2\theta) + \sinh(4\theta) + \sinh(\theta))}{h\sigma}, \\
c_j &= -\frac{1}{2\sigma} (-5 + 4 \cosh(2\theta) - 2 \sinh(2\theta) - 4 \cosh(3\theta) + 3 \sinh(3\theta) + \cosh(4\theta) - \sinh(4\theta) + 4 \cosh(\theta) - \sinh(\theta)), \\
d_j &= -\frac{1}{2\sigma} (\cosh(4\theta) + \sinh(4\theta) - 5 - 4 \cosh(3\theta) - 3 \sinh(3\theta) + 4 \cosh(\theta) + \sinh(\theta) + 4 \cosh(2\theta) + 2 \sinh(2\theta)), \\
a_{j+1} &= -\frac{\omega\theta}{\sigma}, \\
b_{j+1} &= \frac{\theta(-3 \sinh(3\theta) + 2 \sinh(2\theta) + \sinh(4\theta) + \sinh(\theta))}{h\sigma}, \\
c_{j+1} &= \frac{1}{4\sigma} (-5 + 4 \cosh(2\theta) + 10 \sinh(2\theta) - 4 \cosh(3\theta) + \cosh(4\theta) - \sinh(4\theta) + 4 \cosh(\theta) - 16 \sinh(\theta)), \\
d_{j+1} &= \frac{1}{4\sigma} (\cosh(4\theta) + \sinh(4\theta) - 5 - 4 \cosh(3\theta) + 4 \cosh(\theta) + 16 \sinh(\theta) + 4 \cosh(2\theta) - 10 \sinh(2\theta)), \\
a_{j+2} &= 0, \\
b_{j+2} &= \frac{\omega\theta}{h\sigma}, \\
c_{j+2} &= \frac{\omega}{2\sigma}, \\
d_{j+2} &= -\frac{\omega}{2\sigma},
\end{aligned} \tag{12}$$

where

$$\begin{aligned}
\omega &= 5 \sinh(\theta) - 4 \sinh(2\theta) + \sinh(3\theta), \\
\sigma &= 5 + \theta \sinh(4\theta) - 4\theta \sinh(\theta) + 6\theta \sinh(2\theta) - 4\theta \sinh(3\theta) \\
&\quad + 4 \cosh(3\theta) - 4 \cosh(\theta) - \cosh(4\theta) - 4 \cosh(2\theta), \\
\theta &= \tau h.
\end{aligned} \tag{13}$$

Define a function

$$B_j(x) = \begin{cases} s_{j-1}(x), & x \in I_{j-1}, \\ s_j(x), & x \in I_j, \\ s_{j+1}(x), & x \in I_{j+1}, \\ s_{j+2}(x), & x \in I_{j+2}, \\ 0, & \text{otherwise,} \end{cases} \tag{14}$$

$j = 2, 3, \dots, n-2,$

where the coefficients of $s_{j-1}(x)$, $s_j(x)$, $s_{j+1}(x)$, and $s_{j+2}(x)$ are given by the solution of function (9). Besides, for

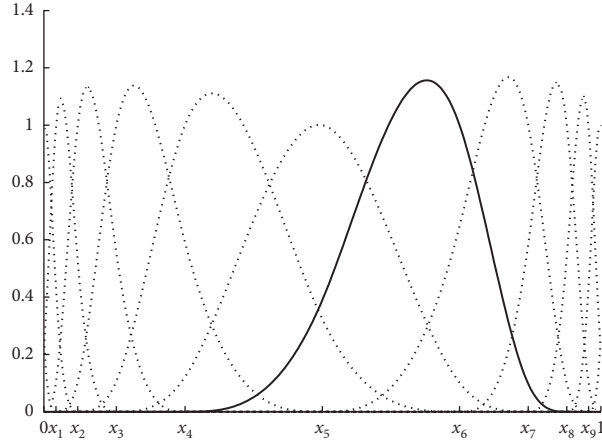


FIGURE 1: Basis function set $\{B_j(x)\}_{j=-1}^{n+1}$ of the exponential spline function space.

$j = -1, 0, 1, n - 1, n, n + 1$, an interval expansion will be conducted, i.e., (x_0, x_1, \dots, x_n) will be extended to be

$$(x_{-3}, x_{-2}, x_{-1}, x_0, x_1, \dots, x_n, x_{n+1}, x_{n+2}, x_{n+3}). \quad (15)$$

Thus, j in (11) can take the values of $-1, 0, 1, \dots, n, n + 1$. Of course, the function domain is still $[x_0, x_n]$.

For the space basis of $\mathcal{E}_3^2(\Delta_n)$, we have the following proposition.

Proposition 1. When $\tau_1 \neq \tau_2$, the function set of $\{B_j(x)\}_{j=-1}^{n+1}$ is a set of basis of $\mathcal{E}_3^2(\Delta_n)$.

For special cases, we can prove the following.

Theorem 1. When $\tau_2 = -\tau_1 = \tau \neq 0$ and $h_i = h, i = -2, -1, \dots, n + 3$, the function set of $\{B_j(x)\}_{j=-1}^{n+1}$ is a set of basis of $\mathcal{E}_3^2(\Delta_n)$.

Proof. Obviously, $B_j(x) \in \mathcal{E}_3^2(\Delta_n), j = -1, 0, 1, \dots, n, n + 1$, and the number of functions equals the dimension of $\mathcal{E}_3^2(\Delta_n)$. Therefore, we need to show that $\{B_j(x)\}_{j=-1}^{n+1}$ is linearly independent.

For $x = x_i, i = -1, 0, \dots, n, n + 1$, let $\mathbf{B} = (\beta_{ij}) = (B_j(x_i))_{(n+3) \times (n+3)}$, if matrix \mathbf{B} is invertible, then $\{B_j(x)\}_{j=-1}^{n+1}$ is linearly independent. It is easy to know that \mathbf{B} is a tridiagonal matrix, and

$$\begin{aligned} b_{i,i-1} &= a_{i-1} + c_{i-1} + d_{i-1}, \\ b_{i,i} &= a_i + c_i + d_i = 1, \\ b_{i,i+1} &= a_{i+1} + c_{i+1} + d_{i+1}, \end{aligned} \quad (16)$$

where $i = -1, 0, \dots, n + 1$. Because

$$\begin{aligned} |b_{i,i-1}| + |b_{i,i+1}| &= |a_{i-1} + c_{i-1} + d_{i-1}| + |a_{i+1} + c_{i+1} + d_{i+1}| \\ &= \left| \frac{8}{\sigma} \left((\cosh(\theta) - 1)^2 (1 - \cosh(\theta))^2 + \theta \sinh(\theta) \right) \right| \\ &= \left| \frac{1 - \cosh(\theta)^2 + \theta \sinh(\theta)}{1 - \cosh(\theta)^2 + \theta \sinh(\theta) \cosh(\theta)} \right| \\ &\leq \frac{1}{2} < 1 = |b_{ii}|. \end{aligned} \quad (17)$$

\mathbf{B} is a strictly tridiagonal matrix. Thus, \mathbf{B} is invertible.

This proves that $\{B_j(x)\}_{j=-1}^{n+1}$ is linearly independent.

When $h_i = h, i = -2, -1, \dots, n + 3$, $\{B_j(x)\}_{j=-1}^{n+1}$ has the following properties. \square

Proposition 2. For any $x \in [a, b]$

$$\sum_{j=-1}^{n+1} B_j(x) = C, \quad (18)$$

where C is not related to x , and

$$C = \frac{\tau_1 \tau_2 h (\tau_2 - \tau_1) (e^{(-\tau_1 h)} + e^{(-\tau_2 h)} - e^{(-h(\tau_1 + \tau_2))} - 1)}{(\tau_2^2 - \tau_1^2) e^{-h(\tau_1 + \tau_2)} + (\tau_1^2 + \tau_2^2 + \tau_1 \tau_2^2 h - \tau_1^2 \tau_2 h) e^{(-\tau_1 h)} - (\tau_1^2 + \tau_2^2 - \tau_1 \tau_2^2 h + \tau_1^2 \tau_2 h) e^{(-\tau_2 h)} + \tau_1^2 - \tau_2^2} \quad (19)$$

The basis function $B_j(x)$ has a local supporting set of $[x_{i-2}, x_{i+2}]$. Figure 1 shows all functions in the function set of $\{B_j(x)\}_{j=-1}^{n+1}$ at the same coordinate.

3. Properties of Exponential Spline Functions

The relationship between the function value and the first derivative and that between the function value and the second derivative are commonly used in numerically solving DEs. Next, we will derive some properties of the functions in $\mathcal{E}_3^2(\Delta_n)$, and these relationships will be used in numerically calculating DEs.

Let $s(x) \in \mathcal{E}_3^2(\Delta_n)$; then,

$$s(x) = s_i(x), \quad x \in I_i, \quad i = 1, 2, \dots, n. \quad (20)$$

Denote

$$\begin{aligned} S_i &= s(x_i), \\ D_i &= s'(x_i), \\ M_i &= s'', \quad i = 1, 2, \dots, n, \end{aligned} \quad (21)$$

since $s_i(x_i) = s_{i+1}(x_i)$, $s_i''(x_i) = s_{i+1}''(x_i)$, the factors of a_i , b_i , c_i , and d_i can be written as

$$\begin{aligned} a_i &= \frac{1}{\tau_1^2 \tau_2^2 \rho_i} \left((\tau_1^2 - \tau_2^2) M_{i-1} + (\tau_2^2 e^{-\tau_2 h_i} - \tau_1^2 e^{-\tau_1 h_i}) M_i + \tau_1^2 \tau_2^2 \rho_i S_i \right), \\ b_i &= \frac{1}{h_i \tau_1^2 \tau_2^2 \rho_i} \left((\tau_2^2 e^{-\tau_1 h_i} - \tau_1^2 e^{-\tau_2 h_i} + \tau_1^2 - \tau_2^2) M_{i-1} \right. \\ &\quad \left. + (\tau_1^2 e^{-\tau_1 h_i - \tau_2 h_i} - \tau_2^2 e^{-\tau_1 h_i - \tau_2 h_i} - \tau_1^2 e^{-\tau_1 h_i} + \tau_2^2 e^{-\tau_2 h_i}) M_i \right. \\ &\quad \left. + \tau_1^2 \tau_2^2 \rho_i S_i + \tau_1^2 \tau_2^2 e^{-\tau_2 h_i} S_{i-1} - \tau_1^2 \tau_2^2 e^{-\tau_1 h_i} S_{i-1} \right), \\ c_i &= \frac{1}{\tau_1^2 \rho_i} (M_{i-1} - e^{-\tau_2 h_i} M_i), \\ d_i &= -\frac{1}{\tau_2^2 \rho_i} (M_{i-1} - e^{-\tau_1 h_i} M_i), \end{aligned} \quad (22)$$

where $\rho_i = e^{-\tau_1 h_i} - e^{-\tau_2 h_i}$, $i = 1, 2, \dots, n$ (the same applies hereinafter). Using the continuous condition of the first derivative

$$s_i'(x_i) = s_{i+1}'(x_i), \quad i = 1, 2, \dots, n-1, \quad (23)$$

we obtain

$$\alpha_{1i} M_{i-1} + \alpha_{2i} M_i + \alpha_{3i} M_{i+1} - \frac{1}{h_i} S_{i-1} + \frac{h_{i+1} + h_i}{h_i h_{i+1}} S_i - \frac{1}{h_{i+1}} S_{i+1} = 0, \quad (24)$$

where $i = 1, 2, \dots, n-1$,

$$\begin{aligned} \alpha_{1i} &= -\frac{(h_i \tau_1 \tau_2^2 - h_i \tau_1^2 \tau_2 - \tau_1^2 e^{(-\tau_2 h_i)} + \tau_2^2 e^{(-\tau_1 h_i)} + \tau_1^2 - \tau_2^2)}{\tau_1^2 \tau_2^2 \rho_i h_i}, \\ \alpha_{2i} &= \frac{1}{\tau_1^2 \tau_2^2 \rho_i \rho_{i+1} h_i h_{i+1}} \left((h_{i+1} \tau_1^2 - h_{i+1} \tau_2^2) e^{(-\tau_1 h_i - \tau_2 h_i - \tau_1 h_{i+1})} + (h_{i+1} \tau_2^2 - h_{i+1} \tau_1^2) e^{(-\tau_1 h_i - \tau_2 h_i - \tau_2 h_{i+1})} \right. \\ &\quad \left. + (-h_i \tau_1^2 + h_i \tau_2^2) e^{(-\tau_1 h_i)} + (h_i \tau_1^2 - h_i \tau_2^2) e^{(-\tau_2 h_i)} + (h_{i+1} \tau_1^2 + h_i \tau_1^2) e^{(-\tau_2 h_{i+1} - \tau_1 h_i)} \right. \\ &\quad \left. + (h_i \tau_2^2 + h_{i+1} \tau_2^2) e^{(-\tau_1 h_{i+1} - \tau_2 h_i)} + (-h_{i+1} \tau_2^2 - h_i \tau_1^2 + h_i h_{i+1} \tau_1 \tau_2^2 - h_i h_{i+1} \tau_1^2 \tau_2) e^{(-\tau_2 (h_{i+1} + h_i))} \right. \\ &\quad \left. + (-h_{i+1} \tau_1^2 - h_i \tau_2^2 - h_i h_{i+1} \tau_1 \tau_2^2 + h_i h_{i+1} \tau_1^2 \tau_2) e^{(-\tau_1 (h_{i+1} + h_i))} \right), \\ \alpha_{3i} &= \frac{\tau_2^2 e^{-\tau_2 h_{i+1}} - \tau_1^2 e^{-\tau_1 h_{i+1}} + (h_{i+1} \tau_1^2 \tau_2 - h_{i+1} \tau_1 \tau_2^2 + \tau_1^2 - \tau_2^2) e^{-h_{i+1} (\tau_1 + \tau_2)}}{\tau_1^2 \tau_2^2 \rho_{i+1} h_{i+1}}. \end{aligned} \quad (25)$$

If $h_i = h > 0$, $i = 1, 2, \dots, n$ and $\tau_2 = -\tau_1 = \tau$, then the corresponding coefficients become

$$\begin{aligned} \alpha_{1i} &= \frac{(e^{2\tau h} - 2\tau h e^{\tau h} - 1)}{h\tau^2(e^{2\tau h} - 1)}, \\ \alpha_{2i} &= \frac{2(-e^{2\tau h} + \tau h e^{2\tau h} + 1 + \tau h)}{h\tau^2(e^{2\tau h} - 1)}, \\ \alpha_{3i} &= \frac{(e^{2\tau h} - 2\tau h e^{\tau h} - 1)}{h\tau^2(e^{2\tau h} - 1)}, \\ \alpha_{4i} &= \frac{1}{h}, \\ \alpha_{5i} &= \frac{2}{h}, \\ \alpha_{6i} &= -\frac{1}{h}. \end{aligned} \tag{26}$$

Let $\tau \rightarrow 0$; then, (24) is equivalent to $h^2(M_{i-1} + 4M_i + M_{i+1}) - 6S_{i-1} + 12S_i - 6S_{i+1} = 0$. (27)

In a similar way, we can obtain the relationship between the function value and the first derivative:

$$\beta_{1i}D_{i-1} + \beta_{2i}D_i + \beta_{3i}D_{i+1} + \beta_{4i}S_{i-1} + \beta_{5i}S_i + \beta_{6i}S_{i+1} = 0, \tag{28}$$

where

$$\begin{aligned} \beta_{1i} &= \frac{1}{K_i K_{i+1}} \left[(\tau_1 - \tau_2)^2 (-\tau_1 + \tau_1 \tau_2 h_i - \tau_2) e^{(-h_{i+1}(\tau_1 + \tau_2))} - \tau_2^2 (\tau_1 - \tau_2) e^{(-\tau_1 h_{i+1} - \tau_2 h_{i+1} - \tau_1 h_i)} \right. \\ &\quad + \tau_1^2 (\tau_1 - \tau_2) e^{(-\tau_1 h_{i+1} - \tau_2 h_{i+1} - \tau_2 h_i)} - \tau_2^2 (-\tau_1 + \tau_1 \tau_2 h_{i+1} + \tau_2) e^{(-\tau_1 (h_{i+1} + h_i))} \\ &\quad - \tau_1^2 (\tau_1 \tau_2 h_{i+1} + \tau_1 - \tau_2) e^{(-\tau_2 (h_{i+1} + h_i))} + \tau_2^2 (\tau_2 - \tau_1) e^{(-\tau_1 h_i)} - \tau_1^2 (\tau_2 - \tau_1) e^{(-\tau_2 h_i)} \\ &\quad + (\tau_1 - \tau_2) (-\tau_1 + \tau_1 \tau_2 h_i - \tau_2) (-\tau_1 + \tau_1 \tau_2 h_{i+1} + \tau_2) e^{(-\tau_1 h_{i+1})} \\ &\quad - (\tau_1 - \tau_2) (-\tau_1 + \tau_1 \tau_2 h_i - \tau_2) (\tau_1 \tau_2 h_{i+1} + \tau_1 - \tau_2) e^{(-\tau_2 h_{i+1})} \\ &\quad \left. + \tau_1^2 (-\tau_1 + \tau_1 \tau_2 h_{i+1} + \tau_2) e^{(-\tau_1 h_{i+1} - \tau_2 h_i)} + \tau_2^2 (\tau_1 \tau_2 h_{i+1} + \tau_1 - \tau_2) e^{(-\tau_1 h_i - \tau_2 h_{i+1})} \right. \\ &\quad \left. + (\tau_1 - \tau_2)^2 (-\tau_1 + \tau_1 \tau_2 h_i - \tau_2) \right], \end{aligned} \tag{29}$$

$$\begin{aligned} \beta_{2i} &= \frac{1}{K_i K_{i+1}} \left[-\tau_1^2 (\tau_1 - \tau_2) (-1 + \tau_2 h_{i+1}) e^{(-\tau_1 h_{i+1} - \tau_1 h_i - \tau_2 h_i)} + \tau_2^2 (\tau_1 h_{i+1} - 1) (\tau_1 - \tau_2) e^{(-\tau_2 h_{i+1} - \tau_1 h_i - \tau_2 h_i)} \right. \\ &\quad - \tau_1^2 (\tau_1 - \tau_2) (-1 + \tau_2 h_i) e^{(-\tau_1 h_{i+1} - \tau_2 h_{i+1} - \tau_1 h_i)} + \tau_2^2 (\tau_1 - \tau_2) (\tau_1 h_i - 1) e^{(-\tau_1 h_{i+1} - \tau_2 h_{i+1} - \tau_2 h_i)} - \\ &\quad (-\tau_2^3 - \tau_1^2 \tau_2 + \tau_1^3 \tau_2^2 Z h_i h_{i+1} - \tau_1^3 \tau_2 h_i - \tau_1 \tau_2^3 h_{i+1} - \tau_1 \tau_2^3 h_i + \tau_1^2 \tau_2^2 h_{i+1} - \tau_1^2 \tau_2^3 h_i h_{i+1} \\ &\quad - \tau_1^3 \tau_2 h_{i+1} + \tau_1^2 \tau_2^2 h_i + \tau_1^3 + \tau_1 \tau_2^2) e^{(-\tau_1 (h_i + h_{i+1}))} - (\tau_1 + \tau_2) (\tau_1 - \tau_2)^2 e^{(-\tau_1 + \tau_2) (h_i + h_{i+1})} \\ &\quad + (-\tau_1^2 \tau_2 + \tau_1 \tau_2^2 - \tau_1^2 \tau_2^3 h_i h_{i+1} + \tau_1^3 + \tau_1^3 \tau_2^2 h_i h_{i+1} + \tau_1 \tau_2^3 h_i - \tau_2^3 \\ &\quad - \tau_1^2 \tau_2^2 h_i + \tau_1^3 \tau_2 h_i - \tau_1^2 \tau_2^2 h_{i+1} + \tau_1^3 \tau_2 h_{i+1} + \tau_1 \tau_2^3 h_{i+1}) e^{(-\tau_2 (h_i + h_{i+1}))} \\ &\quad - \tau_2^2 (\tau_2 - \tau_1) (\tau_1 h_i + 1) e^{(-\tau_1 h_i)} - \tau_1^2 (\tau_2 h_i + 1) (\tau_1 - \tau_2) e^{(-\tau_2 h_i)} \\ &\quad + \tau_2^2 (\tau_1 h_{i+1} + 1) (\tau_1 - \tau_2) e^{(-\tau_1 h_{i+1})} + \tau_1^2 (\tau_2 - \tau_1) (\tau_2 h_{i+1} + 1) e^{(-\tau_2 h_{i+1})} \\ &\quad \left. - \tau_1^2 \tau_2^2 (h_i + h_{i+1}) e^{(-\tau_1 h_{i+1} - \tau_2 h_i)} - \tau_1^2 \tau_2^2 (h_i + h_{i+1}) e^{(-\tau_1 h_i - \tau_2 h_{i+1})} + (\tau_1 + \tau_2) (\tau_1 - \tau_2)^2 \right], \end{aligned} \tag{30}$$

$$\begin{aligned} \beta_{3,i} = & \frac{1}{K_i K_{i+1}} \left[(\tau_1 - \tau_2)^2 (\tau_1 \tau_2 h_{i+1} + \tau_1 + \tau_2) e^{(-h_{i+1}(\tau_1 + \tau_2))} + \tau_1^2 (\tau_2 - \tau_1) e^{(-\tau_1 h_{i+1} - \tau_1 h_i - \tau_2 h_i)} \right. \\ & - \tau_2^2 (\tau_2 - \tau_1) e^{(-\tau_2 h_{i+1} - \tau_1 h_i - \tau_2 h_i)} - (\tau_2 - \tau_1) (\tau_2 + \tau_1 \tau_2 h_i - \tau_1) (\tau_1 \tau_2 h_{i+1} + \tau_1 + \tau_2) e^{(-\tau_1 h_{i+1} - \tau_2 h_{i+1} - \tau_1 h_i)} \\ & - (\tau_1 - \tau_2) (\tau_1 \tau_2 h_i + \tau_1 - \tau_2) (\tau_1 \tau_2 h_{i+1} + \tau_1 + \tau_2) e^{(-\tau_1 h_{i+1} - \tau_2 h_{i+1} - \tau_2 h_i)} \\ & - \tau_1^2 (\tau_2 + \tau_1 \tau_2 h_i - \tau_1) e^{(-\tau_1 (h_{i+1} + h_i))} + (\tau_1 - \tau_2)^2 (\tau_1 \tau_2 h_{i+1} + \tau_1 + \tau_2) e^{(-(\tau_1 + \tau_2) (h_{i+1} + h_i))} \\ & - \tau_2^2 (\tau_1 \tau_2 h_i + \tau_1 - \tau_2) e^{(-\tau_2 (h_{i+1} + h_i))} - \tau_1^2 (\tau_1 - \tau_2) e^{(-\tau_1 h_{i+1})} + \tau_2^2 (\tau_1 - \tau_2) e^{(-\tau_2 h_{i+1})} \\ & \left. + \tau_1^2 (\tau_1 \tau_2 h_i + \tau_1 - \tau_2) e^{(-\tau_1 h_{i+1} - \tau_2 h_i)} + \tau_2^2 (\tau_2 + \tau_1 \tau_2 h_i - \tau_1) e^{(-\tau_1 h_i - \tau_2 h_{i+1})} \right], \end{aligned} \quad (31)$$

$$\begin{aligned} \beta_{4,i} = & \frac{\tau_1 \tau_2}{K_i K_{i+1}} \left[(\tau_1 - \tau_2)^2 e^{(-h_{i+1}(\tau_1 + \tau_2))} + \tau_2 (\tau_1 - \tau_2) e^{(-\tau_1 h_{i+1} - \tau_2 h_{i+1} - \tau_1 h_i)} \right. \\ & - \tau_1 (\tau_1 - \tau_2) e^{(-\tau_1 h_{i+1} - \tau_2 h_{i+1} - \tau_2 h_i)} + \tau_2 (\tau_1 \tau_2 h_{i+1} + \tau_2 - \tau_1) e^{(-\tau_1 (h_{i+1} + h_i))} \\ & + \tau_1 (\tau_1 + \tau_1 \tau_2 h_{i+1} - \tau_2) e^{(-\tau_2 (h_{i+1} + h_i))} + \tau_2 (\tau_1 - \tau_2) e^{(-\tau_1 h_i)} \\ & - \tau_1 (\tau_1 - \tau_2) e^{(-\tau_2 h_i)} + (\tau_1 - \tau_2) (\tau_1 \tau_2 h_{i+1} + \tau_2 - \tau_1) e^{(-\tau_1 h_{i+1})} \\ & - (\tau_1 - \tau_2) (\tau_1 + \tau_1 \tau_2 h_{i+1} - \tau_2) e^{(-\tau_2 h_{i+1})} - \tau_1 (\tau_1 \tau_2 h_{i+1} + \tau_2 - \tau_1) e^{(-\tau_1 h_{i+1} - \tau_2 h_i)} \\ & \left. - \tau_2 (\tau_1 + \tau_1 \tau_2 h_{i+1} - \tau_2) e^{(-\tau_1 h_i - \tau_2 h_{i+1})} + (\tau_1 - \tau_2)^2 \right], \end{aligned} \quad (32)$$

$$\begin{aligned} \beta_{6,i} = & \frac{\tau_1 \tau_2}{K_i K_{i+1}} \left[-(\tau_1 - \tau_2)^2 e^{(-h_{i+1}(\tau_1 + \tau_2))} + \tau_1 (\tau_1 - \tau_2) e^{(-\tau_1 h_{i+1} - \tau_1 h_i - \tau_2 h_i)} \right. \\ & - \tau_2 (\tau_1 - \tau_2) e^{(-\tau_2 h_{i+1} - \tau_1 h_i - \tau_2 h_i)} - (\tau_1 - \tau_2) (-\tau_1 + \tau_1 \tau_2 h_i + \tau_2) e^{(-\tau_1 h_{i+1} - \tau_2 h_{i+1} - \tau_1 h_i)} \\ & + (\tau_1 - \tau_2) (-\tau_2 + \tau_1 \tau_2 h_i + \tau_1) e^{(-\tau_1 h_{i+1} - \tau_2 h_{i+1} - \tau_2 h_i)} + \tau_1 (-\tau_1 + \tau_1 \tau_2 h_i + \tau_2) e^{(-\tau_1 (h_{i+1} + h_i))} \\ & - (\tau_1 - \tau_2)^2 e^{(-(\tau_1 + \tau_2) (h_{i+1} + h_i))} + \tau_2 (-\tau_2 + \tau_1 \tau_2 h_i + \tau_1) e^{(-\tau_2 (h_{i+1} + h_i))} + \tau_1 (\tau_1 - \tau_2) e^{(-\tau_1 h_{i+1})} \\ & \left. - \tau_2 (\tau_1 - \tau_2) e^{(-\tau_2 h_{i+1})} - \tau_1 (-\tau_2 + \tau_1 \tau_2 h_i + \tau_1) e^{(-\tau_1 h_{i+1} - \tau_2 h_i)} - \tau_2 (-\tau_1 + \tau_1 \tau_2 h_i + \tau_2) e^{(-\tau_1 h_i - \tau_2 h_{i+1})} \right], \end{aligned} \quad (33)$$

$$K_i = (-\tau_1 + \tau_1 \tau_2 h_i + \tau_2) e^{(-\tau_1 h_i)} + (-\tau_1 - \tau_1 \tau_2 h_i + \tau_2) e^{(-\tau_2 h_i)} + (\tau_1 - \tau_2) e^{(-h_i(\tau_1 + \tau_2))} + \tau_1 - \tau_2. \quad (34)$$

If $\tau_2 = -\tau_1 = \tau$ and $h_i = h, i = 1, 2, \dots, n$, then

$$\begin{aligned} \beta_{1i} &= \frac{(-2\tau h e^{(\tau h)} + e^{(2\tau h)} - 1)\tau}{4e^{(\tau h)} - 2 - 2e^{(2\tau h)} + \tau h e^{(2\tau h)} - \tau h}, \\ \beta_{2i} &= \frac{2(\tau h e^{(2\tau h)} - e^{(2\tau h)} + \tau h + 1)\tau}{4e^{(\tau h)} - 2 - 2e^{(2\tau h)} + \tau h e^{(2\tau h)} - \tau h}, \\ \beta_{3i} &= \frac{(-2\tau e^{(\tau h)} h + e^{(2\tau h)} - 1)\tau}{4e^{(\tau h)} - 2 - 2e^{(2\tau h)} + \tau h e^{(2\tau h)} - \tau h}, \\ \beta_{4i} &= \frac{(-1 + e^{(\tau h)})\tau^2}{-2e^{(\tau h)} + \tau e^{(\tau h)} h + 2 + \tau h}, \\ \beta_{5i} &= 0, \\ \beta_{6i} &= \frac{(-1 + e^{(\tau h)})\tau^2}{-2e^{(\tau h)} + \tau e^{(\tau h)} h + 2 + \tau h}. \end{aligned} \quad (35)$$

Let $\tau \rightarrow 0$; then, (28) is equivalent to

$$h(D_{i-1} + 4D_i + D_{i+1}) + 3S_{i-1} - 3S_{i+1} = 0. \quad (36)$$

This is consistent with the cubic 2nd-order polynomial spline function relationship.

Besides, using

$$\begin{aligned} s_i(x_i) &= S_i, \\ s'_i(x_i) &= D_i, \\ s''_i(x_i) &= M_i, \\ s''_i(x_{i-1}) &= M_{i-1}, \end{aligned} \quad (37)$$

we can obtain

$$\begin{aligned} a_i &= \frac{(\tau_1^2 - \tau_2^2)M_{i-1} + (\tau_2^2 e^{(-\tau_2 h_i)} - \tau_1^2 e^{(-\tau_1 h_i)})M_i + \tau_1^2 \tau_2^2 \rho_i S_i}{\tau_1^2 \tau_2^2 \rho_i}, \\ b_i &= \frac{(\tau_1 - \tau_2)M_{i-1} + (\tau_2 e^{(-\tau_2 h_i)} - \tau_1 e^{(-\tau_1 h_i)})M_i + \tau_1 \tau_2 \rho_i D_i}{\tau_1 \tau_2 \rho_i}, \\ c_i &= \frac{-M_{i-1} + e^{(-\tau_2 h_i)} M_i}{\tau_1^2 \rho_i}, \\ d_i &= \frac{-M_{i-1} + e^{(-\tau_1 h_i)} M_i}{\tau_2^2 \rho_i}. \end{aligned} \quad (38)$$

Then, using continuous condition of $s_i(x_i) = s_{i+1}(x_i)$, $s'_i(x_i) = s'_{i+1}(x_i)$, we obtain

$$\begin{aligned}
 & - \frac{(h_{i+1}\tau_1\tau_2^2 - h_{i+1}\tau_1^2\tau_2 + \tau_2^2e^{-\tau_1h_{i+1}} - \tau_1^2e^{-\tau_2h_{i+1}} + \tau_1^2 - \tau_2^2)}{\tau_1^2\tau_2^2\rho_{i+1}}M_i \\
 & + \frac{(\tau_1^2e^{-\tau_1h_{i+1}} - \tau_2^2e^{-\tau_2h_{i+1}} + h_{i+1}\tau_1\tau_2^2e^{-\tau_2h_{i+1}} - h_{i+1}\tau_1^2\tau_2e^{-\tau_1h_{i+1}} + \tau_2^2e^{-h_{i+1}(\tau_1+\tau_2)} - \tau_1^2e^{-h_{i+1}(\tau_1+\tau_2)})}{\tau_1^2\tau_2^2\rho_{i+1}}M_{i+1} \\
 & + S_i - S_{i+1} + h_{i+1}D_{i+1} = 0,
 \end{aligned} \tag{39}$$

$$\begin{aligned}
 & - \frac{(\tau_2e^{(-\tau_2h_{i+1})} - \tau_1e^{-\tau_1h_{i+1}}\tau_1e^{-h_{i+1}(\tau_1+\tau_2)} - \tau_2e^{-h_{i+1}(\tau_1+\tau_2)})}{\tau_1\tau_2\rho_{i+1}}M_{i+1} \\
 & - \frac{(\tau_2e^{-\tau_1h_{i+1}} - \tau_1e^{-\tau_2h_{i+1}} + \tau_1 - \tau_2)}{\tau_1\tau_2\rho_{i+1}}M_i + D_i - D_{i+1} = 0.
 \end{aligned} \tag{40}$$

Solving (39) yields

$$\begin{aligned}
 D_i = & - \frac{(\tau_1^2e^{-\tau_2h_i} - \tau_2^2e^{-\tau_1h_i} - h_i\tau_1\tau_2^2 + h_i\tau_1^2\tau_2 - \tau_1^2 + \tau_2^2)}{h_i\tau_1^2\tau_2^2\rho_i}M_{i-1} \\
 & + \frac{((-h_i\tau_1\tau_2^2 + \tau_2^2)e^{-\tau_2h_i} + (-\tau_1^2 + h_i\tau_1^2\tau_2)e^{-\tau_1h_i} + (\tau_1^2 - \tau_2^2)e^{-h_i(\tau_2+\tau_1)})}{h_i\tau_1^2\tau_2^2\rho_i}M_i \\
 & - \frac{S_{i-1}}{h_i} + \frac{S_i}{h_i}.
 \end{aligned} \tag{41}$$

Meanwhile, by eliminating D_{i+1} with (39) and (40) and rearranging, we obtain

$$\begin{aligned}
 D_i = & \frac{((- \tau_1^2 - h_{i+1}\tau_1^2\tau_2)e^{-\tau_2h_{i+1}} + (\tau_2^2 + h_{i+1}\tau_1\tau_2^2)e^{-\tau_1h_{i+1}} - \tau_2^2 + \tau_1^2)}{h_{i+1}\tau_1^2\tau_2^2\rho_{i+1}}M_i \\
 & - \frac{(-\tau_1^2 + h_{i+1}\tau_1\tau_2^2 - h_{i+1}\tau_1^2\tau_2 + \tau_2^2)e^{-h_{i+1}(\tau_1+\tau_2)} + \tau_1^2e^{-\tau_1h_{i+1}} - \tau_2^2e^{-\tau_2h_{i+1}}}{h_{i+1}\tau_1^2\tau_2^2\rho_{i+1}}M_{i+1},
 \end{aligned} \tag{42}$$

$$\frac{S_i}{h_{i+1}} + \frac{S_{i+1}}{h_{i+1}}. \tag{43}$$

We can also use $s_{i+1}(x_{i+1}) = S_{i+1}$, $s_{i+1}(x_i) = S_i$, $s'_{i+1}(x_{i+1}) = D_{i+1}$, and $s'_{i+1}(x_i) = D_i$ to obtain

$$\begin{aligned}
 a_i &= \frac{1}{\varrho_i} \left((\tau_1 h_i - \tau_2 h_i + \rho_i) D_{i-1} + (h_i \tau_2 e^{-\tau_2 h_i} - \tau_1 e^{-\tau_1 h_i} h_i - \rho_i) D_i \right. \\
 &\quad \left. + (\tau_2 e^{-\tau_2 h_i} + \tau_1 - \tau_2 - \tau_1 e^{-\tau_1 h_i}) S_{i-1} \right. \\
 &\quad \left. + \left((-\tau_1 - \tau_1 h_i \tau_2) e^{-\tau_2 h_i} + (\tau_1 h_i \tau_2 + \tau_2) e^{-\tau_1 h_i} + (\tau_1 - \tau_2) e^{-h_i(\tau_1 + \tau_2)} \right) S_i \right), \\
 b_i &= \frac{1}{\varrho_i} \left((\tau_1 - \tau_2 - \tau_1 e^{-\tau_2 h_i} + \tau_2 e^{-\tau_1 h_i}) D_{i-1} + (\tau_2 e^{-\tau_2 h_i} - \tau_1 e^{-\tau_1 h_i} + (\tau_1 - \tau_2) e^{-h_i(\tau_1 + \tau_2)}) D_i \right. \\
 &\quad \left. - \tau_1 \tau_2 \rho_i S_{i-1} + \tau_1 \tau_2 \rho_i S_i \right), \\
 c_i &= \frac{1}{\varrho_i} \left((e^{-\tau_2 h_i} - 1 + \tau_2 h_i) D_{i-1} + (-e^{-\tau_2 h_i} + 1 - h_i \tau_2 e^{-\tau_2 h_i}) D_i \right. \\
 &\quad \left. + (-\tau_2 e^{-\tau_2 h_i} + \tau_2) S_{i-1} + (-\tau_2 + \tau_2 e^{-\tau_2 h_i}) S_i \right), \\
 d_i &= \frac{1}{\varrho_i} \left((-\tau_1 h_i - e^{-\tau_1 h_i} + 1) D_{i-1} + (\tau_1 e^{-\tau_1 h_i} h_i + e^{-\tau_1 h_i} - 1) D_i \right. \\
 &\quad \left. + (-\tau_1 + \tau_1 e^{-\tau_1 h_i}) S_{i-1} + (-\tau_1 e^{-\tau_1 h_i} + \tau_1) S_i \right),
 \end{aligned} \tag{44}$$

where $\varrho_i = (-\tau_1 h_i \tau_2 + \tau_2 - \tau_1) e^{-\tau_2 h_i} + (\tau_1 h_i \tau_2 + \tau_2 - \tau_1) e^{-\tau_1 h_i} + (\tau_1 - \tau_2) e^{-h_i(\tau_1 + \tau_2)} + \tau_1 - \tau_2$. Fast Hermite interpolation can be achieved by using this set of relations.

4. Exponential Spline Difference Method

The spline difference method uses the relationship between the spline function and its derivative to construct the differential expression to numerically solve DEs, by which the numerical solution at nodes can be obtained, and that within the subintervals can also be calculated by using the spline function expressions. It is the advantage of this method compared with the general difference schemes. In fact, it can be said that the approximate analytical solution using the splines is obtained.

4.1. Differential Expression. The following presents a spline difference method for solving (1) which satisfies one of the boundary conditions (2)–(5) for the boundary value problems of ODEs. Due to the limitation of this method, we only consider the case of $q(x) = 0$ in this section. For convenience of description, we first consider the boundary condition (2). From (1), we can obtain

$$u'' = g(x) - p(x)u, \quad x \in [a, b]. \tag{45}$$

By discretization the above equation, we obtain

$$u''_i = g_i - p_i u_i, \quad i = 0, 1, 2, \dots, n, \tag{46}$$

where $g_i = g(x_i)$ and $p_i = p(x_i)$.

Substitute S with u and M with u'' in (24), and we obtain

$$t_i = (\alpha_{1i} u''_{i-1} + \alpha_{2i} u''_i + \alpha_{3i} u''_{i+1}) - \frac{u_{i-1}}{h_i} + \frac{(h_i + h_{i+1})u_i}{h_i h_{i+1}} - \frac{u_{i+1}}{h_{i+1}}, \tag{47}$$

where $i = 1, \dots, n-1$, $u_i = u(x_i)$ and $u''_i = u''(x_i)$. t_i is the local truncation error at x_i . By substituting (46) into (47) and rearranging, we obtain

$$\begin{aligned}
 &\left(-\frac{1}{h_i} - \alpha_{1i} p_{i-1} \right) u_{i-1} + \left(\frac{h_i + h_{i+1}}{h_i h_{i+1}} - \alpha_{2i} p_i \right) u_i \\
 &\quad + \left(-\frac{1}{h_{i+1}} - \alpha_{3i} p_{i+1} \right) u_{i+1} + \alpha_{1i} g_{i-1} + \alpha_{2i} g_i + \alpha_{3i} g_{i+1} = t_i,
 \end{aligned} \tag{48}$$

where $i = 1, 2, \dots, n-1$. Thus, we get $n-1$ equations about u_0, u_1, \dots, u_n .

The following equation can also be derived from the boundary conditions (2):

$$\begin{aligned}
 u_0 &= \mu_0, \\
 u_n &= \mu_1.
 \end{aligned} \tag{49}$$

So, there will be $n+1$ equations in (48) and (49) in total, and its matrix form can be written as

$$\mathbf{A}\mathbf{U} = \mathbf{F} + \mathbf{T}, \tag{50}$$

where $\mathbf{A} = \mathbf{B} - \mathbf{W}$, with

$$\mathbf{B} = \begin{bmatrix} 1 & 0 & 0 \\ \frac{1}{h_1} & \frac{h_1+h_2}{h_1h_2} & \frac{1}{h_2} \\ & \frac{1}{h_2} & \frac{h_2+h_3}{h_2h_3} & \frac{1}{h_3} \\ & & \ddots & \\ & & & \frac{1}{h_{n-2}} & \frac{h_{n-2}+h_{n-1}}{h_{n-2}h_{n-1}} & \frac{1}{h_{n-1}} \\ & & & & \frac{1}{h_{n-1}} & \frac{h_{n-1}+h_n}{h_{n-1}h_n} & \frac{1}{h_n} \\ & & & & 0 & 0 & 1 \end{bmatrix}, \tag{51}$$

$$\mathbf{W} = \begin{bmatrix} 0 & 0 & 0 \\ \alpha_{11}p_0 & \alpha_{21}p_1 & \alpha_{31}p_2 \\ & \alpha_{12}p_1 & \alpha_{22}p_2 & \alpha_{32}p_3 \\ & & \ddots & \\ & & & \alpha_{1,n-2}p_{n-3} & \alpha_{2,n-2}p_{n-2} & \alpha_{3,n-2}p_{n-1} \\ & & & & \alpha_{1,n-1}p_{n-2} & \alpha_{2,n-1}p_{n-1} & \alpha_{3,n-1}p_n \\ & & & & 0 & 0 & 0 \end{bmatrix}, \tag{52}$$

$$\begin{aligned} \mathbf{F} &= [\mu_0, \{-(\alpha_{1i}g_{i-1} + \alpha_{2i}g_i + \alpha_{3i}g_{i+1})\}_{i=1}^{n-1}, \mu_1]^T, \\ \mathbf{T} &= [\{t_i\}_{i=0}^n]^T, \\ \mathbf{U} &= [\{u_i\}_{i=0}^n]^T. \end{aligned} \tag{53}$$

If \mathbf{A} is nonsingular, then equation (50) has a unique solution. Solving (50) yields the approximate values of u_i in $u(x)$ at the splitting points $x_i, i = 0, 1, \dots, n$. Since \mathbf{A} is a tridiagonal matrix, the catch-up method can be used to reduce the calculation in practice.

To obtain the spline function expression, we can calculate u_i'' from (2) after finding u_i and substitute them into (22) to obtain $a_i, b_i, c_i,$ and d_i so that the approximate solution of the spline over the entire interval will be found.

The case of other boundary conditions will be discussed below. For the second boundary conditions, from (41), (42), and (3), we obtain

$$\alpha_{20}M_0 + \alpha_{30}M_1 + \frac{S_0}{h_1} - \frac{S_1}{h_1} = -\mu_0, \tag{54}$$

$$\alpha_{1n}M_{n-1} + \alpha_{2n}M_n - \frac{S_{n-1}}{h_n} + \frac{S_n}{h_n} = \mu_1, \tag{55}$$

where

$$\begin{aligned} \alpha_{20} &= \frac{((\tau_1^2 + h_1\tau_1^2\tau_2)e^{-\tau_2h_1} + (-\tau_2^2 - \tau_1h_1\tau_2^2)e^{-\tau_1h_1} - \tau_1^2 + \tau_2^2)}{h_1\tau_1^2\tau_2^2\rho_1}, \\ \alpha_{30} &= -\frac{(\tau_2^2e^{-\tau_2h_1} - \tau_1^2e^{-\tau_1h_1} + (\tau_1^2 - \tau_1h_1\tau_2^2 + h_1\tau_1^2\tau_2 - \tau_2^2)e^{-h_1(\tau_2+\tau_1)})}{h_1\tau_1^2\tau_2^2\rho_1}, \\ \alpha_{1n} &= -\frac{(\tau_1^2e^{-\tau_2h_n} - \tau_2^2e^{-\tau_1h_n} - h_n\tau_1\tau_2^2 + h_n\tau_1^2\tau_2 - \tau_1^2 + \tau_2^2)}{h_n\tau_1^2\tau_2^2\rho_n}, \\ \alpha_{2n} &= \frac{((-h_n\tau_1\tau_2^2 + \tau_2^2)e^{-\tau_2h_n} + (-\tau_1^2 + h_n\tau_1^2\tau_2)e^{-\tau_1h_n} + (\tau_1^2 - \tau_2^2)e^{-h_n(\tau_2+\tau_1)})}{h_n\tau_1^2\tau_2^2\rho_n}. \end{aligned} \tag{56}$$

Solving this type of boundary problem only needs to modify the first line and the last row of $\mathbf{B}, \mathbf{W},$ and \mathbf{F} in (47), namely,

$$\mathbf{B}_0 = \left[\frac{1}{h_1} \quad \frac{1}{h_1} \quad 0 \quad \dots \quad 0 \right],$$

$$\mathbf{W}_0 = [\alpha_{20}p_0 \quad \alpha_{30}p_1 \quad 0 \quad \dots \quad 0],$$

$$\mathbf{B}_n = \left[0 \quad \dots \quad 0 \quad \frac{1}{h_n} \quad \frac{1}{h_n} \right],$$

$$\mathbf{W}_n = [0 \quad \dots \quad 0 \quad \alpha_{n1}p_{n-1} \quad \alpha_{n2}p_n],$$

$$\mathbf{F}_0 = -\mu_0 - (\alpha_{20}g_0 + \alpha_{30}g_1),$$

$$\mathbf{F}_n = \mu_1 - (\alpha_{1n}g_{n-1} + \alpha_{2n}g_n). \tag{57}$$

And the third and the fourth boundary conditions should also be modified accordingly.

4.2. Error Estimation. Suppose $u(x)$ is sufficiently smooth in $[a, b]$, by Taylor expanding $u_{i-1}, u_{i+1}, u_{i-1}'', u_{i+1}''$ in difference equation (47) at x_i , we obtain

$$t_i = \sum_{j=2}^6 \xi_j u_i^{(j)} + O(h_i^7), \tag{58}$$

where

$$\begin{aligned} \xi_2 &= \alpha_{1i} + \alpha_{2i} + \alpha_{3i} - \frac{1}{2}(h_i + h_{i+1}), \\ \xi_3 &= -\alpha_{1i}h_i + \alpha_{3i}h_{i+1} + \frac{1}{6}(h_i^2 - h_{i+1}^2), \\ \xi_4 &= \frac{1}{2}\alpha_{1i}h_i^2 + \frac{1}{2}\alpha_{3i}h_{i+1}^2 - \frac{1}{24}(h_i^3 + h_{i+1}^3), \\ \xi_5 &= -\frac{1}{6}\alpha_{1i}h_i^3 + \frac{1}{6}\alpha_{3i}h_{i+1}^3 + \frac{1}{120}(h_i^4 + h_{i+1}^4), \\ \xi_6 &= \frac{1}{24}\alpha_{1i}h_i^4 + \frac{1}{24}\alpha_{3i}h_{i+1}^4 - \frac{1}{720}(h_i^5 + h_{i+1}^5). \end{aligned} \tag{59}$$

Let $\tau_1 \rightarrow 0$ and $\tau_2 \rightarrow 0$, we find $\xi_2 = \xi_3 = 0$ and $\xi_4 = (1/24)(h_{i+1}^3 + h_i^3)$. When

$$\begin{aligned} \alpha_{1i} &= \frac{1}{12} \frac{h_i^2 + h_i h_{i+1} - h_{i+1}^2}{h_i}, \\ \alpha_{2i} &= \frac{1}{12} \frac{h_i^3 + 4h_i^2 h_{i+1} + 4h_i h_{i+1}^2 + h_{i+1}^3}{h_i h_{i+1}}, \\ \alpha_{3i} &= -\frac{1}{12} \frac{h_i^2 - h_i h_{i+1} - h_{i+1}^2}{h_{i+1}}, \end{aligned} \tag{60}$$

we obtain $\xi_2 = \xi_3 = \xi_4 = 0$,

$$\xi_5 = \frac{1}{360} (-h_i + h_{i+1})(2h_i + h_{i+1})(h_i + 2h_{i+1})(h_i + h_{i+1}). \tag{61}$$

$\xi_5 = 0$ for an even splitting, i.e., $h_i = h, i = 1, 2, \dots, n$, and $\xi_6 = (1/240)h^6$. This indicates that the even splitting has higher accuracy if $u(x)$ is sufficiently smooth.

4.3. Convergence Analysis. We mainly discuss the convergence of equation (47) and the differential expression of (49) in the sense of $\|E\|_\infty$.

Lemma 1 (see [14]). *If the n -order matrix \mathbf{B} satisfies one of the following two conditions:*

- (1) \mathbf{B} is a strictly diagonally dominant matrix

(2) \mathbf{B} is a second half strong diagonally dominant matrix

Then, \mathbf{B} is nonsingular and $\rho(\mathbf{I} - \mathbf{D}^{-1}\mathbf{B}) < 1$, where $\mathbf{D} = \text{diag}(\mathbf{B})$ and \mathbf{I} is the identity matrix.

By (14),

$$\mathbf{A}\mathbf{S} = \mathbf{F}. \tag{62}$$

If \mathbf{A} is reversible, combining (50), we obtain

$$\mathbf{E} = \mathbf{A}^{-1}\mathbf{T} = (\mathbf{B} - \mathbf{W})^{-1}\mathbf{T} = (\mathbf{I} - \mathbf{B}^{-1}\mathbf{W})^{-1}\mathbf{B}^{-1}\mathbf{T}, \tag{63}$$

where $\mathbf{E} = (e_i) = \mathbf{U} - \mathbf{S}$, and \mathbf{B} , \mathbf{W} , and \mathbf{T} are given by (51)–(53). The reversibility of \mathbf{B} can be proved by 1. From the boundary condition (2), we can get $e_0 = e_n = 0$. Thus, discussing the convergence of $\|E\|_\infty$ is consistent with that of $\|(e_i)_{i=1}^{n-1}\|_\infty$. So, in the following convergence discussion, the first and the last row and the first and the last column will be removed from the original matrices of \mathbf{A} , \mathbf{B} , and \mathbf{W} to obtain the $n - 1$ -order ones, keeping the subscript value unchanged.

If

$$\|\mathbf{B}^{-1}\|_\infty \|\mathbf{W}\|_\infty < 1, \tag{64}$$

then

$$\|E\|_\infty \leq \frac{\|\mathbf{B}^{-1}\|_\infty \|\mathbf{T}\|_\infty}{1 - \|\mathbf{B}^{-1}\|_\infty \|\mathbf{W}\|_\infty} \leq \|\mathbf{B}^{-1}\|_\infty \|\mathbf{T}\|_\infty. \tag{65}$$

To calculate \mathbf{B}^{-1} , the following lemma is needed:

Lemma 2 (see [15]). *Let the square matrix \mathbf{A} be an n -order tridiagonal one, with the following expression:*

$$\mathbf{A} = \begin{bmatrix} a_1 & b_1 & & & \\ c_1 & a_2 & b_2 & & \\ & c_2 & \ddots & \ddots & \\ & & \ddots & \ddots & b_{n-1} \\ & & & c_{n-1} & a_n \end{bmatrix}, \tag{66}$$

and $b_i c_i \neq 0, i = 1, 2, \dots, n - 1, a_i \neq 0, i = 1, 2, \dots, n$; then, the expression of $\mathbf{A}^{-1} = (a_{ij}^{(-1)})$ can be written as

$$a_{ij}^{(-1)} = \begin{cases} (-1)^{i+j} \left(\prod_{k=i}^{j-1} b_k \right) \frac{\det(\mathbf{A}[1, \dots, i-1]) \det(\mathbf{A}[j+1, \dots, n])}{\det(\mathbf{A})}, & i < j, \\ (-1)^{i+j} \left(\prod_{k=j}^{i-1} c_k \right) \frac{\det(\mathbf{A}[1, \dots, i-1]) \det(\mathbf{A}[j+1, \dots, n])}{\det(\mathbf{A})}, & i \geq j, \end{cases} \tag{67}$$

where $\mathbf{A}[i_1, i_2, \dots, i_k]$ denotes the matrix consisting of the elements of i_1, i_2, \dots, i_k rows crossed with the columns in \mathbf{A} . Specifically, $\mathbf{A}[1, \dots, i - 1] = 1$ for $i = 1$.

Using (2), $\mathbf{B}^{-1} = (b_{ij}^{(-1)})$ in (65) can be written as (with $\sum_{k=1}^n h_k = b - a$)

TABLE 1: The maximum error $\|E\|_\infty$ in solving (72) with the exponential spline difference method.

	$n = 32$	$n = 64$	$n = 128$	$n = 256$	$n = 512$
Ref. [7]	$1.84e-4$	$4.61e-5$	$1.15e-5$	$2.88e-6$	$7.21e-7$
Our method ($\tau = [n^{1/4}, -n^{1/4}]$)	$8.11e-6$	$2.03e-6$	$5.09e-7$	$1.28e-7$	$4.25e-8$

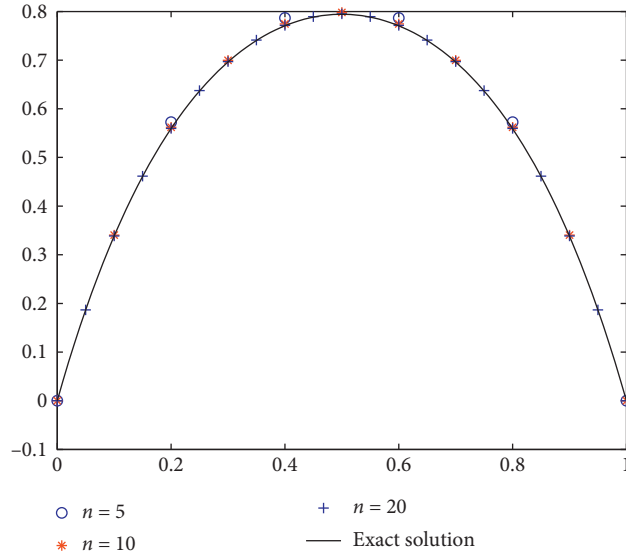


FIGURE 2: Results of the boundary value problem (72) for $\epsilon = 0.1$, and $n = 5, 10$, and 20 , respectively.

TABLE 2: The maximum error $\|E\|_\infty$ and root mean square error for problem (74).

	$n = 10$	$n = 20$	$n = 40$	$n = 80$
Ref. [11]	$1.02e-3$	$2.96e-5$	$3.69e-6$	$5.11e-8$
Our method ($\tau = [10.11, -0.012]$)	$8.57e-7$	$8.18e-7$	$8.03e-7$	$7.97e-7$

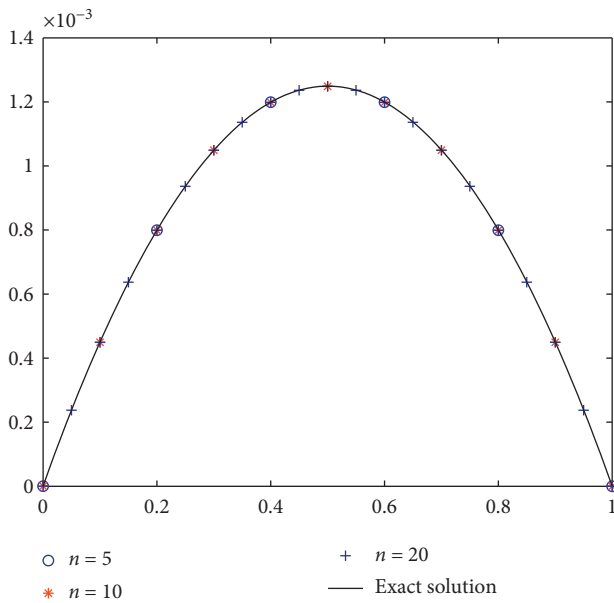


FIGURE 3: Results of the boundary value problem (74) for $\epsilon = 0.01$, and $n = 5, 10$, and 20 , respectively.

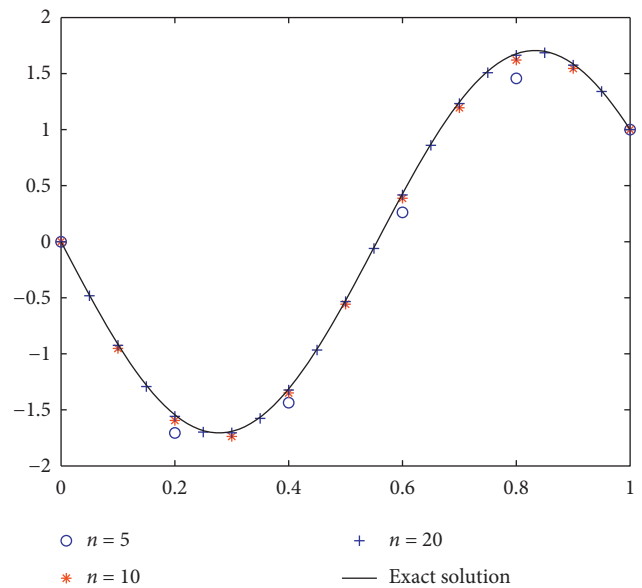


FIGURE 4: Results of the boundary value problem (76) for $\epsilon = 1/32$, and $n = 5, 10$, and 20 , respectively.

TABLE 3: The maximum error $\|E\|_\infty$ and root mean square error for problem (76).

ε	Method	$n = 16$	$n = 32$	$n = 64$	$n = 128$	$n = 256$	$n = 512$	$n = 1024$
1/2	Ref. [16]	$2.6e-4$	$6.5e-5$	$1.6e-5$	$4.1e-6$	$1.0e-6$	$2.6e-7$	$6.4e-8$
	Our method ($\tau = [1.18, -12.75]$)	$2.34e-4$	$6.37e-5$	$1.65e-5$	$4.20e-6$	$1.06e-6$	$2.72e-7$	$5.21e-8$
1/4	Ref. [16]	$1.9e-3$	$4.7e-4$	$1.2e-4$	$2.9e-5$	$7.4e-6$	$1.8e-6$	$4.6e-7$
	Our method ($\tau = [1.91, -11.77]$)	$3.04e-3$	$8.19e-4$	$2.11e-4$	$5.38e-5$	$1.35e-5$	$3.36e-6$	$1.94e-7$
1/8	Ref. [16]	$7.3e-2$	$1.9e-2$	$4.7e-3$	$1.2e-3$	$2.9e-4$	$7.3e-5$	$1.8e-5$
	Our method ($\tau = [1.91, -11.77]$)	$8.23e-2$	$2.39e-2$	$6.13e-3$	$1.54e-3$	$3.93e-4$	$9.66e-5$	$6.74e-7$
1/16	Ref. [16]	$2.9e-2$	$7.1e-3$	$1.8e-3$	$4.4e-4$	$1.1e-4$	$2.8e-5$	$6.9e-6$
	Our method ($\tau = [13, -1]$)	$1.61e-2$	$4.03e-3$	$1.04e-3$	$2.67e-4$	$6.80e-5$	$1.66e-5$	$3.74e-6$
1/32	Ref. [16]	—	$3.8e-2$	$9.8e-3$	$2.5e-3$	$6.2e-4$	$1.5e-4$	$3.9e-5$
	Our method ($\tau = [1, -13]$)	$7.52e-2$	$1.99e-2$	$5.06e-3$	$1.30e-3$	$3.25e-4$	$7.93e-5$	$1.12e-5$
1/64	Ref. [16]	—	$3.4e-2$	$8.7e-3$	$2.2e-3$	$5.5e-4$	$1.4e-4$	$3.4e-5$
	Our method ($\tau = [12.51, -1.48]$)	$8.54e-2$	$2.33e-2$	$6.39e-3$	$1.63e-3$	$4.10e-4$	$1.03e-4$	$1.85e-5$
1/128	Ref. [16]	—	—	$2.8e-2$	$7.2e-3$	$1.8e-3$	$4.5e-4$	$1.1e-4$
	Our method ($\tau = [11.53, -2.46]$)	—	$6.46e-2$	$1.69e-2$	$4.33e-3$	$1.09e-3$	$2.73e-4$	$5.70e-5$
1/256	Ref. [16]	—	—	—	—	$6.3e-2$	$1.6e-2$	$3.9e-3$
	Our method ($\tau = [13, -1]$)	—	—	—	—	$3.21e-2$	$8.09e-3$	$9.13e-4$
1/512	Ref. [16]	—	—	—	—	$4.2e-2$	$1.0e-2$	$2.5e-3$
	Our method ($\tau = [11.53, -2.46]$)	—	—	—	—	$2.12e-2$	$5.35e-3$	$6.92e-4$
1/1024	Ref. [16]	—	—	—	—	—	$3.4e-2$	$8.5e-3$
	Our method ($\tau = [3.93, -10]$)	—	—	—	—	—	$1.92e-2$	$2.55e-3$

$$b_{ij}^{(-1)} = \begin{cases} \frac{1}{b-a} \sum_{k=1}^i h_k \sum_{k=j+1}^n h_k, & i < j, \\ \frac{1}{b-a} \sum_{k=1}^j h_k \sum_{k=i+1}^n h_k, & i \geq j, \end{cases} \quad (68)$$

$$\|E\|_\infty = O\left(\frac{h_{\max}^2}{h_{\min}}\right), \quad (71)$$

that is, the differential expression of (47) is convergent if $h_{\max} = O(h_{\min})$.

then $0 < b_{ij}^{(-1)} \leq (b-a)/4$. Thus,

$$\|B^{-1}\|_\infty \leq \frac{1}{4} n(b-a) \leq \frac{(b-a)^2}{4h_{\min}}. \quad (69)$$

According to (27), we find $|t_i| = O(h_i^2)$. Thus,

$$\|B^{-1}\|_\infty \|T\|_\infty \leq \frac{(b-a)^2}{4} \frac{h_{\max}^2}{h_{\min}}. \quad (70)$$

So, if $h_{\max} = O(h_{\min})$, then $\|B^{-1}\|_\infty \|W\|_\infty \rightarrow 0$ when $h_{\max} \rightarrow 0$.

So far, we have proved that

Theorem 2. For given τ_1, τ_2 , and $\Delta: 0 = x_0 < x_1 < \dots < x_n = 1, h_i = x_i - x_{i-1}, i = 1, 2, \dots, n, h_{\max} = \max_{1 \leq i \leq n} \{h_i\}, h_{\min} = \min_{1 \leq i \leq n} \{h_i\}$, if $\|B^{-1}\|_\infty \|W\|_\infty < 1$, then

5. Example

Example 1. Solve the following singular boundary value problem (see [7]):

$$\begin{cases} -\varepsilon u'' + p(x)u = g(x), & 0 \leq x \leq 1, \\ u(0) = u(1) = 0. \end{cases} \quad (72)$$

where $p(x) = 1 + x(1-x)$ and $g(x) = 1 + x(1-x) + [2\sqrt{\varepsilon} - x(1-x)^2]e^{-x/\sqrt{\varepsilon}} + [2\sqrt{\varepsilon} - x^2(1-x)]e^{-(1-x)/\sqrt{\varepsilon}}$, and its analytical solution is

$$u(x) = 1 + (x-1)e^{-x/\sqrt{\varepsilon}} - xe^{-(1-x)/\sqrt{\varepsilon}}. \quad (73)$$

Table 1 lists the results of the exponential spline difference method for $\varepsilon = 0.1$ and that of the method proposed in [7].

Figure 2 shows the results for $\varepsilon = 0.1$, and $n = 5$ and 10, respectively. To show the difference between the exact

solution and the numerical one, we deliberately use fewer split points and simply connect two adjacent solutions with straight lines. A smoother exponential spline function which is closer to the exact solution can be constructed using these obtained numerical solutions.

Example 2. Consider the convection-dominated equation (see [11]):

$$\begin{cases} u'' - \epsilon u' - \epsilon u = -\epsilon, & 0 < x < 1, \\ u(0) = u(1) = 0. \end{cases} \quad (74)$$

The analytical solution is given by

$$u(x) = 1 + \frac{\left(e^{(1-\sqrt{(1+4)/\lambda})/2/\lambda} - 1 \right) e^{((1+\sqrt{(1+4)/\lambda})/2/\lambda)x} + \left(1 - e^{(1+\sqrt{(1+4)/\lambda})/2/\lambda} \right) e^{((1-\sqrt{(1+4)/\lambda})/2/\lambda)x}}{\left((1 + \sqrt{(1+4)/\lambda})/2/\lambda \right) - \left(1 - \sqrt{(1+4)/\lambda} \right)/2/\lambda}. \quad (75)$$

The computational results are shown in Table 2 for $\epsilon = 0.01$ and various values of n (Figure 3).

Example 3. Consider the convection-dominated equation (see [16–19]) Figure 4:

$$\begin{cases} \epsilon u'' + u = 0, & 0 < x < 1, \\ u(0) = 0, u(1) = 1, \end{cases} \quad (76)$$

$$u(x) = \frac{\sin(x/\sqrt{\epsilon})}{\sin(1/\sqrt{\epsilon})}, \epsilon \neq (n\pi)^{-2}. \quad (77)$$

The computational results are shown in Table 3 for $\epsilon = 1/2$ and various values of n .

6. Conclusions

Exponential spline, which is a generalization of polynomial spline, is an ideal function approximation tool due to its excellent curve fitting ability. High accuracy can be achieved in solving second-order ODEs using the exponential spline scheme. The spline difference method is an ideal scheme because it can give not only the numerical results but also the spline function expressions by reusing these numerical results at the same time, whereas it is only suitable for solving certain types of equations and does not have generality. And the selection of the appropriate parameters is also needed for this method, but there is no better guideline for the selecting.

Data Availability

The data used to support the findings of this study are included within the article.

Conflicts of Interest

The authors declare that there are no conflicts of interest regarding the publication of this paper.

Acknowledgments

This work was supported by the Education Department of Guangxi Province in 2015 (KY2015YB081).

References

- [1] E. L. Albasiny and W. D. Hoskins, “Cubic spline solution to two-point boundary value problems,” *Computer Journal*, vol. 12, no. 2, pp. 151–153, 1969.
- [2] C. V. Raghavarao, Y. V. S. S. Sanyasiraju, and S. Suresh, “A note on application of cubic splines to two point boundary value problems,” *Computers & Mathematics with Applications*, vol. 27, no. 11, pp. 45–48, 1994.
- [3] J. L. Blue, “Spline function methods for nonlinear boundary-value problems,” *Communications of the ACM*, vol. 12, no. 6, pp. 327–330, 1969.
- [4] H. Caglar, N. Caglar, and K. Elfaituri, “B-spline interpolation compared with finite difference, finite element and finite volume methods which applied to two-point boundary value problems,” *Applied Mathematics and Computation*, vol. 175, no. 1, pp. 72–79, 2006.
- [5] M. M. Chawla and P. N. Shivakumar, “A finite difference method for a class of two-point boundary value problems over a semi-infinite range,” *Journal of Computational and Applied Mathematics*, vol. 15, no. 2, pp. 251–256, 1986.
- [6] W. K. Zahra, “Exponential spline solutions for a class of two point boundary value problems over a semi-infinite range,” *Numerical Algorithms*, vol. 52, no. 4, pp. 561–573, 2009.
- [7] S. C. S. Rao and M. Kumar, “Exponential B-spline collocation method for self-adjoint singularly perturbed boundary value problems,” *Applied Numerical Mathematics*, vol. 58, no. 10, pp. 1572–1581, 2008.
- [8] I. A. Tirmizi, F. Fazal-i-Haq, and S. Siraj-ul-Islam, “Non-polynomial spline solution of singularly perturbed boundary-value problems,” *Applied Mathematics and Computation*, vol. 196, no. 1, pp. 6–16, 2008.
- [9] M. A. Ramadan, I. F. Lashien, and W. K. Zahra, “Polynomial and nonpolynomial spline approaches to the numerical solution of second order boundary value problems,” *Applied Mathematics and Computation*, vol. 184, no. 2, pp. 476–484, 2007.
- [10] K. Surla and M. Stojanović, “Solving singularly perturbed boundary-value problems by spline in tension,” *Journal of Computational and Applied Mathematics*, vol. 24, no. 3, pp. 355–363, 1988.
- [11] N. Jha and R. K. Mohanty, “Quintic hyperbolic non-polynomial spline and finite difference method for nonlinear second order differential equations and its application,” *Journal of the Egyptian Mathematical Society*, vol. 22, no. 1, pp. 115–122, 2014.
- [12] N. Jha, “High order accurate quintic nonpolynomial spline finite difference approximations for the numerical solution of non-linear two point boundary value problems,” *International*

- Journal of Modeling, Simulation, and Scientific Computing*, vol. 5, no. 1, p. 1350018, 2014.
- [13] M. K. Kadalbajoo and K. C. Patidar, "Numerical solution of singularly perturbed two-point boundary value problems by spline in tension," *Applied Mathematics and Computation*, vol. 131, no. 2-3, pp. 299–320, 2002.
- [14] Z. You, *Non-singular M-Matrix*, pp. 89–108, Huazhong Institute of Technology Press, Wuhan, China, 1981.
- [15] C. Yang, C. Xu, and Y. Gao, "Explicit inverses of nonsingular tridiagonal matrices," *Journal of Engineering Mathematics*, vol. 21, no. 1, pp. 48–52, 2004.
- [16] M. K. Kadalbajoo and K. C. Patidar, "Numerical solution of singularly perturbed two point boundary value problems by spline in compression," *International Journal of Computer Mathematics*, vol. 77, no. 2, pp. 263–28310, 2001.
- [17] S.-T. Liu and Y. Xu, "Galerkin methods based on hermite splines for singular perturbation problems," *SIAM Journal on Numerical Analysis*, vol. 43, no. 6, pp. 2607–2623, 2006.
- [18] H. Liu, Y. Pan, S. Li, and Y. Chen, "Adaptive fuzzy backstepping control of fractional-order nonlinear systems," *IEEE Transactions on Systems, Man, and Cybernetics: Systems*, vol. 47, no. 8, pp. 2209–2217, 2017.
- [19] H. Liu, H. Wang, J. Cao, A. Alsaedi, and T. Hayat, "Composite learning adaptive sliding mode control of fractional-order nonlinear systems with actuator faults," *Journal of the Franklin Institute*, vol. 356, no. 16, pp. 9580–9599, 2019.

Research Article

Multiple Criteria Decision-Making Based on Vector Similarity Measures under the Framework of Dual Hesitant Fuzzy Sets

Juan Luis García Guirao ¹, M. Sarwar Sindhu,² Tabasam Rashid ² and Agha Kashif²

¹Departamento de Matematica Aplicada y Estadística, Universidad Politecnica de Cartagena, Cartagena, Spain

²Department of Mathematics, University of Management and Technology, Lahore 54770, Pakistan

Correspondence should be addressed to Tabasam Rashid; tabasam.rashid@gmail.com

Received 27 April 2020; Accepted 30 July 2020; Published 17 August 2020

Academic Editor: Garyfalos Papashinopoulos

Copyright © 2020 Juan Luis García Guirao et al. This is an open access article distributed under the Creative Commons Attribution License, which permits unrestricted use, distribution, and reproduction in any medium, provided the original work is properly cited.

Similarity measures have a great importance in the decision-making process. In order to identify the similarity between the options, many experts have established several types of similarity measures on the basis of vectors and distances. The Cosine, Dice, and Jaccard are the vector similarity measures. The present work enclosed the modified Jaccard and Dice similarity measures. Founded on the Dice and Jaccard similarity measures, we offered a multiple criteria decision-making (MCDM) model under the dual hesitant fuzzy sets (DHFSS) situation, in which the appraised values of the alternatives with respect to criteria are articulated by dual hesitant fuzzy elements (DHFES). Since the weights of the criteria have a much influence in making the decisions, therefore decision makers (DMs) allocate the weights to each criteria according to their knowledge. In the present work, we get rid of the doubt to allocate the weights to the criteria by taking an objective function under some constraints and then extended the linear programming (LP) technique to evaluate the weights of the criteria. The Dice and Jaccard weighted similarity measures are practiced amongst the ideal and each alternative to grade all the alternatives to get the best one. Eventually, two practical examples, about investment companies and selection of smart phone accessories are assumed to elaborate the efficiency of the proposed methodology.

1. Introduction

In everyday life, decision-making plays a central role in choosing the best option out of certain choices. Generally, the decision-making [1, 2] process enables the experts or decision makers (DMs) to tackle problems by analyzing alternative selection and choosing the best course to adopt. However, an inconvenience is encountered by the DMs when they deal with the vague and ambiguous information. Zadeh [3] reduced the difficulties of the DMs by introducing the idea of fuzzy sets (FSs). FSs have opened the new horizons to treat the hesitation and vagueness involved in the process of decision-making. Recently, Citil [4] analyzed the fuzzy issues by using the fuzzy Laplace transform. In the FSs' environment, DMs consider only membership values. In [5], Atanassov further extended by adding a nonmembership value in FSs, known as intuitionistic fuzzy sets (IFSs). Later

on, Torra [6] presented a novel extension of FSs, the hesitant fuzzy sets (HFSs), which augmented by adding diverse values to the membership. Researchers divert their attention towards HFSs and ample work is carried out in the MCDM process with the help of HFSs [7–9]. The DMs feel that the above extensions of FSs have inadequacy of data because FSs treat only one membership value; IFSs deal two kinds of information that are membership and nonmembership while HFSs consider the set values in its membership value but ignore the nonmembership value. In order to overcome this deficiency, Zhu et al. [10] defined another extension of FSs, named dual hesitant fuzzy sets (DHFSS) which have the behavior of HFSs as well as IFSs. DHFSSs can take more information into account because DHFSSs have a set of hesitant values as belonging and nonbelonging values. More values are obtained from the decision makers due to which DHFSSs can be regarded as a more comprehensive set which

supports a more flexible approach when the DMs provide their decisions. Xia and Xu [11] presented the idea of dual hesitant fuzzy element (DHFE), which can be considered as the fundamental unit of the DHFSs and thereby becomes the basic and successful instrument used to express the DMs reluctant inclinations in the procedure of decision-making.

In order to develop the theory of DHFSs, Zhu and Xu [12] presented the idea of typical DHFSs (T-DHFSs) and deliberate certain distinct properties of T-DHFSs. Chen and Huang [13] presented the concept of dual hesitant fuzzy probability (DHFP) dependent on some important outcomes, including the characteristic of DHFP, dual hesitant fuzzy contingent probability, and dual hesitant fuzzy complete probability. Recently, MCDM techniques have been established under the DHFSs environment. For example, Ren et al. [14] used DHFS-based VIKOR method for multicriteria group decision-making. Afterwards, the distance and similarity measures [15, 16], the correlation measures [17, 18], and the entropy measures [19] based on DHFSs have been constructed to handle the MCDM problems. Jamil and Rashid [20] developed the weighted geometric Bonferroni and Choquet geometric Bonferroni means based on DHFSs and then applied it in MCDM issue to elect the best alternative. Moreover, due to the specification of DHFSs, DMs are working more and more in different fields of management sciences by using DHFSs [21–23].

The similarity measure denotes the most resemblance amongst the two particles, and it is plausible to give the preferred arrangement according to the significance. Most of the similarity measures are developed on the basis of distances under the dual hesitant fuzzy environment. Beg and Ashraf discussed the various characteristic of similarity measures under the framework of FSs [24]. Measures of vector similarity also play a dominant role in decision-making, such as Ye [25] applied the Cosine similarity measures to pattern recognition and medical diagnosis under IFSS' environment. Intarapaiboon [26] applied two new similarity measures to pattern recognition under IFSS situations. Furthermore, Song and Hu [27] established two similarity measures between hesitant fuzzy linguistic term sets and used it for MCDM problems. Recently, Zang et al. [28] developed the Heronian mean aggregation operators and applied them for multiattribute decision-making (MADM) under the interval-valued dual hesitant fuzzy framework. Zhang et al. [29] introduced a new concept of Cosine similarity measure based on DHFSs and implemented it for the weapon selection problem. Jiang et al. [30] presented a novel similarity measure dependent on distance between IFSS by transforming the isosceles triangles from IFSS and determined the validity and practicality of the proposed similarity measure by employing on different pattern recognition examples. Chen and Barman [31] proposed an adaptive weighted fuzzy interpolative reasoning (AWFIR) method on the basis of representative values (RVs) and similarity measures of interval type-2 polygonal fuzzy sets to handle the flaws of adaptive fuzzy interpolative reasoning (AFIR) method given by Cheng et al. [32]. Moreover, Chen and Barman [33] established a novel adaptive fuzzy interpolative reasoning (AFIR) method on the basis of similarity measures under the polygonal fuzzy

sets' (PFSS) framework to diagnose the diarrheal disease in the specified persons.

The linear programming (LP) [34] technique allows some target function to be minimized or maximized inside the system of giving situational limitations. LP is a computational technique that enables DMs to solve the problems which they face in a decision-making process. It encourages the DMs to deal with the constrained ideal conditions which they need to make the best of their resources. For example, one limitation for a business is the number of employees it can contract. Another could identify the measure of crude material it has access. Wang and Chen [35] presented a new MCDM method on the basis of the linear programming model, new score, and accuracy function of interval-valued intuitionistic fuzzy values (IVIFVs). He et al. [36] presented an input-output LP model to study energy-economic recovery resilience of an economy. Wang and Chen [37] presented LP methodology and the extended TOPSIS method for interval-valued intuitionistic fuzzy numbers for the selection of the best alternative, which deals with two interval values: belonging and nonbelonging. Lanbaran et al. [38] used the interval-valued fuzzy TOPSIS to determine the opportunities of investment in an MCDM problem. Aliyev [39] presented interval LP where the ambiguous location is termed by interval numbers. Recently, Sindhu et al. implemented the LP technique to evaluate the weights of criteria under distinct extensions of FSs [40–42].

In order to show preference strength among the alternatives, the similarity measures have achieved more attention from the DMs from the previous few decades. Many experts have presented a number of similarity measures for MCDM problems to select the most favorable alternative from the various options having identical features under the certain criteria, for example, similarity measures based on distance, Cosine similarity measure, Jaccard similarity measure, and Dice similarity measure. Since DHFSs have adequate information on their formation, therefore, we can deal well with the circumstances that allow both the membership and the non-membership of an element to a particular set having some diverse values. The LP model is simple, user friendly, and responds quickly with the adoptability of Matlab. Also Jaccard and Dice similarity measures are modest and easy to compute. However, it has not been studied under the DHFSs' framework. This motivated us to deal with the problems under the influence of DHFSs' environment. It is noteworthy that the decision-making under DHFSs' environment may acquire more attention and is deserved wider recognition and further research. Thereby, we modified the Jaccard and Dice similarity measures and applied them for the information provided by DMs under DHFSs' environment.

The remaining part of the present work is organized as follows. Section 2 encompasses the basics of DHFSs, the similarity measures, and the LP model. Section 3 comprises the Jaccard and Dice similarity measures with their modified forms. We proposed a MCDM model on the basis of Jaccard and Dice weighted vector similarity measures of DHFSs in Section 4. In Section 5, we utilize MCDM problems to examine the outcomes of the proposed model. A comparative analysis and conclusions are given in Sections 6 and 7, respectively.

2. Preliminaries

A brief review about the fundamentals of IFSSs, HFSs, the Jaccard and Dice vector similarity measures, and the LP model is discussed in the present section.

Definition 1 (see [5]). Let $X = \{x_1, x_2, \dots, x_n\}$ be a discourse set, an intuitionistic fuzzy set (IFS) A on X is represented in terms of two functions $m: X \rightarrow [0, 1]$ and $n: X \rightarrow [0, 1]$ such as

$$A = \{\langle x, m_A(x), n_A(x) \rangle: x \in X\}, \quad (1)$$

with the condition $0 \leq m_A(x) + n_A(x) \leq 1$, for all $x \in X$. Moreover, $\pi(x) = 1 - m_A(x) - n_A(x)$ is called a degree of hesitancy or an intuitionistic index of x in A . For the special case when $\pi(x) = 0$, that is, $m_A(x) + n_A(x) = 1$, then the IFS A becomes a fuzzy set.

Definition 2 (see [6]). Let $X = \{x_1, x_2, \dots, x_n\}$ be a universal set; a hesitant fuzzy set B on X is defined in terms of a function $h_B(x)$ that when applied to X returns a finite subset of $[0, 1]$. For convenience, the HFS can be written mathematically as described by Xia and Xu [11]:

$$H = \{\langle x, h_{H(x)} \rangle: x \in X\}, \quad (2)$$

where $h_{H(x)}$ is the collection of some different values in $[0, 1]$ representing the plausible belonging degrees of the component $x \in X$ to the set H .

Xia and Xu [11] also presented the core element of HFSs called the hesitant fuzzy element (HFE) and simply written as $h = h(x)$. The hesitant fuzzy elements, $h = \{0\}$ and $h = \{1\}$, are called the empty and full HFEs, respectively. For our convenience, HFSs can be calculated with the help of HFEs by using aggregation techniques or some other actions involved in the decision-making methods.

Definition 3 (see [10]). Let $X = \{x_1, x_2, \dots, x_n\}$ be a discourse set; then, a dual hesitant fuzzy set DHFS D on X is defined as follows:

$$D = \{\langle x, h(x), g(x) \rangle: x \in X\}, \quad (3)$$

where $h(x)$ and $g(x)$ are the collections of set values which lie in $[0, 1]$, denoting the plausible MD_g and NMD_g of the element $x \in X$ to the set D , respectively, and satisfying the conditions penned below: $0 \leq \alpha, \beta \leq 1, 0 \leq \alpha^+ + \beta^+ \leq 1$, where

$$\begin{aligned} \alpha &\in h(x), \\ \beta &\in g(x), \\ \alpha^+ \in h^+(x) &= \bigcup_{\alpha \in h(x)} \max\{h(x)\}, \\ \beta^+ \in g^+(x) &= \bigcup_{\beta \in g(x)} \max\{g(x)\}, \\ x &\in X. \end{aligned} \quad (4)$$

For the sake of convenience, the order pair $d(x) = (h(x), g(x))$ is used as DHFE and simply written as $d(h, g)$ in the thesis with a few limitations:

$$\begin{aligned} \alpha &\in h, \\ \beta &\in g, \\ \alpha^+ \in h^+ &= \bigcup_{\alpha \in h} \max\{h\}, \\ \beta^+ \in g^+ &= \bigcup_{\beta \in g} \max\{g\}, \\ 0 \leq \alpha, \beta \leq 1, & 0 \leq \alpha^+ + \beta^+ \leq 1. \end{aligned} \quad (5)$$

Sometimes DMs gave their information in the form of HFSs with distinct cardinalities such as $|h_1| \neq |h_2|$ and $|g_1| \neq |g_2|$ which are the belonging and nonbelonging components of two DHFSs D_1 and D_2 . In order to make the cardinalities to be equal, we can increase or decrease the number of elements by using the definition given by Xu and Zhang [43]. To calculate the distance between two DHFEs $d_1 = (h_1, g_1)$ and $d_2 = (h_2, g_2)$ with unequal lengths, i.e., $|h_1| \neq |h_2|$ and $|g_1| \neq |g_2|$, we will first equalize the cardinalities of d_1 and d_2 .

Definition 4 (see [10]). Let $Y = \{y_1, y_2, \dots, y_n\}$ be a universe set and $\mathcal{D} = \{\{h\}, \{g\}\}$ be the DHFSs on X ; then, the complement of \mathcal{D} denoted by \mathcal{D}^c is defined as follows:

$$\mathcal{D}^c = \bigcup_{\alpha \in h, \beta \in g} \{\{\beta\}, \{\alpha\}\}. \quad (6)$$

Definition 5. Let $S = \{s_1, s_2, \dots, s_n\}$ and $T = \{t_1, t_2, \dots, t_n\}$ be two positive vectors having length n . The Jaccard $J(S, T)$ and Dice $D(S, T)$ similarity measures [44, 45] are defined as follows:

$$\begin{aligned} J(S, T) &= \left(\frac{S \cdot T}{\|S\|^2 + \|T\|^2 - S \cdot T} \right) = \left(\frac{\sum_{k=1}^n s_k \cdot t_k}{\sum_{k=1}^n s_k^2 + \sum_{k=1}^n t_k^2 - \sum_{k=1}^n s_k \cdot t_k} \right), \\ D(S, T) &= \left(\frac{2S \cdot T}{\|S\|^2 + \|T\|^2} \right) = \left(\frac{2 \sum_{k=1}^n s_k \cdot t_k}{\sum_{k=1}^n s_k^2 + \sum_{k=1}^n t_k^2} \right), \end{aligned} \quad (7)$$

where $S \cdot T = \sum_{k=1}^n s_k t_k$ is the inner product of the vectors S and T and $\|S\| = \sqrt{\sum_{k=1}^n s_k^2}$ and $\|T\| = \sqrt{\sum_{k=1}^n t_k^2}$ are the Euclidean norms of S and T . Both Jaccard $J(S, T)$ and Dice $D(S, T)$ similarity measures fulfil the following conditions:

- (1) $J(S, T) = J(T, S)$ and $D(S, T) = D(T, S)$
- (2) $J(S, T) = 1$ and $D(S, T) = 1$ if $S = T$
- (3) $0 \leq J(S, T) \leq 1$ and $0 \leq D(S, T) \leq 1$

Definition 6 (see [34]). The linear programming model is constructed as follows:

$$\begin{aligned}
\text{Maximize: } & S = c_1 t_1 + c_2 t_2 + c_3 t_3 + \dots + c_n t_n \\
& a_{11} t_1 + a_{12} t_2 + a_{13} t_3 + \dots + a_{1n} t_n \leq b_1 \\
& a_{21} t_1 + a_{22} t_2 + a_{23} t_3 + \dots + a_{2n} t_n \leq b_2 \\
\text{Subject to: } & \vdots \\
& a_{m1} t_1 + a_{m2} t_2 + a_{m3} t_3 + \dots + a_{mn} t_n \leq b_m \\
& t_1, t_2, \dots, t_n \geq 0,
\end{aligned} \tag{8}$$

where m and n denote the number of constraints and the number of decision variables, respectively. A solution (t_1, t_2, \dots, t_n) is called feasible point if it fulfils all of the restrictions. The LP model is used to find the optimal solution of the decision variables t_1, t_2, \dots, t_n to maximize the linear function S .

3. Jaccard and Dice Similarity Measures for DHFSs

Let \mathcal{A} and \mathcal{B} be two DHFSs defined on a fixed set $X = \{x_1, x_2, \dots, x_n\}$ represented as $\mathcal{A} = \{\langle x, h_{\mathcal{A}}(x), g_{\mathcal{A}}(x) \rangle : x \in X\}$ and $\mathcal{B} = \{\langle x, h_{\mathcal{B}}(x), g_{\mathcal{B}}(x) \rangle : x \in X\}$, respectively. We can consider any two dual hesitant fuzzy elements $d_1 = (h_1(x), g_1(x)) \in \mathcal{A}$ and $d_2 = (h_2(x), g_2(x)) \in \mathcal{B}$ as two vectors. Then, according to the aforementioned similarity measures in the vector space, we can modify the Jaccard and Dice similarity measures between DHFSs as follows.

Definition 7. Let \mathcal{A} and \mathcal{B} be two DHFSs defined on a fixed set $X = \{x_1, x_2, \dots, x_n\}$; then, the modified Jaccard $J_s(\mathcal{A}, \mathcal{B})$ is defined as follows:

$$\begin{aligned}
J_s(\mathcal{A}, \mathcal{B}) = \frac{1}{2} & \left\{ \frac{\sum(\alpha.\bar{\alpha})}{\sum(\alpha)^2 + \sum(\bar{\alpha})^2 - \sum(\alpha.\bar{\alpha})} \right. \\
& \left. + \frac{\sum(\beta.\bar{\beta})}{\sum(\beta)^2 + \sum(\bar{\beta})^2 - \sum(\beta.\bar{\beta})} \right\}, \tag{9}
\end{aligned}$$

where $\alpha \in h_1, \beta \in g_1 \in \mathcal{A}$ and $\bar{\alpha} \in h_2, \bar{\beta} \in g_2 \in \mathcal{B}$, respectively.

Definition 8. Let \mathcal{A} and \mathcal{B} be two DHFSs defined on a universal set $X = \{x_1, x_2, \dots, x_n\}$; then, the modified Dice $D_s(\mathcal{A}, \mathcal{B})$ is defined as follows:

$$D_s(\mathcal{A}, \mathcal{B}) = \frac{\sum(\alpha.\bar{\alpha})}{\sum(\alpha)^2 + \sum(\bar{\alpha})^2} + \frac{\sum(\beta.\bar{\beta})}{\sum(\beta)^2 + \sum(\bar{\beta})^2}, \tag{10}$$

where $\alpha \in h_1, \beta \in g_1 \in \mathcal{A}$ and $\bar{\alpha} \in h_2, \bar{\beta} \in g_2 \in \mathcal{B}$, respectively.

Since the weights of the criteria has a great worth in making decision. Thus, we can further extend the Jaccard and Dice similarity measures into the Jaccard and Dice weighted similarity measures. Let $w = (w_1, w_2, \dots, w_m)^T$ be a weight vector of the m criteria with $\sum_{j=1}^m w_j = 1$. Then, the Jaccard and Dice similarity measures take the form:

$$J_s^w(\mathcal{A}, \mathcal{B}) = \frac{1}{2} \left\{ \frac{\sum_{j=1}^m w_j(\alpha.\bar{\alpha})}{\sum(\alpha)^2 + \sum(\bar{\alpha})^2 - \sum(\alpha.\bar{\alpha})} + \frac{\sum_{j=1}^m w_j(\beta.\bar{\beta})}{\sum(\beta)^2 + \sum(\bar{\beta})^2 - \sum(\beta.\bar{\beta})} \right\}, \tag{11}$$

$$D_s^w(\mathcal{A}, \mathcal{B}) = \frac{\sum_{j=1}^m w_j(\alpha.\bar{\alpha})}{\sum(\alpha)^2 + \sum(\bar{\alpha})^2} + \frac{\sum_{j=1}^m w_j(\beta.\bar{\beta})}{\sum(\beta)^2 + \sum(\bar{\beta})^2}. \tag{12}$$

Theorem 1. The Jaccard similarity measure $J_s(\mathcal{A}, \mathcal{B})$ between two DHFSs with $d_1 = (h_1, g_1) \in \mathcal{A}$ and $d_2 = (h_2, g_2) \in \mathcal{B}$ satisfies the following properties:

- (1) $J_s(\mathcal{A}, \mathcal{B}) = J_s(\mathcal{B}, \mathcal{A})$
- (2) $J_s(\mathcal{A}, \mathcal{B}) = 1$, if and only if \mathcal{A} is equivalent to \mathcal{B} by definition given in [10]
- (3) $0 \leq J_s(\mathcal{A}, \mathcal{B}) \leq 1$

Proof

(1–2) are obvious.

From (3), let $\alpha \in h_1, \beta \in g_1 \in \mathcal{A}$ and $\bar{\alpha} \in h_2, \bar{\beta} \in g_2 \in \mathcal{B}$, respectively. However, we know that

$$\begin{aligned}
(x - y)^2 & \geq 0 \\
\implies x^2 + y^2 - xy - xy & \geq 0 \\
\implies x^2 + y^2 - xy & \geq xy \\
\implies \sum(\alpha)^2 + \sum(\bar{\alpha})^2 - \sum(\alpha.\bar{\alpha}) - \sum(\alpha.\bar{\alpha}) & \geq 0 \tag{13} \\
\implies \sum(\alpha)^2 + \sum(\bar{\alpha})^2 - \sum(\alpha.\bar{\alpha}) & \geq \sum(\alpha.\bar{\alpha}) \\
\implies \frac{\sum(\alpha.\bar{\alpha})}{\sum(\alpha)^2 + \sum(\bar{\alpha})^2 - \sum(\alpha.\bar{\alpha})} & \leq 1.
\end{aligned}$$

Similarly,

$$\begin{aligned} \sum (\beta)^2 + \sum (\bar{\beta})^2 - \sum (\beta \cdot \bar{\beta}) &\geq \sum (\beta \cdot \bar{\beta}) \\ \implies \frac{\sum (\beta \cdot \bar{\beta})}{\sum (\beta)^2 + \sum (\bar{\beta})^2 - \sum (\beta \cdot \bar{\beta})} &\leq 1. \end{aligned} \tag{14}$$

By adding equations (13) and (14), we obtain

$$\begin{aligned} \frac{\sum (\alpha \cdot \bar{\alpha})}{\sum (\alpha)^2 + \sum (\bar{\alpha})^2 - \sum (\alpha \cdot \bar{\alpha})} + \frac{\sum (\beta \cdot \bar{\beta})}{\sum (\beta)^2 + \sum (\bar{\beta})^2 - \sum (\beta \cdot \bar{\beta})} &\leq 2 \\ \implies \frac{1}{2} \left\{ \frac{\sum (\alpha \cdot \bar{\alpha})}{\sum (\alpha)^2 + \sum (\bar{\alpha})^2 - \sum (\alpha \cdot \bar{\alpha})} + \frac{\sum (\beta \cdot \bar{\beta})}{\sum (\beta)^2 + \sum (\bar{\beta})^2 - \sum (\beta \cdot \bar{\beta})} \right\} &\leq 1, \end{aligned} \tag{15}$$

that is, $0 \leq J_s(\mathcal{A}, \mathcal{B}) \leq 1$.

Lemma 1. Let $X = \{x_1, x_2, \dots, x_n\}$ be a given universe. The modified Jaccard similarity measure $J_s(\mathcal{A}, \mathcal{B})$ satisfies the properties given below:

- (1) $J_s(\mathcal{A}, \mathcal{A}^c) = 0$ if and only if $\mathcal{A} = \{\{1\}, \{0\}\}$
- (2) $J_s(\mathcal{A}, \mathcal{A}^c) = 1$ if and only if $\mathcal{A} = \{\{0.5\}, \{0.5\}\}$
- (3) $J_s(\mathcal{A}, \mathcal{B}) = J_s(\mathcal{A}^c, \mathcal{B}^c)$

Proof

- (1) It is obvious.
- (2) Let $\alpha, \beta \in \mathcal{A}$ and $\alpha_1, \beta_1 \in \mathcal{A}^c$. We obtain

$$\begin{aligned} J_s(\mathcal{A}, \mathcal{A}^c) &= \frac{1}{2} \left\{ \frac{\sum (\alpha \cdot \alpha_1)}{\sum (\alpha)^2 + \sum (\alpha_1)^2 - \sum (\alpha \cdot \alpha_1)} \right. \\ &\quad \left. + \frac{\sum (\beta \cdot \beta_1)}{\sum (\beta)^2 + \sum (\beta_1)^2 - \sum (\beta \cdot \beta_1)} \right\}. \end{aligned} \tag{16}$$

Since $\alpha = \alpha_1$ and $\beta = \beta_1$, therefore,

$$\begin{aligned} J_s(\mathcal{A}, \mathcal{A}^c) &= \frac{1}{2} \left\{ \frac{\sum (\alpha \cdot \alpha)}{\sum (\alpha)^2 + \sum (\alpha)^2 - \sum (\alpha \cdot \alpha)} \right. \\ &\quad \left. + \frac{\sum (\beta \cdot \beta)}{\sum (\beta)^2 + \sum (\beta)^2 - \sum (\beta \cdot \beta)} \right\} = 1. \end{aligned} \tag{17}$$

- (3) Let $\mathcal{A} = \{\{h_1\}, \{g_1\}\}$ and $\mathcal{B} = \{\{h_2\}, \{g_2\}\}$ be two DHFSs and $\mathcal{A}^c = \{\{g_1\}, \{h_1\}\}$ and $\mathcal{B}^c = \{\{g_2\}, \{h_2\}\}$ their complements. Suppose that $\alpha_1, \beta_1 \in \mathcal{A}$, $\alpha_2, \beta_2 \in \mathcal{B}$, $\alpha'_1, \beta'_1 \in \mathcal{A}^c$, and $\alpha'_2, \beta'_2 \in \mathcal{B}^c$, then

$$\begin{aligned} J_s(\mathcal{A}, \mathcal{B}) &= \frac{1}{2} \left\{ \frac{\sum (\alpha_1 \cdot \alpha_2)}{\sum (\alpha_1)^2 + \sum (\alpha_2)^2 - \sum (\alpha_1 \cdot \alpha_2)} \right. \\ &\quad \left. + \frac{\sum (\beta_1 \cdot \beta_2)}{\sum (\beta_1)^2 + \sum (\beta_2)^2 - \sum (\beta_1 \cdot \beta_2)} \right\}. \end{aligned} \tag{18}$$

However, $\alpha_1 = \beta'_1, \alpha_2 = \beta'_2, \beta_1 = \alpha'_1$, and $\beta_2 = \alpha'_2$. Hence,

$$\begin{aligned} J_s(\mathcal{A}, \mathcal{B}) &= \frac{1}{2} \left\{ \frac{\sum (\beta'_1 \cdot \beta'_2)}{\sum (\beta'_1)^2 + \sum (\beta'_2)^2 - \sum (\beta'_1 \cdot \beta'_2)} \right. \\ &\quad \left. + \frac{\sum (\alpha'_1 \cdot \alpha'_2)}{\sum (\alpha'_1)^2 + \sum (\alpha'_2)^2 - \sum (\alpha'_1 \cdot \alpha'_2)} \right\} \\ \implies J_s(\mathcal{A}, \mathcal{B}) &= \frac{1}{2} \left\{ \frac{\sum (\alpha'_1 \cdot \alpha'_2)}{\sum (\alpha'_1)^2 + \sum (\alpha'_2)^2 - \sum (\alpha'_1 \cdot \alpha'_2)} \right. \\ &\quad \left. + \frac{\sum (\beta'_1 \cdot \beta'_2)}{\sum (\beta'_1)^2 + \sum (\beta'_2)^2 - \sum (\beta'_1 \cdot \beta'_2)} \right\} \\ \implies J_s(\mathcal{A}, \mathcal{B}) &= J_s(\mathcal{A}^c, \mathcal{B}^c). \end{aligned} \tag{19}$$

Theorem 2. The Dice similarity measure $D_s(\mathcal{A}, \mathcal{B})$ between two DHFSs with $d_1 = (h_1, g_1) \in \mathcal{A}$ and $d_2 = (h_2, g_2) \in \mathcal{B}$ satisfies the following properties:

- (1) $D_s(\mathcal{A}, \mathcal{B}) = D_s(\mathcal{B}, \mathcal{A})$
- (2) $D_s(\mathcal{A}, \mathcal{B}) = 1$, if and only if \mathcal{A} is equivalent to \mathcal{B} by definition given in [10]
- (3) $0 \leq D_s(\mathcal{A}, \mathcal{B}) \leq 1$

Proof

(1-2) are obvious.

From (3), let $\alpha \in h_1, \beta \in g_1 \in \mathcal{A}$ and $\bar{\alpha} \in h_2, \bar{\beta} \in g_2 \in \mathcal{B}$, respectively.

However, we know that

$$(x - y)^2 \geq 0$$

$$\implies x^2 + y^2 \geq 2xy$$

$$\sum (\alpha)^2 + \sum (\bar{\alpha})^2 \geq 2 \sum (\alpha \cdot \bar{\alpha}) \tag{20}$$

$$\implies \frac{2 \sum (\alpha \cdot \bar{\alpha})}{\sum (\alpha)^2 + \sum (\bar{\alpha})^2} \leq 1,$$

$$\sum (\beta)^2 + \sum (\bar{\beta})^2 \geq 2 \sum (\beta \cdot \bar{\beta})$$

$$\implies \frac{2 \sum (\beta \cdot \bar{\beta})}{\sum (\beta)^2 + \sum (\bar{\beta})^2} \leq 1. \tag{21}$$

By adding equations (20) and (21), we obtain

$$\frac{2 \sum (\alpha \cdot \bar{\alpha})}{\sum (\alpha)^2 + \sum (\bar{\alpha})^2} + \frac{2 \sum (\beta \cdot \bar{\beta})}{\sum (\beta)^2 + \sum (\bar{\beta})^2} \leq 2 \tag{22}$$

$$\implies \frac{\sum (\alpha \cdot \bar{\alpha})}{\sum (\alpha)^2 + \sum (\bar{\alpha})^2} + \frac{\sum (\beta \cdot \bar{\beta})}{\sum (\beta)^2 + \sum (\bar{\beta})^2} \leq 1,$$

which shows that $0 \leq D_s(d_1, d_2) \leq 1$.

Lemma 2. Let $X = \{x_1, x_2, \dots, x_n\}$ be a given universe. The modified Dice similarity measure $D_s(\mathcal{A}, \mathcal{B})$ satisfies the properties given below:

- (1) $D_s(\mathcal{A}, \mathcal{A}^c) = 0$ if and only if $\mathcal{A} = \{\{1\}, \{0\}\}$
- (2) $D_s(\mathcal{A}, \mathcal{A}^c) = 1$ if and only if $\mathcal{A} = \{\{0.5\}, \{0.5\}\}$
- (3) $D_s(\mathcal{A}, \mathcal{B}) = D_s(\mathcal{A}^c, \mathcal{B}^c)$

Proof

- (1) It is obvious.
- (2) Let $\alpha, \beta \in \mathcal{A}$ and $\alpha_1, \beta_1 \in \mathcal{A}^c$. We obtain

$$D_s(\mathcal{A}, \mathcal{A}^c) = \frac{\sum(\alpha)(\alpha_1)}{\sum\alpha^2 + \sum\alpha_1^2} + \frac{\sum(\beta)(\beta_1)}{\sum\beta^2 + \sum\beta_1^2}. \quad (23)$$

Since $\alpha = \alpha_1$ and $\beta = \beta_1$, therefore,

$$D_s(\mathcal{A}, \mathcal{A}^c) = \frac{\sum(\alpha)(\alpha)}{\sum\alpha^2 + \sum\alpha^2} + \frac{\sum(\beta)(\beta)}{\sum\beta^2 + \sum\beta^2} \quad (24)$$

$$\implies D_s(\mathcal{A}, \mathcal{A}^c) = 1.$$

- (3) Let $\mathcal{A} = \{\{h_1\}, \{g_1\}\}$ and $\mathcal{B} = \{\{h_2\}, \{g_2\}\}$ be two DHFSs and $\mathcal{A}^c = \{\{g_1\}, \{h_1\}\}$ and $\mathcal{B}^c = \{\{g_2\}, \{h_2\}\}$ are their complements. Suppose that $\alpha_1, \beta_1 \in \mathcal{A}$, $\alpha_2, \beta_2 \in \mathcal{B}$, $\alpha'_1, \beta'_1 \in \mathcal{A}^c$, and $\alpha'_2, \beta'_2 \in \mathcal{B}^c$, then

$$D_s(\mathcal{A}, \mathcal{B}) = \frac{\sum(\alpha_1)(\alpha_2)}{\sum\alpha_1^2 + \sum\alpha_2^2} + \frac{\sum(\beta_1)(\beta_2)}{\sum\beta_1^2 + \sum\beta_2^2}. \quad (25)$$

However, $\alpha_1 = \beta'_1, \alpha_2 = \beta'_2, \beta_1 = \alpha'_1$, and $\beta_2 = \alpha'_2$. Hence,

$$\begin{aligned} D_s(\mathcal{A}, \mathcal{B}) &= \frac{\sum(\beta'_1)(\beta'_2)}{\sum(\beta'_1)^2 + \sum(\beta'_2)^2} + \frac{\sum(\alpha'_1)(\alpha'_2)}{\sum(\alpha'_1)^2 + \sum(\alpha'_2)^2} \\ \implies D_s(\mathcal{A}, \mathcal{B}) &= \frac{\sum(\alpha'_1)(\alpha'_2)}{\sum(\alpha'_1)^2 + \sum(\alpha'_2)^2} + \frac{\sum(\beta'_1)(\beta'_2)}{\sum(\beta'_1)^2 + \sum(\beta'_2)^2} \\ \implies D_s(\mathcal{A}, \mathcal{B}) &= D_s(\mathcal{A}^c, \mathcal{B}^c). \end{aligned} \quad (26)$$

We can follow the same way to prove the Jaccard- and Dice-weighted similarity measures:

- (1) $J_s^w(\mathcal{A}, \mathcal{B}) = J_s^w(\mathcal{B}, \mathcal{A})$ and $D_s^w(\mathcal{A}, \mathcal{B}) = D_s^w(\mathcal{B}, \mathcal{A})$
- (2) $J_s^w(\mathcal{A}, \mathcal{B}) = D_s^w(\mathcal{A}, \mathcal{B}) = 1$, if and only if $\mathcal{B} = \mathcal{A}$
- (3) $0 \leq J_s^w(\mathcal{A}, \mathcal{B}) \leq 1$ and $0 \leq D_s^w(\mathcal{A}, \mathcal{B}) \leq 1$

4. Multiple Criteria Decision-Making under DHF Environment

The present segment comprises the model for MCDM in which we use the two vector similarity measures based on

DHFSs. For an MCDM problem, under the dual hesitant fuzzy (DHF) environment, let $P = \{P_1, P_2, \dots, P_n\}$ be a discrete set of alternatives and $G = \{G_1, G_2, \dots, G_m\}$ be a discrete set of criteria. If the DMs gave the various values for the alternative $P_i (i = 1, 2, \dots, n)$ under the attribute $G_j (j = 1, 2, \dots, m)$, these values can be considered as a dual hesitant fuzzy element $d_{ij} (i = 1, 2, \dots, n; j = 1, 2, \dots, m)$. Thereby, we can form a dual hesitant fuzzy decision matrix $\mathcal{D} = [\{h_{ij}\}, \{g_{ij}\}]_{n \times m}$. The concept of optimal solution assists the DMs to identify the best alternative from the decision set in the MCDM framework. In spite of the fact that the perfect option does not exist in actual realm, it provides a valuable paradigm to appraise alternatives. Hence, we can find the ideal options P^* from the given information as $P^* = \{\{\max_i h_{i1}, \max_i h_{i2}, \dots, \max_i h_{im}\}, \{\min_i g_{i1}, \min_i g_{i2}, \dots, \min_i g_{im}\}\}$, where $i = 1, 2, \dots, n$. Since the weights of the criteria have excessive importance, therefore a weighting vector of criteria is provided as $w = (w_1, w_2, w_3, \dots, w_m)^T$, where $\sum_{j=1}^m w_j = 1, j = 1, 2, \dots, m$ and $w_j > 0$.

We propose a MCDM model based on the two weighted vector similarity under dual hesitant fuzzy data, which can be formulated as follows:

Step 1: construct a dual hesitant fuzzy decision matrix (DHFM) denoted by $\mathcal{D} = [d_{ij}]_{n \times m}$ according to the given data presented by the DM

Step 2: transform the matrix \mathcal{D} into normalized dual hesitant fuzzy decision matrix NDHFM, $\tilde{\mathcal{D}} = [\tilde{d}_{ij}]_{n \times m}$

Step 3: find the optimal solution P^* from the NDHFM, $\tilde{\mathcal{D}} = [\tilde{d}_{ij}]_{n \times m}$

Step 4: based on Definition 5, using the LP model to find weights of criteria under the given constraints provided by the DM

Step 5: by using equations (11) and (12), calculate the weighted vector similarity measures amongst the alternative $P_i (i = 1, 2, \dots, n)$ and the optimal alternative P^*

5. Practical Examples

Example 1. A particular example is used as a demonstration of the application of the proposed MCDM method in reality-based scenario. For an investment company, who want to invest a sum of money in the best option, there is a particular panel with four possible alternatives to invest the amount: Pakistan microfinance, investment company (P_1), national investment trust limited (P_2), Pak China investment company limited (P_3), power cement limited (P_4), and Pak Kuwait investment company (P_5). In order to make a decision, the investment company follows the following criteria: the risk G_1 , the economic growth G_2 , the environmental impact G_3 , and the interest rate G_4 . The information about the alternatives P_i under the criteria G_j is represented by a dual hesitant fuzzy decision matrix \mathcal{D} in Table 1. Since the weights of the criteria have a great significance in making the decision. DM has an ambiguity to assign the weights to the criteria. DM assumed that the weights of criteria under the constraint conditions are as follows.

TABLE 1: Dual hesitant fuzzy decision matrix \mathcal{D} .

	G_1	G_2	G_3	G_4
P_1	{{0.1, 0.2, 0.3}, {0.6, 0.7}}	{{0.5, 0.6, 0.7}, {0.1, 0.2}}	{{0.3, 0.4, 0.5}, {0.1, 0.2}}	{{0.1, 0.2, 0.3}, {0.4, 0.5}}
P_2	{{0.4, 0.5, 0.6}, {0.1, 0.2}}	{{0.6, 0.7}, {0.1, 0.2}}	{{0.6, 0.7}, {0.1, 0.2}}	{{0.1, 0.2}, {0.3, 0.4}}
P_3	{{0.3, 0.4}, {0.1, 0.2}}	{{0.4, 0.5}, {0.1, 0.2}}	{{0.3, 0.4}, {0.4, 0.5}}	{{0.6, 0.7}, {0.1, 0.2}}
P_4	{{0.7, 0.8}, {0.1, 0.2}}	{{0.2, 0.3, 0.4}, {0.3, 0.4}}	{{0.2, 0.3}, {0.3, 0.4, 0.5}}	{{0.3, 0.4}, {0.2, 0.3}}
P_5	{{0.5, 0.6}, {0.2, 0.3}}	{{0.4, 0.5, 0.6}, {0.1, 0.2, 0.3}}	{{0.1, 0.2, 0.3}, {0.1, 0.2}}	{{0.6, 0.7}, {0.2, 0.3}}

Maximize the objective function $w_1 - 0.2w_2 - 0.3w_3 - w_4$ subject to the constraints $w_j > 0$, where $j = 1, 2, 3, 4$ and $\sum_{j=1}^4 w_j = 1$:

$$\begin{aligned}
 w_1 - w_2 - 0.2w_3 - w_4 &\leq 0.4, \\
 0.2w_1 + w_3 - 0.4w_4 &\leq 0.2, \\
 -0.2w_1 + w_2 + w_4 &\leq 0.1, \\
 0.2 \leq w_1 &\leq 0.4, \\
 0 \leq w_2 &\leq 0.5, \\
 0.2 \leq w_3 &\leq 0.6, \\
 0.1 \leq w_4 &\leq 0.7.
 \end{aligned} \tag{27}$$

We implemented the MCDM approach described in Section 4 to get the preference order of the alternatives to select the best alternative.

Step 1: the information given by the DM is illustrated in Table 1 by a DHFM \mathcal{D}

Step 2: a normalized dual hesitant fuzzy decision matrix, $\tilde{\mathcal{D}}$, is shown in Table 2

Step 3: the optimal solution P^* is obtained from the NDHFM $\tilde{\mathcal{D}}$ as $P^* = \{0.5000, 0.7000, 0.8000\}, \{0.1000, 0.1500, 0.2000\}$

Step 4: we obtained the weights of the criteria by using the LP model on the objective function under the given constraints provided by the DM in equation (27) as $w_1 = 0.2333, w_2 = 0.1000, w_3 = 0.3000,$ and $w_4 = 0.3667$

Step 5: based on equations (11) and (12), calculate the weighted vector similarity measures amongst the alternative $P_i (i = 1, 2, \dots, 5)$ and the optimal alternative P^*

From Table 3, we obtain P_3 is the best choice by utilizing the Jaccard and Dice similarity measures. However, we have another ranking order by using Cosine similarity measure presented in Zhang et al. [29], which shows that the alternative P_3 is the best alternative. The preference arrangements may be distinct according to distinct measures because each algorithm emphasizes on different points of interpretation.

Example 2. A newly established mobile phone firm wants to launch a smart phone. In order to defeat the global market, we must choose the exceptional fixtures suppliers to fit its supply necessities and technology tactics. The system on chip (SoC) is

the pivot of smart phones which is the main concern of the productive growth. The firm hires the suppliers as alternatives according to their level of effort and market investigation. The alternatives can be represented as $P = \{P_1, P_2, P_3, P_4, P_5\}$ and can be evaluated under the criteria as cost (G_1), technical ability (G_2), product performance (G_3), and financial strength (G_4). Assume that all the criteria are beneficial.

Step 1: the information given by the DM is expressed in Table 4 by a DHFM \mathcal{D} .

Step 2: a normalized dual hesitant fuzzy decision matrix (NDHFM), $\tilde{\mathcal{D}}$, is shown in Table 5.

Step 3: the optimal solution P^* is obtained from the NDHFM $\tilde{\mathcal{D}}$ as $P^* = \{0.7000, 0.7500, 0.8000\}, \{0.1000, 0.1500, 0.2000\}$.

Step 4: same weights are used as calculated for Example 1.

Step 5: based on equations (11) and (12), calculate the weighted vector similarity measures amongst the alternative $P_i (i = 1, 2, \dots, 5)$ and the optimal alternative P^* . Table 6 shows the decision outcomes by applying Jaccard and Dice weighted similarity measures.

Table 6 shows that the two preferences' order of the alternatives are same, and we get P_2 as a best choice by using the Jaccard and Dice similarity measures which coincides with another ranking order obtained by using Cosine similarity measure given in Zhang et al. [29].

The above examples clearly indicate that the proposed decision-making model is simple and effective under dual hesitant fuzzy environments and the true need of new types of models based on the vector similarity measures of DHFSs for dealing with dual hesitant fuzzy MCDM problems. The graphical representation of the preference order of the alternatives achieved by the proposed model and the method used by Zhang et al. [29] are shown in Figures 1 and 2.

6. Comparative Analysis

In order to demonstrate merit and the strength of the proposed modified Jaccard and Dice similarity measures for the selection of investment company and supplier of smart phone accessories, we now apply the already presented Cosine similarity measure by Zhang et al. [29] under the DHFSs situations for the comparison analysis. In Example 1, the results of Table 3 indicate that the alternatives selected by using the Jaccard and Dice similarity measures are the same, that is, P_5 is the best alternative, but on the contrary, P_3 is

TABLE 2: The normalized dual hesitant fuzzy decision matrix $\tilde{\mathcal{D}}$.

	G_1	G_2	G_3	G_4
P_1	{{0.1, 0.2, 0.3}, {0.6, 0.65, 0.7}}	{{0.5, 0.6, 0.7}, {0.1, 0.15, 0.2}}	{{0.3, 0.4, 0.5}, {0.1, 0.15, 0.2}}	{{0.1, 0.2, 0.3}, {0.4, 0.45, 0.5}}
P_2	{{0.4, 0.5, 0.6}, {0.1, 0.15, 0.2}}	{{0.6, 0.65, 0.7}, {0.1, 0.15, 0.2}}	{{0.6, 0.65, 0.7}, {0.1, 0.15, 0.2}}	{{0.1, 0.15, 0.2}, {0.3, 0.35, 0.4}}
P_3	{{0.3, 0.35, 0.4}, {0.1, 0.15, 0.2}}	{{0.4, 0.45, 0.5}, {0.1, 0.15, 0.2}}	{{0.3, 0.35, 0.4}, {0.4, 0.45, 0.5}}	{{0.6, 0.65, 0.7}, {0.1, 0.15, 0.2}}
P_4	{{0.7, 0.75, 0.8}, {0.1, 0.15, 0.2}}	{{0.2, 0.3, 0.4}, {0.3, 0.35, 0.4}}	{{0.2, 0.25, 0.3}, {0.3, 0.4, 0.5}}	{{0.3, 0.35, 0.4}, {0.2, .25, 0.3}}
P_5	{{0.5, 0.55, 0.6}, {0.2, 0.25, 0.3}}	{{0.4, 0.5, 0.6}, {0.1, 0.2, 0.3}}	{{0.1, 0.2, 0.3}, {0.1, 0.15, 0.2}}	{{0.6, 0.65, 0.7}, {0.2, .25, 0.3}}

TABLE 3: Decision results obtained by Jaccard, Dice, and Cosine similarity measures.

	$J_s^w (\mathcal{P}_i, \mathcal{P}^*)$	$D_s^w (\mathcal{P}_i, \mathcal{P}^*)$	$C_s^w (\mathcal{P}_i, \mathcal{P}^*)$ Zhang et al. [29]
P_1	0.3921	0.7353	0.3430
P_2	0.4658	0.8442	0.4122
P_3	0.4920	0.8939	0.4796
P_4	0.4391	0.7976	0.4146
P_5	0.4965	0.8947	0.4661
Preference order	$P_5 > P_3 > P_2 > P_4 > P_1$	$P_5 > P_3 > P_2 > P_4 > P_1$	$P_3 > P_5 > P_4 > P_2 > P_1$

TABLE 4: Dual hesitant fuzzy decision matrix \mathcal{D} .

	G_1	G_2	G_3	G_4
P_1	{{0.5, 0.6}, {0.1, 0.2}}	{{0.7, 0.8}, {0.1, 0.2}}	{{0.6, 0.7}, {0.1, 0.2}}	{{0.3, 0.4}, {0.3, 0.4}}
P_2	{{0.4, 0.5, 0.6}, {0.1, 0.2, 0.3}}	{{0.5, 0.6}, {0.3, 0.4}}	{{0.6, 0.7}, {0.1, 0.2}}	{{0.6, 0.7}, {0.2, 0.3}}
P_3	{{0.1, 0.2, 0.3}, {0.3, 0.4, 0.5}}	{{0.5, 0.6}, {0.2, 0.3}}	{{0.4, 0.5}, {0.1, 0.2}}	{{0.6, 0.7}, {0.1, 0.2}}
P_4	{{0.2, 0.3}, {0.1, 0.2}}	{{0.6, 0.7, 0.8}, {0.1, 0.2}}	{{0.1, 0.2}, {0.3, 0.4}}	{{0.6, 0.7}, {0.2, 0.3}}
P_5	{{0.6, 0.7}, {0.1, 0.2}}	{{0.2, 0.3}, {0.4, 0.5, 0.6}}	{{0.3, 0.4}, {0.1, 0.2}}	{{0.3, 0.4}, {0.4, 0.5}}

TABLE 5: The normalized Dual hesitant fuzzy decision matrix $\tilde{\mathcal{D}}$.

	G_1	G_2	G_3	G_4
P_1	{{0.5, 0.55, 0.6}, {0.1, 0.15, 0.2}}	{{0.7, 0.75, 0.8}, {0.7, 0.75, 0.8}}	{{0.6, 0.65, 0.7}, {0.1, 0.15, 0.2}}	{{0.3, 0.35, 0.4}, {0.3, 0.35, 0.4}}
P_2	{{0.4, 0.5, 0.6}, {0.1, 0.2, 0.3}}	{{0.5, 0.55, 0.6}, {0.3, 0.35, 0.4}}	{{0.6, 0.65, 0.7}, {0.1, 0.15, 0.2}}	{{0.6, 0.65, 0.7}, {0.2, 0.25, 0.3}}
P_3	{{0.1, 0.2, 0.3}, {0.3, 0.4, 0.5}}	{{0.5, 0.55, 0.6}, {0.2, 0.25, 0.3}}	{{0.4, 0.45, 0.5}, {0.1, 0.15, 0.2}}	{{0.6, 0.65, 0.7}, {0.1, 0.15, 0.2}}
P_4	{{0.2, 0.25, 0.3}, {0.1, 0.15, 0.2}}	{{0.6, 0.7, 0.8}, {0.1, 0.15, 0.2}}	{{0.1, 0.15, 0.2}, {0.3, 0.35, 0.4}}	{{0.6, 0.65, 0.7}, {0.2, 0.25, 0.3}}
P_5	{{0.6, 0.65, 0.7}, {0.1, 0.15, 0.2}}	{{0.2, 0.25, 0.3}, {0.4, 0.5, 0.6}}	{{0.3, 0.35, 0.4}, {0.1, 0.15, 0.2}}	{{0.3, 0.35, 0.4}, {0.4, 0.45, 0.5}}

TABLE 6: Decision results obtained by Jaccard, Dice, and Cosine similarity measures.

	$J_s^w (\mathcal{P}_i, \mathcal{P}^*)$	$D_s^w (\mathcal{P}_i, \mathcal{P}^*)$	$C_s^w (\mathcal{P}_i, \mathcal{P}^*)$ Zhang et al. [29]
P_1	0.5108	0.9010	0.4432
P_2	0.5439	0.9541	0.4973
P_3	0.4949	0.8943	0.4602
P_4	0.4484	0.8079	0.4103
P_5	0.4534	0.8345	0.4205
Preference order	$P_2 > P_1 > P_3 > P_5 > P_4$	$P_2 > P_1 > P_3 > P_4 > P_5$	$P_2 > P_3 > P_1 > P_5 > P_4$

selected with the help of Cosine similarity measure. In Example 2, Table 6 shows that the alternative P_2 is the best choice obtained by applying the three similarity measures (Jaccard, Dice, and Cosine similarity measures) under the framework of DHFSs. According to the rule of the maximum level of similarity, that is, the similarity increases if the value of the similarity measures approaches to one and become

perfectly similar if the value of the similarity measure become one. From Tables 3 and 6, we can see that value of Jaccard and Dice similarity measures are much greater than Cosine similarity measure. Hence, we can say that our modified Jaccard and Dice similarity measures are more realistic than Cosine similarity measure under the environment of DHFSs.

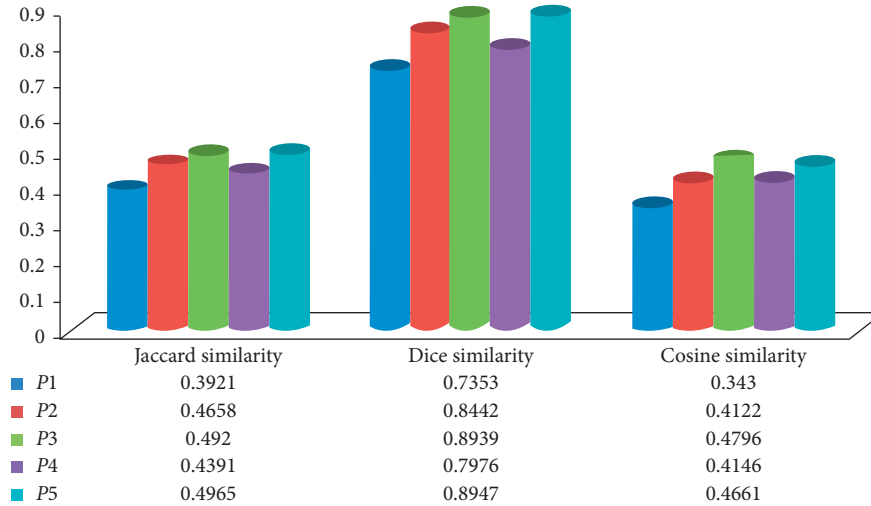


FIGURE 1: Ranking order of alternatives.

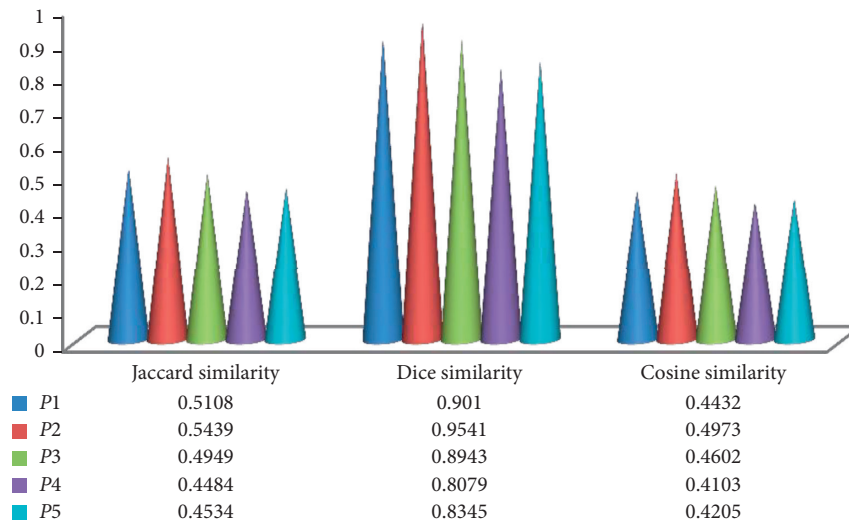


FIGURE 2: Ranking order of alternatives.

7. Conclusions

Jaccard and Dice similarity measures are easy to compute, and LP technique is also user friendly and responds quickly through Matlab. So far, the Jaccard and Dice similarity measures have not been considered under the framework of DHFSs. In the present work, we established the Jaccard and Dice similarity measures between two DHFSs. Most of the DMs assigned the weights to the criteria which are partially or completely known. However, in the present work, we used an objective function which is maximized under the given constraints and then applied the LP technique to find the weights of the criteria. Based on the Jaccard and Dice weighted similarity measures defined in Section 3, we propose an MCDM model to choose the best alternative under the influence of various criteria. Lastly, two practical examples of the constructed model are given to choose the investment company and for the selection of smart phone accessories. Then, we compared the results obtained by using the proposed model and the Cosine

similarity measure presented by Zhang et al. [29]. The decision outcomes illustrate that the Jaccard and Dice similarity measures are more reliable than the Cosine similarity measure because both (Jaccard and Dice) have the same option in the similarity identification and follow the rule of level of maximum similarity. Thus, the numerical examples show that the proposed model in this work is applicable and more effective. In the future research direction, the modified Jaccard and Dice similarity measures will be extended to the picture fuzzy sets, and it can be applied in other related decision-making problem.

Data Availability

No data were used to support the findings of the study.

Conflicts of Interest

The authors declare no conflicts of interest.

Acknowledgments

The first author was partially supported by the Ministerio de Ciencia, Innovación y Universidades under Grant no. PGC2018-097198-B-I00 and Fundación Seneca de la Región de Murcia under Grant no. 20783/PI/18.

References

- [1] T. Li, L. Qiao, and Y. Ding, "Factors influencing the cooperative relationship between enterprises in the supply chain of China's marine engineering equipment manufacturing industry—an study based on GRNN-DEMATEL method," *Applied Mathematics and Nonlinear Sciences*, vol. 5, no. 1, pp. 121–138, 2020.
- [2] L. Li, Y. Wang, and X. Li, "Tourists forecast Lanzhou based on the Baolan high-speed railway by the Arima model," *Applied Mathematics and Nonlinear Sciences*, vol. 5, no. 1, pp. 55–60, 2020.
- [3] L. A. Zadeh, "Fuzzy sets," *Information and Control*, vol. 8, no. 3, pp. 338–353, 1965.
- [4] H. G. Çitil, "Investigation of a fuzzy problem by the fuzzy Laplace transform," *Applied Mathematics and Nonlinear Sciences*, vol. 4, no. 2, pp. 407–416, 2019.
- [5] K. T. Atanassov, "Intuitionistic fuzzy sets," *Fuzzy Sets and Systems*, vol. 20, no. 1, pp. 87–96, 1986.
- [6] V. Torra, "Hesitant fuzzy sets," *International Journal of Intelligent Systems*, vol. 25, pp. 529–539, 2010.
- [7] M. Hu, J. Lan, and Z. Wang, "A distance measure, similarity measure and possibility degree for hesitant interval-valued fuzzy sets," *Computers & Industrial Engineering*, vol. 137, p. 106088, 2019.
- [8] H. B. Liu, Y. Liu, and L. Xu, "Dombi interval-valued hesitant fuzzy aggregation operators for information security risk assessment," *Mathematical Problems in Engineering*, vol. 2020, Article ID 3198645, 15 pages, 2020.
- [9] M. Zhang, T. Zheng, W. Zheng, and L. Zhou, "Interval-valued pythagorean hesitant fuzzy set and its application to multi-attribute group decision-making," *Complexity*, vol. 2020, Article ID 1724943, 26 pages, 2020.
- [10] B. Zhu, Z. Xu, and M. Xia, "Dual hesitant fuzzy sets," *Journal of Applied Mathematics*, vol. 2012, Article ID 879629, 13 pages, 2012.
- [11] M. Xia and Z. Xu, "Hesitant fuzzy information aggregation in decision making," *International Journal of Approximate Reasoning*, vol. 52, no. 3, pp. 395–407, 2011.
- [12] B. Zhu and Z. Xu, "Some results for dual hesitant fuzzy sets," *Journal of Intelligent & Fuzzy Systems*, vol. 26, no. 4, pp. 1657–1668, 2014.
- [13] J. Chen and X. Huang, "Dual hesitant fuzzy probability," *Symmetry*, vol. 9, no. 4, p. 52, 2017.
- [14] Z. Ren, Z. Xu, and H. Wang, "Dual hesitant fuzzy VIKOR method for multi-criteria group decision making based on fuzzy measure and new comparison method," *Information Sciences*, vol. 388–389, pp. 1–16, 2017.
- [15] X. J. Huang, J. J. Chen, and J. Tang, "Distance measures for higher order dual hesitant fuzzy sets," *Computational and Applied Mathematics*, vol. 37, no. 2, pp. 1784–1806, 2017.
- [16] Z. Su, Z. Xu, H. Liu, and S. Liu, "Distance and similarity measures for dual hesitant fuzzy sets and their applications in pattern recognition," *Journal of Intelligent & Fuzzy Systems*, vol. 29, no. 2, pp. 731–745, 2015.
- [17] S. K. Tyagi, "Correlation coefficient of dual hesitant fuzzy sets and its applications," *Applied Mathematical Modelling*, vol. 39, no. 22, pp. 7082–7092, 2015.
- [18] J. Ye, "Correlation coefficient of dual hesitant fuzzy sets and its application to multiple attribute decision making," *Applied Mathematical Modelling*, vol. 38, no. 2, pp. 659–666, 2014.
- [19] N. Zhao and Z. S. Xu, "Entropy measures for dual hesitant fuzzy information," in *Proceedings of the 2015 Fifth International Conference on Communication Systems and Network Technologies*, pp. 1152–1156, Gwalior, India, April 2015.
- [20] R. N. Jamil and T. Rashid, "Application of dual hesitant fuzzy geometric bonferroni mean operators in deciding an energy policy for the society," *Mathematical Problems in Engineering*, vol. 2018, Article ID 4541982, 14 pages, 2018.
- [21] H. Garg and G. Kaur, "Quantifying gesture information in brain hemorrhage patients using probabilistic dual hesitant fuzzy sets with unknown probability information," *Computers & Industrial Engineering*, vol. 140, p. 106211, 2020.
- [22] K. Gong and C. Chen, "Multiple-attribute decision making based on equivalence consistency under probabilistic linguistic dual hesitant fuzzy environment," *Engineering Applications of Artificial Intelligence*, vol. 85, pp. 393–401, 2019.
- [23] B. Li, Y. Yang, J. Su, N. Zhang, and S. Wang, "Two-sided matching model for complex product manufacturing tasks based on dual hesitant fuzzy preference information," *Knowledge-Based Systems*, vol. 186, p. 104989, 2019.
- [24] I. Beg and S. Ashraf, "Similarity measures for fuzzy sets," *Applied and Computational Mathematics*, vol. 8, no. 2, pp. 192–202, 2009.
- [25] J. Ye, "Cosine similarity measures for intuitionistic fuzzy sets and their applications," *Mathematical and Computer Modelling*, vol. 53, no. 1–2, pp. 91–97, 2011.
- [26] P. Intarapaiboon, "New similarity measures for intuitionistic fuzzy sets," *Applied Mathematical Sciences*, vol. 8, no. 45, pp. 2239–2250, 2014.
- [27] Y. Song and J. Hu, "Vector similarity measures of hesitant fuzzy linguistic term sets and their applications," *PLoS One*, vol. 12, no. 12, Article ID e0189579, 2017.
- [28] Y. Zang, X. Zhao, and S. Li, "Interval-valued dual hesitant fuzzy Heronian mean aggregation operators and their application to multi-attribute decision making," *International Journal of Computational Intelligence and Applications*, vol. 17, no. 1, Article ID 1850005, 2018.
- [29] Y. Zhang, L. Wang, X. Yu, and C. Yao, "A new concept of cosine similarity measures based on dual hesitant fuzzy sets and its possible applications," *Cluster Computing*, vol. 22, no. 6, pp. 15483–15492, 2018.
- [30] Q. Jiang, X. Jin, S.-J. Lee, and S. Yao, "A new similarity/distance measure between intuitionistic fuzzy sets based on the transformed isosceles triangles and its applications to pattern recognition," *Expert Systems with Applications*, vol. 116, pp. 439–453, 2019.
- [31] S.-M. Chen and D. Barman, "Adaptive weighted fuzzy interpolative reasoning based on representative values and similarity measures of interval type-2 fuzzy sets," *Information Sciences*, vol. 478, pp. 167–185, 2019.
- [32] S.-H. Cheng, S.-M. Chen, and C.-L. Chen, "Adaptive fuzzy interpolation based on ranking values of polygonal fuzzy sets and similarity measures between polygonal fuzzy sets," *Information Sciences*, vol. 342, pp. 176–190, 2016.
- [33] S.-M. Chen and D. Barman, "Adaptive fuzzy interpolative reasoning based on similarity measures of polygonal fuzzy sets and novel move and transformation techniques," *Information Sciences*, vol. 489, pp. 303–315, 2019.
- [34] R. J. Vanderbei, *Linear Programming: Foundations and Extensions*, Springer-Verlag, Berlin, Germany, 2014.
- [35] C. Wang and S. Chen, "A new multiple attribute decision making method based on linear programming methodology

- and novel score function and novel accuracy function of interval-valued intuitionistic fuzzy values,” *Information Sciences*, vol. 429, no. C, pp. 421–432, 2018.
- [36] P. He, T. S. Ng, and B. Su, “Energy economic recovery resilience with input-output linear programming models,” *Energy Economics*, vol. 68, pp. 177–191, 2017.
- [37] C.-Y. Wang and S.-M. Chen, “Multiple attribute decision making based on interval-valued intuitionistic fuzzy sets, linear programming methodology, and the extended TOPSIS method,” *Information Sciences*, vol. 397–398, pp. 155–167, 2017.
- [38] N. M. Lanbaran, E. Celik, and M. Yiğider, “Evaluation of investment opportunities with interval-valued fuzzy TOPSIS method,” *Applied Mathematics and Nonlinear Sciences*, vol. 5, no. 1, pp. 461–474, 2020.
- [39] R. R. Aliyev, “Interval linear programming based decision making on market allocations,” *Procedia Computer Science*, vol. 120, pp. 47–52, 2017.
- [40] M. S. Sindhu, T. Rashid, A. Kashif, and J. L. Guirao, “Multiple criteria decision making based on probabilistic interval-valued hesitant fuzzy sets by using LP methodology,” *Discrete Dynamics in Nature and Society*, vol. 2019, Article ID 1527612, 12 pages, 2019.
- [41] M. S. Sindhu, T. Rashid, and A. Kashif, “Modeling of linear programming and extended TOPSIS in decision making problem under the framework of picture fuzzy sets,” *PLoS One*, vol. 14, no. 8, Article ID e0220957, 2019.
- [42] T. Rashid and M. S. Sindhu, “Application of linear programming model in multiple criteria decision making under the framework of interval-valued hesitant fuzzy sets,” in *Proceedings of the International Conference on Intelligent and Fuzzy Systems*, pp. 282–290, Istanbul, Turkey, July 2020.
- [43] Z. Xu and X. Zhang, “Hesitant fuzzy multi-attribute decision making based on TOPSIS with incomplete weight information,” *Knowledge-Based Systems*, vol. 52, pp. 53–64, 2013.
- [44] L. R. Dice, “Measures of the amount of ecologic association between species,” *Ecology*, vol. 26, no. 3, pp. 297–302, 1945.
- [45] P. Jaccard, “Distribution de la flore alpine dans le bassin des drouces et dans quelques regions voisines,” *Bulletin de la Societe Vaudoise des Sciences Naturelles*, vol. 37, no. 140, pp. 241–272, 1901.

Research Article

Some Properties of Double Roman Domination

Hong Yang  and Xiaoqing Zhou

School of Information Science and Engineering, Chengdu University, Chengdu 610106, China

Correspondence should be addressed to Hong Yang; yanghong01@cdu.edu.cn

Received 22 May 2020; Accepted 18 July 2020; Published 14 August 2020

Academic Editor: Juan L. G. Guirao

Copyright © 2020 Hong Yang and Xiaoqing Zhou. This is an open access article distributed under the Creative Commons Attribution License, which permits unrestricted use, distribution, and reproduction in any medium, provided the original work is properly cited.

A *double Roman dominating function* on a graph G is a function $f: V(G) \rightarrow \{0, 1, 2, 3\}$ satisfying the conditions that every vertex u for which $f(u) = 0$ is adjacent to at least one vertex v for which $f(v) = 3$ or two vertices v_1 and v_2 for which $f(v_1) = f(v_2) = 2$ and every vertex u for which $f(u) = 1$ is adjacent to at least one vertex v for which $f(v) \geq 2$. The weight of a double Roman dominating function f is the value $w(f) = \sum_{u \in V(G)} f(u)$. The minimum weight of a double Roman dominating function on a graph G is called the *double Roman domination number* $\gamma_{dR}(G)$ of G . A graph with $\gamma_{dR}(G) = 3c(G)$ is called a *double Roman graph*. In this paper, we study properties of double Roman domination in graphs. Moreover, we find a class of double Roman graphs and give characterizations of trees with $\gamma_{dR}(T) = c_R(T) + k$ for $k = 1, 2$.

1. Introduction

In this paper, we shall only consider graphs without multiple edges or loops. Let G be a graph, $v \in V(G)$, and the *neighborhood* of v in G is denoted by $N(v)$. That is to say, $N(v) = \{u \mid uv \in E(G), u \in V(G)\}$. The closed neighborhood $N[v]$ of v in G is defined as $N[v] = \{v\} \cup N(v)$. The complementary graph of G is denoted by \overline{G} . A vertex of degree one is called a *leaf*. A graph is *trivial* if it has a single vertex. The degree of a vertex v is denoted by $d(v)$, i.e., $d(v) = |N(v)|$. Denote by K_n , P_n , and C_n the complete graph, path, and cycle on n vertices, respectively. The maximum degree and the minimum degree of a graph are denoted by $\Delta(G)$ and $\delta(G)$, respectively. For a set $S \subseteq V(G)$, the graph induced by S is denoted by $G[S]$. Let $e \in E(G)$, and we denote by G/e the graph obtained from G by contracting the edge e . For an edge $e \in E(G)$, we denote by $G - e$ the graph obtained from G by deleting e .

A subset D of the vertex set of a graph G is a *dominating set* if every vertex not in D has at least one neighbour in D . The domination number $\gamma(G)$ is the minimum cardinality of a dominating set of G .

The domination and its variations of graphs have attracted considerable attention [1, 2]. Many varieties of dominating sets are listed in the book *Fundamentals of Domination in Graphs* [3]. However, Roman domination

and double Roman domination are not listed in this book. Roman domination and double Roman domination appear to be a new variety of interest [4–11].

A Roman dominating function (RDF) of a graph G is a function $f: V(G) \rightarrow \{0, 1, 2\}$ such that every vertex u for which $f(u) = 0$ is adjacent to at least one vertex v for which $f(v) = 2$. The weight $w(f)$ of a Roman dominating function f is the value $w(f) = \sum_{u \in V(G)} f(u)$. The minimum weight of a Roman dominating function on a graph G is called the *Roman domination number* $\gamma_R(G)$ of G . An RDF f of G with $w(f) = \gamma_R(G)$ is called a $\gamma_R(G)$ function.

A *double Roman dominating function* (DRDF) on a graph G is a function $f: V(G) \rightarrow \{0, 1, 2, 3\}$ satisfying the condition that every vertex u for which $f(u) = 0$ is adjacent to at least one vertex v for which $f(v) = 3$ or two vertices v_1 and v_2 for which $f(v_1) = f(v_2) = 2$ and every vertex u for which $f(u) = 1$ is adjacent to at least one vertex v for which $f(v) \geq 2$. The weight $w(f)$ of a double Roman dominating function f is the value $w(f) = \sum_{u \in V(G)} f(u)$. The minimum weight of a double Roman dominating function on a graph G is called the *double Roman domination number* $\gamma_{dR}(G)$ of G . A DRDF f of G with $w(f) = \gamma_{dR}(G)$ is called a $\gamma_{dR}(G)$ function. We denote by $w_S(f)$ the weight of a double Roman dominating function f in $S \subseteq V(G)$, i.e., $w_S(f) = \sum_{x \in S} f(x)$.

Beeler et al. [12] initiated the study of the double Roman domination in graphs. They showed that $2\gamma(G) \leq \gamma_{dR}(G) \leq 3\gamma(G)$ and defined a graph G to be double Roman if $\gamma_{dR}(G) = 3\gamma(G)$. Moreover, they suggest to find double Roman graphs.

In this paper, we study properties of double Roman domination in graphs and show that the double Roman domination problem is NP-complete for bipartite graphs. Moreover, we find a class of double Roman graphs and give characterizations of trees with $\gamma_{dR}(T) = \gamma_R(T) + k$ for $k = 1, 2$.

2. Properties of Double Roman Domination

Proposition 1 (see [12]). *In a double Roman dominating function of weight $\gamma_{dR}(G)$, no vertex needs to be assigned the value 1.*

By Proposition 1, when we consider a $\gamma_{dR}(G)$ function, we assume no vertex has been assigned the value 1.

Proposition 2 (see [12])

- (i) *Let G be a graph and $f = (V_0, V_1, V_2)$ be a $\gamma_R(G)$ function. Then, $\gamma_{dR}(G) \leq 2|V_1| + 3|V_2|$.*
- (ii) *For any graph G , $\gamma_{dR}(G) \leq 2\gamma_R(G)$ with equality if and only if $G = \overline{K}_n$.*

Proposition 3 (see [12])

- (i) *For every graph G , $\gamma_R(G) < \gamma_{dR}(G)$.*
- (ii) *If $f = (V_0, \emptyset, V_2, V_3)$ is any $\gamma_{dR}(G)$ function, then $\gamma_R(G) \leq 2(|V_2| + |V_3|) = \gamma_{dR}(G) - |V_3|$.*

The following result is immediate.

Proposition 4. *For any graph G , $\gamma_{dR}(G) \geq (3|V(G)|)/(\Delta(G) + 1)$.*

Proof. The desired inequality obviously holds if $\Delta(G) \leq 1$. In order to prove the proposition for $\Delta(G) \geq 2$, we introduce the discharging approach. Let $f = (V_0, \emptyset, V_2, V_3)$ be a $\gamma_{dR}(G)$ function. The initial charge of every vertex $v \in V(G)$ is set to be $s(v) = f(v)$. We apply the discharging procedure defined by applying the following rule.

For each vertex $v \in V_3$, we send $3/(d(v) + 1)$ charge to each adjacent vertex in V_0 . Then, the final charge of v is satisfying with $s(v) = (3/(d(v) + 1)) \geq (3/(\Delta(G) + 1))$.

For each vertex $v \in V_2$, we send $(2/(d(v) + 1)) - (3/(d(v)(\Delta(G) + 1))) = ((2\Delta(G) - 1)/(d(v)(\Delta(G) + 1))) \geq ((2\Delta(G) - 1)/(\Delta(G)(\Delta(G) + 1)))$ charge to each adjacent vertex in V_0 . Then, the final charge of v is satisfying with $s(v) = (3/(d(v) + 1)) \geq (3/(\Delta(G) + 1))$.

For each vertex $v \in V_0$, by the definition of double Roman domination, v has a neighbor assigned 3 or two vertices u_1 and u_2 assigned 2. Due to the discharging rule above, if v has a neighbor u assigned 3, v receives charge from u . We have $s(v) \geq (3/(\Delta(G) + 1))$.

If v has two vertices u_1 and u_2 assigned 2, v receives charge from u_1 and u_2 . We have $s(v) \geq ((4\Delta(G) - 2)/(\Delta(G)(\Delta(G) + 1))) \geq (3/(\Delta(G) + 1))$. Thus, $\gamma_{dR}(G) = \sum_{v \in V(G)} f(v) = \sum_{v \in V(G)} s(v) \geq ((3|V(G)|)/(\Delta(G) + 1))$. The proof is complete. \square

Proposition 5. *Let G be a graph. If $\gamma_R(G) + 1 = \gamma_{dR}(G)$ and $f = (V_0, \emptyset, V_2, V_3)$ is a $\gamma_{dR}(G)$ function,*

- (i) *then $|V_3| \leq 1$*
- (ii) *if $|V_3| = 1$, then $|V_2| = 0$ and there exists a vertex v with degree $|V(G)| - 1$.*

Proof

- (i) By Proposition 3, we have $\gamma_R(G) \leq \gamma_{dR}(G) - |V_3| = \gamma_R(G) + 1 - |V_3|$. So we have $|V_3| \leq 1$.
- (ii) If $|V_3| = 1$, let $V_3 = \{v\}$ and $H = G[V(G) - N[V_3]]$. We have the following claim. \square

Claim 1. H is empty.

Proof. Otherwise, any vertex in H assigned with 0 has at least two vertices assigned with 2. Let w be a vertex in H assigned with 2, we consider a function f' with $f'(w) = 1$, $f'(v) = 2$, and $f'(x) = f(x)$ for any $x \in V(G) - \{v, w\}$. Then, f' is an RDF of G with weight $\gamma_{dR}(G) - 2$. So $\gamma_R(G) \leq \gamma_{dR}(G) - 2$, a contradiction.

Since H is empty, we have v as a vertex with degree $|V(G)| - 1$. Now, we have $\gamma_{dR}(G) = 3$ and $\gamma_R(G) = 2$, and so the result holds. \square

Theorem 1. *For every graph G on n vertices without isolated vertex, $\gamma_{dR}(G) \leq 3n - (3n/(2(1 + \delta(G))))e^{1/\delta(G)}$.*

Proof. Clearly, we have $\delta(G) \geq 1$. We select a subset S of $V(G)$, where each vertex is selected with probability p independently. Let $T = V(G) - N[S]$, we consider a function $f: V(G) \rightarrow \{0, 2, 3\}$ with $f(x) = 3$ for $x \in S$, $f(x) = 2$ for $x \in T$, and $f(x) = 0$ for other vertex x . Then, f is a DRDF of G . We have $\gamma_{dR}(G) \leq 3|S| + 2|T|$. When we consider the expectation, we also have $\gamma_{dR}(G) \leq E[3|S| + 2|T|] = 3E[|S|] + 2E[|T|]$. First, it is clear that $E[|S|] = np$. For each vertex with degree $d(x)$, if neither x nor any neighbor is selected, then $x \in T$. So we have $P(x \in T) = (1 - p)^{1+d(x)}$, and thus, $E[|T|] \leq n(1 - p)^{1+\delta(G)}$. Consequently, $\gamma_{dR}(G) \leq 3np + 2n(1 - p)^{1+\delta(G)}$. Let $F(p) = 3np + 2n(1 - p)^{1+\delta(G)}$. By $F(p) = 3np - 2n(1 + \delta(G))(1 - p)^{\delta(G)} = 0$, the maximum of F is given by $F_{max} = 3n - (3n/(2(1 + \delta(G))))e^{1/\delta(G)}$ at $p = 1 - (3/(2(1 + \delta(G))))e^{1/\delta(G)} \in (0, 1)$. Thus, $\gamma_{dR}(G) \leq 3n - (3n/(2(1 + \delta(G))))e^{1/\delta(G)}$.

If G is a graph with some isolated vertices, then $\delta(G) = 0$. Let W be the set of isolated vertices of G and let $G' = G - W$. Therefore, $\delta(G') \geq 1$. Because all isolated vertices must be assigned 3, it is easy to prove that $\gamma_{dR}(G) \leq 3n - (3n'/(2(1 + \delta(G'))))e^{1/\delta(G')}$, where $n' = |V(G')|$.

Proposition 6. *If G is a connected graph of order n , then $\gamma_{dR}(G) + 1 = 2\gamma_R(G)$ if and only if there exists a vertex v of degree $n + 1 - ((\gamma_{dR}(G) + 1)/2)$ in G .*

Proof

(\Rightarrow) Let $f = (V_0, V_1, V_2)$ be a $\gamma_R(G)$ function with minimum $|V_1|$. Then, we have V_1 being independent. Together with Proposition 2, we have $\gamma_{dR}(G) \leq 2|V_1| + 3|V_2| \leq 2|V_1| + 4|V_2| = 2\gamma_R(G) = \gamma_{dR}(G) + 1$. Then, we have $|V_2| \leq 1$. If $|V_2| = 0$, we have $|V_0| = 0$, and thus $\gamma_R(G) = n = |V_1|$. Since V_1 is independent, it is impossible. If $|V_2| = 1$, we have $\gamma_{dR}(G) = 2|V_1| + 3|V_2| < 2|V_1| + 4|V_2| = 2\gamma_R(G) = \gamma_{dR}(G) + 1$. Let $V_2 = \{v\}$, $V_0 = N(v)$, and $V_1 = V(G) - V_0 - V_2$. Then, we have $\gamma_R(G) = n - 1 - d(v) + 2$ and so $d(v) = n + 1 - \gamma_R(G) = n + 1 - ((\gamma_{dR}(G) + 1)/2)$.

(\Leftarrow) By Proposition 2 (ii), we have $\gamma_{dR}(G) + 1 \leq 2\gamma_R(G)$ for a connected graph G . Assume G contains a vertex v of degree $n + 1 - (\gamma_{dR}(G) + 1)/2$ in G . Let $V_2 = \{v\}$, $V_0 = N(v)$, and $V_1 = V(G) - V_0 - V_2$. Then, $f = (V_0, V_1, V_2)$ is a $\gamma_R(G)$ function and so $\gamma_R(G) \leq |V_1| + 2|V_2| = (\gamma_{dR}(G) + 1)/2$. Hence, $\gamma_{dR}(G) + 1 \geq 2\gamma_R(G)$.

Let \mathcal{F} be the family of connected graphs G such that for any $\gamma_{dR}(G)$ function $f = (V_0, \emptyset, V_2, V_3)$, we have $|V_3| = 0$.

Proposition 7. *Let $G \in \mathcal{F}$, then*

- (i) G contains no strong support vertex
- (ii) if $f(u) = f(v) = 2$ for an edge $uv \in E(G)$, then $G - e \in \mathcal{F}$ and $G/e \in \mathcal{F}$.

Proof

- (i) Suppose v be a strong support vertex, then there exist two leaves $x, y \in N(v)$. Since $f(v) \neq 3$, we have $f(x) = f(y) = 2$. Now consider the function f' with $f'(z) = 0$ for any $z \in L(v)$, $f'(v) = 3$, and $f'(z) = f(z)$ for any $z \in V(G) \setminus L[v]$. Then, f' is a DRDF of G with fewer weight than f , a contradiction.
- (ii) If $f(u) = f(v) = 2$ for an edge $uv \in E(G)$, we have f as also a DRDF of $G - e$. So $\gamma_{dR}(G - e) \leq w(f) = \gamma_{dR}(G)$. Since for any graph G , we have $\gamma_{dR}(G - e) \geq \gamma_{dR}(G)$, so $\gamma_{dR}(G - e) = \gamma_{dR}(G)$. Suppose to the contrary that there exists a $\gamma_{dR}(G - e)$ function such that $f(v) = 3$ for a vertex $v \in V(G - e)$. Then, f is also a $\gamma_{dR}(G)$ function, contradicting with $|V_3| = 0$. For the graph G/e , the proof is similar. \square

Lemma 1. *Let G be a graph on $n \geq 4$ vertices, then $\gamma_{dR}(G) = 4$ if and only if G contains a complete bipartite graph $K_{2,n-2}$ as a subgraph and $\Delta(G) \leq n - 2$.*

Proof

(\Rightarrow) If $\gamma_{dR}(G) = 4$, then no vertex is assigned with 3 and thus we have two vertices v and w assigned with 2 and the others 0. Also, each vertex 0 must be adjacent to both v and w . Therefore, G contains a complete bipartite graph $K_{2,n-2}$ as a subgraph. Since $\gamma_{dR}(G) > 3$, we have $\Delta(G) \leq n - 2$.

(\Leftarrow) If G contains a complete bipartite graph $K_{2,n-2}$ with partitions X, Y ($|X| = 2, |Y| = n - 2$) as a subgraph and $\Delta(G) \leq n - 2$. Then, let $f(x) = 2$ for any $x \in X$ and $f(x) = 0$ for $x \in Y$. Then, f is a DRDF of G and so $\gamma_{dR}(G) \leq 4$. Since G contains no vertex with degree $|V(G)| - 1$, we have $\gamma_{dR}(G) \geq 4$.

Note that $\Delta(G) \geq n - 2$ if G contains a complete bipartite graph $K_{2,n-2}$ as a subgraph. Thus, $\Delta(G) \leq n - 2$ can be replaced with $\Delta(G) = n - 2$ in the lemma.

Theorem 2. *Let G be a graph on $n \geq 3$ vertices, then $8 \leq \gamma_{dR}(G) + \gamma_{dR}(\overline{G}) \leq 2n + 3$. Furthermore, equality holds in the upper bound if G or \overline{G} is K_n .*

Proof. If G is a graph on $n \geq 3$ vertices, we have $\gamma_{dR}(G) \geq 3$, and if $\gamma_{dR}(G) = 3$, then G has a vertex with degree $n - 1$. But its complement is neither a star nor a graph G with $\gamma_{dR}(G) = 4$ (see the graph stated in Lemma 1). So we have $\gamma_{dR}(\overline{G}) \geq 5$ and thus, $\gamma_{dR}(G) + \gamma_{dR}(\overline{G}) \geq 8$. If G is a star, then $\gamma_{dR}(\overline{G}) = 5$ and so the lower bound is attainable.

Let v be a vertex with maximum degree $\Delta(G)$; consider a function f with $f(v) = 3, f(x) = 0$ for any $x \in N(v)$, and $f(x) = 2$ for $x \in V(G) - N[v]$. Then, f is a DRDF of G and so $\gamma_{dR}(G) \leq w(f) = 2n - 2\Delta(G) + 1$. Since $\Delta(\overline{G}) + \delta(G) = n - 1$, we have $\gamma_{dR}(\overline{G}) \leq 2n - 2\Delta(\overline{G}) + 1 = 2\delta(G) + 3$. Therefore, $\gamma_{dR}(G) + \gamma_{dR}(\overline{G}) \leq 2n + 4 - 2\Delta(G) + 2\delta(G) \leq 2n + 4$. It can be seen that if $\gamma_{dR}(G) + \gamma_{dR}(\overline{G}) = 2n + 4$, then $\Delta(G) = \delta(G)$. Hence, G is k -regular for some k . By symmetry, we may assume that $k \leq (n - 1)/2$. Then, if $\gamma_{dR}(G) + \gamma_{dR}(\overline{G}) = 2n + 4$, we have $\gamma_{dR}(G) = 2n - 2k + 1$ and $\gamma_{dR}(\overline{G}) = 2k + 3$. Let $v \in V(G)$. If $|N(u) \cap N(v)| \leq k - 2$ for some $u \in V(G) - N[v]$, then $f = (N(v) \cup N(u), \emptyset, V(G) - N[u] - N[v], \{u, v\})$ is a DRDF of G with fewer weight than $2n - 2k + 1$, a contradiction. Therefore, each vertex not in $N[v]$ has at least $k - 1$ neighbors in $N(v)$. Analogously, each vertex in $N[v]$ has at most 2 neighbors outside $N[v]$. Then, we have $(k - 1)(n - k - 1) \leq 2k$. Since $k \leq (n - 1)/2$, we have $k \leq 2 + 2/(k - 1)$. If $k = 3$, then $n = 7$. This is impossible. If $k = 2$, then $n \in \{5, 6, 7\}$. If $G = C_5$, we have $\gamma_{dR}(G) = \gamma_{dR}(\overline{G}) = 6$, and so $\gamma_{dR}(G) + \gamma_{dR}(\overline{G}) \neq 2n + 4$, a contradiction. If $G = C_6$, we have $\gamma_{dR}(G) = \gamma_{dR}(\overline{G}) = 6$, and so $\gamma_{dR}(G) + \gamma_{dR}(\overline{G}) \neq 2n + 4$, a contradiction. If $G = C_7$, we have $\gamma_{dR}(G) = 8$ and $\gamma_{dR}(\overline{G}) = 6$, and so $\gamma_{dR}(G) + \gamma_{dR}(\overline{G}) \neq 2n + 4$, a contradiction. If $k = 1$, then $G = (n/2)K_2$, and we have $\gamma_{dR}(G) = 3n/2$ and $\gamma_{dR}(\overline{G}) = 4$, and so $\gamma_{dR}(G) + \gamma_{dR}(\overline{G}) \neq 2n + 4$, a contradiction. Therefore, we conclude that $8 \leq \gamma_{dR}(G) + \gamma_{dR}(\overline{G}) \leq 2n + 3$. If $G = K_n$, then $\gamma_{dR}(G) = 3$ and $\gamma_{dR}(\overline{G}) = 2n$ and thus the upper bound is attainable. \square

3. Some Double Roman Graphs

The Cartesian product of graphs G and H is the graph $G \square H$ with vertex set $G \times H$ and $(x_1, x_2)(y_1, y_2) \in E(G \square H)$ whenever $x_1 y_1 \in E(G)$ and $x_2 = y_2$, or $x_2 y_2 \in E(H)$ and $x_1 = y_1$. The Cartesian product is commutative and associative, having the trivial graph as a unit (cf. [13]).

Let f be a double Roman dominating function of $C_m \square C_n$, and we write $V_i^f = \{v \in V(C_m \square C_n) \mid f(v) = i\}$ for $i \in \{0, 1, 2, 3\}$. When no confusion arise, we simply write V_i^f as V_i . We use $f(i, j)$ to denote the value $f(v)$ for $v = (i, j) \in V(C_m \square C_n)$. Let x_i be the weight of \mathcal{C}^i , i.e., $x_i = \{\sum_{x \in \mathcal{C}^i} f(x)\}$.

Theorem 3. *Let $m, n \geq 1$. Then, the Cartesian product graphs $C_{5m} \square C_{5n}$ are double Roman.*

Proof. The lower bound follows from Proposition 4. Let $V(C_{5m} \square C_{5n}) = \{v_{ij} \mid 0 \leq i \leq 5m - 1, 0 \leq j \leq 5n - 1\}$, $V_1 = V_2 = \emptyset$, $V_3 = \{v_{(5i)(5j+2)}, v_{(5i+1)(5j)}, v_{(5i+2)(5j+3)}, v_{(5i+3)(5j+1)}, v_{(5i+4)(5j+4)}, 0 \leq i \leq m - 1, 0 \leq j \leq n - 1\}$, and $V_0 = N(V_3)$. Then, $N[V_3] = V(C_{5m} \square C_{5n})$ and so $f = (V_0, V_1, V_2, V_3)$ is a DRDF of $C_{5m} \square C_{5n}$ with weight $15mn$ and we have $\gamma_{dR}(C_{5m} \square C_{5n}) \leq 15mn$. Since $\gamma(C_{5m} \square C_{5n}) = 5mn$, we have $C_{5m} \square C_{5n}$ is double Roman. \square

4. Trees T with $\gamma_{dR}(T) = \gamma_R(T) + k$

Theorem 4. *If T is a tree, then $\gamma_R(T) + 1 = \gamma_{dR}(T)$ if and only if T is a star $K_{1,s}$ for $s \geq 1$.*

Proof

(\Leftarrow) If T is a star $K_{1,s}$ for $s \geq 1$, it is clear that $\gamma_{dR}(T) = 3$ and $\gamma_R(T) = 2$, and the theorem holds.

(\Rightarrow) By Proposition 3, we have $|V_3| \leq 1$. If $|V_3| = 1$, by Proposition 5, we have T is a star $K_{1,s}$ for some $s \geq 1$. If $|V_2| = 0$, then each vertex in T is assigned 2 or 0. Since T is a tree, T has a least two leaves v and w and $f(v) = f(w) = 2$. If v and w are adjacent to the same vertex x , then we can obtain a DRDF of T with fewer weight by changing $f(x)$ to 3 and $f(v)$ and $f(w)$ to 0 and obtaining a contradiction. If v and w are adjacent to different vertices, we consider a function f' with $f'(w) = 1$, $f'(v) = 1$, and $f'(x) = f(x)$ for any $x \in V(T) - \{v, w\}$. Then, f' is an RDF of T with weight $\gamma_{dR}(T) - 2$. So $\gamma_R(T) \leq \gamma_{dR}(T) - 2$, a contradiction.

For a positive integer t , a wounded spider is a star $K_{1,t}$ with at most $t - 1$ of its edges subdivided. In a wounded spider, a vertex of degree t will be called the head vertex, and the vertices at distance two from the head vertex will be the foot vertices. \square

Theorem 5. *If T is a tree, then $\gamma_R(T) + 2 = \gamma_{dR}(T)$ if and only if T is a wounded spider with only one foot or T is obtained by adding an edge between two stars $K_{1,s}$ and $K_{1,t}$ for $s, t \geq 2$.*

Proof

(\Leftarrow) If T is a wounded spider with only one foot, it is clear that $\gamma_{dR}(T) = 5$ and $\gamma_R(T) = 3$, and the theorem holds. If T is a tree obtained by adding an edge between two stars $K_{1,s}$ and $K_{1,t}$ for $s, t \geq 2$, then $\gamma_{dR}(T) = 6$ and $\gamma_R(T) = 4$, and the theorem holds.

(\Rightarrow) By Proposition 3, we have $|V_3| \leq 2$. If $|V_3| = 2$, let $V_3 = \{v, w\}$ and $H = G[V(G) - N[w] - N[v]]$. Similar to the proof of Theorem 5, we have H as empty. Otherwise, there exists a vertex u in H assigned with 2. Now, we change the function values of v, w, u from 3, 3, 2 to 2, 2, 1, respectively, and obtain an RDF of T with weight $\gamma_{dR}(T) - 3$, a contradiction. In this case, T is a tree obtained by adding an edge between two stars $K_{1,s}$ and $K_{1,t}$ for $s, t \geq 2$. If $|V_3| = 1$, let $V_3 = \{v\}$ and $H = G[V(G) - N[v]]$. Then, H has at most one connected component. Otherwise, we can make a vertex in each connected component to change the function values including the vertex v to obtain an RDF of T with weight $\gamma_{dR}(T) - 3$. Since H contains no vertex assigned with 3, then H is not a star with at least two leaves. We claim that the leaves of H are at most two. Otherwise, we change the function values of v and choose two leaves to obtain an RDF of T with weight $\gamma_{dR}(T) - 3$. Therefore, H is a path on at least four vertices. In this case, we can obtain an RDF of T with weight at most $\gamma_{dR}(T) - 3$, a contradiction. Therefore, T is a wounded spider with only one foot. \square

Data Availability

No data were used to support this study.

Conflicts of Interest

The authors declare that there are no conflicts of interest regarding the publication of this paper.

Acknowledgments

This work was supported by Sichuan Science and Technology Program under grant 2018ZR0265, Sichuan Military and Civilian Integration Strategy Research Center under grant JMRH-1818, and Sichuan Provincial Department of Education (Key Project) under grant 18ZA0118.

References

- [1] M. R. Garey and D. S. Johnson, *Computers and Intractability: A Guide to the Theory of NP-Completeness*, W. H. Freeman, San Francisco, CA, USA, 1979.
- [2] O. Ore, *Theory of Graphs*, American Mathematical Society, Providence, RI, USA, 1967.
- [3] T. W. Haynes, S. T. Hedetniemi, and P. J. Slater, *Fundamentals of Domination in Graphs*, Marcel Dekker, New York, NY, USA, 1998.
- [4] X. Zhang, Z. Li, H. Jiang, and Z. Shao, "Double roman domination in trees," *Information Processing Letters*, vol. 134, pp. 31–34, 2018.

- [5] E. Zhu and Z. Shao, "Extremal problems on weak roman domination number," *Information Processing Letters*, vol. 138, pp. 12–18, 2018.
- [6] Z. Shao, P. Wu, H. Jiang, Z. Li, J. Žerovnik, and X. Zhang, "Discharging approach for double roman domination in graphs," *IEEE Access*, vol. 6, pp. 63345–63351, 2018.
- [7] Z. Shao, J. Amjadi, S. M. Sheikholeslami, and M. Valinavaz, "On the total double roman domination," *IEEE Access*, vol. 7, pp. 52035–52041, 2019.
- [8] J.-B. Liu, C. Wang, S. Wang, and B. Wei, "Zagreb indices and multiplicative zagreb indices of Eulerian graphs," *Bulletin of the Malaysian Mathematical Sciences Society*, vol. 42, no. 1, pp. 67–78, 2019.
- [9] J.-B. Liu, X.-F. Pan, F.-T. Hu, and F.-F. Hu, "Asymptotic Laplacian-energy-like invariant of lattices," *Applied Mathematics and Computation*, vol. 253, pp. 205–214, 2015.
- [10] J.-B. Liu and X.-F. Pan, "Minimizing Kirchhoff index among graphs with a given vertex bipartiteness," *Applied Mathematics and Computation*, vol. 291, pp. 84–88, 2016.
- [11] H. Yang, P. Wu, S. Nazari-Moghaddam et al., "Bounds for signed double roman k -domination in trees," *RAIRO-Operations Research*, vol. 53, no. 2, pp. 627–643, 2019.
- [12] R. A. Beeler, T. W. Haynes, and S. T. Hedetniemi, "Double roman domination," *Discrete Applied Mathematics*, vol. 211, pp. 23–29, 2016.
- [13] R. Hammack, W. Imrich, and S. Klavžar, *Handbook of Product Graphs*, CRC Press, Boca Raton, FL, USA, Second edition, 2011.

Retraction

Retracted: Analysis of the Impact of Climate Change on National Vulnerability Based on Fuzzy Comprehensive Evaluation

Discrete Dynamics in Nature and Society

Received 15 August 2023; Accepted 15 August 2023; Published 16 August 2023

Copyright © 2023 Discrete Dynamics in Nature and Society. This is an open access article distributed under the Creative Commons Attribution License, which permits unrestricted use, distribution, and reproduction in any medium, provided the original work is properly cited.

This article has been retracted by Hindawi following an investigation undertaken by the publisher [1]. This investigation has uncovered evidence of one or more of the following indicators of systematic manipulation of the publication process:

- (1) Discrepancies in scope
- (2) Discrepancies in the description of the research reported
- (3) Discrepancies between the availability of data and the research described
- (4) Inappropriate citations
- (5) Incoherent, meaningless and/or irrelevant content included in the article
- (6) Peer-review manipulation

The presence of these indicators undermines our confidence in the integrity of the article's content and we cannot, therefore, vouch for its reliability. Please note that this notice is intended solely to alert readers that the content of this article is unreliable. We have not investigated whether authors were aware of or involved in the systematic manipulation of the publication process.

Wiley and Hindawi regrets that the usual quality checks did not identify these issues before publication and have since put additional measures in place to safeguard research integrity.

We wish to credit our own Research Integrity and Research Publishing teams and anonymous and named external researchers and research integrity experts for contributing to this investigation.

The corresponding author, as the representative of all authors, has been given the opportunity to register their agreement or disagreement to this retraction. We have kept a record of any response received.

References

- [1] J. Zhu, Y. Chen, and S. Zhang, "Analysis of the Impact of Climate Change on National Vulnerability Based on Fuzzy Comprehensive Evaluation," *Discrete Dynamics in Nature and Society*, vol. 2020, Article ID 3527540, 10 pages, 2020.

Research Article

Analysis of the Impact of Climate Change on National Vulnerability Based on Fuzzy Comprehensive Evaluation

Jia-Ming Zhu,¹ Yang Chen,² and Su Zhang³ 

¹School of Statistics and Applied Mathematics, Anhui University of Finance and Economics, Bengbu 233030, China

²School of Finance, Anhui University of Finance and Economics, Bengbu 233030, China

³Department of Physical Education, Anhui University of Finance and Economics, Bengbu 233030, China

Correspondence should be addressed to Su Zhang; zs0625@163.com

Received 11 June 2020; Accepted 18 July 2020; Published 13 August 2020

Guest Editor: Shaohui Wang

Copyright © 2020 Jia-Ming Zhu et al. This is an open access article distributed under the Creative Commons Attribution License, which permits unrestricted use, distribution, and reproduction in any medium, provided the original work is properly cited.

Climate change has become one of the major threats to global security. On the impact of climate change on national vulnerability, the researchers firstly select relevant factors and data and analyze the principal components to determine the weight of climate change on vulnerability so as to analyze the impact of climate change on national vulnerability. Secondly, based on the influencing factors, we obtain the national vulnerability score through the fuzzy comprehensive evaluation method, delineate the impact scope according to the score, and predict climate change by means of regression analysis and time series analysis. Finally, according to the characteristics of cities and continents, the model is revised, a PSR model and a cluster analysis model are established, and the prediction accuracy is improved.

1. Introduction

Climate change is one of the most universal global threats to peace and security in the 21st century. The damage, loss, and impact caused by various natural disasters worldwide are becoming serious. The research on vulnerability, adaptability, and resilience has become the focus of attention in the fields of global change, disaster prevention and mitigation, and sustainable development. As a key element of international relations and domestic welfare, it covers all areas of security, construction, peace, and development. The impact of climate change has had a negative impact on vulnerable groups, while improving the response capacity of the government [1].

This paper argues that climate change is a “threat multiplier” which interacts with existing pressures, such as social conflict, economic inequality, mass migration, or competition for resources. Then, further countermeasures will be proposed to eliminate these problems and the instability that may arise in violent conflicts [2].

Vulnerability is used to describe the systems and components that are vulnerable to damage, lack

antijamming capabilities, and restore their structure and function. The state is a highly socioeconomically complex integrated system. It interacts with the natural environment and the social environment. According to the definition of vulnerability, national vulnerability refers to the probability of turning risk into disaster when a country's system is adversely affected by the outside world, but the system has the ability to resist and reduce risk and self-recovery.

Vulnerability manifests itself in a variety of areas [3], mainly including physical vulnerability, economic vulnerability, social vulnerability, and political vulnerability. Physical vulnerability refers to the risk of anthropogenic impacts on the climate, and other factors such as natural disasters and human-induced pollution. Economic vulnerability refers to the perception of internal and external threats to the economy. Social vulnerability refers to the potential disaster factors, the degree of damage, and the coping capacity of a social group, organization, or country exposed to disaster impact. Political vulnerability refers to the territorial integrity, core values, and internal unity which are exposed to internal and external threats.

In the study of vulnerability, early scholars mainly focus on the ecological environment and then extend their research to humanities and regional economy. This paper establishes a national vulnerability assessment model, analyzes the impact of climate change on national vulnerability, predicts the critical point of national vulnerability, and gives government intervention measures. The overall idea is shown in Figure 1.

The data in this paper come from Question E of the 2018 American College Students Mathematical Modeling Competition and the statistics of the World Bank.

2. Basic Assumptions

In order to solve the problem, we make the following assumptions:

- (i) Assuming the sovereign government can exercise its executive power during its time in office to control the factors affecting climate change.
- (ii) Assuming the selected indicator adequately reflects the country's vulnerability and does not affect the simulation below.
- (iii) Assuming that in the process of state intervention in climate change, the country will not be affected by economic and political crisis, extreme natural disasters, etc. It can achieve the desired state, when we control the variables.
- (iv) No unexpected factors affecting our assessment during the study period.

3. How to Evaluate a Country's Vulnerability and Measure the Impact of Climate Change

3.1. Analysis Approach. With the research on the impact of climate change in recent years, climate change has become one of the important factors affecting national vulnerability directly or indirectly. The main manifestations of climate change are temperature, precipitation, etc., which, on the one hand, directly affect the vulnerability through subtle changes. On the other hand, climate change is indirectly affected by glaciers and sea levels. Economical, political, and social factors, such as species of flora and fauna, food production, have further affected the vulnerability of the country [4].

In order to measure national vulnerability reasonably and to analyze the direct and indirect impact of climate change on vulnerability, we firstly create an index system for measuring national vulnerability, and then a fuzzy comprehensive evaluation model is established based on the analysis of the principal components.

3.2. Fuzzy Comprehensive Evaluation Model Based on PCA Model

3.2.1. Model Preparation. Considering the influencing factors of the state vulnerability, we should establish the hierarchical structure to evaluate the vulnerability. The

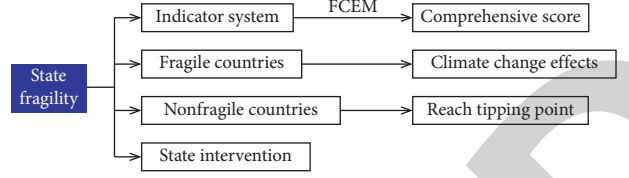


FIGURE 1: Overall thinking process.

decision-making problem is divided into three layers: target layer (T), criterion layer (C), and program layer (P), and each layer has several factors [5], as shown in Table 1.

3.2.2. Model Establishing and Solving. Suppose $U = \{u_1, u_2, \dots, u_n\}$ is a group of n countries to be evaluated, $V = \{v_1, v_2, \dots, v_m\}$ is a set of evaluation factors, and each solution in U is measured by each factor in V , and we select the observation matrix X from the observation data of 16 countries in 2015 [6]:

$$X = \begin{bmatrix} 2720 & 2990 & 6270 & \cdots & 63930 \\ 36.7 & 43.2 & 48.5 & \cdots & 21.456 \\ 3.967 & 2.31 & 1.323 & \cdots & 0.666 \\ \vdots & \vdots & \vdots & \ddots & \vdots \\ -0.738 & 0.976 & 0.075 & \cdots & 1.549 \end{bmatrix}. \quad (1)$$

In the formula, x_{ij} represents the indicator value of the j -th program on the i -th evaluation factor, and the vector $x_j = \{x_{1j}, x_{2j}, \dots, x_{mj}\}$ denotes the evaluation vector of the j -th program on the m -th evaluation indicator.

Suppose the ideal urban air quality indicator vector is u :

$$u = (u_1^0, u_2^0, \dots, u_m^0) = (63930, 21.456, 0.17, 7.357, 0.075, -0.824, 17620, -0.91, -0.738), \quad (2)$$

where

$$u_i^0 = \begin{cases} \max_{1 \leq j \leq n} \{x_{ij}\}, & \text{when } x_{ij} \text{ is a benefit index,} \\ \min_{1 \leq j \leq n} \{x_{ij}\}, & \text{when } x_{ij} \text{ is a cost index,} \\ \frac{x_{ij} - x_0}{x_0}, & \text{when } x_{ij} \text{ is a neutral index.} \end{cases} \quad (3)$$

According to the established ideal scheme, the relative deviation fuzzy matrix R is calculated by substituting the observed data from 16 countries:

$$\tilde{R} = \begin{bmatrix} r_{11} & r_{12} & \cdots & r_{131} \\ r_{21} & r_{22} & \cdots & r_{231} \\ \vdots & \vdots & \ddots & \vdots \\ r_{71} & r_{72} & \cdots & r_{731} \end{bmatrix}, \quad (4)$$

where

TABLE 1: Hierarchy table.

Level 1 indicator	Level 2 indicator	Level 3 indicator	Mark
National vulnerability	Economic factors	Per capita GNI	X_1
		Gini coefficient	X_2
	Political factors	Military expenditure as a share of GDP	X_3
		Public education expenditure as a share of GDP	X_4
	Social factors	Per capita carbon dioxide emissions	X_5
		Population growth rate	X_6
		International migrant share of total population	X_7
	Climatic factors	Temperature	X_8
		Precipitation	X_9

$$Y_{ij} = \frac{|x_{ij} - u_i^0|}{\max_{1 \leq j \leq n} \{x_{ij}\} - \min_{1 \leq j \leq n} \{x_{ij}\}}, \quad i = 1, 2, \dots, 9; j = 1, 2, \dots, 16. \tag{5}$$

So, we can get

$$\tilde{R} = \begin{bmatrix} 0.975 & 0.989 & 0.97 & \dots & 0 \\ 0.564 & 0.804 & 1 & \dots & 0 \\ 0.698 & 0.394 & 0.212 & \dots & 0.091 \\ \vdots & \vdots & \vdots & \ddots & \vdots \\ 0 & 0.175 & 0.171 & \dots & 0.48 \end{bmatrix}. \tag{6}$$

We use the principal component analysis method to calculate the weight of each evaluation indicator. When calculating, the number of principal components can be selected to make the contribution rate of cumulative variance of factors large enough (larger than 85% here) so as to protect the interpretation ability of the common factor to data [7].

As can be seen from Table 2, when the 5 principal components are selected, the cumulative variance contribution rate of the factor has reached 88.508% and meets the requirements, so the first 5 factors are selected for analysis. The column vector of the i factor in Table 3 is divided by the square root of the corresponding characteristic root, and the variation coefficient vector of principal components is obtained, which is shown in Table 4.

According to the proportion of the contribution rate of each principal component to the total contribution rate, the comprehensive coefficient of each factor is calculated and the weight vector of each evaluation index is obtained:

$$W = (-0.1214, 0.2750, 0.0798, 0.2515, -0.0911, 0.1597, 0.12, 0.272, 0.1218)^T. \tag{7}$$

Then, we establish a comprehensive evaluation model [8] as follows:

$$F_j = \sum_{i=1}^7 w_i r_{ij}. \tag{8}$$

Based on this model, the higher the comprehensive score is, the stronger the national vulnerability has. We calculated data from 16 countries, and the ranking of comprehensive score and vulnerability is shown in Table 4 and Figure 2.

TABLE 2: The principal component eigenvalues and cumulative contribution rate.

Components	Total	Rate of change	Cumulative (%)
1	3.638	40.427	40.427
2	1.889	20.991	61.418
3	0.968	10.758	72.175
4	0.834	9.264	81.440
5	0.636	7.068	88.508
6	0.464	5.156	93.664
7	0.405	4.500	98.164
8	0.097	1.074	99.238
9	0.069	0.762	100.000

TABLE 3: Comprehensive score sheet.

Country	Comprehensive score	Rank
Angola	0.7801	1
Zimbabwe	0.7527	2
Yemen	0.7209	3
Kenya	0.7156	4
Laos	0.6823	5
Malawi	0.6419	6
India	0.6040	7
Malaysia	0.5748	8
Indonesia	0.4792	9
Namibia	0.4757	10
Mongolia	0.2821	11
Azerbaijan	0.2597	12
Poland	0.2419	13
Croatia	0.1829	14
Slovenia	0.1193	15
Switzerland	0.0890	16

3.3. Result Analysis. According to the score and ranking, the score is divided into three levels, respectively, marked as follows: fragile, vulnerable, and stable, as shown in Table 5.

When a country has a combined score between 0 and 0.4 in a given year, the country is stable. When the score is between 0.4 and 0.7, the country is fragile. When score is between 0.7 and 1, it is fragile [9].

Temperature and precipitation are the main manifestations of climate and also direct factors affecting national vulnerability. When temperatures and precipitation deviate from a reasonable range, national vulnerability increases. According to principle component analysis model, it can be

TABLE 4: Principal component coefficient matrix.

Factors	Z_1	Z_2	Z_3	Z_4	Z_5
X_1	-0.4323	0.1663	0.1069	0.2852	-0.0776
X_2	0.4696	0.1602	-0.1040	0.0981	0.3115
X_3	0.1390	-0.4562	0.5560	0.1630	0.4992
X_4	0.2449	0.2840	-0.0267	0.8202	-0.1289
X_5	-0.3985	0.0760	-0.0033	0.2620	0.5745
X_6	0.4083	-0.1013	-0.0053	0.1540	-0.2289
X_7	-0.0732	0.3808	0.7851	-0.0793	-0.3003
X_8	0.4246	0.2834	0.1792	-0.2803	0.2308
X_9	-0.0469	0.6454	-0.1393	-0.1803	0.3244

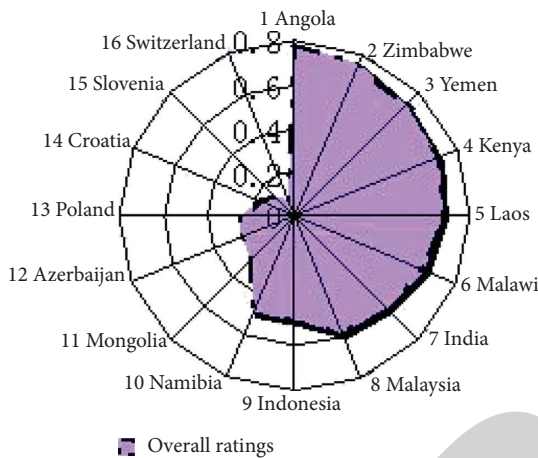


FIGURE 2: Distribution maps of comprehensive score.

TABLE 5: The rating level.

Comprehensive score	0-0.4	0.4-0.7	0.7-1
National vulnerability	Stable	Vulnerable	Fragile

found that there is a direct correlation between indicators affecting national vulnerability. As a result, temperature is also vulnerable to indirect impacts of national vulnerability, thus affecting other indicators [10].

4. Take the Top 10 Most Fragile States to Illustrate How Climate Change Has Increased Their Vulnerability

4.1. *Problem Analysis.* According to the model, the national vulnerability indicators include purchasing power index, gross national income, Gini coefficient, military expenditure, public education, carbon dioxide emissions, population growth rate, international migration, temperature, and precipitation. The weight vector is W .

From the above description, we know that climate change affects national vulnerability through changes in temperature, precipitation, and carbon dioxide emissions. In the absence of climate change, other indicators can reduce national vulnerability by changing the data to change the relative error fuzzy matrix, thereby affecting national vulnerability scores. To determine the impact of climate change

on national vulnerability, we use control variables to process data analyze the impact of the vulnerability of selected countries.

Taking Sudan as an example, we analyzed the impact of other factors on national vulnerability when the initial temperature increased or decreased by 5%, 10%, and 15%. Similarly, we take Sudan to analyze the impact of other factors on the vulnerability of the country [11].

4.2. Problem Solving

4.2.1. *The Impact of Temperature on Vulnerability.* Combined with the above problem, we get the national vulnerability score of Sudan under different temperature data, as shown in Table 6.

The relationship between national vulnerability and temperature was fitted, and the trend of national vulnerability was observed. From Table 6, we know that when the temperature deviates from the baseline temperature, as the temperature rises, the state fragility score increases, which means the state vulnerability increases.

4.2.2. *The Impact of Precipitation on Vulnerability.* The national vulnerability score of Sudan under different precipitation can be found in Table 7.

As can be seen from the result of simulation, Sudan's national vulnerability score varies with the change of precipitation. We can see from Table 7 that the score of national vulnerability increases with the increase of precipitation; that is, the national vulnerability increases [12].

4.2.3. *The Impact of Carbon Dioxide (CO₂) Emissions on Vulnerability.* The national vulnerability score of Sudan under different CO₂ emissions is shown in Table 8.

We fit national vulnerability and carbon dioxide emissions and observe the changing trends in state fragility as shown in Figure 3.

As shown in Figure 3, with the increase of CO₂ emissions, national vulnerability score increases and the national vulnerability increases. Thus, under certain conditions, the reduction of CO₂ emissions may reduce the vulnerability. Carbon dioxide emissions are largely influenced by human factors. In order to reduce the emission, the state should advocate low-carbon and environment-friendly production and life style.

5. Identify a Tipping Point and Predict When to Reach It and Become More Fragile

5.1. Problem Analysis

5.1.1. *Evaluation of Non Top Ten Fragile Countries.* We chose Mongolia, which is not one of the ten most vulnerable countries to analyze this problem. Based on the indicator data in 2015, Mongolia's vulnerability score was calculated and the range of the score was determined, thereby determining its vulnerability. By means of control variables, we dynamically analyze the changes in national vulnerability

TABLE 6: Impact of temperature on vulnerability.

Temperature changes	Drop			Raw data	Rise		
	15%	10%	5%		5%	10%	15%
Temperature	25.48	25.48	26.90	28.31	29.73	31.14	29.73
Comprehensive score	0.5085	0.5795	0.6506	0.6861	0.7216	0.7599	0.7799

TABLE 7: Impact of precipitation on vulnerability.

Precipitation changes	Decrease			Raw data	Increase		
	30%	20%	10%		10%	20%	30%
Precipitation deviation	-0.7145	-0.6003	-0.4861	-0.429	-0.3719	-0.2577	-0.1435
Comprehensive score	0.8216	0.7754	0.7392	0.6861	0.643	0.5768	0.5206

TABLE 8: Impact of CO₂ emissions on vulnerability.

CO ₂ emission changes	Decrease			Raw data	Increase		
	15%	10%	5%		5%	10%	15%
CO ₂ emissions	0.2627	0.2782	0.2936	0.3091	0.3246	0.3400	0.3555
Comprehensive score	0.5121	0.5733	0.6218	0.6861	0.7084	0.7431	0.7956

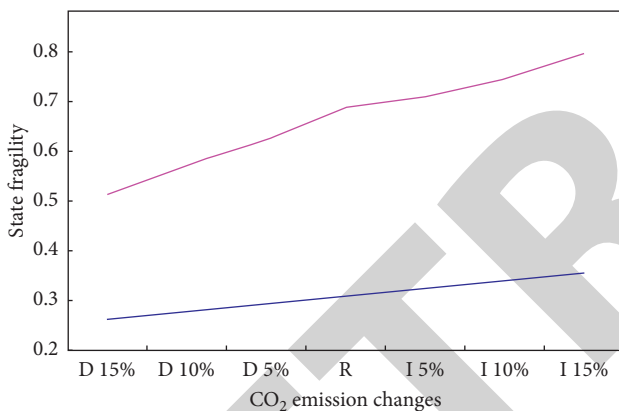


FIGURE 3: Impact of CO₂ emissions on state fragility.

under different temperature conditions and find the trend that national vulnerability scores change with temperature, so as to predict the contribution of climate change to national vulnerability [11–13].

5.1.2. Prediction about Reaching Critical Value. From the previous analysis, we know that CO₂ emissions have a significant impact on national vulnerability. With the increase of CO₂ emissions, the score of national vulnerability increase and the national vulnerability also increase. So we choose CO₂ emissions as an indicator. The comprehensive national vulnerability score of Mongolia under different CO₂ concentrations is calculated by using the control variable method, the direct functional relationship between the national vulnerability score and CO₂ emissions is obtained, and the tipping point of vulnerability is also identified. Based on the annual CO₂ emission data of the World Bank of Mongolia, we use the time series model to predict concentrations of CO₂ in the coming decades, when to reach the

tipping point of concentrations, and when to reach the international year record and become more fragile.

5.2. Problem Solving of Evaluating Non Top Ten Fragile Countries. According to the indicator system model, the national vulnerability scores of Mongolia are 0.2821 and $0 < 0.2821 < 0.4$, which can be judged that Mongolia is stable in 2015. We change the temperature indicator data to make the temperature change by 5%, 10%, and 15%, respectively, and obtain the national vulnerability score at different temperatures, as shown in Figure 4.

As can be seen from Figure 4, the national vulnerability of Mongolia also increases with the rise of temperature. In addition, we can see from the figure that, when the temperature rises from 10% to 15%, the national vulnerability score rises from 0.3829 to 0.4113; that is, Mongolia is transitioning from a stable state to a fragile state. Therefore, the Mongolian government should pay attention to the factors affecting temperature rise and strengthen climate management to prevent instability in the country.

5.3. Linear Regression Model [14]

5.3.1. Model Preparation. We fit national vulnerabilities and carbon dioxide emissions and observe the changing trends in national vulnerability, as shown in Figure 5.

5.3.2. Model Establishment. We have known that the increase in CO₂ emissions will lead to the increase in national vulnerability scores. Therefore, we establish a linear regression model between CO₂ emissions and national vulnerability scores as follows [15]:

$$Y_i = b_0 + b_1 X_i + \varepsilon_i, \quad i = 1, 2, 3, \dots, n. \quad (9)$$

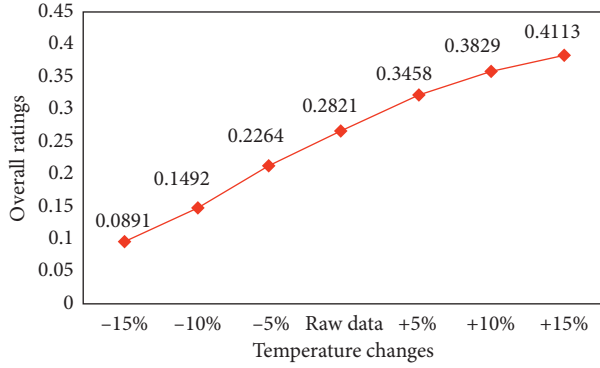


FIGURE 4: Impact of temperature on vulnerability.

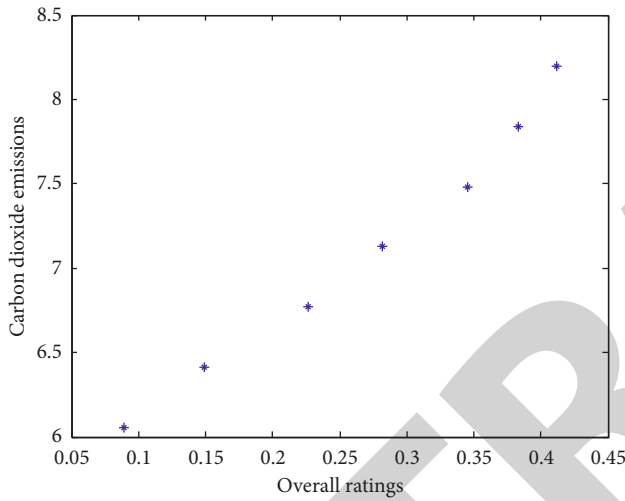


FIGURE 5: Scatter plot.

In solving the normal equations, the least squares estimators of the two parameters are obtained as follows:

$$\hat{b}_1 = \frac{SCP}{SS_X}, \quad (10)$$

$$\hat{b}_0 = \bar{Y} - \hat{b}_1 \bar{X},$$

where

$$\begin{aligned} SCP &= \sum_{i=1}^n X_i Y_i = n \bar{X} \bar{Y}, \\ SS_X &= \sum_{i=1}^n X_i^2 - n \bar{X}^2. \end{aligned} \quad (11)$$

5.3.3. Model Solving and Result Analysis. With the help of MATBLE regression, we obtain the regression model of CO₂ emissions and national vulnerability score as follows:

$$y = 23.4768x + 0.5672. \quad (12)$$

Based on the regression model, we calculate that the CO₂ emissions of Mongolia are 9.95792 when the national vulnerability threshold is 0.4.

5.4. Time Series Prediction Model Based on Exponential Smoothing

5.4.1. Model Establishment. An exponential smoothing formula is as follows:

$$S_t^{(1)} = aY_t + (1-a)S_{t-1}^{(1)}, \quad (13)$$

where $S_t^{(1)}$ is the exponential smoothing value of t period, a is smoothing constant, $0 < a < 1$, and Y_t is current data:

$$\begin{aligned} S_t^{(1)} &= aY_t + a(1-a)Y_{t-1} + (1-a)^2Y_{t-2} + \dots \\ &\quad + a(1-a)^tY_{t-t} + \dots + a(1-a)^{t-1}Y_{t-(t-1)} + (1-a)^tS_0^{(1)} \\ &= a \sum_{k=0}^{t-1} (1-a)^k Y_{t-k} + (1-a)^t S_0^{(1)}. \end{aligned} \quad (14)$$

So, $Y_t, Y_{t-1}, Y_{t-2}, \dots$, weights are $a, a(1-a), a(1-a)^2, \dots$, and the change in weights decreases exponentially.

The smooth value of period T is taken as the predicted value of period $T+1$ [16]:

$$\hat{Y}_{t+1} = S_t^{(1)} = aY_t + (1-a). \quad (15)$$

5.4.2. Model Solving and Result Analysis. We use the time series model to predict the emissions of carbon dioxide in the coming 11 years and get data shown in Table 9.

From Table 9, we can see that in 2025, carbon dioxide emissions of Mongolia will reach 9.9602 metric tons per capita; that is, Mongolia may reach the critical state of fragility [17].

6. Empirical Analysis of Mitigating Climate Vulnerability by Intervention Measures

6.1. Problem Analysis. According to the ranking of the national vulnerability indicator, we selected 177 representative countries. Combined with the fuzzy comprehensive evaluation model, we study national interventions to mitigate the risks posed by climate change, while other conditions remain the same [18]. We select representative three-level countries, including fragile countries (South Sudan and Somalia), vulnerable countries (Indonesia and China), and stable countries (the UK and USA). In the absence of extreme weather events, natural disasters, and economic and political crises, intervention in the climate environment will gradually improve the postintervention climate conditions [19].

6.2. Empirical Analysis of Intervention Measures. According to the indicator system model, carbon dioxide emissions are selected as the main factor for climate change intervention. After the intervention, CO₂ emissions are 50%

TABLE 9: Prediction data (metric tons/person).

Year	2017	2018	2019	2020	2021	2022
Carbon dioxide emissions	7.3172	7.6258	7.8401	8.1964	8.5148	8.9027
Year	2023	2024	2025	2026	2027	—
Carbon dioxide emissions	9.3816	9.6931	9.9602	10.1858	10.3374	—

TABLE 10: Score chart.

Carbon dioxide emissions	South Sudan	Somalia	China	Indonesia	The United States	England
0.1	0.6907	0.6667	0.4971	0.4313	0.1919	0.1419
0.2	0.7274	0.6974	0.5262	0.4662	0.2221	0.1721
0.3	0.7618	0.7318	0.5540	0.4940	0.2440	0.1940
0.4	0.7845	0.7545	0.5750	0.5150	0.2622	0.2122
0.5	0.8064	0.7764	0.5896	0.5296	0.2782	0.2282
0.6	0.8233	0.7933	0.6047	0.5447	0.2927	0.2427
0.7	0.8349	0.8049	0.6145	0.5545	0.3022	0.2522
0.8	0.8459	0.8159	0.6280	0.5680	0.3103	0.2603
0.9	0.8514	0.8214	0.6411	0.5811	0.3143	0.2643
1	0.8543	0.8243	0.6434	0.5834	0.3160	0.2659

to 95% of the previous emissions. To facilitate the statistics, we take 5% as the step size [20]. In order to compare the countries more clearly, we standardize CO₂ emissions in data processing and obtain the following scores, as shown in Table 10.

In the case of other indicators unchanged, we calculate the contribution rate of the country to CO₂ emissions and obtain the weight vector of the evaluation indicator [21]. According to the comprehensive evaluation model, the calculation score is shown in Figures 6–8 [22].

Through data processing, we find that for countries with different levels of vulnerability, intervention in carbon dioxide emissions can effectively reduce national vulnerability indicators and enhance national stability [23]. By changing CO₂ emissions to the same extent, the country’s vulnerability score decreases slowly as the country becomes more stable [24].

7. Evaluation and Spread of the Model

7.1. Revision of the Model to Make It Work on Smaller “States” or Cities. Combining with the evaluation system based on the abovementioned national vulnerability evaluation model, as well as the specific characteristics of cities, we rank and classify the indicators according to the risk level, sensitivity, and adaptability [25]. We have established a selection database of urban vulnerability indicators to prepare for future indicator screening.

7.2. The PSR Model. Firstly, the index data are standardized, and the entropy method is used to determine the indicator weight, and then the comprehensive weight method is used to calculate the indicator of urban vulnerability. After that, we use factor analysis in SPSS to find out the main factors influencing factors [26].

The framework of the PSR model (risk sensitivity and adaptability) is adopted to establish the indicator evaluation system of urban vulnerability. National risk

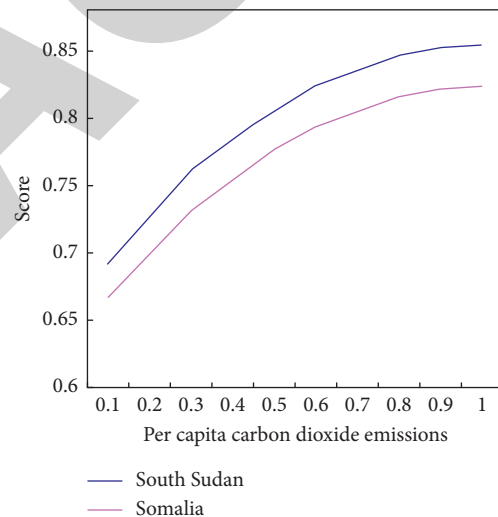


FIGURE 6: Score of fragile countries.

indicators are selected in terms of climate change, global and external pressure factors, including annual average precipitation change, annual average temperature change, frequency of extreme climate events, urban population density, and situation of economic development [27]. Urban sensitivity indicators are selected from the factors to explain situation of urban natural and social environment, including water resources, relative humidity, vegetation ecosystem, political conflict, social equity, and primary industrial structure. Urban resilience refers to the city’s ability to respond to climate change, including GDP per capita, education level, hospital beds, science and technology expenditure, ecological construction, pollution control, and other factors [28].

- (1) Building the original index data matrix: it is composed of city and evaluation indexes.

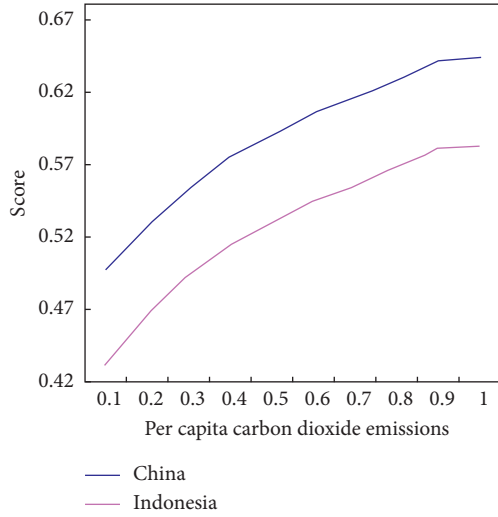


FIGURE 7: Score of vulnerable countries.

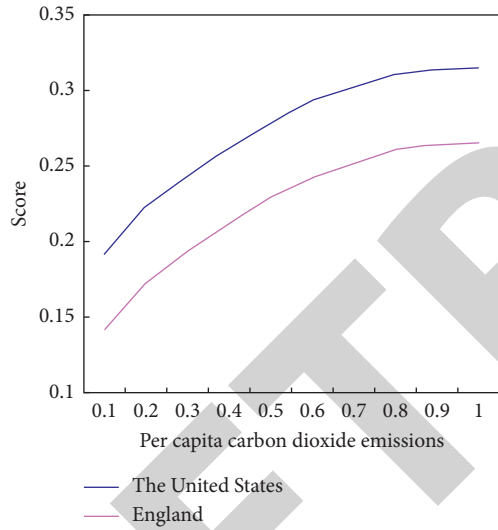


FIGURE 8: Score of stable countries.

There are m cities and n evaluation indicators that form the original indicator data matrix:

$$X = (x_{ij})_{m \times n} \quad (0 \leq i \leq m, 0 \leq j \leq n), \quad (16)$$

where x_{ij} is the j -th indicator value of the i -th city. Firstly, standardize the original indicator data.

The standardized calculation of positive indicators is as follows:

$$X = \frac{[X_{ij} - \min(X_{ij})]}{[\max(X_i) - \min(X_i)]} \quad (17)$$

The standardized calculation of negative indicators is as follows:

$$X = \frac{[\max(X_i) - X_i]}{[\max(X_i) - \min(X_i)]} \quad (18)$$

After processing, calculate the proportion of the indicator value P_{ij} of the i -th city under the j -th indicator:

$$P_{ij} = \frac{y_{ij}}{\sum_{i=1}^m y_{ij}}. \quad (19)$$

Then, calculate the entropy of the j -th indicator:

$$E_{ij} = -\frac{k}{\sum_{i=1}^m P_{ij} \ln P_{ij}}, \quad k = \frac{1}{\ln m}. \quad (20)$$

- (2) Calculating the weights of the j -th evaluation indicator W_j : $w_j = g_j / \sum g_j$.
- (3) Calculating the difference coefficient of the j -th evaluation indicator: based on the above method, the weight of the evaluation indicators at all levels of the urban vulnerability evaluation index system in the context of climate change has been finally determined.

8. Conclusion

In the irrational world political and economic order dominated by the Western developed countries, poverty and war occur in the underdeveloped countries, social vulnerability exists in developed countries, and human beings in the industrial age are faced with the vulnerability of the natural environment [29].

The research on the new theory of fragile countries can break through the limitations of the past, improve the ambiguity of the concept and the subjectivity of the evaluation criteria, and gradually improve the conceptual framework and evaluation indicator system of the national instability studies [30–35].

At the same time, the evaluation system defines the vulnerability and incentive mechanism for national vulnerability, puts forward effective control or response measures, enhances the country's ability to respond to various adverse effects, and strengthens the application of national vulnerability in the early warning of security risks. More importantly, it provides a scientific basis for our country to formulate sustainable development strategy.

Data Availability

The data in this paper come from Question E of the 2018 American College Students Mathematical Modeling Competition and the statistics of the World Bank.

Conflicts of Interest

The authors declare that there are no conflicts of interest regarding the publication of this paper.

Acknowledgments

This study was funded by the Humanities and Social Sciences Research Major Project of the Education Department of Anhui Province (SK2017A0452), the Teaching and Research Fund Project of the Education Department of Anhui

Province (2018jyxm1305), and the Teaching and Research Fund Project of the Anhui University of Finance and Economics (acxksjy201803zd).

References

- [1] A. R. Krakowka, N. HeimeI, and F. Galgan, "Modeling environmental security in Sub-Saharan Africa-ProQuest," *The Geographical Bulletin*, vol. 53, no. 1, pp. 21–38, 2012.
- [2] P. Schwartz and D. Randall, "An Abrupt climate change Scenario and its implications for United States national security," *Futures*, vol. 53, no. 6, 2004.
- [3] O. M. Theisen, N. P. Gleditsch, and H. Buhaug, "Is climate change a driver of armed conflict?" *Climatic Change*, vol. 117, no. 3, pp. 613–625, 2013.
- [4] L. Gong and C. L. Jin, "Fuzzy comprehensive evaluation model for water resources carrying capacity in Tarim river basin, Xinjiang, China," *Chinese Geographical Science*, vol. 19, no. 1, pp. 89–95, 2009.
- [5] H. L. Santos and L. F. L. Legey, "A model for long-term electricity expansion planning with endogenous environmental costs," *International Journal of Electrical Power & Energy Systems*, vol. 51, no. 10, pp. 98–105, 2013.
- [6] J. Barnett and W. N. Adger, "Climate change, human security and violent conflict," *Political Geography*, vol. 26, no. 6, pp. 639–655, 2007.
- [7] K. K. Yen, S. Ghoshray, and G. Roig, "A linear regression model using triangular fuzzy number coefficients," *Fuzzy Sets and Systems*, vol. 106, no. 2, pp. 167–177, 1999.
- [8] J. Uche, A. Martínez, and B. Carrasquer, "A study of the application of the physical hydromonics methodology to assess environmental costs of European rivers," *Management of Environmental Quality: An International Journal*, vol. 25, no. 3, pp. 324–334, 2014.
- [9] W. Easterly, "Empirics of strategic interdependence: the case of the racial tipping point," *B.e.journal of Macroeconomics*, vol. 9, no. 1, pp. 145–174, 2009.
- [10] Q.-Q. Song, Q.-Z. Jiang, and Z.-Z. Song, "Optimization of CO₂ separation technologies for Chinese refineries based on a fuzzy comprehensive evaluation model," *Petroleum Science*, vol. 12, no. 1, pp. 197–206, 2015.
- [11] I. Gengut, N. Davaahuu, E. Alnykina, and I. Potravnyy, "Environmental costs management of the project: the experience of Russia and Mongolia," *Baltic Journal of Real Estate Economics and Construction Management*, vol. 3, no. 1, pp. 140–150, 2015.
- [12] J. S. Chou and K. C. Yeh, "Life cycle carbon dioxide emissions simulation and environmental cost analysis for building construction," *Journal of Cleaner Production*, vol. 101, pp. 137–147, 2015.
- [13] H. J. Lynch, M. Rhainds, and J. M. Calabrese, "How climate extremes-not means-define a species' geographic range boundary via a demographic tipping point," *Ecological Monographs*, vol. 84, no. 1, pp. 131–149, 2016.
- [14] C. Antoniou, E. Papadimitriou, and G. Yannis, "Road Safety forecasts in five European countries using structural time series models," *Traffic Injury Prevention*, vol. 15, no. 6, pp. 58–605, 2014.
- [15] P. C. Padhi, S. S. Mahapatra, S. N. Yadav, and D. K. Tripathy, "Optimization of correlated quality characteristics in WEDM process using Taguchi approach coupled with principal component analysis," *Journal for Manufacturing Science & Production*, vol. 13, no. 3, pp. 199–208, 2013.
- [16] O. O. Aalen, "Further results on the non-parametric linear regression model in survival analysis," *Statistics in Medicine*, vol. 12, no. 17, pp. 1569–1588, 1993.
- [17] R. Coppi, P. D'Urso, P. Giordani, and A. Santoro, "Least squares estimation of a linear regression model with LR fuzzy response," *Computational Statistics & Data Analysis*, vol. 51, no. 1, pp. 267–286, 2006.
- [18] B. M. Brentan, E. Luvizotto Jr., and M. Herrera, "Hybrid regression model for near real-time urban water demand forecasting," *Journal of Computational and Applied Mathematics*, vol. 309, pp. 532–541, 2017.
- [19] S.-K. Oh, M.-S. Kim, T.-D. Eom, and J.-J. Lee, "Heterogeneous local model networks for time series prediction," *Applied Mathematics and Computation*, vol. 168, no. 1, pp. 164–177, 2005.
- [20] R. Al-Hmouz, W. Pedrycz, and A. Balamash, "Description and prediction of time series: a general framework of Granular Computing," *Expert Systems With Applications*, vol. 42, no. 10, pp. 4830–4839, 2015.
- [21] A. Laukaitis, "Functional data analysis for cash flow and transactions intensity continuous-time prediction using Hilbert-valued autoregressive processes," *European Journal of Operational Research*, vol. 185, no. 3, pp. 1607–1614, 2006.
- [22] O. Valenzuela, I. Rojas, F. Rojas et al., "Hybridization of intelligent techniques and ARIMA models for time series prediction," *Fuzzy Sets and Systems*, vol. 159, no. 7, pp. 821–845, 2008.
- [23] S. Franke, J. Meixensberger, and T. Neumuth, "Intervention time prediction from surgical low-level tasks," *Journal of Biomedical Informatics*, vol. 46, no. 1, pp. 152–159, 2013.
- [24] I. S. David, "An atmosphere-ocean time series model of global climate change," *Computational Statistics and Data Analysis*, vol. 51, no. 2, pp. 1330–1334, 2006.
- [25] B. Evanoff, A. M. Dale, A. Zeringue et al., "Results of a fall prevention educational intervention for residential construction," *Safety Science*, vol. 89, pp. 301–307, 2016.
- [26] L. M. Braun, D. A. Rodriguez, T. Cole-Hunter et al., "Short-term planning and policy interventions to promote cycling in urban centers: findings from a commute mode choice analysis in Barcelona, Spain," *Transportation Research Part A: Policy and Practice*, vol. 89, pp. 164–183, 2016.
- [27] K. Basen-Engquist, K. S. Hudmon, M. Tripp, and R. Chamberlain, "Worksite health and safety climate: scale development and effects of a health promotion intervention," *Preventive Medicine*, vol. 27, no. 1, pp. 111–119, 1998.
- [28] L. W. Sussams, W. R. Sheate, and R. P. Eales, "Green infrastructure as a climate change adaptation policy intervention: muddying the waters or clearing a path to a more secure future?" *Journal of Environmental Management*, vol. 147, pp. 184–193, 2015.
- [29] S. M. Rice and L. J. McIver, "Climate change and mental health: rationale for research and intervention planning," *Asian Journal of Psychiatry*, vol. 20, pp. 1–2, 2016.
- [30] S. C. Sekhar, "A critical evaluation of variable air volume system in hot and humid climates," *Energy and Buildings*, vol. 26, no. 2, pp. 223–232, 1997.
- [31] J. B. Liu, J. Zhao, and J. Min, "On the Hosoya index of graphs formed by a fractal graph," *Fractals-Complex Geometry Patterns and Scaling in Nature and Society*, vol. 27, no. 8, pp. 19–35, 2019.
- [32] J.-B. Liu, J. Zhao, H. He, and Z. Shao, "Valency-based Topological descriptors and structural property of the generalized Sierpiński networks," *Journal of Statistical Physics*, vol. 177, no. 6, pp. 1131–1147, 2019.

Research Article

Maximum Reciprocal Degree Resistance Distance Index of Unicyclic Graphs

Gai-Xiang Cai ¹, Xing-Xing Li,¹ and Gui-Dong Yu ^{1,2}

¹School of Mathematics and Physics, Anqing Normal University, Anqing 246133, China

²Basic Department, Hefei Preschool Education College, Hefei 230013, China

Correspondence should be addressed to Gui-Dong Yu; guidongy@163.com

Received 7 May 2020; Accepted 26 June 2020; Published 8 August 2020

Guest Editor: Muhammad Javaid

Copyright © 2020 Gai-Xiang Cai et al. This is an open access article distributed under the Creative Commons Attribution License, which permits unrestricted use, distribution, and reproduction in any medium, provided the original work is properly cited.

The reciprocal degree resistance distance index of a connected graph G is defined as $\text{RDR}(G) = \sum_{\{u,v\} \subseteq V(G)} ((d_G(u) + d_G(v)) / (r_G(u, v)))$, where $r_G(u, v)$ is the resistance distance between vertices u and v in G . Let \mathcal{U}_n denote the set of unicyclic graphs with n vertices. We study the graph with maximum reciprocal degree resistance distance index among all graphs in \mathcal{U}_n and characterize the corresponding extremal graph.

1. Introduction

Let $G = (V, E)$ be a simple connected graph of order n with vertex set $V = V(G) = \{v_1, v_2, \dots, v_n\}$ and edge set $E = E(G)$. For any $u \in V(G)$, $d_G(u)$ is the degree of vertex u , and the distance between vertices of u and v , denoted by $d_G(u, v)$, is the length of a shortest path between them. Topological indices are numbers associated with molecular structures which serve for quantitative relationships between chemical structures and properties. The first such index was published by Wiener [1], but the name topological index was invented by Hosoya [2]. Many of them are based on the graph distance [3] and the vertex degree [4]. In addition, several graph invariants are based on both the vertex degree and the graph distance [5].

One of the most intensively studied topological indices is the Wiener index. The Wiener index was introduced by American chemist Wiener in [1], defined as

$$W(G) = \sum_{\{u,v\} \subseteq V(G)} d_G(u, v). \quad (1)$$

Another distance-based graph invariant Harary index has been introduced by Plavšić et al. [6] and independently by Ivanciuc et al. [7] in 1993 for the characterization of molecular graphs. The Harary index $H(G)$ of graph G is defined as

$$H(G) = \sum_{\{u,v\} \subseteq V(G)} \frac{1}{d_G(u, v)}. \quad (2)$$

For more results related to Harary index, refer to [8, 9–17].

The resistance distance $r(u, v)$ (if more than one graphs are considered, we write $r_G(u, v)$ in order to avoid confusion) between vertices u and v in G is defined as the effective resistance between the two nodes of the electronic network obtained so that its nodes correspond to the vertices of G and each edges of G is replaced by a resistor of unit resistance, which is compared by the methods of the theory of resistive electrical networks based on Ohm's and Kirchoff's laws.

The Kirchoff index $\text{Kf}(G)$ of a graph G is defined as [18, 19]

$$\text{Kf}(G) = \sum_{\{u,v\} \subseteq V(G)} r_G(u, v). \quad (3)$$

As a new structure descriptor, the Kirchoff index is well studied (see recent papers [20–31]). In 2017, Chen et al. [32] introduced a new graph invariant reciprocal to Kirchoff index, named Resistance-Harary index:

$$\text{RH}(G) = \sum_{\{u,v\} \subseteq V(G)} \frac{1}{r_G(u, v)}. \quad (4)$$

For more results related to Resistance-Harary index, refer to [32–34].

The first and the second Zagreb indices are defined as

$$\begin{aligned} M_1 = M_1(G) &= \sum_{u \in V(G)} d_G(u)^2 = \sum_{uv \in E(G)} (d_G(u) + d_G(v)), \\ M_2 = M_2(G) &= \sum_{uv \in E(G)} d_G(u)d_G(v), \end{aligned} \quad (5)$$

respectively. These are the oldest [35, 36] and best studied degree-based topological indices (see the reviews [4], recent papers [37, 38], and the references cited therein).

Dobrynin and Kochtova [39] and Gutman [40] independently proposed a vertex-degree-weighted version of Wiener index called degree distance, which is defined for a connected graph G as

$$\text{DD}(G) = \frac{1}{2} \sum_{\{u,v\} \in V(G)} (d_G(u) + d_G(v))d_G(u, v). \quad (6)$$

The reciprocal degree distance [41] is defined as

$$\text{RDD}(G) = \frac{1}{2} \sum_{\{u,v\} \in V(G)} \frac{d_G(u) + d_G(v)}{d_G(u, v)}. \quad (7)$$

Hua and Zhang [42] have obtained lower and upper bounds for the reciprocal degree distance of graph in terms of other graph invariants. The chemical applications and mathematical properties of the reciprocal degree distance are well studied in [41, 43].

Analogous to the relationship between degree distance and reciprocal degree distance, we introduce here a new graph invariant based on both the vertex degree and the graph distance, named the reciprocal degree resistance distance index:

$$\text{RDR}(G) = \sum_{\{u,v\} \subseteq V(G)} \frac{d_G(u) + d_G(v)}{r_G(u, v)}. \quad (8)$$

A unicyclic graph is a connected graph with n vertices and n edges. Let \mathcal{U}_n denote the set of unicyclic graphs with n vertices. In this paper, we determine the graph with maximum reciprocal degree resistance distance index among all graphs in \mathcal{U}_n and characterize the corresponding extremal graph.

2. Preliminaries

In this section, we will introduce some useful lemmas and three transformations.

Let $C_g = v_1 v_2 \cdots v_g v_1$ be the cycle on $g \geq 3$ vertices. For any two vertices $v_i, v_j \in V(C_g)$ with $i < j$, by Ohm's law, one has

$$r_{C_g}(v_i, v_j) = \frac{(j-i)(g+i-j)}{g}. \quad (9)$$

Lemma 1 (see [19]). *Let x be a cut vertex of a connected graph G and let a and b be vertices occurring in different components which arise upon deletion of x . Then,*

$$r_G(a, b) = r_G(a, x) + r_G(x, b). \quad (10)$$

2.1. Edge-Lifting Transformation. Let G_1 and G_2 be two graphs with $n_1 \geq 2$ and $n_2 \geq 2$ vertices, respectively. G is the graph obtained from G_1 and G_2 by adding an edge between a vertex u_0 of G_1 to a vertex v_0 of G_2 . And G' is the graph obtained by identifying u_0 of G_1 to a vertex v_0 of G_2 and adding a pendant edge to u_0 (v_0). We say that G' is obtained from G by an edge-lifting transformation at $e = \{u_0, v_0\}$ (see Figure 1).

Lemma 2. *If G' can be obtained from G by an edge-lifting transformation, then $\text{RDR}(G) < \text{RDR}(G')$.*

Proof. Consider G and G' shown in Figure 1. By the definition of $\text{RDR}(G)$,

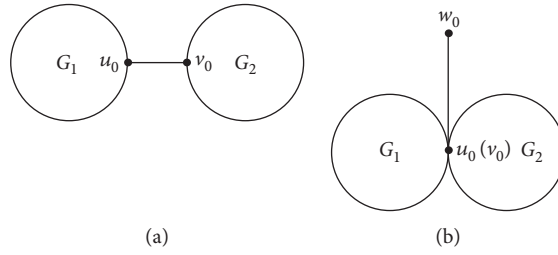


FIGURE 1: The edge-lifting transformation. (a) G . (b) G' .

$$\begin{aligned}
 \text{RDR}(G) &= \sum_{x,y \in V(G_1) \setminus \{u_0\}} \frac{d_G(x) + d_G(y)}{r_G(x,y)} + \sum_{x,y \in V(G_2) \setminus \{v_0\}} \frac{d_G(x) + d_G(y)}{r_G(x,y)} \\
 &+ \sum_{x \in V(G_1) \setminus \{u_0\}} \frac{d_G(u_0) + d_G(x)}{r_G(u_0,x)} + \sum_{x \in V(G_2) \setminus \{v_0\}} \frac{d_G(u_0) + d_G(x)}{r_G(v_0,x) + 1} \\
 &+ \sum_{x \in V(G_1) \setminus \{u_0\}} \frac{d_G(v_0) + d_G(x)}{r_G(u_0,x) + 1} + \sum_{x \in V(G_2) \setminus \{v_0\}} \frac{d_G(v_0) + d_G(x)}{r_G(v_0,x)} \\
 &+ \sum_{x \in V(G_1) \setminus \{u_0\}, y \in V(G_2) \setminus \{v_0\}} \frac{d_G(x) + d_G(y)}{r_G(x,u_0) + 1 + r_G(v_0,y)} + \frac{d_G(u_0) + d_G(v_0)}{r_G(u_0,v_0)}, \\
 \text{RDR}(G') &= \sum_{x,y \in V(G_1) \setminus \{u_0\}} \frac{d_{G'}(x) + d_{G'}(y)}{r_{G'}(x,y)} + \sum_{x,y \in V(G_2) \setminus \{v_0\}} \frac{d_{G'}(x) + d_{G'}(y)}{r_{G'}(x,y)} \\
 &+ \sum_{x \in V(G_1) \setminus \{u_0\}} \frac{d_{G'}(u_0) + d_{G'}(x)}{r_{G'}(u_0,x)} + \sum_{x \in V(G_2) \setminus \{v_0\}} \frac{d_{G'}(v_0) + d_{G'}(x)}{r_{G'}(v_0,x)} \\
 &+ \sum_{x \in V(G_1) \setminus \{u_0\}} \frac{d_{G'}(w_0) + d_{G'}(x)}{r_{G'}(u_0,x) + 1} + \sum_{x \in V(G_2) \setminus \{v_0\}} \frac{d_{G'}(w_0) + d_{G'}(x)}{r_{G'}(v_0,x) + 1} \\
 &+ \sum_{x \in V(G_1) \setminus \{u_0\}, y \in V(G_2) \setminus \{v_0\}} \frac{d_{G'}(x) + d_{G'}(y)}{r_{G'}(x,u_0) + r_{G'}(v_0,y)} + \frac{d_{G'}(u_0) + d_{G'}(w_0)}{r_{G'}(u_0,w_0)}.
 \end{aligned} \tag{11}$$

(i) Note that $d_G(x) + d_G(y) = d_{G'}(x) + d_{G'}(y)$, $r_G(x,y) = r_{G'}(x,y)$ for $x, y \in V(G_1) \setminus \{u_0\}$ or $x, y \in V(G_2) \setminus \{v_0\}$, and $d_G(u_0) + d_G(v_0) = d_{G'}(u_0) + d_{G'}(w_0)$, $r_G(u_0, v_0) = r_{G'}(u_0, w_0)$; then, we have

$$\begin{aligned}
 \sum_{x,y \in V(G_1) \setminus \{u_0\}} \frac{d_G(x) + d_G(y)}{r_G(x,y)} &= \sum_{x,y \in V(G_1) \setminus \{u_0\}} \frac{d_{G'}(x) + d_{G'}(y)}{r_{G'}(x,y)}, \\
 \sum_{x,y \in V(G_2) \setminus \{v_0\}} \frac{d_G(x) + d_G(y)}{r_G(x,y)} &= \sum_{x,y \in V(G_2) \setminus \{v_0\}} \frac{d_{G'}(x) + d_{G'}(y)}{r_{G'}(x,y)}, \\
 \frac{d_G(u_0) + d_G(v_0)}{r_G(u_0, v_0)} &= \frac{d_{G'}(u_0) + d_{G'}(w_0)}{r_{G'}(u_0, w_0)}.
 \end{aligned} \tag{12}$$

(ii) Note that $d_G(x) + d_G(y) = d_{G'}(x) + d_{G'}(y)$, $r_G(x, u_0) + r_G(v_0, y) = r_{G'}(x, u_0) + r_{G'}(v_0, y)$ for $x \in V(G_1) \setminus \{u_0\}$, $y \in V(G_2) \setminus \{v_0\}$; then, we have

$$\begin{aligned}
 &\sum_{x \in V(G_1) \setminus \{u_0\}, y \in V(G_2) \setminus \{v_0\}} \frac{d_G(x) + d_G(y)}{r_G(x, u_0) + 1 + r_G(v_0, y)} \\
 &< \sum_{x \in V(G_1) \setminus \{u_0\}, y \in V(G_2) \setminus \{v_0\}} \frac{d_{G'}(x) + d_{G'}(y)}{r_{G'}(x, u_0) + r_{G'}(v_0, y)}.
 \end{aligned} \tag{13}$$

(iii) Note that $r_{G'}(u_0, x) = r_G(u_0, x)$ for any $x \in V(G_1) \setminus \{u_0\}$, and $d_{G'}(u_0) = d_G(u_0) + d_G(v_0) - 1$; then, we have

$$\begin{aligned}
& \left(\sum_{x \in V(G_1) \setminus \{u_0\}} \frac{d_{G'}(u_0) + d_{G'}(x)}{r_{G'}(u_0, x)} - \sum_{x \in V(G_1) \setminus \{u_0\}} \frac{d_G(u_0) + d_G(x)}{r_G(u_0, x)} \right) \\
& + \left(\sum_{x \in V(G_1) \setminus \{u_0\}} \frac{d_{G'}(u_0) + d_{G'}(x)}{r_{G'}(u_0, x) + 1} - \sum_{x \in V(G_1) \setminus \{u_0\}} \frac{d_G(u_0) + d_G(x)}{r_G(u_0, x) + 1} \right) \\
& = \sum_{x \in V(G_1) \setminus \{u_0\}} \frac{d_G(v_0) - 1}{r_G(u_0, x)} + \sum_{x \in V(G_1) \setminus \{u_0\}} \frac{1 - d_G(v_0)}{r_G(u_0, x) + 1} > 0.
\end{aligned} \tag{14}$$

(iv) Note that $r_{G'}(v_0, x) = r_G(v_0, x)$, $d_{G'}(x) = d_G(x)$ for any $x \in V(G_2)$, and $d_{G'}(v_0) = d_G(u_0) + d_G(v_0) - 1$; then, we have

$$\begin{aligned}
& \left(\sum_{x \in V(G_2) \setminus \{v_0\}} \frac{d_{G'}(v_0) + d_{G'}(x)}{r_{G'}(v_0, x)} - \sum_{x \in V(G_2) \setminus \{v_0\}} \frac{d_G(v_0) + d_G(x)}{r_G(v_0, x)} \right) \\
& + \left(\sum_{x \in V(G_2) \setminus \{v_0\}} \frac{d_{G'}(v_0) + d_{G'}(x)}{r_{G'}(v_0, x) + 1} - \sum_{x \in V(G_2) \setminus \{v_0\}} \frac{d_G(v_0) + d_G(x)}{r_G(v_0, x) + 1} \right) \\
& = \sum_{x \in V(G_2) \setminus \{v_0\}} \frac{d_G(u_0) - 1}{r_G(v_0, x)} + \sum_{x \in V(G_2) \setminus \{v_0\}} \frac{1 - d_G(u_0)}{r_G(v_0, x) + 1} > 0.
\end{aligned} \tag{15}$$

Thus, by (i)–(iv), we get $RDR(G') - RDR(G) > 0$. \square

2.2. Cycle-Lifting Transformation. Let G be a graph as shown in Figure 2. Take a cycle C in G , say $C = v_1 v_2 \cdots v_p v_1$; G can be viewed as a graph obtained by coalescing C with a number of star subgraphs of G , say G_1, G_2, \dots, G_p , by identifying v_i with the center of G_i for all i ($1 \leq i \leq p$), denoted as $|E(G_i)| = s_i$ and $|V(G_i)| = s_i + 1$. Deleting all edges in G_i and joining v_1 to all pendant vertices of G_i ($2 \leq i \leq p$), we obtained a new graph, denoted by G' (see Figure 2). This operation is called a cycle-lifting transformation of G with respect to C .

Lemma 3. *If G' can be obtained from G by a cycle-lifting transformation, then $RDR(G) < RDR(G')$.*

Proof. Consider G and G' shown in Figure 2. By the definition of $RDR(G)$,

$$\begin{aligned}
RDR(G) &= \sum_{i=1}^p \sum_{x, y \in V(G_i) \setminus \{v_i\}} \frac{d_G(x) + d_G(y)}{r_G(x, y)} + \sum_{i=1}^p \sum_{x \in V(G_i) \setminus \{v_i\}} \frac{d_G(v_i) + d_G(x)}{r_G(v_i, x)} \\
&+ \sum_{i, j=1}^p \sum_{\substack{x \in V(G_i) \setminus \{v_i\} \\ i \neq j \\ y \in V(G_j) \setminus \{v_j\}}} \frac{d_G(x) + d_G(y)}{r_G(x, v_i) + r_G(v_i, v_j) + r_G(v_j, y)} + \sum_{i=1}^p \sum_{\substack{x \in V(G_i) \setminus \{v_i\} \\ y \in V(G_j) \setminus \{v_j\}}} \frac{d_G(x) + d_G(y)}{r_G(x, y)} \\
&+ \sum_{x, y \in V(C_p)} \frac{d_G(x) + d_G(y)}{r_G(x, y)},
\end{aligned} \tag{16}$$

$$\begin{aligned}
RDR(G') &= \sum_{i=1}^p \sum_{x, y \in V(G_i) \setminus \{v_i\}} \frac{d_{G'}(x) + d_{G'}(y)}{r_{G'}(x, y)} + \sum_{i=1}^p \sum_{x \in V(G_i) \setminus \{v_i\}} \frac{d_{G'}(v_1) + d_{G'}(x)}{r_{G'}(v_1, x)} \\
&+ \sum_{i, j=1}^p \sum_{\substack{x \in V(G_i) \setminus \{v_i\} \\ i \neq j \\ y \in V(G_j) \setminus \{v_j\}}} \frac{d_{G'}(x) + d_{G'}(y)}{r_{G'}(x, v_1) + r_{G'}(v_1, y)} + \sum_{i=1}^p \sum_{\substack{x \in V(C_p) \setminus \{v_1\} \\ y \in V(G_i) \setminus \{v_i\}}} \frac{d_{G'}(x) + d_{G'}(y)}{r_{G'}(x, y)} \\
&+ \sum_{x, y \in V(C_p)} \frac{d_{G'}(x) + d_{G'}(y)}{r_{G'}(x, y)}.
\end{aligned}$$

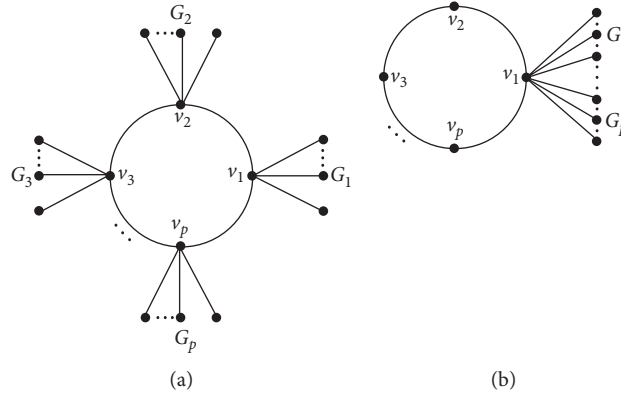


FIGURE 2: The cycle-lifting transformation. (a) G . (b) G' .

(i) Note that $d_G(x) + d_G(y) = d_{G'}(x) + d_{G'}(y)$, $r_G(x, y) = r_{G'}(x, y)$ for $x, y \in V(G_i) \setminus \{v_i\}$ in G , and $x, y \in V(G_i) \setminus \{v_1\}$ in G' ; then, we have

$$\begin{aligned} & \sum_{i=1}^p \sum_{x, y \in V(G_i) \setminus \{v_i\}} \frac{d_G(x) + d_G(y)}{r_G(x, y)} \\ &= \sum_{i=1}^p \sum_{x, y \in V(G_i) \setminus \{v_i\}} \frac{d_{G'}(x) + d_{G'}(y)}{r_{G'}(x, y)}. \end{aligned} \tag{17}$$

(ii) Let $r_G(v_i, v_j) = r_{G'}(v_i, v_j) = r_i$; when $|j - i| = t$, then $r_t = r_{p-t}$. $d_G(v_i) = s_i + 2$ for any $v_i \in V(C_p)$ in G and $d_{G'}(v_1) = s_1 + \dots + s_p + 2$ for $v_1 \in V(C_p)$ in G' ; then, we have

$$\begin{aligned} \sum_{x, y \in V(C_p)} \frac{d_G(x) + d_G(y)}{r_G(x, y)} &= \sum_{i=2}^p \frac{d_G(v_1) + d_G(v_i)}{r_G(v_1, v_i)} \\ &+ \sum_{i=3}^p \frac{d_G(v_2) + d_G(v_i)}{r_G(v_2, v_i)} + \dots \\ &+ \frac{d_G(v_{p-1}) + d_G(v_p)}{r_G(v_{p-1}, v_p)}. \end{aligned} \tag{18}$$

Thus,

$$\begin{aligned} \sum_{i=2}^p \frac{d_G(v_1) + d_G(v_i)}{r_G(v_1, v_i)} &= \frac{s_1 + s_2 + 4}{r_1} + \frac{s_1 + s_3 + 4}{r_2} + \dots + \frac{s_1 + s_p + 4}{r_{p-1}}, \\ \sum_{i=3}^p \frac{d_G(v_2) + d_G(v_i)}{r_G(v_2, v_i)} &= \frac{s_2 + s_3 + 4}{r_1} + \dots + \frac{s_2 + s_p + 4}{r_{p-2}}, \\ &\dots \\ \frac{d_G(v_{p-1}) + d_G(v_p)}{r_G(v_{p-1}, v_p)} &= \frac{s_{p-1} + s_p + 4}{r_1}. \end{aligned} \tag{19}$$

Thus,

$$\begin{aligned} \sum_{x,y \in V(C_p)} \frac{d_G(x) + d_G(y)}{r_G(x,y)} &= \frac{(s_1 + \cdots + s_{p-1}) + (s_2 + \cdots + s_p) + 4(p-1)}{r_1} \\ &+ \frac{(s_1 + \cdots + s_{p-2}) + (s_3 + \cdots + s_p) + 4(p-2)}{r_2} \\ &+ \cdots + \frac{s_1 + s_p + 4}{r_{p-1}}. \end{aligned} \quad (20)$$

Similarly,

$$\begin{aligned} \sum_{x,y \in V(C_p)} \frac{d_{G'}(x) + d_{G'}(y)}{r_{G'}(x,y)} &= \frac{(s_1 + \cdots + s_p) + 4(p-1)}{r_1} \\ &+ \frac{(s_1 + \cdots + s_p) + 4(p-2)}{r_2} \\ &+ \cdots + \frac{s_1 + \cdots + s_p + 4}{r_{p-1}}. \end{aligned} \quad (21)$$

Then,

$$\begin{aligned} \sum_{x,y \in V(C_p)} \frac{d_G(x) + d_G(y)}{r_G(x,y)} - \sum_{x,y \in V(C_p)} \frac{d_{G'}(x) + d_{G'}(y)}{r_{G'}(x,y)} \\ = \frac{s_2 + \cdots + s_{p-1}}{r_1} + \frac{s_3 + \cdots + s_{p-2}}{r_2} \\ + \cdots + \frac{-(s_2 + \cdots + s_{p-1})}{r_{p-1}} = 0. \end{aligned} \quad (22)$$

(iii) Note that $d_G(x) + d_G(y) = d_{G'}(x) + d_{G'}(y)$, $r_G(x, v_i) + r_G(v_j, y) = r_{G'}(x, v_1) + r_{G'}(v_1, y)$ for $x \in V(G_i) \setminus \{v_i\}$, $y \in V(G_j) \setminus \{v_j\}$ in G and for $x \in V(G_i) \setminus \{v_1\}$, $y \in V(G_j) \setminus \{v_1\}$ in G' ; then, we have

$$\begin{aligned} \sum_{\substack{i,j=1 \\ i \neq j}}^p \sum_{\substack{x \in V(G_i) \setminus \{v_i\} \\ y \in V(G_j) \setminus \{v_j\}}} \frac{d_G(x) + d_G(y)}{r_G(x, v_i) + r_G(v_i, v_j) + r_G(v_j, y)} \\ < \sum_{\substack{i,j=1 \\ i \neq j}}^p \sum_{\substack{x \in V(G_i) \setminus \{v_1\} \\ y \in V(G_j) \setminus \{v_1\}}} \frac{d_{G'}(x) + d_{G'}(y)}{r_{G'}(x, v_1) + r_{G'}(v_1, y)}. \end{aligned} \quad (23)$$

(iv) Note that $r_G(v_i, x) = r_{G'}(v_1, x) = 1$, $d_G(v_i) + d_G(x) = s_i + 3$ for $x \in V(G_i) \setminus \{v_i\}$ in G , and $d_{G'}(v_1) + d_{G'}(x) = s_1 + \cdots + s_p + 3$ for $x \in V(G_i) \setminus \{v_1\}$ in G' ; then, we have

$$\begin{aligned} \sum_{i=1}^p \sum_{x \in V(G_i) \setminus \{v_i\}} \frac{d_G(v_i) + d_G(x)}{r_G(v_i, x)} &= s_1(s_1 + 3) + s_2(s_2 + 3) \\ &+ \cdots + s_p(s_p + 3) \\ &= \sum_{i=1}^p s_i(s_i + 3), \\ \sum_{i=1}^p \sum_{x \in V(G_i) \setminus \{v_1\}} \frac{d_{G'}(v_1) + d_{G'}(x)}{r_{G'}(v_1, x)} &= s_1(s_1 + \cdots + s_p + 3) + \cdots \\ &+ s_p(s_1 + \cdots + s_p + 3) \\ &= \sum_{i=1}^p s_i(s_1 + \cdots + s_p + 3). \end{aligned} \quad (24)$$

Thus, we have

$$\begin{aligned} \sum_{i=1}^p \sum_{x \in V(G_i) \setminus \{v_i\}} \frac{d_{G'}(v_1) + d_{G'}(x)}{r_{G'}(v_1, x)} - \sum_{i=1}^p \sum_{x \in V(G_i) \setminus \{v_i\}} \frac{d_G(v_i) + d_G(x)}{r_G(v_i, x)} \\ = \sum_{\substack{i,j=1 \\ i \neq j}}^p s_i \cdot s_j. \end{aligned} \quad (25)$$

(v) Note that $d_G(x) + d_G(y) = 3 + s_i$, $d_{G'}(x) + d_{G'}(y) = 3$, $r_G(x, y) = r_{G'}(x, y)$ for any $x \in V(C_p) \setminus \{v_i\}$, $y \in V(G_i) \setminus \{v_i\}$ in G and for $x \in V(C_p) \setminus \{v_1\}$, $y \in V(G_i) \setminus \{v_1\}$ in G' ; when $s_{i+t} > s_p$ ($1 \leq t \leq p-1$), then $s_{i+t} = s_{i+t-p}$; we have

$$\begin{aligned}
 \sum_{i=1}^p \sum_{\substack{x \in V(C_p) \setminus \{v_i\} \\ y \in V(G_i) \setminus \{v_i\}}} \frac{d_G(x) + d_G(y)}{r_G(x, y)} &= \sum_{\substack{x \in V(C_p) \setminus \{v_1\} \\ y \in V(G_1) \setminus \{v_1\}}} \frac{d_G(x) + d_G(y)}{r_G(x, y)} \\
 &+ \sum_{\substack{x \in V(C_p) \setminus \{v_2\} \\ y \in V(G_1) \setminus \{v_2\}}} \frac{d_G(x) + d_G(y)}{r_G(x, y)} \\
 &+ \dots + \sum_{\substack{x \in V(C_p) \setminus \{v_p\} \\ y \in V(G_p) \setminus \{v_p\}}} \frac{d_G(x) + d_G(y)}{r_G(x, y)}.
 \end{aligned} \tag{26}$$

Thus,

$$\begin{aligned}
 \sum_{\substack{x \in V(C_p) \setminus \{v_1\} \\ y \in V(G_1) \setminus \{v_1\}}} \frac{d_G(x) + d_G(y)}{r_G(x, y)} &= \frac{s_1(3 + s_2)}{r_1 + 1} + \frac{s_1(3 + s_3)}{r_2 + 1} + \dots + \frac{s_1(3 + s_p)}{r_{p-1} + 1}, \\
 \sum_{\substack{x \in V(C_p) \setminus \{v_2\} \\ y \in V(G_1) \setminus \{v_2\}}} \frac{d_G(x) + d_G(y)}{r_G(x, y)} &= \frac{s_2(3 + s_3)}{r_1 + 1} + \frac{s_2(3 + s_4)}{r_2 + 1} + \dots + \frac{s_2(3 + s_1)}{r_{p-1} + 1}, \\
 &\dots \\
 \sum_{\substack{x \in V(C_p) \setminus \{v_p\} \\ y \in V(G_p) \setminus \{v_p\}}} \frac{d_G(x) + d_G(y)}{r_G(x, y)} &= \frac{s_p(3 + s_1)}{r_1 + 1} + \frac{s_p(3 + s_2)}{r_2 + 1} + \dots + \frac{s_p(3 + s_{p-1})}{r_{p-1} + 1},
 \end{aligned} \tag{27}$$

and we have

$$\sum_{i=1}^p \sum_{\substack{x \in V(C_p) \setminus \{v_j\} \\ y \in V(G_p) \setminus \{v_j\}}} \frac{d_G(x) + d_G(y)}{r_G(x, y)} = \sum_{i=1}^p \frac{s_i(3 + s_{(i+1) \bmod p})}{r_1 + 1} + \sum_{i=1}^p \frac{s_i(3 + s_{(i+2) \bmod p})}{r_2 + 1} + \dots + \sum_{i=1}^p \frac{s_i(3 + s_{(i+p-1) \bmod p})}{r_{p-1} + 1}. \tag{28}$$

Thus,

$$\sum_{i=1}^p \sum_{\substack{x \in V(C_p) \setminus \{v_i\} \\ y \in V(G_p) \setminus \{v_i\}}} \frac{d_G(x) + d_G(y)}{r_G(x, y)} = \sum_{\substack{i, j=1 \\ i \neq j}}^p \frac{s_i \cdot (3 + s_j)}{r_G(v_i, v_j) + 1}. \quad (29)$$

Similarly,

$$\begin{aligned} \sum_{i=1}^p \sum_{\substack{x \in V(C_p) \setminus \{v_i\} \\ y \in V(G_i) \setminus \{v_i\}}} \frac{d_{G'}(x) + d_{G'}(y)}{r_{G'}(x, y)} &= \sum_{\substack{x \in V(C_p) \setminus \{v_1\} \\ y \in V(G_1) \setminus \{v_1\}}} \frac{d_{G'}(x) + d_{G'}(y)}{r_{G'}(x, y)} + \sum_{\substack{x \in V(C_p) \setminus \{v_1\} \\ y \in V(G_2) \setminus \{v_1\}}} \frac{d_{G'}(x) + d_{G'}(y)}{r_{G'}(x, y)} \\ &\quad + \dots + \sum_{\substack{x \in V(C_p) \setminus \{v_1\} \\ y \in V(G_i) \setminus \{v_1\}}} \frac{d_{G'}(x) + d_{G'}(y)}{r_{G'}(x, y)}, \\ \sum_{\substack{x \in V(C_p) \setminus \{v_1\} \\ y \in V(G_1) \setminus \{v_1\}}} \frac{d_{G'}(x) + d_{G'}(y)}{r_{G'}(x, y)} &= \frac{3s_1}{r_1 + 1} + \frac{3s_1}{r_2 + 1} + \dots + \frac{3s_1}{r_{p-1} + 1}, \\ \sum_{\substack{x \in V(C_p) \setminus \{v_1\} \\ y \in V(G_2) \setminus \{v_1\}}} \frac{d_{G'}(x) + d_{G'}(y)}{r_{G'}(x, y)} &= \frac{3s_2}{r_1 + 1} + \frac{3s_2}{r_2 + 1} + \dots + \frac{3s_2}{r_{p-1} + 1}, \\ &\quad \dots \\ \sum_{\substack{x \in V(C_p) \setminus \{v_1\} \\ y \in V(G_i) \setminus \{v_1\}}} \frac{d_{G'}(x) + d_{G'}(y)}{r_{G'}(x, y)} &= \frac{3s_p}{r_1 + 1} + \frac{3s_p}{r_2 + 1} + \dots + \frac{3s_p}{r_{p-1} + 1}. \end{aligned} \quad (30)$$

Thus, we have

$$\begin{aligned} \sum_{i=1}^p \sum_{\substack{x \in V(C_p) \setminus \{v_i\} \\ y \in V(G_i) \setminus \{v_i\}}} \frac{d_{G'}(x) + d_{G'}(y)}{r_{G'}(x, y)} \\ = \sum_{i=1}^p \frac{3s_i}{r_1 + 1} + \sum_{i=1}^p \frac{3s_i}{r_2 + 1} + \dots + \sum_{i=1}^p \frac{3s_i}{r_{p-1} + 1}. \end{aligned} \quad (31)$$

Then,

$$\begin{aligned} \sum_{i=1}^p \sum_{\substack{x \in V(C_p) \setminus \{v_i\} \\ y \in V(G_i) \setminus \{v_i\}}} \frac{d_{G'}(x) + d_{G'}(y)}{r_{G'}(x, y)} \\ - \sum_{i=1}^p \sum_{\substack{x \in V(C_p) \setminus \{v_i\} \\ y \in V(G_i) \setminus \{v_i\}}} \frac{d_G(x) + d_G(y)}{r_G(x, y)} = - \sum_{\substack{i, j=1 \\ i \neq j}}^p \frac{s_i \cdot s_j}{r_G(v_i, v_j) + 1}. \end{aligned} \quad (32)$$

Thus, by (i)–(v), we get $RDR(G') - RDR(G) > 0$. \square

2.3. Cycle-Shrinking Transformation. Denote by S_n^p the unicyclic graph obtained from cycle C_p by attaching $n - p$ pendant edges to a vertex v_1 of C_p (see Figure 3). Let $G = S_n^p$ ($p \geq 4$); deleting the edges $v_2v_3, \dots, v_{p-1}v_p$ and adding the edges $v_2v_p, v_3v_1, \dots, v_{p-1}v_1$, we obtain the graph $G' = S_n^3$. This operation is called cycle-shrinking transformation. Denote by W (W' , resp) the set of pendant vertices of G (G' , resp). Let $|W| = k$, $|W'| = k'$. It is clear that $p + k = n$ and $3 + k' = n$. Then, $k' = k + (p - 3)$; thus, W' can be

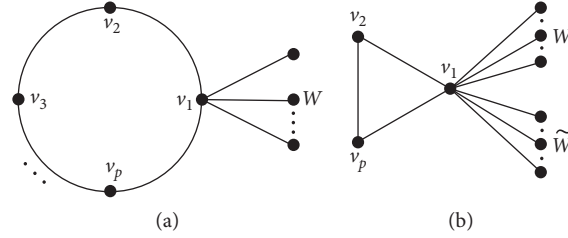
partitioned into two subsets. One has k vertices, which is naturally corresponding to W . So, we also denote it by W ; another has $p - 3$ vertices, denoted by \tilde{W} .

Lemma 4. *Let G be an unicyclic graph of order n and a cycle C_p with $p \geq 4$; if G' can be obtained from G by a cycle-shrinking transformation, then $RDR(G) < RDR(G')$.*

Proof. Consider G and G' shown in Figure 3. By the definition of $RDR(G)$,

$$\begin{aligned}
 RDR(G) &= \sum_{x,y \in W} \frac{d_G(x) + d_G(y)}{r_G(x,y)} + \sum_{x \in W} \frac{d_G(v_1) + d_G(x)}{r_G(v_1,x)} + \sum_{\substack{x \in W \\ y \in \{v_2, v_p\}}} \frac{d_G(x) + d_G(y)}{r_G(x,y)} \\
 &+ \sum_{\substack{x \in W \\ y \in V(C_p) \setminus \{v_1, v_2, v_p\}}} \frac{d_G(x) + d_G(y)}{r_G(x,y)} + \sum_{x \in \{v_2, v_p\}} \frac{d_G(v_1) + d_G(x)}{r_G(v_1,x)} \\
 &+ \sum_{x \in V(C_p) \setminus \{v_1, v_2, v_p\}} \frac{d_G(v_1) + d_G(x)}{r_G(v_1,x)} + \sum_{\substack{x \in V(C_p) \setminus \{v_1, v_2, v_p\} \\ y \in \{v_2, v_p\}}} \frac{d_G(x) + d_G(y)}{r_G(x,y)} \\
 &+ \sum_{x,y \in V(C_p) \setminus \{v_1, v_2, v_p\}} \frac{d_G(x) + d_G(y)}{r_G(x,y)} + \frac{d_G(v_2) + d_G(v_p)}{r_G(v_2, v_p)}, \tag{33}
 \end{aligned}$$

$$\begin{aligned}
 RDR(G') &= \sum_{x,y \in W} \frac{d_{G'}(x) + d_{G'}(y)}{r_{G'}(x,y)} + \sum_{x \in W} \frac{d_{G'}(v_1) + d_{G'}(x)}{r_{G'}(v_1,x)} + \sum_{\substack{x \in W \\ y \in \{v_2, v_p\}}} \frac{d_{G'}(x) + d_{G'}(y)}{r_{G'}(x,y)} \\
 &+ \sum_{x \in W, y \in \tilde{W}} \frac{d_{G'}(x) + d_{G'}(y)}{r_{G'}(x,y)} + \sum_{x \in \{v_2, v_p\}} \frac{d_{G'}(v_1) + d_{G'}(x)}{r_{G'}(v_1,x)} + \sum_{x \in \tilde{W}} \frac{d_{G'}(v_1) + d_{G'}(x)}{r_{G'}(v_1,x)} \\
 &+ \sum_{\substack{x \in W \\ y \in \{v_2, v_p\}}} \frac{d_{G'}(x) + d_{G'}(y)}{r_{G'}(x,y)} + \sum_{x,y \in \tilde{W}} \frac{d_{G'}(x) + d_{G'}(y)}{r_{G'}(x,y)} + \frac{d_{G'}(v_2) + d_{G'}(v_p)}{r_{G'}(v_2, v_p)}.
 \end{aligned}$$

FIGURE 3: The cycle-shrinking transformation. (a) G . (b) G' .

(i) Note that $d_G(x) + d_G(y) = d_{G'}(x) + d_{G'}(y)$, $r_G(x, y) = r_{G'}(x, y)$ for any $x, y \in W$; then, we have

$$\sum_{x, y \in W} \frac{d_G(x) + d_G(y)}{r_G(x, y)} = \sum_{x, y \in W} \frac{d_{G'}(x) + d_{G'}(y)}{r_{G'}(x, y)}. \quad (34)$$

(ii) Note that $d_G(x) + d_G(y) = d_{G'}(x) + d_{G'}(y) = 3$, $r_G(x, y) = (p-1)/p + 1 \geq r_{G'}(x, y) = (2/3) + 1$ for any $x \in W, y \in \{v_2, v_p\}$ in G and $x \in W, y \in \{v_2, v_p\}$ in G' ; then, we have

$$\sum_{\substack{x \in W \\ y \in \{v_2, v_p\}}} \frac{d_{G'}(x) + d_{G'}(y)}{r_{G'}(x, y)} - \sum_{\substack{x \in W \\ y \in \{v_2, v_p\}}} \frac{d_G(x) + d_G(y)}{r_G(x, y)} \geq 0. \quad (35)$$

(iii) Note that $d_G(v_1) + d_G(x) = k + 3$, $d_{G'}(v_1) + d_{G'}(x) = k + p$, $r_G(v_1, x) = r_{G'}(v_1, x) = 1$, for $x \in W$ in G and G' , respectively; then, we have

$$\begin{aligned} \sum_{x \in W} \frac{d_{G'}(v_1) + d_{G'}(x)}{r_{G'}(v_1, x)} - \sum_{x \in W} \frac{d_G(v_1) + d_G(x)}{r_G(v_1, x)} \\ = k(k + p) - k(k + 3) = k(p - 3). \end{aligned} \quad (36)$$

(iv) Note that $d_G(x) + d_G(y) = 3$, $r_G(x, y) = r_G(v_i, v_1) + 1 \geq 2$ ($3 \leq i \leq p-1$) for $x \in W, y \in V(C_p) \setminus \{v_1, v_2, v_p\}$ and $d_{G'}(x) + d_{G'}(y) = 2$, $r_{G'}(x, y) = 2$ for $x \in W, y \in \tilde{W}$; then, we have

$$\begin{aligned} \sum_{\substack{x \in W \\ y \in \tilde{W}}} \frac{d_{G'}(x) + d_{G'}(y)}{r_{G'}(x, y)} - \sum_{\substack{x \in W \\ y \in V(C_p) \setminus \{v_1, v_2, v_p\}}} \frac{d_G(x) + d_G(y)}{r_G(x, y)} \\ \geq k(p - 3) - \frac{3k(p - 3)}{2} = -\frac{k(p - 3)}{2}. \end{aligned} \quad (37)$$

Combing (iii) – (iv), we have

$$\begin{aligned} \left(\sum_{x \in W} \frac{d_{G'}(v_1) + d_{G'}(x)}{r_{G'}(v_1, x)} - \sum_{x \in W} \frac{d_G(v_1) + d_G(x)}{r_G(v_1, x)} \right) \\ + \left(\sum_{\substack{x \in W \\ y \in \tilde{W}}} \frac{d_{G'}(x) + d_{G'}(y)}{r_{G'}(x, y)} \right. \\ \left. - \sum_{\substack{x \in W \\ y \in V(C_p) \setminus \{v_1, v_2, v_p\}}} \frac{d_G(x) + d_G(y)}{r_G(x, y)} \right) \\ \geq \frac{k(p - 3)}{2} \geq 0. \end{aligned} \quad (38)$$

(v) Note that $d_G(v_1) + d_G(x) = k + 4$, $r_G(v_1, x) = (p-1)/p$, and $d_{G'}(v_1) + d_{G'}(x) = k + p + 1$, $r_{G'}(v_1, x) = 2/3$, for $x \in \{v_2, v_p\}$ in G and G' , respectively; then, we have

$$\begin{aligned} \sum_{x \in \{v_2, v_p\}} \frac{d_{G'}(v_1) + d_{G'}(x)}{r_{G'}(v_1, x)} - \sum_{x \in \{v_2, v_p\}} \frac{d_G(v_1) + d_G(x)}{r_G(v_1, x)} \\ = 3(k + p + 1) - \frac{2p(k + 4)}{p - 1} = \frac{(k + 3p + 1)(p - 3)}{p - 1}. \end{aligned} \quad (39)$$

(vi) Note that $d_G(v_1) + d_G(x) = k + 4$, $r_G(v_1, x) = r_G(v_1, v_i) \geq 1$ ($3 \leq i \leq p-1$) for $x \in V(C_p) \setminus \{v_1, v_2, v_p\}$ and $d_{G'}(v_1) + d_{G'}(x) = k + p$, $r_{G'}(v_1, x) = 1$ for $x \in \tilde{W}$; then, we have

$$\sum_{x \in \tilde{W}} \frac{d_{G'}(v_1) + d_{G'}(x)}{r_{G'}(v_1, x)} - \sum_{x \in V(C_p) \setminus \{v_1, v_2, v_p\}} \frac{d_G(v_1) + d_G(x)}{r_G(v_1, x)} \geq (p-3)(k+p) - (p-3)(k+4) = (p-3)(p-4). \tag{40}$$

(vii) Note that $d_G(x) + d_G(y) = 3$ for $x \in V(C_p) \setminus \{v_1, v_2, v_p\}$, $y \in \{v_2, v_p\}$ and $d_{G'}(x) + d_{G'}(y) = 4$, $r_{G'}(x, y) = r_{G'}(v_2, v_1) + 1 = (2/3) + 1 = (5/3)$ for $x \in \tilde{W}$, $y \in \{v_2, v_p\}$; by the symmetry between v_2 and v_p , we have

$$\sum_{\substack{x \in \tilde{W} \\ y \in \{v_2, v_p\}}} \frac{d_{G'}(x) + d_{G'}(y)}{r_{G'}(x, y)} - \sum_{\substack{x \in V(C_p) \setminus \{v_1, v_2, v_p\} \\ y \in [v_2, v_p]}} \frac{d_G(x) + d_G(y)}{r_G(x, y)} = 2 \sum_{i=3}^{p-1} \frac{3}{r_{G'}(v_2, v_1) + 1} - 2 \sum_{i=3}^{p-1} \frac{4}{r_G(v_2, v_i)} = \frac{18(p-3)}{5} - \left(\frac{8p}{p-1} + 2 \sum_{i=4}^{p-1} \frac{4}{r_G(v_2, v_i)} \right). \tag{41}$$

Since $r_G(v_2, v_i) \geq r_G(v_2, v_4) = ((2(p-2))/p)$ ($4 \leq i \leq p-1$), if $((2(p-2))/p) \geq (5/3)$, then $p \geq 12$.

Then,

$$2 \sum_{i=4}^{p-1} \frac{4}{r_G(v_2, v_i)} \leq \frac{24(p-4)}{5}. \tag{42}$$

Thus,

$$\sum_{\substack{x \in \tilde{W} \\ y \in \{v_2, v_p\}}} \frac{d_{G'}(x) + d_{G'}(y)}{r_{G'}(x, y)} - \sum_{\substack{x \in V(C_p) \setminus \{v_1, v_2, v_p\} \\ y \in [v_2, v_p]}} \frac{d_G(x) + d_G(y)}{r_G(x, y)} \geq \frac{18(p-3)}{5} - \left(\frac{8p}{p-1} + \frac{24(p-4)}{5} \right). \tag{43}$$

(viii) Note that $d_G(x) + d_G(y) = 4$, $r_G(x, y) = r_G(v_i, v_j)$ ($3 \leq i < j \leq p-1$) for $x, y \in V(C_p) \setminus \{v_1, v_2, v_p\}$ and $d_{G'}(x) + d_{G'}(y) = 2$, $r_{G'}(x, y) = 2$ for $x, y \in \tilde{W}$; then, we have

$$\sum_{x, y \in \tilde{W}} \frac{d_{G'}(x) + d_{G'}(y)}{r_{G'}(x, y)} - \sum_{x, y \in V(C_p) \setminus \{v_1, v_2, v_p\}} \frac{d_G(x) + d_G(y)}{r_G(x, y)} = \frac{(p-3)(p-4)}{2} - \sum_{i, j=3, i < j}^{p-1} \frac{4}{r_G(v_i, v_j)}. \tag{44}$$

Then,

$$\sum_{i, j=3, i < j}^{p-1} \frac{4}{r_G(v_i, v_j)} = \sum_{i=4}^p \frac{d_G(v_3) + d_G(v_i)}{r_G(v_3, v_i)} + \sum_{i=5}^p \frac{d_G(v_4) + d_G(v_i)}{r_G(v_4, v_i)} + \dots + \frac{d_G(v_{p-2}) + d_G(v_{p-1})}{r_G(v_{p-2}, v_{p-1})}. \tag{45}$$

When $j - i = t$ ($i < j$), $r_G(v_i, v_j) = r_t = r_{p-t}$; thus,

$$\sum_{i=4}^p \frac{d_G(v_3) + d_G(v_i)}{r_G(v_3, v_i)} = \frac{4}{r_1} + \frac{4}{r_2} + \dots + \frac{4}{r_{p-4}},$$

$$\sum_{i=5}^p \frac{d_G(v_4) + d_G(v_i)}{r_G(v_4, v_i)} = \frac{4}{r_1} + \dots + \frac{4}{r_{p-5}},$$

...

$$\frac{d_G(v_{p-2}) + d_G(v_{p-1})}{r_G(v_{p-2}, v_{p-1})} = \frac{4}{r_1}$$

and

$$\sum_{x, y \in V(C_p) \setminus \{v_1, v_2, v_p\}} \frac{d_G(x) + d_G(y)}{r_G(x, y)} = \frac{4(p-4)}{r_1} + \frac{4(p-5)}{r_2} + \dots + \frac{4}{r_{p-4}}. \tag{47}$$

Since $r_1 = ((p-1)/p)$, $r_t \geq r_2 = (2(p-2))/p$ ($2 \leq t \leq p-4$), if $(2(p-2))/p \geq (5/3)$, then $p \geq 12$.

Then,

$$\sum_{x, y \in V(C_p) \setminus \{v_1, v_2, v_p\}} \frac{d_G(x) + d_G(y)}{r_G(x, y)} \leq \frac{4p(p-4)}{p-1} + \frac{6(p-4)(p-5)}{5}. \tag{48}$$

Thus,

$$\begin{aligned} & \sum_{x,y \in \tilde{W}} \frac{d_{G'}(x) + d_{G'}(y)}{r_{G'}(x,y)} - \sum_{x,y \in V(C_p) \setminus \{v_1, v_2, v_p\}} \frac{d_G(x) + d_G(y)}{r_G(x,y)} \\ & \geq \frac{(p-3)(p-4)}{2} - \left(\frac{4p(p-4)}{p-1} + \frac{6(p-4)(p-5)}{5} \right). \end{aligned} \quad (49)$$

When $p \geq 12$, combing (v) – (viii), we have

$$\begin{aligned} & \left(\sum_{x \in \{v_2, v_p\}} \frac{d_{G'}(v_1) + d_{G'}(x)}{r_{G'}(v_1, x)} - \sum_{x \in \{v_2, v_p\}} \frac{d_G(v_1) + d_G(x)}{r_G(v_1, x)} \right) \\ & + \left(\sum_{x \in \tilde{W}} \frac{d_{G'}(v_1) + d_{G'}(x)}{r_{G'}(v_1, x)} - \sum_{x \in V(C_p) \setminus \{v_1, v_2, v_p\}} \frac{d_G(v_1) + d_G(x)}{r_G(v_1, x)} \right) \\ & + \left(\sum_{x \in \tilde{W}} \sum_{y \in \{v_2, v_p\}} \frac{d_{G'}(x) + d_{G'}(y)}{r_{G'}(x,y)} - \sum_{x \in V(C_p) \setminus \{v_1, v_2, v_p\}} \sum_{y \in \{v_2, v_p\}} \frac{d_G(x) + d_G(y)}{r_G(x,y)} \right) \\ & + \left(\sum_{x,y \in \tilde{W}} \frac{d_{G'}(x) + d_{G'}(y)}{r_{G'}(x,y)} - \sum_{x,y \in V(C_p) \setminus \{v_1, v_2, v_p\}} \frac{d_G(x) + d_G(y)}{r_G(x,y)} \right) \\ & \geq \frac{(k+3p+1)(p-3)}{p-1} + \frac{3(p-3)(p-4)}{2} + \frac{18(p-3)}{5} - \frac{4p(p-2)}{p-1} - \frac{6(p-1)(p-4)}{5} \\ & = \frac{3p^3 - 22p^2 + 33p - 54 + k(10p - 30)}{10(p-1)}. \end{aligned} \quad (50)$$

Let $f(p) = 3p^3 - 22p^2 + 33p - 54$, $p \in [12, +\infty)$; this function is strictly increasing in this interval; thus, $f(p) \geq f(12) = 2358 > 0$.

Hence,

$$\frac{3p^3 - 22p^2 + 33p - 54 + k(10p - 30)}{10(p-1)} > 0. \quad (51)$$

(ix) Note that $d_G(x) + d_G(y) = 4$, $r_G(v_2, v_p) = ((2(p-2))/p)$ for $x \in \{v_2, v_p\}$ in G and $d_{G'}(x) + d_{G'}(y) = 4$, $r_{G'}(v_2, v_p) = (2/3)$ for $x \in \{v_2, v_p\}$ in G' ; then, we have

$$\frac{d_{G'}(v_2) + d_{G'}(v_p)}{r_{G'}(v_2, v_p)} - \frac{d_G(v_2) + d_G(v_p)}{r_G(v_2, v_p)} = 6 - \frac{2p}{p-2}$$

$$= \frac{4p-12}{p-2} > 0. \quad (52)$$

Thus, by (i)–(ix), when $p \geq 12$, we get $\text{RDR}(G') - \text{RDR}(G) > 0$.

When $4 \leq p \leq 11$, $U_n(G_0) = \{S_n^4, S_n^5, S_n^6, S_n^7, S_n^8, S_n^9, S_n^{10}, S_n^{11}\}$. By comparison of direct calculation, we can obtain $\text{RDR}(S_n^3) > \text{RDR}(S_n^p)$.

The proof is completed. \square

3. Maximum Reciprocal Degree Resistance Distance Index of Unicyclic Graphs

Let G be a connected graph with exactly one cycle, say $C_p = v_1 v_2 \cdots v_p v_1$. G can be viewed as a graph obtained by coalescing C_p with a number of trees, denoted by G_1, G_2, \dots, G_p , by identifying v_i with some vertex of G_i for all i ($1 \leq i \leq p$). Denote S_n^3 by the unicyclic graph obtained from cycle C_3 by attaching $n - 3$ pendant edges to a vertex of C_3 . The next theorem discusses the maximum reciprocal degree resistance distance index in \mathcal{U}_n , which is the main result of our work.

Theorem 1. *Let G be a unicyclic graph of order n ; then, $RDR(G) \leq RDR(S_n^3)$, and the equality holds if and only if $G \cong S_n^3$.*

Proof. Let G be a unicyclic graph of order n such that $\xi(G)$ is as big as possible. By Lemmas 2–4, we have $RDR(G) \leq RDR(S_n^3)$; the equality holds if and only if $G \cong S_n^3$. \square

Data Availability

The data used to support the findings of this study are included within the article.

Conflicts of Interest

The authors declare that there are no conflicts of interest regarding the publication of this paper.

Acknowledgments

This study was jointly supported by the National Natural Science Foundation of China (11871077), the Natural Science Foundation of Anhui Province (1808085MA04), and the Natural Science Foundation of Department of Education of Anhui Province (KJ2017A362).

References

- [1] H. Wiener, "Structural determination of paraffin boiling points," *Journal of the American Chemical Society*, vol. 69, no. 1, pp. 17–20, 1947.
- [2] H. Hosoya, "Topological index. A newly proposed quantity characterizing the topological nature of structural isomers of saturated hydrocarbons," *Bulletin of the Chemical Society of Japan*, vol. 44, no. 9, pp. 2332–2339, 1971.
- [3] K. Xu, M. Liu, K. C. Das, I. Gutman, and B. Furtula, "A survey on graphs extremal with respect to distancebased topological indices," *MATCH Communications in Mathematical and in Computer Chemistry*, vol. 71, pp. 461–508, 2014.
- [4] I. Gutman, "Degree-based topological indices," *Croatica Chemica Acta*, vol. 86, no. 4, pp. 351–361, 2013.
- [5] K. C. Das, I. Gutman, and M. J. Nadjafi-Arani, "Relations between distance-based and degree-based topological indices," *Applied Mathematics and Computation*, vol. 270, pp. 142–147, 2015.
- [6] D. Plavšić, S. Nikolić, N. Trinajstić, and Z. Mihalić, "On the Harary index for the characterization of chemical graphs," *Journal of Mathematical Chemistry*, vol. 12, no. 1, pp. 235–250, 1993.
- [7] O. Ivanciuc, T.-S. Balaban, and A. T. Balaban, "Design of topological indices. Part 4. Reciprocal distance matrix, related local vertex invariants and topological indices," *Journal of Mathematical Chemistry*, vol. 12, no. 1, pp. 309–318, 1993.
- [8] B. Furtula, I. Gutman, and V. Katanic, "Three-center Harary index and its applications," *Iranian Journal of Mathematical Chemistry*, vol. 7, pp. 61–68, 2016.
- [9] L. Feng, Y. Lan, W. Liu, and X. Wang, "Minimal Harary index of graphs with small parameters," *MATCH Communications in Mathematical and in Computer Chemistry*, vol. 76, pp. 23–42, 2016.
- [10] X.-X. Li and Y.-Z. Fan, "The connectivity and the Harary index of a graph," *Discrete Applied Mathematics*, vol. 181, pp. 167–173, 2015.
- [11] S. Pirzada, H. A. Ganie, and I. Gutman, "On laplacian-energy-like invariant and Kirchhoff index," *MATCH Communications in Mathematical and in Computer Chemistry*, vol. 73, pp. 41–59, 2015.
- [12] K. Xu and K. C. Das, "On Harary index of graphs," *Discrete Applied Mathematics*, vol. 159, no. 15, pp. 1631–1640, 2011.
- [13] K. Xu, "Trees with the seven smallest and eight greatest Harary indices," *Discrete Applied Mathematics*, vol. 160, no. 3, pp. 321–331, 2012.
- [14] K. Xu and K. C. Das, "Extremal unicyclic and bicyclic graphs with respect to Harary index," *Bulletin of the Malaysian Mathematical Sciences Society*, vol. 36, pp. 373–383, 2013.
- [15] K. Xu, J. Wang, K. C. Das, and S. Klavžar, "Weighted Harary indices of apex trees and k -apex trees," *Discrete Applied Mathematics*, vol. 189, pp. 30–40, 2015.
- [16] G. Yu and L. Feng, "On the maximal Harary index of a class of bicyclic graphs," *Utilitas Mathematica*, vol. 82, pp. 285–292, 2010.
- [17] B. Zhou, X. Cai, and N. Trinajstić, "On Harary index," *Journal of Mathematical Chemistry*, vol. 44, no. 2, pp. 611–618, 2008.
- [18] D. Bonchev, A. T. Balaban, X. Liu, and D. J. Klein, "Molecular cyclicity and centrality of polycyclic graphs. I. Cyclicity based on resistance distances or reciprocal distances," *International Journal of Quantum Chemistry*, vol. 50, no. 1, pp. 1–20, 1994.
- [19] D. J. Klein and M. Randić, "Resistance distance," *Journal of Mathematical Chemistry*, vol. 12, no. 1, pp. 81–95, 1993.
- [20] R. B. Bapat, M. Karimi, and J.-B. Liu, "Kirchhoff index and degree Kirchhoff index of complete multipartite graphs," *Discrete Applied Mathematics*, vol. 232, pp. 41–49, 2017.
- [21] H. Deng, "On the minimum Kirchhoff index of graphs with a given number of cutedges," *MATCH Communications in Mathematical and in Computer Chemistry*, vol. 63, pp. 171–180, 2010.
- [22] J.-B. Liu, J. Cao, A. Alofi, A. Al-Mazrooei, and A. Elaiw, "Applications of Laplacian spectra for n -prism networks," *Neurocomputing*, vol. 198, pp. 69–73, 2016.
- [23] J.-B. Liu, W.-R. Wang, Y.-M. Zhang, and X.-F. Pan, "On degree resistance distance of cacti," *Discrete Applied Mathematics*, vol. 203, pp. 217–225, 2016.
- [24] J.-B. Liu and X.-F. Pan, "Minimizing Kirchhoff index among graphs with a given vertex bipartiteness," *Applied Mathematics and Computation*, vol. 291, pp. 84–88, 2016.
- [25] A. Nikseresht, "On the minimum Kirchhoff index of graphs with a fixed number of cut vertices," *Discrete Applied Mathematics*, vol. 207, pp. 99–105, 2016.
- [26] J. L. Palacios, "On the Kirchhoff index of graphs with diameter 2," *Discrete Applied Mathematics*, vol. 184, pp. 196–201, 2015.

- [27] K. Xu, H. Liu, Y. Yang, and K. Das, "The minimal Kirchhoff index of graphs with a given number of cut vertices," *Filomat*, vol. 30, no. 13, pp. 3451–3463, 2016.
- [28] K. Xu, K. C. Das, and X.-D. Zhang, "Ordering connected graphs by their Kirchhoff indices," *International Journal of Computer Mathematics*, vol. 93, no. 10, pp. 1741–1755, 2016.
- [29] Y. Yang, "The Kirchhoff index of subdivisions of graphs," *Discrete Applied Mathematics*, vol. 171, pp. 153–157, 2014.
- [30] B. Zhou and N. Trinajstić, "A note on Kirchhoff index," *Chemical Physics Letters*, vol. 455, no. 1–3, pp. 120–123, 2008.
- [31] H. Zhang, X. Jiang, and Y. Yang, "Bicyclic graphs with extremal Kirchhoff index," *MATCH Communications in Mathematical and in Computer Chemistry*, vol. 61, pp. 697–712, 2009.
- [32] S. Chen, Z. Guo, T. Zeng, and L. Yang, "On the resistance-Harary index of unicyclic graphs," *MATCH Communications in Mathematical and in Computer Chemistry*, vol. 78, pp. 189–198, 2017.
- [33] H. Wang, H. Hua, L. Zhang, and S. Wen, "On the resistance-harary index of graphs given cut edges," *Journal of Chemistry*, vol. 2017, Article ID 3531746, 7 pages, 2017.
- [34] W. Fang, Y. Wang, J.-B. Liu, and G. Jing, "Maximum resistance-Harary index of cacti," *Discrete Applied Mathematics*, vol. 251, pp. 160–170, 2018.
- [35] I. Gutman, B. Rušćić, N. Trinajstić, and C. F. Wilcox, "Graph theory and molecular orbitals. xii. Acyclic polyenes," *The Journal of Chemical Physics*, vol. 62, no. 9, pp. 3399–3045, 1975.
- [36] I. Gutman and N. Trinajstić, "Graph theory and molecular orbitals. Total ϕ -electron energy of alternant hydrocarbons," *Chemical Physics Letters*, vol. 17, no. 4, pp. 535–538, 1972.
- [37] I. Gutman, "An exceptional property of first zagreb index," *MATCH Communications in Mathematical and in Computer Chemistry*, vol. 72, pp. 733–740, 2014.
- [38] H. Lin, "Vertices of degree two and the first zagreb index of trees," *MATCH Communications in Mathematical and in Computer Chemistry*, vol. 72, pp. 301–310, 2014.
- [39] A. A. Dobrynin and A. A. Kochtova, "Degree distance of a graph: a degree analogue of the Wiener index," *Journal of Chemical Information and Modeling*, vol. 34, 1994.
- [40] I. Gutman, "Selected properties of the Schultz molecular topological index," *Journal of Chemical Information and Modeling*, vol. 34, no. 5, pp. 1087–1089, 1994.
- [41] Y. Alizadeh, A. Iranmanesh, and T. Došlić, "Additively weighted Harary index of some composite graphs," *Discrete Mathematics*, vol. 313, no. 1, pp. 26–34, 2013.
- [42] H. Hua and S. Zhang, "On the reciprocal degree distance of graphs," *Discrete Applied Mathematics*, vol. 160, no. 7–8, pp. 1152–1163, 2012.
- [43] S. C. Li and X. Meng, "Four edge-grafting theorems on the reciprocal degree distance of graphs and their applications," *Journal of Combinatorial Optimization*, vol. 30, no. 3, pp. 468–488, 2015.

Research Article

DNA Origami Model for Simple Image Decoding

Risheng Wang,¹ Zhixiang Yin ,² Jianzhong Cui,¹ Jing Yang,¹ Zhen Tang,¹ Xinmu Yang,¹ and Xianya Geng¹

¹Anhui University of Science and Technology, Huainan, China

²Shanghai University of Engineering Science, Songjiang, China

Correspondence should be addressed to Zhixiang Yin; zxyin66@163.com

Received 24 April 2020; Accepted 18 May 2020; Published 3 August 2020

Academic Editor: Jia-Bao Liu

Copyright © 2020 Risheng Wang et al. This is an open access article distributed under the Creative Commons Attribution License, which permits unrestricted use, distribution, and reproduction in any medium, provided the original work is properly cited.

DNA origami is the application of self-assembly in nanotechnology. The combination of DNA origami and hybridization chain reaction is one of the important application methods of DNA origami. In this paper, DNA origami is used to design the cipher pattern on the base of origami. The cipher chain, which is put into the reaction solution, hybridizes with the molecular beacon and the hairpin structure that form the cipher pattern to build a DNA origami model that can decode the pattern. The cipher chain consists of the starting chain and the intermediate chain. When the cipher is correct, the cipher chain can open the molecular beacon and the hairpin structure to display the cipher pattern on the origami base in the solution.

1. Introduction

DNA origami is a DNA self-assembly method proposed in recent years. The concept of DNA origami was proposed firstly by Rothemund [1]. Compared with traditional DNA self-assembly, DNA origami is easier in constructing highly complex and structurally stable nanostructures. It also has addressability, which is a significant progress in the field of DNA self-assembly and DNA nanotechnology. Through DNA origami technology, Qian and his team successfully constructed the map of China, further proving that DNA origami has the ability to construct almost any complex two-dimensional nanoshape [2]. In 2011, Han et al. studied the stereoscopic vase structure that can precisely regulate the three-dimensional surface and pushed the research of DNA origami in the structural design and manufacturing to the climax [3, 4]. In 2013, the bipedal DNA Walker played a key role in the research of DNA origami “orbit” [5]. In 2014, DNA origami robots were designed for conventional computing [6]. In the same year, Koirala and his team combined DNA origami nanostructures to mechanochemical sensors [7]. In 2017, Tikhomirov et al. used the square DNA origami as the basic unit to obtain the pattern of the Mona Lisa at the micron level, further proving the ability

of DNA origami to construct any complex pattern, indicating the addressability of DNA origami [8]. In 2018, Chao combined DNA origami with hybridization chain reaction to solve the maze problem [9]. The substrate constructed by DNA origami has great advantages in assembling functional carbon nanotubes, nanoparticles, and proteins. Many complex and diverse nanostructures have been designed and assembled [10–12]. DNA origami can construct highly complex nanostructures, which has great potential in the “nano” field. Wang and his team used DNA origami nanostructures to visualize cell uptake and metastasis in tumor cells [13]. In fact, DNA origami has been applied to single molecule detection [14, 15] and logic operation [16, 17]. DNA origami has been used as the carbon nanotubes, protein structure, and the basic template for the assembly of functional metal nanoparticles [18–22].

The combination of DNA origami and hybridization chain reaction is one of the important application methods of DNA origami. Hybridization chain reaction (HCR) is a new signal amplification method based on DNA hybridization proposed by Dirks and Pierce in 2004. This is an isothermal amplification technology, which greatly simplifies the requirements of the instrument. It only needs simple temperature control equipment such as heating

module and water bath pot to complete the signal amplification of hybridization chain reaction [23]. When there are only two kinds of DNA strands in the test tube solution, they are stable in the solution and will not be hybridized and opened. Once the starting DNA strand is added, the two kinds of DNA strands will be hybridized alternately to form a long double stranded DNA polymer with a gap. The use of hybridization chain reaction can not only amplify the signal of single strand DNA, but also amplify the signal of other biological molecules. It can induce oligonucleotides to hybridize with each other using a small segment of nucleotide chain as initiator to form a single strand DNA with two-dimensional or three-dimensional spatial structure by designing different oligonucleotides reasonably [23, 24]. At present, hybridization chain reaction has been widely used in nucleic acid, protein detection, biosensor, and other fields [25–29]. Dong and his team combined the hybridization chain reaction with G-quadruplex to construct a fluorescent sensor for target DNA unmarked detection. The target DNA can be detected by changing the fluorescence intensity before and after the reaction [30]. Xiao et al. designed a variety of chemiluminescence imaging technologies by combining DNA microarray with hybridization chain reaction amplification induced by adjacent binding and used them in sensitive screening and detection of protein biomarkers [31]. Li et al. proposed a method to light up the fluorescent sensor by using hybridization chain reaction and DNA three-strand assembly [32]. Because of the advantages of simple operation and low cost, this method has high application value in biomarker determination, clinical diagnosis, and biomedical detection.

We use DNA origami to design the cipher pattern on the base of origami. We put the cipher chain into the reaction solution, which carry on the hybridization chain reaction with the molecular beacon and the hairpin structure that form the cipher pattern. It could establish the DNA origami model, which can decode the pattern. It has been proved that hybridization chain reaction and DNA origami structure have the good application prospect in this field [33–46]. The cipher chain is composed of the starting chain and the intermediate chain containing the password. Through the reaction with the origami base containing the cipher pattern in the solution, the pattern is displayed when the cipher is correct. The pattern is observed by imaging with atomic force microscope.

2. DNA Origami and Hybridization Chain Reaction

2.1. DNA Origami. DNA origami refers to folding a long *M13mp18 phage* DNA strand back and forth as a scaffold chain and using multiple staples to fix the shape to obtain fine and complex two-dimensional structure. Compared with the self-assembly of DNA module, the design of DNA strand in DNA origami is relatively simple. It also have high assembly efficiency, nano-addressable characteristics (realized by redesigning the single strand at the designated position of staple chain and scaffold chain), and the ability to construct more complex and fine patterns. The substrate

constructed by DNA origami has great advantages in assembling functional carbon nanotubes, nanoparticles, proteins, and so on.

2.2. Hybridization Chain Reaction. Hybridization chain reaction (HCR) is a new signal amplification method proposed by Dirks and Pierce. It can induce oligonucleotides to hybridize with each other to form DNA with spatial structure using a small segment of nucleotide chain as initiator by rationally designing different oligonucleotides. The hybridization chain reaction is to induce DNA molecules of two different types of hairpin structures to hybridize alternately by using the starting chain, open the hairpin structure alternately, and form a double strand DNA nanowire with a gap. And this process does not need enzyme participation; the reaction conditions are mild; the operation is simple. The reaction principle is shown in Figure 1.

C_1 and C_2 are two DNA strands of hairpin structure, which can exist in solution at the same time and can remain stable without any hybridization reaction. C_1 and C_2 are all composed of three parts, the sticky end, the “stem” in the form of double chain, and the ring part of single chain, as shown in Figure 1 (1). Among them, b and b^* are base complementary and exist in the form of double chain, called the stem of $C_1(C_2)$ chain; a is the single chain sticky extending from the “stem” of C_1 chain, and the single chain segment c of hairpin is called the ring of C_1 chain; accordingly, a^* is the C_2 chain ring, and c^* is the single chain sticky end extending from the “stem” of C_2 chain. We can call T initiation chain, which is a DNA single strand composed of a^* and b^* parts. When the initiation chain T is added, the a^* and b^* segments hybridize with the sticky end a and stem b of C_1 , respectively. The hairpin segment of C_1 is opened, and the segment $c - b^*$ is exposed in the form of a single chain, as shown in Figure 1 (2). The segment $c - b^*$ exposed by C_1 and segment $c^* - b$ of C_2 have a hybridization chain reaction. The hairpin section of C_2 is opened, and the segment $a^* - b^*$ is exposed by C_2 , as shown in Figure 1 (3). The exposed segment $a^* - b^*$ of C_2 continues to hybridize with the next C_1 and open the hairpin structure. It will circulate and react successively until the C_1 and C_2 in the solution are exhausted. Finally, alternating hybridization of C_1 and C_2 assembled spontaneously a long DNA nanowire. Each initiation chain T is equivalent to the growth site of a DNA nanowire. With the concentration of “fuel” C_1 and C_2 being constant and sufficient, the higher the concentration of the initiation chain T is, the shorter the nanowire is and the smaller the molecular weight is.

3. DNA Origami Model

3.1. Composition of the Model. Because of the simple image design, we give a simple cipher image circuit diagram of “Tian,” shaped as the Chinese character “Field.”

There are three lines in the horizontal and vertical direction of the circuit diagram, and each line has two short paths (two short edges) with a total of 12 edges. The 12 edges of the circuit diagram can be used to design simple cipher

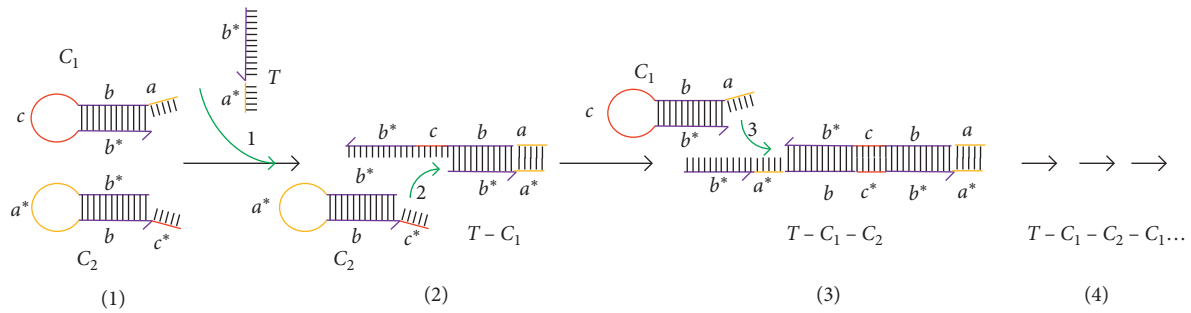


FIGURE 1: Basic principle of hybridization chain reaction.

image. The circuit diagram is mapped on the origami base, which is composed of several molecular beacons and ordinary hairpin structure fixed on the DNA origami base. Among them, there are nine ordinary hairpin structures at the vertices and intersections of the circuit diagram, which are fixed on the origami base in the form of three in each row and three rows in total; there are molecular beacons with a fluorescence group and a quenching group on each edge (between the two adjacent hairpin structures) of the circuit diagram, a total of 12, as shown in Figure 2(a). We use the short chain to fold the circular phage into a two-dimensional rectangle as the origami base (shown in gray in the figure). At a certain distance on the origami base, we extend the staple chain with the sticky end (shown in light blue in the figure), which is connected with the hairpin structures (including molecular beacon and ordinary hairpin structure). The red one is the molecular beacon with fluorescence and quenching group, and the dark blue one is the ordinary hairpin structure.

The structure of molecular beacon and hairpin structure is basically the same. They are all composed of five-segment oligonucleotide fragments, with two segments that complement each other to form the “stems” of the chain. One is the “ring” of the chain, and the other is complementary to the sticky end of a stapling chain extending on the origami base, which fixes the chain on the origami base. Only compared with the ordinary hairpin structure, the two sticky ends of the molecular beacon have luminescent fluorescence groups and quenching groups. They do not light up when they are not turned on. And they only turn on and shine when the starting chain and the intermediate auxiliary chain (collectively referred to here as “the cipher chain”) are added. And the ordinary hairpin structure plays a role of route guidance to avoid causing other neighboring molecular beacons to open in advance when opening these molecular beacons, so that it can be opened according to the designed route. In this way, the molecular beacons fixed on the origami base can be used for simple cipher image design, and the corresponding molecular beacons need to be opened to display the cipher pattern.

To open the corresponding molecular beacon, a cipher chain needs to be added, which is composed of a starting chain and an intermediate chain, as shown in Figure 2(b). The starting chain consists of two oligonucleotide fragments, as shown in the left side of Figure 2(b); the intermediate chain consists of four oligonucleotide fragments, as shown in

the right side of Figure 2(b). Only the chain containing the correct fragment can open the corresponding molecular beacon, and then the cipher pattern can be displayed.

3.2. *The Construction of Cipher and the Realization of Decoding.* According to the composition of the model, we designed a cipher pattern and according to the cipher pattern, we designed the base sequence of hairpin structure (including molecular beacon and hairpin structure) on origami base. The base sequence of each hairpin structure passed by the pattern is almost the same. It is only different from the base sequence of molecular beacon and hairpin structure at the binding marker, and the base sequence of hairpin structure of the starting point at the junction of the starting chain, as shown in Figure 3(a). We set the top left as the starting point of the cipher pattern, and the cipher pattern we designed is the dotted brown line on the graph below. The base sequence of hairpin structure in other positions is different from it, so it will not react with it and open it.

In the cipher pattern on this origami substrate, all hairpin structures can be regarded as consisting of five segments of oligonucleotide fragments. One of the segments is complementary to the sticky end of a staple chain extending on the origami base and is not marked with letters. The remaining four segments are marked with letters as shown in the hairpin structure on Figure 3(a). Segments a and a^* are the stems of the hairpin structure, and they are complementary; segment c is the loop of the hairpin structure. The above oligonucleotide fragments are the same in all the hairpin structures. Only compared to the ordinary hairpin structure, the two sticky ends of the a and a^* segments of the molecular beacon have luminescent fluorescent groups and quenching groups. The hairpin structure of the starting point is different from other hairpin structures in the oligonucleotide fragment combined with the starting chain, and we mark it as the x segment. We mark other hairpin structures of this segment as the e segment.

The base sequence of the hairpin structure in the position of noncipher pattern is different from that in the position of cipher pattern, so that the cipher chain will not react with it and this hairpin structure will not be opened. In order to simplify the design of hairpin structure, we can only design different noncipher pattern hairpin structure adjacent to the

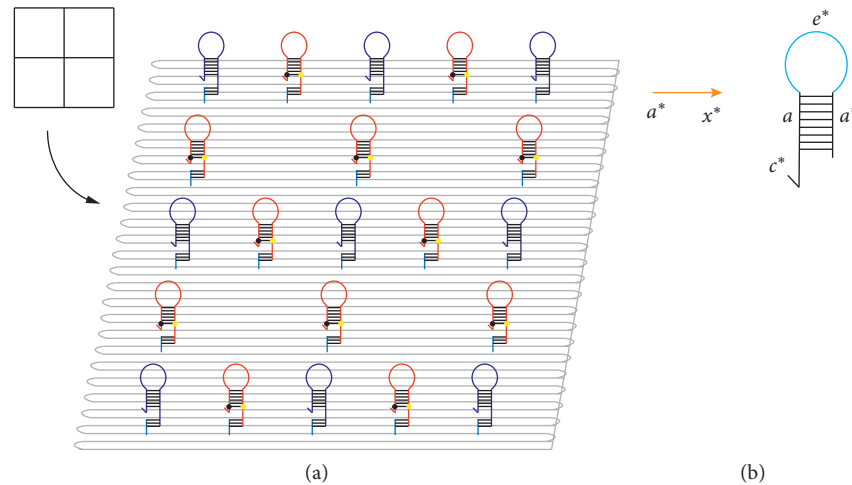


FIGURE 2: (a) Circuit diagram of origami base and hairpin structure; (b) cipher chain, consisting of starting chain (left) and intermediate chain (right).

hairpin structure at the location of cipher pattern to avoid other hairpin structures participating in the reaction.

We put the designed origami base into the solution in advance. Then we add the cipher chain to the solution. The hairpin structure of the starting point has a special oligonucleotide fragment, which can be specifically combined with the starting chain in the cipher chain, thereby ensuring the uniqueness of the starting point.

When the cipher chain is added to the solution, the starting chain will open the hairpin structure of the starting point. The opening process is shown in Figure 3(b). The x^* segment of the starting chain will complement and pair with the x segment of the starting point hairpin structure, and the a^* segment of the starting chain will complement and pair with the a segment of the starting point hairpin structure, thereby opening the hairpin structure. The hairpin c segment and a^* segment of the hairpin structure will be complementarily paired with the intermediate chain c^* segment and the a segment of the cipher chain, thereby opening the intermediate chain. The loop e^* segment and a^* segment of the intermediate chain can continue to be complementary paired with the e segment and a segment of the molecular beacon, thereby opening the molecular beacon to make the pattern glow.

Another molecular beacon adjacent to the starting point hairpin structure will not open (that is, the cipher pattern will not pass through) because its base sequence structure is different from the intermediate chain. In this way, according to the designed cipher pattern, the hairpin structure can be opened in sequence; the starting chain can open the hairpin structure of the starting point; the hairpin structure opens the intermediate chain; the intermediate chain is opening the molecular beacon; the molecular beacon lights up; and then the molecular beacon opens the intermediate chain so as to finally display the cipher pattern, as shown in Figure 3(c). At the same time, the intermediate chain can only open the

adjacent hairpin structure of the previous one, thereby avoiding mismatches.

The circuit diagram of cipher pattern we designed does not directly arrange the molecular beacons in order. The addition of ordinary hairpin structures between the molecular beacons can avoid the situation that there is a fold back in the path of cipher pattern and the opening sequence cannot follow the design image. As shown in Figure 4(a), T_1 goes through T_2 to T_3 instead of directly from T_1 to T_3 . The correct and wrong opening methods are shown in Figure 4(b).

We pour the cipher chain into the solution. If the cipher chain is correct, the starting chain can open the hairpin structure at the starting point, and then the intermediate chain of the cipher chain can sequentially open the hairpin structure that the cipher pattern passes through. And the opened molecular beacon will light up to display the cipher pattern. If the cipher is not correct, no matter the base sequence in the starting chain or the intermediate chain is wrong, the hairpin structure cannot be opened to display the cipher pattern. As shown in Figure 4(c), the upper part is the open figure with correct cipher chain display, and the lower part is the figure with wrong cipher chain display (this is the starting chain error).

We also consider hiding the base code of the intermediate chain, and the correct code is its password. Since the encryption algorithm of DNA coding has been very mature, we hide the base sequence of intermediate chain. After only obtaining its decoding method, completing the decoding, and finding the corresponding intermediate chain to match, we could get the correct cipher pattern while putting the cipher chain into the solution. If the decoding is not successful, we will not get the final correct cipher pattern. In this way, we can make the cipher chain more secure. We should have not only the cipher chain but also the correct method for decoding the cipher chain, so

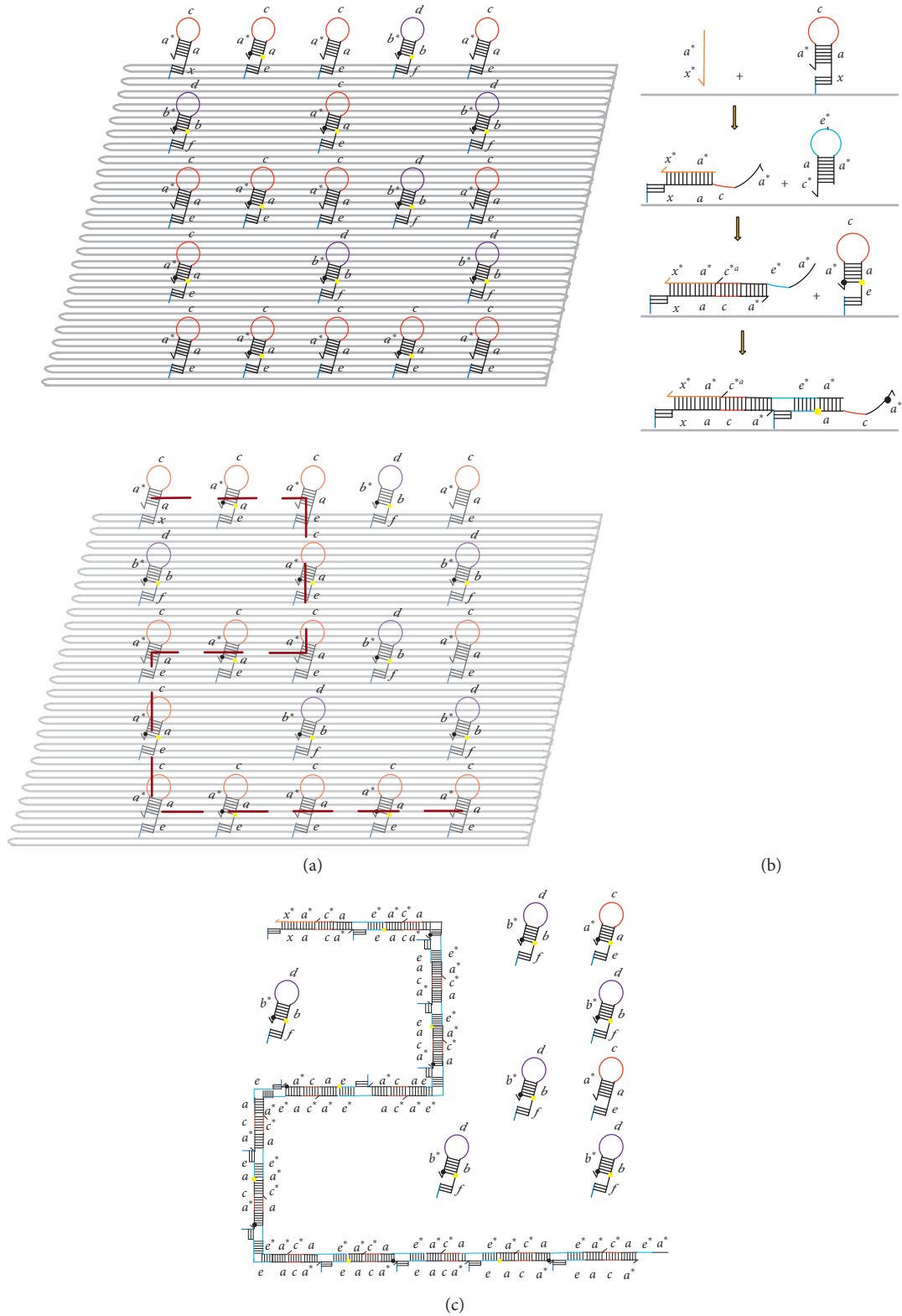


FIGURE 3: (a) The hairpin structure and cipher pattern designed on origami base; (b) the opening process after adding the cipher chain; (c) the cipher pattern after opening.

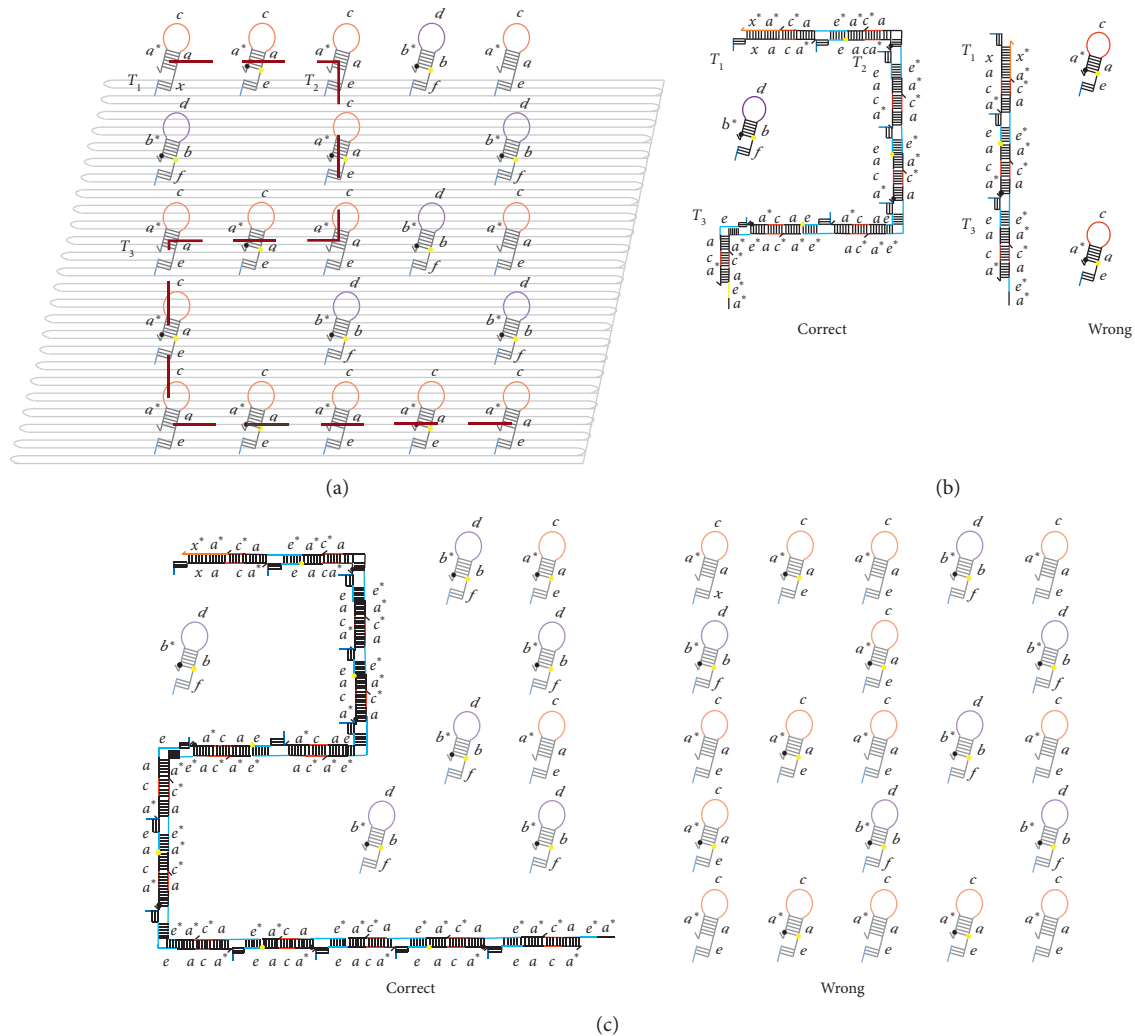


FIGURE 4: (a) Cipher pattern to be displayed on the origami base; (b) the correct and wrong ways to open the designed cipher diagram in the reaction; (c) origami base figure after adding cipher chain to react.

that the correct answer can form the correct path. This is what we will do next.

4. Conclusion

In this paper, DNA origami model for simple image decoding is established by combining DNA origami with hybridization chain reaction. We design the hairpin structure on the origami base, which can decode the simple cipher pattern. The correct cipher chain composed of a starting chain and an intermediate chain can open the molecular beacon and display the cipher pattern. But the hairpin structure is a one-time channel, which cannot be reused; the cipher pattern cannot be designed to crossovers. With the development of molecular biology and bioengineering, the method is expected to have more progress in reusability and can further be expanded to solve more complex decoding problems.

Data Availability

The data used to support the findings of this study are available from the corresponding author upon request.

Conflicts of Interest

The authors declare that they have no conflicts of interest.

References

- [1] P. W. K. Rothemund, "Folding DNA to create nanoscale shapes and patterns," *Nature*, vol. 440, no. 7082, pp. 297–302, 2006.
- [2] L. Qian, Y. Wang, Z. Zhang et al., "Analogic China map constructed by DNA," *Chinese Science Bulletin*, vol. 51, no. 24, pp. 2973–2976, 2006.
- [3] D. Han, S. Pal, J. Nangreave, Z. Deng, Y. Liu, and H. Yan, "DNA origami with complex curvatures in three-dimensional space," *Science*, vol. 332, no. 6027, pp. 342–346, 2011.

- [4] D. Han, S. Pal, Y. Yang et al., "DNA gridiron nanostructures based on four-arm junctions," *Science*, vol. 339, no. 6126, pp. 1412–1415, 2011.
- [5] T. E. Tomov, R. Tsukanov, M. Liber, R. Masoud, N. Plavner, and E. Nir, "Rational design of DNA motors: fuel optimization through single-molecule fluorescence," *Journal of the American Chemical Society*, vol. 135, no. 32, pp. 11935–11941, 2013.
- [6] Y. Amir, E. Ben-Ishay, D. Levner, S. Ittah, A. Abu-Horowitz, and I. Bachelet, "Universal computing by DNA origami robots in a living animal," *Nature Nanotechnology*, vol. 9, no. 5, pp. 353–357, 2014.
- [7] D. Koirala, P. Shrestha, T. Emura et al., "Single-molecule mechanochemical sensing using DNA origami nanostructures," *Angewandte Chemie International Edition*, vol. 53, no. 31, pp. 8137–8141, 2014.
- [8] G. Tikhomirov, P. Petersen, and L. Qian, "Fractal assembly of micrometre-scale DNA origami arrays with arbitrary patterns," *Nature*, vol. 552, no. 7683, pp. 67–71, 2017.
- [9] J. Chao, J. Wang, F. Wang et al., "Solving mazes with single-molecule DNA navigators," *Nature Materials*, vol. 18, no. 3, pp. 273–279, 2018.
- [10] F. Zhang, J. Nangreave, Y. Liu, and H. Yan, "Reconfigurable DNA origami to generate quasifractal patterns," *Nano Letters*, vol. 12, no. 6, pp. 3290–3295, 2012.
- [11] B. Wei, M. Dai, and P. Yin, "Complex shapes self-assembled from single-stranded DNA tiles," *Nature*, vol. 485, no. 7400, pp. 623–626, 2012.
- [12] Y. Ke, J. Sharma, M. Liu, K. Jahn, Y. Liu, and H. Yan, "Scaffolded DNA origami of a DNA tetrahedron molecular container," *Nano Letters*, vol. 9, no. 6, pp. 2445–2447, 2009.
- [13] P. Wang, M. A. Rahman, Z. Zhao et al., "Visualization of the cellular uptake and trafficking of DNA origami nanostructures in cancer cells," *Journal of the American Chemical Society*, vol. 140, no. 7, 2018.
- [14] M. Endo, Y. Katsuda, K. Hidaka, and H. Sugiyama, "A versatile DNA nanochip for direct analysis of DNA base-excision repair," *Angewandte Chemie International Edition*, vol. 49, no. 49, pp. 9412–9416, 2010.
- [15] Y. Sannohe, M. Endo, Y. Katsuda, K. Hidaka, and H. Sugiyama, "Visualization of dynamic conformational switching of the G-quadruplex in a DNA nanostructure," *Journal of the American Chemical Society*, vol. 132, no. 46, pp. 16311–16313, 2010.
- [16] C. Zhang, J. Yang, S. Jiang, Y. Liu, and H. Yan, "DNAzyme-based logic gate-mediated DNA self-assembly," *Nano Letters*, vol. 16, no. 1, pp. 736–741, 2015.
- [17] D. Wang, Y. Fu, J. Yan et al., "Molecular logic gates on DNA origami nanostructures for MicroRNA diagnostics," *Analytical Chemistry*, vol. 86, no. 4, pp. 1932–1936, 2014.
- [18] J. Sharma, R. Chhabra, Y. Liu, Y. Ke, and H. Yan, "DNA-templated self-assembly of two-dimensional and periodical gold nanoparticle arrays," *Angewandte Chemie International Edition*, vol. 45, no. 5, pp. 730–735, 2006.
- [19] M. Pilo-Pais, S. Goldberg, E. Samano, T. H. Labean, and G. Finkelstein, "Connecting the nanodots: programmable nanofabrication of fused metal shapes on DNA templates," *Nano Letters*, vol. 11, no. 8, pp. 3489–3492, 2011.
- [20] H. Yan, S. H. Park, and G. Finkelstein, "DNA-templated self-assembly of protein arrays and highly conductive nanowires," *Science*, vol. 301, no. 5641, pp. 1882–1884, 2003.
- [21] N. V. Voigt, T. Tørring, A. Rotaru et al., "Single-molecule chemical reactions on DNA origami," *Nature Nanotechnology*, vol. 5, no. 3, pp. 200–203, 2010.
- [22] H. T. Maune, S.-p. Han, R. D. Barish et al., "Self-assembly of carbon nanotubes into two-dimensional geometries using DNA origami templates," *Nature Nanotechnology*, vol. 5, no. 1, pp. 61–66, 2010.
- [23] R. M. Dirks and N. A. Pierce, "From the Cover: triggered amplification by hybridization chain reaction," *Proceedings of the National Academy of Sciences*, vol. 101, no. 43, pp. 15275–15278, 2004.
- [24] D. Evanko, "Hybridization chain reaction," *Nature Methods*, vol. 1, no. 3, p. 186, 2004.
- [25] D. Peng and R. Yuan, "A novel electrochemical aptasensor for thrombin detection based on hybridization chain reaction as enhanced signals," *Chemical Sensors*, vol. 34, no. 4, pp. 14–19, 2014.
- [26] B. Zhang, B. Liu, D. Tang, R. Niessner, G. Chen, and D. Knopp, "DNA-based hybridization chain reaction for amplified bioelectronic signal and ultrasensitive detection of proteins," *Analytical Chemistry*, vol. 84, no. 12, pp. 5392–5399, 2012.
- [27] Y. Chen, J. Xu, J. Su, Y. Xiang, R. Yuan, and Y. Chai, "In situ hybridization chain reaction amplification for universal and highly sensitive electrochemiluminescent detection of DNA," *Analytical Chemistry*, vol. 84, no. 18, pp. 7750–7755, 2012.
- [28] J. Huang, Y. Wu, Y. Chen et al., "Pyrene-excimer probes based on the hybridization chain reaction for the detection of nucleic acids in complex biological fluids," *Angewandte Chemie International Edition*, vol. 50, no. 2, pp. 401–404, 2011.
- [29] D. Yang, Y. Tang, and P. Miao, "Hybridization chain reaction directed DNA superstructures assembly for biosensing applications," *TrAC Trends in Analytical Chemistry*, vol. 94, pp. 1–13, 2017.
- [30] J. Dong, X. Cui, Y. Deng, and Z. Tang, "Amplified detection of nucleic acid by G-quadruplex based hybridization chain reaction," *Biosensors and Bioelectronics*, vol. 38, no. 1, pp. 258–263, 2012.
- [31] Q. Xiao, P. J. Wu, and H. Ju, "Multiplexed chemiluminescence imaging assay of protein biomarkers using DNA microarray with proximity binding-induced hybridization chain reaction amplification," *Analytica Chimica Acta*, vol. 1032, no. 1032, pp. 130–137, 2018.
- [32] Z. Li, L. Tingting, and S. Ruidi, "A label-free light-up fluorescent sensing platform based upon hybridization chain reaction amplification and DNA triplex assembly," *Talanta*, vol. 189, pp. 137–142, 2018.
- [33] Z. Zhang, Y. Yang, F. Pincet, M. C. Llaguno, and C. Lin, "Placing and shaping liposomes with reconfigurable DNA nanocages," *Nature Chemistry*, vol. 9, no. 7, pp. 653–659, 2017.
- [34] N. Y. Wong, H. Xing, L. H. Tan, and Y. Lu, "Nano-encrypted morse code: a versatile approach to programmable and reversible nanoscale Assembly and disassembly," *Journal of the American Chemical Society*, vol. 135, no. 8, pp. 2931–2934, 2013.
- [35] S. D. Mason, Y. Tang, Y. Li, X. Xie, and F. Li, "Emerging bioanalytical applications of DNA walkers," *TrAC Trends in Analytical Chemistry*, vol. 107, pp. 212–221, 2018.
- [36] Z. Li and K. Bošković, "Nanopore-based DNA hard drives for rewritable and secure data storage," *Nano Letters*, vol. 20, no. 5, pp. 3754–3760, 2020.
- [37] T. G. W. Edwardson, K. L. Lau, D. Bousmail, C. J. Serpell, and H. F. Sleiman, "Transfer of molecular recognition information from DNA nanostructures to gold nanoparticles," *Nature Chemistry*, vol. 8, no. 2, pp. 162–170, 2016.
- [38] S. Shah, A. K. Dubey, and J. Reif, "Improved optical multiplexing with temporal DNA barcodes," *ACS Synthetic Biology*, vol. 8, no. 5, pp. 1100–1111, 2019.

- [39] M. Xiao, W. Lai, T. Man et al., "Rationally engineered nucleic acid architectures for biosensing applications," *Chemical Reviews*, vol. 119, no. 22, pp. 11631–11717, 2019.
- [40] K. Chen, X. Li, and J. Yang, "Precise control of gold nanoparticles on DNA origami for logic operation," *Journal of Nanomaterials*, vol. 2019, pp. 1–9, 2019.
- [41] J. O'Brien and A. Murugan, "Temporal pattern recognition through analog molecular computation," *ACS Synthetic Biology*, vol. 8, no. 4, pp. 826–832, 2019.
- [42] G. Chatterjee, N. Dalchau, R. A. Muscat, A. Phillips, and G. Seelig, "A spatially localized architecture for fast and modular DNA computing," *Nature Nanotechnology*, vol. 12, no. 9, pp. 920–927, 2017.
- [43] K. Sergio, W. J. Paschoalino, and L. T. Kubota, "Supramolecular DNA origami nanostructures for use in bioanalytical applications," *TrAC Trends in Analytical Chemistry*, vol. 108, pp. 88–97, 2018.
- [44] K. E. Bujold, A. Lacroix, and H. F. Sleiman, "DNA nanostructures at the interface with biology," *Chem*, vol. 4, no. 3, pp. 495–521, 2018.
- [45] T. Fu, Y. Lyu, and H. Liu, "DNA-based dynamic reaction networks[J]," *Trends in Biochemical Sciences*, vol. 43, no. 7, pp. 457–560, 2018.
- [46] X. Song and J. Reif, "Nucleic acid databases and molecular-scale computing," *ACS Nano*, vol. 13, no. 6, pp. 6256–6268, 2019.

Research Article

On Face Index of Silicon Carbides

Xiujun Zhang ¹, **Ali Raza**,² **Asfand Fahad** ², **Muhammad Kamran Jamil** ³,
Muhammad Anwar Chaudhry ⁴, and **Zahid Iqbal** ^{4,5}

¹School of Information Science and Engineering, Chengdu University, Chengdu 610106, China

²Department of Mathematics, COMSATS University Islamabad, Vehari Campus, Vehari 61110, Pakistan

³Department of Mathematics, Riphah Institute of Computing and Applied Sciences, Riphah International University, 14 Ali Road, Lahore, Pakistan

⁴Department of Mathematics and Statistics, Institute of Southern Punjab, Multan 66000, Pakistan

⁵School of Natural Sciences, National University of Sciences and Technology, Sector H-12, Islamabad, Pakistan

Correspondence should be addressed to Muhammad Kamran Jamil; m.kamran.sms@gmail.com

Received 13 May 2020; Accepted 4 July 2020; Published 1 August 2020

Academic Editor: Juan L. G. Guirao

Copyright © 2020 Xiujun Zhang et al. This is an open access article distributed under the Creative Commons Attribution License, which permits unrestricted use, distribution, and reproduction in any medium, provided the original work is properly cited.

Several graph invariants have been defined and studied, which present applications in nanochemistry, computer networks, and other areas of science. One vastly studied class of the graph invariants is the class of the topological indices, which helps in the studies of chemical, biological, and physical properties of a chemical structure. One recently introduced graph invariant is the face index, which can assist in predicting the energy and the boiling points of the certain chemical structures. In this paper, we derive the analytical closed formulas of face index of silicon carbides $Si_2C_3 - I[a, b]$, $Si_2C_3 - II[a, b]$, $Si_2C_3 - III[a, b]$, and $SiC_3 - III[a, b]$.

1. Introduction

Several invariants assigning a matrix, a polynomial, a numeric number, or a sequence (of numbers) to a graph have been defined and studied during the last few decades. One such significant class among such invariants is the class of topological indices (TIs), which assigns a number to the given graph. The value of a TI of a molecular structure is dependent on its shape, size, symmetry, patterns of the bonds, and the contents of heteroatoms in it. Consequently, the notion of the TI provides the quantitative characterization of the molecular structures. Several researchers have studied different aspects and applications of the TIs. For contents related to studies on lower/upper bounds maxima/minima of TIs, see [1–5], studies on chemistry and drugs see [6–10], and other applications, see [11–13]. Another vital contribution of the study of the TIs is their effectiveness in studying the different aspects of new drugs and chemical compounds, which is an immense need of the medical science and industry. For details, we refer [14, 15] to the readers. Consequently, computing and studying the behavior

of the values of the TIs of the molecular structures provide significant information and hence is one of the trends in modern research.

Before proceeding further with the study of a specific index, we set the notations used in this paper. The notions of a planar graph, its faces, and an infinite face are well known in the literature. Let G be a graph with vertex set $V(G)$, edge set $E(G)$, and face set $F(G)$. A face f is said to be incident with an edge e , whenever e is among the edges which surrounds f . Moreover, face is said to be incident with a vertex w , whenever w is incident to an edge e which surrounds f . The incidence of w to the face f is represented by $w \sim f$. The degree of a face f in G is given as $d(f) = \sum_{w \sim f} d_w$. For the notions and notations not given here, we refer [16] to the readers. Recently, Jamil et al. [17] introduced a novel topological index named as the face index. They showed that the face index can help to predict the boiling points and the energy of selected benzenoid hydrocarbons with the correlation coefficient $r > 0.99$. For a planar graph G , the face index (FI) can be defined as

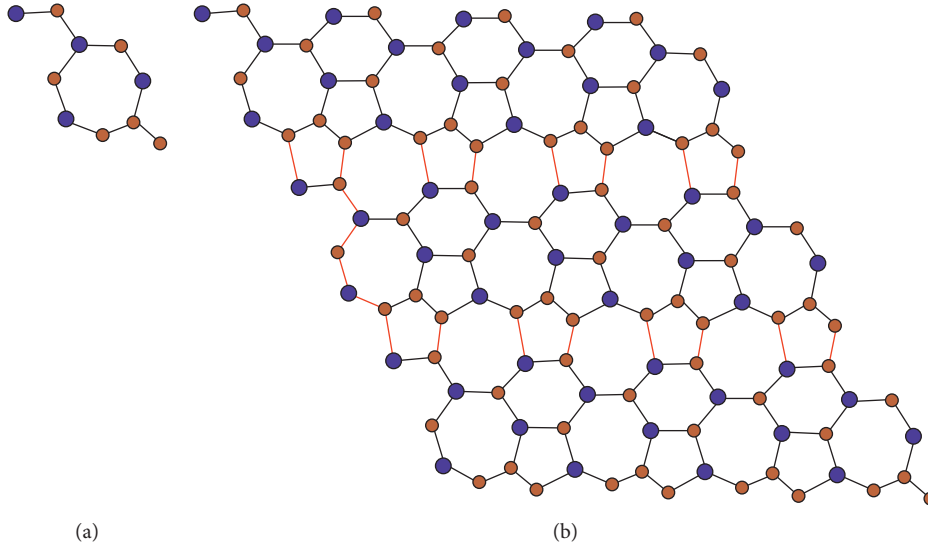


FIGURE 1: The unit cell and $Si_2C_3 - I[3,4]$, respectively.

$$FI(G) = \sum_{f \in F(G)} d(f) = \sum_{w \sim f \in F(G)} d_w, \quad (1)$$

where $w \sim f$ represents the incidence of the vertex w with the face f .

On the contrary, the Silicon Carbide (SiC) is the first and foremost material that contained the covalent bound of C and Si atoms, typically in biatomic layers. These layers form tetrahedrally oriented molecules of C and Si atoms, with a very short bound length and hence a very high bound strength. This is the base of extremely high mechanically and chemical stability of SiC [18, 19]. SiC occurs in nature as the incredibly uncommon mineral moissanite. SiC being one of the most extensively used wide bandgap materials, performs a vital role in power industries by setting new principles in power savings as rectifiers or switches in the system for data centers, solar cells, wind turbines, and electric vehicles, as well as high temperature and radiation tolerant electronic applications [20–23]. There are several silicon carbides which we are going to study in this paper, such as $Si_2C_3 - I[a, b]$, $Si_2C_3 - II[a, b]$, $Si_2C_3 - III[a, b]$, and $SiC_3 - III[a, b]$. Several papers have been devoted to the study of silicon, carbon-based structures, for details, see [24–26]. The main objective of this paper is to find the analytic formula of the face index of these silicon carbides. Moreover, we also present the graphical analysis of the obtained results. For this, we use the Chemscketch for plotting the figures of silicon carbides, Maple for calculations, and MATLAB for graphical analysis.

Before presenting the results, we include Euler's formula for planar graphs. Evidently, we may observe that the silicon structures presented in Section 2 are consistent with this formula.

Theorem 1. For a finite, connected, and planar graph G with vertex set $V(G)$, edge set $E(G)$, and face set $F(G)$, we have

$$|V(G)| - |E(G)| + |F(G)| = 2. \quad (2)$$

2. Results

In this section, we investigate the exact formulas of the face index for $Si_2C_3 - I[a, b]$, $Si_2C_3 - II[a, b]$, $Si_2C_3 - III[a, b]$, and $SiC_3 - III[a, b]$. To find the face indices of the molecular graphs, we partitioned the face set depending on the degrees of each face.

2.1. Face Index for $Si_2C_3 - II[a, b]$ and Graphical Representations. The molecular graphs of silicon carbides $Si_2C_3 - I[a, b]$ are given in Figure 1. Figure 1(a) consists of unit cell of the silicon carbide $Si_2C_3 - I[a, b]$ and $Si_2C_3 - I[a, b]$ for $a = 1$ and $b = 1$. Figure 1(b) is $Si_2C_3 - I[a, b]$ for $a = 3$ and $b = 4$.

Theorem 2. Let $G = Si_2C_3 - I[a, b]$, where $a, b \geq 1$. Then,

$$FI(G) = \begin{cases} 70a - 34, & \text{if } b = 1 \\ 90ab - 20a - 30b - 4, & \text{if } a, b \neq 1 \\ 18(3b - 1), & \text{if } a = 1. \end{cases} \quad (3)$$

Proof. We consider the following three cases:

Case-I If $b = 1$, let f_j and $|f_j|$ denote the face with the property $\sum_{w \sim f_j} d_w = j$ and the number of such faces, respectively. The structure $Si_2C_3 - I[a, 1]$ contains four types of internal faces f_{14} , f_{16} , f_{18} , and f_{20} and an external face, f_{∞} . So, the face index of $Si_2C_3 - I[a, 1]$ is

TABLE 1: Numbers of f_{14} , f_{15} , f_{16} , f_{18} , f_{19} , f_{20} , and f_{21} with given number of rows.

Rows	$ f_{14} $	$ f_{15} $	$ f_{16} $	$ f_{18} $	$ f_{19} $	$ f_{20} $	$ f_{21} $
2	$a + 1$	$2a - 3$	$a - 1$	$a + 1$	2	$a - 2$	$2a - 3$
3	$a + 3$	$2(2a - 3)$	$a - 1$	$2a$	4	$a - 2$	$2(2a - 3)$
4	$a + 5$	$3(2a - 3)$	$a - 1$	$3a - 1$	6	$a - 2$	$3(2a - 3)$
\vdots	\vdots	\vdots	\vdots	\vdots	—	—	—
\vdots	\vdots	\vdots	\vdots	\vdots	—	—	—
\vdots	\vdots	\vdots	\vdots	\vdots	—	—	—
B	$a + 2b - 3$	$(b - 1)(2a - 3)$	$a - 1$	$ab - a - b + 3$	$2(b - 1)$	$a - 2$	$(b - 1)(2a - 3)$

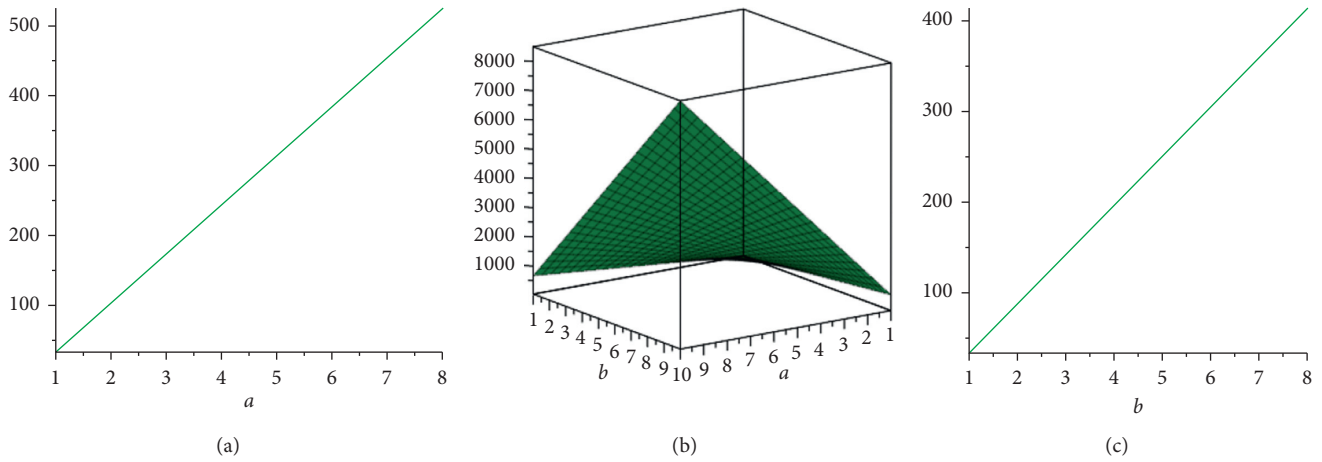


FIGURE 2: $FI(Si_2C_3 - I[a, 1])$, $FI(Si_2C_3 - I[a, b])$, and $FI(Si_2C_3 - I[1, b])$, respectively.

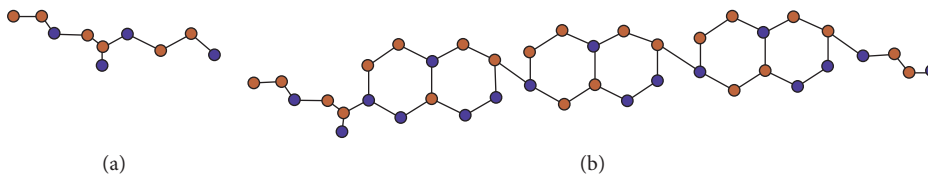


FIGURE 3: The unit cell and $Si_2C_3 - II[4, 1]$, respectively.

$$\begin{aligned}
 FI(G) &= \sum_{w \sim f \in F(G)} d_w \\
 &= \sum_{w \sim f_{14}} d_w + \sum_{w \sim f_{16}} d_w + \sum_{w \sim f_{18}} d_w + \sum_{w \sim f_{20}} d_w + \sum_{w \sim f_{\infty}} d_w \\
 &= |f_{14}|(14) + |f_{16}|(16) + |f_{18}|(18) + |f_{20}|(20) + 20a \\
 &= 14(a - 1) + 16(a - 1) + 18(2) + 20(a - 2) + 20a \\
 &= 70a - 34.
 \end{aligned}
 \tag{4}$$

Case-II When $a, b \neq 1$, then, we notice that the structure $Si_2C_3 - I[a, b]$ contains seven types of faces, which are $f_{14}, f_{15}, f_{16}, f_{18}, f_{19}, f_{20}$, and f_{21} and an external face, f_{∞} . Moreover, the sum of vertex degrees of external

TABLE 2: Numbers of f_{16} , f_{17} , and f_{18} with given number of rows.

No. of rows	$ f_{16} $	$ f_{17} $	$ f_{18} $
2	$2a$	$2a$	$3a - 5$
3	$2a + 2$	$2a + 2$	$8a - 12$
4	$2a + 4$	$2a + 4$	$13a - 19$
\vdots	\vdots	\vdots	\vdots
\vdots	\vdots	\vdots	\vdots
\vdots	\vdots	\vdots	\vdots
B	$2(a + b) - 4$	$2(a + b) - 4$	$5ab - 7(a + b) + 9$

The rest follows from the definition of the face index.

face is $20a + 30(b - 1)$. In each row of Table 1, the number of internal faces is written.

The face index of $Si_2C_3 - I[a, b]$ is

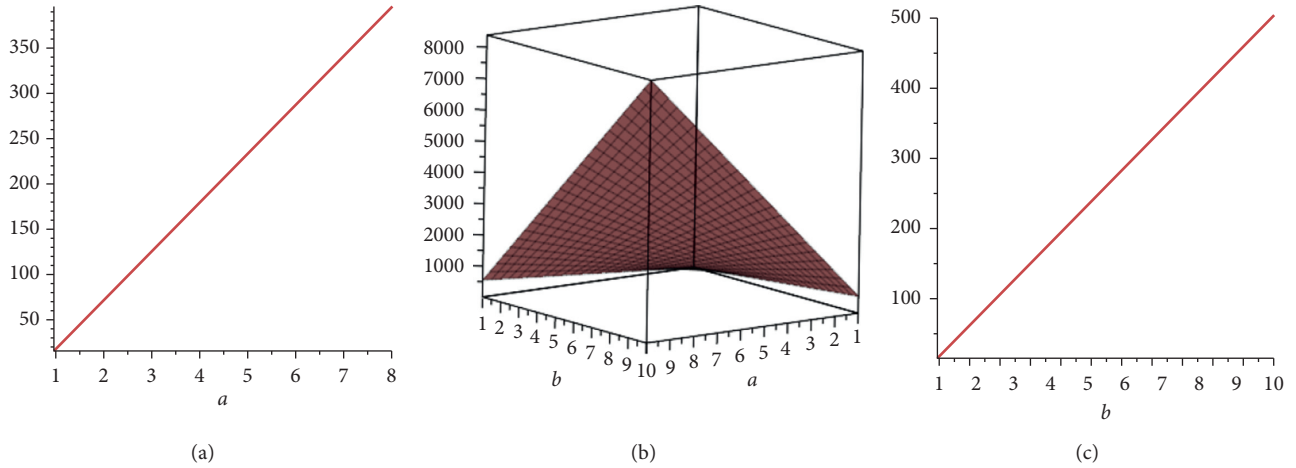


FIGURE 4: $FI(Si_2C_3 - II[a, 1])$, $FI(Si_2C_3 - II[a, b])$, and $FI(Si_2C_3 - II[1, b])$, respectively.

$$\begin{aligned}
 FI(G) &= \sum_{w \sim f \in F(G)} d_w \\
 &= \sum_{w \sim f_{14}} d_w + \sum_{w \sim f_{15}} d_w + \sum_{w \sim f_{16}} d_w + \sum_{w \sim f_{18}} d_w \\
 &\quad + \sum_{w \sim f_{19}} d_w + \sum_{w \sim f_{20}} d_w + \sum_{w \sim f_{21}} d_w + \sum_{w \sim f_{\infty}} d_w \\
 &= |f_{14}|(14) + |f_{15}|(15) + |f_{16}|(16) + |f_{18}|(18) \\
 &\quad + |f_{19}|(19) + |f_{20}|(20) + |f_{21}|(21) + 20a + 30(b-1) \\
 &= 14(a+2b-3) + 15(b-1)(2a-3) + 16(a-1) \\
 &\quad + 18(ab-a-b+3) + 19(2(b-1)) + 20(a-2) \\
 &\quad + 21(b-1)(2a-3) + 20a + 30(b-1) \\
 &= 90ab - 20a - 30b - 4.
 \end{aligned} \tag{5}$$

Case-III When $a = 1$, the structure $Si_2C_3 - I[a, b]$ contains three types of internal faces f_{13} , f_{16} , and f_{17} and an external face f_{∞} with sum of degrees $24b - 4$. Moreover, $|f_{13}| = b - 1$, $|f_{16}| = 1$, and $|f_{17}| = b - 1$. So, the face index of $Si_2C_3 - I[a, b]$ is

$$\begin{aligned}
 FI(G) &= \sum_{w \sim f \in F(G)} d_w \\
 &= \sum_{w \sim f_{13}} d_w + \sum_{w \sim f_{16}} d_w + \sum_{w \sim f_{17}} d_w + \sum_{w \sim f_{\infty}} d_w \\
 &= |f_{13}|(13) + |f_{16}|(16) + |f_{17}|(17) + 24b - 4 \\
 &= 13(b-1) + 16(1) + 17(b-1) + 24b - 4 \\
 &= 18(3b-1),
 \end{aligned} \tag{6}$$

which completes the proof. \square

Remark 1. It is interesting to observe that $|V(Si_2C_3 - I[a, b])| = 10ab$, $|E(Si_2C_3 - I[a, b])| = 15ab - 2a - 3b$, and $|F(Si_2C_3 - I[a, b])| = 5ab - 2a - 3b + 2$. Hence, the structure $Si_2C_3 - I[a, b]$ satisfies the Euler formula.

Now, we present the results obtained for $Si_2C_3 - I[a, b]$ in a graphical way in Figure 2. Every silicon carbide structure depends on two variables a and b . We use two kinds of graphs to show the outcomes of face index. One is the 2D graph where the reliance of a face index is drawn against one variable of the structure a or b while other is kept fixed. Here, we demonstrate 2D graphs for $b = 1$ and change a , and for $a = 1$ and change b . The second tool is the 3D graph where reliance of a face index is drawn against both parameters, and we gained a surface that tells about the trends of face index against both parameters a and b at the same time.

2.2. Face Index for $Si_2C_3 - II[a, b]$ and Graphical Representations. The molecular graphs of silicon carbides $Si_2C_3 - II[a, b]$ are given in Figure 3, which consists of unit cell of silicon carbide $Si_2C_3 - II[a, b]$ and $Si_2C_3 - II[a, b]$ for $a = 4$ and $b = 1$.

Theorem 3. Let $H = Si_2C_3 - II[a, b]$, where $a, b \geq 1$. Then, the face index of H is given as

$$FI(H) = \begin{cases} 18(3a-2), & \text{if } b = 1, \\ 90ab - 30(a+b) - 15, & \text{if } a, b \neq 1, \\ 18(3b-2), & \text{if } a = 1. \end{cases} \tag{7}$$

Proof. We consider the following three cases.

Case-I If $b = 1$, then the graph of $Si_2C_3 - II[a, 1]$ consists of two faces, an internal face f_{15} with $|f_{15}| = 2a - 2$ and an external face, f_{∞} having the sum of vertex degrees $24a - 6$. The rest follows from the definition of the face index.

Case-II When $a, b \neq 1$, then, we notice that the structure $Si_2C_3 - II[a, b]$ contains three types of internal faces, which are f_{16} , f_{17} , and f_{18} and an external face, f_{∞} . Moreover, the sum of vertex degrees of external face is $30(a+b) - 45$. The number of internal faces in each row is given in Table 2. \square

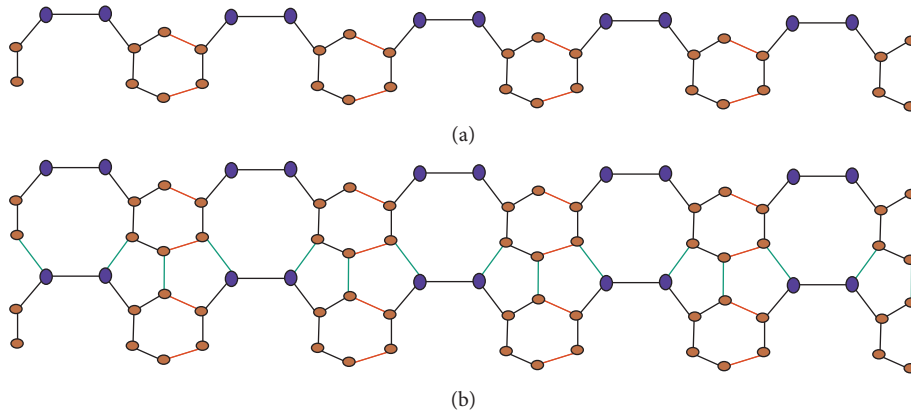


FIGURE 5: (a) $SiC_3 - III[5, 1]$ and (b) $SiC_3 - III[5, 2]$.

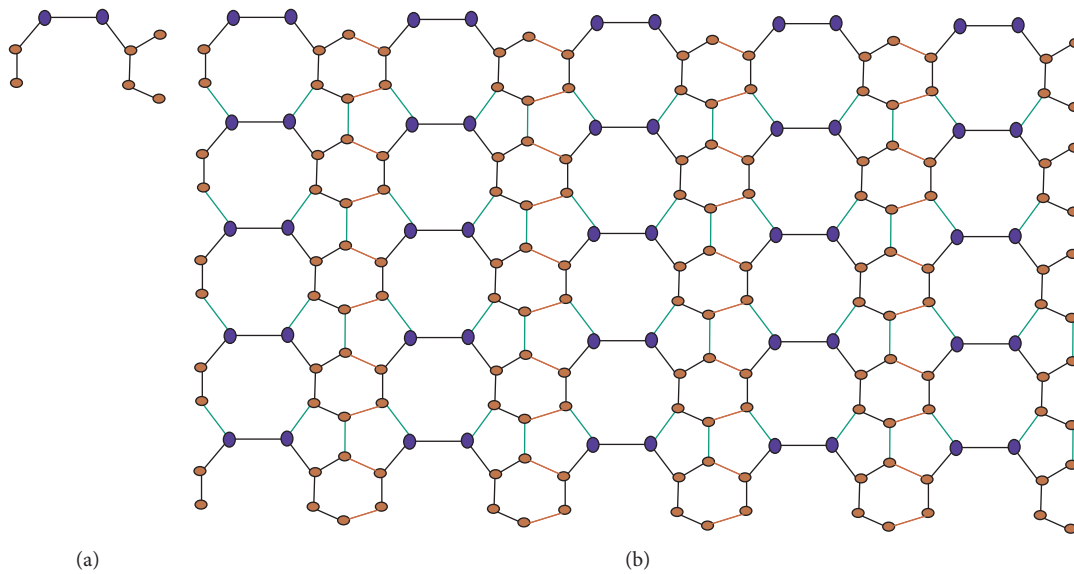


FIGURE 6: The unit cell and $SiC_3 - III[5, 5]$, respectively.

Case-III When $a = 1$, the structure $Si_2C_3 - II[a, b]$ contains an internal face f_{15} and an external face f_{∞} with sum of degrees $24b - 6$. Moreover, $|f_{15}| = 2b - 2$. The rest follows from the definition of the face index.

Remark 2. It is interesting to observe that $|V(Si_2C_3 - II[a, b])| = 10ab$, $|E(Si_2C_3 - II[a, b])| = 15ab - 2a - 3b$, and $|F(Si_2C_3 - II[a, b])| = 5ab - 2a - 3b + 2$. Hence, the structure $Si_2C_3 - II[a, b]$ satisfies the Euler formula.

With the same settings as in Section 2.1, we present the results obtained for $Si_2C_3 - II[a, b]$ in graphical way in Figure 4.

2.3. Face Index for $SiC_3 - III[a, b]$ and Graphical Representations. The molecular graphs of silicon carbides $SiC_3 - III[a, b]$ are given in Figures 5 and 6. Figure 5(a) is for $a = 5$ and $b = 1$, Figure 5(b) is for $a = 5$ and $b = 2$, and Figure 6 consists of unit cell and $SiC_3 - III[a, b]$ for $a = 5$ and $b = 5$.

TABLE 3: Numbers of $f_{13}, f_{15}, f_{17}, f_{18}, f_{20}, f_{22}$, and f_{24} with given number of rows.

Rows	$ f_{13} $	$ f_{15} $	$ f_{17} $	$ f_{18} $	$ f_{20} $	$ f_{22} $	$ f_{24} $
2	1	$3(a-1)$	$a-1$	—	1	$a-1$	—
3	2	$5(a-1)$	$a-1$	$a-1$	1	A	$a-1$
4	3	$7(a-1)$	$a-1$	$2(a-1)$	1	$a+1$	$2(a-1)$
⋮	⋮	⋮	⋮	⋮	⋮	⋮	⋮
⋮	⋮	⋮	⋮	⋮	⋮	⋮	⋮
⋮	⋮	⋮	⋮	⋮	⋮	⋮	⋮
B	$b-1$	$(2b-1)$ $(a-1)$	$a-1$	$(b-2)$ $(a-1)$	1	$a+b-3$	$(b-2)$ $(a-1)$

The rest follows from the definition of the face index.

Theorem 4. Let $K = SiC_3 - III[a, b]$, where $a, b \geq 1$. Then,

$$FI(K) = \begin{cases} 32a - 18; & \text{for } b = 1 \\ 72ab - 30a - 20b - 7; & \text{for } b > 1. \end{cases} \quad (8)$$

Proof. When $b = 1$, then the graph of $SiC_3 - III[a, 1]$ consists of two faces, an internal face f_{14} with $|f_{14}| = a - 1$, and

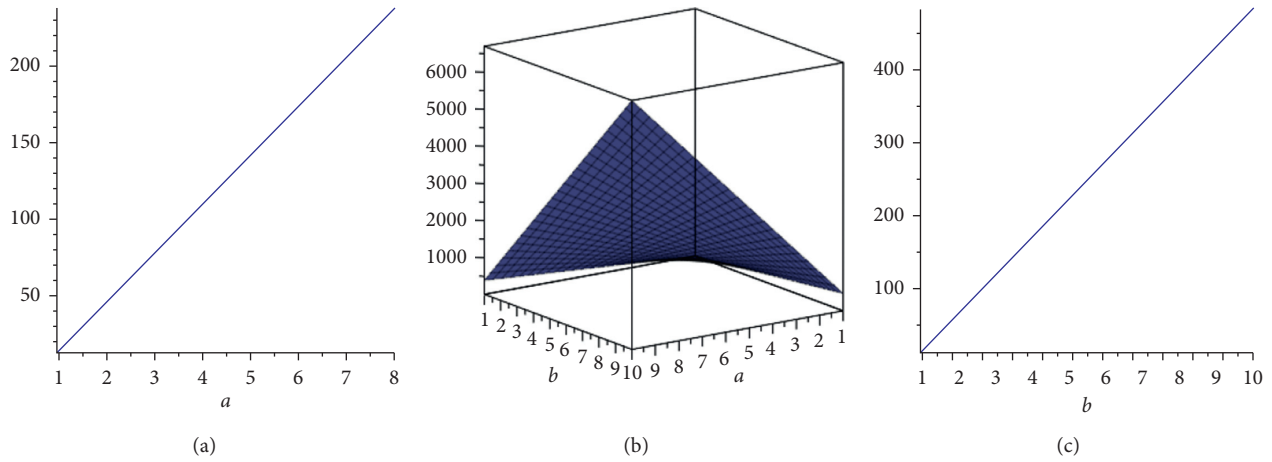


FIGURE 7: $FI(SiC_3 - III[a, 1])$, $FI(SiC_3 - III[a, b])$, and $FI(SiC_3 - III[1, b])$, respectively.

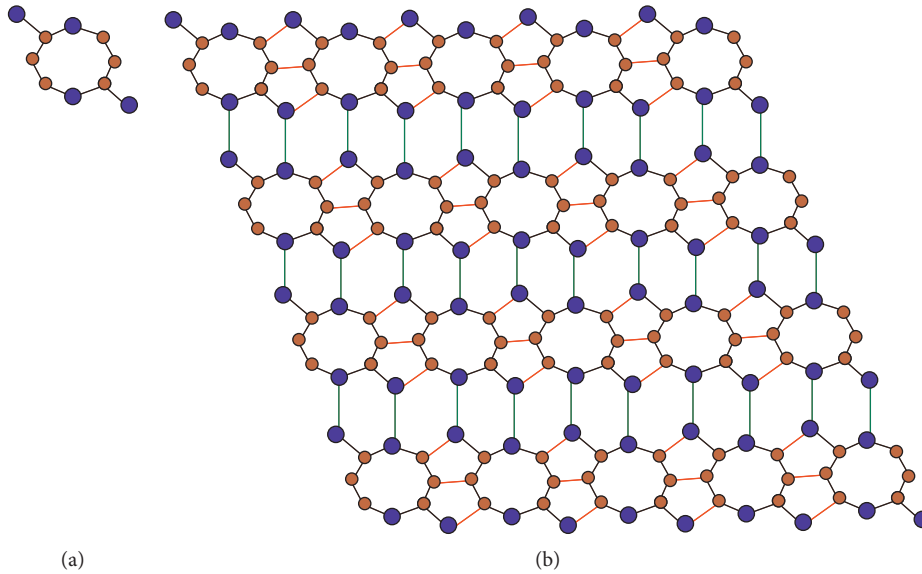


FIGURE 8: The unit cell and $SiC_3 - III[5, 4]$, respectively.

an external face, f_∞ having the sum of degrees $18a - 4$. The rest follows from the definition of the face index. Now, when $b > 1$, then we notice that the structure $SiC_3 - III[a, b]$ contains seven types of internal faces which are f_{13} , f_{15} , f_{17} , f_{18} , f_{20} , f_{22} , and f_{24} and an external face, f_∞ . Moreover, the sum of vertex degrees of external face is $30a + 17b - 30$. In each row of Table 3, the number of internal faces is written. \square

Remark 3. It is interesting to observe that $|V(SiC_3 - III[a, b])| = 8ab$, $|E(SiC_3 - III[a, b])| = 12ab - 3a - 2b$, and $|F(SiC_3 - III[a, b])| = 4ab - 3a - 2b + 2$. Hence, the structure $SiC_3 - III[a, b]$ satisfies the Euler formula.

With the same settings as in Section 2.1, we present the results obtained for $SiC_3 - III[a, b]$ in a graphical way in Figure 7.

2.4. Face Index for $SiC_3 - III[a, b]$ and Graphical Representations. The molecular graphs of silicon carbides $SiC_3 - III[a, b]$ are given in Figure 8.

Theorem 5. Let $L = SiC_3 - III[a, b]$, where $a, b \geq 1$. Then,

$$FI(L) = \begin{cases} 70a - 32, & \text{for } b = 1, \\ 90ab - 20a - 30b - 2, & \text{for } b > 1. \end{cases} \quad (9)$$

TABLE 4: Numbers of $f_{14}, f_{15}, f_{17}, f_{18}, f_{21}, f_{22}, f_{23}$, and f_{24} with given number of rows.

No. of rows	$ f_{14} $	$ f_{15} $	$ f_{17} $	$ f_{18} $	$ f_{21} $	$ f_{22} $	$ f_{23} $	$ f_{24} $
2	$2(a-1)$	$2(a-1)$	2	$(2a-3)$	4	—	$2(a-2)$	—
3	$2(a-1)$	$4(a-1)$	4	$2(2a-3)$	4	2	$2(a-2)$	$a-2$
4	$2(a-1)$	$6(a-1)$	6	$3(2a-3)$	4	4	$2(a-2)$	$2(a-2)$
⋮	⋮	⋮	⋮	⋮	⋮	⋮	⋮	⋮
⋮	⋮	⋮	⋮	⋮	⋮	⋮	⋮	⋮
⋮	⋮	⋮	⋮	⋮	⋮	⋮	⋮	⋮
B	$2(a-1)$	$2(b-1)(a-1)$	$2(b-1)$	$(b-1)(2a-3)$	4	$2(b-2)$	$2(a-2)$	$(b-2)(a-2)$

The rest follows from the definition of the face index.

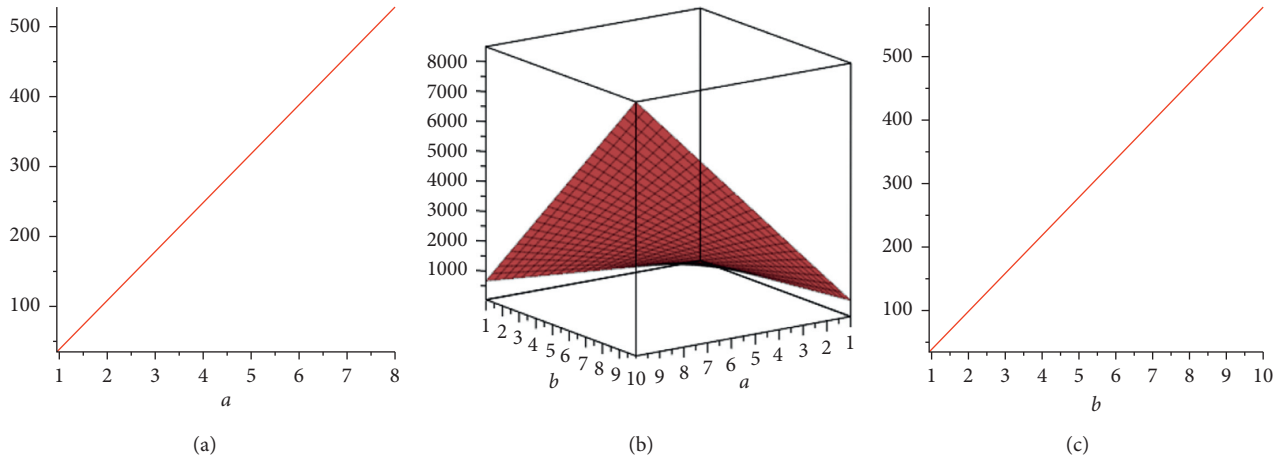


FIGURE 9: $FI(Si_2C_3 - III[a, 1])$, $FI(Si_2C_3 - III[a, b])$, and $FI(Si_2C_3 - III[1, b])$, respectively.

Proof. When $b = 1$, then the graph of $Si_2C_3 - III[a, 1]$ consists of four types of faces, three internal faces f_{14}, f_{20} , and f_{22} and an external face f_{∞} having the sum of degrees $20a$. Moreover, the values of $|f_{14}|, |f_{20}|$, and $|f_{22}|$ are $2(a - 1), 2$, and $(a - 2)$, respectively. The rest follows from the definition of the face index. Now, when $b > 1$, then we notice that the structure $Si_2C_3 - III[a, b]$ contains eight types of internal faces, which are $f_{14}, f_{15}, f_{17}, f_{18}, f_{21}, f_{22}, f_{23}$, and f_{24} and an external face, f_{∞} . Moreover, the sum of vertex degrees of external face is $20a + 24(b - 1)$. In each row of Table 4, the number of internal faces is written. \square

Remark 4. It is interesting to observe that $|V(Si_2C_3 - III[a, b])| = 10ab, |E(Si_2C_3 - III[a, b])| = 15ab - 2a - 3b$, and $|F(Si_2C_3 - III[a, b])| = 5ab - 32 - 3b + 2$. Hence, the structure $Si_2C_3 - III[a, b]$ satisfies the Euler formula.

With the same settings as in Section 2.1, we present the results obtained for $Si_2C_3 - III[a, b]$ in a graphical way in Figure 9.

3. Conclusions

An ongoing direction in mathematical and computational chemistry is the assessment of various properties of molecular structures with the help of numerical graph descriptors. These invariants have also established the feasible applications in QSAR/QSPR studies, which are beneficial for the new molecular designs, drug discoveries, and hazard

estimation of chemicals. Hence, the novel index, named as the face index for the molecular graphs of silicon carbides, is presented through the numerical way, and we have also displayed our numeric outcomes in the graphical way. Our consequences could be applicable in assessing and comparing the properties of these molecular structures.

Data Availability

The data used to support the findings of the study are included within the article.

Conflicts of Interest

The authors declare no conflicts of interest.

Acknowledgments

This work was supported in part by the National Key Research and Development Program under Grants 2017YFB0802300 and 2018YFB0904205 and Key Laboratory of Pattern Recognition and Intelligent Information Processing, Institutions of Higher Education of Sichuan Province under Grant MSSB-2020-12.

References

- [1] L. Luo, N. Dehgardi, and A. Fahad, "Lower bounds on the entire Zagreb indices of trees," *Discrete Dynamics in Nature and Society*, vol. 2020, Article ID 8616725, 8 pages, 2020.

- [2] Z. Shao, P. Wu, Y. Gao, I. Gutman, and X. Zhang, "On the maximum ABC index of graphs without pendent vertices," *Applied Mathematics and Computation*, vol. 315, no. 315, pp. 298–312, 2017.
- [3] Z. Shao, P. Wu, H. Jiang, S. M. Sheikholeslami, and S. Wang, "On the maximum ABC index of bipartite graphs without pendent vertices," *Open Chemistry*, vol. 18, no. 1, pp. 39–49, 2020.
- [4] Z. Shao, P. Wu, X. Zhang, D. Dimitrov, and J.-B. Liu, "On the maximum ABC index of graphs with prescribed size and without pendent vertices," *IEEE Access*, vol. 6, no. 6, pp. 27604–27616, 2018.
- [5] S. Wang, C. Wang, L. Chen, J. B. Liu, and Z. Shao, "Maximizing and Minimizing Multiplicative Zagreb Indices of graphs subject to given number of cut edges," *Mathematics*, vol. 6, pp. 1–10, 2018.
- [6] W. Gao, W. Wang, and M. R. Farahani, "Topological indices study of molecular structure in anticancer drugs," *Journal of Chemistry*, vol. 2016, Article ID 3216327, 8 pages, 2016.
- [7] A. Ye, M. I. Qureshi, A. Fahad et al., "Zagreb connection number index of nanotubes and regular hexagonal lattice," *Open Chemistry*, vol. 17, no. 1, pp. 75–80, 2019.
- [8] D. Zhao, Z. Iqbal, R. Irfan et al., "Comparison of irregularity indices of several dendrimers structures," *Processes*, vol. 7, no. 10, p. 662, 2019.
- [9] J. Zheng, Z. Iqbal, A. Fahad et al., "Some eccentricity-based topological indices and polynomials of oly (EThyleneAmidoAmine) (PETAA) dendrimers, processes," vol. 7, no. 433, pp. 1–14, 2019.
- [10] X. Zuo, J.-B. Liu, H. Iqbal, K. Ali, and S. T. R. Rizvi, "Topological indices of certain transformed chemical structures," *Journal of Chemistry*, vol. 2020, Article ID 3045646, 7 pages, 2020.
- [11] J.-B. Liu, M. Javaid, and H. M. Awais, "Computing zagreb indices of the subdivision-related generalized operations of graphs," *IEEE Access*, vol. 7, pp. 105479–105488, 2019.
- [12] J.-B. Liu, J. Zhao, S. Wang, M. Javaid, and J. Cao, "On the topological properties of the certain neural networks," *Journal of Artificial Intelligence and Soft Computing Research*, vol. 8, no. 4, pp. 257–268, 2018.
- [13] W. F. Wang and W. Gao, "Second atom-bond connectivity index of special chemical molecular structures," *Journal of Chemistry*, vol. 2014, Article ID 906254, 8 pages, 2014.
- [14] A. R. Katritzky, R. Jain, A. Lomaka, R. Petrukhin, U. Maran, and M. Karelson, "Perspective on the relationship between melting points and chemical structure," *Crystal Growth & Design*, vol. 1, no. 4, pp. 261–265, 2001.
- [15] H. Wiener, "Structural determination of paraffin boiling points," *Journal of the American Chemical Society*, vol. 69, no. 1, pp. 17–20, 1947.
- [16] J. A. Bondy and U. S. R. Murty, *Graph Theory*, Springer, Berlin, Germany, 2008.
- [17] M. K. Jamil, M. Imran, and K. Abdul Sattar, "Novel face index for benzenoid hydrocarbons," *Mathematics*, vol. 8, no. 3, p. 312, 2020.
- [18] A. Norlin, J. Pan, and C. Leygraf, "Investigation of interfacial capacitance of Pt, Ti and TiN coated electrodes by electrochemical impedance spectroscopy," *Biomolecular Engineering*, vol. 19, no. 2-6, pp. 67–71, 2002.
- [19] S. Singh and R. C. Buchanan, "SiC-C fiber electrode for biological sensing," *Materials Science and Engineering: C*, vol. 27, no. 3, pp. 551–557, 2007.
- [20] R. Gerhardt, *Properties and Applications of Silicon Carbide*, BoDBooks on Demand, Norderstedt, Germany, 2011.
- [21] G. L. Harris, *Properties of Silicon Carbide*, IET, London, UK, 1995.
- [22] H. J. Kang, J. H. Moon, W. Bahng et al., "Oxygen- and photoresist-related interface states of 4H-SiC Schottky diode observed by deep-level transient spectroscopy," *Journal of Applied Physics*, vol. 122, no. 9, Article ID 094504, 2017.
- [23] S. M. Koo, *Design and process issues of junction-and ferroelectric-field effect transistors in silicon carbide*, Ph.D. thesis, Doctoral dissertation, Mikroelektronik och informationsteknik, KTH Royal Institute of Technology, Stockholm, Sweden, 2003.
- [24] Z.-Q. Cai, A. Rauf, M. Ishtiaq, and M. K. Siddiqui, "On v-degree and ev-degree based topological properties of silicon carbide Si₂C₃-II [p, q]," *Polycyclic Aromatic Compounds*, pp. 1–15, 2020.
- [25] W. Gao and W. F. Wang, "The fifth geometric-arithmetic index of bridge graph and carbon nanocones," *Journal of Difference Equations and Applications*, vol. 23, no. 1-2, pp. 100–109, 2017.
- [26] X.-L. Wang, J.-B. Liu, A. Jahanbani, M. K. Siddiqui, N. J. Rad, and R. Hasni, "On generalized topological indices of silicon-carbon," *Journal of Mathematics*, vol. 2020, Article ID 2128594, 21 pages, 2020.

Research Article

Minimum Variable Connectivity Index of Trees of a Fixed Order

Shamaila Yousaf,^{1,2} Akhlaq Ahmad Bhatti ¹ and Akbar Ali ^{3,4}

¹Department of Sciences and Humanities, National University of Computer and Emerging Sciences, Lahore Campus, B-Block, Faisal Town, Lahore, Pakistan

²Department of Mathematics, University of Gujrat, Hafiz Hayat Campus, Gujrat, Pakistan

³Department of Mathematics, Faculty of Science, University of Ha'il, Ha'il, Saudi Arabia

⁴Knowledge Unit of Science, University of Management and Technology, Sialkot, Pakistan

Correspondence should be addressed to Akbar Ali; akbarali.maths@gmail.com

Received 13 May 2020; Accepted 29 June 2020; Published 20 July 2020

Academic Editor: Juan L. G. Guirao

Copyright © 2020 Shamaila Yousaf et al. This is an open access article distributed under the Creative Commons Attribution License, which permits unrestricted use, distribution, and reproduction in any medium, provided the original work is properly cited.

The connectivity index, introduced by the chemist Milan Randić in 1975, is one of the topological indices with many applications. In the first quarter of 1990s, Randić proposed the variable connectivity index by extending the definition of the connectivity index. The variable connectivity index for graph G is defined as $\sum_{vw \in E(G)} ((d(v) + \gamma)(d(w) + \gamma))^{-1/2}$, where γ is a nonnegative real number, $E(G)$ is the edge set of G , and $d(t)$ denotes the degree of an arbitrary vertex t in G . Soon after the innovation of the variable connectivity index, its various chemical applications have been reported in different papers. However, to the best of the authors' knowledge, mathematical properties of the variable connectivity index, for $\gamma > 0$, have not yet been discussed explicitly in any paper. The main purpose of the present paper is to fill this gap by studying this topological index in a mathematical point of view. More precisely, in this paper, we prove that the star graph has the minimum variable connectivity index among all trees of a fixed order n , where $n \geq 4$.

1. Introduction

All the graphs that we discuss in the present study are simple, connected, undirected, and finite. For a graph $G = (V, E)$, the number $|V(G)|$ is called its order, and $|E(G)|$ is the size of G . Neighbor of a vertex $v \in V(G)$ is a vertex adjacent to v . The set of all neighbors of vertex v of G is denoted by $N(v)$. The number $|N(v)|$ is called the degree of a vertex, $v \in G$, and it is denoted by $d(v)$. If $d(v) = 1$, then v is called a pendent vertex or a leaf. A graph of order n is called an n -vertex graph. Denote by P_n and S_n the n -vertex path graph and the n -vertex star graph, respectively. The class of all n -vertex trees is denoted by T_n . For the (chemical) graph theoretical notation and terminology that are not defined in this paper, refer to [1, 2].

One of the fundamental ideas in CGT (chemical graph theory) is molecular connectivity. Chemical behavior of a compound is dependent upon its structure. QSPR/QSAR (quantitative structure-property/activity relationship)

studies are progressive fields of chemical research that focus on the behavior of this dependency. The quantitative relationships are mathematical models that either enable the prediction of a continuous variable (e.g., boiling point and LC_{50} toxicity) or the classification of a discrete variable (e.g., sweet/bitter and toxic/nontoxic) from structural parameters. Actually, CGT has provided many topological indices that have been and are being used in QSPR/QSAR studies for predicting the physicochemical properties of chemical compounds. Topological indices are those graph invariants that found some applications in chemistry [3–6]. For further details about the topological indices and their applications, refer to [3, 7–11] and the references therein.

Molecules can be modeled using graphs in which vertices correspond to atoms of the considered molecules, and the edges correspond to the covalent bonds between atoms [6]. To model the heteroatom molecules, it is better to use the vertex-weighted graphs, which are the graphs whose one or more vertices are distinguished in some way from the rest of

the vertices [12]. Let G be a vertex-weighted graph with the vertex set $\{v_1, v_2, \dots, v_n\}$, and let w_i be the weight of the vertex v_i for $i = 1, 2, \dots, n$. The augmented vertex-adjacency matrix of G is an $n \times n$ matrix denoted by ${}^{av}\mathbf{A}(G)$ and is defined as ${}^{av}\mathbf{A}(G) = [a_{i,j}]_{n \times n}$ where

$$a_{i,j} = \begin{cases} 1, & \text{if } v_i v_j \in E(G); \\ w_i, & \text{if } i = j; \\ 0, & \text{otherwise.} \end{cases} \quad (1)$$

The variable connectivity index [13, 14], proposed by Randić, for graph G is defined as

$${}^1\chi^f(G) = \sum_{v_i v_j \in E(G)} \frac{1}{\sqrt{(d(v_i) + w_i)(d(v_j) + w_j)}} \quad (2)$$

We associate this index's name with its inventor Randić by calling it as the variable Randić index. This index was actually introduced within the QSPR/QSAR studies of heteroatomic molecules. If G is the molecular graph of a homoatomic molecule, then $w_1 = w_2 = \dots = w_n = \gamma$ (say), and hence, the variable Randić index ${}^1\chi^f(G)$ becomes

$${}^1\chi^f(G) = {}^vR_\gamma(G) = \sum_{v_i v_j \in E(G)} \frac{1}{\sqrt{(d(v_i) + \gamma)(d(v_j) + \gamma)}} \quad (3)$$

In the rest of this paper, we denote this index by ${}^vR_\gamma$ instead of ${}^1\chi^f$. Clearly, if we take $\gamma = 0$, then the invariant

${}^vR_\gamma(G)$ is the classical Randić index [10, 15]. Liu and Zhong [5] showed that the variable Randić index has more flexibility in characterizing polymers, which can lead to simpler correlations with better correlative accuracy. Details about the chemical applications of the variable Randić index can be found in [5, 7, 9, 12, 15–22] and related references listed therein. It needs to be mentioned here that the variable Randić index seems to have more chemical applications than the several well-known variable indices, for example, the indices considered in [23–33]. However, to the best of the authors' knowledge, mathematical properties of the variable Randić index, for $\gamma > 0$, have not yet been discussed explicitly in any paper. The main purpose of the present paper is to fill this gap by studying this topological index in a mathematical point of view. Since the trees (that are the connected graphs without cycles) form an important class of graphs both in chemical graph theory as well as in general graph theory, in this paper, we study an extremal problem related to the variable Randić index of the class of trees. We prove that the star graph S_n has the minimum variable Randić index among all trees of a fixed order n , where $n \geq 4$.

2. Main Result

To establish the main result, we prove a lemma first.

Lemma 1. *If $\gamma \geq 0$ and $s, t \geq 2$, then function f defined as*

$$f(\gamma, s, t) = (s + t - 1)\sqrt{s + t - 1 + \gamma} - (s - 1)\sqrt{s + \gamma} - (t - 1)\sqrt{t + \gamma} - \sqrt{\frac{(s + \gamma)(t + \gamma)}{1 + \gamma}}, \quad (4)$$

is positive-valued.

Proof. We note that the function $\partial f/\partial s$ is strictly increasing in t on the interval $(1, \infty)$ because

$$\begin{aligned} \frac{\partial f}{\partial s} &= \sqrt{s + t - 1 + \gamma} + \frac{s + t - 1}{2\sqrt{s + t - 1 + \gamma}} - \sqrt{s + \gamma} - \frac{s - 1}{2\sqrt{s + \gamma}} - \frac{\sqrt{t + \gamma}}{2\sqrt{(1 + \gamma)(s + \gamma)}}, \\ \frac{\partial}{\partial t} \left(\frac{\partial f}{\partial s} \right) &= \frac{3\sqrt{(1 + \gamma)(t + \gamma)(s + \gamma)} - \sqrt{s + t - 1 + \gamma}}{4\sqrt{(1 + \gamma)(t + \gamma)(s + \gamma)}\sqrt{s + t - 1 + \gamma}} + \frac{\gamma}{4(s + t - 1 + \gamma)^{3/2}} > 0, \end{aligned} \quad (5)$$

where the last inequality holds because

$$(\gamma + 1)(s + \gamma)(t + \gamma) \geq (s + \gamma)(t + \gamma) > (s + \gamma) + (t + \gamma) - 1 \geq s + t + \gamma - 1. \quad (6)$$

Also, note that the value of the function $\partial f/\partial s$ at $t = 1$ is 0, which implies that the function $\partial f/\partial s$ is positive-valued for $t > 1$, and hence, function f is strictly increasing in s on the interval $(1, \infty)$. Due to the identity $f(\gamma, s, t) = f(\gamma, t, s)$, function f is strictly increasing also in t on the interval

$(1, \infty)$. It holds that $f(\gamma, 1, t) = f(\gamma, t, 1) = 0$, and hence, $f(\gamma, s, t) > 0$ for all $s, t > 1$ and $\gamma \geq 0$. \square

Transformation 1. For $n \geq 4$, let T be a tree of order n containing at least two nonpendent vertices. Let $u \in V(T)$ be

a vertex of maximum degree, and let $N_T(u) = \{v, u_1, u_2, \dots, u_{s-1}\}$, where $d(v) \geq d(u_i)$ for $i = 1, 2, \dots, s-1$. Also, take $N_T(v) = \{u, v_1, v_2, \dots, v_{t-1}\}$. Note that $s \geq t \geq 2$. We transform T into another tree T' by removing the edges $vv_1, vv_2, \dots, vv_{t-1}$ and adding the edges $uv_1, uv_2, \dots, uv_{t-1}$.

Lemma 2. Let T and T' be the trees defined in Transformation 1. For $\gamma \geq 0$, it holds that

$${}^vR_\gamma(T') < {}^vR_\gamma(T). \tag{7}$$

Proof. By using the definition of the variable Randić index, one has

$$\begin{aligned} {}^vR_\gamma(T) - {}^vR_\gamma(T') &= \sum_{i=1}^{s-1} [f(s, d(u_i)) - f(s+t-1, d(u_i))] \\ &\quad + \sum_{i=1}^{t-1} [f(t, d(v_i)) - f(s+t-1, d(v_i))] \\ &\quad + f(s, t) - f(s+t-1, 1), \end{aligned} \tag{8}$$

where

$$f(a, b) = \frac{1}{\sqrt{(a+\gamma)(b+\gamma)}} \tag{9}$$

Equation (8) gives

$$\begin{aligned} {}^vR_\gamma(T) - {}^vR_\gamma(T') &= \sum_{i=1}^{s-1} f(s, d(u_i)) \left[1 - \frac{f(s+t-1, d(u_i))}{f(s, d(u_i))} \right] \\ &\quad + \sum_{i=1}^{t-1} f(t, d(v_i)) \left[1 - \frac{f(s+t-1, d(v_i))}{f(t, d(v_i))} \right] \\ &\quad + f(s, t) - f(s+t-1, 1) \\ &= \sum_{i=1}^{s-1} f(s, d(u_i)) \left(1 - \frac{\sqrt{s+\gamma}}{\sqrt{s+t-1+\gamma}} \right) \\ &\quad + \sum_{i=1}^{t-1} f(t, d(v_i)) \left(1 - \frac{\sqrt{t+\gamma}}{\sqrt{s+t-1+\gamma}} \right) \\ &\quad - \frac{1}{\sqrt{(1+\gamma)(s+t-1+\gamma)}} + \frac{1}{\sqrt{(s+\gamma)(t+\gamma)}} \end{aligned} \tag{10}$$

Since the vertex $u \in V(T)$ has the maximum degree, that is, $d(u) = s \geq d(w)$ for every $w \in V(T)$ and $d(v) = t \geq d(u_i)$ for $i = 1, 2, \dots, s-1$, thus, $f(s, d(u_i)) \geq f(s, t)$ and $f(t, d(v_i)) \geq f(t, s) = f(s, t)$. Hence, equation (10) yields

$$\begin{aligned} {}^vR_\gamma(T) - {}^vR_\gamma(T') &\geq \frac{s-1}{\sqrt{(s+\gamma)(t+\gamma)}} \left(1 - \frac{\sqrt{s+\gamma}}{\sqrt{s+t-1+\gamma}} \right) \\ &\quad + \frac{t-1}{\sqrt{(s+\gamma)(t+\gamma)}} \left(1 - \frac{\sqrt{t+\gamma}}{\sqrt{s+t-1+\gamma}} \right) \\ &\quad - \frac{1}{\sqrt{(1+\gamma)(s+t-1+\gamma)}} + \frac{1}{\sqrt{(s+\gamma)(t+\gamma)}} \\ &= \frac{s-1}{\sqrt{(s+\gamma)(t+\gamma)}} + \frac{t-1}{\sqrt{(s+\gamma)(t+\gamma)}} + \frac{1}{\sqrt{(t+\gamma)(s+\gamma)}} \\ &\quad - \frac{s-1}{\sqrt{(t+\gamma)(s+t-1+\gamma)}} - \frac{t-1}{\sqrt{(s+\gamma)(s+t-1+\gamma)}} \\ &\quad - \frac{1}{\sqrt{(1+\gamma)(s+t-1+\gamma)}} \\ &= \frac{1}{\sqrt{(s+\gamma)(t+\gamma)(s+t-1+\gamma)}} [(s+t-1)\sqrt{s+t-1+\gamma} \\ &\quad - (s-1)\sqrt{s+\gamma} - (t-1)\sqrt{t+\gamma} - \sqrt{\frac{(s+\gamma)(t+\gamma)}{1+\gamma}}]. \end{aligned} \tag{11}$$

By using Lemma 1 in (11), we get ${}^vR_\gamma(T) - {}^vR_\gamma(T') > 0$, as desired.

Next result is a direct consequence of Lemma 2. \square

Theorem 1. For $n \geq 4$ and $\gamma \geq 0$, among all trees of a fixed order n , star graph S_n is the unique tree with minimum variable Randić index ${}^vR_\gamma$, which is

$$\frac{n-1}{\sqrt{(n-1+\gamma)(1+\gamma)}} \tag{12}$$

For $\gamma \geq 0$ and small values of n , we calculate the variable Randić index ${}^vR_\gamma$ of the trees of order n and find that the value of this index does not exceed from

$${}^vR_\gamma(P_n) = \frac{2}{\sqrt{(1+\gamma)(2+\gamma)}} + \frac{n-3}{2+\gamma} \tag{13}$$

This suggests the following conjecture.

Conjecture 1. For $n \geq 4$ and $\gamma \geq 0$, among all trees of a fixed order n , path graph P_n is the unique tree with maximum variable Randić index ${}^vR_\gamma$, which is

$$\frac{2}{\sqrt{(1+\gamma)(2+\gamma)}} + \frac{n-3}{2+\gamma} \tag{14}$$

Data Availability

There are no data concerning the present study except those presented in this manuscript.

Conflicts of Interest

The authors declare that there are no conflicts of interest.

Acknowledgments

This work was supported by the National University of Computer and Emerging Sciences, Lahore, Pakistan.

References

- [1] J. L. Gross and J. Yellen, *Graph Theory*, CRC Press, Boca Raton, FL, USA, 2000.
- [2] F. Harary, *Graph Theory*, Addison-Wesley, Toronto, Canada, 1969.
- [3] I. Gutman and O. E. Polansky, *Mathematical Concepts in Organic Chemistry*, Springer-Verlag, New York, NY, USA, 1986.
- [4] L. B. Kier and L. H. Hall, *Molecular Connectivity in Structure-Activity Analysis*, John Wiley and Sons Inc., New York, NY, USA, 1986.
- [5] D. Liu and C. Zhong, "Modeling of the heat capacity of polymers with the variable connectivity index," *Polymer Journal*, vol. 34, no. 12, pp. 954–961, 2002.
- [6] N. Trinajstić, *Chemical Graph Theory*, CRC Press, Boca Raton, FL, USA, 1992.
- [7] G. Caporossi, I. Gutman, P. Hansen, and L. Pavlović, "Graphs with maximum connectivity index," *Computational Biology and Chemistry*, vol. 27, no. 1, pp. 85–90, 2003.
- [8] E. Estrada and D. Bonchev, "Chemical graph theory," in *Discrete Mathematics and Its Applications*, CRC Press, Boca Raton, FL, USA, 2013.
- [9] M. Randić, "On the history of the connectivity index: from the connectivity index to the exact solution of the protein alignment problem," *SAR and QSAR in Environmental Research*, vol. 26, no. 7-9, pp. 523–555, 2015.
- [10] M. Randić, "On characterization of molecular branching," *Journal of the American Chemical Society*, vol. 97, no. 23, 1975.
- [11] M. Randić, "High quality structure-property regressions. Boiling points of smaller alkanes," *New Journal of Chemistry*, vol. 24, no. 3, pp. 165–171, 2000.
- [12] M. Randić, M. Pompe, D. Mills, and S. C. Basak, "Variable connectivity index as a tool for modeling structure-property relationships," *Molecules (Basel, Switzerland)*, vol. 9, no. 12, pp. 1177–1193, 2004.
- [13] M. Randić, "Novel graph theoretical approach to heteroatoms in quantitative structure-activity relationships," *Chemo-metrics and Intelligent Laboratory Systems*, vol. 10, no. 1-2, pp. 213–227, 1991.
- [14] M. Randić, "On computation of optimal parameters for multivariate analysis of structure-property relationship," *Journal of Computational Chemistry*, vol. 12, no. 8, pp. 970–980, 1992.
- [15] M. Randić, "On history of the Randić index and emerging hostility toward chemical graph theory," *MATCH Communications in Mathematical and in Computer Chemistry*, vol. 59, no. 1, pp. 5–124, 2008.
- [16] J. C. Dearden, "The use of topological indices in QSAR and QSPR modeling," in *Advances in QSAR Modeling*, K. Roy, Ed., pp. 57–88, Springer, Berlin, Germany, 2017.
- [17] R. G. Domenech, J. Gálvez, J. V. de Julián-Ortiz, and L. Pogliani, "Some new trends in chemical graph theory," *Chemical Reviews*, vol. 108, pp. 1127–1169, 2008.
- [18] M. Pompe, "Variable connectivity index as a tool for solving the anti connectivity problem," *Chemical Physics Letters*, vol. 404, pp. 296–299, 2004.
- [19] M. Randić and S. C. Basak, "On use of the variable connectivity index $1\chi^f$ in QSAR: toxicity of aliphatic ethers," *Journal of Chemical Information and Computer Sciences*, vol. 41, no. 3, pp. 614–618, 2001.
- [20] M. Randić and M. Pompe, "The variable connectivity index $1\chi^f$ versus the traditional molecular descriptors: a comparative study of $1\chi^f$ against descriptors of CODESSA," *Journal of Chemical Information and Computer Sciences*, vol. 41, no. 3, pp. 631–638, 2001.
- [21] M. Randić, D. Plavšić, and N. Leš, "Variable connectivity index for cycle-containing structures," *Journal of Chemical Information and Computer Sciences*, vol. 41, pp. 657–662, 2001.
- [22] S. Yousaf, A. A. Bhatti, and A. Ali, "On the minimum variable connectivity index of unicyclic graphs with a given order," *Discrete Dynamics in Nature and Society*.
- [23] S. Akhter, M. Imran, and Z. Raza, "Bounds for the general sum-connectivity index of composite graphs," *Journal of Inequalities and Applications*, vol. 2017, no. 1, p. 76, 2017.
- [24] A. Ali, Z. Du, and K. Shehzadi, "Estimating some general molecular descriptors of saturated hydrocarbons," *Molecular Informatics*, vol. 38, no. 11-12, 2019.
- [25] D. Amić, D. Davidovic-Amić, D. Bešlo, B. Lučić, N. Trinajstić, and S. Nikolić, "The vertex-connectivity index revisited," *Journal of Chemical Information and Computer Sciences*, vol. 38, no. 5, pp. 819–822, 1998.
- [26] A. Behtoei, "Some relations and bounds for the general first zagreb index," *MATCH Communications in Mathematical and in Computer Chemistry*, vol. 81, no. 2, pp. 361–370, 2019.
- [27] D. Dimitrov and A. Ali, "On the extremal graphs with respect to the variable sum exdeg index," *Discrete Mathematics Letters*, vol. 1, pp. 42–48, 2019.
- [28] S. Elumalai and T. Mansour, "On the general zeroth-order Randić index of bargraphs," *Discrete Mathematics Letters*, vol. 2, pp. 6–9, 2019.
- [29] F. Hayat, "On generalized atom-bond connectivity index of cacti," *Iranian Journal of Mathematical Chemistry*, vol. 10, pp. 319–330, 2019.
- [30] M. Imran, A. Q. Baig, and H. Ali, "On molecular topological properties of hex-derived networks," *Journal of Chemo-metrics*, vol. 30, no. 3, pp. 121–129, 2016.
- [31] J.-B. Liu, J. Zhao, and Z.-Q. Cai, "On the generalized adjacency, Laplacian and signless Laplacian spectra of the weighted edge corona networks," *Physica A: Statistical Mechanics and Its Applications*, vol. 540, p. 123073, 2020.
- [32] J.-B. Liu, J. Zhao, H. He, and Z. Shao, "Valency-based topological descriptors and structural property of the generalized sierpiński networks," *Journal of Statistical Physics*, vol. 177, no. 6, pp. 1131–1147, 2019.
- [33] A. Martínez-Pérez and J. M. Rodríguez, "A unified approach to bounds for topological indices on trees and applications," *MATCH Communications in Mathematical and in Computer Chemistry*, vol. 82, pp. 679–698, 2019.

Research Article

On Computation of Face Index of Certain Nanotubes

Ansheng Ye,¹ Aisha Javed,² Muhammad Kamran Jamil ,³ Kanza Abdul Sattar,³
Adnan Aslam ,⁴ Zahid Iqbal ,^{5,6} and Asfand Fahad ⁷

¹School of Information Science and Engineering, Chengdu University, Chengdu 610106, China

²Abdus Salam School of Mathematical Sciences, GC University, Lahore, Pakistan

³Department of Mathematics, Riphah International University, 14 Ali Road, Lahore, Pakistan

⁴Department of Natural Sciences and Humanities, University of Engineering and Technology, Lahore (RCET), Lahore, Pakistan

⁵National University of Science and Technology, Islamabad, Pakistan

⁶Department of Mathematics and Statistics, Institute of Southern Punjab, Multan, Pakistan

⁷Department of Mathematics, COMSATS University Islamabad, Vehari Campus, Vehari 61110, Pakistan

Correspondence should be addressed to Adnan Aslam; adnanaslam15@yahoo.com

Received 22 May 2020; Accepted 18 June 2020; Published 16 July 2020

Guest Editor: Muhammad Javaid

Copyright © 2020 Ansheng Ye et al. This is an open access article distributed under the Creative Commons Attribution License, which permits unrestricted use, distribution, and reproduction in any medium, provided the original work is properly cited.

Topological index is a number that can be used to characterize the graph of a molecule. Topological indices describe the physical, chemical, and biological properties of a chemical structure. In this paper, we derive the analytical closed formulas of face index of some planar molecular structures such as TUC_4 , $TUC_4C_8(S)$, $TUHC_6$, $TUC_4C_8(R)$, and armchair $TUVC_6$.

1. Introduction

In this time of rapid technological development, the pharmacological techniques have evolved rapidly during the recent years. Consequently, a large number of new drugs and chemical compounds have been obtained. A huge amount of work is required to study the biological, chemical, and pharmacological aspects of these new drugs and chemical compounds. This workload is becoming more and more cumbersome as it requires sufficient tools, reagents, human resources, and a lot of time to check the performance of these new chemical compounds. However, the developing countries cannot afford these equipment and reagents to check up these biochemical properties and are resultantly unable to compete with the developed world in the areas of medical science and industry. To some extent, the chemical graph theory solved this problem as it assists to measure the pharmaceutical, chemical, and physical properties of the chemical compounds. Fortunately, previous research has revealed that chemical properties of a molecule such as boiling point, melting point, and toxicity are closely related to their molecular structures (see [1, 2]). This relationship is

one of the key reasons for the development of the mathematical chemistry. In the chemical graph theory, a molecular structure can be represented in the form of a graph $G = (V(G), E(G))$, where vertices $V = V(G)$ and edges $E = E(G)$ of a graph G show the atoms and the bonds of a molecular structure, respectively.

A topological index (TI) is an invariant that is assigned to a molecular structure (graph) and is used to characterize the molecule. It may be thought as a convenient device which converts a chemical constitution into a unique number, which is independent of the way in which the corresponding graph has been drawn or labeled. TIs were employed in developing a suitable correlation between the chemical structure and chemical or biological activities and physical properties. Several researchers working in the area of chemical and mathematical sciences have introduced TIs, such as the Wiener index, Randić indices, Zagreb indices, PI index, eccentric index, atom-bond connectivity index, and forgotten index, which have been used to predict the characteristics of the nanomaterials, drugs, and other chemical compounds. There are several papers to calculate the topological indices of some special molecular graphs [3–12].

The notions of a planar graph, its faces, and an infinite face are well known in the literature. Let $G = (V(G), E(G), F(G))$ be a finite simple connected planar graph, where $V(G)$, $E(G)$, and $F(G)$ represent the vertex, edge, and face sets, respectively. A face $f \in F(G)$ is incident to an edge $e \in E(G)$ if e is one of those which surrounds the face. Similarly, a face $f \in F(G)$ is incident to a vertex v in G if v is at the end of one of those incident edges; the incidence of v to the face f is represented by $v \sim f$. The face degree f in G is given as $d(f) = \sum_{v \sim f} d(v)$. For the notions and notations not given here, we refer [13] to the readers.

Recently, Jamil et al. [14] introduced a novel topological index named as the face index. The face index helped to predict the energy and the boiling points of selected benzenoid hydrocarbons with the correlation coefficient $r > 0.99$. For a graph G , the face index (FI) can be defined as

$$FI(G) = \sum_{f \in F(G)} d(f) = \sum_{v \sim f \in F(G)} d(v). \quad (1)$$

In this paper, we calculate the face index of some special molecular graphs which have been widely used in drugs.

2. Main Results

In this section, we investigate the exact formulas of the face index for the molecular structures of vastly studied nanotubes with wide range of applications: $TUC_4C_8(S)$, $TUC_4C_8(R)$, $TUHC_6$, TUC_4 , and $TUVC_6$. To find the face indices of the molecular graphs of these nanotubes, we partitioned the face set depending on the degrees of each face.

2.1. Face Index of $TUC_4C_8(S)[n, q, r]$ and $TUC_4C_8(R)[n, q, r]$ Nanotubes. The 2-dimensional lattice of $TUC_4C_8(S)$ $[n, q, r]$ is constructed by the alternately positioned squares C_4 and octagons C_8 (see Figure 1(a)), where n, q , and r represent the number of rows, octagons in each row, and squares in each row. A $TUC_4C_8(S)[n, q, r]$ nanotube can be constructed by rolling the 2D lattice of carbon atoms and can be seen in Figure 1(b).

Firstly, we prove the following formula which provides the exact values of the face index for $TUC_4C_8(S)[n, q, r]$.

Theorem 1. *Let $G = TUC_4C_8(S)[n, q, r]$, where $n, q, r \geq 1$, be the 2-dimensional lattice of $TUC_4C_8(S)$ nanotube; then, the face index of G is given as*

$$FI(G) = 24nq + 12nr + 4q + 12r. \quad (2)$$

Proof. Let G be the 2-dimensional lattice of $TUC_4C_8(S)[n, q, r]$ nanotube with n number of rows and let q and r be the number of octagons and number of squares in each row, respectively. In $TUC_4C_8(S)[n, q, r]$, the total number of faces in one row is $q + r$. Let f_j denote the faces having $\sum_{w \sim f_j} d_w = j$ and $|f_j|$ denote the number of faces with degree j . From Figure 1(a), it can be noticed that 2D lattice of $TUC_4C_8(S)[7, 4, 4]$ contains four types of internal faces f_{12} , f_{20} , f_{22} , and f_{24} and an external face, f_∞ . When

$TUC_4C_8(S)[n, q, r]$ has n rows, then sum of vertex degrees of external face is $8q + 12r$. The number of internal faces in each row is given in Table 1.

The face index of $TUC_4C_8(S)[n, q, r]$ is

$$\begin{aligned} FI(G) &= \sum_{w \sim f \in F(G)} d_w \\ &= \sum_{w \sim f_{12}} d_w + \sum_{w \sim f_{22}} d_w + \sum_{w \sim f_{24}} d_w + \sum_{w \sim f_\infty} d_w \\ &= |f_{12}|(12) + |f_{22}|(22) + |f_{24}|(24) + 8q + 12r \quad (3) \\ &= nr(12) + 2q(22) + q(n-2)(24) + 8q + 12r \\ &= 12nr + 44q + 24nq - 48q + 8q + 12r \\ &= 24nq + 12nr + 4q + 12r. \end{aligned}$$

This completes the proof. \square

Theorem 2. *Let $n, q, r \geq 1$ and $H = TUC_4C_8(R)[n, q, r]$ be the graph of 2-dimensional lattice of $TUC_4C_8(R)$ nanotube. Then, the face index of the graph H is given as*

$$FI(H) = 24nq + 6nr + 12q + 18r. \quad (4)$$

Proof. Consider a $TUC_4C_8(R)[n, q, r]$ nanotube with n number of rows, q number of octagons, and r number of squares in each row as shown in Figure 2(a). The 2-dimensional lattice (H) of $TUC_4C_8(R)[n, q, r]$ is shown in Figure 2(b). In H , the total number of faces in one row is $q + r$. Let f_j and $|f_j|$ denote the face with degree j and the number of faces with degree j , respectively. From the structure of H , one can notice that there are three types of internal faces f_{11} , f_{12} , and f_{24} and an external face f_∞ . The external face has degree $12q + 2r$. Table 2 illustrates the number of internal faces in $TUC_4C_8(R)[n, q, r]$ based on the degree of each face.

The face index of the graph $H = TUC_4C_8(R)[n, q, r]$ is

$$\begin{aligned} FI(H) &= \sum_{w \sim f \in F(H)} d_w \\ &= \sum_{w \sim f_{11}} d_w + \sum_{w \sim f_{12}} d_w + \sum_{w \sim f_{24}} d_w + \sum_{w \sim f_\infty} d_w \\ &= |f_{11}|(11) + |f_{12}|(12) + |f_{24}|(24) + 12q + 2r \\ &= r(11) + \frac{(n-1)r}{2}(12) + nq(24) + 12q + 2r \\ &= 11r + 6nr - 6r + 24nq + 12q + 2r \\ &= 24nq + 6nr + 12q + 7r. \end{aligned} \quad (5)$$

This completes the proof. \square

2.2. Face Index of $TUC_4[p, q]$ Nanotube. For $p \geq 2$ and $q \geq 3$, the 2-dimensional lattice of $TUC_4[p, q]$ nanotube is obtained by the Cartesian product of the path P_p and the cycle C_q . For $p = 8$ and $q = 4$, the example of $TUC_4[p, q]$ is shown in Figure 3(b).

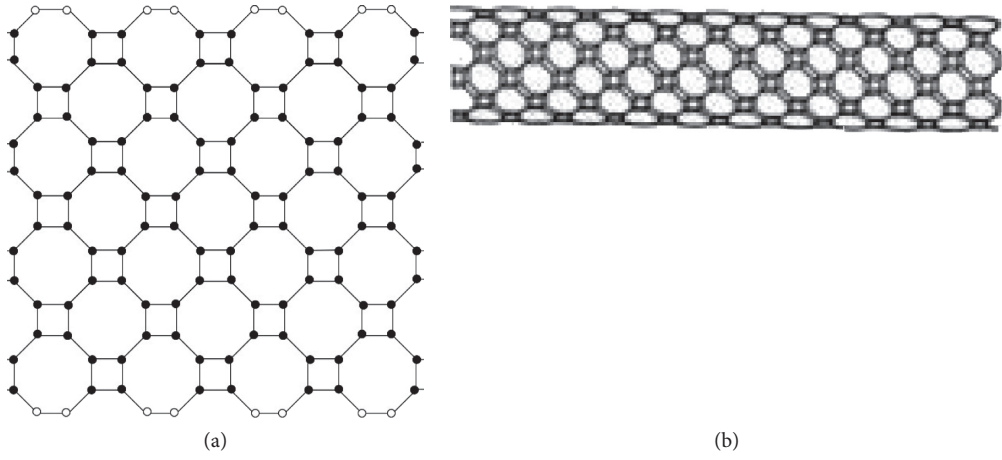


FIGURE 1: (a) 2D lattice of $TUC_4C_8(S)[7,4,4]$. (b) 3D nanotube $TUC_4C_8(S)$.

TABLE 1: Numbers of f_{12} , f_{20} , f_{22} , and f_{24} with given number of rows.

n	$ f_{12} $	$ f_{20} $	$ f_{22} $	$ f_{24} $
1	R	q	—	—
2	$2r$	—	$2q$	—
3	$3r$	—	$2q$	Q
4	$4r$	—	$2q$	$2q$
⋮	⋮	⋮	⋮	⋮
⋮	⋮	⋮	⋮	⋮
N	Nr	—	$2q$	$(n-2)q$

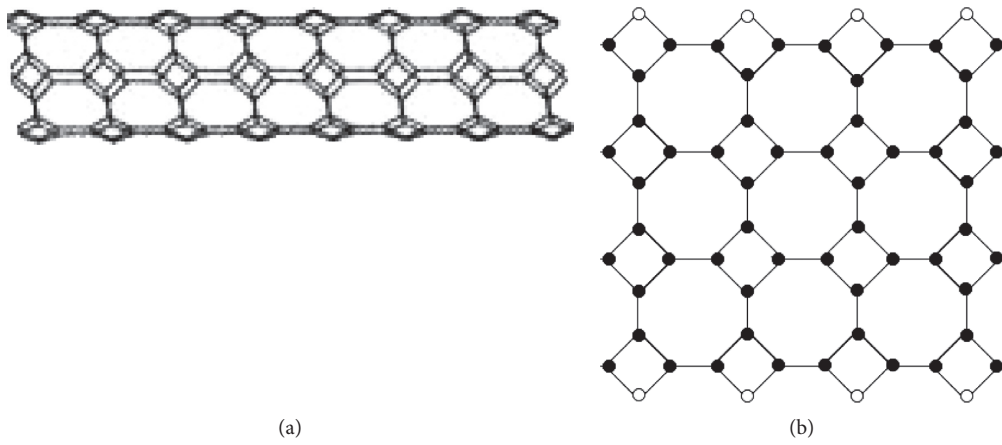


FIGURE 2: (a) 3D nanotube $TUC_4C_8(R)$. (b) 2D lattice of $TUC_4C_8(R)$.

TABLE 2: Numbers of f_{11} , f_{12} , and f_{24} with given number of rows.

n	$ f_{11} $	$ f_{12} $	$ f_{24} $
1	R	—	Q
2	R	$r/2$	$2q$
3	R	R	$3q$
4	R	$3r/2$	$4q$
5	5	$2r$	$5q$
⋮	⋮	⋮	⋮
⋮	⋮	⋮	⋮
N	R	$(n-1)r/2$	Nq

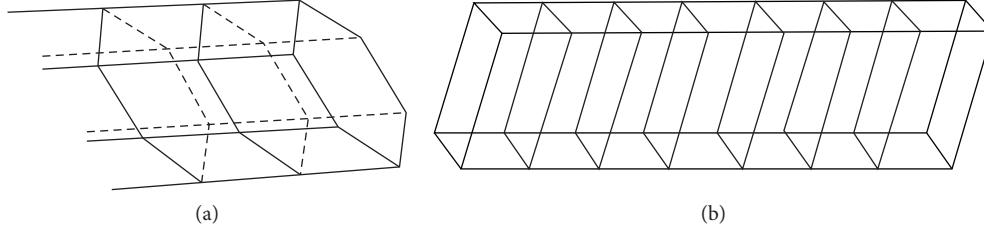


FIGURE 3: (a) Nanotube $TUC_4[p, 6]$. (b) Nanotube $TUC_4[8, 4]$.

Theorem 3. Let K be the graph of $TUC_4[p, q]$ nanotube structure, where $p \geq 2$ and $q \geq 3$. Then, the face index of K is equal to

$$FI(K) = \begin{cases} 18q; & \text{if } p = 2, \\ 34q; & \text{if } p = 3, \\ 2q(8p - 7); & \text{if } p > 3. \end{cases} \quad (6)$$

Proof. We will prove the result for $p > 3$. Let K denote the graph of $TUC_4C[p, q]$ nanotube structure. From Figure 3, we can notice that the graph K contains three types of internal faces, namely, f_{3q} , f_{14} , and f_{16} , and an external face of degree $3q$. By applying the definition and using the values from Table 3, the face index of K can be computed as

$$\begin{aligned} FI(K) &= \sum_{w \sim f \in F(K)} d_w \\ &= \sum_{w \sim f_{3q}} d_w + \sum_{w \sim f_{14}} d_w + \sum_{w \sim f_{16}} d_w \\ &= |f_{3q}|(3q) + |f_{14}|(14) + |f_{16}|(16) \\ &= 2(3q) + 14(2q) + 16(p - 3)q \\ &= 2q(8p - 7). \end{aligned} \quad (7)$$

This completes the proof.

2.3. Zig-Zag $TUHC_6[n, q]$ Nanotube. Consider the graph K of $TUHC_6[n, q]$ zig-zag polyhex nanotube structure, where n denotes the number of rows and the number of hexagons in each row is represented by q . Figure 4 illustrates the nanotube $TUHC_6[n, q]$ and its 2-dimensional structure.

Theorem 4. For $n, q \geq 1$, let K represent the 2-dimensional graph of $TUHC_4[n, q]$ structure. The face index of K is

$$FI(K) = 18nq + 8q. \quad (8)$$

Proof. Let $TUHC_6[n, q]$ be a polyhex nanotube with n number of rows and q number of hexagons in each row and K be the 2-dimensional graph of $TUHC_6[n, q]$ structure. The molecular graph of $TUHC_6[n, q]$ is shown in Figure 4. Let f_j denote the face having degree j , i.e., $\sum_{w \sim f_j} d_w = j$, and let $|f_j|$ denote the number of f_j . The molecular graph of $TUHC_6[n, q]$ contains two types of internal faces f_{17} and f_{18} and an external face f_{∞} . When $TUHC_6[n, q]$ has n rows, then the face degree of f_{∞} is $10q$. The number of internal faces with the given number of rows is listed in Table 4.

TABLE 3: Numbers of f_{11} , f_{12} , and f_{24} with given number of rows.

$TUC_4[k, q]$	$ f_{3q} $	$ f_{12} $	$ f_{14} $	f_{16}
$k=2$	2	Q	—	—
$k=3$	2	—	$2q$	—
$k=4$	2	—	$2q$	Q
$k=5$		—	$2q$	$2q$
\vdots	\vdots	\vdots	\vdots	\vdots
\vdots	\vdots	\vdots	\vdots	\vdots
\vdots	\vdots	\vdots	\vdots	\vdots
$k=p$	2	—	$2q$	$(p-3)q$

The face index of the graph $K = TUHC_6[n, q]$ is

$$\begin{aligned} FI(K) &= \sum_{w \sim f \in F(K)} d_w \\ &= \sum_{w \sim f_{17}} d_w + \sum_{w \sim f_{18}} d_w + \sum_{w \sim f_{\infty}} d_w \\ &= |f_{17}|(17) + |f_{18}|(18) + 10q \\ &= 2q(17) + (n - 2)q(18) + 10q \\ &= 34q + 18nq - 36q + 10q \\ &= 18nq + 8q, \end{aligned} \quad (9)$$

which is the required result. \square

2.4. $TUVC_6[n, q]$ Nanotube. The 2-dimensional graph of $TUVC_6[n, q]$ is shown in Figure 5(b), and the $TUVC_6[n, q]$ nanotube can be constructed by rolling this lattice of carbon atoms (Figure 5(a)), where n represents the number of rows and q is the hexagons in each row.

Theorem 5. Let $L = TUVC_4[n, q]$, where $n, q \geq 1$, be the graph of 2-dimensional lattice of $TUVC_6[n, q]$ armchair polyhex nanotube. The face index of L is

$$FI(L) = 36nq - 8q. \quad (10)$$

Proof. Let L represent the 2-dimensional molecular graph of $TUVC_6[n, q]$ with n number of rows and q number of hexagons in each row. From Figure 5(b), we can easily notice that L contains 2 types of internal faces f_{16} and f_{18} and an external face, and the degree of external face is $14q$. The cardinalities of internal faces with given degree and given number of rows are explained in Table 5.

The face index of $L = TUVC_6[n, q]$ is

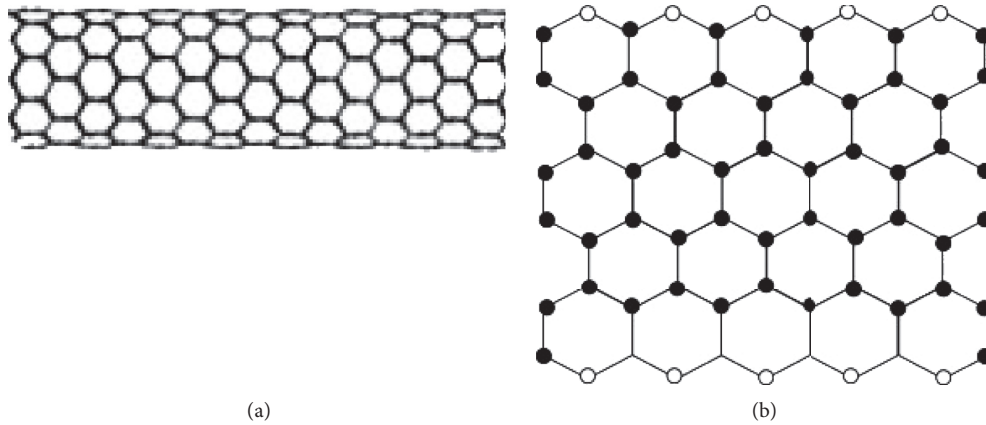


FIGURE 4: (a) 3D nanotube TUHC₆[n, q]. (b) 2D lattice of TUHC₆[5, 5].

TABLE 4: The cardinalities of the faces with given degree for given number of rows.

n	$ f_{16} $	$ f_{17} $	$ f_{18} $
1	q	—	—
2	—	$2q$	—
3	—	$2q$	Q
4	—	$2q$	$2q$
⋮	⋮	⋮	⋮
⋮	⋮	⋮	⋮
N	—	$2q$	$(n-2)q$

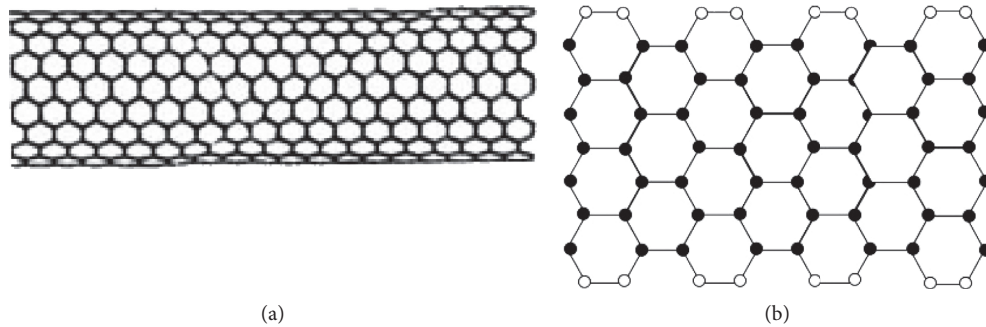


FIGURE 5: (a) Armchair 3D nanotube TUV C₆[n, q]. (b) 2D lattice of TUV C₆[4, 4].

TABLE 5: The cardinalities of f_{14} , f_{16} , and f_{18} with given number of rows.

n	$ f_{14} $	$ f_{16} $	$ f_{18} $
1	q	—	—
2	—	$2q$	Q
3	—	$2q$	$3q$
4	—	$2q$	$5q$
⋮	⋮	⋮	⋮
⋮	⋮	⋮	⋮
N	—	$2q$	$(2n-3)q$

$$\begin{aligned}
 FI(L) &= \sum_{w \sim f \in F(L)} d_w \\
 &= \sum_{w \sim f_{16}} d_w + \sum_{w \sim f_{18}} d_w + \sum_{w \sim f_{\infty}} d_w \\
 &= |f_{16}|(16) + |f_{18}|(18) + 14q \\
 &= 2q(16) + (2n-3)q(18) + 14q \\
 &= 32q + 36nq - 54q + 14q \\
 &= 36nq - 8q,
 \end{aligned}
 \tag{11}$$

and the proof is complete. \square

3. Conclusion

In [14], using multiple linear regression, it has been shown that the novel face index can predict the π electron energy and boiling point of benzenoid hydrocarbon with a correlation coefficient greater than 0.99. Therefore, this index can be useful in QSPR/QSAR studies. In this paper, we have computed the novel face index of some nanotubes.

Data Availability

No data were used to support the study.

Disclosure

This research was carried out as a part of the employment of the authors.

Conflicts of Interest


The authors declare that they have no conflicts of interest.

References

- [1] H. Wiener, "Structural determination of paraffin boiling points," *Journal of the American Chemical Society*, vol. 69, no. 1, pp. 17–20, 1947.
- [2] A. R. Katritzky, R. Jain, A. Lomaka, R. Petrukhin, U. Maran, and M. Karelson, "Perspective on the relationship between melting points and chemical structure," *Crystal Growth & Design*, vol. 1, no. 4, pp. 261–265, 2001.
- [3] J.-B. Liu, M. Javaid, and H. M. Awais, "Computing Zagreb indices of the subdivision-related generalized operations of graphs," *IEEE Access*, vol. 7, pp. 105479–105488, 2019.
- [4] J.-B. Liu, S. Javed, M. Javaid, and K. Shabbir, "Computing first general Zagreb index of operations on graphs," *IEEE Access*, vol. 7, pp. 47494–47502, 2019.
- [5] J.-H. Tang, U. Ali, M. Javaid, and K. Shabbir, "Zagreb connection indices of subdivision and semi-total point operations on graphs," *Journal of Chemistry*, vol. 2019, Article ID 9846913, 14 pages, 2019.
- [6] M. Javaid, M. U. Rehman, and J. Cao, "Topological indices of rhombus type silicate and oxide networks," *Canadian Journal of Chemistry*, vol. 95, no. 2, pp. 134–143, 2017.
- [7] A. Aslam, Y. Bashir, S. Ahmad, and W. Gao, "On topological indices of certain dendrimer structures," *Zeitschrift für Naturforschung A*, vol. 72, no. 6, pp. 559–566, 2017.
- [8] A. Aslam, S. Ahmad, and W. Gao, "On certain topological indices of boron triangular nanotubes," *Zeitschrift für Naturforschung A*, vol. 72, no. 8, pp. 711–716, 2017.
- [9] A. Aslam, M. K. Jamil, W. Gao, and W. Nazeer, "Topological aspects of some dendrimer structures," *Nanotechnology Reviews*, vol. 7, no. 2, pp. 123–129, 2018.
- [10] A. Aslam, S. Ahmad, M. A. Binyamin, and W. Gao, "Calculating topological indices of certain OTIS interconnection networks," *Open Chemistry*, vol. 17, no. 1, pp. 220–228, 2019.
- [11] Z. Shao, P. Wu, Y. Gao, I. Gutman, and X. Zhang, "On the maximum ABC index of graphs without pendent vertices," *Applied Mathematics and Computation*, vol. 315, pp. 298–312, 2017.
- [12] Z. Shao, P. Wu, X. Zhang, D. Dimitrov, and J.-B. Liu, "On the maximum ABC index of graphs with prescribed size and without pendent vertices," *IEEE Access*, vol. 6, no. 6, pp. 27604–27616, 2018.
- [13] J. A. Bondy and U. S. R. Murty, *Graph Theory*, Springer, Berlin, Germany, 2008.
- [14] M. K. Jamil, M. Imran, and K. Abdul Sattar, "Novel face index for benzenoid hydrocarbons," *Mathematics*, vol. 8, no. 3, p. 312, 2020.

Research Article

Design of Computational Model for Cyanobacterial Pollutant Diffusion Change in Chaohu Lake of China Based on Large Data

Junping Yao ¹ and Guilan He ²

¹*School of Electronic and Information Engineering, Chongqing Radio & TV University, Chongqing, China*

²*School of Artificial Intelligence and Big Data, Chongqing College of Electronic Engineering, Chongqing, China*

Correspondence should be addressed to Junping Yao; yao_junping@126.com

Received 29 April 2020; Accepted 28 May 2020; Published 11 July 2020

Academic Editor: Jia-Bao Liu

Copyright © 2020 Junping Yao and Guilan He. This is an open access article distributed under the Creative Commons Attribution License, which permits unrestricted use, distribution, and reproduction in any medium, provided the original work is properly cited.

Cyanobacteria in Chaohu Lake multiply rapidly and diffuse in large quantities every summer, which has a serious impact on the normal life of the surrounding residents and the local economic development. Therefore, it is urgent to control the cyanobacterial pollutants in Chaohu Lake. In this context, in order to improve the scientificity and feasibility of control measures, it is an important prerequisite and condition to grasp the change of cyanobacterial pollutant diffusion in Chaohu Lake. For this reason, a computational model for cyanobacterial pollutant diffusion in Chaohu Lake, China, was designed based on the relevant large data. The design of the model is divided into three parts: the first part builds an area calculation model to analyze the change of cyanobacterial pollutant diffusion area; the second part builds a concentration calculation model to analyze the change of cyanobacterial pollutant concentration; and the third part combines the previous two to build a diffusion change calculation model to analyze the rule of cyanobacterial pollutant diffusion change in Chaohu Lake. In order to verify the feasibility and validity of the model, simulation experiments were carried out. The results show that, under the large data related to cyanobacteria pollution in Chaohu Lake, China, from May to August 2017, the calculation model is used to calculate the cyanobacteria pollutant diffusion change. The data obtained are basically consistent with the actual situation, which proves the feasibility and validity of the model. This provides data support for the cyanobacteria pollution control in Chaohu Lake and improves the efficiency and effect of the control.

1. Introduction

China is a vast land with many rivers and lakes, such as Junyang Lake in Jiangxi Province, Dongting Lake in Hunan Province, Taihu Lake and Hongze Lake in Jiangsu, and Chaohu Lake in Anhui Province, which are five major freshwater rivers in China and important part of fresh water resource. Taking Chaohu Lake in China as an example, this paper analyzes the change of cyanobacterial pollutant diffusion. Located in central Anhui Province and between the Yangtze River and the Huaihe River, Chaohu River covers a total area of 769.5 square kilometers and stretches across 6 counties and cities, Hefei, Feixi, Shucheng, Lujiang, Chaohu, and Feidong, with multiple functions such as transportation, fish breeding, and agricultural irrigation [1]. However, as the

economy develops rapidly and urban population increases quickly, there are increasing pollutants discharged into Chaohu Lake, especially industrial wastewater, which causes serious water heavy metal pollution. According to the data of satellite monitoring, the frequency and the maximum area of cyanobacterial outbreak were higher than those of the same period last year; in the first half of this year, the total nitrogen concentration of Chaohu Lake was basically equal to that of the same period last year, and the total phosphorus concentration increased by 7.32%; the average algae density of the whole lake was 78.1% higher than that of the same period last year [2]. In addition, since this summer, there have been 29 cyanobacterial outbreaks in Chaohu Lake. The maximum outbreak area reached 130 square kilometers, accounting for 17.1% of the area of Chaohu Lake, which not only had a

serious impact on the normal life of the surrounding residents but also caused serious losses to local transportation and fishery development. In this context, it is urgent to control the cyanobacterial pollutants in Chaohu Lake, China. However, due to insufficient mastery of the information related to the change of cyanobacterial pollutant diffusion, the adopted treatment measures could not suit the remedy to the case. Therefore, based on big data, this paper designs a calculation model for cyanobacterial pollutant diffusion change in Chaohu Lake, China. In order to roundly grasp the changing situation of cyanobacterial pollutant diffusion in Chaohu Lake, China, this model comprehensively evaluates pictures and data and concludes the comprehensive result including the change of pollutant diffusion area and concentration distribution situation in water body as time goes by integrating all results [3]. Among them, the former two were realized based on remote sensing data, while the latter was realized on the detection data from the sensor. Finally, in order to test the validity of the calculation model in this paper, the relevant historical data from May to August 2015 was taken as sample data for simulation test. After comparing the test result with the actual result recorded in that year, the result showed that data related to the change of cyanobacterial pollutant diffusion in Chaohu Lake obtained by the calculation model in this paper is close to the actual results and proved the validity and feasibility of the model in this paper, which provides important treatment data for cyanobacterial pollutants in Chaohu Lake, China, and improves the water environment of Chaohu Lake to some extent.

2. Design of Calculation Model for Cyanobacterial Pollutant Diffusion Change in Chaohu Lake of China

Cyanophyta, also known as cyanobacteria, is the most primitive and the oldest algae with extremely wide distribution range and strong reproductive ability. Especially with suitable temperature and rich nutrient substances, Cyanophyta will reproduce excessively, which will cause oxygen reduction in water body, affect the growth of other aquatic plants, generate cyanobacterial toxins, harm aquaculture, and influence the normal life of surrounding residents with stink [4]. As one of five major freshwater lakes, Chaohu Lake has Cyanophyta outbreak every year, which causes enormous economic loss. For the above situations, this paper divides the calculation model for cyanobacterial pollutant diffusion change in Chaohu Lake, China, into three parts: the first is the calculation model for the pollutant diffusion area change; the second is the model of pollutant transportation and diffusion concentration; and the third is that the previous two are combined to construct the mathematical model of water quality to describe the pollutant diffusion rule as space and time go by [5]. The specific content is shown in Figure 1.

2.1. Calculation Model for the Pollutant Diffusion Area Change. Pollutant diffusion area is directly related to the

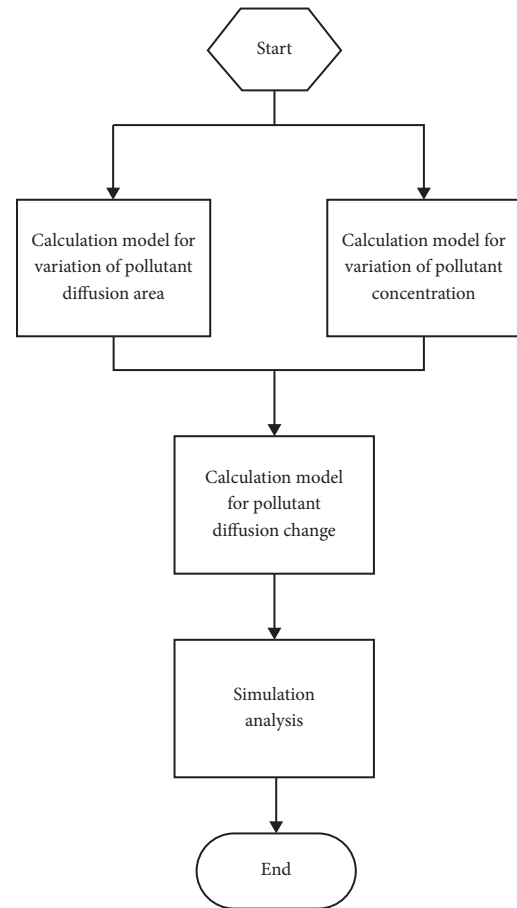


FIGURE 1: Research thought of the calculation model for cyanobacterial pollutant diffusion change in Chaohu Lake of China.

input effort and layout of treatment measures of cyanobacterial pollutants in Chaohu Lake. Therefore, in this chapter, based on satellite remote sensing images, the distribution and area change of cyanobacterial outbreak zone in Chaohu Lake are analyzed [6]. The analysis process of the model is divided into three parts: satellite remote sensing image processing of cyanobacterial pollutants, image identification, and area calculation.

2.1.1. Remote Sensing Image Processing. Remote sensing is a science and technology acquiring its information without touching the target object on the Earth's surface directly. A lot of information can be obtained from remote sensing images, such as water body, vegetation, land, and mountain. However, the original cyanobacterial pollutant images of Chaohu Lake collected by satellite remote sensing shall be processed before image analysis, such as image correction, image mosaic, and cutting [7].

(1) *Image Correction.* Affected by the character of the sensor, ground light conditions (terrain and solar altitude angle influence), and atmospheric action, there is an inconsistency between the measured value of the remote sensing equipment and the actual ground spectral radiant emissivity; namely, radiometric distortion is generated. However,

radiometric distortion will cause the deviation of the geometric position, shape, size, location, and other characteristics of surface features on the original image from the expression requirements in the reference system; namely, geometric distortion is generated. The previous two distortions shall be corrected, and images shall be restored. Radiometric distortion includes sensor correction, topographic correction, and atmospheric correction. Geometric distortion correction mainly involves the selection of control point, transformation of spatial location (transformation of coordinates), and recollection of pixel brightness value [8].

(2) *Image Mosaic*. When the area to be researched cannot be summarized with a remote sensing image, two or more images shall be spliced together to form an image with a wider cover area, so that the collected images are rounder. In order to make image mosaic, based on an image, the contrast ratio matching, pixel size, and data type of mosaic image shall be determined firstly; then, another image shall be inserted into a basic image through hue adjustment, removal of overlapping, and other processings [9].

(3) *Image Cutting*. Among the collected remote sensing images of Chaohu Lake, the research goal is the area covered by Chaohu Lake instead of other areas. Therefore, it is necessary to cut the excessive part and leave the area to be researched, so as to reduce the research difficulty. Due to the large difference between the spectral reflectivity of water body and the spectral reflectivity of other surrounding areas, area growth can be used directly to generate polygon, so as to gain the boundary of Chaohu Lake and cut out Chaohu Lake area from remote sensing image along the boundary.

2.1.2. Identification of Cyanobacterial Pollutants. Because this paper aims to research the cyanobacterial pollutants in Chaohu Lake, Chaohu water area image shall be cut out further to determine the distribution scope of cyanobacterial pollutants, so as to calculate the pollutant diffusion area subsequently.

For target identification, there are many methods, such as deep learning algorithm, SVM, and decision-making tree. Here, the decision-making tree is adopted to identify the cyanobacterial pollutants in Chaohu Lake, China. The identification process is mainly divided into two stages.

(1) *The First Stage*. Characteristic analysis of cyanobacterial pollutants in Chaohu Lake: Due to different properties and characteristics of every substance, there are differences in the reflectivity of remote sensing beam, which makes images show different object characteristics. Therefore, different reflectivity of water body on the remote sensing images of Chaohu Lake will distinguish water body from various substances in water body. Under this principle, except for Chaohu Lake water body, all influencing factors including chlorophyll, suspended matter, and yellow substance can be shown through the inherent optical characteristic parameters of water body. The mathematical description formula of

the relationship between various substances and water body reflectivity influence is as follows:

$$Z_w \approx \frac{x_w + x_s + s_p}{y_w + y_s + y_p + y_y} \quad (1)$$

In formula 1, Z_w represents the water surface reflectivity; x_w refers to the backscattering coefficient of water; x_s means the backscattering coefficient of inorganic suspended matters; s_p represents the backscattering coefficient of algal substances; y_w is the absorption coefficient of water; y_s means the absorption coefficient of suspended matters; y_p represents the absorption coefficient of algal substances; y_y refers to the absorption coefficient of yellow substances.

Containing a lot of chlorophyll, Cyanophyta is also called green alga. Therefore, in the event of the mass propagation of Cyanophyta in Chaohu Lake, the content of chlorophyll a in water will also increase. However, the concentration of chlorophyll a strongly correlates with the spectral ranges of 550~580, 630~670, and 685~715 nm; namely, when the concentration of chlorophyll a in water is high, the accumulation area of cyanobacteria will have spectral characteristics similar to those of plants with high reflectivity [10].

(2) *The Second Stage*. Classification and identification of Cyanophyta pollutants in Chaohu Lake:

Based on the above spectral characteristics of Cyanophyta pollutants in Chaohu Lake, decision-making tree algorithm is used to construct classifier and identify Cyanophyta pollutants in Chaohu Lake. As a machine learning algorithm, decision-making tree is a tree structure similar to flow chart [11]. In a decision-making tree, because the top node of the tree represents the root of the tree, it is called root node; containing all the data to be analyzed, the root node is a data set; branch nodes in the internal structure of the decision-making tree represent the best test for an attribute, and each branch represents the taxonomic structure; the tree structure also includes leaves, namely, leaf nodes that represent categories [12].

The construction of the decision-making tree requires ID3, CART, and C4.5 algorithms. Here, CART algorithm is adopted to construct the decision-making tree [13]. Known as classification and regression tree, CART is a nonparametric classification and regression method [14]. Its mathematical definition is shown below:

$$\text{CART} = 1 - \sum_j R^2\left(\frac{j}{N}\right), \quad (2)$$

$$R\left(\frac{j}{N}\right) = \frac{s_j(N)}{s(N)}, \quad (3)$$

In formulas (2) and (3), $R(j/N)$ is the probability that the value of a sample test variable in training set is N and belongs to the category of j ; $s_j(N)$ represents the number of samples where the value of a test variable in training set is N and belongs to the category of j ; $s(N)$ refers to the number of

samples where a test variable in training set is N ; j means the number of categories.

The basic flow of CART is shown in Algorithm 1.

2.1.3. Calculation of Cyanobacterial Pollutant Diffusion Area. Based on the distribution range of cyanobacterial pollutants in Chaohu Lake identified by the above CART decision-making tree [15], the cyanobacterial pollutant diffusion area can be calculated directly. The calculation mode is shown below.

Given that the density of cyanobacterial pollutants within the polluted area of Chaohu Lake is ρ and the location of the central coordinate in the standard coordinate system is (x, y) , the distribution degree coefficient of cyanobacterial pollutants within the polluted area of Chaohu Lake is

$$\mu = \frac{1}{\rho^2} \sum_{j=1}^j (x^2 + y^2) - v^2 ab. \quad (4)$$

In formula (4), j represents the number of pixels of the cut boundary outline of the polluted area of Chaohu Lake; v represents the number of all pixels of the polluted area of Chaohu Lake; a refers to convection coefficient of water flow; b means the mobile coefficient of boats and ships on water body.

Then, the above distribution degree coefficients of cyanobacterial pollutants within the polluted area of Chaohu Lake are used to calculate partitioning coefficient as shown below:

$$\gamma = \sqrt{(x - y) \cdot \mu \cdot \log ab} - v. \quad (5)$$

Partitioning coefficient describes the partitioning situation between the cyanobacterial polluted area and non-polluted area.

Finally, the distribution degree coefficient and partitioning coefficient of cyanobacterial pollutants within the polluted area of Chaohu Lake are used to calculate the pollutant diffusion area, namely,

$$\lambda = \frac{(\sqrt{\gamma} - \mu)^2}{\mu^2 + v}. \quad (6)$$

The pollutant area can be obtained through pollutant diffusion area coefficient [16]. However, affected by non-linear disordered factors such as water flow and various material activities in water body, the diffusion path is unpredictable. Therefore, error compensation is required [17]. Error calculation formula is as follows:

$$k = \frac{1}{E} \sum_{i=1}^t \left(d - \frac{f}{g} \right)^2. \quad (7)$$

In formula (7), E is the diffusion distance offset parameter of pollutants; t represents spatial location parameters of pollutants; d refers to diffusion factor; f means the coefficient of pollutant diffusion area; g is the pollutant diffusion direction deviation parameter.

2.2. Computational Model for Pollutant Diffusion Concentration Change. In Chapter 1, based on remote sensing

image information, the cyanobacterial pollutant diffusion range and area are calculated. However, diffusion range and area coefficients are a part of the computational model for diffusion change, and the concentration calculation of another part is also very important. The flow and diffusion of cyanobacterial pollutants in Chaohu Lake is a complicated process because the pollutants will spread around or reduce or disappear due to self-cleaning action of water body. Therefore, the distribution and calculation of pollutant concentration in water body are important problems in the environmental engineering of Chaohu Lake. Therefore, in this chapter, the model of pollution diffusion concentration change is established to calculate the concentration of pollution diffusion [18].

As an unsteady diffusion process, the flow and diffusion of cyanobacterial pollutants in Chaohu Lake can be described by diffusion model [19]. Firstly, if all factors are considered, the diffusion model will be complicated, and the calculation will be difficult. Therefore, it is necessary to set hypothesis conditions. Although the exact result cannot be obtained, certain veracity and feasibility can be possessed [20].

- (1) Each section and degree of depth in Chaohu Lake are consistent
- (2) The amount of cyanobacterial pollutants can be represented by certain concentration symbol (such as BOD or COD)
- (3) Certain self-cleaning action that reduces pollutants can be regarded as a kind of first-level reaction
- (4) The diffusion movement of cyanobacterial pollutants has a steady diffusion coefficient

According to Fick's Law, the formula of cyanobacterial pollutant diffusion can be obtained:

$$\frac{q}{t} = u \frac{q}{x^2} - h \frac{q}{x}. \quad (8)$$

In formula (8), q is the pollutant concentration; t means time; u refers to diffusion coefficient; x represents polluted area; h is water velocity of Chaohu Lake.

2.3. Computational Model for Cyanobacterial Pollutant Diffusion Change. Based on the above calculation of the area and concentration of cyanobacterial pollutants in Chaohu Lake, a computational model for cyanobacterial pollutant diffusion change is constructed, which describes the variation laws of pollutant diffusion with the time as well as spatial development. The model derivation formula is as follows:

$$\frac{AC}{t} + \frac{AUC}{x} = \frac{A(D_x + E_x)(q/x)}{x} - KAC + \frac{A}{h} S_r + S. \quad (9)$$

In formula (9), A is the area of the pollutant; C is the average concentration of the pollutants; U is the average flow rate; D_x is the turbulent diffusion coefficient; E_x is the longitudinal diffusion coefficient; K is the pollutant degradation coefficient; h is the average depth of the section; S_r is the speed of releasing pollutants from riverbed sediment; S is

Input: Train data set Y of the remote sensing images of cyanobacterial pollutants; conditions for stopping calculation
 Output: CART Decision-making Tree
 According to training data set, conduct the following operations on each node recursively from root node and construct binary decision-making tree:
 Step 1: Set the training data set of nodes as D , calculate the Gini coefficient of existing characteristics on this data set, test whether to divide D into $D1$ and $D2$ according to sample point $A = a$ for each characteristic A and each possible value a , and then calculate Gini (D, A)
 Step 2: among all possible characteristics A and segmentation points a , select the characteristic with the smallest Gini coefficient and corresponding segmentation points as the optimal characteristic and segmentation point. According to the optimal characteristic and segmentation point, generate two child nodes from the existing node and distribute the training data set into two child nodes according to characteristics
 Step 3: make recursive calls on two child nodes until the stop conditions are met
 Step 4: Generate CART Decision-making Tree
 end
 Note: the conditions for algorithm to stop calculation are that the number of samples in nodes is less than a predefined threshold or Gini coefficient of sample set is smaller than a predefined threshold (samples are basically of the same category), or there are no more characteristics.

ALGORITHM 1: Basic flow of CART algorithm.

the amount of pollutants discharged per unit of riverbed in unit of time.

According to experience, the longitudinal movement of water flow in the lake is the main factor leading to the variation of the pollution area and concentration, so the above model can be simplified on this basis. Regardless of the effects of turbulent diffusion, release of pollutants from lake bed sediments, and discharge of other pollutants, the computational model for pollutant diffusion change is

$$\frac{AC}{t} + \frac{AUC}{x} = AE \frac{q}{x^2} - KAC. \quad (10)$$

In this paper, the implicit difference system in the finite difference method is adopted for solution among the above models. As a numerical method of differential equations, the finite difference method approximates the derivative through finite difference, so as to obtain the approximate solution of the differential equation. The principle diagram is shown in Figure 2.

The finite difference method can be represented by the x - t grid plane. As shown in Figure 2, Δx represents the step size in direction x ; Δt is the step size in direction t ; (x_i, t_j) represents the grid node formed by the intersection of two grid lines; $(0, t_j)$ and $(x_j, 0)$ represent boundary nodes; $C(x_i, t_j)$ or C_i^j represents the water quality and concentration at any point.

After that, the implicit difference equation can be used to solve the computational model for pollutant diffusion change, insert the boundary firstly, and then obtain the solution via the chasing method.

3. Simulation Test Analysis

After finishing building the model, further simulation experiments are needed to verify the feasibility and effectiveness of the model. The data used in this experiment are all cited from the website of Chaohu Lake China Resources Satellite Ground Application Center.

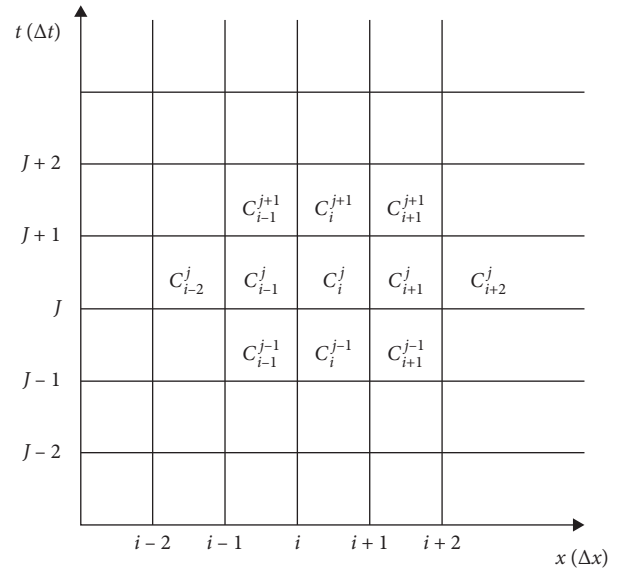


FIGURE 2: x - t grid plane.

3.1. *Experimental Data Set.* In this experiment, data were collected from May to September 2017, generally from 10:00 am to 2:00 pm when the weather is fine, the wind was small, and the water surface was relatively calm. The water is collected once a month on the 15th and 30th days from 5 collection points. There are totally 20 spectrum collection points, which are densely arranged in the western half of the lake while being sparsely arranged in the eastern half of the lake (Table 1).

- (1) Sensing Image Set. The sensing image set contains 1600 images about the cyanobacterial pollutant diffusion in Chaohu Lake, as shown in Figure 3.
- (2) Water Quality Related Data.

3.2. *Test Software.* The experiment was carried out on the virtual simulation platform of smart city pollution control, a

TABLE 1: Water quality related data in June 1st (excerpt).

Item	TN (mg/L)	TP (mg/L)	COD (mg/L)	COD Mn (mg/L)	TOC (mg/L)	Chl (mg/m ³)
Collection point 1	5.562	0.152	12.363	5.487	9.123	4.36
Collection point 2	6.561	0.254	13.15	5.933	9.256	5.33
Collection point 3	8.256	0.256	15.320	7.145	10.363	7.125
Collection point 4	6.522	0.242	14.325	6.692	9.255	5.632
Collection point 5	6.352	0.202	14.201	6.636	9.014	5.201

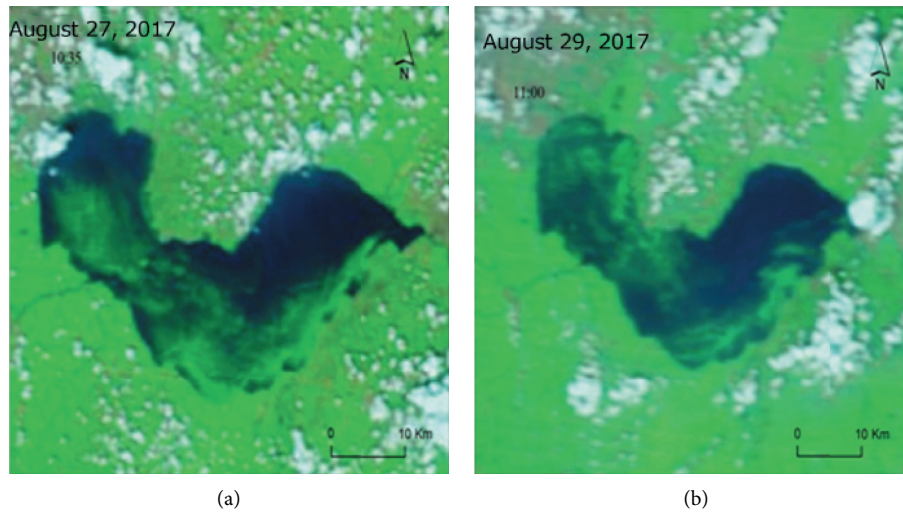


FIGURE 3: Sensing image of cyanobacterial pollutant diffusion in Chaohu lake (excerpt).

monitoring and disposal management platform independently developed by UNISOL directed at various environmental pollutions. By integrating with virtual simulation, BIM model, GIS data, Internet of Things, artificial intelligence, and other complex technologies, this platform is designed to improve real-time monitoring and preventive processing capabilities in wastewater treatment as well as solid waste prevention. The platform is mainly composed of three modules: environmental monitoring and treatment, emergency simulation and disposal, and urban planning and reporting. It can display the integrated water quality monitoring and manual monitoring data of the surrounding lakes and the monitoring data of pollution sources in a visual way, drive the control value, and simulate the variation form of water pollution under different data.

3.3. Test Results. As can be observed from Tables 2 and 3, the data and status of cyanobacterial pollutant change in Chaohu Lake during the period from May to September 2017 are calculated by using the proposed model. These data are almost consistent with those recorded with the website of Chaohu Lake China Resources Satellite Ground Application Center.

Regarding analysis of pollution change, in May, the area of cyanobacterial pollutant in Chaohu Lake was small and the concentration was low. In the middle of June, the level of cyanobacterial pollutant in Chaohu Lake reached its peak

TABLE 2: Test results.

Month	Area (m ²)	Concentration (mg/m ³)
5.1	52123.6	7.36
5.15	52694.5	7.58
6.1	52819.5	7.66
6.15	96922.3	9.25
7.1	82143.3	8.68
7.15	71231.3	8.54
8.1	75692.3	7.36
8.15	81433.3	8.25
9.1	84250.6	8.47
9.15	85361.3	8.65

TABLE 3: Actual results.

Month	Area (m ²)	Concentration (mg/m ³)
5.1	52124.4	7.52
5.15	52694.6	7.45
6.1	52818.0	7.60
6.15	96922.7	9.33
7.1	82145.4	8.47
7.15	71232.4	8.63
8.1	75691.9	7.45
8.15	81435.5	8.32
9.1	84255.0	8.52
9.15	85363.3	8.78

and the relevant departments started treatment since then, so there were fewer pollutants during the middle of July. Then, the monitoring in August and September found that the area and concentration of cyanobacterial pollutant in Chaohu Lake began to increase relatively, but they were less than the peak in the middle of June.

4. Conclusions

To sum up, as one of the five largest freshwater lakes in China, Chaohu Lake provides important freshwater resources for transportation, agricultural irrigation, and domestic water. However, the massive and rapid reproduction of cyanobacteria in Chaohu Lake during summer has serious water pollution and seriously influenced the surrounding residents as well as local economic development. Under this background, it is of great practical significance to study the law of cyanobacterial pollutant change in Chaohu Lake. To this end, a computational model for the cyanobacterial pollutant diffusion change in Chaohu Lake is designed based on big data, which can help grasp the diffusion of cyanobacterial pollutants in Chaohu Lake so as to provide data support for its governance and improve the feasibility as well as scientificity of the treatment plan. Finally, the simulation test is carried out to test the model validity, which shows that the results obtained by the proposed computational model are almost consistent with the actual results. Therefore, the model proposed in this paper is proved to be effective and the research purpose is achieved.

Data Availability

The authors used simulation data, and their model and related hyperparameters are provided in the article.

Conflicts of Interest

The authors declare that they have no conflicts of interest.

References

- [1] H. Yoshioka and Y. Yaegashi, "Robust stochastic control modeling of dam discharge to suppress overgrowth of downstream harmful algae," *Applied Stochastic Models in Business and Industry*, vol. 34, no. 3, pp. 338–354, 2018.
- [2] S. Sen, S. Nandi, and S. Dutta, "Application of RSM and ANN for optimization and modeling of biosorption of chromium (VI) using cyanobacterial biomass," *Applied Water Science*, vol. 8, no. 5, pp. 148–153, 2018.
- [3] S. K. Kurt, M. Akhtar, K. D. P. Nigam, and N. Kockmann, "Modular concept of a smart scale helically coiled tubular reactor for continuous operation of multiphase reaction systems," in *AMSE 2016 14th International Conference on Nanochannels, Microchannels, and Minichannels*, American Society of Mechanical Engineers, Washington, DC, USA, July 2016.
- [4] C. P. Ukpaka, "Empirical model approach for the evaluation of pH and conductivity on pollutant diffusion in soil environment," *Chemistry International*, vol. 2, no. 4, pp. 267–278, 2016.
- [5] A. M. D. A. Ketife, S. Judd, and H. Znad, "A mathematical model for carbon fixation and nutrient removal by an algal photobioreactor," *Chemical Engineering Science*, vol. 153, pp. 354–362, 2016.
- [6] C. Baroukh, R. Muñoz-Tamayo, O. Bernard, and J.-P. Steyer, "Mathematical modeling of unicellular microalgae and cyanobacteria metabolism for biofuel production," *Current Opinion in Biotechnology*, vol. 33, pp. 198–205, 2015.
- [7] X. Cao, Y. Wang, J. He, X. Luo, and Z. Zheng, "Phosphorus mobility among sediments, water and cyanobacteria enhanced by cyanobacteria blooms in eutrophic Lake Dianchi," *Environmental Pollution*, vol. 219, pp. 580–587, 2016.
- [8] H. F. Lobaton, *Mathematical modelling as a research tool in the cyanobacteria cultivation*, Ph.D. thesis, Friedrich-Alexander-Universität Erlangen-Nürnberg, Erlangen, Germany, 2017.
- [9] S. Westermark and R. Steuer, "Toward multiscale models of cyanobacterial growth: a modular approach," *Frontiers in Bioengineering and Biotechnology*, vol. 4, pp. 95–103, 2016.
- [10] L. Pinto, M. Mateus, and A. Silva, "Modeling the transport pathways of harmful algal blooms in the Iberian coast," *Harmful Algae*, vol. 53, pp. 8–16, 2016.
- [11] R. B. Waghmare and S. B. Kivne, "Mathematical modeling of disposal of pollutant in rivers," *International Journal of Computational and Applied Mathematics*, vol. 12, no. 3, pp. 835–842, 2017.
- [12] H. Yoshioka and Y. Yaegashi, "Singular stochastic control model for algae growth management in dam downstream," *Journal of Biological Dynamics*, vol. 12, no. 1, pp. 242–270, 2018.
- [13] Y. Hu and L. Li, "Remote sensing mapping of cyanobacteria blooms in Chaohu based on spatio-temporal-spectrum fusion: improvement on spatial scales," *Journal of Engineering Science & Technology Review*, vol. 12, no. 6, pp. 182–194, 2019.
- [14] S.-B. Hsu, F.-B. Wang, and X.-Q. Zhao, "A reaction-diffusion model of harmful algae and zooplankton in an ecosystem," *Journal of Mathematical Analysis and Applications*, vol. 451, no. 2, pp. 659–677, 2017.
- [15] J. Zhang, J. Shi, and X. Chang, "A mathematical model of algae growth in a pelagic-benthic coupled shallow aquatic ecosystem," *Journal of Mathematical Biology*, vol. 76, no. 5, pp. 1159–1193, 2018.
- [16] J.-I. Ishihara, M. Tachikawa, H. Iwasaki, and A. Mochizuki, "Mathematical study of pattern formation accompanied by heterocyst differentiation in multicellular cyanobacterium," *Journal of Theoretical Biology*, vol. 371, pp. 9–23, 2015.
- [17] Y. Han, J. W. Smithheart, R. L. Smyth, T. N. Aziz, and D. R. Obenour, "Assessing vertical diffusion and cyanobacteria bloom potential in a shallow eutrophic reservoir," *Lake and Reservoir Management*, vol. 36, no. 2, pp. 169–185, 2019.
- [18] M. Nieves-Mori6n, C. W. Mullineaux, and E. Flores, "Molecular diffusion through cyanobacterial septal junctions," *Mbio*, vol. 8, no. 1, pp. 1756–1816, 2017.
- [19] F.-B. Wang, "A PDE system modeling the competition and inhibition of harmful algae with seasonal variations," *Nonlinear Analysis: Real World Applications*, vol. 25, pp. 258–275, 2015.
- [20] A. Torres-Sánchez, J. Gómez-Gardeñes, and F. Falo, "An integrative approach for modeling and simulation of heterocyst pattern formation in cyanobacteria filaments," *PLoS Computational Biology*, vol. 11, no. 3, pp. 109–114, 2015.

Research Article

Regulator-Based Risk Statistics for Portfolios

Xiaochuan Deng¹ and Fei Sun² 

¹School of Economics and Management, Wuhan University, Wuhan 430072, China

²School of Mathematics and Computational Science, Wuyi University, Jiangmen 529020, China

Correspondence should be addressed to Fei Sun; fsun.sci@outlook.com

Received 30 May 2020; Accepted 20 June 2020; Published 9 July 2020

Academic Editor: Jia-Bao Liu

Copyright © 2020 Xiaochuan Deng and Fei Sun. This is an open access article distributed under the Creative Commons Attribution License, which permits unrestricted use, distribution, and reproduction in any medium, provided the original work is properly cited.

Risk statistic is a critical factor not only for risk analysis but also for financial application. However, the traditional risk statistics may fail to describe the characteristics of regulator-based risk. In this paper, we consider the regulator-based risk statistics for portfolios. By further developing the properties related to regulator-based risk statistics, we are able to derive dual representation for such risk.

1. Introduction

Risk measure is a popular topic in both financial application and theoretical research. The quantitative calculation of risk involves two problems: choosing an appropriate risk model and allocating risk to individual institutions. This has led to further research on risk statistics. In a seminal paper, Sun et al. and Liu et al. [1, 2] first introduced the class of natural risk statistics with representation results. Furthermore, Ahmed et al. [3] derived an alternative proof for the natural risk statistics. Later, Tian and Jiang and Tian and Suo [4, 5] obtained the representation results for convex risk statistics and quasiconvex risk statistics, respectively.

However, traditional risk statistics may fail to describe the characteristics of regulator-based risk. Therefore, the study of regulator-based risk statistics is particularly interesting. On the other hand, in the abovementioned research on risk statistics, the set-valued risk was never studied. Jouini et al. [6] pointed out that a set-valued risk measure is more appropriate than a scalar risk measure especially in the case where several different kinds of currencies are involved when one is determining capital requirements for the portfolio. Indeed, a natural set-valued risk statistic can be considered as an empirical (or a data-based) version of a set-valued risk measure. More recent studies of set-valued risk measures include those of [7–14] and the references therein.

The main focus of this paper is regulator-based risk statistics for portfolios. In this context, both empirical

versions and data-based versions of regulator-based risk measures are discussed. By further developing the properties related to regulator-based risk statistics, we are able to derive their dual representations. Indeed, this class of risk statistics can be considered as an extension of those introduced in [15–17].

The remainder of this paper is organized as follows. In Section 2, we briefly introduce some preliminaries. In Section 3, we state the main results of regulator-based risk statistics, including the dual representations. Section 4 investigates the data-based versions of regulator-based risk measures. Finally, in Section 5, the main proofs in this paper are discussed.

2. Preliminary Information

In this section, we briefly introduce some preliminaries that are used throughout this paper. Let $d \geq 1$ be a fixed positive integer. The space $\mathbb{R}^{d \times n}$ represents the set of financial risk positions. With positive values of $X \in \mathbb{R}^{d \times n}$, we denote the gains while the negative denotes the losses. Let n_j be the sample size of $D = (X_1, \dots, X_d)$ in the j^{th} scenario, $j = 1, \dots, l$. Let $n := n_1 + \dots + n_l$. More precisely, suppose that the behavior of D is represented by a collection of data $X = (X_1, \dots, X_d) \in \mathbb{R}^n \times \dots \times \mathbb{R}^n$, where $X_i = (X^{i,1}, \dots, X^{i,l}) \in \mathbb{R}^n$ and $X^{i,j} = (x_1^{i,j}, \dots, x_{n_j}^{i,j}) \in \mathbb{R}^{n_j}$ is the data subset that corresponds to the j^{th} scenario with respect to X_i . For each $j = 1, \dots, l$, $h = 1, \dots, n_j$, $X_h^j :=$

$(x_h^{1,j}, x_h^{2,j}, \dots, x_h^{d,j})$ is the data subset that corresponds to the h^{th} observation of D in the j^{th} scenario.

In this paper, an element z of \mathbb{R}^d is denoted by $z := (z_1, \dots, z_d)$. An element X of $\mathbb{R}^{d \times n}$ is denoted by $X := (X_1, \dots, X_d) := (x_1^{1,1}, \dots, x_{n_1}^{1,1}, \dots, x_1^{1,l}, \dots, x_{n_1}^{1,l}, \dots, x_1^{d,1}, \dots, x_{n_d}^{d,1}, \dots, x_1^{d,l}, \dots, x_{n_d}^{d,l})$. Let K be a closed convex polyhedral cone of \mathbb{R}^d where $K \supseteq \mathbb{R}_+^d := \{(x_1, \dots, x_d) \in \mathbb{R}^d; x_i > 0, 1 \leq i \leq d\}$ and $K \cap \mathbb{R}_-^d = \emptyset$ where $\mathbb{R}_-^d := \{(x_1, \dots, x_d) \in \mathbb{R}^d; x_i \leq 0, 1 \leq i \leq d\}$. Let K^+ be the positive dual cone of K , that is, $K^+ := \{u \in \mathbb{R}^d; u^{\text{tr}} v \geq 0 \text{ for any } v \in K\}$, where u^{tr} means the transpose of u . For any $X = (X_1, \dots, X_d), Y = (Y_1, \dots, Y_d) \in \mathbb{R}^{d \times n}$, $X + Y$ stands for $(X_1 + Y_1, \dots, X_d + Y_d)$ and aX stands for (aX_1, \dots, aX_d) for $a \in \mathbb{R}$. Denote $K1_n := \{(z_1 1_n, z_2 1_n, \dots, z_d 1_n) : z \in K\}$ and $z1_n := \{(z, z, \dots, z) : z \in \mathbb{R}\} \in \mathbb{R}^n$ where $1_n := (1, \dots, 1) \in \mathbb{R}^n$. By $(K1_n)^+$, and we denote the positive dual cone of $K1_n$ in $\mathbb{R}^{d \times n}$, i.e., $(K1_n)^+ := \{w \in \mathbb{R}^{d \times n}; wz^{\text{tr}} \geq 0 \text{ for any } z \in K\}$. The partial order with respect to K is defined as $a \leq_K b$, which means $b - a \in K$ where $a, b \in \mathbb{R}^d$, and $X \leq_{K1_n} Y$ means $Y - X \in K1_n$ where $X, Y \in \mathbb{R}^{d \times n}$.

Let $M := \mathbb{R}^m \times \{0\}^{d-m}$ be the linear subspace of \mathbb{R}^d for $1 \leq m \leq d$. The introduction of M was considered in [6, 9]. Denote $M_+ := M \cap \mathbb{R}_+^d$, where $\mathbb{R}_+^d := \{(x_1, \dots, x_d) \in \mathbb{R}^d; x_i \geq 0, 1 \leq i \leq d\}$ and $M^- := \{0\}^m \times \mathbb{R}^{d-m}$. Therefore, a regulator can only accept security deposits in the first m reference instruments. Denoting $K_M := K \cap M$ by the closed convex polyhedral cone in M , $K_M^+ := \{u \in M; u^{\text{tr}} z \geq 0 \text{ for any } z \in K_M\}$ the positive dual cone of K_M in M and $\text{int } K_M$ is the interior of K_M in M . We denote $Q_M^- := \{A \subset M; A = \text{clco}(A + K_M)\}$ and $Q_M^+ := \{A \subset K_M; A = \text{clco}(A + K_M)\}$, where the $\text{clco}(A)$ represents the closed convex hull of A .

By [18], a set-valued risk statistic is any map ρ ,

$$\rho: \mathbb{R}^{d \times n} \longrightarrow 2^M, \quad (1)$$

which can be considered as an empirical (or a data-based) version of a set-valued risk measure. The axioms related to this set-valued risk statistic are organized as follows:

[A0] Normalization: $K_M \subseteq \rho(0)$ and $\rho(0) \cap -\text{int } K_M = \emptyset$

[A1] Monotonicity: for any $X, Y \in \mathbb{R}^{d \times n}$, $X - Y \in K1_n$ implies that $\rho(X) \supseteq \rho(Y)$

[A2] M-translative invariance: for any $X \in \mathbb{R}^{d \times n}$ and $z \in \mathbb{R}^d$, $\rho(X - z1_n) = \rho(X) + z$

[A3] Convexity: for any $X, Y \in \mathbb{R}^{d \times n}$ and $\lambda \in [0, 1]$, $\rho(\lambda(X) + (1 - \lambda)Y) \supseteq \lambda\rho(X) + (1 - \lambda)\rho(Y)$

[A4] Positive homogeneity: $\rho(\lambda X) = \lambda\rho(X)$ for any $X \in \mathbb{R}^{d \times n}$ and $\lambda > 0$

[A5] Subadditivity: $\rho(X + Y) \supseteq \rho(X) + \rho(Y)$ for any $X, Y \in \mathbb{R}^{d \times n}$

We end this section with more notations. A function $\rho: \mathbb{R}^{d \times n} \longrightarrow 2^M$ is said to be proper if $\text{dom } \rho := \{X \in \mathbb{R}^{d \times n}; \rho(X) \neq \emptyset\} \neq \emptyset$ and $\rho(X) \neq M$ for all $X \in \text{dom } \rho$. ρ is said to be closed if $\text{graph } \rho$ is a closed set. For the properties of the graphs, see [19–21].

3. Empirical Versions of Regulator-Based Risk Measures

In this section, we state the dual representations of regulator-based risk statistics, which are the empirical versions of regulator-based risk measures. Firstly, for any $X \in \mathbb{R}^{d \times n}$, $X \wedge_{K1_n} 0$ is defined as follows:

$$X \wedge_{K1_n} 0 := \begin{cases} X, & X \notin K1_n, \\ 0, & X \in K1_n. \end{cases} \quad (2)$$

Therefore, the position that belongs to K regarded is as 0 position. Next, we derive the properties related to regulator-based risk statistics.

Definition 1. A regulator-based risk statistic is a function $\varrho: \mathbb{R}^{d \times n} \longrightarrow Q_M^+$ that satisfies the following properties:

[P0] Normalization: $K_M \subseteq \varrho(0)$ and $\varrho(0) \cap -\text{int } K_M = \emptyset$

[P1] Cash cover: for any $z \in K_M$, $z \in \varrho(-z1_n)$

[P2] Monotonicity: for any $X, Y \in \mathbb{R}^{d \times n}$, $X - Y \in \mathbb{R}^{d \times n} \cap K1_n$ implies that $\varrho(X) \supseteq \varrho(Y)$

[P3] Regulator-dependence: for any $X \in \mathbb{R}^{d \times n}$, $\varrho(X) = \varrho(X \wedge_{K1_n} 0)$

[P4] Convexity: for any $X, Y \in \mathbb{R}^{d \times n}$ and $\lambda \in [0, 1]$, $\varrho(\lambda(X) + (1 - \lambda)Y) \supseteq \lambda\varrho(X) + (1 - \lambda)\varrho(Y)$

Remark 1. The property of [P1] means any fixed negative risk position $-z$ can be canceled by its positive quality z ; [P2] says that if X_1 is bigger than X_2 for the partial order in K , then the X_1 need less capital requirement than X_2 , so $\varrho(X_1)$ contains $\varrho(X_2)$; [P3] means the regulator-based risk statistics start only from the viewpoint of regulators which only care about the positions that need to pay capital requirements, while the positions that belong to K regarded as 0 position.

We now construct an example for regulator-based risk statistics.

Example 1. The coherent risk measure $AV@R$ was studied by Föllmer and Schied [22] in detail. They have given several representations and many properties such as law invariance and the Fatou property [12]. First, they introduced set-valued $AV@R$, where the representation result is derived. Moreover, they also proved that it is a set-valued coherent risk measure. We now define the regulator-based average value at risk. For any $X \in \mathbb{R}^{d \times n}$ and $0 < \alpha < 1$, we define $\varrho(X)$ as

$$\begin{aligned} \varrho(X) &:= AV@R_\alpha^{\text{loss}}(X), \\ &:= \inf_{z \in \mathbb{R}^d} \left\{ \frac{1}{\alpha} \left(-(X \wedge_{K1_n} 0) \Big|_M + z \right)^+ - z \right\} + \mathbb{R}_+^m, \end{aligned} \quad (3)$$

It is clear that ϱ satisfies the cash cover, monotonicity, regulator dependence properties, and convexity, so ϱ is a regulator-based risk statistic.

Definition 2. Let $Y \in \mathbb{R}^{d \times n}$, $u \in M$. Define a function $S_{(Y,u)}(X) : \mathbb{R}^{d \times n} \rightarrow 2^M$ as

$$S_{(Y,u)}(X) := \{z \in M : X^{\text{tr}}Y \leq u^{\text{tr}}z\}. \quad (4)$$

In fact, the $S_{(Y,u)}(X)$ is the support function of X . Before we derive the dual representations of regulator-based risk statistics, the Legendre–Fenchel conjugate theory ([9]) should be recalled.

Lemma 1 (see [9], Theorem 2). *Let $R : \mathbb{R}^{d \times n} \rightarrow Q_M^t$ be a set-valued closed convex function. Then, the Legendre–Fenchel conjugate and the biconjugate of R can be defined, respectively, as*

$$-R^*(Y, u) := \text{cl} \bigcup_{X \in \mathbb{R}^{d \times n}} (R(X) + S_{(Y,u)}(-X)), \quad (5)$$

$$Y \in \mathbb{R}^{d \times n}, u \in \mathbb{R}^d,$$

$$R(X) = R^{**}(X) := \bigcap_{(Y,u) \in \mathbb{R}^{d \times n} \times K_M^+ \setminus \{0\}} [-R^*(Y, u) + S_{(Y,u)}(X)], \quad X \in \mathbb{R}^{d \times n}. \quad (6)$$

Definition 3 (indicator function). For any $Z \subseteq \mathbb{R}^{d \times n}$, the Q_M^t -valued indicator function $I_Z : \mathbb{R}^{d \times n} \rightarrow Q_M^t$ is defined as

$$I_Z(X) := \begin{cases} \text{cl} K_M, & X \in Z, \\ \phi, & X \notin Z. \end{cases} \quad (7)$$

Remark 2. The conjugate of Q_M^t -valued indicator function I_Z is

$$-(I_Z)^*(Y, u) := \text{cl} \bigcup_{X \in Z} S_{(Y,u)}(-X). \quad (8)$$

Remark 3. It is easy to see that the regulator-based risk statistic ϱ does not have cash additivity, see [9]. However, ϱ has cash subadditivity introduced in [23, 24]. Indeed, from

$$W = \left\{ (Y, u) \in (-\mathbb{R}_+^{d \times n} \cap K^+ \mathbf{1}_n) \times K_M^+ \setminus \{0\} \mid u \in \left(-\sum_{j=1}^l \sum_{h=1}^{n_j} Y_h^{1,j}, \dots, -\sum_{j=1}^l \sum_{h=1}^{n_j} Y_h^{d,j} \right) + M^\perp \right\}, \quad (13)$$

such that for any $X \in \mathbb{R}^{d \times n}$,

$$\varrho(X) = \bigcap_{(Y,u) \in W} \{-\alpha(Y, u) + S_{(Y,u)}(X \wedge_{K \mathbf{1}_n} 0)\}. \quad (14)$$

4. Alternative Data-Based Versions of Regulator-Based Risk Measures

In this section, we develop another framework, the data-based versions of regulator-based risk measures. This framework is a little different from the previous one. However, almost all the arguments are the same as those in the previous section.

Theorem 2 of [10], ϱ satisfies the Fatou property. Then, considering any $X \in \mathbb{R}^{d \times n}$ and $z \in K_M$, for any $\varepsilon \in (0, 1)$, we have

$$\begin{aligned} \varrho((1-\varepsilon)X - z\mathbf{1}_n) &= \varrho\left((1-\varepsilon)X + \varepsilon\left(-\frac{z}{\varepsilon}\mathbf{1}_n\right)\right), \\ &\supseteq (1-\varepsilon)\varrho(X) + \varepsilon\varrho\left(-\frac{z}{\varepsilon}\mathbf{1}_n\right), \\ &\supseteq (1-\varepsilon)\varrho(X) + z, \end{aligned} \quad (9)$$

where the last inclusion is due to the property [P1]. Using the arbitrariness of ε , we have the following lemma.

Lemma 2. *Assume that ϱ is a regulator-based risk statistic. For any $z \in \mathbb{R}_+^d$, $X \in \mathbb{R}^{d \times n}$,*

$$\varrho(X - z\mathbf{1}_n) \supseteq \varrho(X) + z, \quad (10)$$

which also implies

$$\varrho(X + z\mathbf{1}_n) \subseteq \varrho(X) - z. \quad (11)$$

Proposition 1. *Let $\varrho : \mathbb{R}^{d \times n} \rightarrow Q_{M^+}^t$ be a proper closed convex regulator-based risk statistic with $u \in \{(-\sum_{j=1}^l \sum_{h=1}^{n_j} Y_h^{1,j}, \dots, -\sum_{j=1}^l \sum_{h=1}^{n_j} Y_h^{d,j}) + M^\perp\} \cap K_M^+ \setminus \{0\}$. Then,*

$$-\varrho^*(Y, u) = \begin{cases} \text{cl} \bigcup_{X \in \mathbb{R}^{d \times n}} S_{(Y,u)}(-X), & Y \in -\mathbb{R}_+^{d \times n} \cap (K^+ \mathbf{1}_n), \\ M, & \text{elsewhere.} \end{cases} \quad (12)$$

Now, we state the main result of this paper, the dual representations of regulator-based risk statistics.

Theorem 1. *If $\varrho : \mathbb{R}^{d \times n} \rightarrow Q_{M^+}^t$ is a proper closed convex regulator-based risk statistic, then there is a $-\alpha : (-\mathbb{R}_+^{d \times n} \cap K^+ \mathbf{1}_n) \times K_M^+ \setminus \{0\} \rightarrow Q_{M^+}^t$, which is not identically M of the set*

Therefore, we only state the corresponding notations and results and omit all the proofs and relevant explanations.

We replace M by $\tilde{M} \in \mathbb{R}^{d \times n}$ that is a linear subspace of $\mathbb{R}^{d \times n}$. We also replace K by $\tilde{K} \in \mathbb{R}^{d \times n}$ that is a closed convex polyhedral cone where $\tilde{K} \supseteq \mathbb{R}_+^{d \times n}$. The partial order with respect to \tilde{K} is defined as $X \leq_{\tilde{K}} Y$, which means $Y - X \in \tilde{K}$. Let $\tilde{M}_+ := \tilde{M} \cap \mathbb{R}_+^{d \times n}$. Denoting $\tilde{K}_{\tilde{M}} := \tilde{K} \cap \tilde{M}$ by the closed convex polyhedral cone in \tilde{M} , $\tilde{K}_{\tilde{M}}^+ := \{\tilde{u} \in \tilde{M} : \tilde{u}^{\text{tr}}\tilde{z} \geq 0 \text{ for any } \tilde{z} \in \tilde{K}_{\tilde{M}}\}$ is the positive dual cone of $\tilde{K}_{\tilde{M}}$ in \tilde{M} and $\text{int} \tilde{K}_{\tilde{M}}^+$ is the interior of $\tilde{K}_{\tilde{M}}^+$ in \tilde{M} . We denote $Q_{\tilde{M}}^t := \{\tilde{A} \subset \tilde{M} : \tilde{A} = \text{clco}(\tilde{A} + \tilde{K}_{\tilde{M}}^+)\}$ and

$Q_M^{t,+} := \{\tilde{A} \subset \tilde{K}_M^- : \tilde{A} = \text{clco}(\tilde{A} + \tilde{K}_M^-)\}$. We still start from the viewpoint of regulators which only care about the positions that need to pay capital requirements. Therefore, for any $X \in \mathbb{R}^{d \times n}$, we define $X \wedge_{\tilde{K}} 0$ as

$$X \wedge_{\tilde{K}} 0 := \begin{cases} X, & X \notin \tilde{K}, \\ 0, & X \in \tilde{K}, \end{cases} \quad (15)$$

Then, we state the axioms related to regulator-based risk statistics.

Definition 4. A regulator-based risk statistic is a function $\tilde{q} : \mathbb{R}^{d \times n} \rightarrow Q_M^{t,+}$ that satisfies the following properties:

- [Q0] Normalization: $\tilde{K}_M^- \subseteq \tilde{q}(0)$ and $\tilde{q}(0) \cap -\text{int} \tilde{K}_M^- = \emptyset$
- [Q1] Cash cover: for any $\tilde{z} \in \tilde{K}_M^-$, $\tilde{z} \in \tilde{q}(-\tilde{z})$
- [Q2] Monotonicity: for any $X_1, X_2 \in \mathbb{R}^{d \times n}$, $X_1 - X_2 \in \mathbb{R}^{d \times n} \cap \tilde{K}$ implies that $\tilde{q}(X_1) \supseteq \tilde{q}(X_2)$
- [Q3] Regulator-dependence: for any $X \in \mathbb{R}^{d \times n}$, $\tilde{q}(X) = \tilde{q}(X \wedge_{\tilde{K}} 0)$
- [Q4] Convexity: for any $X, Y \in \mathbb{R}^{d \times n}$, $\lambda \in [0, 1]$, $\tilde{q}(\lambda X + (1 - \lambda)Y) \supseteq \lambda \tilde{q}(X) + (1 - \lambda)\tilde{q}(Y)$

We need more notations. Let $Y \in \mathbb{R}^{d \times n}$, $\tilde{u} \in \tilde{M}$. Define a function $S_{(Y, \tilde{u})}(X) : \mathbb{R}^{d \times n} \rightarrow 2^M$ as

$$S_{(Y, \tilde{u})}(X) := \{\tilde{z} \in \tilde{M} : X^{\text{tr}} Y \leq \tilde{u}^{\text{tr}} \tilde{z}\}, \quad (16)$$

let $\tilde{R} : \mathbb{R}^{d \times n} \rightarrow Q_M^{t,+}$ be a set-valued closed convex function. Then, the Legendr e-Fenchel conjugate and the biconjugate of \tilde{R} can be defined, respectively, as

$$-\tilde{R}^*(Y, u) := \text{cl} \bigcup_{X \in \mathbb{R}^{d \times n}} (\tilde{R}(X) + S_{(Y, \tilde{u})}(-X)), \quad (17)$$

$$Y \in \mathbb{R}^{d \times n}, \tilde{u} \in \mathbb{R}^{d \times n},$$

$$\tilde{R}(X) = \tilde{R}^{**}(X) := \bigcap_{(Y, \tilde{u}) \in \mathbb{R}^{d \times n} \times \tilde{K}_M^+ \setminus \{0\}} \{-\tilde{R}^*(Y, \tilde{u}) + S_{(Y, \tilde{u})}(X)\}, \quad X \in \mathbb{R}^{d \times n}. \quad (18)$$

$$\tilde{W} = \left\{ (Y, \tilde{u}) \in (-\mathbb{R}_+^{d \times n} \cap \tilde{K}^+) \times \tilde{K}_M^+ \setminus \{0\} : \tilde{u} \in \left(-\sum_{j=1}^l \sum_{h=1}^{n_j} Y_h^{1,j}, \dots, -\sum_{j=1}^l \sum_{h=1}^{n_j} Y_h^{d,j} \right) + \tilde{M}^\perp \right\} \quad (24)$$

such that for any $X \in \mathbb{R}^{d \times n}$,

$$\tilde{q}(X) = \bigcap_{(Y, \tilde{u}) \in \tilde{W}} \{-\alpha(Y, \tilde{u}) + S_{(Y, \tilde{u})}(X \wedge_{\tilde{K}} 0)\}. \quad (25)$$

5. Proofs of Main Results

Proof of Lemma 2. the proof of Lemma 2 is straightforward from Remark 3.

Proof of Proposition 1. if $Y \notin -\mathbb{R}_+^{d \times n} \cap (K^+ 1_n)$, there exists an $\bar{X} \in \mathbb{R}^{d \times n} \cap (K 1_n)$ such that $\bar{X}^{\text{tr}} Y > 0$. Using the definition of

For any $\tilde{Z} \subseteq \mathbb{R}^{d \times n}$, the $Q_M^{t,+}$ -valued indicator function $I_{\tilde{Z}} : \mathbb{R}^{d \times n} \rightarrow Q_M^{t,+}$ is defined as

$$I_{\tilde{Z}}(X) := \begin{cases} \text{cl} \tilde{K}_M^-, & X \in \tilde{Z}, \\ \emptyset, & X \notin \tilde{Z}. \end{cases} \quad (19)$$

The conjugate of $Q_M^{t,+}$ -valued indicator function $I_{\tilde{Z}}$ is

$$-(I_{\tilde{Z}})^*(Y, \tilde{u}) := \text{cl} \bigcup_{X \in \tilde{Z}} S_{(Y, \tilde{u})}(-X). \quad (20)$$

Assume that \tilde{q} is a regulator-based risk statistic. For any $\tilde{z} \in \mathbb{R}_+^{d \times n}$, $X \in \mathbb{R}^{d \times n}$,

$$\tilde{q}(X - \tilde{z}) \supseteq \tilde{q}(X) + \tilde{z}, \quad (21)$$

which also implies

$$\tilde{q}(X + \tilde{z}) \subseteq \tilde{q}(X) - \tilde{z}. \quad (22)$$

Next, we state the dual representations of regulator-based risk statistics.

Proposition 2. Let $\tilde{q} : \mathbb{R}^{d \times n} \rightarrow Q_M^{t,+}$ be a proper closed convex regulator-based risk statistic with $\tilde{u} \in \{(-\sum_{j=1}^l \sum_{h=1}^{n_j} Y_h^{1,j}, \dots, -\sum_{j=1}^l \sum_{h=1}^{n_j} Y_h^{d,j}) + \tilde{M}^\perp\} \cap \tilde{K}_M^+ \setminus \{0\}$. Then,

$$-\tilde{q}^*(Y, \tilde{u}) = \begin{cases} \text{cl} \bigcup_{X \in \mathbb{R}^{d \times n}} S_{(Y, \tilde{u})}(-X), & Y \in -\mathbb{R}_+^{d \times n} \cap (\tilde{K}^+), \\ \tilde{M}, & \text{elsewhere.} \end{cases} \quad (23)$$

Theorem 2. If $\tilde{q} : \mathbb{R}^{d \times n} \rightarrow Q_M^{t,+}$ is a proper closed convex regulator-based risk statistic, then there is a $-\alpha : (-\mathbb{R}_+^{d \times n} \cap \tilde{K}^+) \times \tilde{K}_M^+ \setminus \{0\} \rightarrow Q_M^{t,+}$, that is not identically \tilde{M} of the set

$S_{(Y, \tilde{u})}$, we have $S_{(Y, \tilde{u})}(-t\bar{X}) = \{z \in M : -t\bar{X}^{\text{tr}} Y \leq \tilde{u}^{\text{tr}} z\}$ for $t > 0$. Therefore,

$$\text{cl} \bigcup_{X \in \mathbb{R}^{d \times n}} S_{(Y, \tilde{u})}(-X) \supseteq \bigcup_{t > 0} S_{(Y, \tilde{u})}(-t\bar{X}) = M. \quad (26)$$

The last equality is due to $-t\bar{X}^{\text{tr}} Y \rightarrow -\infty$ when $t \rightarrow +\infty$. Using the definition of $S_{(Y, \tilde{u})}$, we conclude that $\text{cl} \bigcup_{X \in \mathbb{R}^{d \times n}} S_{(Y, \tilde{u})}(-X) \subseteq M$. Hence,

$$\text{cl} \bigcup_{X \in \mathbb{R}^{d \times n}} S_{(Y, \tilde{u})}(-X) = M, \quad Y \notin -\mathbb{R}_+^{d \times n} \cap (K^+ 1_n). \quad (27)$$

It is easy to check that for any $X \in \mathbb{R}^{d \times n}$ and $v \in M$,

$$\begin{aligned} S_{(Y,u)}(-X - v1_n) &= \{z \in M : -X^{\text{tr}}Y \leq u^{\text{tr}}z + Y^{\text{tr}}(v1_n)\}, \\ &= \{z - v \in M : -X^{\text{tr}}Y \leq u^{\text{tr}}(z - v) + (Y + u1_n)^{\text{tr}}(v1_n)\} + v, \\ &= \{z \in M : -X^{\text{tr}}Y \leq u^{\text{tr}}z + (Y + u1_n)^{\text{tr}}(v1_n)\} + v, \end{aligned} \quad (28)$$

when $(-\sum_{j=1}^l \sum_{h=1}^{n_j} Y_h^{1,j}, \dots, -\sum_{j=1}^l \sum_{h=1}^{n_j} Y_h^{d,j}) + u \in M^\perp$, and we have $S_{(Y,u)}(-X - v1_n) = S_{(Y,u)}(-X) + v$. However, $u \notin ((-\sum_{j=1}^l \sum_{h=1}^{n_j} Y_h^{1,j}, \dots, -\sum_{j=1}^l \sum_{h=1}^{n_j} Y_h^{d,j}) + M^\perp)$. Therefore, $(-\sum_{j=1}^l \sum_{h=1}^{n_j} Y_h^{1,j}, \dots, -\sum_{j=1}^l \sum_{h=1}^{n_j} Y_h^{d,j}) + u \notin M^\perp$, and we can find $v \in M$ such that for any $z \in M$,

$$-X^{\text{tr}}Y \leq u^{\text{tr}}z + (Y + u1_n)^{\text{tr}}(v1_n). \quad (29)$$

Therefore, we have

$$z + v \in S_{(Y,u)}(-X - v1_n). \quad (30)$$

Therefore,

$$\bigcup_{z,v \in M} (z + v) \subset \bigcup_{v \in M} S_{(Y,u)}(-X - v1_n). \quad (31)$$

Therefore,

$$M \subset \bigcup_{v \in M} S_{(Y,u)}(-X - v1_n). \quad (32)$$

From the definition of $S_{(Y,u)}$, the inverse inclusion is always true. So, we conclude that

$$M = \bigcup_{v \in M} S_{(Y,u)}(-X - v1_n). \quad (33)$$

It is also easy to check that

$$\begin{aligned} -\varrho^*(Y, u) &= \text{cl} \bigcup_{X \in \mathbb{R}^{d \times n}, v \in M} (\varrho(X + v1_n) + S_{(Y,u)}(-X - v1_n)), \\ &= \text{cl} \bigcup_{X \in \mathbb{R}^{d \times n}, v \in M} (\varrho(X + v1_n) + M), \\ &= M, \end{aligned} \quad (34)$$

where the last equality comes from the fact that M is a linear space and $\varrho(X) \subseteq M$. We now derive that $-\varrho^*(Y, u) = \text{cl} \bigcup_{X \in \mathbb{R}^{d \times n}} S_{(Y,u)}(-X)$. In this context, from $-\varrho^*(Y, u) = \text{cl} \bigcup_{X \in \mathbb{R}^{d \times n}} (\varrho(X) + S_{(Y,u)}(-X))$, we derive it in two cases.

Case 1. When $X \wedge_{K1_n} 0 = 0$, using the definition, we have $\varrho(X) = \varrho(0) \ni 0$. Hence,

$$\text{cl} \bigcup_{X \in \mathbb{R}^{d \times n}} (\varrho(X) + S_{(Y,u)}(-X)) \stackrel{\text{cl} \bigcup_{X \in \mathbb{R}^{d \times n}} S_{(Y,u)}(-X)}{=} \text{cl} \bigcup_{X \in \mathbb{R}^{d \times n}} S_{(Y,u)}(-X). \quad (35)$$

Case 2. When $X \wedge_{K1_n} 0 = X$, we can always find an $\alpha \in K_M$ such that $\alpha \in \varrho(X)$. Then,

$$\varrho(X) + S_{(Y,u)}(-X) \supseteq \alpha + S_{(Y,u)}(-X) = S_{(Y,u)}(-X - \alpha 1_n) = S_{(Y,u)}(-\beta), \quad (36)$$

where $\beta = X + \alpha 1_n$. It is relatively simple to check that $\beta \in \mathbb{R}^{d \times n}$. Therefore,

$$\text{cl} \bigcup_{X \in \mathbb{R}^{d \times n}} (\varrho(X) + S_{(Y,u)}(-X)) \supseteq \text{cl} \bigcup_{z \in \mathbb{R}^{d \times n}} S_{(Y,u)}(-z), \quad (37)$$

that is,

$$-\varrho^*(Y, u) \supseteq \text{cl} \bigcup_{X \in \mathbb{R}^{d \times n}} S_{(Y,u)}(-X). \quad (38)$$

Consequently, we have

$$-\varrho^*(Y, u) \supseteq \text{cl} \bigcup_{X \in \mathbb{R}^{d \times n}} S_{(Y,u)}(-X). \quad (39)$$

We now need only to derive that $-\varrho^*(Y, u) \subseteq \text{cl} \bigcup_{X \in \mathbb{R}^{d \times n}} S_{(Y,u)}(-X)$. In fact, for any $z \in \varrho(X)$ and $X \in \mathbb{R}^{d \times n}$, $X + z1_n \in \mathbb{R}^{d \times n}$. Therefore,

$$\begin{aligned} \text{cl} \bigcup_{X \in \mathbb{R}^{d \times n}} S_{(Y,u)}(-X) &= \text{cl} \bigcup_{X \in \mathbb{R}^{d \times n}} S_{(Y,u)}(-X) \supseteq S_{(Y,u)}(-X - z1_n) \\ &= S_{(Y,u)}(-X) + z. \end{aligned} \quad (40)$$

Using the arbitrariness of z , we have

$$\varrho(X) + S_{(Y,u)}(-X) \subseteq \text{cl} \bigcup_{X \in \mathbb{R}^{d \times n}} S_{(Y,u)}(-X). \quad (41)$$

Therefore,

$$-\varrho^*(Y, u) \subseteq \text{cl} \bigcup_{X \in \mathbb{R}^{d \times n}} S_{(Y,u)}(-X). \quad (42)$$

Proof of Theorem 1. the proof is straightforward from Lemma 1 and Proposition 1.

Data Availability

No data and code were generated or used during the study.

Disclosure

This manuscript has been released as a preprint at arXiv: 1904.08829v4.

Conflicts of Interest

The authors declare no conflicts of interest.

Acknowledgments

This work was supported by funds from Education Department of Guangdong (2019KQNCX156).

References

- [1] C. C. Heyde, S. G. Kou, and X. H. Peng, *What is a Good External Risk Measure: Bridging the Gaps between Robustness, Subadditivity, and Insurance Risk Measures*, Columbia University, New York City, NY, USA, 2007.
- [2] S. Kou, X. Peng, and C. C. Heyde, "External risk measures and basel accords," *Mathematics of Operations Research*, vol. 38, no. 3, pp. 393–417, 2013.
- [3] S. Ahmed, D. Filipović, and G. Svindland, "A note on natural risk statistics," *Operations Research Letters*, vol. 36, no. 6, pp. 662–664, 2008.
- [4] D. Tian and L. Jiang, "Quasiconvex risk statistics with scenario analysis," *Mathematics and Financial Economics*, vol. 9, no. 2, pp. 111–121, 2015.
- [5] D. Tian and X. Suo, "A note on convex risk statistic," *Operations Research Letters*, vol. 40, no. 6, pp. 551–553, 2012.
- [6] E. Jouini, M. Meddeb, and N. Touzi, "Vector-valued coherent risk measures," *Finance Stoch*, vol. 8, no. 4, pp. 531–552, 2004.
- [7] C. Ararat, A. H. Hamel, and B. Rudloff, "Set-valued shortfall and divergence risk measures," 2017, <https://arxiv.org/abs/1405.4905>.
- [8] W. Farkas, P. Koch-Medina, and C. Munari, "Measuring risk with multiple eligible assets," *Mathematics and Financial Economics*, vol. 9, no. 1, pp. 3–27, 2015.
- [9] A. H. Hamel, "A duality theory for set-valued functions i: fenchel conjugation theory," *Set-Valued and Variational Analysis*, vol. 17, no. 2, pp. 153–182, 2009.
- [10] A. H. Hamel and F. Heyde, "Duality for set-valued measures of risk," *SIAM Journal on Financial Mathematics*, vol. 1, no. 1, pp. 66–95, 2010.
- [11] A. H. Hamel, F. Heyde, and B. Rudloff, "Set-valued risk measures for conical market models," *Mathematics and Financial Economics*, vol. 5, no. 1, pp. 1–28, 2011.
- [12] A. H. Hamel, B. Rudloff, and M. Yankova, "Set-valued average value at risk and its computation," *Mathematics and Financial Economics*, vol. 7, no. 2, pp. 229–246, 2013.
- [13] C. C. A. Labuschagne and T. M. Offwood-Le Roux, "Representations of set-valued risk measures defined on the \mathbb{R}^n -tensor product of banach lattices," *Positivity*, vol. 18, no. 3, pp. 619–639, 2014.
- [14] I. Molchanov and I. Cascos, "Multivariate risk measures: a constructive approach based on selections," *Mathematical Finance*, vol. 26, no. 4, pp. 867–900, 2016.
- [15] Y. Chen, F. Sun, and Y. Hu, "Coherent and convex loss-based risk measures for portfolio vectors," *Positivity*, vol. 22, no. 1, pp. 399–414, 2018.
- [16] R. Cont, R. Deguest, and X. D. He, "Loss-based risk measures," *Statistics & Risk Modeling*, vol. 30, no. 2, pp. 133–167, 2013.
- [17] F. Sun, Y. Chen, and Y. Hu, "Set-valued loss-based risk measures," *Positivity*, vol. 22, no. 3, pp. 859–871, 2018.
- [18] Y. Chen and Y. Hu, "Set-valued risk statistics with scenario analysis," *Statistics & Probability Letters*, vol. 131, pp. 25–37, 2017.
- [19] J.-B. Liu, C. Wang, S. Wang, and B. Wei, "Zagreb indices and multiplicative zagreb indices of eulerian graphs," *Bulletin of the Malaysian Mathematical Sciences Society*, vol. 42, no. 1, pp. 67–78, 2019.
- [20] J. Liu, J. Zhao, J. Min, and J. Cao, "On the hosoya index of graphs formed by a fractal graph," *Fractals-Complex Geometry Patterns and Scaling in Nature and Society*, vol. 27, no. 8, pp. 19–35, 2019.
- [21] J.-B. Liu, J. Zhao, H. He, and Z. Shao, "Valency-based topological descriptors and structural property of the generalized sierpiński networks," *Journal of Statistical Physics*, vol. 177, no. 6, pp. 1131–1147, 2019.
- [22] H. Föllmer and A. Schied, *Stochastic Finance: An Introduction in Discrete Time*, Walter de Gruyter Berlin, Berlin, Germany, Third edition, 2011.
- [23] N. El Karoui and C. Ravanelli, "Cash subadditive risk measures and interest rate ambiguity," *Mathematical Finance*, vol. 19, no. 4, pp. 561–590, 2009.
- [24] F. Sun and Y. Hu, "Set-valued cash sub-additive risk measures," *Probability in the Engineering and Information Sciences*, vol. 33, no. 2, pp. 241–257, 2019.

Research Article

A Mathematical Model for Calculating the “Brittleness-Ductility” Drop Coefficient of Sandstone in Mining Zones

Guodong Shi,^{1,2} Baoquan Cheng ,^{1,2} and An Li^{1,2}

¹School of Civil Engineering, Anhui Jianzhu University, Hefei, Anhui 230601, China

²National-Local Joint Engineering Laboratory of Structural Health Monitoring and Disaster Prevention Technology, Hefei, Anhui 230601, China

Correspondence should be addressed to Baoquan Cheng; curtis_ch@163.com

Received 25 April 2020; Accepted 21 May 2020; Published 8 July 2020

Guest Editor: Shaohui Wang

Copyright © 2020 Guodong Shi et al. This is an open access article distributed under the Creative Commons Attribution License, which permits unrestricted use, distribution, and reproduction in any medium, provided the original work is properly cited.

Sandstone is different from pure brittle rocks such as marble and granite. Its brittleness weakens and then increases with increasing confining pressure. This paper establishes a calculation model of the “brittleness-ductility” energy drop coefficient that characterizes the whole process of sandstone failure from the perspective of energy. The obtained result was compared with the result of traditional calculation model. The results show that the established model is more consistent with the experimental phenomenon and can describe the whole process of sandstone failure more precisely at a macro level. Moreover, the model is more practical since it avoids the tedious integration calculation process. The model and tests have extended the applicable range and applied rock types of the energy drop coefficient and enriched the knowledge system of elastoplastic mechanics. At the same time, they carry important significance for environmental restoration and geological disaster prevention and control in sedimentary rock mining zones, which can promote the sustainable development of related industries in the mining zones.

1. Introduction

China is one of the few countries in the world which use coal as the main energy source. Its coal output has exceeded one-third of the world's total [1, 2]. Resource destruction, environmental damage, and industrial accidents related to coal production are very prominent [3, 4]. In particular, during the construction of new mine and waste mine backfilling, frequent mine collapses threaten the safety of workers and their property, seriously damage the ecological environment and groundwater quality, or even trigger more severe geographic hazards [5–7]. The sustainable development of coal resources and related industries is facing challenges. Sandstone is the most common surrounding rock in coal mines in China [8]. Frequent landslides are often closely related to the failure of sandstone. Therefore, a deep understanding of its failure mechanism can ensure the safety of mine construction and exploitation [9, 10]. In addition, it helps to prevent the negative impact of mining industry on the surroundings and has far-reaching significance for

environmental restoration and disaster prevention and control in the mining zones.

In traditional elastic-plastic mechanics theory, the stress-strain curve is usually used to describe the process of material deformation and failure, thus establishing the constitutive model of the material and the corresponding strength theory. For linear elastic materials, this method can be used to reflect mechanical characteristics of the material accurately. However, due to the anisotropy and inhomogeneity of the material, the stress-strain relationship of the rock is distinctively nonlinear [5, 11]. As a result, for stones it is difficult to establish a reasonable strength criterion based on the stress-strain curve alone. In fact, the loading process is a process of exerting external energy input. Before its stress reaches the peak, the rock absorbs and stores the external energy taking advantage of its own elastoplasticity to maintain a stable state [12–14]. At the peak intensity, the rock is in a critical state of high energy instability [15]. With the continuous input of external energy, the rock finally releases the stored energy and loses its stability, and the

stress quickly drops to the residual strength [16, 17]. This means that the rock deformation and failure process is an irreversible process of energy release and dissipation. The ultimate failure of the rock is actually a sudden change in the process of energy dissipation. Therefore, to describe the deformation and failure process of rocks from the perspective of energy can better reflect the physical nature of its failure mechanism.

In recent years, many researchers have studied the failure mechanism of brittle rocks based on energy analysis. Zhao et al. demonstrated in detail that the failure mode and energy dissipation process change with the anisotropy, inhomogeneity, and stress state of rocks and proposed the principle of minimum energy for dynamic failure based on the findings [18]. Yang et al. performed triaxial tests on marble rocks by using servo machines to investigate the deformation and failure process of rock samples and their energy characteristics [19]. Su et al. studied the patterns of plastic deformation, uniaxial compression strength, average modulus, energy dissipation, and failure characteristics of rock samples during triaxial tests [20]. Xie et al. proposed failure criterion for stratified rock based on distortion energy and generalized volume expansion potential energy, which was in good agreement with the results of the double pressure tests. The established rock damage evolution equation was verified through experiments, and related parameter indicators were determined [21]. Zuo et al. analyzed the shortcomings of the stress drop coefficient of brittle rocks and put forward a new characterization parameter of rock failure—the energy drop coefficient [22]. Song et al. analyzed the applicability and limitation of the energy drop coefficient and further considered the proportion of releasable elastic energy in the total energy before peak stage to present an improved energy drop coefficient [23]. Liu et al. presented valency-based topological indices of chemical networks [24, 25]. By using some real world data, we performed certain comparative testing to investigate the performance of almost all well-known valency-based indices. In light of this, many scholars have rediscovered the changes in the stress-strain state of rocks under external loads from an energy perspective and analyzed the energy transfer and conversion in the process of rock deformation and failure in order to establish the strength theory using energy changes as failure criteria, which is a more realistic description of the failure mechanism of rocks.

However, there are some strong limitations in current researches. First, these energy threshold values reflecting rock strength usually only take into account the energy evolution characteristics of the postpeak stage and thus cannot reflect the entire process of rock deformation and failure [26]. Second, the calculation of the traditional energy drop coefficient of rocks mainly requires a large number of integral calculations, which is cumbersome and inconvenient. Third, previous studies have used magmatic rocks and metamorphic rocks such as marble and granite as research objects more, and few studies have been conducted on sedimentary rocks such as sandstone [27]. To address these research gaps, this paper obtains the whole stress-strain curves of sandstones under different confining pressures based on triaxial tests and proposes a calculation model of

“brittleness-ductility” energy drop coefficient applicable to sandstone. Based on established model, the mechanism of sandstone failure is explained and influence of confining pressure on energy release and dissipation during rock deformation and failure is discussed.

The calculation model of “brittleness-ductility” energy drop coefficient proposed in this paper can truly describe the no-linear deformation and failure process of sandstone. The model fully considers the two states before and after the failure of the rock samples and further enriches the physical meaning of the traditional stress-strain curve in describing material failure mechanism, which can provide references for studies on other rocks with similar mechanical characteristics. In addition, the model can efficiently calculate and characterize the mechanical properties of sandstone and provide a reference for the comprehensive development and management of mining zones, which is beneficial to the environmental restoration and geological disaster prevention in these zones. The study can promote the sustainable development of related industries as well.

2. Energy Drop Coefficient of Rock Based on Triaxial Tests

The rock triaxial test is essentially a simulation of the mechanical properties of the rock in a three-way compression environment. Compared to conventional test methods, triaxial tests are more intricately advanced tests, which can obtain compressive strength, shear strength, elastic modulus, Poisson’s ratio, cohesion, and internal friction angle under different confining pressures (or depths) of rocks. Without changing the ambient temperature, the heat exchange between the test piece and the environment can be ignored. Therefore, the energy conversion of the test piece during the tests is mainly mechanical energy exchange with the test machine.

In the test, the work done by the testing machine for the axial compression of test piece is

$$W_z = \int F_z dz = \frac{\pi d^2}{4} h \int \sigma_z d\varepsilon_z, \quad (1)$$

where W_z is the work done by the testing machine for the axial compression, and it is also the total energy input into the test piece. F_z is the axial equivalent effect, d the diameter of the test piece, h the height, σ_z the axial stress, and ε_z the axial strain.

For the triaxial test with constant confining pressure, the work done by the test piece in the circumferential direction on the hydraulic oil is

$$W_r = \int F_r dr = \frac{\pi d^2}{2} h \int \sigma_r d\varepsilon_r, \quad (2)$$

where F_r is the circumferential equivalent force, d the diameter of the test piece, h the height, σ_r the radial stress, and ε_r the radial strain.

From (1) and (2), it can be known that the actual mechanical energy absorbed by the sample W is the difference between W_z and W_r :

$$W = W_z - W_r. \quad (3)$$

It is difficult to measure W_z and W_r directly from the tests. In fact, the deformation and failure of the pieces essentially result from the continuous dissipation and rapid release of energy. It means that part of the input mechanical energy is released as elastic energy and the other converted to dissipative energy. Therefore, the actual mechanical energy W absorbed when the test piece reaches the peak pressure can be divided into dissipative energy and releasable elastic energy:

$$W = W_p + W_e, \quad (4)$$

where W_p is dissipative energy and W_e is releasable elastic energy. Figure 1 shows the typical stress-strain curve of rocks. W_p corresponds to the area enclosed by the OAB and W_e corresponds to the area enclosed by the BAC.

When the axial strain is ε , according to (1)–(4), the energy absorbed by the test piece is $W(\varepsilon)$ and is equal to the work performed by the test machine on the test piece:

$$W = W_p W(\varepsilon) = V \left[\int_0^\varepsilon \sigma_z d\varepsilon_z - 2 \int_0^{\mu\varepsilon} \sigma_r d\varepsilon_r \right] + W_e, \quad (5)$$

where V is the volume of the test piece; σ_z , ε_z , σ_r , and ε_r are integral variables; ε is the axial strain; and μ is the Poisson's ratio.

When the confining pressure remains unchanged, W_e , the elastic energy released by the rock, can be measured by the unloading test. If the elastic modulus of the test piece is E ,

$$W_e(\varepsilon) = V \left(\frac{1}{2} \sigma_z \varepsilon^e + \mu \varepsilon^e \sigma_r \right), \quad (6)$$

where E is the elastic modulus of the test piece and ε^e is recoverable elastic strain:

$$\varepsilon^e = \frac{1}{E} (\sigma_z - 2\mu\sigma_r). \quad (7)$$

From (6) and (7), it can be known that

$$W_e(\varepsilon) = \frac{V}{E} (\sigma_z - 2\mu\sigma_r) \left(\frac{1}{2} \sigma_z + \mu\sigma_r \right). \quad (8)$$

When the stress drops from point A to point D, the change of releasable elastic energy is

$$\Delta W_e(\varepsilon) = W_e(\varepsilon_A) - W_e(\varepsilon_D) = V \left(\frac{\sigma_A^2}{2E_A} - \frac{\sigma_D^2}{2E_D} \right). \quad (9)$$

According to (5), when confining pressure is constant, the stress drops from point A to point D, and the externally input mechanical energy ΔW is

$$\Delta W = V \left[\int_{\varepsilon_A}^{\varepsilon_D} \sigma_z d\varepsilon_z - 2\mu(\varepsilon_D - \varepsilon_A)\sigma_r \right]. \quad (10)$$

The ratio of ΔW and ΔW_e is used to characterize the energy change during the stress drop when the test piece fails. This ratio H is defined as the energy drop coefficient of the rocks:

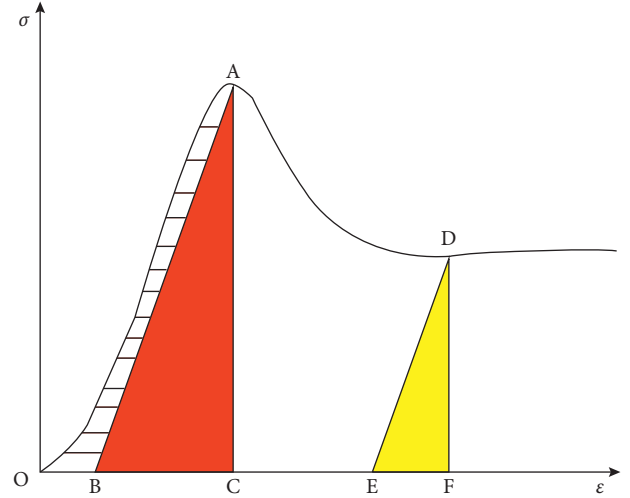


FIGURE 1: Typical stress-strain curve of rocks.

$$H = \frac{\Delta W}{\Delta W_e} = \frac{\int_{\varepsilon_A}^{\varepsilon_D} \sigma_z d\varepsilon_z - 2\mu(\varepsilon_D - \varepsilon_A)\sigma_r}{(\sigma_A^2/2E_A) - (\sigma_D^2/2E_D)}, \quad (11)$$

where σ_A and ε_A are the peak stress and peak strain, respectively; μ is the Poisson's ratio; σ_D and ε_D are the residual stress and residual strain, respectively; and E_A is the elastic modulus of unloading at the peak.

The energy drop coefficient H expresses a proportional relationship between the mechanical energy input into the rock and the releasable elastic energy. It demonstrates that the deformation and failure of the brittle rock are the result of energy dissipation and sudden release. H has a certain correlation with the brittle failure of the rock. The larger the H value, the less obvious the brittle stress drop of the rock, and the stronger the ductility. Therefore, the energy drop coefficient H has important reference value for characterizing the degree of rock brittle failure.

3. Triaxial Test of Sandstone

In order to find out the failure mechanism of sandstone from the energy perspective and to obtain the relevant mechanical parameters, triaxial tests were performed on typical sandstone samples collected from the Hulusu Mine in Inner Mongolia, China. The test pieces were standard cylinder with a diameter of 50 mm and a height of 100 mm.

The tests were conducted on the MTS816 rock test system. The device is shown in Figure 2. This system uses a three-axis servo press, which can record the stress-strain curve and thus obtain the data of test piece including residual stress and permanent deformation. The 1-hydraulic system was adopted to load hydraulic oil into 6-triaxial cavity to simulate and control the confining pressure stress state of the test piece. The 3-control system was used to control and operate 9-loading device and to load the test piece [28]. The test adopted the force-displacement mixed control loading system. In the initial stage, different confining pressures were applied to the test piece through force control. Confining pressures were applied to predetermined

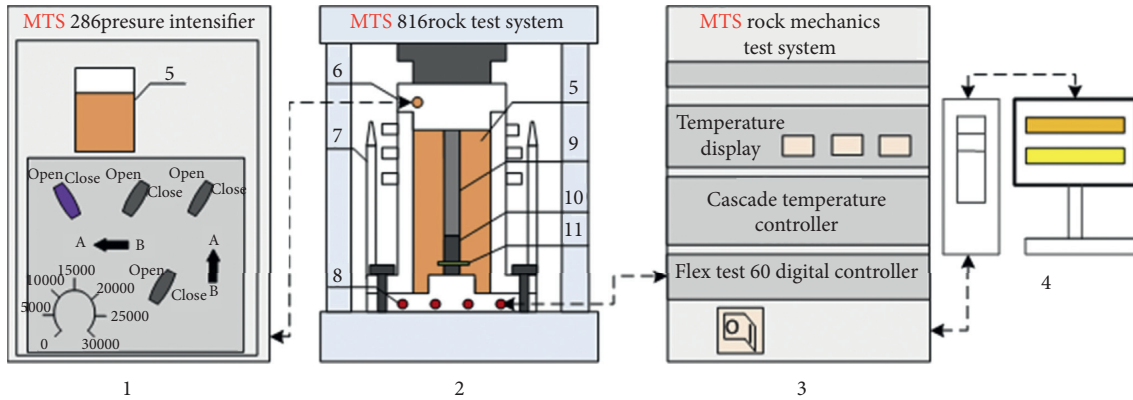


FIGURE 2: MTS816 test system. (1) Hydraulic control system. (2) Triaxial experimental platform. (3) Control cabinet. (4) Data acquisition system. (5) Hydraulic oil. (6) Confining pressure cavity. (7) Positioning rod. (8) Sensor interface. (9) Loading device. (10) Specimen. (11) Ring extensometer.

values according to different hydrostatic pressures, which were 4, 6, 8, and 10 MPa. Each confining pressure was applied to five distinct rock test pieces repeatedly. When the confining pressures reached the preset value, the displacement control was used instead, and the axial loading was performed at a loading speed of 0.01 mm/s until the test piece failed.

Figure 3 shows the triaxial compressive stress-strain curves of sandstone samples under confining pressures of 4, 6, 8, and 10 MPa, respectively.

It can be learned that before the stress reached its peak value, it increased linearly with the rise of the strain, showing relatively good elasticity. When it reached its peak value, the sample went through buckling failure rapidly, exhibiting obvious brittle stress drop phenomenon. After that, an obvious yielding plateau appeared, which indicated that the sandstones still maintained some ductility under the confining pressures. The carrying capacity increased with the rise of confining pressure. As the confining pressure increased from 4 MPa to 8 MPa, the magnitude of stress drop also gradually went up. However, as the confining pressure continued to do so, the magnitude dropped instead. It showed that as the confining pressure increased, the sandstone exhibited the mechanical characteristics of changing from brittleness to ductility and then back to brittleness. This is inconsistent with the characteristic that the brittleness of granite and marble gradually declines with increasing confining pressure. It is difficult to reveal its failure mechanism using traditional energy drop coefficient.

Figure 4 shows the characteristics of the failure surfaces of sandstone samples under different confining pressures. It can be concluded that the samples under different confining pressures had only one shear failure surface which changed along with different confining pressures. Under 4 MPa, the macroscopic fracture surfaces of the samples were cracked from the middle, indicating that they had already been completely destroyed under the low confining pressure state, exhibiting distinguished brittleness. As the confining pressure increased, the angles θ_1 – θ_3 between the normal direction of the sandstone failure surface and the horizontal line gradually increased, and the macroscopic failure

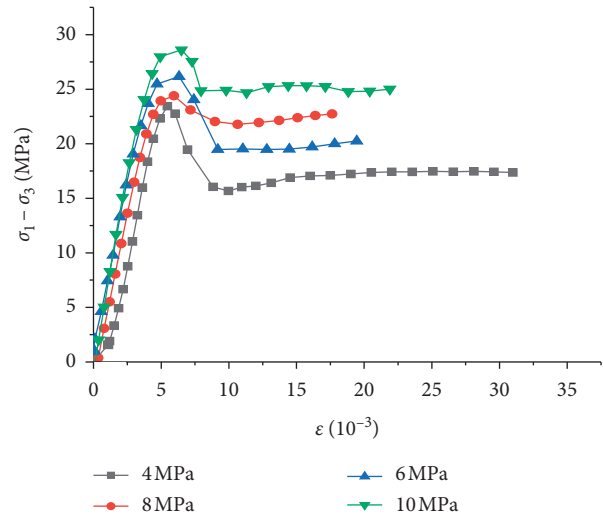


FIGURE 3: Stress-strain curves of sandstone samples under different confining pressures.

surfaces became more and more flat, indicating enhanced ductility of the samples. At 10 MPa, the fracture surfaces corresponding to the confining pressures were obviously different from those under other confining pressure states, with θ_3 being the largest angle. The surrounding areas were severely fragmented, showing more severe brittleness. This again showed that sandstone has different mechanical properties from marble and granite rocks.

4. “Brittleness-Ductility” Energy Drop Coefficient

The traditional calculation method of energy drop coefficient has been well applied in rocks such as marble and granite. Based on the results of triaxial tests, it can be concluded that sandstone exhibits transformative characteristics of “brittleness-ductility-brittleness” with increasing confining pressure, which makes it difficult for the energy drop coefficient of brittle rock to fully reflect the deformation and failure process of sandstone. In addition, the traditional

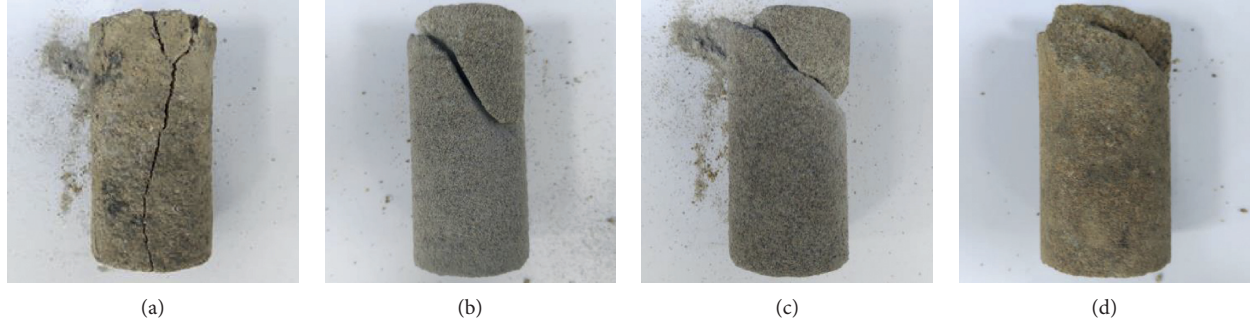


FIGURE 4: Failure surfaces of sandstone samples under different confining pressures. (a) 4 MPa, (b) 6 MPa, (c) 8 MPa, (d) 10 MPa.

TABLE 1: Calculation of sandstone energy drop coefficients.

Pressures (MPa)	$S_{BAC}-S_{EDF}$ (10^3 J/m ³)	$2\mu(\varepsilon_D - \varepsilon_A)\sigma_r$ (10^3 J/m ³)	$\int_{\varepsilon_A}^{\varepsilon_D} \sigma_z d\varepsilon_z$ (10^3 J/m ³)	S_{CADF} (10^3 J/m)	H	He	θ
4	29.95	6.19	100.8	60.82	0.314	1.82	—
6	24.78	9.29	110.9	70.06	0.377	2.45	56°
8	10.07	12.38	118.8	71.30	0.381	5.85	75°
10	15.56	15.48	165.5	82.36	0.393	4.30	82°

method requires the calculation of a large number of integrals. The complicated and cumbersome process is difficult to be applied in practical engineering. Therefore, it is necessary to establish a calculation model that is easy to use and more suitable for sandstone failure characteristics.

When the sandstone enters the ductility stage, the elastic modulus E_A corresponding to the unloading at the peak in (11) cannot accurately reflect the stress-strain relationship of the samples at this time. When the effect of sandstone damage and defect is not considered, the rock damage factor D is considered to be 0. At this time, according to $E_D = (1 - D)E_A$, it can be replaced by the elastic modulus E_D corresponding to the residual strength unloading. In Figure 1, AB and DE stand for E_A and E_D , respectively. In order to simplify the calculation method, the area of the stress-strain curve is used to represent the energy involved in the deformation and failure process.

$\int_{\varepsilon_A}^{\varepsilon_D} \sigma_z d\varepsilon_z$ is represented by the area of trapezoid ACDF, which represents the external input of the mechanical energy into the samples after the peak point A. The releasable elastic energy of the samples can be expressed by the difference between SBAC (in red in Figure 1) and SEDF (in yellow in Figure 1). This value represents the relative magnitudes of the ductility and brittleness of the samples—the smaller the value, the higher the ductility. $2\mu(\varepsilon_D - \varepsilon_A)\sigma_r$ is represented by W_C . Therefore, the energy drop coefficient calculation model for sandstone can be expressed as

$$He = \frac{S_{CADF} - W_C}{S_{vac} - S_{EDF}}. \quad (12)$$

He can better characterize the relative magnitudes of the ductility and brittleness of the rock, which is called the “brittleness-ductility” energy drop coefficient. The coefficient calculation model is more in line with the energy change of the actual failure process of sandstone and can

better reflect the energy conversion of the collapse of sandstone at various depths.

5. Comparison Analysis

The residual energy, elastic energy, work done by rock samples to hydraulic oil under different confining pressures, and the drop coefficients H and He obtained by the two different calculation models according to (11) and (12) are calculated, and the results are shown in Table 1.

It can be learned that as the confining pressure increases, the mechanical energy input of the samples gradually increases; the energy loss caused by the work performed by the samples to the hydraulic oil rises as well; and the releasable elastic energy gradually decreases. The traditional energy drop coefficient of sandstone H and the “brittle-ductility” energy drop coefficient He have basically the same variation tendency. As the confining pressure increases, the energy drop coefficient also gradually goes up, the brittleness exhibited by the failure of the samples weakens, and the ductility enhances. This proves the correctness of the “brittle-ductility” energy drop coefficient. However, when the confining pressure rises to 10 MPa, the H value of the sandstone continues to increase while He drops. The results show that when the confining pressure rises to 10 MPa, the brittleness enhances. This demonstrates that the calculation of the coefficient He proposed in this paper can better characterize the relative magnitudes of the ductility and brittleness of the rock and thus reflect the physical failure mechanism of sandstone failure more precisely.

6. Conclusions and Recommendations

6.1. Conclusions. This paper establishes a calculation model of the “brittle-ductility” energy drop coefficient that characterizes the whole process of sandstone deformation and

failure from the perspective of energy based on the stress-strain curves of sandstone samples obtained from triaxial tests. It also discusses the influence of confining pressure on energy drop during sandstone failure. The following conclusions are reached:

- (1) According to the fracture surface characteristics and stress-strain curves of the sandstone obtained from the triaxial tests, as the confining pressure increases, the brittleness of the failed samples diminishes and then gradually enhances after reaching the peak. This is different from other rocks such as granite and marble.
- (2) Compared with traditional energy drop coefficients, the calculation model of “brittleness-ductility” energy drop coefficient proposed in this paper can accurately describe the whole process of sandstone deformation and failure from an energy perspective. At the same time, the improved model is easy to adopt because it can avoid tedious integration calculations.

This model extends the applicable rock types of the energy drop coefficient and enriches the knowledge system of elastoplastic mechanics. At the same time, a deep understanding of the sandstone failure mechanism can ensure the safety of construction and exploitation in mining zones while reducing the environmental damage. It is of great significance for environmental restoration and geological disaster prevention.

6.2. Recommendations. For future research, the following research directions deserve scholarly attention:

This paper only establishes a calculation model for the “brittle-ductility” energy drop coefficient suitable for characterizing the sandstone failure mechanism but does not explain why the tendency of sandstone brittleness to change with confining pressure differs from that of marble and granite. Future research can try to explain the mechanism from the composition and mechanical properties.

According to the genesis, rocks can be divided into magmatic rocks, sedimentary rocks, and metamorphic rocks. In addition to sandstone, there are other common surrounding rocks like mudstone in the mining zones. Difference between different types of rocks is actually very large. The new calculation model proved to be feasible and efficient to describe the failure of sandstone. However, whether it can suit other types of rocks is still unclear. Therefore, more samples could be collected to study the energy drop law. In light of this, the strength thresholds of rocks can be identified by applying correspondent energy coefficients according to rock types to better guide the safe and sustainable production in the mining zones.

Data Availability

The data are generated from experiments.

Conflicts of Interest

The authors declare no conflicts of interest.

Acknowledgments

The authors thank Anhui University for providing laboratory and test system for this study. This research was funded by National Nature Science Foundation of China (51774007), Nature Science Research Project of Anhui Education Department (KJ2018JD03), and AHJZU-Anhui Huali Construction Co. Ltd. Joint Research Project (HYB20190152).

References

- [1] K. Xie, W. Li, and W. Zhao, “Coal chemical industry and its sustainable development in China,” *Energy*, vol. 35, no. 11, pp. 4349–4355, 2010.
- [2] M. Cheng and B. Liu, “Analysis on the influence of China’s energy consumption on economic growth,” *Sustainability*, vol. 11, no. 14, p. 3982, 2019.
- [3] J. L. Hao, B. Q. Cheng, W. S. Lu et al., “Carbon emission reduction in prefabrication construction during materialization stage: a BIM-based life-cycle assessment approach,” *Science of Total Environment*, vol. 723, Article ID 131870, 2020.
- [4] Q. Wang, X. Song, and Y. Liu, “China’s coal consumption in a globalizing world: insights from multi-regional input-output and structural decomposition analysis,” *Science of the Total Environment*, vol. 711, Article ID 134790, 2019.
- [5] B. Q. Cheng, J. W. Li, and W. Y. Vivian, “A case study on large deformation failure mechanism and control techniques for soft rock roadways in tectonic stress areas,” *Sustainability*, vol. 11, no. 13, p. 3510, 2019.
- [6] H. Li, B. Zhang, H. Bai et al., “Surface water resource protection in a mining process under varying strata thickness—A case study of buliangou coal mine, China,” *Sustainability*, vol. 10, no. 12, p. 4634, 2018.
- [7] S. G. Lei and Z. F. Bian, “Research progress on the environment impacts from underground coal mining in arid western area of China,” *Acta Ecologica Sinica*, vol. 34, no. 11, pp. 2837–2843, 2014.
- [8] Q. Liu, X. Li, and M. Hassall, “Evolutionary game analysis and stability control scenarios of coal mine safety inspection system in China based on system dynamics,” *Safety Science*, vol. 80, pp. 13–22, 2015.
- [9] J. Liu, H. Liu, X.-L. Yao, and Y. Liu, “Evaluating the sustainability impact of consolidation policy in China’s coal mining industry: a data envelopment analysis,” *Journal of Cleaner Production*, vol. 112, pp. 2969–2976, 2016.
- [10] M. He, L. R. e Sousa, T. Miranda, and G. Zhu, “Rockburst laboratory tests database - application of data mining techniques,” *Engineering Geology*, vol. 185, pp. 116–130, 2015.
- [11] Y. Kang, Q. Liu, G. Gong, and H. Wang, “Application of a combined support system to the weak floor reinforcement in deep underground coal mine,” *International Journal of Rock Mechanics and Mining Sciences*, vol. 71, pp. 143–150, 2014.
- [12] H. Xie and D. Rui, “Progress in strength theory of rocks based on fracture mechanics and damage mechanics,” *Progress in Nature*, vol. 14, no. 10, pp. 1086–1092, 2004.
- [13] D. A. Beck and B. H. G. Brady, “Evaluation and application of controlling parameters for seismic events in hard-rock

- mines,” *International Journal of Rock Mechanics and Mining Sciences*, vol. 39, no. 5, pp. 633–642, 2002.
- [14] Z. You, H. Fu, and J. Shi, “Design-by-analogy: a characteristic tree method for geotechnical engineering,” *Automation in Construction*, vol. 87, pp. 13–21, 2018.
- [15] M. Q. You and A. Z. Hua, “Fracture of rock specimen and decrement of bearing capacity in uniaxial compression,” *Chinese Journal of Rock Mechanics and Engineering*, vol. 17, no. 3, pp. 292–296, 1998.
- [16] J. J. Zhang and B. J. Fu, “Rock burst and its criteria and control,” *Chinese Journal of Rock Mechanics and Engineering*, vol. 27, no. 10, pp. 2034–2042, 2008.
- [17] R. Altindag, “Correlation of specific energy with rock brittleness concepts on rock cutting,” *Journal of South African Institute of Mining and Metallurgy*, vol. 103, no. 3, pp. 163–171, 2003.
- [18] Y. S. Zhao, Z. C. Feng, and Z. J. Wan, “Least energy principle of dynamical failure of rock mass,” *Chinese Journal of Rock Mechanics and Engineering*, vol. 22, no. 11, pp. 1781–1783, 2003.
- [19] S. Q. Yang, W. Y. Xu, and C. D. Su, “Study on the deformation failure and energy properties of marble specimen under triaxial,” *Engineering Mechanics*, vol. 24, no. 1, pp. 136–142, 2007.
- [20] C. Su and Z. H. Zhang, “Analysis of plastic deformation and energy property of marble under pseudo-triaxial,” *Chinese Journal of Rock Mechanics and Engineering*, vol. 27, no. 2, pp. 273–280, 2008.
- [21] H. P. Xie and Y. Ju, “Energy mechanism of deformation and failure of rock masses,” *Chinese Journal of Rock Mechanics and Engineering*, vol. 27, no. 9, pp. 1729–1740, 2008.
- [22] J. Zuo and Y. Huang, “Study of energy-drop coefficient of brittle rock failure,” *Rock and Soil Mechanics*, vol. 35, no. 2, pp. 321–327, 2014.
- [23] H. Song and J. P. Zuo, “Revised energy drop coefficient based on energy characteristics in the whole process of rock failure,” *Rock and Soil Mechanics*, vol. 40, no. 1, pp. 1–9, 2019.
- [24] J.-B. Liu, J. Zhao, H. He, and Z. Shao, “Valency-based topological descriptors and structural property of the generalized sierpiński networks,” *Journal of Statistical Physics*, vol. 177, no. 6, pp. 1131–1147, 2019.
- [25] J. B. Liu, J. Zhao, and Z. Cai, “On the generalized adjacency, Laplacian and sign less Laplacian spectra of the weighted edge corona networks,” *Physica A*, vol. 540, Article ID 123073, 2020.
- [26] Z. H. Wang, L. Li, Y. X. Zhang et al., “Reinforcement model considering slip effect,” *Engineering Structures*, vol. 198, Article ID 109493, 2019.
- [27] Z. H. Wang, L. Li, and Y. X. Zhang, “Bond-slip model considering freeze-thaw damage effect of concrete and its application,” *Engineering Structures*, vol. 201, Article ID 109831, 2019.
- [28] W. Ma, Y. Li, K. W. Ding et al., “Mechanical properties of new dry-type beam-column bolt connection Joint,” *Sustainability*, vol. 11, Article ID 134790, no. 12, 3348 pages, 2019.

Research Article

Analytical and Approximate Solutions of a Novel Nervous Stomach Mathematical Model

Yolanda Guerrero Sánchez ¹, Zulqurnain Sabir,² Hatira Günerhan,³
and Haci Mehmet Baskonus ⁴

¹Universidad de Murcia, Departamento de Anatomía y Psicobiología, 30001 Murcia, Spain

²Department of Mathematics and Statistics, Hazara University, Mansehra, Pakistan

³Mathematics Department, Faculty of Education, Kafkas University, Kars, Turkey

⁴Faculty of Education, Harran University, Sanliurfa, Turkey

Correspondence should be addressed to Yolanda Guerrero Sánchez; yolanda.guerreros@um.es

Received 20 April 2020; Accepted 8 June 2020; Published 4 July 2020

Academic Editor: Jia-Bao Liu

Copyright © 2020 Yolanda Guerrero Sánchez et al. This is an open access article distributed under the Creative Commons Attribution License, which permits unrestricted use, distribution, and reproduction in any medium, provided the original work is properly cited.

The stomach is usually considered as a hollow muscular sac, which initiates the second segment of digestion. It is the most sophisticated endocrine structure having unique biochemistry, physiology, microbiology, and immunology. The pivotal aim of the present study is to propose the nonlinear mathematical model of the nervous stomach system based on three compartments namely, tension (T), food (F), and medicine (M). The detailed description of each compartment is provided along with the mathematical form and different rates/factors, such as sleep factor, food rate, tension rate, medicine term, and death rate. The solution of the designed model is presented numerically by using the well-known differential transformation technique. The behavior of the obtained solution has been captured with respect to time as well as presentations of the numerical simulations.

1. Introduction

The importance of every organ in the human body has its individual value, and without having any organ or having a weak organ, the human body feels troubles. In human body, every organ is linked to other organs, e.g., eye has a connection with the nose and the nose is connected with the ear. The stomach is one of the most significant organ in the human body that has connection with many organs. The stomach's role is maintaining the health of every living being, and it magnetizes the attention of the research community [1]. The earliest Greeks observed the gastric contents with the bitter nature. In the sixteenth century, both van Helmont [2] and Paracelsus [3] believed that an acid is present in the stomach, and it is essential for digestion. Consequent observations by Spallanzani [4] and De Reaumur [5] recommended the 'solvent' properties of

digestive juice on the tissue of animals. Prout [6] did not publish his work related to the gastric acid secretion nature until 1823. Beaumont [7] provided the first interpretations on his patient with gastric fistula, and that was published by Alexis St Martin three years later in the second decade of the eighteenth century. These observations based on meticulous were discussed for about a hundred years, and the core of his investigations was gastric ingestion in a human body with the stress effects.

At the beginning of the twentieth century, the control of gastric secretion was discovered by ablation of the coeliac axis and vagotomy as therapeutic interferences. This highlighted the complex nature of the gastric secretion's control, and it led to a quick increase in interest and the work of Laidlaw and Dale on histamine [8], which led to the serious discovery by Popielski on the effects of histamine on gastric secretion [9]. Bayliss and Starling presented the secretin [10]

and Edkins dissertation on gastrin [11]. These discoveries helped us to understand the gastric disease leading to dramatic advances in the pharmacological organization of peptic ulcer disease with the finding of the H₂-receptor antagonists by Sir James Black in the seventh decade of the nineteenth century [12]. Marshall and Warren discussed the acid-related disease in the twentieth century until the groundbreaking discovery of *Helicobacter pylori* in 1983 [13]. The stomach was reflected microbiologically sterile, although Jaworski [14] has presented many observations of several bacterial populations in gastric juice.

The present study aims to illustrate the mathematical form of the nervous stomach model and the performance of the numerical solutions by considering all the parameters of the designed model via the differential transformation (DT) method. The considered novel technique is proposed by Zhou [15], called as a differential transformation method, with the help of the Taylor series expansion in the 8th decade of the nineteenth century. The designed nervous stomach model is obtained by considering the three compartments namely, tension (T), food (F), and medicine (M). Furthermore, for more convince, this model is named as TFM. Three different cases based on the designed model have been taken, and the numerical results are drawn using the DT method. The obtained results show the efficiency of the proposed scheme.

Some salient geographies of the designed TFM model are given as follows:

- (i) The nervous stomach model is presented effectively by using the three compartments namely tension (T), food (F), and medicine (M)
- (ii) The detailed descriptions of all the compartments of the TFM model are provided along with different factors and rates
- (iii) The nonlinear system of ordinary differential equations is obtained by using the three above-mentioned compartments
- (iv) The numerical solutions of the designed TFM model are performed by using the DT numerical scheme

The rest of the paper is organized as follows. Section 2 describes the structure of the designed model. Section 3 presents the procedure of the DT scheme and essential results. Section 4 shows the detailed results and discussion of the TFM model. Conclusions along with future research directions are presented in the last section of the paper.

2. Structure of the TFM Model

The mathematical form of the nervous stomach model will be presented along with the three compartments namely tension (T), food (F), and medicine (M). The details of each compartment are presented as follows:

- (i) $T(t)$: the indications caused by mental health are always present in the mind. There are various physical symptoms; one of them that may target anybody and cause anxiousness and stress is a nervous stomach. The effect of a nervous stomach is extremely inconvenient for the human body and may forbid them from completing the projects due to stress. It is one of the main reasons to disturb the stomach at time t .
- (ii) $F(t)$: the oily, spicy, and crispy food are the main factors to disturb the stomach. Especially, anybody who does not frequently consume spicy foods and has no patience may cause havoc on the digestive system. The presence of some compounds in spicy food such as capsaicin is not broken down in digestion and can annoy the lining of the intestines or stomach. This is the main cause to disturb the stomach at time t .
- (iii) $M(t)$: the overuse of medicine is also an important factor to disturb the stomach. Most medicines are used to recover different disease that can also disturb the stomach. These medicines straightly upset the stomach, and through this way, the stomach feels irregularity and gets affected badly.

The mathematical form of the TFM model is presented in the nonlinear system of ordinary differential equations, which is achieved by using the three above compartments namely, tension, food, and medicine at time t , and it is defined as

$$\begin{cases} \frac{dT(t)}{dt} = -\alpha F(t)T(t) - \beta, & T(0) = I_1, \\ \frac{dF(t)}{dt} = \delta T(t) + \gamma M(t)F(t), & F(0) = I_2, \\ \frac{dM(t)}{dt} = -\delta T(t) + \beta F(t)M(t) - d, & M(0) = I_3, \end{cases} \quad (1)$$

where α represents the quantity of food, and negative sign indicates the lesser quantity of food. β shows the sleep factor, δ is used for the tension rate, γ indicates the recovery term, and d shows the death rate. Moreover, I_1 , I_2 , and I_3 are the initial conditions for all compartments of the TFM model. For the verification of the designed model, three different cases are considered based on the designed TFM model and solved by using a well-known DT method. The historical DT method is famous to solve the singular, nonlinear, and fractional differential models [16–23].

3. Differential Transformation Scheme

Taking one-dimensional arbitrary function $w(x)$ in Taylor's series about a point $x = x_0$, we have

$$W(k) = \frac{1}{k!} \left[\frac{d^k w(x)}{dx^k} \right]_{x=0}. \tag{2}$$

The original function is $w(x)$ in the above equation (2), whereas the transformed function is $W(k)$, which is also known as T-function. The differential transform of the inverse of $W(k)$ is provided as follows:

$$w(x) = \sum_{k=0}^{\infty} Y(k)(x-x_0)^k \equiv D^{-1}W(k). \tag{3}$$

Using equations (2) and (3) and taking $x_0 = 0$, the obtained form is written as follows:

$$w(x) = \sum_{k=0}^{\infty} \frac{x^k}{k!} \left[\frac{d^k w(x)}{dx^k} \right]_{x=0}. \tag{4}$$

Equation (4) gives the concepts of differential transform derived from the expansion of the Taylor series, and this scheme is not applied for symbolical evaluation of the derivatives. Moreover, comparative derivatives are found by using an iterative procedure. In the present study, the lower case letter is used to show the original function, and upper case letter is used to represent the transformed function. From the definition of the above two equations, one can easily prove that the transformed functions have the basic mathematics values provided in Table 1.

In real applications, $w(x)$ is obtained by a finite series, and equation (3) can be described as follows:

$$w(x) = \sum_{k=0}^m x^k W(k). \tag{5}$$

Equation (5) shows that $w(x) = \sum_{k=m+1}^{\infty} x^k W(k)$ is very small and can be neglected. In fact, it denotes the error. Hence, in the present study, m is used for the convergence of natural frequency.

Theorem 1. If $w(x) = a(x)b(x)$, then $W(k) = A(k) \otimes B(k) = \sum_{l=0}^k A(l)B(k-l)$ (here \otimes denotes the convolution):

$$\begin{aligned} w(x) &= \sum_{k=0}^{\infty} A(k)(x-x_0)^k \times \sum_{k=0}^{\infty} B(k)(x-x_0)^k \\ &= (A(0) + A(1)(x-x_0) + A(2)(x-x_0)^2 + \dots) \\ &\quad \times (B(0) + B(1)(x-x_0) + B(2)(x-x_0)^2 + \dots) \\ &= A(0)B(0) + (A(0)B(1) + A(1)B(0))(x-x_0) \\ &\quad + (A(0)B(2) + A(1)B(1) + A(2)B(0))(x-x_0)^2 + \dots \\ &= \sum_{k=0}^{\infty} \sum_{l=0}^k A(l)B(k-l)(x-x_0)^k. \end{aligned} \tag{6}$$

By using equation (3), we can write

$$W(k) = \sum_{l=0}^k A(l)B(k-l). \tag{7}$$

Theorem 2. If $w(x) = x^m$, then $W(k) = \delta(k-m) = \begin{cases} 1, & k=m, \\ 0, & k \neq m, \end{cases}$ where $\delta(k) = \begin{cases} 1, & k=0, \\ 0, & k \neq 0, \end{cases}$.

Proof. By using equation (2), we have

$$W(k) = \frac{1}{k!} \left. \frac{\partial (x^m)}{\partial x^k} \right|_{t=0} = \begin{cases} \frac{1}{k!} \frac{\partial^k (x^k)}{\partial x^k} = \frac{k!}{k!} = 1, & k=m, \\ \frac{1}{k!} \frac{\partial^k (x^m)}{\partial x^k} = 0, & k \neq m. \end{cases} \tag{8}$$

□

Theorem 3. If $w(t) = u_1(t)u_2(t)u_3(t) \dots u_{n-1}(t)u_n(t)$, then $W(k) = \sum_{l_{n-1}=0}^k \sum_{l_{n-2}=0}^{l_{n-1}} \dots \sum_{l_2=0}^{l_3} \sum_{l_1=0}^{l_2} U_1(l_1)U_2(l_2-l_1) \dots U_{n-1}(l_{n-1}-l_{n-2})U_n(k-l_{n-1})$.

Proof. By using equation (2), we have

TABLE 1: The essential operations of the unique and transformed functions of the DT method.

Unique function	Transformed function
$w(x) = a(x) \pm b(x)$	$W(k) = A(k) \pm B(k)$
$w(x) = ca(x)$	$W(k) = cA(k)$
$w(x) = (d^m a(x))/dx^m$	$W(k) = (k+1) + (k+2) \cdots (k+m) \cdot A(k+m)$
$w(x) = a(cx)$	$W(k) = c^k \cdot A(k)$
$w(x) = a(x/c)$	$W(k) = A(k)/c^k$
$w(x) = (d^m/dx^m)a(cx)$	$W(k) = (k+1) + (k+2) \cdots (k+m) \cdot c^{k+m} \cdot A(k+m)$
$w(x) = e^{x+c}$	$W(k) = e^c/k!$

$$\begin{aligned}
W(0) &= \frac{1}{0!} [u_1(t)u_2(t) \cdots u_{n-1}(t)u_n(t)]_{t=t_0} \\
&= U_1(0)U_2(0) \cdots U_{n-1}(0)U_n(0), \\
W(1) &= \frac{1}{1!} \frac{\partial}{\partial t} [u_1(t)u_2(t) \cdots u_{n-1}(t)u_n(t)]_{t=t_0} \\
&= [u_1'(t)u_2(t) \cdots u_{n-1}(t)u_n(t) + u_1(t)u_2'(t) \cdots u_{n-1}(t)u_n(t) + \cdots + u_1(t)u_2(t) \cdots u_{n-1}'(t)u_n(t) \\
&\quad + u_1(t)u_2(t) \cdots u_{n-1}(t)u_n'(t)]_{t=t_0} \\
&= U_1(1)U_2(0) \cdots U_{n-1}(0)U_n(0) + U_1(0)U_2(1) \cdots U_{n-1}(0)U_n(0) + \cdots + U_1(0)U_2(0) \cdots U_{n-1}(1)U_n(0) \\
&\quad + U_1(0)U_2(0) \cdots U_{n-1}(0)U_n(1), \\
W(2) &= U_1(1)U_2(1)U_3(0) \cdots U_{n-2}(0)U_{n-1}(0)U_n(0) + U_1(0)U_2(1)U_3(1) \cdots U_{n-2}(0)U_{n-1}(0)U_n(0) + \cdots \\
&\quad + U_1(0)U_2(0)U_3(0) \cdots U_{n-2}(1)U_{n-1}(1)U_n(0) + U_1(0)U_2(0)U_3(0) \cdots U_{n-2}(0)U_{n-1}(1)U_n(1).
\end{aligned} \tag{9}$$

We have

$$\begin{aligned}
W(k) &= \sum_{l_{n-1}=0}^k \sum_{l_{n-2}=0}^{l_{n-1}} \cdots \sum_{l_2=0}^{l_3} \sum_{l_1=0}^{l_2} U_1(l_1)U_2(l_2 - l_1) \\
&\quad \cdots U_{n-1}(l_{n-1} - l_{n-2})U_n(k - l_{n-1}). \quad \square
\end{aligned} \tag{10}$$

Theorem 4. If $w(t) = \sin(\omega t + \alpha)$, then $W(h) = (w^h/h!) \sin((h\pi/2) + \alpha)$.

Proof. By using equation (2), we have

$$\begin{aligned}
k = 1: W(1) &= \frac{1}{1!} \frac{\partial \sin(\omega t + \alpha)}{\partial t} \Big|_{t=0} = \frac{1}{1!} \omega \cos(\omega t + \alpha) \Big|_{t=0} = \frac{1}{1!} \omega \sin\left(\left(\frac{\pi}{2} + \alpha\right) + \omega t\right) \Big|_{t=0} = \frac{1}{1!} \omega \sin\left(\frac{\pi}{2} + \alpha\right), \\
k = 2: W(2) &= \frac{1}{2!} \frac{\partial^2 \sin(\omega t + \alpha)}{\partial t^2} \Big|_{t=0} = \frac{1}{2!} \omega^2 \cos\left(\frac{\pi}{2} + (\alpha + \omega t)\right) \Big|_{t=0} = \frac{1}{2!} \omega^2 \sin\left(\frac{\pi}{2} + \left(\alpha + \frac{\pi}{2}\right) + \omega t\right) \Big|_{t=0} \\
&= \frac{1}{2!} \omega^2 \sin\left(\frac{2\pi}{2} + \alpha + \omega t\right) \Big|_{t=0} = \frac{1}{2!} \omega^2 \sin\left(\frac{2\pi}{2} + \alpha\right), \dots, \\
k = h: W(h) &= \frac{1}{h!} \frac{\partial^h \sin(\omega t + \alpha)}{\partial t^h} \Big|_{t=0} = \frac{\omega^h}{h!} \sin\left(\frac{h\pi}{2} + \alpha + \omega t\right) \Big|_{t=0} = \frac{\omega^h}{h!} \sin\left(\frac{h\pi}{2} + \alpha\right).
\end{aligned} \tag{11}$$

We have

$$W(h) = \frac{\omega^h}{h!} \sin\left(\frac{h\pi}{2} + \alpha\right). \tag{12} \quad \square$$

4. Results and Discussion

In this section, three different cases will be discussed by taking different values of the sleep factor, food rate, tension rate, medicine term, and death rate. These cases numerically

TABLE 2: Numerical investigations of the $T(t)$, $F(t)$, and $M(t)$ for Case 1 of the TFM model.

t	Case 1		
	$T(t)$	$F(t)$	$M(t)$
0	0.9999	0.0001	0
0.4	0.62731	0.67810	-0.15969
0.8	-0.11289	0.87141	-0.11953
1.2	-0.76466	0.47571	-0.02268
1.6	-0.91441	-0.24356	0.05255
2	-0.31034	-0.72335	-0.03076
2.4	1.51535	0.02444	-0.60601
2.8	6.55651	4.51745	-2.65702
3.2	21.0587	20.2326	-8.88120
3.6	60.1631	67.4145	-25.7791
4	154.959	194.152	-67.3316
4.4	362.400	502.590	-160.990
4.8	778.453	1191.23	-356.890
5.2	1554.77	2619.56	-741.403
5.6	2919.070	5402.54	-1456.36
6	5199.07	10544	-2725.58
6.4	8850.05	19620	-4890.42
6.8	14485.3	35024.04	-8456.69
7.2	22909.1	60288.6	-14155.1
7.6	35150.96	100501	-23018.7
8	52500.24	162828	-36478.7
8.4	76539.23	257180	-56485
8.8	109172.9	397018	-85652.1
9.2	152653.1	600357	-127437
9.6	209593.8	890972	-186354
10	282975.4	129984	-0.15969

TABLE 3: Numerical investigations of the obtained results $T(t)$, $F(t)$, and $M(t)$ for Case 2 of the TFM model.

t	Case 2		
	$T(t)$	$F(t)$	$M(t)$
0	0.9999	0.0001	0
0.4	0.99711	0.38141	-0.16480
0.8	1.14519	0.76386	-0.35228
1.2	1.45588	1.20409	-0.58365
1.6	1.96438	1.76437	-0.88481
2	2.73324	2.52173	-1.28985
2.4	3.85971	3.57910	-1.84568
2.8	5.48681	5.08036	-2.61842
3.2	7.81825	7.23190	-3.70235
3.6	11.1371	10.3342	-5.23279
4	15.8281	14.8287	-7.40436
4.4	22.4012	21.3651	-10.4966
4.8	31.5164	30.8991	-14.9098
5.2	44.0051	44.8295	-21.2138
5.6	60.8851	65.1876	-30.2136
6	83.3624	94.8947	-43.0369
6.4	112.814	138.106	-61.2485
6.8	150.746	200.663	-86.9977
7.2	198.705	290.679	-123.207
7.6	258.144	419.281	-173.809
8	330.223	601.560	-244.041
8.4	415.518	857.740	-340.814
8.8	513.633	1214.63	-473.152
9.2	622.681	1707.40	-652.739
9.6	738.609	2381.74	-894.564
10	854.345	3296.39	-1217.70

TABLE 4: Numerical investigations of the $T(t)$, $F(t)$, and $M(t)$ for Case 3 of the TFM model.

t	Case 3		
	$T(t)$	$F(t)$	$M(t)$
0	0.9999	0.0001	0
0.4	0.91790	0.08917	-0.32811
0.8	0.83361	0.11440	-0.67315
1.2	0.74964	0.07287	-1.03638
1.6	0.66871	-0.03826	-1.41954
2	0.59367	-0.22183	-1.82483
2.4	0.52746	-0.48070	-2.25501
2.8	0.47317	-0.81787	-2.71345
3.2	0.43398	-1.23656	-3.20419
3.6	0.41323	-1.74029	-3.73200
4	0.41439	-2.33302	-4.30250
4.4	0.44111	-3.01924	-4.92219
4.8	0.49724	-3.80409	-5.59860
5.2	0.58682	-4.69357	-6.34036
5.6	0.71418	-5.69461	-7.15737
6	0.88394	-6.81533	-8.06087
6.4	1.10104	-8.06514	-9.06365
6.8	1.37086	-9.45503	-10.1801
7.2	1.69921	-10.9977	-11.4268
7.6	2.09246	-12.7080	-12.8221
8	2.55758	-14.6031	-14.3867
8.4	3.10226	-16.7024	-16.1442
8.8	3.73500	-19.0287	-18.1207
9.2	4.46520	-21.6077	-20.3460
9.6	5.30331	-24.4691	-22.8529
10	6.26098	-27.6464	-25.6788

solve by using the DT method. The values are taken between 0 and 10 with the step size of 0.4. These cases based on the above system of equations are written as follows:

Case 1. Taking the values of $\alpha = 0.1$, $\beta = 0.2$, $\delta = 0.3$, $\gamma = 0.4$, $d = 0.5$, $I_1 = 0.9999$, $I_2 = 0.0001$, and $I_3 = 0$, model (1) takes the form as

$$\begin{cases} \frac{dT(t)}{dt} = -0.1F(t) - 0.2, & T(0) = 0.9999, \\ \frac{dF(t)}{dt} = 0.3T(t) + 0.4M(t), & F(0) = 0.0001, \\ \frac{dM(t)}{dt} = -0.3T(t) + 0.2M(t) - 0.5, & M(0) = 0. \end{cases} \quad (13)$$

The DT method is applied to solve the above model. By using the definitions of one-dimensional differential transformation and the corresponding transformation of equation (13), the obtained system becomes

$$\begin{cases} (k+1)T(k+1) = -0.1F(k) - 0.2\delta(k), & T(0) = 0.9999, \\ (k+1)F(k+1) = 0.3T(k) + 0.4M(k), & F(0) = 0.0001, \\ (k+1)M(k+1) = -0.3T(k) + 0.2M(k) - 0.5\delta(k), & M(0) = 0. \end{cases} \quad (14)$$

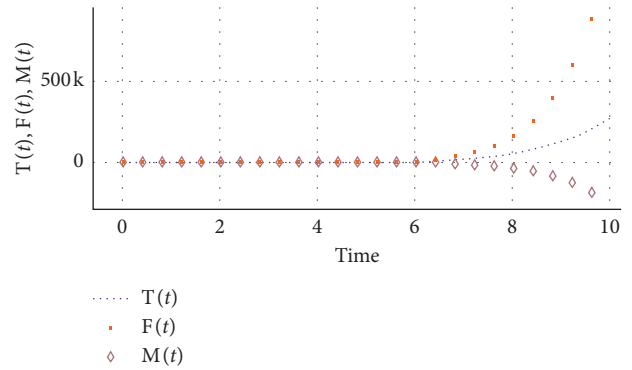


FIGURE 1: Nature of the $T(t)$, $F(t)$, and $M(t)$ for Case 1 of the TFM model.

Case 2. Taking the values of $\alpha = -1$, $\beta = 0.2$, $\delta = 1$, $\gamma = 0.4$, $d = 0.1$, $I_1 = 0.9999$, $I_2 = 0.0001$, and $I_3 = 0$, model (1) becomes

$$\begin{cases} \frac{dT(t)}{dt} = F(t) - 0.2, & T(0) = 0.9999, \\ \frac{dF(t)}{dt} = T(t) + 0.4M(t), & F(0) = 0.0001, \\ \frac{dM(t)}{dt} = -0.3T(t) + 0.2M(t) - 0.1, & M(0) = 0. \end{cases} \quad (15)$$

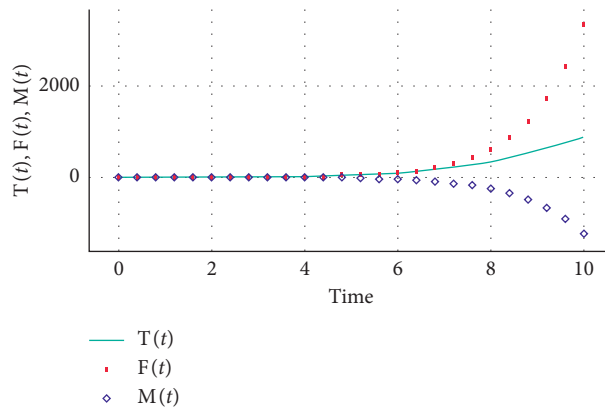


FIGURE 2: Behavior of the $T(t)$, $F(t)$, and $M(t)$ for Case 2 of the TFM model.

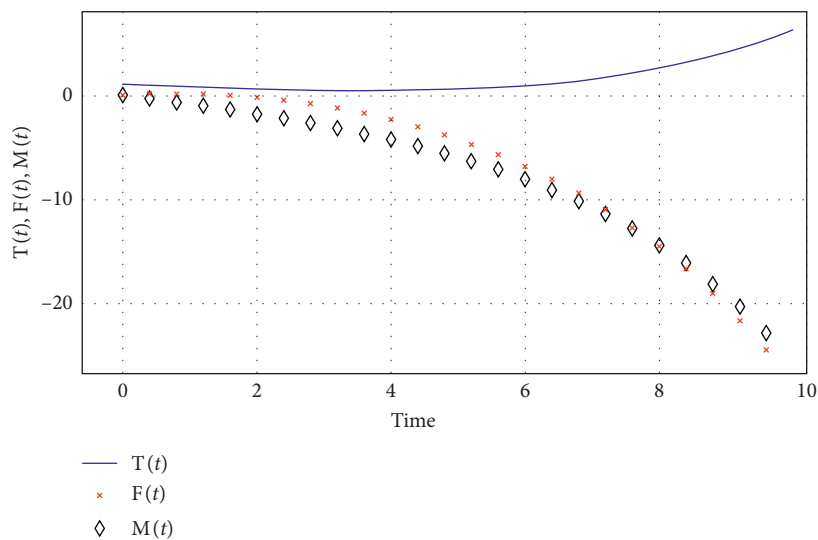


FIGURE 3: Behavior of the $T(t)$, $F(t)$, and $M(t)$ for Case 3 of the TFM model.

The DT method is applied to solve the above equation (15). By using the definitions of one-dimensional differential

transformation and the corresponding transformation of equation (15), the obtained system becomes

$$\begin{cases} (k+1)T(k+1) = F(k) - 0.2\delta(k), & T(0) = 0.9999, \\ (k+1)F(k+1) = T(k) + 0.4M(k), & F(0) = 0.0001, \\ (k+1)M(k+1) = -0.3T(k) + 0.2M(k) - 0.1\delta(k), & M(0) = 0. \end{cases} \quad (16)$$

Case 3. Taking the values of $\alpha = 2$, $\beta = 0.2$, $\delta = 2$, $\gamma = 0.4$, $d = 0.01$, $I_1 = 0.9999$, $I_2 = 0.0001$ and $I_3 = 0$, model (1) becomes

$$\begin{cases} \frac{dT(t)}{dt} = -2F(t) - 0.2, & T(0) = 0.9999, \\ \frac{dF(t)}{dt} = 2T(t) + 0.4M(t), & F(0) = 0.0001, \\ \frac{dM(t)}{dt} = -0.3T(t) + 0.2M(t) - 0.01, & M(0) = 0. \end{cases} \quad (17)$$

The DTM is applied to solve the above model. By using the definitions of one-dimensional differential transformation and the corresponding transformation of equation (17), the obtained system becomes

$$\begin{cases} (k+1)T(k+1) = -2F(k) - 0.2\delta(k), & T(0) = 0.9999, \\ (k+1)F(k+1) = 2T(k) + 0.4M(k), & F(0) = 0.0001, \\ (k+1)M(k+1) = -0.3T(k) + 0.2M(k) - 0.01\delta(k), & M(0) = 0. \end{cases} \quad (18)$$

Tables 2–4 show the different values of the $T(t)$, $F(t)$, and $M(t)$ in the interval $[0,10]$ with the step size of 0.4. The fixed initial values have been taken for all three cases. The

numerical experimentations have been achieved by using the DT method. The details of each compartment for all the cases are provided in Tables 2–4. In Table 3, it is seen that by increasing the time, increment is seen in factors $T(t)$ and $F(t)$, while decrement is noticed in the values of $M(t)$.

5. Conclusion

In the present study, a novel mathematical form of the nervous stomach model is introduced, which is based on three compartments namely tension, food, and medicine. The detail of each compartment is discussed and provided. The mathematical form of the TFM model is obtained in the form of three nonlinear differential equations, and numerical solutions have been tabulated and plotted in Tables 2–4 and Figures 1–3 by using a well-known differential transform scheme. The differential transformation scheme is recommended for all forms of differential equations due to the rapidity of its convergence and fewer computations. The considered method offers fast converging serial solutions, and furthermore, the accuracy of this solution can be improved by taking more terms in the solution. The differential transformation method is highly effective and produces approximate results of the model that have been investigated in this paper.

In the future, the novel nonlinear stomach model can be solved by using well-known artificial neural networks [24–33], and the differential transformation scheme can be applied by using fluid dynamics problems [34–36].

Data Availability

Our paper is not based on any data.

Conflicts of Interest

The authors declare that they have no conflicts of interest.

Acknowledgments

This work was partially supported by Ministerio de Ciencia, Innovacion y Universidades (grant number PGC2018-0971-B-100) and Fundacion Seneca de la Region de Murcia (grant no. 20783/PI/18).

References

- [1] I. M. Modlin, *From Prout to the Proton Pump*, Schnetztor-Verlag, Zeppelinstraße, Germany, 1995.
- [2] W. Pagel, *Joan Baptista Van Helmont: Reformer of Science and Medicine*, Cambridge University Press, England, UK, 2002.
- [3] N. Goodrick-Clarke, *Paracelsus*, vol. 1, North Atlantic Books, Berkeley, CA, USA, 1999.
- [4] L. Spallanzani, *Dissertazioni di Fisica animale e Vegetabile*, Vol. 2, Presso La Societa' Tipografica, Modena, Italy, 1780.
- [5] R. F. De Réaumur, "Observations sur la digestion des oiseaux," *Histoire de l'Académie Royale des Sciences*, vol. 266, p. 461, 1752.
- [6] W. Prout, III, *On the Nature of the Acid and Saline Matters Usually Existing in the Stomachs of Animals*, vol. 114, pp. 45–49, Philosophical Transactions of the Royal Society of London, London, UK, 1824.
- [7] W. Beaumont, "Further experiments on the case of Alexis san martin who was wounded in the stomach by a load of duck-shot: detailed in the recorder for January 1825," 1825.
- [8] H. H. Dale, "Comment on paper 23 in: adventures in physiology, a selection from the scientific publications of Sir Henry Hallett Dale," 1953.
- [9] L. Popielski, " β -imidazolyläthylamin und die Organextrakte," *Pflügers Archiv für die Gesamte Physiologie des Menschen und der Tiere*, vol. 178, no. 1, pp. 214–236, 1920.
- [10] W. M. Bayliss and E. Starling, "Preliminary communication on the causation of the so-called "peripheral reflex secretion" of the pancreas," *The Lancet*, vol. 159, no. 4099, p. 813, 1902.
- [11] J. S. Edkins, "The chemical mechanism of gastric secretion 1," *The Journal of Physiology*, vol. 34, no. 1-2, pp. 133–144, 1906.
- [12] J. W. Black, W. A. M. Duncan, C. J. Durant, C. R. Ganellin, and E. M. Parsons, "Definition and antagonism of histamine H₂-receptors," *Nature*, vol. 236, no. 5347, pp. 385–390, 1972.
- [13] J. R. Warren and B. Marshall, "Unidentified curved Bacilli on gastric epithelium in active chronic gastritis," *The Lancet*, vol. 321, no. 8336, pp. 1273–1275, 1983.
- [14] W. Jaworski, *Podręcznikchoróbżoladka (Handbook of Gastric Diseases)*, Wydawnictwa Dziel Lekarskich Polskich, Warsaw, Poland, 1899.
- [15] J. K. Zhou, *Differential Transformation and Its Applications for Electrical Circuits*, Huazhong University Press, Wuhan, China, 1986.
- [16] D. Arslan, "The comparison study of the hybrid method with RDTM for solving Rosenau–Hyman equation," *Applied Mathematics and Nonlinear Sciences*, vol. 5, no. 1, pp. 267–274, 2020.
- [17] H. Günerhan and E. Çelik, "Analytical and approximate solutions of fractional partial differential-algebraic equations," *Applied Mathematics and Nonlinear Sciences*, vol. 5, no. 1, pp. 109–120, 2020.
- [18] Z. Sabir, H. Günerhan, and J. L. Guirao, "On a new model based on third-order nonlinear multisingular functional differential equations," *Mathematical Problems in Engineering*, vol. 2020, Article ID 1683961, 9 pages, 2020.
- [19] M. Modanli and A. Akgül, "On solutions of fractional order telegraph partial differential equation by Crank–Nicholson finite difference method," *Applied Mathematics and Nonlinear Sciences*, vol. 5, no. 1, pp. 163–170, 2020.
- [20] E. İlhan and İ.O. Kıymaz, "A generalization of truncated M-fractional derivative and applications to fractional differential equations," *Applied Mathematics and Nonlinear Sciences*, vol. 5, no. 1, pp. 171–188, 2020.
- [21] M. S. M. Selvi and L. Rajendran, "Application of modified wavelet and homotopy perturbation methods to nonlinear oscillation problems," *Applied Mathematics and Nonlinear Sciences*, vol. 4, no. 2, pp. 351–364, 2019.
- [22] W. Adel and Z. Sabir, "Solving a new design of nonlinear second-order Lane–Emden pantograph delay differential model via Bernoulli collocation method," *The European Physical Journal Plus*, vol. 135, no. 6, p. 427, 2020.
- [23] D. Ziane, M. H. Cherif, C. Cattani, and K. Belghaba, "Yang-laplace decomposition method for nonlinear system of local fractional partial differential equations," *Applied Mathematics and Nonlinear Sciences*, vol. 4, no. 2, pp. 489–502, 2019.
- [24] Z. Sabir, M. A. Z. Raja, M. Umar, and M. Shoaib, "Design of neuro-swarmling-based heuristics to solve the third-order nonlinear multisingular Emden–Fowler equation," *The European Physical Journal Plus*, vol. 135, no. 6, p. 410, 2020.

- [25] Z. Sabir, F. Amin, D. Pohl, and J. L. Guirao, "Intelligence computing approach for solving second order system of the Emden–Fowler model," *Journal of Intelligent & Fuzzy Systems*, pp. 1–16, 2020.
- [26] Z. Sabir, H. A. Wahab, M. Umar, and F. Erdoğan, "Stochastic numerical approach for solving second order nonlinear singular functional differential equation," *Applied Mathematics and Computation*, vol. 363, Article ID 124605, 2019.
- [27] Z. Sabir, H. A. Wahab, M. Umar, M. G. Sakar, and M. A. Z. Raja, "Novel design of the Morlet wavelet neural network for solving second order Lane-Emden equation," *Mathematics and Computers in Simulation*, vol. 172, pp. 1–14, 2020.
- [28] M. Umar, Z. Sabir, and M. A. Z. Raja, "Intelligent computing for numerical treatment of nonlinear prey-predator models," *Applied Soft Computing*, vol. 80, pp. 506–524, 2019.
- [29] M. A. Z. Raja, M. Umar, Z. Sabir, J. A. Khan, and D. Baleanu, "A new stochastic computing paradigm for the dynamics of nonlinear singular heat conduction model of the human head," *The European Physical Journal Plus*, vol. 133, no. 9, p. 364, 2018.
- [30] Z. Sabir, M. A. Manzar, M. A. Z. Raja, M. Sheraz, and A. M. Wazwaz, "Neuro-heuristics for nonlinear singular Thomas-Fermi systems," *Applied Soft Computing*, vol. 65, pp. 152–169, 2018.
- [31] M. A. Z. Raja, J. Mehmood, Z. Sabir, A. K. Nasab, and M. A. Manzar, "Numerical solution of doubly singular nonlinear systems using neural networks-based integrated intelligent computing," *Neural Computing and Applications*, vol. 31, no. 3, pp. 793–812, 2019.
- [32] M. A. Z. Raja, Z. Sabir, N. Mehmood, E. S. Al-Aidarous, and J. A. Khan, "Design of stochastic solvers based on genetic algorithms for solving nonlinear equations," *Neural Computing and Applications*, vol. 26, no. 1, pp. 1–23, 2015.
- [33] Z. Sabir and M. A. Z. Raja, "Numeric treatment of nonlinear second order multipoint boundary value problems using ANN, Gas, and the sequential quadratic programming technique," *International Journal of Industrial Engineering Computations*, vol. 5, no. 3, pp. 431–442, 2014.
- [34] H. A. Wahab, Z. Zhiyu, M. Shoaib et al., "Numerical treatment for the three-dimensional Eyrin–Powell fluid flow over a stretching sheet with velocity slip and activation energy," *Advances in Mathematical Physics*, vol. 2019, Article ID 9860471, 12 pages, 2019.
- [35] Z. Sabir, R. Akhtar, Z. Zhiyu et al., "A computational analysis of two-phase Casson nanofluid passing a stretching sheet using chemical reactions and gyrotactic microorganisms," *Mathematical Problems in Engineering*, vol. 2019, Article ID 1490571, 12 pages, 2019.
- [36] M. Umar, Z. Sabir, A. Imran, A. Wahab, M. Shoaib, and M. Raja, "Three-dimensional flow of Casson nanofluid over a stretched sheet with chemical reactions, velocity slip, thermal radiation, and Brownian motion," *Thermal Science*, vol. 24, no. 5, pp. 2929–2939, 2020.